Research Topics

Lithospheric diversity: New perspective on structure, composition and evolution

Edited by
Weijia Sun, Erdinc Saygin, Zengxi Ge, Christian Sippl,
Chunquan Yu and Kazunori Yoshizawa

Published in
Frontiers in Earth Science

ISSN 1664-8714
ISBN 978-2-8325-2385-8
DOI 10.3389/978-2-8325-2385-8

About Frontiers

Frontiers is more than just an open access publisher of scholarly articles: it is a pioneering approach to the world of academia, radically improving the way scholarly research is managed. The grand vision of Frontiers is a world where all people have an equal opportunity to seek, share and generate knowledge. Frontiers provides immediate and permanent online open access to all its publications, but this alone is not enough to realize our grand goals.

Frontiers journal series

The Frontiers journal series is a multi-tier and interdisciplinary set of open-access, online journals, promising a paradigm shift from the current review, selection and dissemination processes in academic publishing. All Frontiers journals are driven by researchers for researchers; therefore, they constitute a service to the scholarly community. At the same time, the *Frontiers journal series* operates on a revolutionary invention, the tiered publishing system, initially addressing specific communities of scholars, and gradually climbing up to broader public understanding, thus serving the interests of the lay society, too.

Dedication to quality

Each Frontiers article is a landmark of the highest quality, thanks to genuinely collaborative interactions between authors and review editors, who include some of the world's best academicians. Research must be certified by peers before entering a stream of knowledge that may eventually reach the public - and shape society; therefore, Frontiers only applies the most rigorous and unbiased reviews. Frontiers revolutionizes research publishing by freely delivering the most outstanding research, evaluated with no bias from both the academic and social point of view. By applying the most advanced information technologies, Frontiers is catapulting scholarly publishing into a new generation.

What are Frontiers Research Topics?

Frontiers Research Topics are very popular trademarks of the *Frontiers journals series*: they are collections of at least ten articles, all centered on a particular subject. With their unique mix of varied contributions from Original Research to Review Articles, Frontiers Research Topics unify the most influential researchers, the latest key findings and historical advances in a hot research area.

Find out more on how to host your own Frontiers Research Topic or contribute to one as an author by contacting the Frontiers editorial office: frontiersin.org/about/contact

Lithospheric diversity: New perspective on structure, composition and evolution

Topic editors
Weijia Sun — Key Laboratory of Earth and Planetary Physics, Institute of Geology and Geophysics (CAS), China
Erdinc Saygin — Commonwealth Scientific and Industrial Research Organisation (CSIRO), Australia
Zengxi Ge — Peking University, China
Christian Sippl — Institute of Geophysics (ASCR), Czechia
Chunquan Yu — Southern University of Science and Technology, China
Kazunori Yoshizawa — Hokkaido University, Japan

Citation
Sun, W., Saygin, E., Ge, Z., Sippl, C., Yu, C., Yoshizawa, K., eds. (2023). *Lithospheric diversity: New perspective on structure, composition and evolution*. Lausanne: Frontiers Media SA. doi: 10.3389/978-2-8325-2385-8

Table of contents

frontiers in Earth Science

ORIGINAL RESEARCH
published: 08 February 2022
doi: 10.3389/feart.2022.838751

Crustal S-Wave Velocity Structure Beneath the Northwestern Bohemian Massif, Central Europe, Revealed by the Inversion of Multimodal Ambient Noise Dispersion Curves

Qingbo Ma[1,2], *Lei Pan*[2,3], *Jian-nan Wang*[2,3], *Zhentao Yang*[2,3] *and Xiaofei Chen*[2,3,4]*

[1]*School of Earth and Space Sciences, University of Science and Technology of China, Hefei, China,* [2]*Shenzhen Key Laboratory of Deep Offshore Oil and Gas Exploration Technology, Southern University of Science and Technology, Shenzhen, China,* [3]*Southern Marine Science and Engineering Guangdong Laboratory (Guangzhou), Guangzhou, China,* [4]*Department of Earth and Space Sciences, Southern University of Science and Technology, Shenzhen, China*

The northwestern Bohemian Massif and adjacent areas are a tectonically active region associated with complex geodynamic activities, that manifest as Quaternary volcanism, earthquake swarms in the upper and middle crust, degassing of CO_2, and crustal fluid migration. The intricate tectonic evolution and activities of this region reflect the complexity of the crustal structure therein. However, the crustal models derived from previous studies in this area offer different, even contradictory information regarding the existence of a mid-crustal low-velocity zone (LVZ). In this study, we apply the frequency-Bessel transform (F-J) method to extract the fundamental-mode and up to five higher-mode Rayleigh wave dispersion curves from ambient seismic noise data recorded in the study area and perform multimodal ambient noise dispersion curves inversion. The addition of higher-mode dispersion curves enhances the vertical resolution of the velocity structure inversion results. Our models support the view that the general S-wave velocity level of the crust is high within the study area. We detect two S-wave LVZs beneath the study area that are distributed mainly in the middle crust rather than the lower crust, and these LVZs are separated by a high-velocity zone. Considering the results of previous studies in the area, we infer that these S-wave LVZs may be the consequence of crustal fluids, plastic deformation and even partial melting of the felsic middle crust at relatively high crustal temperatures. Furthermore, these S-wave LVZs could be responsible for the origin and foci depth distribution of earthquake swarms. S-wave low-velocity anomalies are also observed in the uppermost mantle beneath the study area. These S-wave models based on the joint inversion of multimodal dispersion curves can provide new references for understanding the tectonic activity and geodynamic evolution of the northwestern Bohemian Massif and adjacent areas.

Keywords: Europe, Bohemian Massif, ambient seismic noise, S-wave low-velocity zone, frequency-Bessel transform method

Edited by:
Weijia Sun,
Institute of Geology and Geophysics (CAS), China

Reviewed by:
Zhi Guo,
China Earthquake Administration, China
Huaiyu Yuan,
Macquarie University, Australia

Correspondence:
Xiaofei Chen
chenxf@sustech.edu.cn

Specialty section:
This article was submitted to Solid Earth Geophysics, a section of the journal Frontiers in Earth Science

Received: *18 December 2021*
Accepted: *13 January 2022*
Published: *08 February 2022*

Citation:
Ma Q, Pan L, Wang J-n, Yang Z and Chen X (2022) Crustal S-Wave Velocity Structure Beneath the Northwestern Bohemian Massif, Central Europe, Revealed by the Inversion of Multimodal Ambient Noise Dispersion Curves.
Front. Earth Sci. 10:838751.
doi: 10.3389/feart.2022.838751

INTRODUCTION

The Bohemian Massif, which consists of four geological units, namely, the Saxo-Thuringian (ST), Teplá-Barrandian (TB), Moldanubian and Sudetes zones, is one of the largest stable outcrops of basement rocks in Central Europe (Růžek et al., 2003; Karousová et al., 2012; Plomerová et al., 2012). Tectonically, the Bohemian Massif forms the easternmost rim of the Variscan belt that developed between approximately 480 and 290 Ma during the collision between Laurussia and Gondwana (Matte, 2001; Heuer et al., 2006; Hrubcová et al., 2008; Valentová et al., 2017). The area studied herein is the key tectonic area of the Bohemian Massif, namely, the convergence area of the four geological units mentioned above (as shown in **Figure 1**), including the northwestern part of the Bohemian Massif and adjacent areas. This region, which is presently tectonically active and exhibits complex geological features (Kolínský and Brokešová, 2007; Mousavi et al., 2017), composes a part of the European Cenozoic Rift System and is characterized by a relic Devonian oceanic suture (Karousová et al., 2012; Plomerová et al., 2007). The ongoing geodynamic activities manifest as Quaternary volcanism, earthquake swarms in the upper and middle crust, degassing of CO_2, and crustal fluid migration (Fischer and Horálek., 2003; Horálek and Fischer., 2008; Babuška et al., 2016). The signatures of the intricate regional tectonic evolution and ongoing tectonic activities are recorded in and reflect the complexity of the crustal structure in this area.

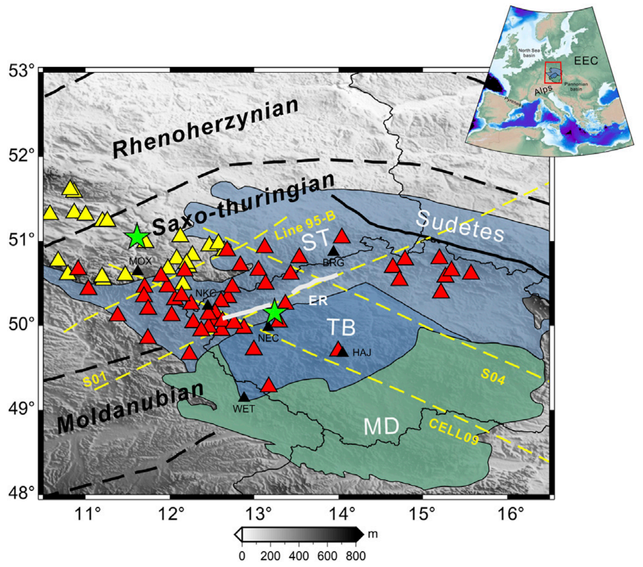

FIGURE 1 | Study area and distribution of stations. A simplified overview of the northwestern Bohemian Massif and adjacent areas (modified after Knapmeyer-Endrun et al. (2014) showing the major tectonic units and seismic stations (yellow and red triangles) used in this study. Major tectonic units and zones of the Bohemian Massif: ST, Saxo-Thuringian zone; TB, Teplá-Barrandian zone; MD, Moldanubian zone; ER, Eger Rift. EEC, Eastern European Craton. Black triangles denote the stations MOX, NKC, WET, and BRG used in Wilde-Piórko et al. (2005) and the stations NEC and HAJ used in Kolínský et al. (2011). Yellow and red triangles denote the seismic stations of arrays "TH" and "ZV", respectively; and green pentagrams denote the center positions of the two arrays. The yellow dashed lines denote profile 95-B of the GRANU95 project, profile CEL09, profile S01 and profile S04.

Previous studies on the crust of the northwestern Bohemian Massif and adjacent areas have relied mainly on seismic sounding experiments, that principally provided P-wave velocity models, such as the NW-SE-trending CEL09 profile (Růžek et al., 2007; Hrubcová et al., 2005; Novotný, 2012) and S04 profile (Růžek et al., 2007; Hrubcová et al., 2010) and the NE-SW-trending S01 profile (Růžek et al., 2007; Grad et al., 2008) and 95-B profile (Enderle et al., 1998). These seismic sounding experiments revealed that the middle crust is generally laterally homogeneous, while the lower crust is laterally inhomogeneous. Along profile 95-B, some regions exhibit high P-wave velocities in the upper and middle crust (depths of ~5 and ~16 km, respectively), suggesting the presence of a low-velocity zone (LVZ) in the depth range of ~5–16 km. The crustal structure is more complicated under the Eger Rift along profile S01; P-wave high-velocity bodies (HVBs) exist mainly in the upper crust (~2–10 km) and feature deep roots extending into the middle crust (~18 km).

Moreover, some studies have recently applied passive seismic techniques in this area. By analyzing teleseismic records with the receiver function technique (e.g., the receiver functions at stations MOX, WET, BRG, and NKC shown in **Figure 1**), Wilde-Piórko et al. (2005) revealed the existence of an S-wave LVZ in the middle crust (depth range of 10–15 km) of the northwestern Bohemian Massif. With the help of Love wave phase velocity dispersion curves, Kolínský et al. (2011) discovered an S-wave LVZ in the middle and lower crust beneath the TB zone and a gradually increasing S-wave velocity structure in the crust of the ST zone. By applying ambient seismic noise interferometric surface wave tomography (ASNT) to the recordings of broadband seismic stations, Růžek et al. (2016) inverted group and phase dispersion curves to obtain crustal velocity models for the Bohemian Massif that monotonically increase with depth; they concluded that the differences among different tectonic units are small and that the most homogeneous part among them generally being the middle crust. Some researchers utilized the ASNT method with data from additional seismic stations in Europe to extract phase velocity dispersion curves (e.g., Kästle et al., 2018) and group velocity dispersion curves (e.g., Lu et al., 2018) for the inversion and derived high-resolution S-wave velocity models that present the almost smoothly increasing velocity structure of the crust in the study area. More recently, Kvapil et al. (2021) reported that the velocity-drop interface (negative velocity gradient) in the lower part of the crust of the Bohemian Massif (depth of 18–30 km); however, the general group velocity level of dispersion curves is lower than the level presented in Lu et al. (2018).

Nevertheless, the crustal models derived from previous studies for the Bohemian Massif present different, even contradictory results regarding the existence of the LVZ in the middle crust (e.g., Enderle et al., 1998; Wilde-Piórko et al., 2005; Grad et al., 2008; Kolínský et al., 2011; Růžek et al., 2016; Kästle et al., 2018; Lu et al., 2018; Kvapil et al., 2021). To address this inconsistency, in this study, we apply our newly developed multimodal ambient noise dispersion curve tomography method, denoted the frequency-Bessel transform (F-J) method (Wang et al., 2019), to investigate the crustal structure beneath the study area by using available ambient seismic noise datasets.

In the following, we describe how to process the ambient noise data used in this study. Then, we briefly summarize the principle of the F-J method and apply it to extract the fundamental-mode and higher-mode Rayleigh wave phase velocity dispersion curves from ambient seismic noise data, after which we carry out the joint inversion of these multimodal dispersion curves to obtain the S-wave velocity model for the crust and uppermost mantle with a higher vertical resolution. Finally, we compare our models with the results of previous studies conducted in our region of interest.

DATA AND PREPROCESSING

The continuous ambient seismic noise data analyzed in this study are derived from two independent datasets. The first dataset is from the Bohema digital seismic network (FDSN code: ZV), which is a part of the Bohemian Massif Anisotropy and Heterogeneity (BOHEMA) project (Babuška et al., 2005; Plomerová et al., 2003), from which we select continuous broadband vertical-component seismic noise data (channel code: BHZ/HHZ, sampling rate: 20–100 Hz) from January 2001 to December 2005 recorded by 49 stations. The second dataset is from the Thuringer Seismisches Netz (TSN) network (FDSN code: TH; Jena, 2009), from which we select continuous broadband vertical-component seismic noise data (channel code: HHZ, sampling rate: 100 Hz) from January 2015 to December 2017 recorded by 23 stations. All stations are located mainly in the northwestern Bohemian Massif and adjacent areas and span the area of approximately 6 ° × 3 °, as shown in **Figure 1**. We take the central longitude and latitude of the area where the seismic array is located as the center of the array (green pentagrams in **Figure 1**).

The procedures for preprocessing the data are similar to those described in Bensen et al. (2007), including downsampling, tapering, detrending, removing the mean, removing the instrumental response, time-domain normalization and spectral whitening. Finally, we split the whole records from each station into 1-h segments. After processing the data from all stations, we use linear stacking method to compute 1-h stacked noise cross-correlation functions (NCFs) of all station pairs in the two datasets. **Supplementary Figure S1** shows the cross-correlation functions of different arrays (period band 1–50 s).

METHODOLOGY

F-J Method

We recently proposed the F-J method (Wang et al., 2019), which can effectively extract multimodal dispersion curves from ambient seismic noise data (e.g., Wu et al., 2020; Zhan et al., 2020). Having obtained the stacked NCFs in the preprocessing step, we then extract the multimodal dispersion curves of the areas beneath each dataset by using the F-J method. The main procedures of the F-J method are briefly summarized as follows.

After preprocessing the ambient seismic noise data, we can obtain the frequency spectra $\tilde{C}(r,\omega)$ of the NCFs of a series of station pairs, where r is the interstation distance. If the station pair cross-correlation functions are continuously distributed, and the number is infinite, we can calculate the F-J spectrogram of $\tilde{C}(r,\omega)$ as follows:

$$I(\omega,c)=\int_0^{+\infty}\tilde{C}(r,\omega)J_0\left(\frac{\omega}{c}r\right)rdr, \tag{1}$$

Where J_0 is Bessel function of order 0. We have theoretically proven that when c and ω satisfy the dispersion relationship, the value of $I(\omega,c)$ tends to infinity. When scanning with limited pixels, the F-J spectrogram $I(\omega,c)$ shows significant maximum values in the narrow neighborhood of the dispersion curve of each mode, and thus, we can identify the dispersion curves of the fundamental mode and higher modes from the $I(\omega,c)$ diagram. However, in practical applications, the number of stations is finite; hence, we cannot directly apply **Eq. 1** to obtain $I(\omega,c)$. We can approximate the infinite integral in **Eq. 1** by the following truncation:

$$I(\omega,c)=\int_0^{+\infty}\tilde{C}(r,\omega)J_0\left(\frac{\omega}{c}r\right)rdr\approx\sum_{j=1}^{N}\int_{r_{j-1}}^{r_j}\tilde{C}(r,\omega)J_0\left(\frac{\omega}{c}r\right)rdr, \tag{2}$$

where $0=r_0<r_1<r_2<\ldots<r_j\ldots<r_N$.

Within the interval $[r_{j-1},r_j]$, the $\tilde{C}(r,\omega)$ can be approximated by a linear function as follows:

$$\tilde{C}(r,\omega)\approx a_j+b_jr, \tag{3}$$

with

$$a_j=\tilde{C}\left(r_{j-1},\omega\right)-\left[\frac{\tilde{C}\left(r_j,\omega\right)-\tilde{C}\left(r_{j-1},\omega\right)}{r_j-r_{j-1}}\right]r_{j-1}\text{ and }b_j=\frac{\tilde{C}\left(r_j,\omega\right)-\tilde{C}\left(r_{j-1},\omega\right)}{r_j-r_{j-1}}. \tag{4}$$

Substituting **Eq. 3** into **Eq. 2**, and with the following formulas (J_1 is Bessel function of order 1):

$$\int xJ_0(x)dx=\mathrm{x}\mathrm{J}_1(x), \tag{5}$$

$$\int x^2J_0(x)dx=x^2J_1(x)+xJ_0(x)-\int J_0(x)dx. \tag{6}$$

We can get the following approximation formula which can be used when scanning to obtain the F-J spectrogram (Wang et al., 2019):

$$I(\omega,c)\approx\sum_{j=1}^{N}\left\{\left(\frac{c}{\omega}\right)\tilde{C}(r,\omega)rJ_1\left(\frac{w}{c}r\right)+b_j\left(\frac{c}{\omega}\right)^3\left[\frac{\omega}{c}rJ_0\left(\frac{\omega}{c}r\right)-B_0\left(\frac{\omega}{c}r\right)\right]\right\}\Bigg|_{r_{j-1}}^{r_j}, \tag{7}$$

where c and r_j denote the phase velocity and the interstation distance of station pair j, respectively. $B_0(x)=\int_0^xJ_0(\eta)d\eta$.

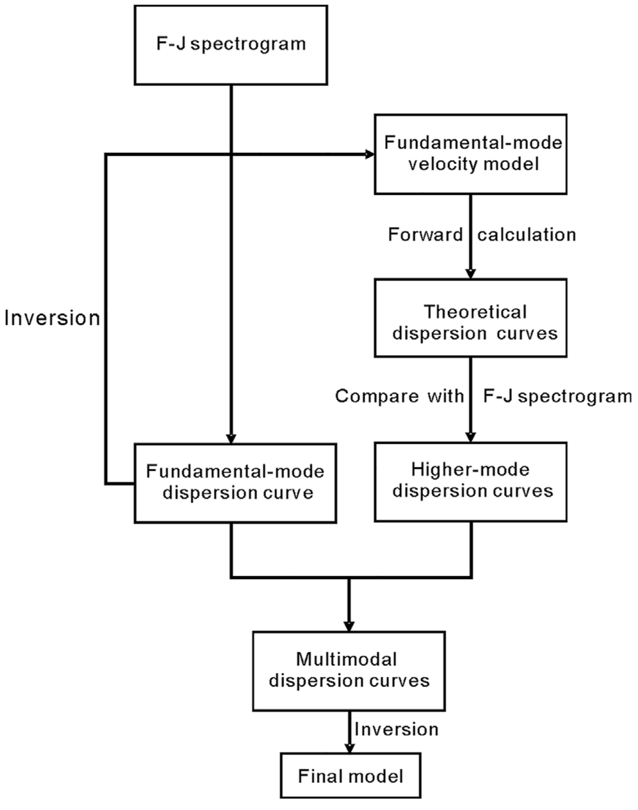

FIGURE 2 | Multimodal dispersion curve identification workflow.

Identification of Multimodal Dispersion Curves

To accurately extract higher-mode dispersion curves, we extract the multimodal dispersion curves in two steps. The workflow is illustrated in **Figure 2**. First, we extract the fundamental-mode dispersion curve from the F-J spectrogram and invert the dispersion curve to obtain a preliminary S-wave velocity model (hereinafter referred to as the fundamental-mode velocity model). Then, we calculate the theoretical higher-mode dispersion curves of the model using the generalized reflection-transmission coefficient method (Chen, 1993) and project them onto the F-J spectrogram. Finally, taking these theoretical higher-mode dispersion curves as a reference, we identify the highlighted areas on the F-J spectrogram and extract the higher-mode dispersion curves.

Inversion Method

Having obtained the dispersion curves, we carry out the inversion by using the Broyden-Fletcher-Goldfarb-Shanno (BFGS) algorithm (e.g., Byrd et al., 1995). The detailed procedures are described in Pan et al. (2019) and Zhan et al. (2020); a brief summary is given as follows. First, an objective function of multimodal dispersion curves is defined by:

$$f(\boldsymbol{V}_{\mathbf{s}}) = \frac{1}{m}\sum_{k=0}^{m}\frac{a_k}{n_k}\left\{\sum_i \left[c_{ik}^{s}(\boldsymbol{V}_{\mathbf{s}}) - c_{ik}^{o}\right]^2\right\} + \gamma\left\|\hat{D}\mathbf{V}_{\mathbf{s}}\right\|_2^2, \quad (8)$$

where i and k are the indices for the sampled frequency and dispersion curve mode, respectively; c_{ik}^{S} is the phase velocity of the synthetic dispersion curve at the ith frequency and kth mode; c_{ik}^{O} is the observed velocity; m is the number of modes of the dispersion curves used for the inversion; n_k is the number of sampled data points for the kth mode; and a_k is a weight factor for the kth mode. In this study, we set the weight factor of each higher-mode dispersion curve to 1, and the weight factor of the fundamental mode dispersion curve is equal to the number of all higher-mode dispersion curves. Through this simple strategy, it is possible to ensure that the fundamental mode makes the main contribution to the inversion, as well as the improvement of the inversion by the higher modes. The second term is the smoothing regularization. $\boldsymbol{V}_S$ is the shear velocity model; $\hat{D} = e^{\frac{-|z_i - z_j|}{d}}$, where z_i and z_j are the depths at the top of the ith and jth layers; and d is a smoothing distance (Haney and Tsai, 2017). The smoothing factor γ is near the maximum curvature of the L-curve (Hansen, 2001) and the value is between 3e-3 and 3e-2. In the inversion, we set the layer thickness to 2 km in the depth range of 0–68 km.

In the process of iteratively solving the nonlinear inversion problem, the P-wave velocity v_p and density ρ of each iteration are converted by the following empirical formulas: $v_p = 1.67v_s$ and $\rho = 0.77 + 0.32v_p$ (Růžek et al., 2016). For the first step in inverting the fundamental-mode dispersion curve, 200 initial models are randomly generated in the range of ±0.4 km/s with the Eurasian 1D average reference model (Marone et al., 2004) as the intermediate value for the inversion, and the best-fitting model is taken as the fundamental-mode velocity model. After obtaining the higher-mode dispersion curves, the fundamental-mode velocity model is used to randomly generate 200 initial models within the range of ±0.4 km/s for the multimodal dispersion curve inversion. The model that minimizes the objective function is taken as the final model for the inversion of multimodal dispersion curves.

RESULTS

Identification of Multimodal Dispersion Curves and Inversion Results

The distribution area of stations in seismic array "TH" is adjacent to the northwestern Bohemian Massif (yellow triangles in **Figure 1**). We apply the F-J method to this array and the results are shown in **Figure 3**. **Figure 3A** clearly shows the fundamental-mode dispersion curve, as well as the possible higher-mode dispersion curves. The fundamental-mode velocity model is obtained by inverting the fundamental-mode dispersion curve. **Figure 3B** shows the first ten well-fitting inversion results; the red line represents the model with the smallest objective function, namely, the fundamental-mode velocity model, and its fundamental-mode dispersion curve fitting is shown in **Figure 3C**. According to the fundamental-mode velocity model, we calculate the theoretical higher-mode

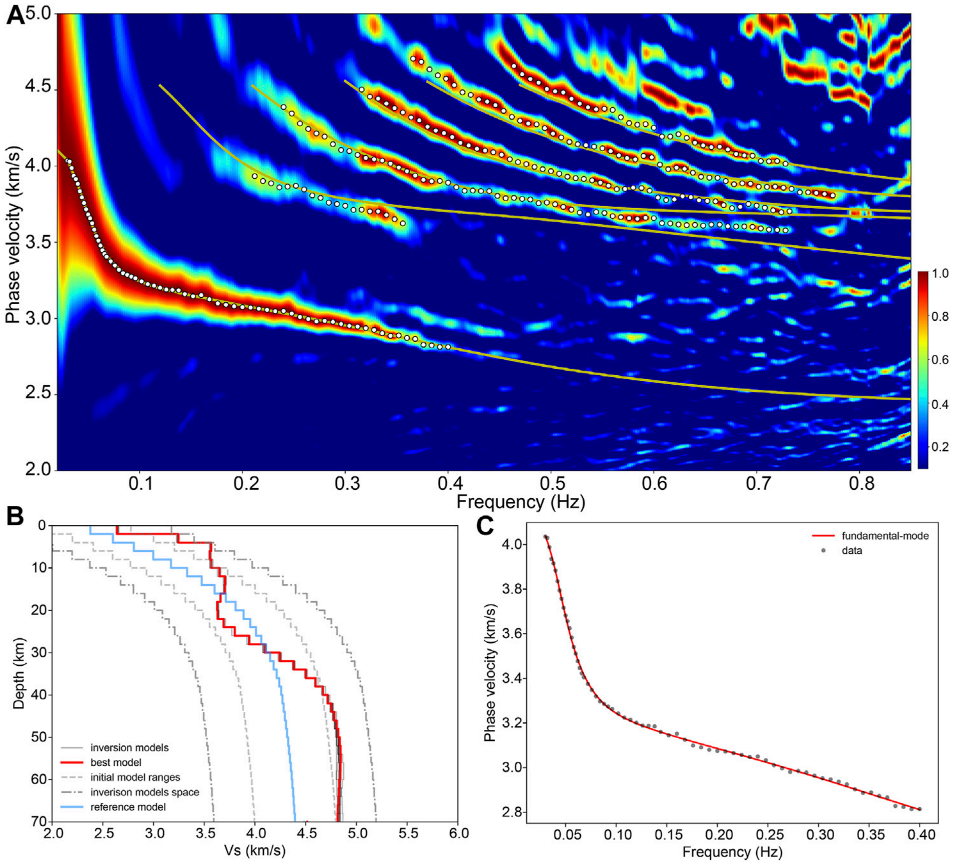

FIGURE 3 | Identification of the multimodal dispersion curves for array "TH". **(A)** The F-J spectrogram of seismic array "TH"; the yellow solid lines denote the theoretical multimodal dispersion curves corresponding to the fundamental-mode velocity model, and the white dotted lines denote the picked fundamental-mode and higher-mode dispersion curves. **(B)** The fundamental-mode dispersion curve inversion results; the blue line is the reference velocity model; the red and black lines are the first ten well-fitting models obtained from inverting the fundamental-mode dispersion curve; the red line denotes the best-fitting inversion model with the smallest objective function value; the gray dashed line lines represent the range of the initial models. the gray dash-dotted lines represent the inversion model space. **(C)** The fitting result of the fundamental-mode velocity model; the black points are the picked fundamental-mode dispersion points, and the red line denotes the theoretical dispersion curve corresponding to the fundamental-mode velocity model.

dispersion curves (yellow solid lines in **Figure 3A**) and project them onto the F-J spectrogram. With this projection as a reference, we extract the fundamental-mode and five higher-mode dispersion curves (white dotted lines in **Figure 3A**).

To invert the multimodal dispersion curves in the area of seismic array "TH", we use the fundamental-mode velocity model (red line in **Figure 3B**) as the intermediate value within the range of the fundamental-mode velocity model (±0.4 km/s, gray dashed lines in **Figure 4A**) to randomly generate 200 initial models for the multimodal dispersion curve inversion. **Figure 4A** shows the first ten well-fitting inversion results (the standard deviations of the ten models are shown in **Supplementary Figure S2**), while the red line represents the best-fitting model with the smallest objective function value, that is, the final model of the multimodal dispersion curve inversion. The multimodal dispersion curve fitting result of this model is shown in **Figure 4B**. The model depicts an S-wave LVZ in the middle crust (depths of 12–22 km), and the low-velocity anomalies in the uppermost mantle (depths of 42–62 km).

The stations of seismic array "ZV" are distributed mainly in the northwestern Bohemian Massif (red triangles in **Figure 1**). **Figure 5A** shows the picked points of the multimodal dispersion curves and the theoretical multimodal dispersion curves corresponding to the fundamental-mode velocity model (blue line in **Figure 5B**). The inversion and fitting results of the multimodal dispersion curves are shown in **Figures 5B,C**. The final model (red line in **Figure 5B**) of the multimodal dispersion curve inversion similarly reveals an S-wave LVZ in the middle crust (depths of 8–12 km) and low-velocity anomalies in the uppermost mantle (below 50 km).

Sensitivity Kernel Analysis

To illustrate the influence of the higher-mode Rayleigh wave dispersion curves on the velocity structure inversion results, we employ the method of Pan et al. (2019) to calculate both the depth and the frequency distributions of the S-wave sensitivity kernel function of the final inversion model in each of the above two regions (as shown in **Figure 6** and **Figure 7**). The distributions of

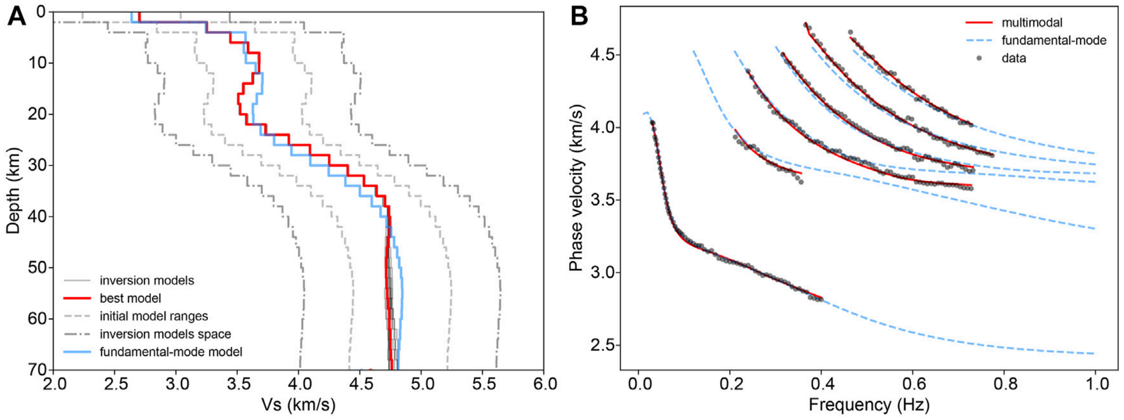

FIGURE 4 | Inversion and fitting results of the multimodal dispersion curves of array "TH". **(A)** The blue line is the fundamental-mode velocity model, and the red and black lines are the first ten well-fitting models obtained from the inversion of multimodal dispersion curves, where the red line denotes the best-fitting inversion model with the smallest objective function value, namely, the final model of the multimodal dispersion curve inversion. **(B)** The black points are the picked multimodal dispersion points, the red lines denote the theoretical multimodal dispersion curves of the final model of the multimodal dispersion curve inversion, and the blue dashed lines are the theoretical multimodal dispersion curves of the fundamental-mode velocity model.

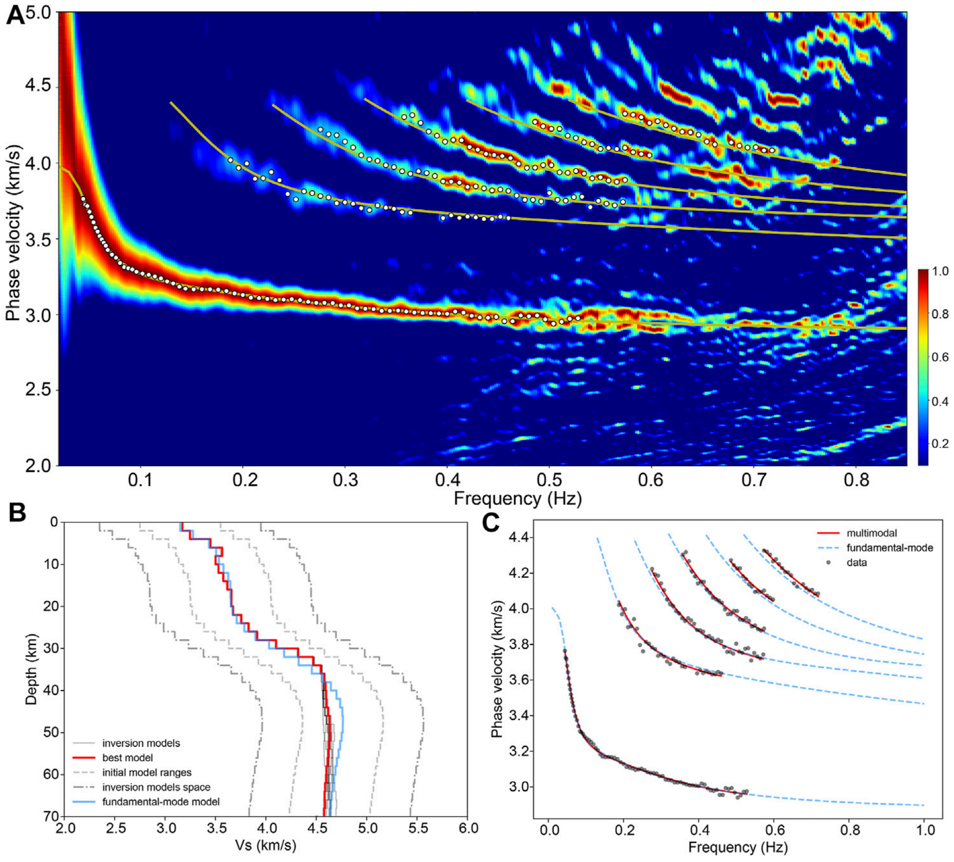

FIGURE 5 | Identification of the multimodal dispersion curves of array "ZV" and inversion results and fitting results. **(A)** The F-J spectrogram of seismic array "ZV". **(B)** and **(C)** The inversion and fitting results of the multimodal dispersion curves.

these sensitivity kernel functions show that the fundamental-mode dispersion curve offers constraint on the entire crust and uppermost mantle in the study area, and the constraint is the strongest at the surface and weakens with depth. Furthermore, the higher-mode dispersion curves strongly constrain both the entire crust and the structure near the crust-mantle boundary

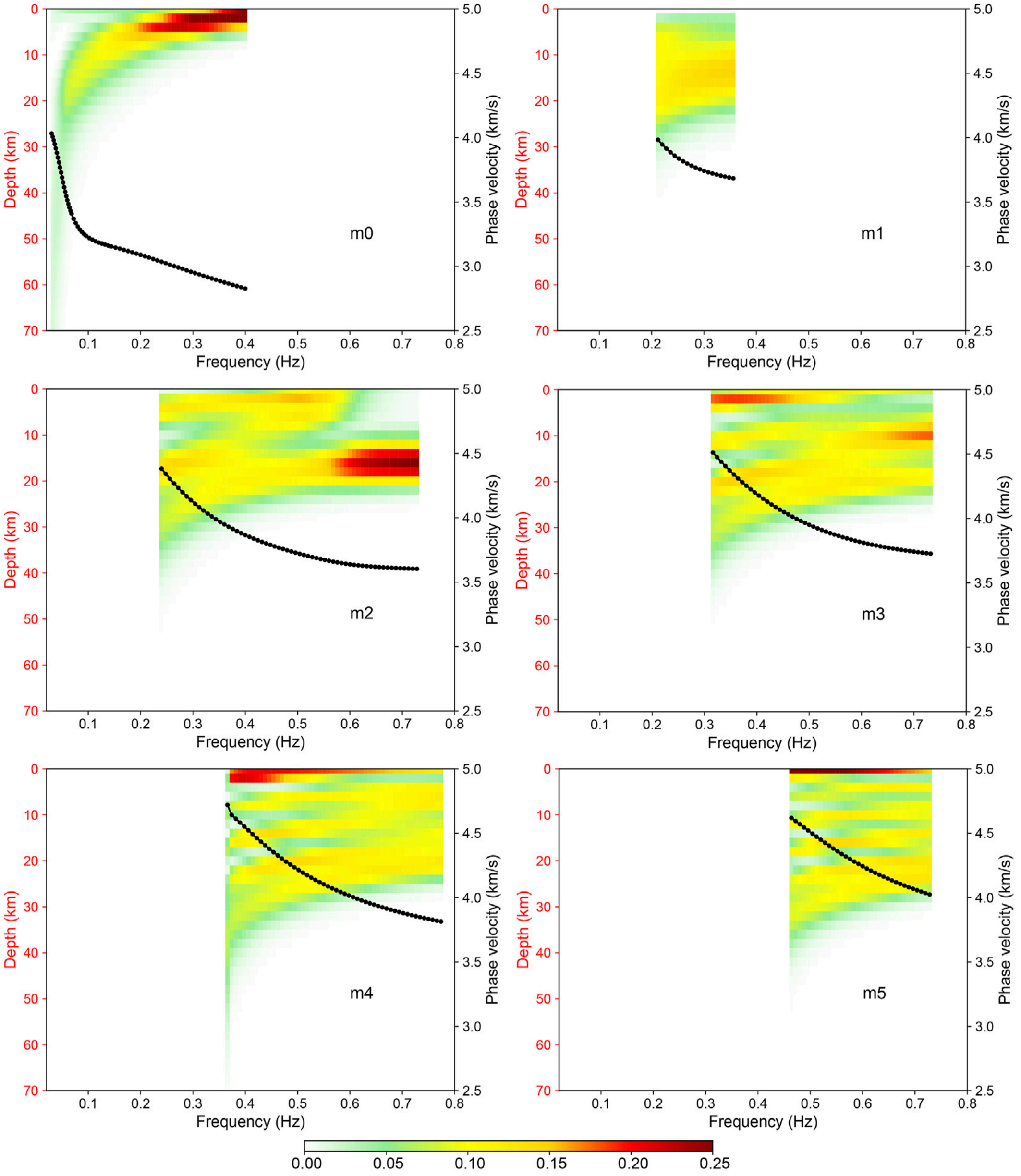

FIGURE 6 | Depth and frequency distributions of the sensitivity kernel function of the final model of the multimodal dispersion curve inversion for array "TH". The black dotted lines are the theoretical dispersion curves corresponding to the final model (truncated according to the frequency range of the picked data points).

(depth of approximately 40 km). We also employ the final models of the two arrays as the true models to test the improvement effect of higher modes on the inversion. The **Supplementary Figure S3** and **Supplementary Figure S4** clearly show that when only the fundamental mode is used for the inversion, the inversion models are considerably different from the true models; with the addition of higher modes to the inversion, the inversion models are much closer to the true models at depths of 0–40 km, and the inversion accuracy at depths of 40–70 km is also improved. Therefore, the addition of higher-mode dispersion curves to the inversion directly and significantly improves the inversion accuracy in the depth range of 0–40 km and thus improves the inversion accuracy in the whole inversion depth range. Introducing higher-mode dispersion curves on the basis of the fundamental-mode dispersion curve can provide more constraints on inversion, which can help mitigate the non-uniqueness problem.

Subregion Division

Obvious S-wave LVZs are detected in the middle crust from the velocity structure inversion results beneath the two seismic arrays. To further study the distributions of the S-wave LVZs, we divide the stations on the west side of the study area into two subarrays, as shown in **Figure 8**. Although some of the stations of the two subarrays overlap, the geometric centers of the subarrays

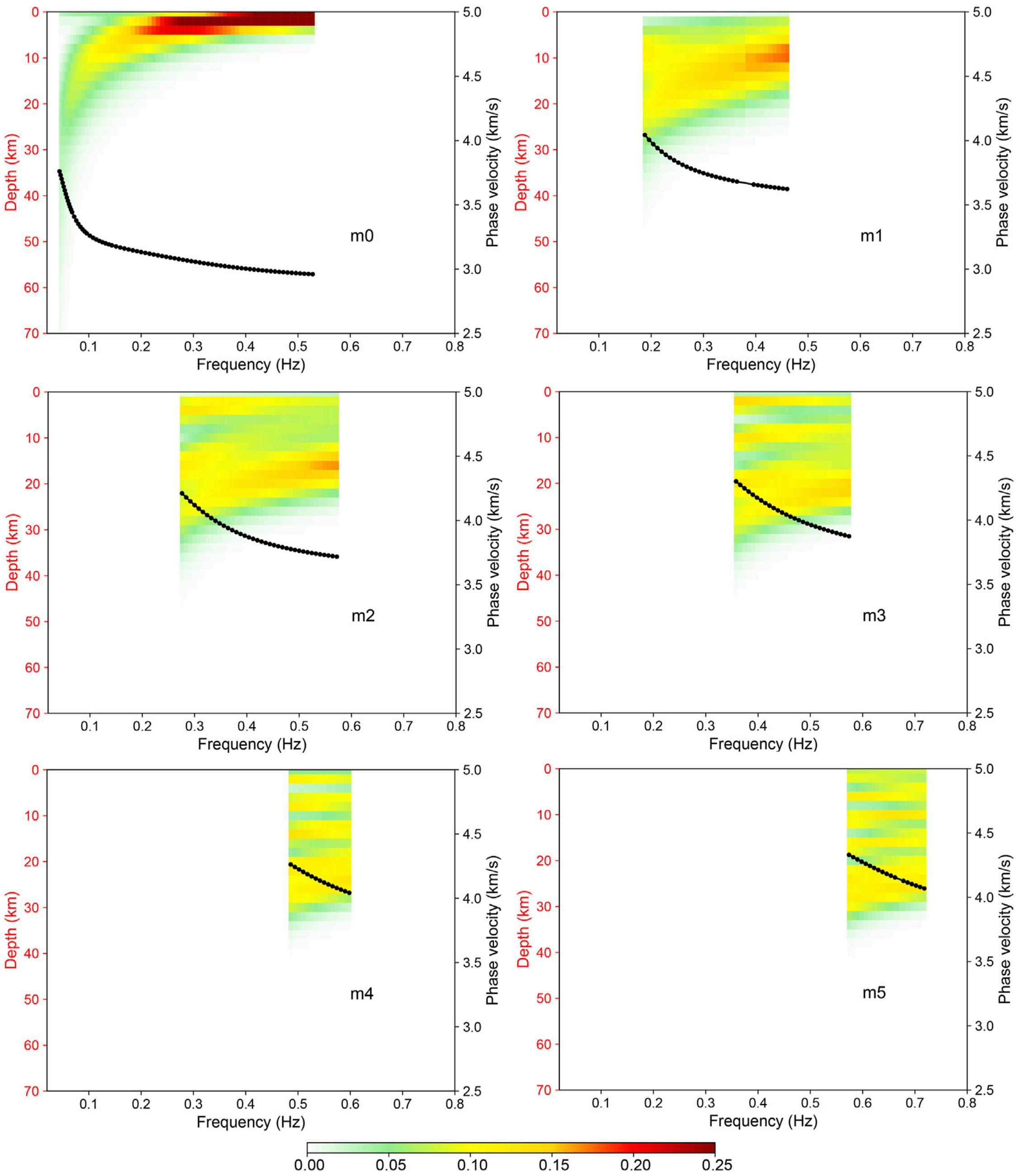

FIGURE 7 | Depth and frequency distributions of the sensitivity kernel function of the final model of the multimodal dispersion curve inversion for array “ZV”.

are different (the green pentagrams in **Figure 8**) and are approximately 60 km apart.

Figure 9 shows the F-J spectrogram of subarray 1 and the picked points of the dispersion curves, the final inversion model, and the fitting results of the dispersion curves. The inversion result in this area reveals a LVZ at depths of 12–16 km in the middle crust; furthermore, the velocity gradient at depths of 22–26 km is very small, and the velocity in the uppermost mantle (below 42 km) decreases with depth. Likewise, the F-J spectrogram, the picked points of the dispersion curves, and the inversion results for subarray 2 are shown in **Figure 10**. The final inversion model of this area shows two S-wave LVZs in the crust at depths of 8–12 km and 18–24 km; in addition, low-velocity features appear in the uppermost mantle at depths of 36–44 km and below 50 km.

The current sub-division method considers the quality of the F-J spectrogram and the regional structural characteristics as much as possible. If we try to divide into smaller subregions, the quality of the F-J spectrogram will be lower. For example, based on **Figure 8**, we remove the stations on the northwest edge of the two subarrays; the

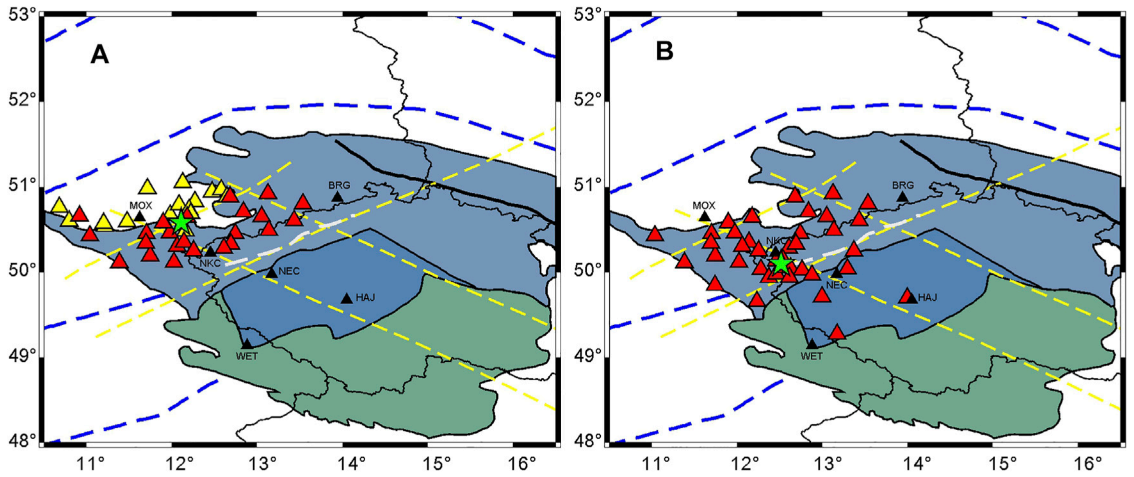

FIGURE 8 | (A) Distribution of stations in subarray 1 (yellow and red triangles). **(B)** Distribution of stations in subarray 2 (red triangles). The two green pentagrams are the centers of the two subarrays; see **Figure 1** for explanations of the other symbols.

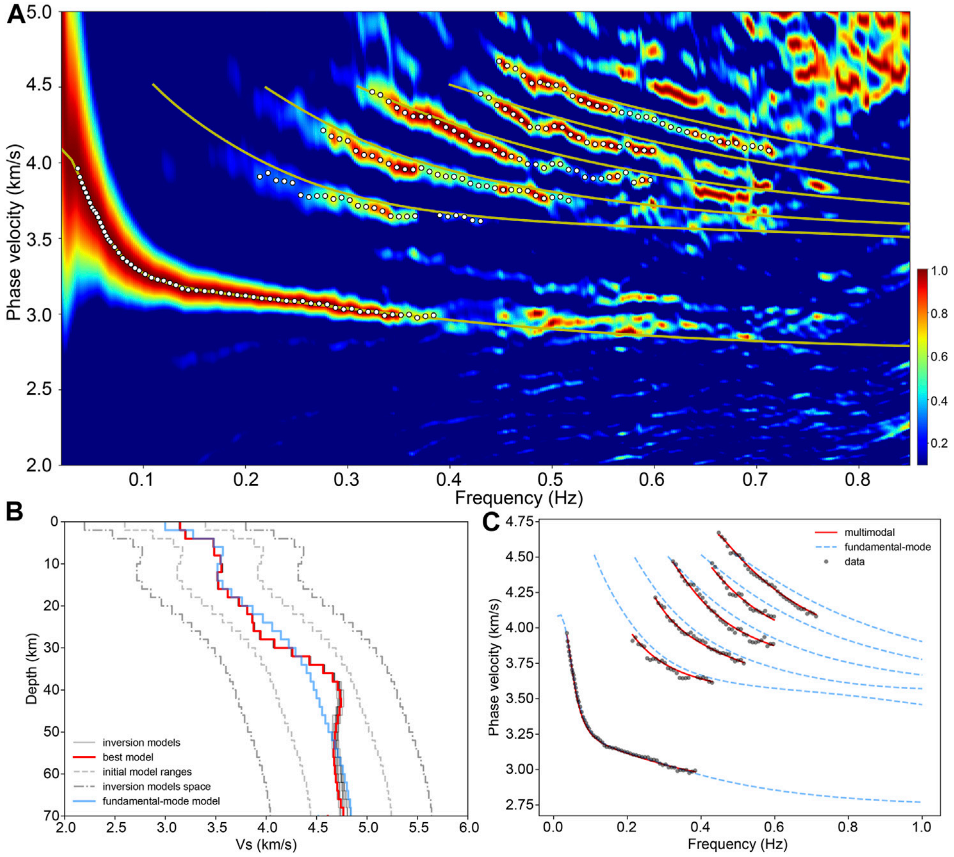

FIGURE 9 | Identification of the multimodal dispersion curves of subarray 1 and the inversion and fitting results. **(A)** The F-J spectrogram of seismic array “subarray 1”. **(B)** and **(C)** The inversion and fitting results of the multimodal dispersion curves.

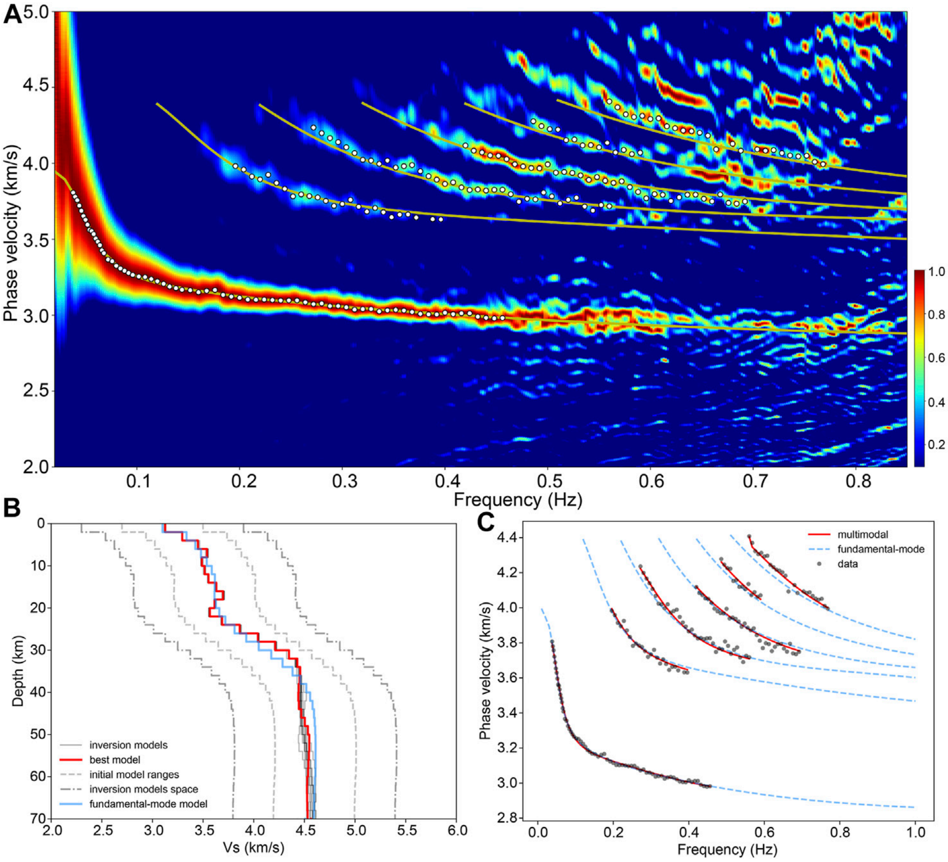

FIGURE 10 | Identification of the multimodal dispersion curves of subarray 2 and the inversion and fitting results. **(A)** The F-J spectrogram of seismic array "subarray 2". **(B)** and **(C)** The inversion and fitting results of the multimodal dispersion curves.

two new subarrays are shown in **Supplementary Figure S5** and the F-J spectrograms of the two new subarrays are shown in **Supplementary Figure S6**. It is clear that the quality of the F-J spectrograms decreases, especially for the higher modes.

DISCUSSION

The Robustness of the LVZs in the Middle Crust

To verify the robustness of the LVZs in our models, we carry out the random inversions while prohibiting a decrease in velocity with depth. For the joint inversion of multimodal dispersion curves, we obtain 200 inversion models without LVZ for each array. **Figure 11** shows the first ten well-fitting models of each array. We calculate the objective function values of the initial models and the inversion models of each array when the velocity decrease is prohibited, and compare them with those when the velocity is allowed to decrease (shown in **Figure 12**). According to the statistical significance tests and the comparisons shown in **Figure 12**, the objective function values of the initial models in two cases have little difference (p-value >0.05); furthermore, compared to the initial models, the inversion models in each case are significantly improved (p-value< 0.01), and the inversion models obtained by allowing the velocity to decrease are obviously better than those when the velocity is prohibited from decreasing with depth (p-value <0.01); that is, the models in which the velocity is allowed to decrease are more reasonable. These outcomes confirm that the LVZs in the inversion results are robust. In addition, based on 3D gravity modeling, geological data, seismic refraction (CEL09) and reflection (9HR), Guy et al. (2011) suggested the lower-density middle crust of the ST zone (~10–25 km).

Crustal S-Wave Velocity Models in the Northwestern Bohemian Massif

Recently, some researchers have used the traditional ASNT method to extract phase velocity dispersion curves (e.g., Růžek et al., 2016; Kästle et al., 2018) and group velocity dispersion curves (e.g., Růžek et al., 2016; Lu et al., 2018; Kvapil et al., 2021) to study the velocity structure in the study region and obtained S-wave velocity models. Based on the velocity models of the previous studies, we obtain average 1D S-wave velocity models (**Figures 13A,B**; **Supplementary Figure S7A**, **Supplementary Figure S7B**) beneath the stations of the four arrays (we select the

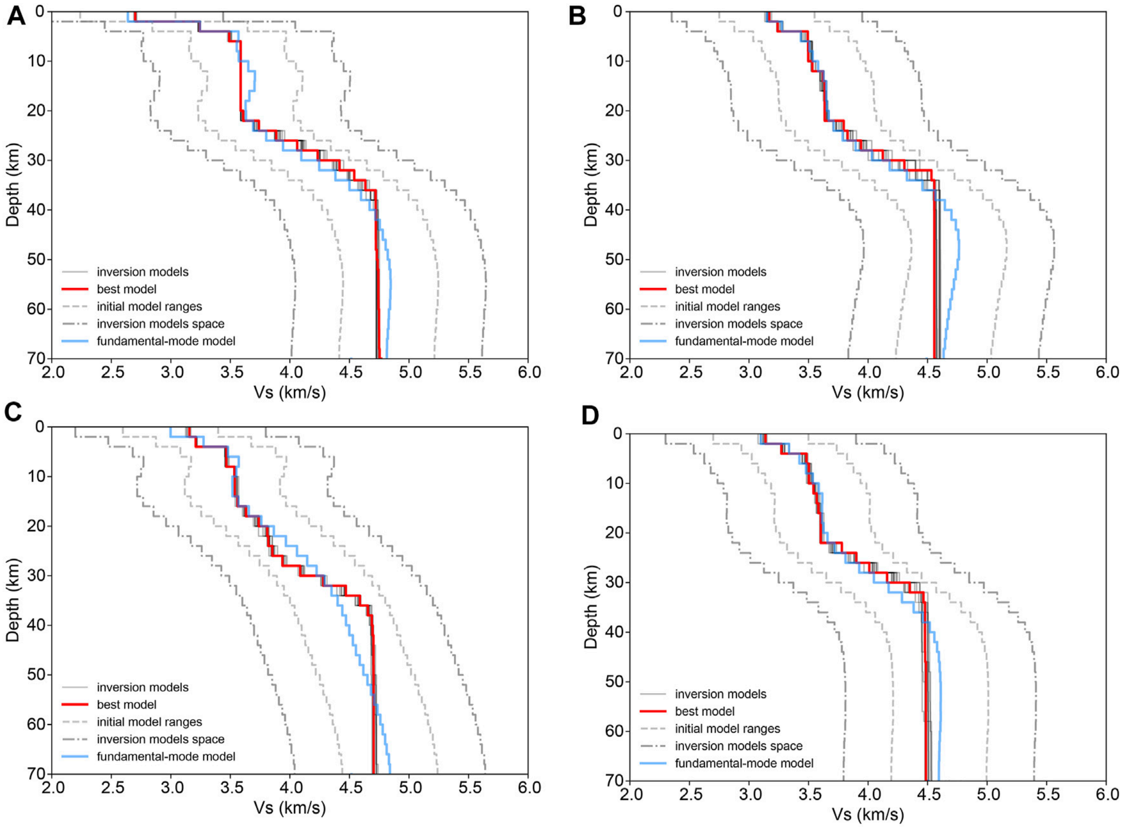

FIGURE 11 | Inversion results (the velocity is prohibited from decreasing with depth) of the multimodal dispersion curves. **(A)** TH array; **(B)** ZV array; **(C)** subarray 1; **(D)** subarray 2.

velocity models of the grid points nearest to the stations to calculate the averaged 1D models). Furthermore, the average 1D velocity model under the area of arrays "ZV" and subarray 2 (yellow line in **Figure 13B** and **Supplementary Figure S7B**) is obtained according to the 1D models of Růžek et al. (2016) in the ST and TB units. In comparison, the S-wave velocities in our models are higher than those in the other models at depths of ~30–40 km. In addition, the S-wave velocities in the models from Kvapil et al. (2021) are obviously lower than those in other models (shown in **Figure 13**, **Supplementary Figure S7** and **Supplementary Figure S8**), even the models of Lu et al. (2018), who also used group velocity dispersion curves for inversion. The general group velocity level of the dispersion curves in Kvapil et al. (2021) is lower than the level presented in Lu et al. (2018), which may be the main reason for the models' discrepancy.

For a comparison with the picked data, we calculate the theoretical dispersion curves of these 1D velocity models (**Figures 13C,D**; **Supplementary Figure S7C, Supplementary Figure S7D**), the results of which clearly demonstrate an unsatisfactory match between the theoretical dispersion curves of these models and the F-J spectrograms (especially at the higher modes). Specifically, the theoretical dispersion curves corresponding to the 1D models under the four arrays extracted from the models of Lu et al. (2018) and Kvapil et al. (2021) are overall lower than picked data; the two 1D models using the phase velocity dispersion curves for the inversion (Kästle et al., 2018; Růžek et al., 2016), especially the models from Kästle et al. (2018) present better fitting results for fundamental mode, but large deviations at the higher modes are still observed for the two models. Our models obtained *via* the joint inversion of the multimodal dispersion curves match well with the fundamental mode and higher modes for the four arrays. Therefore, introducing higher-mode dispersion curves on the basis of the fundamental-mode dispersion curve is crucial to constrain the structure of the crust in the study area.

S-Wave LVZs in the Middle Crust of Northwestern Bohemian Massif

The models obtained via the joint inversion of multimodal dispersion curves based on the F-J method reveal obvious low-velocity characteristics in the crust and uppermost mantle beneath the study area. Other studies similarly provided evidence for the existence of an LVZ in this region (e.g., Wilde-Piórko et al., 2005; Kolínský et al., 2011; Kvapil et al., 2021). Based on our inversion results, we construct a simple S-wave velocity profile of the crust and uppermost mantle

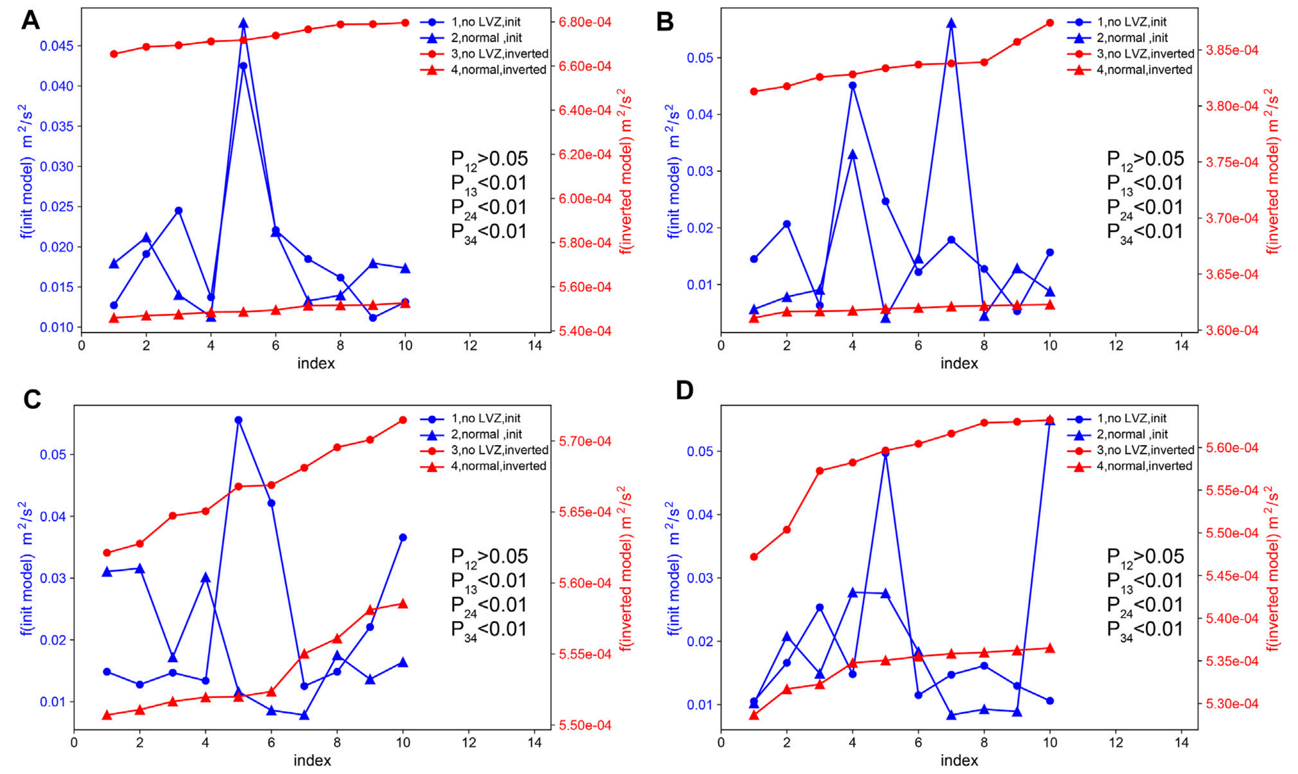

FIGURE 12 | Objective function values of the models and the results of the statistical significance test. The blue and red lines denote the objective function values of the initial models and inversion models, respectively. The triangles and circles denote the inversion that allows the velocity to decrease and the inversion that prohibits the velocity from decreasing, respectively. **(A)** TH array; **(B)** ZV array; **(C)** subarray 1; **(D)** subarray 2

beneath the western side of the study area (**Figure 14B**). The surface line corresponding to this profile in the study area trends NW-SE (the direction of the black arrow in **Figure 14A**) and mainly covers two geological tectonic units: ST and TB. Along the profile, there are two obvious LVZs (depth range of 8–24 km) in the middle crust separated by the high-velocity zone (HVZ, depth range of 12–18 km), which is different from the crustal S-wave velocity models of previous investigations (e.g., Wilde-Piórko et al., 2005; Růžek et al., 2016; Kästle et al., 2018; Lu et al., 2018; Kvapil et al., 2021). In the middle crust, the uppermost LVZ is thick in the west and thin in the east, and the velocity contrast of the LVZ is strong in the west and weak in the east; the thickness of the lowermost LVZ is relatively uniform, and the velocity contrast of the LVZ is weak in the west and strong in the east. The negligible HVZ between the upper and lower LVZs in the middle crust may be caused by the high-velocity crust beneath the Eger Rift.

In addition to this mid-crustal S-wave LVZs, S-wave low-velocity anomalies are also discovered in the uppermost mantle beneath the study area. The thickness of uppermost-mantle low-velocity anomalies is about ~8–20 km. These S-wave low-velocity anomalies may be related to the partial melting in the mantle near the Eger Rift or the upwelling of materials from the lithosphere-asthenosphere transition zone (e.g., Plomerová et al., 2007; Grad et al., 2008).

Causes of the Mid-crustal S-Wave LVZs in the Study Area

The mid-crustal S-wave LVZs in the study area and the low-velocity anomalies in the uppermost mantle are not directly connected; instead, they are separated by the high-velocity lower crust. Due to the influences of temperature and pressure, the middle crust may be relatively plastic or even partially molten. The surface heat flow is an important parameter for understanding geothermal activity, which is related to regional and global tectonic activities. The average heat flow in the Bohemian Massif is 67.9 mW/m^2; low heat flow values are observed in the southern and central parts, while high heat flow values are measured in the northwestern Bohemian Massif (Čermák, 1976). Previous studies have shown that the middle crust below the study area is predominantly felsic. For example, Förster and Förster (2000) calculated the heat budget based on the surface heat flow and radiogenic heat production of the ST unit, and inferred that the middle crust is relatively felsic and the lower crust may be relatively mafic and less felsic. Based on 3D gravity modeling, geological data, and seismic refraction (CEL09) and reflection (9HR), Guy et al. (2011) suggested that the lower-density middle crust of the ST zone (~10–25 km) is felsic; similarly, they indicated that the lower-density crust underneath the TB area is also felsic. A higher surface heat flow value usually corresponds to a higher crustal temperature. Hence, the felsic middle crust beneath the northwestern Bohemian Massif could have

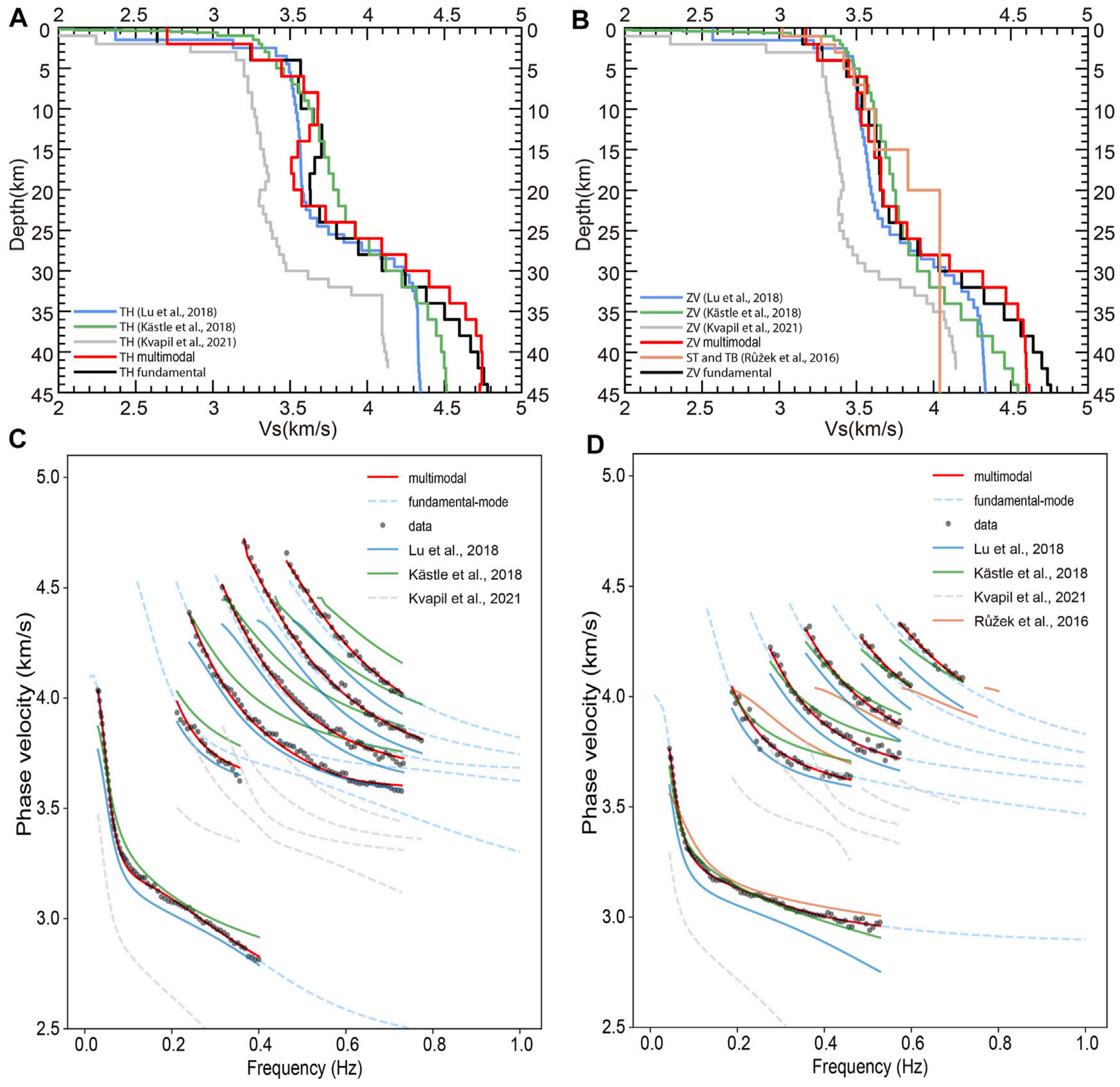

FIGURE 13 | Velocity models of previous studies and their fitting results with the picked data in the study area. **(A)** S-wave velocity models for array “TH”. Different colors denote the different average 1D S-wave velocity models beneath the stations of array “TH” (Kästle et al., 2018; Lu et al., 2018; Kvapil et al., 2021), and the red solid line denotes our model obtained from the inversion of multimodal dispersion curves. The black solid line denotes the model obtained from the inversion using only fundamental mode. **(B)** S-wave velocity models for array “ZV”. The yellow line is the average of the 1D models below the ST and TB units in the study area from Růžek et al. (2016). **(C)** The theoretical dispersion curves of the different 1D velocity models for array “TH”. The different colors denote the theoretical dispersion curves of the different average 1D S-wave velocity models in **(A)**; for additional explanations, see **Figure 4B**. **(D)** The theoretical dispersion curves of different 1D velocity models for array “ZV”. The different colors denote the theoretical dispersion curves of the different average 1D S-wave velocity models in **(B)**; for other explanations, see **Figure 5C**.

undergone plastic deformation and even partial melting at relatively higher crustal temperatures, thereby forming the S-wave LVZs in the middle crust.

Moreover, the gases and fluids originating from activities involving the upper mantle and the lower crust caused a series of geodynamic activities in the crust of the study area. Microearthquake activities, including single events and earthquake swarms, frequently occur in western Bohemia/Vogtland, with the depths of the microearthquake hypocenters varying between 3 and 23 km (Horálek et al., 2000). The Novy Kostel focal zone (near seismic station NKC shown in **Figures 14A,B**) is dominant throughout the whole region of the West Bohemia/Vogtland earthquake swarms. The foci of the microearthquakes in the Novy Kostel focal zone occur at depths of 6–11 km (Fischer and Horálek, 2000). These focal depths may be related to the uppermost mid-crustal S-wave LVZ beneath the study area. The crustal fluids in the Western Bohemia/Vogtland play a key role in bringing the faults from the subcritical to the critical state, which triggers the earthquake swarms in this region (Horálek and Fischer, 2008). Fluids in the crust can lower the S-wave velocity, which may be one explanation for these mid-crustal S-wave LVZs. Špičák et al. (1999) suggested that the earthquake swarms in the western Bohemian Massif may be caused by the magma intrusions and related fluid and gas release at depths of ~10 km. The plasticity and presence of partial melting in the fluid-rich mid-crust resulting in

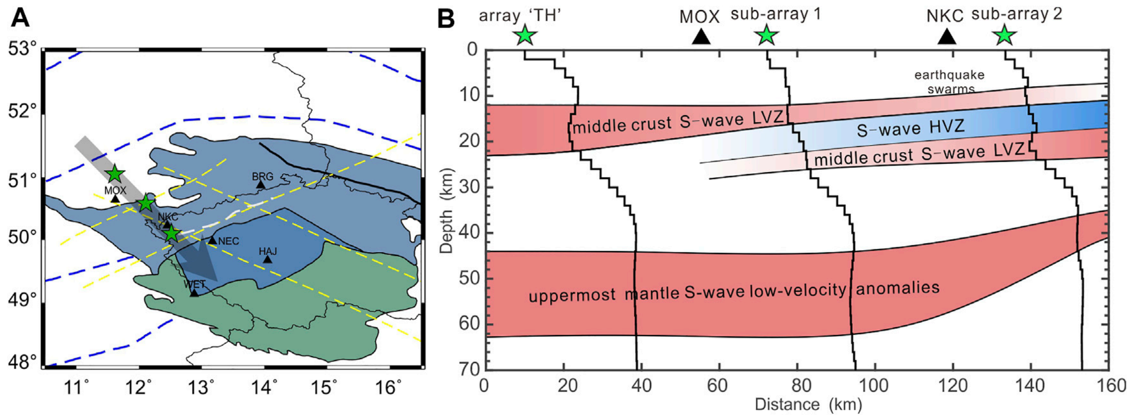

FIGURE 14 | Location of the profile and low-velocity distribution **(A)** The three green pentagrams are the center positions of array "TH", subarray 1, and subarray 2. **(B)** A simple schematic diagram depicting the distribution of the S-wave LVZs in the middle crust and the S-wave low-velocity anomalies in the uppermost mantle along the profile. The earthquake swarms beneath the station NKC occur at depths of 6–11 km.

the S-wave LVZs, which could be responsible for the origin and foci depth distribution of earthquake swarms in the study area.

CONCLUSION

In the northwestern Bohemian Massif and adjacent areas, the F-J method was employed to extract up to five higher-mode dispersion curves in addition to the fundamental-mode dispersion curve. The joint inversion of these fundamental-mode and higher-mode dispersion curves improved the vertical resolution of the velocity structure inversion results, allowing us to obtain high-resolution S-wave velocity models of the crust and uppermost mantle beneath the study area. Based on our models, we report the following novel insights:

1. Introducing higher-mode dispersion curves on the basis of the fundamental-mode dispersion curve is crucial to constrain the structure of the entire crust in the study area;
2. The general S-wave velocity level of the crust in the study area is higher than that in the models from Kvapil et al. (2021), which supports the views of previous studies (Růžek et al., 2016; Kästle et al., 2018; Lu et al., 2018);
3. The S-wave velocity of the crust in the study area is relatively high at depths of ~30–40 km;
4. The S-wave LVZs are distributed mainly in the middle crust of the study area (~10–20 km) rather than the lower crust (e.g., Kvapil et al., 2021);
5. On the western side of the study area, there are two obvious LVZs in the middle crust which are separated by the HVZ, which is different from the crustal S-wave velocity models of previous studies (e.g., Wilde-Piórko et al., 2005; Růžek et al., 2016; Kästle et al., 2018; Lu et al., 2018; Kvapil et al., 2021).

The mid-crustal S-wave LVZs in the northwestern Bohemian Massif and its adjacent areas may be the consequence of crustal fluids, plastic deformation and even partial melting of the felsic middle crust at relatively high crustal temperatures. Furthermore, these S-wave LVZs could be responsible for the origin and foci depth distribution of earthquake swarms in the study area. In addition, we observed S-wave low-velocity anomalies in the uppermost mantle, especially near the Eger Rift, which may be related to partial melting in the mantle or the upwelling of materials from the lithosphere-asthenosphere transition zone. These S-wave models based on the joint inversion of multimodal dispersion curves can provide new references for understanding the tectonic activity and geodynamic evolution of the northwestern Bohemian Massif and adjacent areas. Moreover, considering the recent discovery of a widespread mid-crustal low-velocity layer beneath Northeast China (Zhan et al., 2020), the existence of a mid-crustal LVZ may be a common feature in tectonically active areas. Considerable in-depth research is needed to confirm this speculation.

DATA AVAILABILITY STATEMENT

The datasets analyzed for this study can be found in the GEOFON Data Center (http://geofon.gfzpotsdam.de/fdsnws/dataselect/1/) and BGR Data Center (http://eida.bgr.de/fdsnws/dataselect/1/).

AUTHOR CONTRIBUTIONS

The specific contributions of each author are as follows. QM: Conceptualization, Software, Writing–Original Draft, Validation, Data Curation, Investigation, Visualization; LP: Methodology, Software, Validation, Investigation, Visualization; J-nW: Methodology, Software; ZY: Software, Visualization; XC: Conceptualization, Methodology, Writing–Review; Editing, Resources, Supervision, Project administration. All authors read and approved the final manuscript.

FUNDING

This work was supported by National Natural Science Foundation of China (Grant Nos U1901602, 41790465), Key Special Project for Introduced Talents Team of Southern Marine Science and Engineering Guangdong Laboratory (Guangzhou) (GML2019ZD0203), Shenzhen Key Laboratory of Deep Offshore Oil and Gas Exploration Technology (Grant No. ZDSYS20190902093007855), Shenzhen Science and Technology Program (Grant No. KQTD20170810111725321), the leading talents of Guangdong province program (Grant No. 2016LJ06N652).

SUPPLEMENTARY MATERIAL

The Supplementary Material for this article can be found online at: https://www.frontiersin.org/articles/10.3389/feart.2022.838751/full#supplementary-material

REFERENCES

Babuska, V., Plomerova, J., Vecsey, L., Jedlicka, P., and Ruzek, B. (2005). Non-Reviewed Contribution: Ongoing Passive Seismic Experiments Unravel Deep Lithosphere Structure of the Bohemian Massif. *Stud. Geophys. Geod.* 49, 423–430. doi:10.1007/s11200-005-0018-0

Babuška, V., Růžek, B., and Dolejš, D. (2016). Origin of Earthquake Swarms in the Western Bohemian Massif: Is the Mantle CO2 Degassing, Followed by the Cheb Basin Subsidence, an Essential Driving Force? *Tectonophysics* 668-669, 42–51. doi:10.1016/j.tecto.2015.12.008

Bensen, G. D., Ritzwoller, M. H., Barmin, M. P., Levshin, A. L., Lin, F., Moschetti, M. P., et al. (2007). Processing Seismic Ambient Noise Data to Obtain Reliable Broad-Band Surface Wave Dispersion Measurements. *Geophys. J. Int.* 169, 1239–1260. doi:10.1111/j.1365-246X.2007.03374.x

Beyreuther, M., Barsch, R., Krischer, L., Megies, T., Behr, Y., and Wassermann, J. (2010). ObsPy: A Python Toolbox for Seismology. *Seismological Res. Lett.* 81, 530–533. doi:10.1785/gssrl.81.3.530

Byrd, R. H., Lu, P., Nocedal, J., and Zhu, C. (1995). A Limited Memory Algorithm for Bound Constrained Optimization. *SIAM J. Sci. Comput.* 16, 1190–1208. doi:10.1137/0916069

Čermak, V. (1976). Heat flow map of the Bohemian Massif. *Journal of Geophysics*, 42(1), 455–458. Retrieved from https://journal.geophysicsjournal.com/JofG/article/view/195

Chen, X. (1993). A Systematic and Efficient Method of Computing normal Modes for Multilayered Half-Space. *Geophys. J. Int.* 115, 391–409. doi:10.1111/j.1365-246X.1993.tb01194.x

Enderle, U., Schuster, K., Prodehl, C., Schulze, A., and Bribach, J. (1998). The Refraction Seismic experiment GRANU95 in the Saxothuringian belt, southeastern Germany. *Geophys. J. Int.* 133, 245–259. doi:10.1046/j.1365-246X.1998.00462.x

Fischer, T., and Horálek, J. (2000). Refined Locations of the Swarm Earthquakes in the Nový Kostel Focal Zone and Spatial Distribution of the January 1997 Swarm in Western Bohemia, Czech Republic. *Stud. Geophys. Geod.* 44, 210–226. doi:10.1023/A:1022162826079

Fischer, T., and Horálek, J. (2003). Space-time Distribution of Earthquake Swarms in the Principal Focal Zone of the NW Bohemia/Vogtland Seismoactive Region: Period 1985-2001. *J. Geodynamics* 35, 125–144. doi:10.1016/S0264-3707(02)00058-3

Förster, A., and Förster, H.-J. (2000). Crustal Composition and Mantle Heat Flow: Implications from Surface Heat Flow and Radiogenic Heat Production in the Variscan Erzgebirge (Germany). *J. Geophys. Res.* 105, 27917–27938. doi:10.1029/2000JB900279

Grad, M., Guterch, A., Mazur, S., Keller, G. R., Špičák, A., Hrubcová, P., et al. (2008). Lithospheric Structure of the Bohemian Massif and Adjacent Variscan belt in central Europe Based on Profile S01 from the SUDETES 2003 experiment. *J. Geophys. Res.* 113, B10304. doi:10.1029/2007JB005497

Guy, A., Edel, J.-B., Schulmann, K., Tomek, Č., and Lexa, O. (2011). A Geophysical Model of the Variscan Orogenic Root (Bohemian Massif): Implications for Modern Collisional Orogens. *Lithos* 124, 144–157. doi:10.1016/j.lithos.2010.08.008

Haney, M. M., and Tsai, V. C. (2017). Perturbational and Nonperturbational Inversion of Rayleigh-Wave Velocities. *Geophysics* 82, F15–F28. doi:10.1190/geo2016-0397.1

Hansen, P. C. (2001). "The L-Curve and its Use in the Numerical Treatment of Inverse Problems," in *Computational Inverse Problems in Electrocardiology*. ed. P. Johnston (Southampton: WIT Press), 119–142.

Heuer, B., Geissler, W. H., Kind, R., and Kämpf, H. (2006). Seismic Evidence for Asthenospheric Updoming beneath the Western Bohemian Massif, central Europe. *Geophys. Res. Lett.* 33, 1–4. doi:10.1029/2005GL025158

Horálek, J., Fischer, T., Boušková, A., and Jedlička, P. (2000). The Western Bohemia/Vogtland Region in the Light of the Webnet Network. *Stud. Geophys. Geod.* 44, 107–125. doi:10.1023/A:1022198406514

Horálek, J., and Fischer, T. (2008). Role of Crustal Fluids in Triggering the West Bohemia/Vogtland Earthquake Swarms: Just what We Know (A Review). *Stud. Geophys. Geod.* 52, 455–478. doi:10.1007/s11200-008-0032-0

Hrubcová, P., Środa, P., and CELEBRATION 2000 Working Group (2008). Crustal Structure at the Easternmost Termination of the Variscan belt Based on CELEBRATION 2000 and ALP 2002 Data. *Tectonophysics* 460, 55–75. doi:10.1016/j.tecto.2008.07.009

Hrubcová, P., Środa, P., Grad, M., Geissler, W. H., Guterch, A., Vozár, J., et al. (2010). From the Variscan to the Alpine Orogeny: Crustal Structure of the Bohemian Massif and the Western Carpathians in the Light of the SUDETES 2003 Seismic Data. *Geophys. J. Int.* 183, 611–633. doi:10.1111/j.1365-246X.2010.04766.x

Hrubcová, P., Środa, P., Špičák, A., Guterch, A., Grad, M., Keller, G. R., et al. (2005). Crustal and Uppermost Mantle Structure of the Bohemian Massif Based on CELEBRATION 2000 Data. *J. Geophys. Res.* 110, 1–21. doi:10.1029/2004JB003080

Jena, F. S. U. (2009). "Thüringer Seismologisches Netz (TSN)," in *International Federation of Digital Seismograph Networks*. doi:10.7914/SN/TH

Karousová, H., Plomerová, J., and Vecsey, L. (2012). Seismic Tomography of the Upper Mantle beneath the north-eastern Bohemian Massif (central Europe). *Tectonophysics* 564-565, 1–11. doi:10.1016/j.tecto.2012.06.031

Kästle, E. D., El-Sharkawy, A., Boschi, L., Meier, T., Rosenberg, C., Bellahsen, N., et al. (2018). Surface Wave Tomography of the Alps Using Ambient-Noise and Earthquake Phase Velocity Measurements. *J. Geophys. Res. Solid Earth* 123, 1770–1792. doi:10.1002/2017JB014698

Knapmeyer-Endrun, B., Kruger, F., and Group, t. P. W.the PASSEQ Working Group (2014). Moho Depth across the Trans-European Suture Zone from P- and S-Receiver Functions. *Geophys. J. Int.* 197, 1048–1075. doi:10.1093/gji/ggu035

Kolínský, P., and Brokešová, J. (2007). The Western Bohemia Uppermost Crust Shear Wave Velocities from Love Wave Dispersion. *J. Seismol.* 11, 101–120. doi:10.1007/s10950-006-9040-0

Kolínský, P., Málek, J., and Brokešová, J. (2011). Shear Wave Crustal Velocity Model of the Western Bohemian Massif from Love Wave Phase Velocity Dispersion. *J. Seismol.* 15, 81–104. doi:10.1007/s10950-010-9209-4

Kvapil, J., Plomerová, J., Kampfová Exnerová, H., Babuška, V., Hetényi, G., and Group, A. W. (2021). Transversely Isotropic Lower Crust of Variscan central Europe Imaged by Ambient Noise Tomography of the Bohemian Massif. *Solid Earth* 12, 1051–1074. doi:10.5194/se-12-1051-2021

Li, Z., Zhou, J., Wu, G., Wang, J., Zhang, G., Dong, S., et al. (2021). CC-FJpy: A Python Package for Extracting Overtone Surface-Wave Dispersion from Seismic Ambient-Noise Cross Correlation. *Seismological Res. Lett.* 92, 3179–3186. doi:10.1785/0220210042

Lu, Y., Stehly, L., and Paul, A.AlpArray Working Group (2018). High-resolution Surface Wave Tomography of the European Crust and Uppermost Mantle from Ambient Seismic Noise. *Geophys. J. Int.* 214, 1136–1150. doi:10.1093/gji/ggy188

Marone, F., Van Der Lee, S., and Giardini, D. (2004). Three-dimensional Upper-mantleS-Velocity Model for the Eurasia-Africa Plate Boundary Region. *Geophys. J. Int.* 158, 109–130. doi:10.1111/j.1365-246X.2004.02305.x

Matte, P. (2001). The Variscan Collage and Orogeny (480-290 Ma) and the Tectonic Definition of the Armorica Microplate: a Review. *Terra Nova* 13, 122–128. doi:10.1046/j.1365-3121.2001.00327.x

Mousavi, S., Haberland, C., Bauer, K., Hejrani, B., and Korn, M. (2017). Attenuation Tomography in West Bohemia/Vogtland. *Tectonophysics* 695, 64–75. doi:10.1016/j.tecto.2016.12.010

Novotný, M. (2012). Depth-Recursive Tomography of the Bohemian Massif at the CEL09 Transect-Part B: Interpretation. *Surv. Geophys.* 33, 243–273. doi:10.1007/s10712-011-9155-x

Pan, L., Chen, X., Wang, J., Yang, Z., and Zhang, D. (2019). Sensitivity Analysis of Dispersion Curves of Rayleigh Waves with Fundamental and Higher Modes. *Geophys. J. Int.* 216, 1276–1303. doi:10.1093/gji/ggy479

Plomerová, J., Achauer, U., Babuška, V., and Granet, M. (2003). BOHEMA 2001-2003: Passive Seismic Experiment to Study Lithosphere-Asthenosphere System in the Western Part of the Bohemian Massif. *Stud. Geophys. Geod.* 47, 691–701. doi:10.1023/A:1024784223048

Plomerová, J., Achauer, U., Babuška, V., and Vecsey, L.BOHEMA working group (2007). Upper Mantle beneath the Eger Rift (Central Europe): Plume or Asthenosphere Upwelling. *J. Int.* 169, 675–682. doi:10.1111/j.1365-246X.2007.03361.x

Plomerová, J., Vecsey, L., and Babuška, V. (2012). Mapping Seismic Anisotropy of the Lithospheric Mantle beneath the Northern and Eastern Bohemian Massif (central Europe). *Tectonophysics* 564-565, 38–53. doi:10.1016/j.tecto.2011.08.011

Růžek, B., Vavryčuk, V., Hrubcová, P., Zedník, J., Guterch, A., Grad, M., et al. (2003). Crustal Anisotropy in the Bohemian Massif, Czech Republic: Observations Based on Central European Lithospheric Experiment Based on Refraction (CELEBRATION) 2000. *J. Geophys. Res.* 108. 1–15. doi:10.1029/2002JB002242

Růžek, B., Hrubcová, P., Novotný, M., Špičák, A., and Karousová, O. (2007). Inversion of Travel Times Obtained during Active Seismic Refraction Experiments CELEBRATION 2000, ALP 2002 and SUDETES 2003. *Stud. Geophys. Geod.* 51, 141–164. doi:10.1007/s11200-007-0007-6

Růžek, B., Valentová, L., and Gallovič, F. (2016). Significance of Geological Units of the Bohemian Massif, Czech Republic, as Seen by Ambient Noise Interferometry. *Pure Appl. Geophys.* 173, 1663–1682. doi:10.1007/s00024-015-1191-x

Špičák, A., Horálek, J., Boušková, A., Tomek, Č., and Vaněk, J. (1999). Magma Intrusions and Earthquake Swarm Occurrence in the Western Part of the Bohemian Massif. *Stud. Geophys. Geod.* 43, 87–106. doi:10.1023/A:1023366210017

Valentová, L., Gallovič, F., and Maierová, P. (2017). Three-dimensional S-Wave Velocity Model of the Bohemian Massif from Bayesian Ambient Noise Tomography. *Tectonophysics* 717, 484–498. doi:10.1016/j.tecto.2017.08.033

Wang, J., Wu, G., and Chen, X. (2019). Frequency-Bessel Transform Method for Effective Imaging of Higher-Mode Rayleigh Dispersion Curves from Ambient Seismic Noise Data. *J. Geophys. Res. Solid Earth* 124, 3708–3723. doi:10.1029/2018JB016595

Wessel, P., Smith, W. H. F., Scharroo, R., Luis, J., and Wobbe, F. (2013). Generic Mapping Tools: Improved Version Released. *Eos Trans. AGU* 94, 409–410. doi:10.1002/2013EO450001

Wilde-Piórko, M., Saul, J., and Grad, M. (2005). Differences in the Crustal and Uppermost Mantle Structure of the Bohemian Massif from Teleseismic Receiver Functions. *Stud. Geophys. Geod.* 49, 85–107. doi:10.1007/s11200-005-1627-3

Wu, G. x., Pan, L., Wang, J. n., and Chen, X. (2020). Shear Velocity Inversion Using Multimodal Dispersion Curves from Ambient Seismic Noise Data of USArray Transportable Array. *J. Geophys. Res. Solid Earth* 125, e2019JB018213. doi:10.1029/2019JB018213

Zhan, W., Pan, L., and Chen, X. (2020). A Widespread Mid-crustal Low-Velocity Layer beneath Northeast China Revealed by the Multimodal Inversion of Rayleigh Waves from Ambient Seismic Noise. *J. Asian Earth Sci.* 196, 104372. doi:10.1016/j.jseaes.2020.104372

Conflict of Interest: The authors declare that the research was conducted in the absence of any commercial or financial relationships that could be construed as a potential conflict of interest.

frontiers in Earth Science

METHODS
published: 31 March 2022
doi: 10.3389/feart.2022.855015

Releasing the Time Step Upper Bound of CFL Stability Condition for the Acoustic Wave Simulation With Model-Order Reduction

Yingjie Gao[1,2], *Meng-Hua Zhu*[1,2] *and Huai Zhang*[3,4]*

[1]State Key Laboratory of Lunar and Planetary Sciences, Macau University of Science and Technology, Macau, China, [2]CNSA Macau Center for Space Exploration and Science, Macau, China, [3]Key Laboratory of Computational Geodynamics, Chinese Academy of Sciences, Beijing, China, [4]College of Earth and Planetary Sciences, University of Chinese Academy of Sciences, Beijing, China

The maximum time step size for the explicit finite-difference scheme complies with the Courant–Friedrichs–Lewy (CFL) stability condition, which essentially restricts the optimization and tuning of the communication-intensive massive seismic wave simulation in a parallel manner. This study brings forward the model-order reduction (MOR) method to simulate acoustic wave propagation. It briefly takes advantage of the update matrix's eigenvalues and the expansion coefficients of the variables for the time in the semi-discrete scheme of the wave equation, reducing the computational complexity and enhancing its computing efficiency. Moreover, we introduced the eigenvalue abandonment and eigenvalue perturbation methods to stabilize the unstable oscillations when the time step size breaks the CFL stability upper bound. We then introduced the time-dispersion transform method to eliminate the time-dispersion error caused by the large time step and secure the high accuracy. Numerical experiments exhibit that the MOR method, in conjunction with eigenvalue abandonment (and the eigenvalue perturbation) and the time-dispersion transform method, can capture highly accurate waveforms even when the time step size exceeds the CFL stability condition. The eigenvalue perturbation method is suitable for strongly heterogenous media and can maintain the numerical accuracy and stability even when the time step size is toward the upper bound of the Nyquist sampling.

Keywords: explicit finite-difference scheme, CFL stability upper bound, model-order reduction, time-dispersion error, eigenvalue operation

Edited by:
Weijia Sun,
Institute of Geology and Geophysics (CAS), China

Reviewed by:
Wei Wei,
Institute of Geology and Geophysics (CAS), China
Weijuan Meng,
Tsinghua University, China

Correspondence:
Huai Zhang
hzhang@ucas.ac.cn

Specialty section:
This article was submitted to Solid Earth Geophysics, a section of the journal Frontiers in Earth Science

Received: *14 January 2022*
Accepted: *02 March 2022*
Published: *31 March 2022*

Citation:
Gao Y, Zhu M-H and Zhang H (2022) Releasing the Time Step Upper Bound of CFL Stability Condition for the Acoustic Wave Simulation With Model-Order Reduction.
Front. Earth Sci. 10:855015.
doi: 10.3389/feart.2022.855015

INTRODUCTION

Numerical simulation of seismic wavefields is an important technical means to understand the law of seismic wave propagation and imaging underground complex structures. It is an essential theoretical basis for seismological research and plays an important role in seismology. Simulating the propagation of seismic waves by solving wave equations is the most widely used numerical simulation method. The explicit finite-difference (FD) scheme, the method of explicitly iterating the wavefield in the time domain, is widely used in seismic wavefield numerical simulation due to its simplicity (Etgen and O'Brien, 2007). The size of the time step can directly affect the calculation efficiency of the explicit FD scheme. For a given length of wavefield propagation time, a larger time step means fewer iterations than a smaller time step, which can improve the calculation efficiency. For the explicit FD scheme, two difficulties are observed when a large time step is adopted. First, the numerical simulation using a large time step leads to a numerical dispersion error, which can cause inaccurate amplitude and inaccurate phase information of the simulated seismic waveforms (i.e., time-dispersion error). Second, the time step size must be strictly limited by the Courant–Friedrichs–Lewy (CFL) stability condition (Courant et al., 1928), and a small time step must be accepted in practice to guarantee a stable numerical scheme for the numerical simulation of small-scale structures or high-velocity targets. Especially in the fine structure simulation, the small spatial grid makes the time step even smaller and increases computing complexity. Therefore, finding efficient large time-step numerical algorithms while ensuring the accuracy and stability has become a research hotspot in the field of seismic wavefield numerical simulation in recent years (Stork, 2013; Wang and Xu, 2015; Gao et al., 2016; Koene et al., 2018; Liu, 2020).

As mentioned before, to use a large time step for numerical simulation, the first problem to be handled is to eliminate the time-dispersion error caused by a large time step. In this aspect, researchers have conducted numerous studies in order to suppress the time-dispersion error; for a detailed review refer to Wang and Xu (2015) and Gao et al. (2016). A couple of previous methods for eliminating the time-dispersion error are achieved using higher precision temporal discretization schemes (Dablain, 1986; Kosloff et al., 1989; Chen, 2007; Song and Fomel, 2011). Stork (2013) demonstrated that the time-dispersion error only depends on the frequency, time step size, and total propagation time. The time-dispersion error is independent of both the velocity model and the space dispersion. Therefore, the time dispersion can be handled separately from the space dispersion without considering velocity variations. Based on these theories, Stork (2013) proposed a novel idea to eliminate the time-dispersion error: it is predictable and can be removed by a time-varying filter and interpolation after FD modeling (Dai et al., 2014; Liu et al., 2014; Li et al., 2016).

As a further development of Stork's work, Wang and Xu (2015) constructed analytical time-varying filters with a conventional explicit FD scheme, entitled the time-dispersion transform method. This method includes a time-dispersion prediction algorithm (forward time-dispersion transform, FTDT) and a time-dispersion elimination algorithm (inverse time-dispersion transform, ITDT) to add and remove the time-dispersion error flexibly. Koene et al. (2018) modified the FTDT algorithm and constructed a complete process to remove time-dispersion error for seismic wave numerical simulation by applying FTDT to the source time function before the simulation and applying ITDT to the output waveforms after the simulation. FTDT is preprocessing and ITDT is post-processing, neither of which participates in the iteration of the wavefield and does not affect the main body of the wavefield numerical simulation. The time-dispersion transform method can effectively eliminate the time-dispersion error and can provide a guaranteed accuracy for numerical simulation using a large time step. The total calculation amount of the simulation is less than that of the conventional wavefield simulation with the same accuracy.

The time-dispersion transform method allows us to use a time step size close to the stability condition for numerical simulation without worrying about the inaccuracy caused by the time-dispersion error (Gao et al., 2016; Koene et al., 2018). Then the CFL stability condition becomes the main limitation if a large time step for the explicit FD scheme is used. In recent years, researchers turn to figure out appropriate numerical strategies for releasing the time step size beyond the CFL stability upper bound, which certainly draws attention in the seismic simulation community.

Ecer et al. (2000) proposed that when a time step was beyond the CFL stability upper bound, the unstable component would appear in the high-wavenumber region. Therefore, the instability of the high-wavenumber region can be measured by a spatial filtering algorithm and using a low-pass filter to filter out the unstable components generated in the high-wavenumber area. Later on, Sarris (2011) adopted the spatial filtering algorithm to solve the instability problem for solving Maxwell's equation in the field of electromagnetic wave numerical simulation. Also, the time step of the explicit FD scheme can be successfully released beyond the CFL stability upper bound (Chang and Sarris, 2011; Chang and Sarris, 2012, 2013).

In the field of electromagnetic wave numerical simulation, He et al. (2012) proposed an unconditionally stable method by eigenvalue operation of the updated matrix based on the explicit FD scheme. Gaffar and Jiao (2014, 2015) analyzed the instability when using a time step that exceeds the CFL stability condition of the explicit FD scheme. The unstable eigenvalues are then abandoned from the initial numerical system before the explicit time iteration (Yan and Jiao, 2017), called the eigenvalue abandonment algorithm. Li et al. (2014) implemented the unconditionally stable method by perturbing the modulus of the unstable eigenvalues to be stable, instead of abandoning them, which is called the eigenvalue perturbation algorithm (Li, 2014). Since both methods of removing and perturbing the unstable eigenvalues are preprocessing algorithms, they have little effect on the calculation amount of the wavefield iteration process.

Inspired by the abovementioned explicit unconditionally stable numerical simulation methods, Gao et al. (2018, 2019) introduced the eigenvalue perturbation method and the spatial filtering method to seismic wave numerical simulation, respectively. Meanwhile, the time-dispersion error caused by a large time step was successfully eliminated by the time-dispersion transform method. The combination of eigenvalue perturbation and the time-dispersion transform method is suitable for strong heterogenous media. It can extend the available time step size toward the upper bound of the Nyquist sampling, saving many iterations while ensuring the calculation accuracy (Gao et al., 2018; Lyu et al., 2021).

Although the unconditionally stable algorithms for the explicit FD scheme have been applied in seismic wave numerical simulation, the related algorithms still need to be further modified and improved. The spatial filtering method bears the risk of unreluctantly filtering out the effective wavenumber when the wave propagates at a low velocity but in a strong heterogenous media. The abovementioned eigenvalue operation algorithms are all implemented based on discretizing the wave equation using a global matrix-form operator, which requires a huge amount of memory and computation during the temporal iteration progress of the wavefield for the numerical simulation. Meanwhile, to our knowledge, no literature that compares the effects of the eigenvalue abandonment algorithm and the eigenvalue perturbation algorithm is available to date, neither the selection criteria on how to choose these two methods.

In order to avoid the calculation of the global update-matrix operators during the wavefield iteration progress for the abovementioned eigenvalue operation algorithms, people adopted the model-order reduction (MOR) method (Remis and Van den Berg, 1998; Freund, 2004). The MOR method is implemented by the Krylov subspace projection of the space discretized dynamical system, which can project the original higher-state subspace into a significantly reduced-state subspace. This method captures the most influential eigenvalues of the dynamical system and can guarantee the dynamics of interest with sufficient accuracy. The MOR method has been widely used in the field of numerical simulation for electromagnetic waves and can be well coupled with eigenvalue operation algorithms to release the time step upper bound of CFL stability condition (He et al., 2012; Li, 2014; Gaffar and Jiao, 2014, 2015; Chen et al., 2016; Zhang et al., 2017). The MOR method has also been applied in the field of seismic wavefield numerical simulation in recent years (Pereyra and Kaelin, 2008; Pereyra, 2013; Wu et al., 2013; Basir et al., 2015; Pereyra, 2016; Basir et al., 2018), while no related literature in the field of seismic wavefield numerical simulation discussed extending the limit of CFL stability condition based on the MOR method.

This study introduces the MOR method to solve the scalar wave equation. First, we applied the eigenvalue decomposition to the update matrix for the discrete wave equation based on a given time step. Then we used only the update matrix's eigenvalues and the expansion coefficients of the variables in the wave equation during the time step iteration. It can reduce the excessive dependence on the calculation memory for the wavefield iteration. To release the CFL stability upper bound, we brought forward the eigenvalue abandonment algorithm (He et al., 2012; Gaffar and Jiao, 2015) and the eigenvalue perturbation algorithm (Li, 2014; Gao et al., 2018; Lyu et al., 2021) to operate on the unstable eigenvalues of the update matrix, respectively. The workflows and characteristics of these two methods are introduced and compared in detail. The time-dispersion transform method is presented to eliminate the time-dispersion error caused by the large time step and ensure the accuracy of the numerical simulation (Wang and Xu, 2015; Koene et al., 2018). The FTDT is applied to the source time-discrete scheme during preprocessing, and the ITDT is applied to the seismic waveform during post-processing. Numerical experiments verify that the integration of the MOR method, the eigenvalue abandonment (and the eigenvalue perturbation), and the time-dispersion transform method can simulate highly accurate waveforms when a time step beyond the CFL stability upper bound is accepted. Our proposed numerical method is suitable for strong heterogenous media and can successfully surpass the time step size to the upper bound of the Nyquist sampling.

METHODOLOGY

Scalar Wave Equation and Its Discretization

Consider the following 2D scalar wave equation:

$$\frac{1}{c^2}\frac{\partial^2 u}{\partial t^2} = \frac{\partial^2 u}{\partial x^2} + \frac{\partial^2 u}{\partial z^2} + s, \tag{1}$$

where u and c are the wavefield and the propagation velocity, respectively, and s is the source term. With the second-order finite-difference (FD) method for the temporal discretization, the matrix form of **Eq. 1** can be written as (Gao et al., 2018) follows:

$$U^{n+1} - 2U^n + U^{n-1} = \mathbf{M}U^n + \bar{S}^{\,n}, \tag{2}$$

where U^{n+1} and U^n represent the column vectors that collect the value of the wavefields at all grid nodes at the time $(n+1)\Delta t$ and $n\Delta t$, respectively; the column vector $\bar{S}^n = c^2\Delta t^2 S^n$ and S^n contains entries corresponding to the source location and source time function, respectively; and the size of the update matrix $\mathbf{M}$ is $(N_x \times N_z)^2$, where N_x and N_z are the grid numbers of discrete points along the x- and z-directions, respectively. After applying the Fourier transform in the time domain, the left-hand side of **Eq. 2** in the frequency domain can be expressed as (Gao et al., 2018) follows:

$$\left(e^{i\omega\Delta t} - 2 + e^{-i\omega\Delta t}\right)\tilde{U} = -4\sin^2\left(\frac{\omega\Delta t}{2}\right)\tilde{U}, \tag{3}$$

where $\tilde{U}$ represents the forward Fourier transform of the wavefield u. Obviously, the range of the left-hand side of **Eq. 2** is from −4 to 0. The matrix **M** is a semi-negative definite matrix, and its eigenvalues are non-positive real numbers (Gaffar and Jiao, 2014; Li, 2014; Gao et al., 2018; Lyu et al., 2021). Therefore, the CFL stability upper bound for **Eq. 2** is obtained by requiring $|\varepsilon_i| \le 4$, where ε_i is the eigenvalue of the update matrix **M**, and the subscript i ranges from 1 to $(N_x \times N_z)^2$.

Model-Order Reduction

The MOR method can be realized by singular value decomposition (Pereyra and Kaelin, 2008; Li, 2014) or eigenvalue decomposition (Gaffar and Jiao, 2014, 2015; Basir et al., 2015, 2018). The former method can handle a non-square matrix, while the latter method can only handle a square matrix. The update matrix **M** is a square matrix, and it is completely applicable to eigenvalue decomposition, whose calculation is smaller and more concise than that of the singular value decomposition. Therefore, we adopted the eigenvalue decomposition method to implement the MOR method.

To introduce the MOR method, we first performed eigenvalue decomposition on the update matrix **M** as follows:

$$\mathbf{M} = \mathbf{V}\mathbf{E}\mathbf{V}^{-1}, \tag{4}$$

where the matrix **V** contains the eigenvectors V_i of matrix **M**, while E is a diagonal matrix whose entries are the eigenvalues ε_i of matrix **M**. We used the eigenvalues ε_i in matrix **E** to form a column vector E. Using the MOR method, **Eq. 2** can be abbreviated as follows:

$$A^{n+1} - 2A^n + A^{n-1} = E.*A^n + B^n, \tag{5}$$

where A^n and B^n are the column vector of expansion coefficients for U^n and $\overline{S}^n$, respectively; $U^n = \mathbf{V}A^n = \sum_i \alpha_i^n V_i$ and $\overline{S}^n = \mathbf{V}B^n = \sum_i \beta_i^n V_i$, where the expansion coefficients α_i^n and β_i^n are the ith element of the column vector A^n and B^n, respectively. V_i is the ith column vector of the eigenvector matrix **V**; the calculation symbol ".*" represents multiplying the corresponding elements for the column vectors on both sides.

Column vectors A^n, A^{n-1}, E, and B^n in **Eq. 5** are the input for the wavefield solving iteration, and A^{n+1} is the output for the iteration. After each iteration, we can obtain the updated wavefield by the following equation:

$$U^{n+1} = \mathbf{V}A^{n+1}. \tag{6}$$

The calculation of **Eq. 6** can output the global wavefield values, including all the spatial grid points. If we only need to output the wavefield values of a certain trace at a fixed point, we do not need to calculate **Eq. 6**. For example, to output the wave value at a fixed point $(x_{out},\ z_{out})$ (x_{out} and z_{out} are the corner marks along the x- and z-direction in the discrete coordinate, respectively), we can use the $[(z_{out}-1)\times N_x + x_{out}]$ th row vector in matrix **V** and multiply by A^{n+1}, whose calculation amount is very small.

The input expansion coefficients B^n for the source are obtained by $B^n = \mathbf{V}^{-1}\overline{S}^n$. Generally, the source is located at a fixed location, that is, the column vector $\overline{S}^n$ contains only one element s^n that corresponds to the source; other elements are all zero. The position of the element s^n determines the location of the source, and the value of the element s^n represents the value of the source time function at time $n\Delta t$. Source column vectors $\overline{S}^{n+1}$ and $\overline{S}^n$ at adjacent moments only have one different element with a scalar factor ratio α (e.g., $\overline{S}^{n+1} = \alpha\overline{S}^n$), which is determined by the amplitudes of the source time function at different times. Therefore, there is no need to perform the matrix calculation $B^n = \mathbf{V}^{-1}\overline{S}^n$ for each iteration. We only need to know the ratio α of the source time function at adjacent moments, and the expansion coefficients B^{n+1} can be obtained by $B^{n+1} = \alpha B^n$.

We can see that only the eigenvalues E of the updated matrix and the expansion coefficients A^n, A^{n-1}, and B^n (wavefield and source) in **Eq. 5** are used to do the iteration of wave propagation, which is just an iteration of the column vectors and greatly simplifies numerical simulation compared with **Eq. 2**.

Releasing the Time Step Upper Bound of the CFL Stability Condition

We used the fourth-order FD method for the spatial discretization of **M** in **Eq. 2**. Using the velocity c = 4,000 m/s and the spatial grid interval $\Delta x = \Delta z = h$ = 10 m, we can obtain the maximum time step $\Delta t_{\max}$ = 1.530 ms, according to the CFL stability condition for high-order FD schemes (Liu and Sen, 2009). For a time step Δt over $\Delta t_{\max}$, the discrete update matrix **M** will contain unstable eigenvalues (Li et al., 2014; Gao et al., 2018; Lyu et al., 2021). As shown in **Figure 1**, the eigenvalues of the discrete update matrix for Δt = 1 ms are all distributed in the range of 0 to −4, which means that all the eigenvalues are stable (Gao et al., 2018); in contrast, some eigenvalues of matrix **M** for the time step larger than $\Delta t_{\max}$ (e.g., Δt = 2, 3, 4, 5, 6, 7, 8, and 9 ms) are distributed outside of the range of 0 to −4 (the red zones showed in **Figure 1**). These eigenvalues, whose absolute values violate the basic requirement of $|\varepsilon_i| \leq 4$, cause unstable phenomena when $\Delta t > \Delta t_{\max}$. **Table 1** shows the number of stable eigenvalues for different time steps. We can see that after the time step exceeds $\Delta t_{\max}$, the number of stable eigenvalues decreases sharply as the time step increases (e.g., when Δt = 9 ms, only 965 stable eigenvalues exist, which is 2.39% of the total numbers 40401). To release the CFL stability upper bound on the time step, we introduced two kinds of operations for those unstable eigenvalues of matrix **M**: the eigenvalue abandonment algorithm and the eigenvalue perturbation algorithm.

Eigenvalue Abandonment

We used the eigenvalues ε_i in the diagonal matrix E to form a column vector E, which can be divided into two parts (He et al., 2012; Gaffar and Jiao, 2015) as follows:

$$E = \begin{bmatrix} E_s \\ E_u \end{bmatrix}, \tag{7}$$

where E_s is the column vector that consists of the stable eigenvalues, and E_u is the column vector that consists of the unstable eigenvalues. We classified the eigenvectors in matrix V according to **Eq. 7**, and matrix V can be expressed as follows:

$$\mathbf{V} = [\,\mathbf{V}_s \quad \mathbf{V}_u\,], \tag{8}$$

where matrix $\mathbf{V}_s$ and matrix $\mathbf{V}_u$ are composed of the eigenvectors $\mathbf{V}_i$ that correspond to the eigenvalues ε_i in E_s and E_u, respectively.

The eigenvalue abandonment algorithm (He et al., 2012; Gaffar and Jiao, 2015; Chen et al., 2016) is implemented by abandoning the unstable eigenvalues E_u and the corresponding eigenvectors $\mathbf{V}_u$; while only the column vector is composed of stable eigenvalues E_s, the corresponding eigenvector $\mathbf{V}_s$ participates in the iteration of wavefield calculation. After the eigenvalue abandonment operation, **Eq. 5** can be expressed as follows:

$$A_s^{n+1} - 2A_s^n + A_s^{n-1} = E_s.*A_s^n + B_s^n, \tag{9}$$

where the number of elements in the column vectors A_s^{n+1}, A_s^n, A_s^{n-1}, and B_s^n is equal to the number of elements in the column vector E_s. We can obtain the updated wavefield by $U^{n+1} = \mathbf{V}_s A_s^{n+1}$ after each iteration. The input expansion coefficients B_s^n for the source term are obtained by $B_s^n = \mathbf{V}_s^{-1}\overline{S}_s^n$. The whole workflow for the wavefield iteration using **Eq. 9** is shown in **Figure 2A**.

Eigenvalue Perturbation

For the detailed description for the eigenvalue perturbation process refer to Li et al. (2014) and Gao et al. (2018). Here, we introduced the eigenvalue perturbation algorithm combined

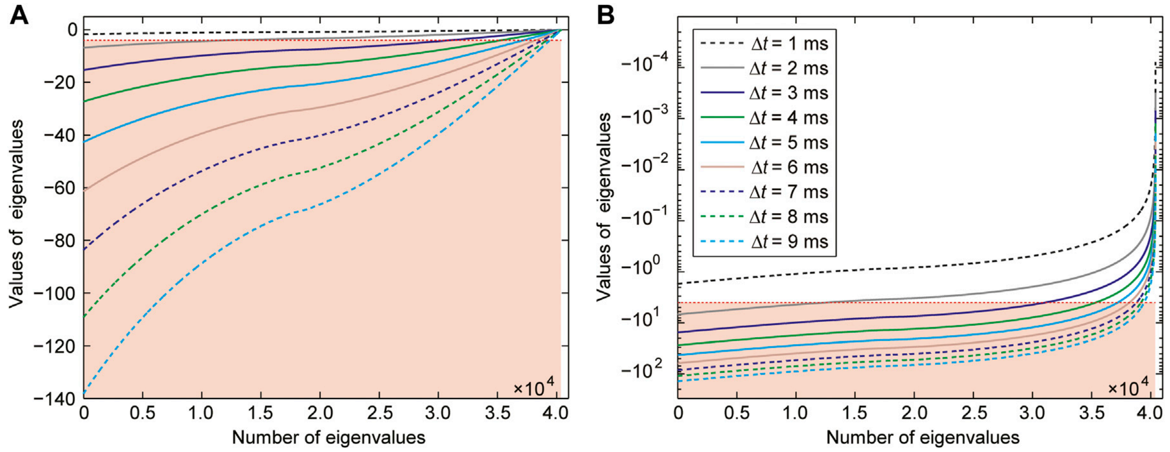

FIGURE 1 | Eigenvalues of the discrete update matrix **M** for different time steps. **(A)** The eigenvalues for time steps of Δt = 1, 2, 3, 4, 5, 6, 7, 8, and 9 ms. **(B)** Logarithmic display for the eigenvalues in **(A)**.

TABLE 1 | Number of stable eigenvalues for the discrete update matrix **M** for different time steps. The table is generated using the second-order temporal FD scheme and the fourth-order spatial FD scheme, with the velocity c = 4000 m/s and the spatial grid interval h = 10 m.

Total number of stable eigenvalues	Δt = 1 ms	Δt = 2 ms	Δt = 3 ms	Δt = 4 ms	Δt = 5 ms	Δt = 6 ms	Δt = 7 ms	Δt = 8 ms	Δt = 9 ms
40,401 (Δt ≤ 1.530 ms)	40,401	21,920	14,683	8,763	5,412	3,460	2,480	1,226	965

with the MOR method. The unstable eigenvalues of **M** (ε_i in column vector E_u) that violate $|\varepsilon_i| \le 4$ can be perturbed by the following :

$$\hat{\varepsilon}_i = \frac{4\varepsilon_i}{|\varepsilon_i|}. \tag{10}$$

In this way, the magnitude of the unstable eigenvalues is normalized to −4, which can guarantee the stability when using a time step beyond the CFL stability upper bound. The perturbed eigenvalues are collected to form a new column vector $\hat{E}_u$, which can form the new matrix column vector $\hat{E}$ with the originally stable eigenvalues column vector E_s, as follows:

$$\hat{E} = \begin{bmatrix} E_s \\ \hat{E}_u \end{bmatrix}. \tag{11}$$

After the eigenvalue perturbation operation, **Eq. 5** can be expressed as follows:

$$A^{n+1} - 2A^n + A^{n-1} = \hat{E}.*A^n + B^n. \tag{12}$$

The calculation process of **Eq. 12** is as same as that of **Eq. 5**, except for using $\hat{E}$ to replace E. The whole workflow for the wavefield iteration using **Eq. 12** is shown in **Figure 2B**.

Eliminating the Time-Dispersion Error

We used the time-dispersion transform method, which includes the forward time-dispersion transform (FTDT) algorithm and the inverse time-dispersion (ITDT) algorithm (Wang and Xu, 2015; Koene et al., 2018). For a detailed description of the time-dispersion transform method process refer to Koene et al. (2018). The whole workflow of the time-dispersion error elimination using the time-dispersion transform method is shown in **Figure 3**.

NUMERICAL EXPERIMENTS

Homogenous Model

We performed numerical experiments on a homogenous square model by the finite-difference time-domain method. The wave velocity is c = 4,000 m/s. The spatial grid interval is $\Delta x = \Delta z$ = 10 m, and the grid point number is 201 × 201. The source is a Ricker wavelet with a dominant frequency of 20 Hz, which is located at x = 1.0 km and z = 1.0 km. According to the CFL stability condition, the maximum time step for the second-order FD method in temporal discretization and fourth-order FD method in spatial discretization is $\Delta t_{\max}$ = 1.530 ms. We tested several large time steps (Δt = 2, 3, 4, 5, 6, 7, 8, and 9 ms) by **Eqs. 9–12**, where all time steps are beyond the CFL stability upper bound. We used the workflow in **Figure 3** to apply the time-dispersion transform method. To examine the results obtained by the different time steps, we performed numerical simulations using a short time step Δt = 1 ms, which is also applied by the time-dispersion transform method. The simulated waveforms can be regarded as theoretical references to examine the accuracy using larger time steps.

Figure 4 shows the waveforms recorded at x = 700 m and z = 700 m. Although the time steps exceed the CFL stability condition, no instability arises after applying the eigenvalue abandonment (shown in **Figure 4A**) and the eigenvalue

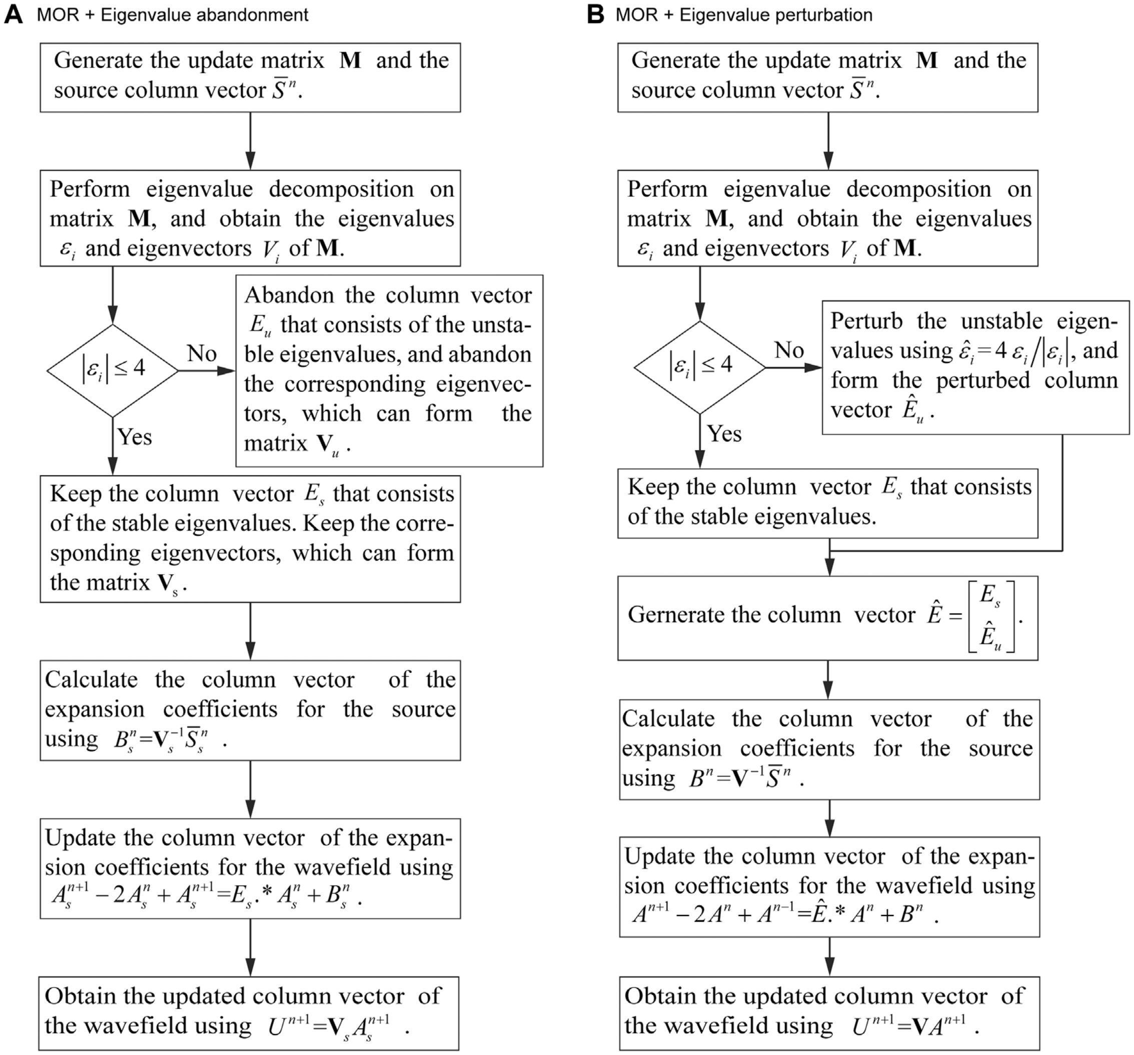

FIGURE 2 | Workflows for releasing the CFL stability limit on the time step for numerical simulation based on the MOR method using eigenvalue operations. **(A)** Workflow for the numerical simulation using eigenvalue abandonment. **(B)** Workflow for the numerical simulation using eigenvalue perturbation.

perturbation (shown in **Figure 4B**). It proves that the combination of the MOR, eigenvalue abandonment (and eigenvalue perturbation) algorithm, and time-dispersion transform methods can extend the CFL stability upper bound successfully.

The time-dispersion error using Δt = 2, 3, 4, 5, and 6 ms is invisible, as shown in **Figures 4A,B**. It indicates that integration of the MOR, eigenvalue abandonment (or eigenvalue perturbation) algorithm, and the time-dispersion transform method can provide highly accurate simulation results even when a much larger time step size beyond the CFL stability upper bound is used.

According to the Nyquist sampling theorem $\Delta t < 1/(2f_{\max})$ (Gaffar and Jiao, 2014; Gao et al., 2018), the time step size cannot be larger than 6.7 ms for the Ricker wavelet with a dominant frequency of 20 Hz, whose maximum frequency is about 75 Hz. Therefore, using Δt = 7 ms has exceeded the Nyquist sampling. Interestingly, starting from Δt = 7 ms, the results of the two processing methods are different. Although 7 ms has exceeded the Nyquist sample for the eigenvalue abandonment operation, the results still seem acceptable except for some slight error. We need to associate the eigenvalue abandonment with the spatial filtering method (Gao et al., 2019). Different eigenvalues of the updated matrix correspond to different wavenumbers: the unstable eigenvalues correspond to the wavefield that distributes in the high-wavenumber region, and stable eigenvalues correspond to the low-wavenumber region (Li, 2014). Abandoning the unstable eigenvalues is equivalent to filtering out the unstable wavefield components with a low-pass filter. The aliasing effect caused by insufficient sampling points (i.e., using a time step that exceeds the Nyquist sampling upper bound) is a high-frequency oscillation, which would be filtered out by a low-pass filtering operation.

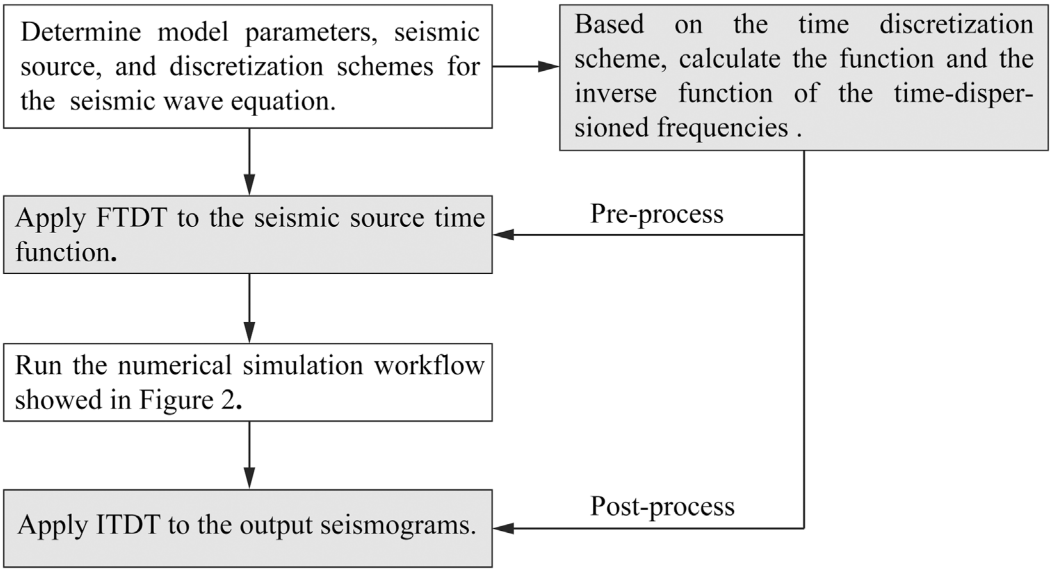

FIGURE 3 | Workflow for the time-dispersion error elimination using the time-dispersion transform method.

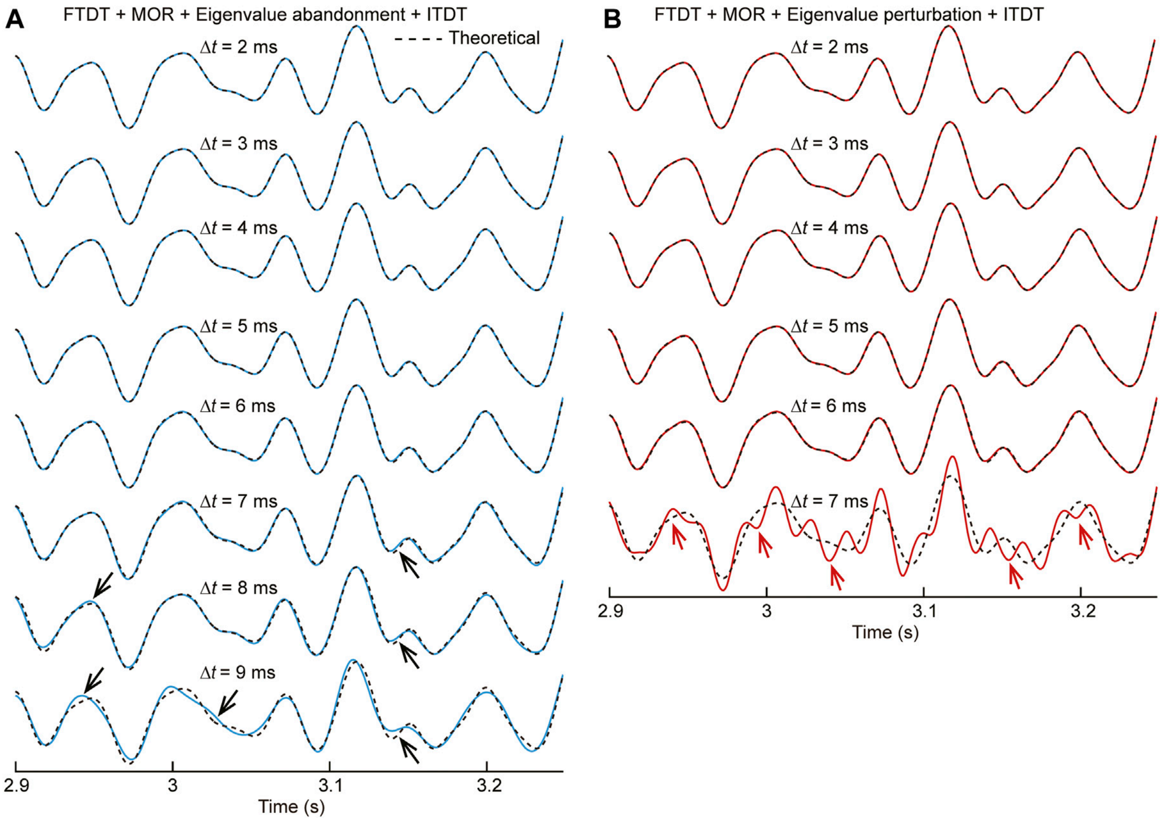

FIGURE 4 | Waveforms that are recorded at a fixed point (x = 700 m, z = 700 m) of the homogenous model using different time steps. The dashed curve obtained using Δt = 1 ms (with the time-dispersion transform method applied) is taken as the theoretical reference. Eight and six time steps are tested for eigenvalue abandonment and eigenvalue perturbation, respectively. The waveforms in **(A)** are obtained using the eigenvalue abandonment algorithm, and the waveforms in **(B)** are obtained using the eigenvalue perturbation algorithm. All the waveforms are the final results after the time-dispersion transform method has been applied according to the workflows showed in **Figure 3**.

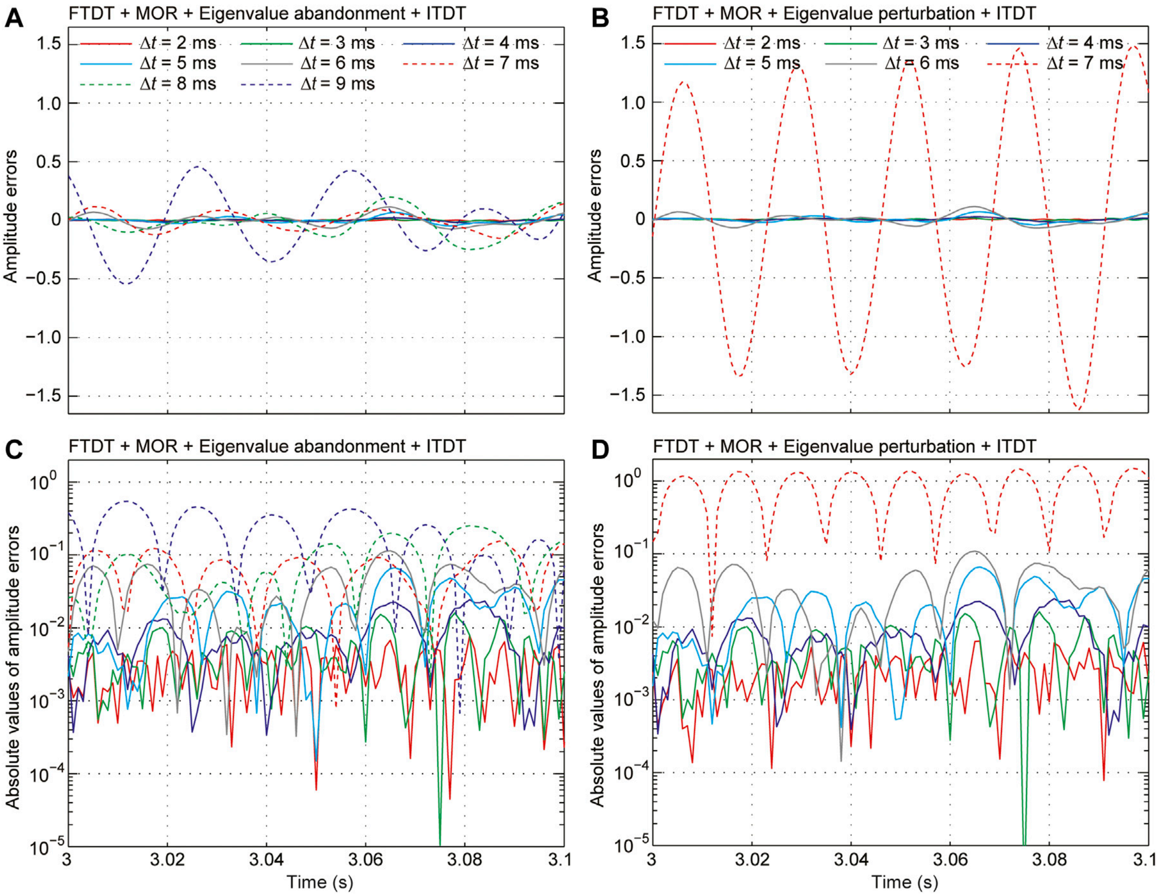

FIGURE 5 | Amplitude errors between the waveforms and the theoretical waveform showed in **Figure 4** (from 3 s to 3.1 s). The amplitude errors in **(A)** and **(B)** are obtained using the eigenvalue abandonment algorithm and the eigenvalue perturbation algorithm, respectively. **(C)** and **(D)** are logarithmic display for the absolute values of the amplitude errors in **(A)** and **(B)**, respectively.

In contrast, the eigenvalue perturbation operation is implemented by perturbing the unstable eigenvalues into stable eigenvalues, which is a normalized operation, rather than a low-pass filter. The high-frequency oscillation caused by insufficient sampling points will be retained. It can explain why the high-frequency oscillation exists resulting from the eigenvalue perturbation algorithm using $\Delta t = 7$ ms in **Figure 4B**.

Next, using the idea of spatial filtering, it is easy to explain the inaccuracy for the result obtained using $\Delta t = 9$ ms in **Figure 3A**. As the time step increases, the number of stable eigenvalues decreases dramatically (as shown in **Table 1**). It is equivalent to a sharp decrease in the threshold of the low-pass filter for spatial filtering. The effective seismic wavefield mainly distributes in a certain bandwidth of low wavenumber. The corresponding low-pass filter would filter out the effective wavefield distributes in the low-wavenumber regions for an excessively large time step. As a result, the wavefield information is incomplete. Even if the time-dispersion transform method is used, the result would still have errors.

We further analyzed the amplitude errors between the waveforms obtained by different time steps and the theoretical waveform (as shown in **Figure 5**). The time ranges from 3 to 3.1 s, which is an intermediate time period of the waveforms in **Figures 4**, **5C,D**, are logarithmic displays for the absolute values of the amplitude errors in **Figures 5A,B**, respectively. The amplitude errors increase with the increasing time step, but the errors are

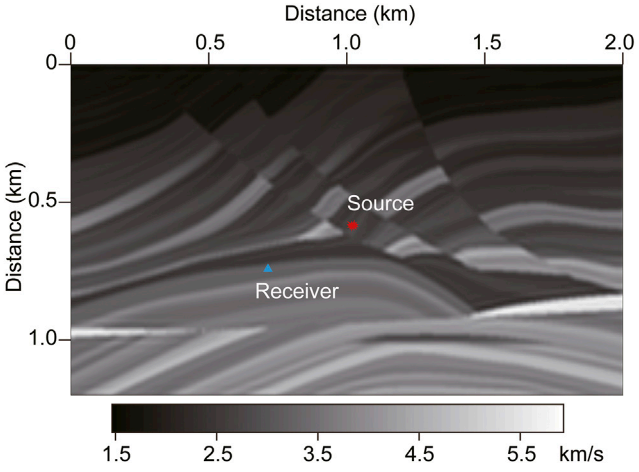

FIGURE 6 | Modified Marmousi model.

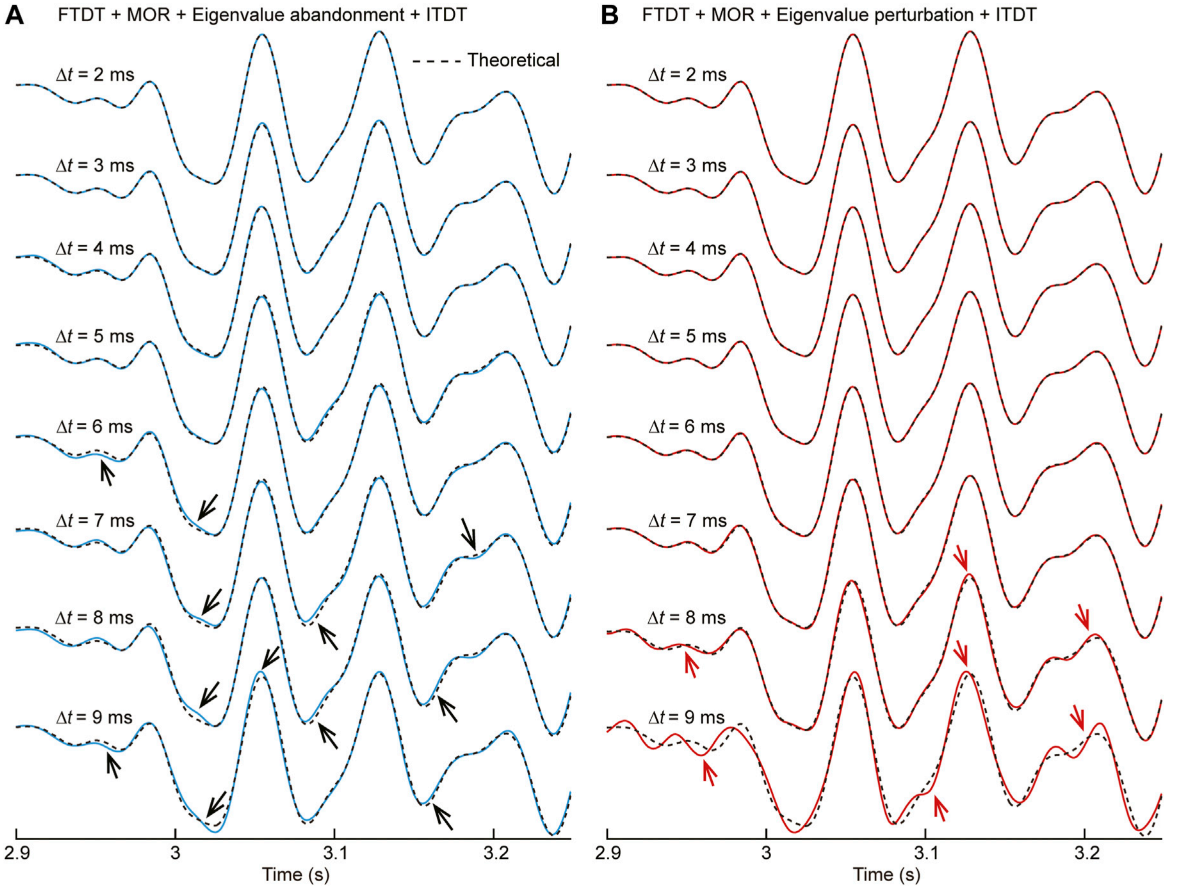

FIGURE 7 | Waveforms that recorded at a fixed point ($x = 700$ m, $z = 700$ m) of the modified Marmousi model using different time steps. The dashed curve obtained using $\Delta t = 1$ ms (with the time-dispersion transform method applied) is taken as the theoretical reference. **(A)** Waveforms obtained using the eigenvalue abandonment algorithm. **(B)** Waveforms obtained using the eigenvalue perturbation algorithm. Eight time steps are tested: Δt = 2, 3, 4, 5, 6, 7, 8, and 9 ms, respectively.

acceptable when $\Delta t \le 6$ ms. For example, using $\Delta t = 2$ ms, the values of amplitude errors are around 0.001 (red lines in **Figures 5C,D**), while the amplitude values of the theoretical waveform range from −3.340 to 4.011, and the error of 0.001 is negligible relative to the overall amplitude values; using $\Delta t = 6$ ms, the maximum error is about 0.1 (grey lines in **Figures 5C,D**), which is only 2.5% of the maximum amplitude value 4.011.

Based on the analysis mentioned before, for a homogenous model, in association with the MOR method and the time-dispersion transform method, both the eigenvalue perturbation algorithm and the eigenvalue abandonment algorithm can release the time step toward the upper bound of the Nyquist sampling and still ensure the accuracy of the numerical simulation. For the eigenvalue abandonment operation, although no high-frequency oscillations appear after the time step size exceeds the Nyquist sampling, there is a risk of filtering out effective wavefield that distributes in the low-wavenumber region if the time step size is too large.

Heterogenous Model

We verified the feasibility of the proposed methods by a heterogenous medium, part of the Marmousi model, as shown in **Figure 6**. In this model, the velocity contrast is strong, the multiple waves are significant, and the velocity range is from 1,467 to 5,928 m/s. The spatial grid interval is $\Delta x = \Delta z = 10$ m, and the grid point number is 121 × 201. The source is a Ricker wavelet with a dominant frequency of 15 Hz, located at x = 1.0 km and z = 0.6 km. The maximum time step size for the second-order FD method in temporal discretization and the fourth-order FD method in spatial discretization schemes are $\Delta t_{\max} = 1.032$ ms. We tested several large time steps (Δt = 2, 3, 4, 5, 6, 7, 8, and 9 ms), and all these time steps are beyond the CFL stability upper bound. We used the workflow in **Figure 3** to apply the time-dispersion transform method. Similar to what has been done in the heterogenous model, we performed numerical simulations using a small time step $\Delta t = 1$ ms, whose results can be regarded as theoretical references to examine the accuracy using larger time steps.

Figure 7 shows the waveforms around 3 s. The residual errors are invisible even for the eigenvalue perturbation algorithm, even for $\Delta t = 7$ ms (shown in **Figure 7B**). Starting from $\Delta t = 8$ ms, the simulation results become inaccurate due to the time step size has exceeded the upper bound of the Nyquist sampling. It demonstrates that the combination of the MOR, the

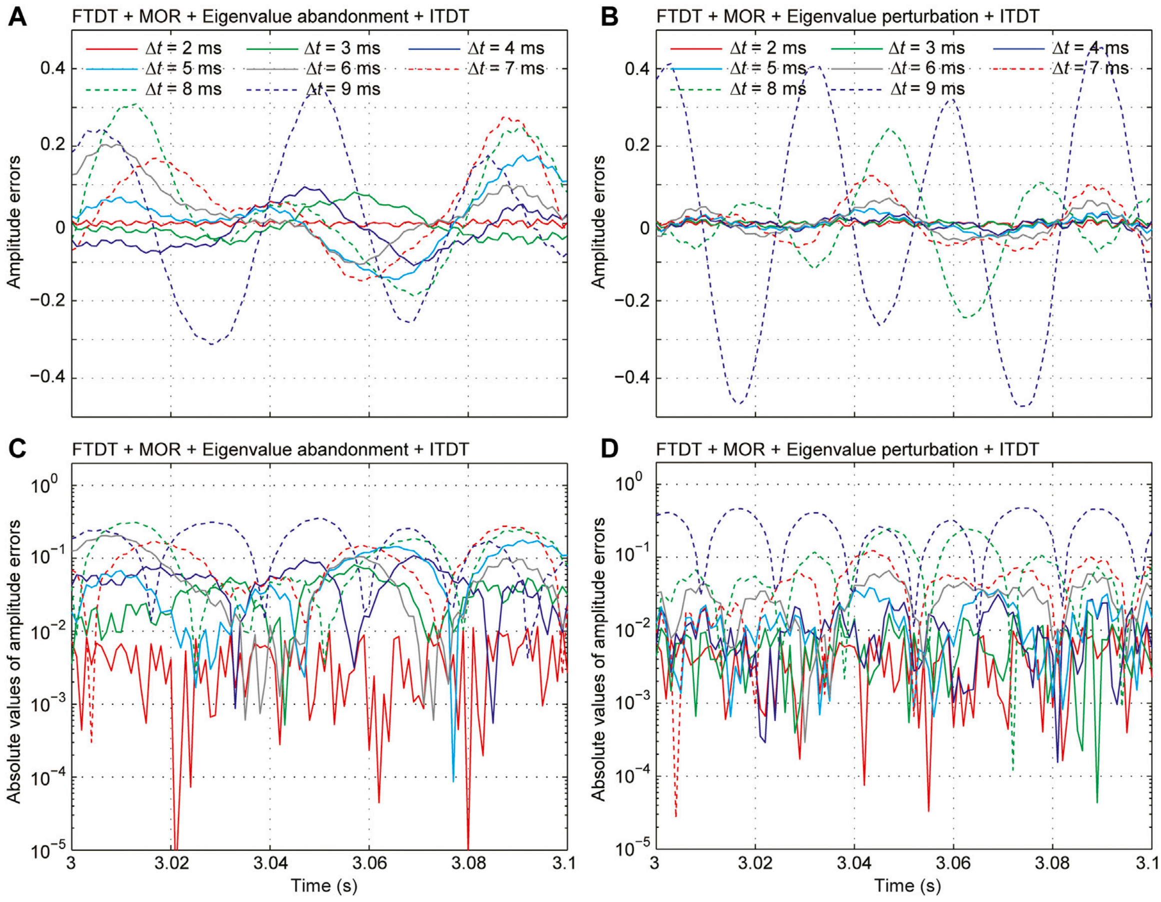

FIGURE 8 | Amplitude errors between the waveforms and the theoretical waveform showed in **Figure 7** (from 3 s to 3.1 s). The amplitude errors in **(A)** and **(B)** are obtained using the eigenvalue abandonment algorithm and the eigenvalue perturbation algorithm, respectively. **(C)** and **(D)** are logarithmic display for the absolute values of the amplitude errors in **(A)** and **(B)**, respectively.

eigenvalue perturbation, and the time-dispersion transform method can still release the time step to the upper bound of the Nyquist sampling even for the heterogenous media with strong velocity contrast.

For the eigenvalue abandonment algorithm, when $\Delta t = 6$ ms, a relatively obvious error appears. Simultaneously, the time step size has not reached the upper bound of the Nyquist sampling yet (shown in **Figure 7A**). This problem still needs to be explained from the perspective of the spatial filtering method. In heterogenous media, instability phenomenon would appear in the high-velocity region according to the CFL stability condition with the time step size increasing. Therefore, the threshold of the low-pass filter is determined by the high-velocity region. However, for the wavefield with a given bandwidth, the wavenumber range in the low-velocity region is wider than that in the high-velocity region (Gao et al., 2019). With the increasing time step size, the low-pass filter of the spatial filtering with decreasing threshold will filter out the effective wavefield in the low-velocity region, which would result in incomplete wavefield components. For the eigenvalue abandonment algorithm, when the time step size is too large (e.g., $\Delta t \geq 6$ ms in this numerical experiment), the unstable eigenvalues are caused by the velocity in the high-velocity region, and this part of eigenvalues corresponds to the wavefield in the high-wavenumber region. Abandoning these unstable eigenvalues is equivalent to filtering out the wavefield of the corresponding wavenumber range, which would filter out the effective wavefield of the low-velocity region.

We further analyzed the amplitude errors between the waveforms obtained by different time steps and the theoretical waveform (as shown in **Figure 8**). The time ranges from 3 to 3.1 s, which is an intermediate time period of the waveforms in **Figure 7**. The amplitude values of the theoretical waveform range from −3.345 to 3.081. Using $\Delta t = 6$ ms, the maximum error of the eigenvalue abandonment algorithm is 0.204 (grey lines in **Figures 8A,C**), which is 6.1% of the maximum absolute amplitude value 3.345; while the maximum error of the eigenvalue abandonment algorithm is 0.059 (grey lines in **Figures 8B,D**), which is only 1.8% of the maximum amplitude value 3.345. Therefore, it is better to perturb this part of the eigenvalues to be stable than to abandon them directly, and this can retain the effective component of the wavefield. The eigenvalue perturbation algorithm is a better choice than the eigenvalue abandonment algorithm. The former is more suitable for the simulation of strongly heterogenous models. The time step can be released beyond the CFL stability upper bound and even toward the upper bound of the Nyquist sampling.

DISCUSSIONS

In the Methodology section, we analyzed and manipulated the eigenvalues of matrix M based on **Eq. 2**, whose stable eigenvalues range from 0 to −4. **Equation 2** can also be written with the following alternative form Gao et al., 2018:

$$\begin{bmatrix} U^{n+1} \\ V^{n+1} \end{bmatrix} = \mathbf{A} \begin{bmatrix} U^{n} \\ V^{n} \end{bmatrix} + \begin{bmatrix} \bar{S}^{n} \\ 0 \end{bmatrix}, \tag{13}$$

where V^{n+1} and V^{n} are the introduced auxiliary variables that represent the wavefields at $n\Delta t$ and $(n-1)\Delta t$, respectively (i.e., $V^{n+1} = U^{n}$ and $V^{n} = U^{n-1}$). According to the CFL stability condition, the stable eigenvalues of matrix **A** range from 0 to 1 (Gao et al., 2018). Since **Eq. 13** is equivalent to **Eq. 2**, the range 0 to −4 for the stable eigenvalues of matrix M is equivalent to the range 0–1 for the stable eigenvalues of matrix A. All the methods involved in this study can also be realized using **Eq. 13**. However, the size of matrix M is $(N_x \times N_z)^2$, which is only a quarter of the size of the matrix A. This means **Eq. 2** is more memory saving than **Eq. 13**. Therefore, we directly used **Eq. 2** to introduce the relevant algorithms instead of starting with **Eq. 13**.

The limitation for the time step of the combination method using the eigenvalue abandonment algorithm is influenced by two factors: wavenumber range of the effective wavefield and the upper bound of the Nyquist sampling, which one is reached first depend on the model parameters. Furthermore, the combination method using the eigenvalue abandonment algorithm has the risk of filtering out the effective wavefield in the low-velocity region in the strongly heteronomous media, which is similar with the combination method using the spatial filtering method mentioned in Gao et al. (2019). The limitation for the time step of the combination method using the eigenvalue perturbation algorithm is only influenced by the upper bound of the Nyquist sampling, and this method is more suitable for strong heterogenous media (Gao et al., 2018). We preferred to use the combination method using the eigenvalue perturbation algorithm to release the time step upper bound of CFL stability condition.

The MOR method can effectively reduce the amount of calculation in the iterative process, but this skill is still implemented based on the global operator M. The eigenvalue decomposition calculation amount in preprocessing is still very large, especially for memory consumption, which is still a challenge faced by this method. Therefore, we still need to research how to release the time step size beyond the CFL stability condition by avoiding the global matrix operators in the future.

CONCLUSION

We introduced the model-order reduction (MOR) method to solve the acoustic wave equation. Only the updated matrix's eigenvalues and the expansion coefficients of the variables in the wave equation are used to iterate the wave propagation, which greatly reduces the amount of calculation in the wavefield iteration process. Moreover, we introduced the eigenvalue abandonment algorithm and the eigenvalue perturbation algorithm to operate on the unstable eigenvalues of the updated matrix. We successfully released the time step size of the CFL stability condition for the explicit FD scheme. We then introduced the time-dispersion transform method to eliminate the time-dispersion error caused by the large time step and ensure numerical simulation's accuracy. Numerical experiments show that the combination of the MOR method, eigenvalue abandonment (and the eigenvalue perturbation), and the time-dispersion method can simulate highly accurate waveforms when applying a time step beyond the CFL stability upper bound. The combination method using the eigenvalue abandonment algorithm has the risk of filtering out the effective wavefield in the low-velocity region in the strongly heteronomous media. The combination method using the eigenvalue perturbation algorithm is suitable for strong heterogenous media and can successfully extend the time step size toward the upper bound of the Nyquist sampling. An unusually sparse time step can be used for the seismic numerical simulation without suffering from the time-dispersion error and stability problems.

AUTHOR CONTRIBUTIONS

YG derived the equations, wrote the program, and performed numerical experiments. M-HZ checked the formula derivation and performed analysis for the numerical experiments. HZ designed the experiments and analyzed the results of the numerical experiments.

FUNDING

This research was supported by the National Natural Science Foundation of China (grant nos. 41725017, 11773087) and the Science and Technology Development Fund, Macau SAR (grant nos. 0002/2019/APD, 0079/2018/A2). YG was also supported by the National Natural Science Foundation of China (grant no. 41704063) and the General Financial Grant from the China Postdoctoral Science Foundation (grant no. 2017M610980).

REFERENCES

Basir, H. M., Javaherian, A., Shomali, Z., Firouzabadi, R. D., and Dalkhani, A. R. (2015). "Using Reduced Order Modeling Algorithm for Reverse Time Migration," in Paper read at Third EAGE Workshop on Iraq.

Basir, H. M., Javaherian, A., Shomali, Z. H., Firouz-Abadi, R. D., and Gholamy, S. A. (2018). Reverse Time Migration by Krylov Subspace Reduced Order Modeling. *J. Appl. Geophys.* 151, 298–308. doi:10.1016/j.jappgeo.2018.02.010

Chang, C., and Sarris, C. D. (2011). "A Spatial Filter-Enabled High-Resolution Subgridding Scheme for Stable FDTD Modeling of Multiscale Geometries," in Paper read at international microwave symposium. doi:10.1109/mwsym.2011.5972916

Chang, C., and Sarris, C. D. (2013). A Spatially Filtered Finite-Difference Time-Domain Scheme with Controllable Stability beyond the CFL Limit: Theory and Applications. *IEEE Trans. Microwave Theor. Techn.* 61 (1), 351–359. doi:10.1109/tmtt.2012.2224670

Chang, C., and Sarris, C. D. (2012). "A Three-Dimensional Spatially Filtered FDTD with Controllable Stability beyond the Courant Limit," in Paper read at Microwave Symposium Digest. doi:10.1109/mwsym.2012.6259570

Chen, J. B. (2007). High-order Time Discretizations in Seismic Modeling. *Geophysics* 72 (5), SM115–SM122. doi:10.1190/1.2750424

Chen, Z., Fan, W., and Yang, S. (2016). "Towards the Wave-Equation Based Explicit FDTD Method without Numerical Instability," in Paper read at 2016 IEEE International Conference on Computational Electromagnetics (Iccem). doi:10.1109/compem.2016.7588616

Courant, R., Friedrichs, K., and Lewy, H. (1928). Über die partiellen Differenzengleichungen der mathematischen Physik. *Math. Ann.* 100 (1), 32–74. (In German). doi:10.1007/bf01448839

Dablain, M. A. (1986). The Application of High-order Differencing to the Scalar Wave Equation. *Geophysics* 51 (1), 54–66. doi:10.1190/1.1442040

Dai, N., Liu, H., and Wu, W. (2014). "Solutions to Numerical Dispersion Error of Time FD in RTM," in Paper read at 84th Annual International Meeting, Society of Exploration Geophysicists, 4027–4031.

Ecer, A., Gopalaswamy, N., Akay, H. U., and Chien, Y. P. (2000). Digital Filtering Techniques for Parallel Computation of Explicit Schemes. *Int. J. Comput. Fluid Dyn.* 13 (3), 211–222. doi:10.1080/10618560008940899

Etgen, J. T., and O'Brien, M. J. (2007). Computational Methods for Large-Scale 3D Acoustic Finite-Difference Modeling: A Tutorial. *Geophysics* 72 (5), SM223–SM230. doi:10.1190/1.2753753

Freund, R. W. (2004). "SPRIM: Structure-Preserving Reduced-Order Interconnect Macromodeling," in Paper read at IEEE/ACM International Conference on Computer Aided Design. ICCAD-2004.

Gaffar, M., and Jiao, D. (2015). Alternative Method for Making Explicit FDTD Unconditionally Stable. *IEEE Trans. Microwave Theor. Techn.* 63 (12), 4215–4224. doi:10.1109/tmtt.2015.2496255

Gaffar, M., and Jiao, D. (2014). An Explicit and Unconditionally Stable FDTD Method for Electromagnetic Analysis. *IEEE Trans. Microwave Theor. Techn.* 62 (11), 2538–2550. doi:10.1109/tmtt.2014.2358557

Gao, Y., Zhang, J., and Yao, Z. (2019). Extending the Stability Limit of Explicit Scheme with Spatial Filtering for Solving Wave Equations. *J. Comput. Phys.* 397, 108853. doi:10.1016/j.jcp.2019.07.051

Gao, Y., Zhang, J., and Yao, Z. (2018). Removing the Stability Limit of the Explicit Finite-Difference Scheme with Eigenvalue Perturbation. *Geophysics* 83 (6), A93–A98. doi:10.1190/geo2018-0447.1

Gao, Y., Zhang, J., and Yao, Z. (2016). Third-order Symplectic Integration Method with Inverse Time Dispersion Transform for Long-Term Simulation. *J. Comput. Phys.* 314, 436–449. doi:10.1016/j.jcp.2016.03.031

He, Q., Gan, H., and Jiao, D. (2012). Explicit Time-Domain Finite-Element Method Stabilized for an Arbitrarily Large Time Step. *IEEE Trans. Antennas Propagat.* 60 (11), 5240–5250. doi:10.1109/tap.2012.2207666

Koene, E. F. M., Robertsson, J. O. A., Broggini, F., and Andersson, F. (2018). Eliminating Time Dispersion from Seismic Wave Modeling. *Geophys. J. Int.* 213, 169–180. doi:10.1093/gji/ggx563

Kosloff, D., Filho, A. Q., Tessmer, E., and Behle, A. (1989). Numerical Solution of the Acoustic and Elastic Wave Equations by a New Rapid Expansion Method1. *Geophys. Prospect* 37 (4), 383–394. doi:10.1111/j.1365-2478.1989.tb02212.x

Li, X. (2014). *Model Order Reduction and Stability Enforcement of Finite-Difference Time-Domain Equations beyond the CFL Limit*. University of Toronto. (Canada).

Li, X., Sarris, C. D., and Triverio, P. (2014). "Overcoming the FDTD Stability Limit via Model Order Reduction and Eigenvalue Perturbation," in Paper read at Microwave Symposium. doi:10.1109/mwsym.2014.6848408

Li, Y. E., Wong, M., and Clapp, R. (2016). Equivalent Accuracy at a Fraction of the Cost: Overcoming Temporal Dispersion. *Geophysics* 81 (5), T189–T196. doi:10.1190/geo2015-0398.1

Liu, H., Dai, N., Niu, F., and Wu, W. (2014). An Explicit Time Evolution Method for Acoustic Wave Propagation. *Geophysics* 79 (3), T117–T124. doi:10.1190/geo2013-0073.1

Liu, Y. (2020). Maximizing the CFL Number of Stable Time-Space Domain Explicit Finite-Difference Modeling. *J. Comput. Phys.* 416, 109501. doi:10.1016/j.jcp.2020.109501

Liu, Y., and Sen, M. K. (2009). Advanced Finite-Difference Methods for Seismic Modeling. *Geohorizons* 14 (2), 5–16.

Lyu, C., Capdeville, Y., Lu, G., and Zhao, L. (2021). Removing the Courant-Friedrichs-Lewy Stability Criterion of the Explicit Time-Domain Very High Degree Spectral-Element Method with Eigenvalue Perturbation. *Geophysics* 86 (5), T411–T419. doi:10.1190/geo2020-0623.1

Pereyra, V., and Kaelin, B. (2008). Fast Wave Propagation by Model Order Reduction. *Electron. Trans. Numer. Anal.* 30, 406–419.

Pereyra, V. (2016). Model Order Reduction with Oblique Projections for Large Scale Wave Propagation. *J. Comput. Appl. Mathematics* 295, 103–114. doi:10.1016/j.cam.2015.01.029

Pereyra, V. (2013). Wave Equation Simulation Using a Compressed Modeler. *J. Comput. Mathematics* 3 (3), 231–241. doi:10.4236/ajcm.2013.33033

Remis, R. F., and Van den Berg, P. M. (1998). Efficient Computation of Transient Diffusive Electromagnetic fields by a Reduced Modeling Technique. *Radio Sci.* 33 (2), 191–204. doi:10.1029/97rs03693

Sarris, C. D. (2011). Extending the Stability Limit of the FDTD Method with Spatial Filtering. *IEEE Microw. Wireless Compon. Lett.* 21 (4), 176–178. doi:10.1109/lmwc.2011.2105467

Song, X., and Fomel, S. (2011). Fourier Finite-Difference Wave Propagation. *Geophysics* 76 (5), T123–T129. doi:10.1190/geo2010-0287.1

Stork, C. (2013). "Eliminating Nearly All Dispersion Error from FD Modeling and RTM with Minimal Cost Increase," in Paper read at 75th Annual International Conference and Exhibition (EAGE). Extended Abstracts, Tu 11 07. doi:10.3997/2214-4609.20130478

Wang, M., and Xu, S. (2015). Finite-difference Time Dispersion Transforms for Wave Propagation. *Geophysics* 80 (6), WD19–WD25. doi:10.1190/geo2015-0059.1

Wu, C., Bevc, D., and Pereyra, V. (2013). "*Model Order Reduction for Efficient Seismic Modeling*," in Paper read at 83rd Annual International Meeting, Society of Exploration Geophysicists, 3360–3364.

Yan, J., and Jiao, D. (2017). Fast Explicit and Unconditionally Stable FDTD Method for Electromagnetic Analysis. *IEEE Trans. Microwave Theor. Techn.* 65 (8), 2698–2710. doi:10.1109/tmtt.2017.2686862

Zhang, X., Bekmambetova, F., and Triverio, P. (2017). "Reduced Order Modeling in FDTD with Provable Stability beyond the CFL Limit," in Paper read at Electrical PERFORMANCE of Electronic Packaging and Systems.

Conflict of Interest: The authors declare that the research was conducted in the absence of any commercial or financial relationships that could be construed as a potential conflict of interest.

frontiers | Frontiers in Earth Science

METHODS
published: 08 April 2022
doi: 10.3389/feart.2022.883160

Application of the Reflectionless Discrete Perfectly Matched Layer for Acoustic Wave Simulation

Yingjie Gao [1,2] *and Meng-Hua Zhu* [1,2]*

[1]*State Key Laboratory of Lunar and Planetary Sciences, Macau University of Science and Technology, Macau, China,* [2]*CNSA Macau Center for Space Exploration and Science, Macau, China*

The perfectly matched layer (PML) is one of the most popular absorbing boundary conditions for simulating seismic waves. In theory, the PML can absorb incident waves at any incident angle and any frequency in a medium. However, numerical reflections will be generated after the PML has been discretized. Therefore, how to reduce the reflections of discrete PML has been a research topic for more than 2 decades. In this paper, we adopt the reflectionless discrete PML (RD-PML) for seismic wave and implement the RD-PML based on the acoustic wave equation, and then compare its absorbing performance with that of the conventional discrete PML. Our numerical experiments show that the RD-PML has advantages over the conventional discrete PML. In homogeneous model, a thick enough RD-PML can effectively eliminate reflections. In heterogeneous model, a thin-layer RD-PML can obtain better absorbing performance even than the thick-layer conventional discrete PML. The absorbing performance of the RD-PML can be improved by using the periodic boundary without increasing the amount of computation and memory. RD-PML provides a new perspective to understand the discretization of PML, and may play an important role in promoting the development of PML technology.

Keywords: absorbing boundary, perfectly matched layer, discrete complex analysis, periodic boundary, boundary reflection

Edited by:
Weijia Sun,
Institute of Geology and Geophysics (CAS), China

Reviewed by:
Enjiang Wang,
Hohai University, China
Na Fan,
Yangtze University, China

****Correspondence:***
Meng-Hua Zhu
mhzhu@must.edu.mo

Specialty section:
This article was submitted to Solid Earth Geophysics, a section of the journal Frontiers in Earth Science

Received: *24 February 2022*
Accepted: *09 March 2022*
Published: *08 April 2022*

Citation:
Gao Y and Zhu M-H (2022) Application of the Reflectionless Discrete Perfectly Matched Layer for Acoustic Wave Simulation.
Front. Earth Sci. 10:883160.
doi: 10.3389/feart.2022.883160

INTRODUCTION

Perfectly matched layer (PML) is one of the most widely used artificial absorbing boundaries that are used to deal with the artificial boundary truncation in the numerical simulation of seismic wave propagation. It was proposed by Bérenger (1994) for electromagnetic wave simulations, and was applied to the wave equation using complex coordinate stretching through the modification of spatial partial derivatives, which introduces an imaginary part of the coordinate that is associated with an attenuation factor (Chew and Weedon, 1994). After its introduction, the PML found widespread use in various fields of numerical simulation due to its good applicability to different types of equations. For example, it is commonly implemented for seismic wave simulation (Chew and Liu, 1996), which includes both the acoustic wave simulation (Liu and Tao, 1997; Yuan et al., 1997; Qi and Geers, 1998; Katsibas and Antonopoulos, 2002; Diaz and Joly, 2006; Bermúdez et al., 2007; Ma et al., 2014) and the elastic wave simulation (Chew and Liu, 1996; Hastings et al., 1996; Collino and Tsogka, 2001; Komatitsch and Tromp, 2003; Pled and Desceliers, 2021).

In theory, the PML can absorb the incident waves of any incident angle and any frequency under continuous medium. However, numerical reflections will still be generated after the PML has been discretized. In order to improve the absorbing performance of discrete PML, several methods have been proposed, which are briefly reviewed in the following paragraphs.

Collino and Monk (1998) optimized the discrete PML by suitable design of the layer, which includes the selection for the number of layers and attenuation coefficients. After that, people carried out further optimization work to choose the layer parameters of PML (Fang and Wu, 1996; Winton and Rappaport, 2000; Travassos et al., 2006; Bermúdez et al., 2007; Nissen and Kreiss, 2011).

The absorbing performance of the discrete PML is proven to vary with the angle of the incident wave, and will continue to decrease as the angle of the incident wave gradually increases (Gao et al., 2017); thus its absorbing performance on grazing incident waves is not satisfactory (Roden and Gedney, 2000; Winton and Rappaport, 2000). Furthermore, the grazing incident waves can be converted into evanescent waves, which cannot be absorbed by the PML and will generate spurious reflections (Drossaert and Giannopoulos, 2007b; Komatitsch and Martin, 2007). Kuzuoglu and Mittra (1996) modified the PML by introducing two new parameters to the complex coordinate stretching operator of PML, which can shift the pole of the complex coordinate stretched operator to a non-zero value. The modified PML is called as complex frequency-shifted PML (CFS-PML), and can improve the absorbing performance of the PML for grazing incident waves (Festa and Vilotte, 2005, Komatitsch and Martin, 2007, Drossaert and Giannopoulos, 2007a, b).

The PML and CFS-PML were both originally implemented based on split-field formulations, which adopts a nonphysical splitting of the variables in the wave equations and lead to two different sets of equations for the inner wavefield simulation area and the outer PML area. Furthermore, the split-field formulation is mathematically weakly well-posed (Abarbanel and Gottlieb, 1997), and will be unstable for long time simulations (Festa et al., 2005). Different unsplit-field implementations of the CFS-PML were developed by using convolutional algorithms (Roden and Gedney, 2000; Wang and Tang, 2003; Wang et al., 2005; Drossaert and Giannopoulos, 2007a, b; Komatitsch and Martin, 2007; Li and Matar, 2010; Pasalic and McGarry, 2010; Matzen, 2011), integral terms (Zeng and Liu, 2004; Drossaert and Giannopoulos, 2007b), matched Z-transform (Shi et al., 2012), and auxiliary differential-equation (ADE) algorithm (Ramadan, 2003; Rejiba et al., 2003; Wang and Liang, 2006; Kristek et al., 2009; Gedney and Zhao, 2010; Martin et al., 2010; Zhang and Shen, 2010; Xie et al., 2014; Deng et al., 2018; He et al., 2019). Among the above methods, the convolutional algorithm and the ADE algorithm are the most widely used in seismic numerical simulations. The ADE algorithm is implemented by introducing auxiliary differential equations, which are a series of first-order partial derivative equations; in contrast, the convolutional algorithm is implemented by convolutional operations, which are solved by recursive convolution technique (Luebbers and Hunsberger, 1992).

For an isotropic medium, the unsplit CFS-PML will be a sufficient choice for long time simulation because of its weak reflections and excellent stability (Komatitsch and Martin, 2007), but in an anisotropic viscoelastic medium, the unsplit CFS-PML suffers from instabilities for long-time simulation. The multi-axial PML (M-PML) was developed to guarantee the long-time stability of PML in an anisotropic medium, which is efficient and stable without dependences on frequencies and directions of wave propagation (Meza-Fajardo and Papageorgiou, 2008, 2010, 2012; Ping et al., 2014, 2016; Gao and Huang, 2017). But it was soon proven that the M-PML is not perfectly matched and thus is not a PML (Dmitriev and Lisitsa, 2011, 2012). Rather, it can be seen as an improved sponge boundary (Xie et al., 2014).

The numerical implementations of the traditional PML and CFS-PML are based on the first-order system of wave equations, and they cannot be directly applied to the second-order wave equation. The second-order wave equation is usually transformed into the first-order form to just to be able to use the PML or CFS-PML, which significantly increases both the memory requirement and computational cost (Liu and Tao, 1997; Yuan et al., 1997; Qi and Geers, 1998; Yuan et al., 1999). Komatitsch and Tromp (2003) were the first to try and construct the PML for the second-order elastic wave equation, and a series of studies were followed (Pasalic and McGarry, 2010; Duru and Kreiss, 2012; Ma et al., 2014; Xie et al., 2014; Gao et al., 2015; Ma et al., 2018, 2019a, 2019b).

It was shown that the CFS-PML could be understood as a low-pass Butterworth filter, which can absorb waves with frequency higher than the cut-off frequency, but cannot efficiently absorb low-frequency waves below the cut-off frequency (Festa and Vilotte, 2005). To absorb both the low-frequency propagating waves and evanescent waves, high-order CFS-PML was proposed (Correia and Jin, 2005, 2006). Unlike the conventional CFS-PML (or called the first-order CFS-PML) that only has a single pole in the coordinate stretching operator, the higher-order CFS-PML has multiple poles that consist of two or more stretching operators. The higher-order CFS-PML has the advantages of both the conventional PML and the CFS-PML in terms of absorbing performance, since the conventional PML is great at the low frequencies but poor at grazing incidences, while the CFS-PML is poor at low frequencies but great at grazing incidences (Martin et al., 2010; Feng and Li, 2013). Feng et al. (2015) proved that the second-order PML is an optimal choice, since it provides almost the same absorbing performance as the third-order PML, while requiring less computational time and memory. Feng et al. (2017) analyzed the different roles of the second-order CFS-PML parameters and proposed optimal selections of these parameters to get satisfactory results for broad-band seismic wave simulations.

The above-mentioned research works have continuously promoted the development of PML technology, both in terms of absorbing performance and realization form. However, none of them has achieved "mechanical zero" absorbing performance after discretization. Chern (2019) presented a new approach to deriving the discrete PML equations using Discrete Complex Analysis (Duffin, 1956; Lovász, 2004; Bobenko et al., 2005; Bobenko and Günther, 2016). Instead of seeking a high-order discretization of the continuous PML equations, Chern (2019) took the discrete wave equation and found its associated PML equations by mimicking the continuous theory but solely in the discrete setting. The resulted discrete PML for the first time "perfectly matches" the discrete wave equation, and it is called reflectionless discrete PML (RD-PML). Furthermore, Chern (2019) proposed to use a constant attenuation coefficient to replace the conventional gradually increasing attenuation coefficients. The RD-PML gained good absorbing performance, but it was originally proposed based on a homogeneous model with the velocity $v = 1\,\mathrm{m/s}$ (Chern, 2019), and the cases of arbitrary velocity and heterogenous model have not been considered and researched yet.

In this paper, we adopt the RD-PML to solve the boundary truncation problem for acoustic equation modelling. Firstly, we briefly introduce the RD-PML algorithm and give the attenuation coefficient with arbitrary velocity v. The model design for periodic boundary is also discussed. Then, we compare the absorbing performance of RD-PML with that of the conventional discrete PML, and verify the improvement effect of the periodic boundary on the absorbing performance. The case of heterogenous model is also considered. Numerical experiments demonstrate the superiority of RD-PML method over conventional methods.

METHODOLOGY

We start with the 2-dimensional acoustic wave equation

$$\frac{1}{v^2}\frac{\partial^2 u}{\partial t^2} = \frac{\partial^2 u}{\partial x^2} + \frac{\partial^2 u}{\partial z^2} + s, \tag{1}$$

where $u(x,z,t)$ is the wavefield, $v(x,z)$ is the velocity, and $s(x,z,t)$ is the source term. Research on the implementation for the PML algorithm mainly focuses on taking operation for the spatial partial derivatives in the wave equation. For simplicity, here we only discuss the PML algorithm along the x-direction as an example in the text, and the operation along the z-direction can be similarly obtained.

To implement the PML, the spatial partial derivative in the wave equation can be extended to complex coordinate by the stretching operator (Johnson, 2008):

$$s_x(x) = 1 + \frac{i d_x(x)}{\omega}, \tag{2}$$

where $s_x(x)$ is the complex stretching function, $d_x(x)$ is the attenuation coefficient of the PML, and $i = \sqrt{-1}$ (Collino and Tsogka, 2001); thus, we have

$$\frac{\partial}{\partial x} \to \frac{\partial}{\partial \tilde{x}} = \frac{1}{s_x}\frac{\partial}{\partial x}, \tag{3}$$

The expression for the complex coordinate is

$$\tilde{x} = x + \frac{i}{\omega}\int_0^x d_x(x)dx. \tag{4}$$

The plane wave solution can be expressed as

$$U = u_0 \exp[i(k_x x - \omega t)], \tag{5}$$

where u_0 is the amplitude of the wave and k_x is the wavenumber along the x-direction. The plane wave solution would be modified by complex stretching in the complex coordinate as

$$\begin{aligned}\hat{U} &= u_0 \exp[i(k_x\tilde{x} - \omega t)] \\ &= u_0 \exp\left\{i\left[k_x\left(x + \frac{i}{\omega}\int_0^x d_x(x)dx\right) - \omega t\right]\right\}.\end{aligned} \tag{6}$$

After further sorting, **Eq. 6** can be written as

$$\begin{aligned}\hat{U} &= u_0 \exp[i(k_x x - \omega t)]\exp\left(-\frac{k_x}{\omega}\int_0^x d_x(x)dx\right) \\ &= U\exp\left(-\frac{k_x}{\omega}\int_0^x d_x(x)dx\right).\end{aligned} \tag{7}$$

Compared with the original expression of the plane wave solution in **Eq. 5**, **Eq. 7** has an extra item $\exp(-k_x/\omega\int_0^x d_x(x)dx)$, which is the attenuation term of the PML. If we don't consider the time term and only consider the space term in **Eq. 6**, the expression can be simplified as

$$\begin{aligned}\exp(ik_x\tilde{x}) &= \exp\left[ik_x\left(x + \frac{i}{\omega}\int_0^x d_x(x)dx\right)\right] \\ &= \exp\{ik_x[\mathrm{Re}(\tilde{x}) + i\mathrm{Im}(\tilde{x})]\} \\ &= \exp[ik_x\mathrm{Re}(\tilde{x})]\exp[-k_x\mathrm{Im}(\tilde{x})],\end{aligned} \tag{8}$$

where $\mathrm{Re}(\tilde{x})$ and $\mathrm{Im}(\tilde{x})$ represent the real and imaginary parts of $\tilde{x}$, respectively. According to Euler's formula $\exp[ik_x\mathrm{Re}(\tilde{x})] = \cos[k_x\mathrm{Re}(\tilde{x})] + i\sin[k_x\mathrm{Re}(\tilde{x})]$, the values of $\exp[ik_x\mathrm{Re}(\tilde{x})]$ distribute along a unit circle in the complex coordinate. The real part of $\exp[ik_x\mathrm{Re}(\tilde{x})]$ is a cosine function $\cos[k_x\mathrm{Re}(\tilde{x})]$, and the real part of $\exp(ik_x\tilde{x})$ in **Eq. 8** can be expressed as:

$$\mathrm{Re}[\exp(ik_x\tilde{x})] = \cos[k_x\mathrm{Re}(\tilde{x})]\exp[-k_x\mathrm{Im}(\tilde{x})], \tag{9}$$

With a positive wavenumber k_x, the values of $\exp[-k_x\mathrm{Im}(\tilde{x})]$ range from 1 to 0 when $\mathrm{Im}(\tilde{x}) > 0$, and this will lead to attenuation for the wave amplitude. The values of **Eq. 9** are shown in **Figure 1A**, which shows the principle of the attenuation for the PML. The negative real coordinate of $\tilde{x}$ represents the normal wavefield propagation area, and the positive real coordinate of $\tilde{x}$ represents the PML attenuation area. The amplitude of the waveform does not attenuate when the wave propagating along the real axis of $\tilde{x}$ (the blue dashed line in **Figures 1B,C**), while the amplitude of the waveform would decrease as the wave propagating along the stretched coordinate (the red dashed line in **Figures 1D,E**).

In theory, the PML can absorb the incident waves of any angle and any frequency before discretization (Bérenger, 1994; Komatitsch and Martin, 2007). However, after the discretization, the numerical reflections will arise at the interface of PML due to the discretization error (Bérenger, 2002; Gao et al., 2017). Here, we analyse why the conventional discrete PML will produce reflected waves. The corresponding

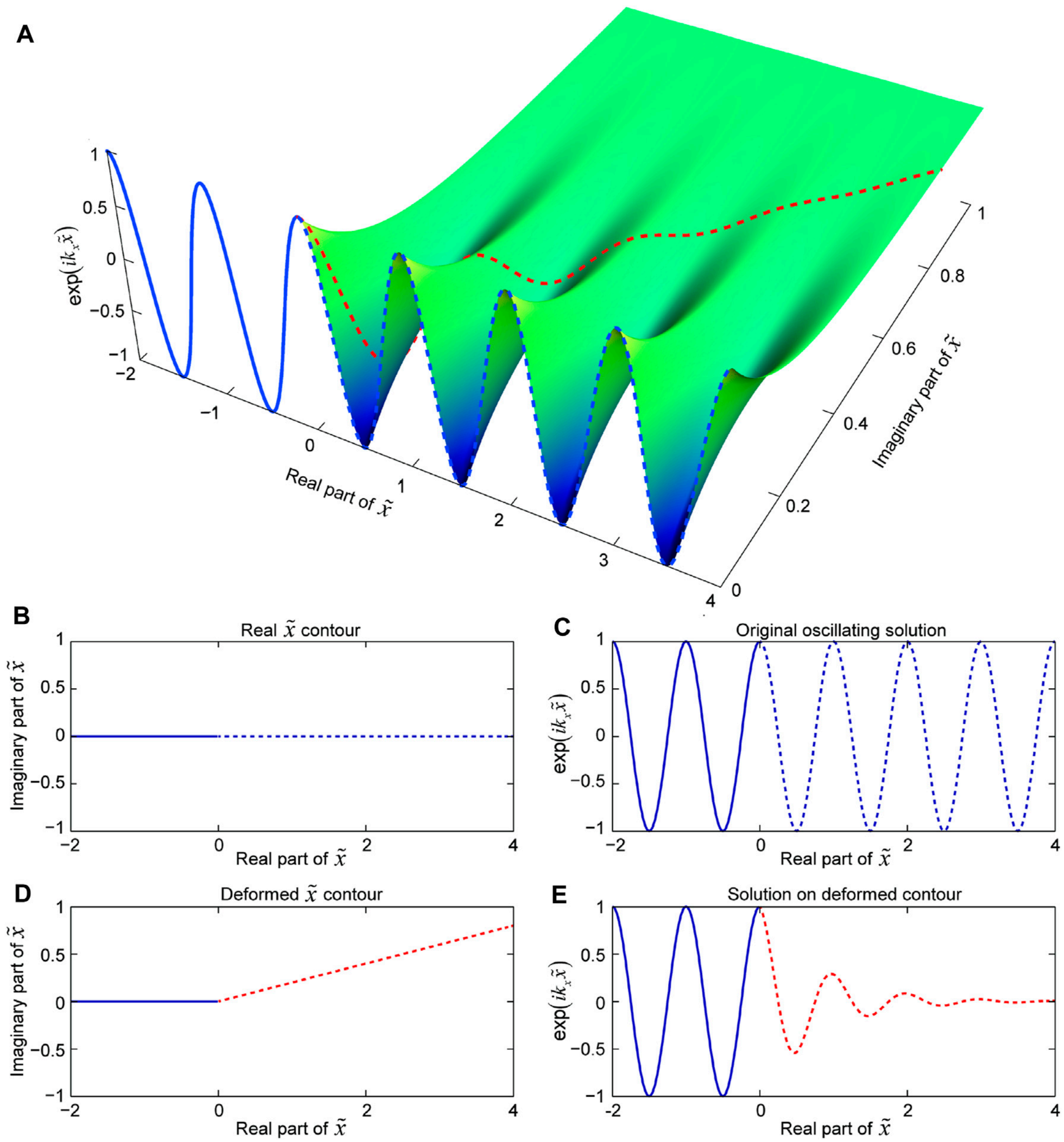

FIGURE 1 | Sketch map of the attenuation principle for the plane waves in the PML region. The coordinate that corresponds to Re ($\tilde{x}$) < 0 represents the normal wave propagation region and no attenuation considered, and the region that corresponds to Re ($\tilde{x}$) > 0 represents the PML region. **(A)** The attenuation process of the plane waves along different stretching directions in the PML region. **(B)** The direction along the real axis in the complex coordinate (the dashed blue line in **(A)**. **(C)** Real part of oscillating solution exp ($ik_x\tilde{x}$) that corresponds to the stretching direction in **(B)**. **(D)** The stretching direction along a deformed contour in the complex coordinate (the dashed red line in **(A)**). **(E)** Real part of oscillating solution exp ($ik_x\tilde{x}$) that corresponds to the stretching direction in **(D)**.

discrete format complex coordinate path for $\tilde{x}$ in **Eq. 4** can be expressed as

$$\tilde{x}(j) = x(j) + \frac{i}{\omega}\sum_{j=1}^{N} d_x(j)\Delta x, \tag{10}$$

which is shown by the blue line in **Figure 2A**. The finite-difference (FD) operators for the spatial partial derivative $\partial^2 u/\partial \tilde{x}^2$ along the blue path that in the PML area cannot "perfectly matched" with the original finite-difference operators for $\partial^2 u/\partial x^2$ that along the real x axis in the non-attenuation area. In addition, the conventional discrete PML uses gradual increasing attenuation coefficients (Collino and Tsogka, 2001; Komatitsch and Martin, 2007; Zhang and Shen, 2010; Gao et al., 2015), which will lead adjacent grid-spacing difference in complex coordinates and the unequal-spacing finite-difference operator would introduce new calculation errors.

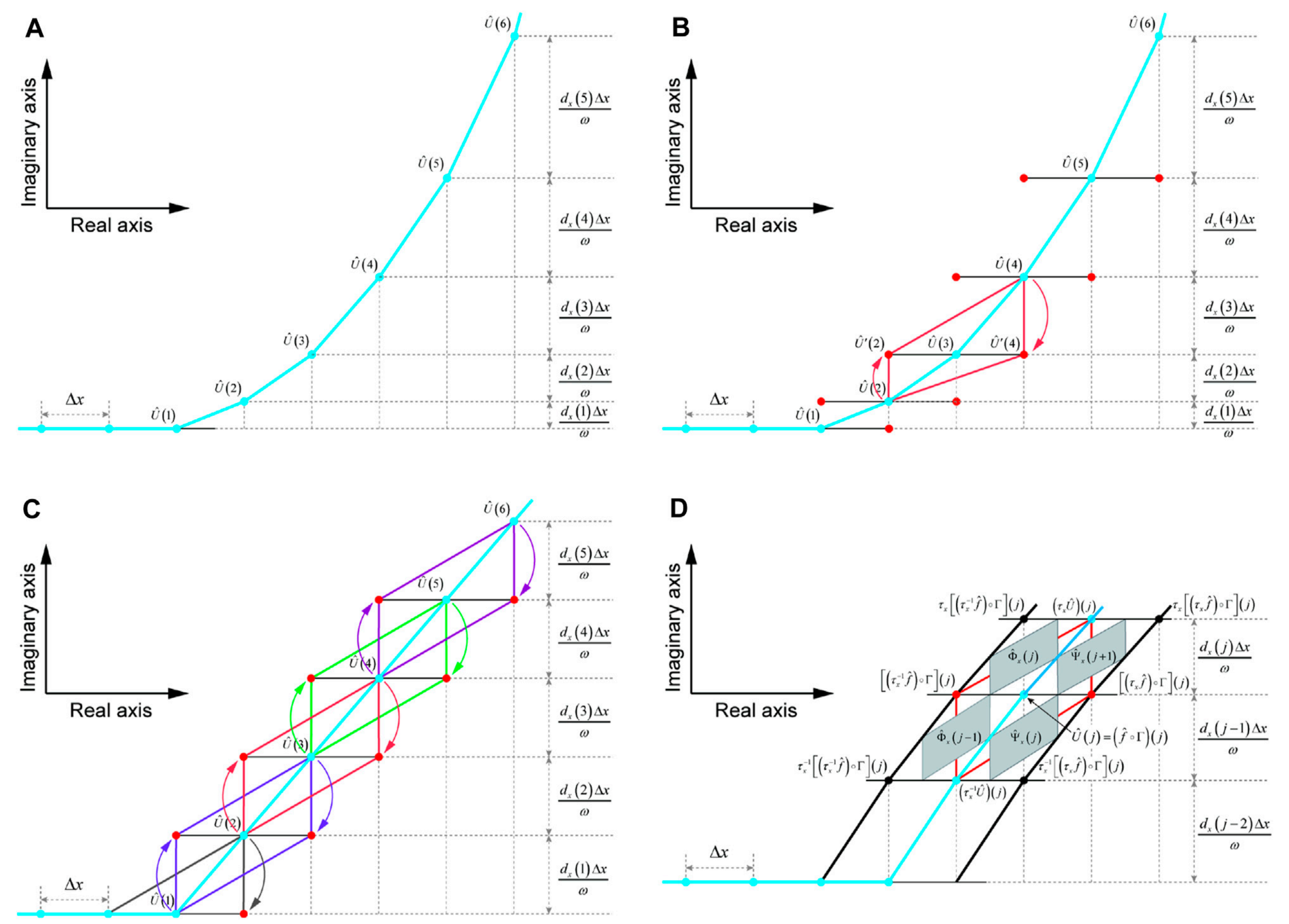

FIGURE 2 | Sketch map of the stretching path for the PML in the complex coordinate after discretization and sketch map of the projection method using discrete complex analysis. **(A)** The discrete stretching path for the PML in the complex coordinate using gradually increasing attenuation coefficients. **(B)** The quadrilateral for the projection using discrete complex analysis for the discrete path in **(A)**. **(C)** The discrete stretching path for the PML in the complex coordinate using constant attenuation coefficients. The quadrilaterals of different colors represent the projection quadrilaterals of the 2nd-order FD operator corresponding to the respective center points. **(D)** Sketch map the projection method of the quadrilateral corresponding to $\hat{U}(i)$ using discrete complex analysis. Symbol ∘ represents compound function operation (e.g., $\hat{f}\circ\Gamma(x)=\hat{f}[\Gamma(x)]$) and $\hat{f}\circ\Gamma$ represents the stretching path of PML. τ_x and τ_x^{-1} are the positive and negative shift operators, respectively.

Chern (2019) presented the reflectionless discrete PML (abbreviated as RD-PML) using Discrete Complex Analysis (Duffin, 1956; Lovász, 2004; Bobenko et al., 2005; Bobenko and Günther, 2016), and this new form discrete PML for the first time "perfectly matches" the discrete wave equation. For example, the FD operator at $\hat{U}(3)$ along the blue line in **Figure 2A** is transformed to an operator that parallel to the real x axis by the equivalent projection method (i.e., Discrete Complex Analysis). In this way, the direction of the projected FD operators in the PML region can be kept parallel with the original FD operators in the normal wave propagation region. Ordinarily the second-order discretization for the FD operator of $\partial^2 u/\partial\tilde{x}^2$ at $\hat{U}(3)$ involves $\hat{U}(2)$, $\hat{U}(3)$, and $\hat{U}(4)$. Instead if we project $\hat{U}(2)$ and $\hat{U}(4)$ to the red points $\hat{U}'(2)$ and $\hat{U}'(4)$ on the horizontal line that passing $\hat{U}(3)$ using Discrete Complex Analysis, respectively (shown by the red quadrilateral in **Figure 2B**). In this way, the original diagonal FD operator composed of $\hat{U}(2)$, $\hat{U}(3)$, and $\hat{U}(4)$ is transformed into a horizontal FD operator composed of $\hat{U}'(2)$, $\hat{U}(3)$, and $\hat{U}'(4)$. After transforming this horizontal FD operator from the frequency domain back to the time domain, it can well match with the original FD operator.

Furthermore, Chern (2019) proposed to use a constant attenuation coefficient to replace the conventional gradually increasing attenuation coefficients. In the example given by Chern (2019), the constant attenuation coefficient is $d_x = 2/\Delta x$ for a homogeneous model with the velocity $v = 1$ m/s. To obtain the attenuation coefficient for the model with the velocity v, we begin with the geometric decay rate ρ, which can be expressed as (Chern, 2019):

$$\rho = \frac{2 + i\frac{d_x}{\omega}\left(1 - e^{-ik_x\Delta x}\right)}{2 + i\frac{d_x}{\omega}\left(1 - e^{ik_x\Delta x}\right)}. \tag{11}$$

The ρ represents the decay rate for a single grid of PML. When $k_x\Delta x \sim O(\Delta x)$ (symbol ~ represents smooth asymptotics), we can obtain (Chern, 2019):

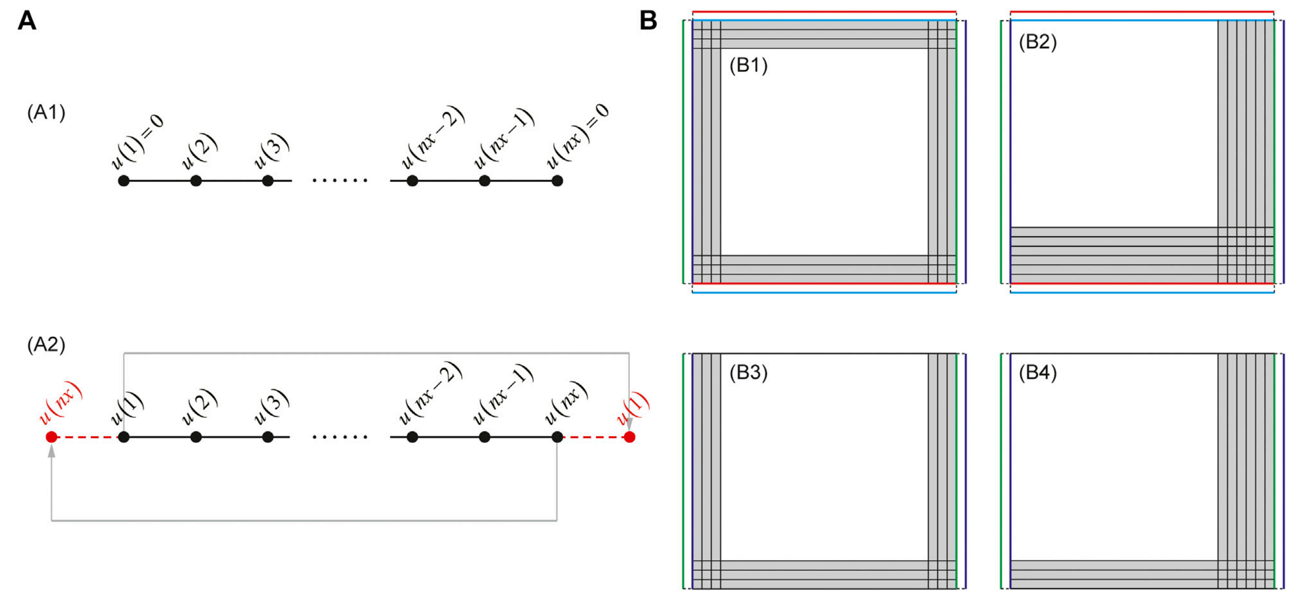

FIGURE 3 | Sketch map of the periodic boundary condition. (a1) The conventional aperiodic boundary condition for 1-dimensional model. (a2) The periodic boundary condition for 1-dimensional model. **(B)** Sketch map of the periodic boundary condition for 2-dimensional model. (b1) and (b2) are the sketch map of the periodic boundaries settled in the four directions of up, down, left, and right. (b3) and (b4) are the sketch map of the periodic boundary condition with the free boundary condition for the up boundary and the PML boundaries for the other three directions. periodic boundary is used only for the left and right boundaries.

$$\rho \sim \frac{2 - d_x \Delta x \frac{k_x}{\omega}}{2 + d_x \Delta x \frac{k_x}{\omega}}. \tag{12}$$

Smooth waves with 0 incident angle can be eliminated within one grid when $\rho \sim 0$. Combined with $\omega = k_x v$, we obtain the attenuation coefficient for the model with the velocity v as

$$d_x = \frac{2v}{\Delta x} \tag{13}$$

With the constant attenuation coefficient, the projection method is shown as **Figure 2C**, the quadrangles with different colours mean different projection unit for each 2nd-order FD operator. **Figure 2D**, which refers to Chern (2019), shows the projection method for the quadrangle of $\hat{U}(i)$. By introducing the auxiliary variables $\hat{f}$, $\hat{\phi}_x$, and $\hat{\psi}_x$, $\tau_x^{-1}\hat{U}$ and $\tau_x \hat{U}$ can be projected to $\tau_x^{-1}\hat{f}$ and $\tau_x \hat{f}$ using Discrete Complex Analysis, where τ_x and τ_x^{-1} are the positive and negative shift operators along x-direction (i. e., $\tau_x \hat{U}(j) = \hat{U}(j+1)$ and $\tau_x^{-1}\hat{U}(j) = \hat{U}(j-1)$), respectively. Chern (2019) gave the detailed process derive the RD-PML expression. Here, we briefly introduce the algorithm and extend this algorithm to the numerical simulation of seismic wavefield. The expressions for $\hat{\phi}_x$ and $\hat{\psi}_x$ can be obtained as following (Chern, 2019)

$$\begin{cases} -i\omega\hat{\phi}_x = -\frac{1}{2}\left[\left(\tau_x^{-1}d_x\right)\left(\tau_x^{-1}\hat{\phi}_x\right) + d_x\hat{\phi}_x\right] - \frac{1}{2\Delta x}\left(\tau_x\hat{U} - \tau_x^{-1}\hat{U}\right), \\ -i\omega\hat{\psi}_x = -\frac{1}{2}\left[\left(\tau_x^{-1}d_x\right)\hat{\psi}_x + d_x\left(\tau_x\hat{\psi}_x\right)\right] - \frac{1}{2\Delta x}\left(\tau_x\hat{U} - \tau_x^{-1}\hat{U}\right). \end{cases} \tag{14}$$

Further, the expression of $\tau_x^{-1}\hat{f}$ and $\tau_x\hat{f}$ can be written as (Chern, 2019)

$$\begin{cases} \tau_x^{-1}\hat{f} = \tau_x^{-1}\hat{U} - \Delta x\left(\tau_x^{-1}d_x\right)\left(\tau_x^{-1}\hat{\phi}_x\right), \\ \tau_x\hat{f} = \tau_x\hat{U} + \Delta x d_x\left(\tau_x\hat{\psi}_x\right). \end{cases} \tag{15}$$

Now, we can convert the 2nd-order FD operator for the spatial partial derivative $\partial^2\hat{U}/\partial\tilde{x}^2$ as

$$\frac{\partial^2\hat{U}}{\partial\tilde{x}^2} = \frac{\tau_x\hat{U} - 2\hat{U} + \tau_x^{-1}\hat{U}}{\Delta\tilde{x}^2} \rightarrow \frac{\partial^2\hat{f}}{\partial x^2} = \frac{\tau_x\hat{f} - 2\hat{f} + \tau_x^{-1}\hat{f}}{\Delta x^2}. \tag{16}$$

Substituting **Eq. 15** into the latter expression of **Eq. 16**, we can obtain

$$\begin{aligned} \frac{\partial^2\hat{f}}{\partial x^2} &= \frac{\tau_x\hat{f} - 2\hat{f} + \tau_x^{-1}\hat{f}}{\Delta x^2} \\ &= \frac{\tau_x\hat{U} - 2\hat{U} + \tau_x^{-1}\hat{U}}{\Delta x^2} + \frac{d_x\left(\tau_x\hat{\psi}_x\right) - \left(\tau_x^{-1}d_x\right)\left(\tau_x^{-1}\hat{\phi}_x\right)}{\Delta x}, \end{aligned} \tag{17}$$

where the attenuation term of the RD-PML is simply added to the original FD operator. This form does not require special treatment of the original wave equation to implement the RD-PML, and we only need to add the corresponding attenuation term in the PML attenuation area during programming, which is very convenient for the realization of numerical simulation.

After transforming **Eqs 14**, **17** back to the time domain using the inverse Fourier transform, and introducing the derivation along the z-direction, we can obtain the whole expressions of the RD-PML for **Eq. 1**:

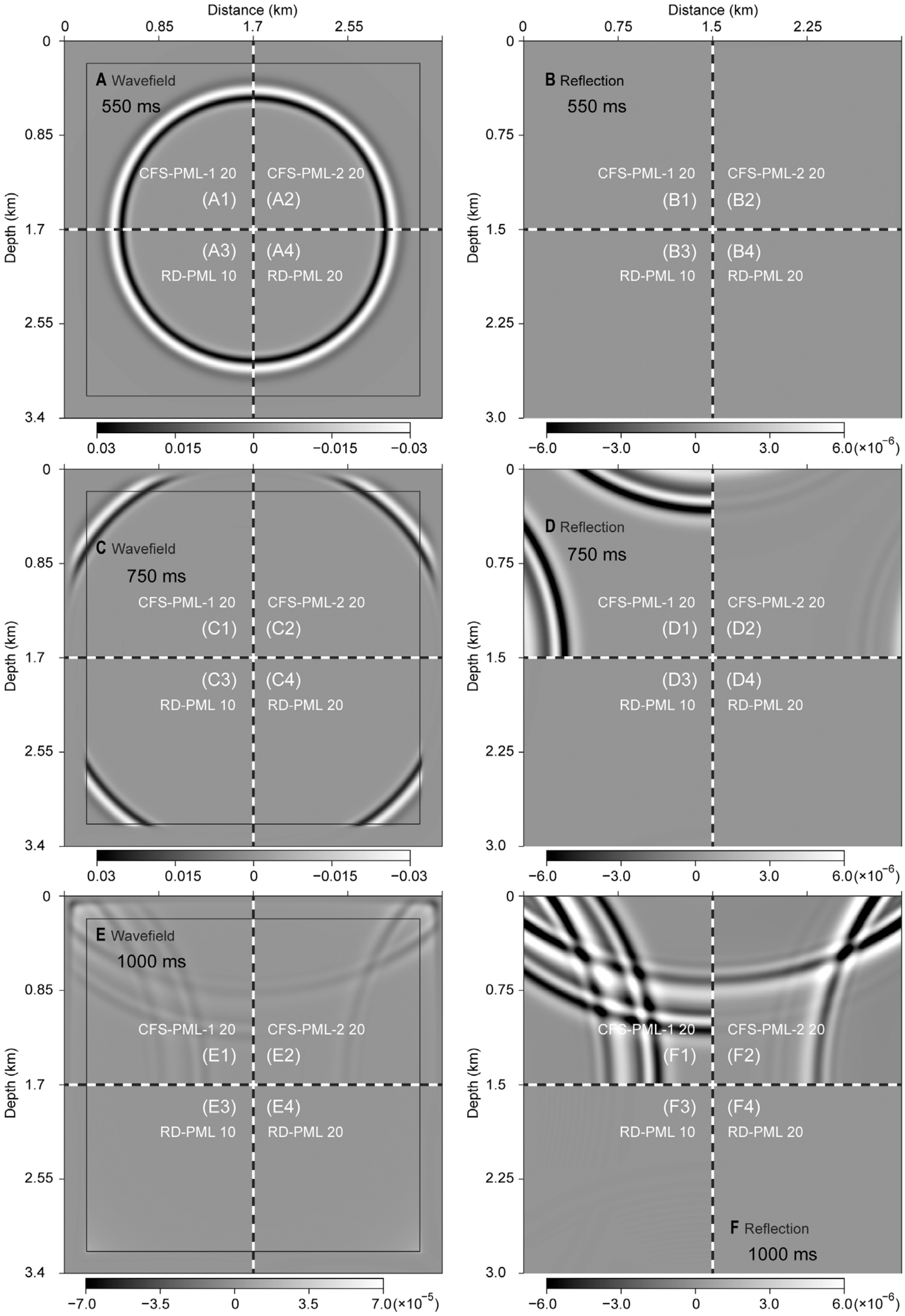

FIGURE 4 | Snapshots and wave reflections obtained using different types of PML. **(A)**, **(C)**, and **(E)** are the snapshots obtained at 550, 750, and 1,000 ms, respectively. The areas in the black boxes are the normal wavefield simulation area, and the areas outside the black boxes are the absorbing area of PML. **(B)**, **(D)**, and **(F)** are the wave reflections obtained at 550, 750, and 1,000 ms in the normal wavefield simulation area, respectively.

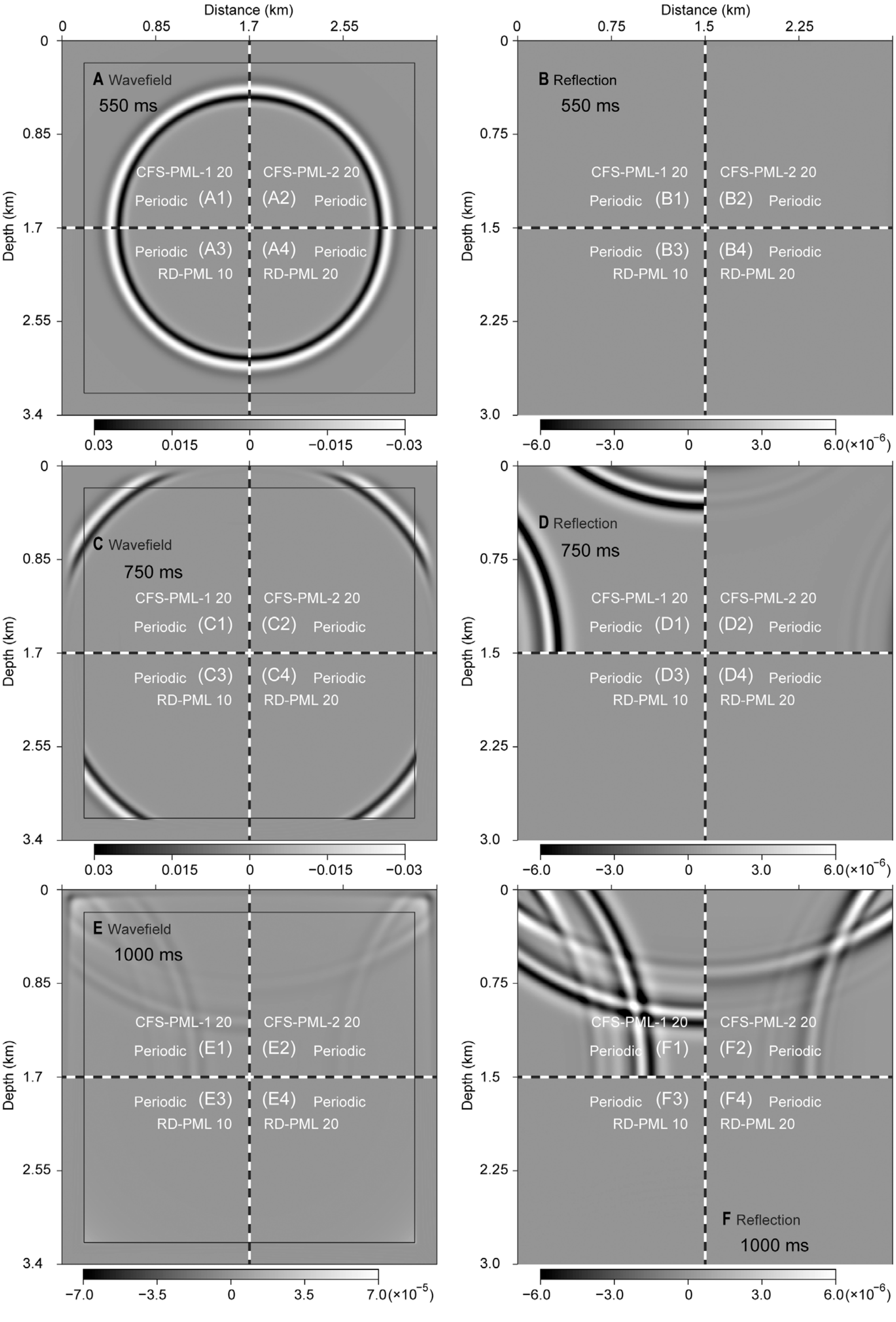

FIGURE 5 | Snapshots and wave reflections obtained using different types of PML using periodic boundary. **(A)**, **(C)**, and **(E)** are the snapshots obtained at 550, 750, and 1,000 ms, respectively. **(B)**, **(D)**, and **(F)** are the wave reflections obtained at 550, 750, and 1,000 ms, respectively.

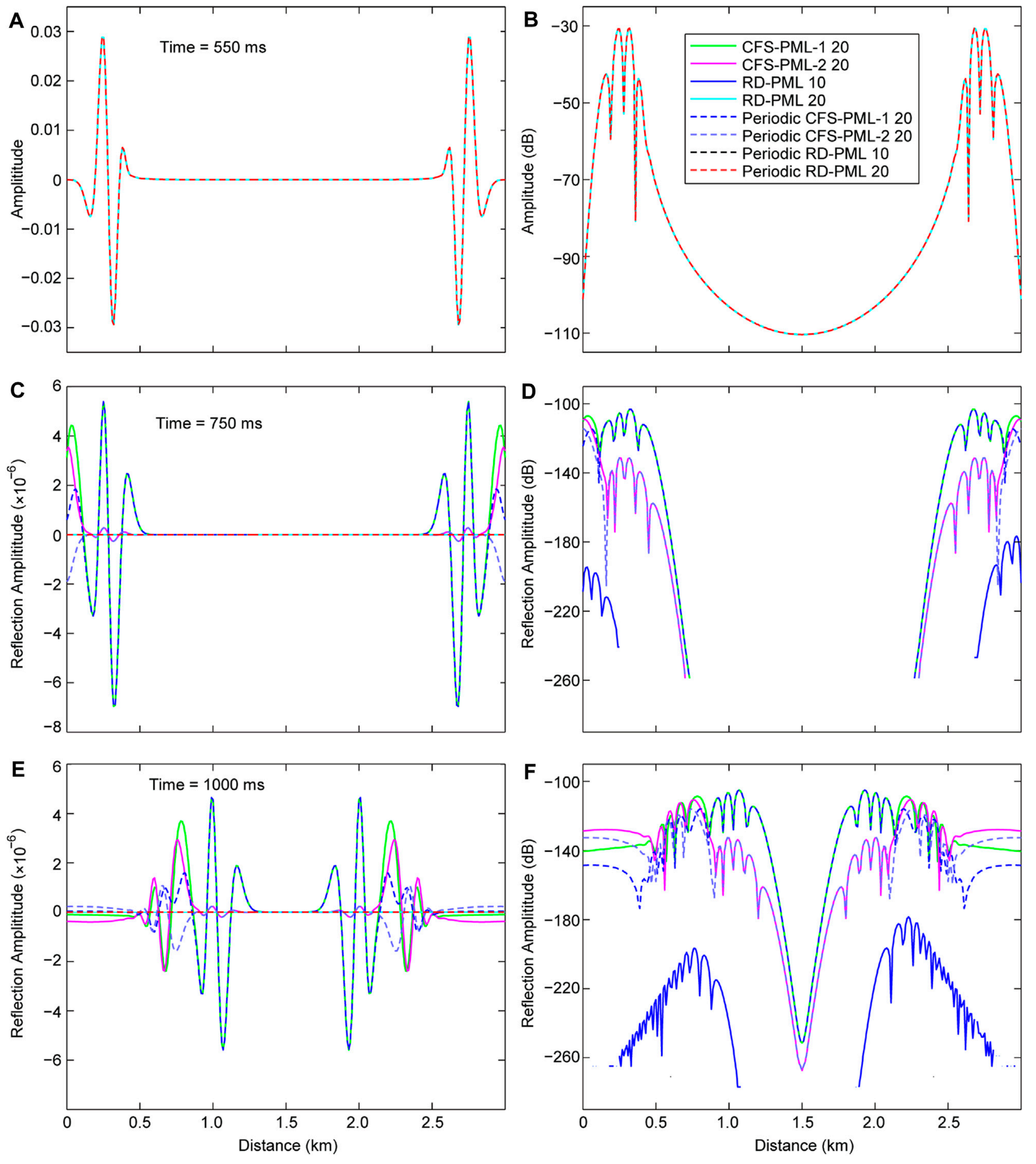

FIGURE 6 | Waveforms along the horizontal dashed line in **Figure 4** and **Figure 5** at different time. **(A)**, **(C)**, and **(E)** are the waveforms obtained at 550, 750, and 1,000 ms, respectively. **(B)**, **(D)**, and **(F)** are the logarithmic display of waveforms in **(A)**. **(C)**, and **(E)**, respectively.

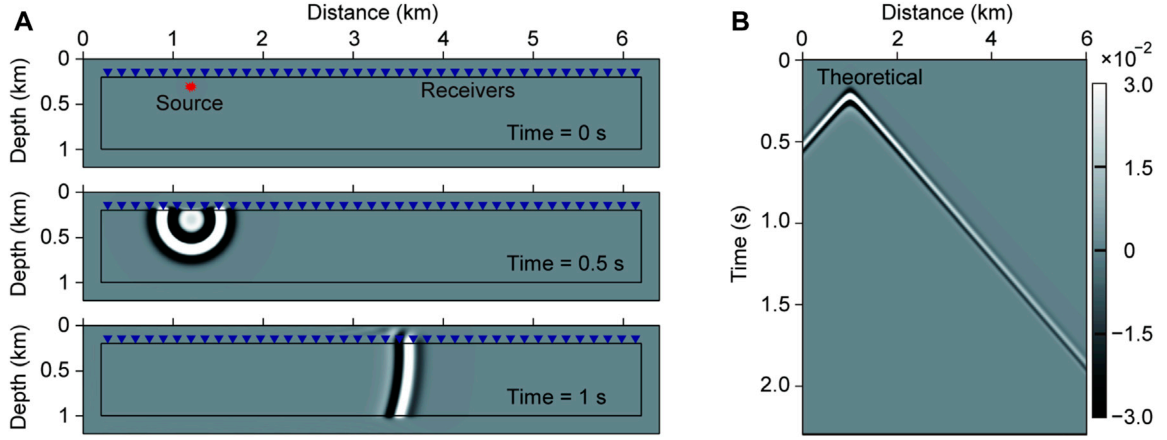

FIGURE 7 | Schematic map of the narrow slice model and wave field record. **(A)** Snapshots of a point source for the narrow slice model at 0, 500, and 1,000 ms. The snapshots are obtained by 20-layer RD-PML. **(B)** Shot records by the receivers along the horizontal line of blue triangles in **(A)**. The shot records are obtained using a very large model to avoid boundary reflections, which can be regarded as a reference to check the performance of different types of PML.

$$\begin{cases} \frac{1}{v^2}\frac{\partial^2 u}{\partial t^2} = \frac{1}{\Delta x^2}\left(\tau_x u - 2u + \tau_x^{-1}u\right) + \frac{1}{\Delta z^2}\left(\tau_z u - 2u + \tau_z^{-1}u\right) \\ +\frac{1}{\Delta x}\left[d_x\left(\tau_x\psi_x\right) - \left(\tau_x^{-1}d_x\right)\left(\tau_x^{-1}\phi_x\right)\right] + \frac{1}{\Delta z}\left[d_z\left(\tau_z\psi_z\right) - \left(\tau_z^{-1}d_z\right)\left(\tau_z^{-1}\phi_z\right)\right], \\ \frac{\partial\phi_x}{\partial t} = -\frac{1}{2}\left[\left(\tau_x^{-1}d_x\right)\left(\tau_x^{-1}\phi_x\right) + d_x\phi_x\right] - \frac{1}{2\Delta x}\left(\tau_x u - \tau_x^{-1}u\right), \\ \frac{\partial\psi_x}{\partial t} = -\frac{1}{2}\left[\left(\tau_x^{-1}d_x\right)\psi_x + d_x\left(\tau_x\psi_x\right)\right] - \frac{1}{2\Delta x}\left(\tau_x u - \tau_x^{-1}u\right), \\ \frac{\partial\phi_z}{\partial t} = -\frac{1}{2}\left[\left(\tau_z^{-1}d_z\right)\left(\tau_z^{-1}\phi_z\right) + d_z\phi_z\right] - \frac{1}{2\Delta z}\left(\tau_z u - \tau_z^{-1}u\right), \\ \frac{\partial\psi_z}{\partial t} = -\frac{1}{2}\left[\left(\tau_z^{-1}d_z\right)\psi_z + d_z\left(\tau_z\psi_z\right)\right] - \frac{1}{2\Delta z}\left(\tau_z u - \tau_z^{-1}u\right), \end{cases} \tag{18}$$

where ψ_x, ϕ_x, ψ_z and ϕ_z are the variables in the time domain after inverse Fourier transform applied to $\hat{\psi}_x$, $\hat{\phi}_x$, $\hat{\psi}_z$ and $\hat{\phi}_z$, respectively. Compared with the expressions for RD-PML in Chern (2019), **Eq. 18** directly introduces the velocity v in the first expression, and there is no change in the other expressions. To implement RD-PML, our target is to handle the discretization and calculation for the spatial partial derivatives of the wave equation in PML region. The introduced auxiliary variables $\hat{\psi}_x$, $\hat{\phi}_x$, $\hat{\psi}_z$ and $\hat{\phi}_z$ actually serve spatial partial derivatives and velocity v is not required to participate in this progress. This form can refer to the previous approach in introducing auxiliary variables for PML (Komatitsch and Martin, 2007; Pasalic and McGarry, 2010; Zhang and Shen, 2010).

In a homogeneous medium, since the PML attenuation coefficient of each layer is the same, Chern (2019) adopted the periodic boundary, which greatly improved the absorbing performance of the RD-PML. **Figure 3** shows the sketch map of the periodic boundary. **Figure 3A1** shows the conventional Dirichlet boundary for 2$^{\text{nd}}$-order FD scheme in 1-dimansional situation, while **Figure 3A2** shows the corresponding periodic boundary processing method, which connects the outmost FD operators on the two sides of discrete grid points. **Figure 3B** shows the sketch maps of the periodic boundary condition in the two-dimensional model, in which **Figures 3B1, 3B2** with the boundaries set in the four directions of up, down, left, and right and **Figure 3B3, 3B4** with the free boundary condition for the up boundary and the PML for the other three boundaries. Neither the top boundary nor the bottom boundary has been specially processed, and the periodic boundaries are only used for the left and right boundaries.

NUMERICAL EXPERIMENTS

Homogenous Model

We perform numerical experiments on a homogeneous square model using different types of PML. The wave velocity is v = 3,000 m/s. The spatial grid interval is $\Delta x = \Delta z = 10$ m, and the grid number is 301 × 301. The source is a Ricker wavelet with a dominant frequency of 15 Hz, which is located at the center of the square model. We use the 2$^{\text{nd}}$-order FD method for the spatial discretization and 4-stage Runge Kutta method for the temporal discretization, and the time step is Δt = 1 ms. We compare the boundary reflections using various types of PML: the AED CFS-PML using collocated grid (abbreviated as CFS-PML-1, Gao et al., 2015) with 20 layers; the convolutional CFS-PML using staggered grid (abbreviated as CFS-PML-2, Pasalic and McGarry, 2010) with 20 layers; and the RD-PML with 10 layers and 20 layers, respectively. We use a very large model to simulate the theoretical wavefield to avoid boundary reflections, which can be regarded as a reference to check the performance of the above-mentioned artificial absorbing boundaries.

Figure 4 shows the snapshots obtained by different types of PML. At 550 ms, the wavefield has not reached the attenuation area of PML, and the reflected waves have not yet arisen, so the value of the reflections in **Figure 4B1–4B4** are all zero. At 750 ms, conspicuous reflections appear in 20-layer CFS-PML-1, and weak reflections appear in 20 CFS-PML-2. This is because the latter one is implemented based on the staggered grid method, and its

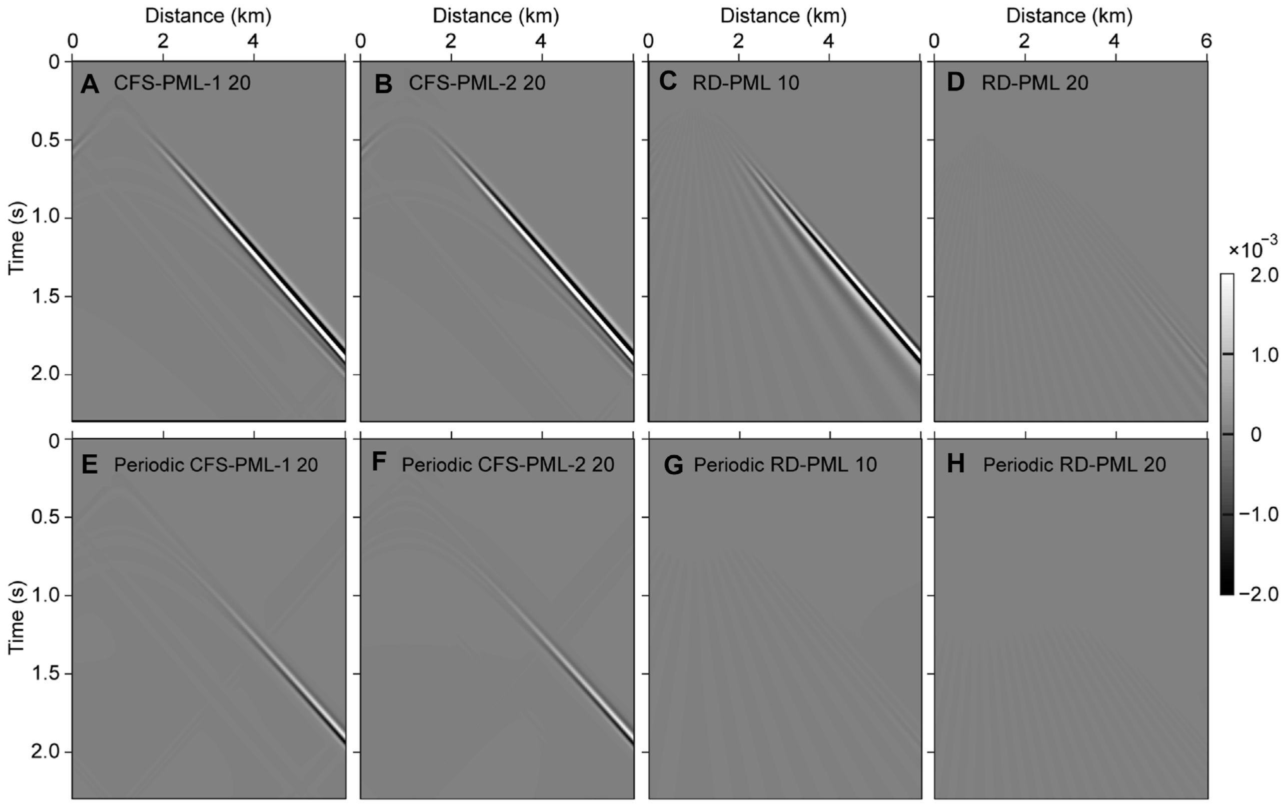

FIGURE 8 | Wavefield difference between the shot records of different types of PML with the theoretical shot records that shown in **Figure 7B**. **(A)**, **(B)**, **(C)**, and **(D)** are the wavefield difference between the shot records of 20-layer CFS-PML-1, 20-layer CFS-PML-2, 10-layer RD-PML, and 20-layer RD-PML with the theoretical records, respectively. **(E)**, **(F)**, **(G)**, and **(H)** are the wavefield difference that the shot records using periodic boundaries for the corresponding types of PML in **(A)**, **(B)**, **(C)**, and **(D)**, respectively.

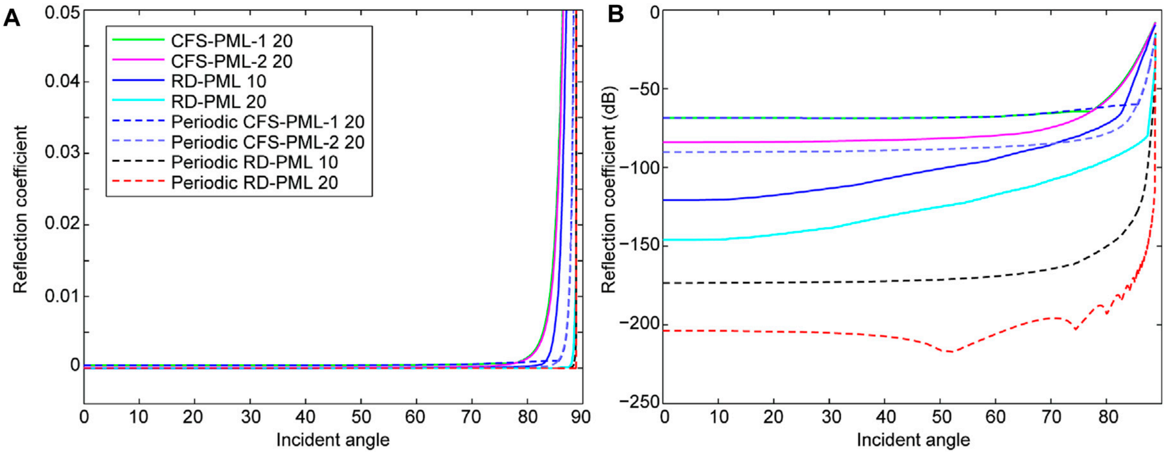

FIGURE 9 | Comparison of the reflection coefficient computed by numerical simulations. **(A)** Absolute values of numerical reflection coefficient. **(B)** The decibel (dB) values of numerical reflection coefficient.

absorbing performance is better than that of the former one, which is implemented based on the collocated grid method. Neither 10-layer RD-PML nor 20-layer RD-PML shows any reflections in the current color scale. At 1,000 ms, there are slight reflections in 10-layer RD-PML, but there are still no visible reflections in 20-layer RD-PML. At the same time, by

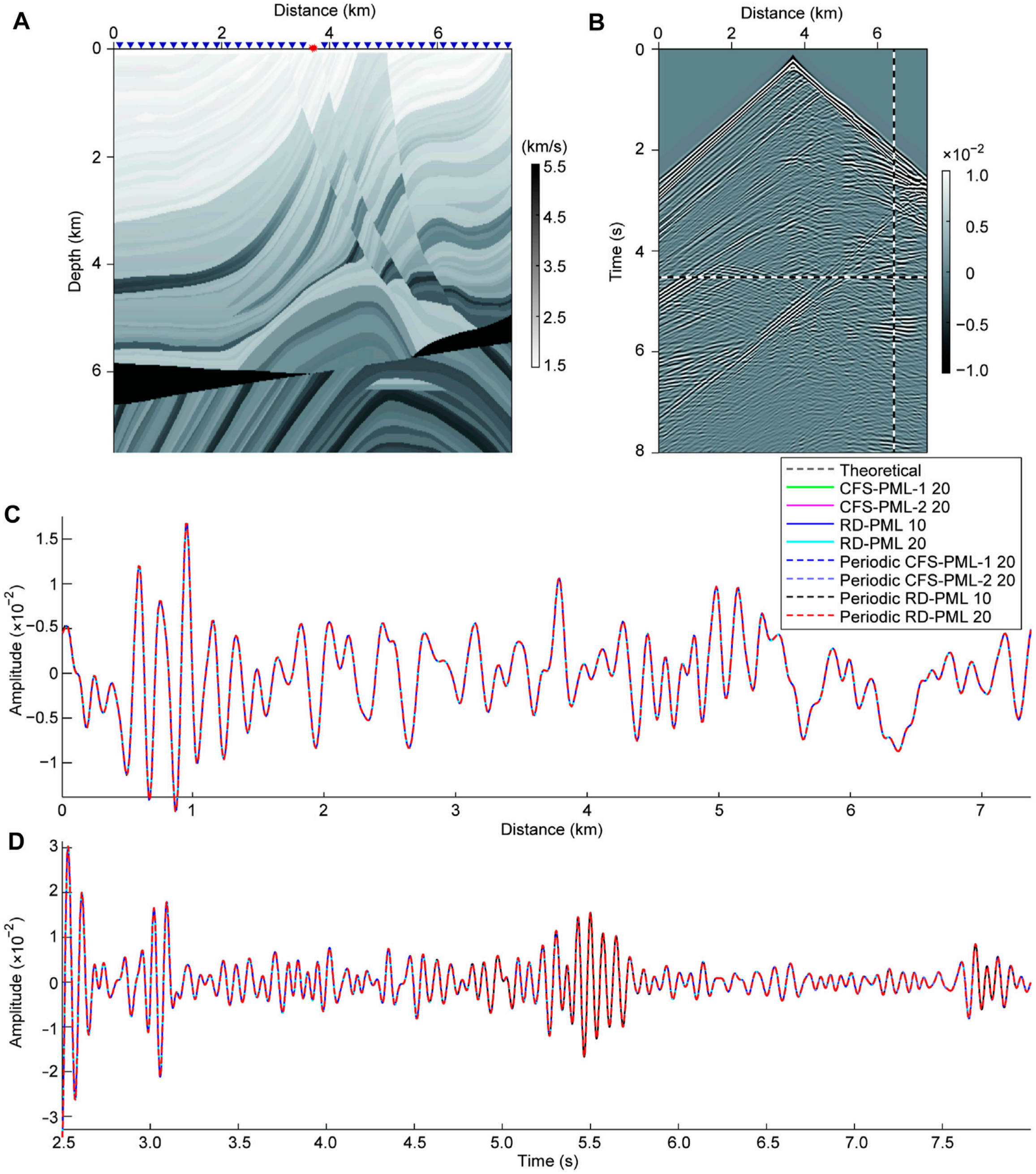

FIGURE 10 | Numerical test on a heterogeneous model. **(A)** Modified Marmousi model. **(B)** Shot records by the receivers along the horizontal line of blue triangles in **(A)**. **(C)** and **(D)** are the waveforms along the horizontal dashed line and the vertical dashed line in **(B)**, respectively.

comparing the reflections of 10-layer RD-PML with that of 20-layer CFS-PML-1 and 20-layer CFS-PML-2, we find that the reflected waves of the conventional discrete PML (20-layer CFS-PML-1 and 20-layer CFS-PML-2) mainly consist of two parts: one part is the reflected wave from the inner boundary of PML, and the other is the reflected wave from the outer boundary of PML.

The reflections of 10-layer RD-PML mainly consist of the reflected waves from the outer boundary, which is caused by the outer boundary of PML due to insufficient thickness. Considering that the parameter settings of each layer of 10-layer RD-PML and 20-layer RD-PML are all the same, which also explains why the latter performs better than the former. At the same time, this conclusion leads to experiments using periodic boundaries.

Figure 5 shows the snapshots obtained by different types of PML after the periodic boundaries used. After adopting the periodic boundaries refer to **Figure 3B1**, the reflections from outer boundary of the conventional discrete PML (20-layer CFS-

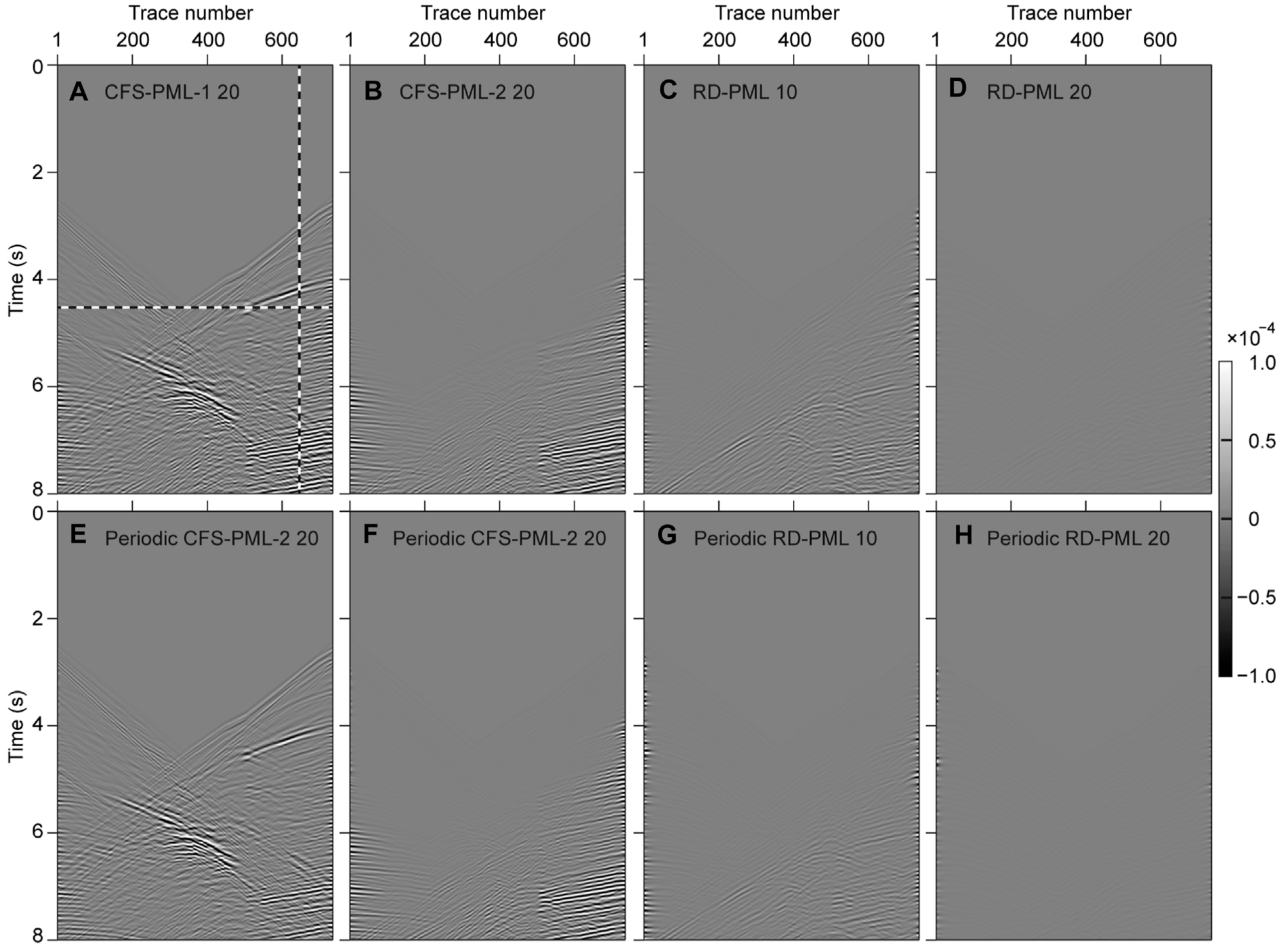

FIGURE 11 | Wavefield difference between the shot records of different types of PML with the reference shot records that shown in **Figure 10B**. **(A)**, **(B)**, **(C)**, and **(D)** are the wavefield difference between the shot records of 20-layer CFS-PML-1, 20-layer CFS-PML-2, 10-layer RD-PML, and 20-layer RD-PML with the theoretical records, respectively. **(E)**, **(F)**, **(G)**, and **(H)** are the wavefield difference that the shot records using periodic boundaries for the corresponding types of PML in **(A)**, **(B)**, **(C)**, and **(D)**, respectively.

PML-1 and 20-layer CFS-PML-2) have been significantly reduced; while the reflections from inner boundary of the conventional discrete PML have not changed (as shown in **Figure 5F**). This is because the periodic boundary can be regarded as a thickening of the original boundary, which cannot improve the absorbing performance of the reflections from the inner boundary and can only improve the absorbing performance of the reflections from the outer boundary. As analyzed above, the reflections of the 10-layer RD-PML mainly consist of the reflections from the outer boundary. Therefore, its absorbing performance has been significantly improved after adopting the periodic boundary. The reflected waves of 10-layer RD-PML are no longer visible in the color scale of **Figure 5F**.

Figure 6 shows the waveforms along the horizontal dashed lines in **Figures 4**, **5**. **Figure 6A** shows the waveforms for different types of PML before reaching the boundaries, and all the unattenuated waveforms are all the same. **Figures 6D,F** are the logarithmic displays for the reflected waves of **Figures 6C,E**, respectively. At 1,000 ms, the reflected waves of the 10-layer RD-PML are the smallest among all the reflections (shown in **Figure 6F**). At the same time, we find that the reflected waves of the 20-layer RD-PML, periodic 10-layer RD-PML, and periodic 20-layer RD-PML all disappear. This is because their reflections are zero and the corresponding logarithmic values don't exist, which demonstrate that the absorbing performance of these three boundaries indeed reach "mechanical zero" (Chern, 2019).

For the convenience of comparing the absorbing performances of different boundary conditions, we further perform numerical experiments using a long model, which can be seen as a narrow strip model (shown in **Figure 7A**). The farther the distance between the receiver and the seismic source, the greater the incident angle of the wave field, and the harder it is to absorb the incident waves for the absorbing boundary. Grazing incident wave would appear in the long model when the wavefield is far from the source (Komatitsch and Martin, 2007; Gao et al., 2017), so we can compare the absorbing performance for the

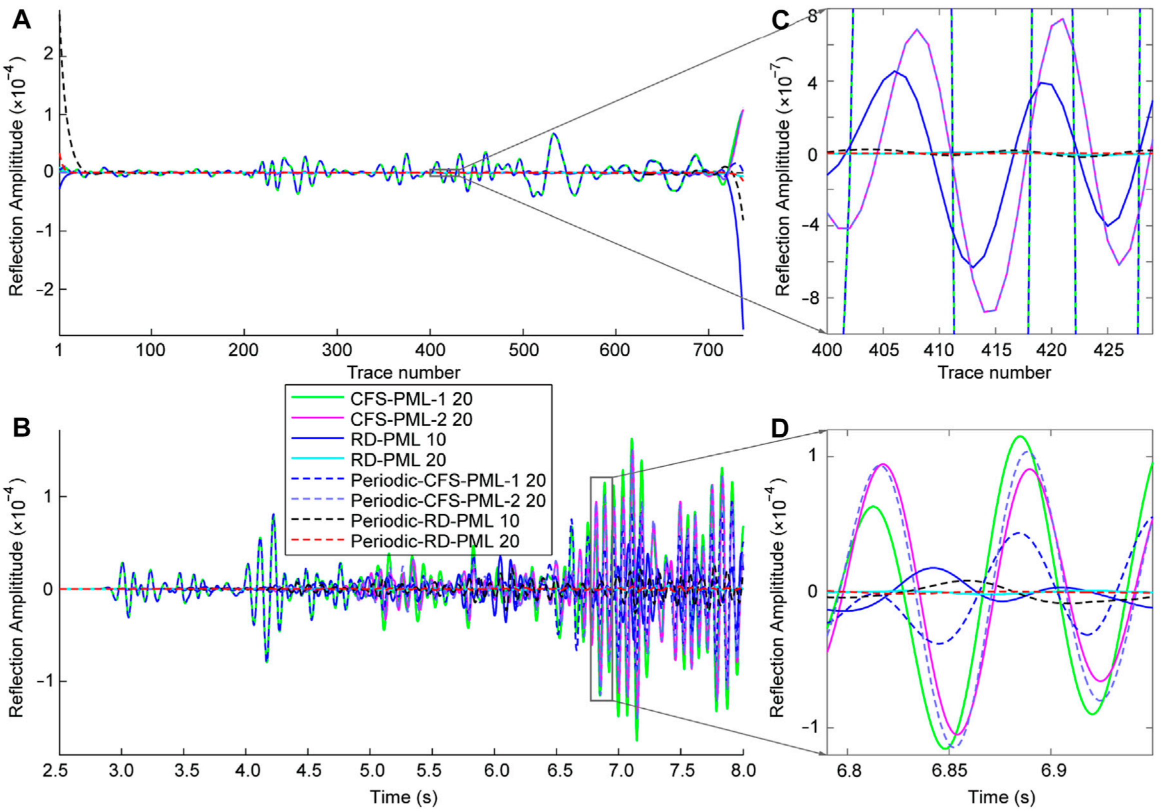

FIGURE 12 | Artificial reflections obtained by the wavefield difference between the shot records and the reference shot records. **(A)** and **(B)** are the waveforms along the horizontal dashed line and the vertical dashed line in **Figure 11**, respectively. **(C)** and **(D)** are the enlarged portions of the frame in **(A)** and **(B)**, respectively.

grazing incident wave of different PML. The wave velocity is v = 3,000 m/s. The spatial grid interval is $\Delta x = \Delta z = 10$ m, and the grid number is 601 × 81. The source is a Ricker wavelet with a dominant frequency of 10 Hz. Seismic source is located at 1,000 m along x-direction and 100 m in depth. We obtain the wavefield records along the line composed of blue inverted triangles in **Figure 7A**. We use a very large model to simulate the theoretical wavefield records to avoid boundary reflections, which can be regarded as a reference (shown in **Figure 7B**).

Figure 8 shows the wavefield difference between the shot records of different types of PML with the theoretical shot records that shown in **Figure 7B**. For absorbing the grazing incident waves, 10-layer RD-PML performs better than 20-layer CFS-PML-1 and 20-layer CFS-PML-2 (shown in **Figures 8A,B**), but performs not as good as Periodic 20-layer CFS-PML-1 and Periodic 20-layer CFS-PML-2 (shown in **Figures 8E,F**). Weak reflected waves appear in 20-layer RD-PML (shown in **Figure 8D**), while no obvious reflected waves appear in Periodic 10-layer RD-PML and Periodic 20-layer RD-PML (shown in **Figures 8D,H**).

Because RD-PML still uses the conventional PML coordinate stretching operator expression (shown as **Eq. 2**), broom-like evanescent waves still appear (shown in **Figures 8C,D,G,H**), which are caused by grazing incident waves. Due to the advantages of the coordinate stretching operator expression of CFS-PML type boundary for grazing waves (Komatitsch and Martin, 2007), no broom-like reflected wave appears (shown in **Figures 8A,B,E,F**). Compared with the main reflected waves, the evanescent waves are very weak and their amplitudes are negligible. The RD-PML here, especially after adopting the periodic absorbing boundary, has obvious advantages over conventional methods.

In order to further compare the absorbing performances, we calculated the numerical reflection coefficients for different types of PML. We calculate the numerical reflection coefficient by

$$R_p = \left| \frac{\max\left(u_{ref}\right) - \max\left(u_{mod}\right)}{\max\left(u_{ref}\right)} \right|, \tag{19}$$

where u_{ref} are the theoretical wavefield records at the outer boundary without artificial reflections, and u_{mod} are the wavefield records at the upper boundary with different artificial boundary conditions. For a given spatial position, the maximum value of the wavefields along the whole temporal duration are taken to compute the numerical reflection coefficient. **Figure 9B** shows the decibel (dB) values of numerical reflection coefficient at different incident angles, where. $dB(R_p) = 20\log_{10} R_p$.

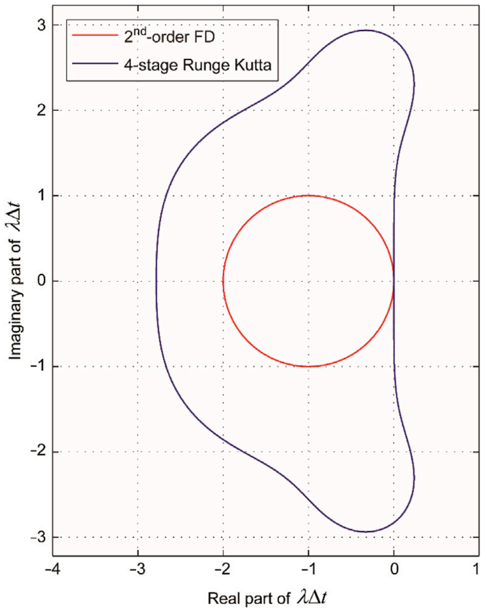

FIGURE 13 | Stability regions for different temporal discretization methods. The stability regions for the 2nd-order FD scheme and the 4-stage Runge Kutta scheme are the regions inside the red curve and the blue curve, respectively; while the instability regions for the 2nd-order FD scheme and the 4-stage Runge Kutta scheme are the regions outside the red curve and the blue curve, respectively. λ represents the eigenvalue of the discrete wave equation.

Obviously, the periodic boundary performs better than the corresponding non-periodic boundary. Periodic-10-layer RD-PML performs even better than 20-layer RD-PML, and periodic 20-layer RD-PML performs the best among all the absorbing boundaries. The jitters in the reflection curve of periodic 20-layer RD-PML is caused by the broom-like evanescent waves in **Figure 8H**, whose amplitudes are negligible.

Heterogenous Model

To illustrate the numerical performance of the proposed method for heterogeneous media, we test on the modified Marmousi model, as shown in **Figure 10A**. The grid spacing is 10 m and the grid number is 737 × 751. The upper boundary of the model is a free surface, and the other three edges are absorbing boundaries. The source is a Ricker wavelet and the dominant frequency is of 8 Hz. The source is added on the free surface and middle of the model. A group of receivers are located along the upper boundary. Eight kinds of boundary conditions are compared. There is no theoretical wavefield available as a reference for the Marmousi model; thus, we take the wavefield generated by 50-layer RD-PML as a reference instead (shown in **Figure 10B**). The periodic boundaries for different types of PML are settled refer to **Figure 3B3**.

Figure 11 shows the wavefield difference, which can be regarded as the reflected waves from the boundaries, between the shot records of different types of PML with the reference shot records that shown in **Figure 10B**. **Figures 12A, B** show the waveforms along the horizontal dashed line and the vertical dashed line in **Figure 11**, respectively. The performances of 10-layer RD-PML are better than that of 20-layer conventional CFS-PML, which demonstrates that RD-PML still has a good absorbing effect and applicability for heterogeneous media. Here we focus on the internal comparison of different layers of RD-PML. There are two points that require special analysis: 1) periodic 10-layer RD-PML performs better than 10-layer RD-PML, but not better than 20-layer RD-PML, which is different from the homogeneous medium. Taking the left and right boundaries as an example, the speed setting of the PML region is a one-dimensional extension of the speed along the outermost boundary of the model. Though we set a constant attenuation coefficient $d_x = 2v_{\max}/\Delta x$, the velocity fields in the left and right boundaries are different, which would lead to reflection at the interface of the left and right boundaries when the periodic boundary is adopted. 2) The reflected waves at the left and right boundaries of the 10-layer periodic RD-PML seem to have reversed positions, compared with that of the 10-layer RD-PML. This is due to the periodic boundary that makes part of the reflected wave propagate to the opposite side.

In summary, the improvement of the absorbing performance in heterogeneous media by the periodic boundary is not as obvious as in a homogeneous medium both for the conventional discrete PML and the RD-PML, but RD-PML is still superior to the conventional discrete PML. Considering that there is almost no increase in the amount of calculation, we recommend the use of RD-PML with periodic boundary.

DISCUSSION

The expression of the coordinate stretching operator used in this article (shown as **Eq. 2**) has a sign difference compared with the regular expression (Collino and Tsogka, 2001; Komatitsch and Martin, 2007; Zhang and Shen, 2010; Gao et al., 2017):

$$s_x(x) = 1 + \frac{d_x(x)}{i\omega}. \tag{19a}$$

This is because that **Eq. 2** is proposed based on the plane wave expression: $U = u_0 \exp[i(k_x x - \omega t)]$, while **Eq. 19** is proposed based on the plane wave expression: $U = u_0 \exp[-i(k_x x - \omega t)]$ (Johnson, 2008; Chern, 2019). Therefore, **Eq. 2** is actually equal to **Eq. 19**. We adopt **Eq. 2** in this article to maintain continuity with Chern's method.

The RD-PML is implemented by directly adding the decay terms to the original wave equation and the original spatial partial derivatives have not been modified (shown as the first expression in **Eq. 18**), which is very easy for programming. In addition, since RD-PML is suitable for periodic boundary, the scheme in **Figures 3B2, 3B4** can be used in programming, which is very easy to load RD-PML outside the normal simulation area. These two advantages make RD-PML have good application prospects in both reverse time migration (RTM) and full waveform inversion (FWI). To implement the RD-PML for an existing RTM or FWI program, we don't have to rewrite the original program; instead, we only need to add a corresponding RD-PML calculation module and load it in the main program.

For the temporal discretization, we tried to implement the RD-PML using the conventional 2$^{\text{nd}}$-order FD method for the temporal discretization. However, a very small time-step size is required to ensure the stability of the wave field iteration, otherwise the wavefield iteration would fail. Instead, we adopt the 4-stage Runge Kutta method for the temporal discretization of the seismic wave equation according to Chern (2019). We give a rough analysis for the reason here. The stability area of the 4-stage Runge Kutta method is larger than that of the second-order FD method (shown in **Figure 13**), which means that the CFL stability condition of the former are more relaxed (Karim, 1966; Frank, 2008). In the case of the same spatial model parameters, the former can use a larger time step, and we can use the time step as we routinely use for simulation. This shows that the stability conditions of the RD-PML method are relatively harsh, although it has been proven to be stable by Chern (2019). The research on the stability conditions of RD-PML can also be a future research work.

CONCLUSION

We introduce the RD-PML to the seismic wave numerical simulation. Firstly, we introduce the principle of PML attenuation in detail and analyze the cause of reflections that produced by conventional discrete PML. Then, we compare the absorbing performance of the RD-PML with that of the conventional discrete PML. Numerical experiments demonstrate the superiority of the RD-PML. In homogenous model, RD-PML with sufficient thickness (e.g., 20 layer) can make the reflected waves reach the effect of mechanical zero; in heterogenous model, 10-layer RD-PML performs better than the 20-layer conventional discrete PML. Furthermore, we adopt periodic boundary to the RD-PML, which can improve the absorbing performance of RD-PML without increasing the amount of memory and calculation. Although in the inhomogeneous medium, the periodic boundary has a very limited improvement in the absorbing performance, it doesn't increase the amount of calculation. Another point is that RD-PML is directly implemented based on the 2$^{\text{nd}}$-order equation, and the attenuation term is directly added to the original wave equation. This kind of system does not need to be rewritten as a first-order system, which is very convenient for programming. The method in this paper provides a new idea to realize discrete PML, and has an important role in promoting the development of PML technology.

DATA AVAILABILITY STATEMENT

The raw data supporting the conclusion of this article will be made available by the authors, without undue reservation.

AUTHOR CONTRIBUTIONS

YG derives the equations, writes the program, and does the numerical experiments. MZ checks the formula derivation and takes analysis for the numerical experiments.

ACKNOWLEDGMENTS

We are especially grateful to Albert Chern for his helpful introduction and discussion on RD-PML. This research is supported by the Science and Technology Development Fund, Macau SAR (grant nos. 0002/2019/APD, 0079/2018/A2). YG is also supported by the National Natural Science Foundation of China (grant no. 41704063, 11773087) and the General Financial Grant from the China Postdoctoral science foundation (grant no. 2017M610980).

REFERENCES

Abarbanel, S., and Gottlieb, D. (1997). A Mathematical Analysis of the PML Method. *J. Comput. Phys.* 134 (2), 357–363. doi:10.1006/jcph.1997.5717

Bérenger, J. P. (1994). A Perfectly Matched Layer for the Absorption of Electromagnetic Waves. *J. Comput. Phys.* 114 (2), 185–200. doi:10.1006/jcph.1994.1159

Bérenger, J. P. (2002). Numerical Reflection from FDTD-PMLs: A Comparison of the Split PML with the Unsplit and CFS PMLs. *IEEE Trans. Antennas Propag.* 50 (3), 258–265. doi:10.1109/8.999615

Bermúdez, A., Hervella-Nieto, L., and Prieto, A. (2007). An Optimal Perfectly Matched Layer with Unbounded Absorbing Function for Tim/j.jcp.2006.09.018

Bobenko, A. I., and Günther, F. (2016). "Discrete Complex Analysis on Planar Quad-Graphs," in *Advances in Discrete Differential Geometry* (Berlin, Heidelberg: Springer), 57–132. doi:10.1007/978-3-662-50447-5_2

Bobenko, A. I., Mercat, C., and Suris, Y. B. (2005). Linear and Nonlinear Theories of Discrete Analytic Functions. Integrable Structure and Isomonodromic Green's Function. *J. für die reine Angew. Math. (Crelles J.)* 2005, 117–161. doi:10.1515/crll.2005.2005.583.117

Chern, A. (2019). A Reflectionless Discrete Perfectly Matched Layer. *J. Comput. Phys.* 381, 91–109. doi:10.1016/j.jcp.2018.12.026

Chew, W. C., and Liu, Q. H. (1996). Perfectly Matched Layers for Elastodynamics: a New Absorbing Boundary Condition. *J. Comp. Acous.* 04 (04), 341–359. doi:10.1142/s0218396x96000118

Chew, W. C., and Weedon, W. H. (1994). A 3D Perfectly Matched Medium from Modified Maxwell's Equations with Stretched Coordinates. *Microw. Opt. Technol. Lett.* 7 (13), 599–604. doi:10.1002/mop.4650071304

Collino, F., and Monk, P. B. (1998). Optimizing the Perfectly Matched Layer. *Comput. Methods Appl. Mech. Eng.* 164 (1-2), 157–171. doi:10.1016/s0045-7825(98)00052-8

Collino, F., and Tsogka, C. (2001). Application of the Perfectly Matched Absorbing Layer Model to the Linear Elastodynamic Problem in Anisotropic Heterogeneous media. *Geophysics* 66 (1), 294–307. doi:10.1190/1.1444908

Correia, D., and Jian-Ming Jin, J.-M. (2005). On the Development of a Higher-Order PML. *IEEE Trans. Antennas Propagat.* 53 (12), 4157–4163. doi:10.1109/tap.2005.859901

Correia, D., and Jin, J.-M. (2006). Performance of Regular PML, CFS-PML, and Second-Order PML for Waveguide Problems. *Microw. Opt. Technol. Lett.* 48 (10), 2121–2126. doi:10.1002/mop.21872

Deng, C., Luo, M., Yuan, M., Zhao, B., Zhuang, M., and Liu, Q. H. (2018). The Auxiliary Differential Equations Perfectly Matched Layers Based on the Hybrid SETD and PSTD Algorithms for Acoustic Waves. *J. Theor. Comput. Acoust.* 26 (1), 1–19. doi:10.1142/s2591728517500311

Diaz, J., and Joly, P. (2006). A Time Domain Analysis of PML Models in Acoustics. *Comput. Methods Appl. Mech. Eng.* 195 (29), 3820–3853. doi:10.1016/j.cma.2005.02.031

Dmitriev, M. N., and Lisitsa, V. V. (2011). Application of M-PML Reflectionless Boundary Conditions to the Numerical Simulation of Wave Propagation in Anisotropic media. Part I: Reflectivity. *Numer. Analys. Appl.* 4 (4), 271–280. doi:10.1134/s199542391104001x

Dmitriev, M. N., and Lisitsa, V. V. (2012). Application of M-PML Absorbing Boundary Conditions to the Numerical Simulation of Wave Propagation in Anisotropic media. Part II: Stability. *Numer. Analys. Appl.* 5 (1), 36–44. doi:10.1134/s1995423912010041

Drossaert, F. H., and Giannopoulos, A. (2007a). Complex Frequency Shifted Convolution PML for FDTD Modelling of Elastic Waves. *Wave Motion* 44 (7), 593–604. doi:10.1016/j.wavemoti.2007.03.003

Drossaert, F. H., and Giannopoulos, A. (2007b). A Nonsplit Complex Frequency-Shifted PML Based on Recursive Integration for FDTD Modeling of Elastic Waves. *Geophysics* 72 (2), T9–T17. doi:10.1190/1.2424888

Duffin, R. J. (1956). Basic Properties of Discrete Analytic Functions. *Duke Math. J.* 23 (2), 335–363. doi:10.1215/s0012-7094-56-02332-8

Duru, K., and Kreiss, G. (2012). A Well-Posed and Discretely Stable Perfectly Matched Layer for Elastic Wave Equations in Second Order Formulation. *Commun. Comput. Phys.* 11 (5), 1643–1672. doi:10.4208/cicp.120210.240511a

Fang, J., and Wu, Z. (1996). Closed-form Expression of Numerical Reflection Coefficient at PML Interfaces and Optimization of PML Performance. *IEEE Microw. Guid. Wave Lett.* 6 (9), 332–334. doi:10.1109/75.535836

Feng, N., and Li, J. (2013). Novel and Efficient FDTD Implementation of Higher-Order Perfectly Matched Layer Based on ADE Method. *J. Comput. Phys.* 232 (1), 318–326. doi:10.1016/j.jcp.2012.08.012

Feng, N., Yue, Y., Zhu, C., Wan, L., and Liu, Q. H. (2015). Second-order PML: Optimal Choice of Nth-Order PML for Truncating FDTD Domains. *J. Comput. Phys.* 285, 71–83. doi:10.1016/j.jcp.2015.01.015

Feng, H., Zhang, W., Zhang, J., and Chen, X. (2017). Importance of Double-Pole CFS-PML for Broad-Band Seismic Wave Simulation and Optimal Parameters Selection. *Geophys. J. Int.* 209 (2), 1148–1167. doi:10.1093/gji/ggx070

Festa, G., and Vilotte, J.-P. (2005). The Newmark Scheme as Velocity-Stress Time-Staggering: an Efficient PML Implementation for Spectral Element Simulations of Elastodynamics. *Geophys. J. Int.* 161 (3), 789–812. doi:10.1111/j.1365-246x.2005.02601.x

Festa, G., Delavaud, E., and Vilotte, J. P. (2005). Interaction between Surface Waves and Absorbing Boundaries for Wave Propagation in Geological Basins: 2D Numerical Simulations. *Geophys. Res. Lett.* 32, 1–4. doi:10.1029/2005gl024091

Frank, J. (2008). Numerical Modelling of Dynamical Systems. Lecture Notes. URL: https://webspace.science.uu.nl/~frank011/Classes/numwisk/ (Accessed 2008).

Gao, K., and Huang, L. (2017). Optimal Damping Profile Ratios for Stabilization of Perfectly Matched Layers in General Anisotropic media. *Geophysics* 83 (1), T15–T30. doi:10.1190/geo2017-0430.1

Gao, Y., Zhang, J., and Yao, Z. (2015). Unsplit Complex Frequency Shifted Perfectly Matched Layer for Second-Order Wave Equation Using Auxiliary Differential Equations. *J. Acoust. Soc. Am.* 138 (6), EL551–EL557. doi:10.1121/1.4938270

Gao, Y., Song, H., Zhang, J., and Yao, Z. (2017). Comparison of Artificial Absorbing Boundaries for Acoustic Wave Equation Modelling. *Explor. Geophys.* 48 (1), 76–93. doi:10.1071/eg15068

Gedney, S. D., and Zhao, B. (2010). An Auxiliary Differential Equation Formulation for the Complex-Frequency Shifted PML. *IEEE Trans. Antennas Propagat.* 58 (3), 838–847. doi:10.1109/tap.2009.2037765

Hastings, F. D., Schneider, J. B., and Broschat, S. L. (1996). Application of the Perfectly Matched Layer (PML) Absorbing Boundary Condition to Elastic Wave Propagation. *J. Acoust. Soc. Am.* 100 (5), 3061–3069. doi:10.1121/1.417118

He, Y., Chen, T., and Gao, J. (2019). Unsplit Perfectly Matched Layer Absorbing Boundary Conditions for Second-Order Poroelastic Wave Equations. *Wave Motion* 89, 116–130. doi:10.1016/j.wavemoti.2019.01.004

Johnson, S. G. (2008). "Notes on Perfectly Matched Layers (PMLs)," in *Lecture Notes* (Massachusetts: Massachusetts Institute of Technology), 29.

Karim, A. I. A. (1966). Stability of the Fourth Order runge-kutta Method for the Solution of Systems of Differential Equations. *Comput. J.* 9 (3), 308–311. doi:10.1093/comjnl/9.3.308

Katsibas, T. K., and Antonopoulos, C. S. (2002). "An Efficient PML Absorbing Medium in FDTD Simulations of Acoustic Scattering in Lossy media," in Proceedings of the 2002 IEEE Ultrasonics Symposium (Munich, Germany: IEEE).

Komatitsch, D., and Martin, R. (2007). An Unsplit Convolutional Perfectly Matched Layer Improved at Grazing Incidence for the Seismic Wave Equation. *Geophysics* 72 (5), SM155–SM167. doi:10.1190/1.2757586

Komatitsch, D., and Tromp, J. (2003). A Perfectly Matched Layer Absorbing Boundary Condition for the Second-Order Seismic Wave Equation. *Geophys. J. Int.* 154 (1), 146–153. doi:10.1046/j.1365-246x.2003.01950.x

Kristek, J., Moczo, P., and Galis, M. (2009). A Brief Summary of Some PML Formulations and Discretizations for the Velocity-Stress Equation of Seismic Motion. *Stud. Geophys. Geod.* 53 (4), 459–474. doi:10.1007/s11200-009-0034-6

Kuzuoglu, M., and Mittra, R. (1996). Frequency Dependence of the Constitutive Parameters of Causal Perfectly Matched Anisotropic Absorbers. *IEEE Microw. Guid. Wave Lett.* 6 (12), 447–449. doi:10.1109/75.544545

Li, Y., and Bou Matar, O. (2010). Convolutional Perfectly Matched Layer for Elastic Second-Order Wave Equation. *J. Acoust. Soc. Am.* 127 (3), 1318–1327. doi:10.1121/1.3290999

Liu, Q., and Tao, J. (1997). The Perfectly Matched Layer for Acoustic Waves in Absorptive media. *J. Acoust. Soc. Am.* 102 (4), 2072–2082. doi:10.1121/1.419657

Lovász, L. (2004). Discrete Analytic Functions: an Exposition. *Surv. Differ. Geom.* 9 (1), 241–273. doi:10.4310/SDG.2004.v9.n1.a7

Luebbers, R. J., and Hunsberger, F. (1992). FDTD for Nth-Order Dispersive Media. *IEEE Trans. Antennas Propagat.* 40 (11), 1297–1301. doi:10.1109/8.202707

Ma, Y., Yu, J., and Wang, Y. (2014). A Novel Unsplit Perfectly Matched Layer for the Second-Order Acoustic Wave Equation. *Ultrasonics* 54, 1568–1574. doi:10.1016/j.ultras.2014.03.016

Ma, X., Yang, D., Huang, X., and Zhou, Y. (2018). Nonsplit Complex-Frequency Shifted Perfectly Matched Layer Combined with Symplectic Methods for Solving Second-Order Seismic Wave Equations—Part 1: Method. *Geophysics* 83 (6), 1–49. doi:10.1190/geo2017-0603.1

Ma, X., Yang, D., He, X., Huang, X., and Song, J. (2019a). Nonsplit Complex-Frequency-Shifted Perfectly Matched Layer Combined with Symplectic Methods for Solving Second-Order Seismic Wave Equations—Part 2: Wavefield Simulations. *Geophysics* 84 (3), T167–T179. doi:10.1190/geo2018-0349.1

Ma, X., Li, Y., and Song, J. (2019b). A Stable Auxiliary Differential Equation Perfectly Matched Layer Condition Combined with Low-Dispersive Symplectic Methods for Solving Second-Order Elastic Wave Equations. *Geophysics* 84 (4), T193–T206. doi:10.1190/geo2018-0572.1

Martin, R., Komatitsch, D., Gedney, S. D., and Bruthiaux, E. (2010). A High-Order Time and Space Formulation of the Unsplit Perfectly Matched Layer for the Seismic Wave Equation Using Auxiliary Differential Equations (ADE-PML). *Comput. Model. Eng. Sci. (Cmes)* 56 (1), 17–41.

Matzen, R. (2011). An Efficient Finite Element Time-Domain Formulation for the Elastic Second-Order Wave Equation: A Non-split Complex Frequency Shifted Convolutional PML. *Int. J. Numer. Meth. Engng.* 88 (10), 951–973. doi:10.1002/nme.3205

Meza-Fajardo, K. C., and Papageorgiou, A. S. (2008). A Nonconvolutional, Split-Field, Perfectly Matched Layer for Wave Propagation in Isotropic and Anisotropic Elastic media: Stability Analysis. *Bull. Seismol. Soc. Am.* 98 (4), 1811–1836. doi:10.1785/0120070223

Meza-Fajardo, K. C., and Papageorgiou, A. S. (2010). On the Stability of a Non-convolutional Perfectly Matched Layer for Isotropic Elastic media. *Soil Dyn. Earthquake Eng.* 30 (3), 68–81. doi:10.1016/j.soildyn.2009.09.002

Meza-Fajardo, K. C., and Papageorgiou, A. S. (2012). Study of the Accuracy of the Multiaxial Perfectly Matched Layer for the Elastic-Wave Equation. *Bull. Seismol. Soc. Am.* 102 (6), 2458–2467. doi:10.1785/0120120061

Nissen, A., and Kreiss, G. (2011). An Optimized Perfectly Matched Layer for the Schrödinger Equation. *Commun. Comput. Phys.* 9 (1), 147–179. doi:10.4208/cicp.010909.010410a

Pasalic, D., and McGarry, R. (2010). "Convolutional Perfectly Matched Layer for Isotropic and Anisotropic Acoustic Wave Equations," in Paper read at 80th Annual International Meeting (Denver, CO: Society of Exploration Geophysicists). doi:10.1190/1.3513453

Ping, P., Zhang, Y., and Xu, Y. (2014). A Multiaxial Perfectly Matched Layer (M-PML) for the Long-Time Simulation of Elastic Wave Propagation in the Second-Order Equations. *J. Appl. Geophys.* 101 (1), 124–135. doi:10.1016/j.jappgeo.2013.12.006

Ping, P., Zhang, Y., Xu, Y., and Chu, R. (2016). Efficiency of Perfectly Matched Layers for Seismic Wave Modeling in Second-Order Viscoelastic Equations. *Geophys. J. Int.* 207 (3), 1367–1386. doi:10.1093/gji/ggw337

Pled, F., and Desceliers, C. (2021). Review and Recent Developments on the Perfectly Matched Layer (PML) Method for the Numerical Modeling and Simulation of Elastic Wave Propagation in Unbounded Domains. *Arch. Comput. Methods Eng.* 29, 471–518. doi:10.1007/s11831-021-09581-y

Qi, Q., and Geers, T. L. (1998). Evaluation of the Perfectly Matched Layer for Computational Acoustics. *J. Comput. Phys.* 139 (1), 166–183. doi:10.1006/jcph.1997.5868

Ramadan, O. (2003). Auxiliary Differential Equation Formulation: an Efficient Implementation of the Perfectly Matched Layer. *IEEE Microw. Wireless Compon. Lett.* 13 (2), 69–71. doi:10.1109/lmwc.2003.808706

Rejiba, F., Camerlynck, C., and Mechler, P. (2003). FDTD-SUPML-ADE Simulation for Ground-Penetrating Radar Modeling. *Radio Sci.* 38 (1), 5-1–5-13. doi:10.1029/2001rs002595

Roden, J. A., and Gedney, S. D. (2000). Convolution PML (CPML): An Efficient FDTD Implementation of the CFS-PML for Arbitrary media. *Microw. Opt. Technol. Lett.* 27 (5), 334–339. doi:10.1002/1098-2760(20001205)27:5<334::aid-mop14>3.0.co;2-a

Shi, R., Wang, S., and Zhao, J. (2012). An Unsplit Complex-Frequency-Shifted PML Based on matchedZ-Transform for FDTD Modelling of Seismic Wave Equations. *J. Geophys. Eng.* 9 (2), 218–229. doi:10.1088/1742-2132/9/2/218

Travassos, X. L., Avila, S. L., Prescott, D., Nicolas, A., and Krahenbuhl, L. (2006). Optimal Configurations for Perfectly Matched Layers in FDTD Simulations. *IEEE Trans. Magn.* 42 (4), 563–566. doi:10.1109/tmag.2006.871471

Wang, L., and Liang, C. (2006). A New Implementation of CFS-PML for ADI-FDTD Method. *Microwave Opt. Technol. Lett.* 48 (10), 1924–1928. doi:10.1002/mop.21816

Wang, T., and Tang, X. (2003). Finite-Difference Modeling of Elastic Wave Propagation: A Nonsplitting Perfectly Matched Layer Approach. *Geophysics* 68 (5), 1749–1755. doi:10.1190/1.1620648

Wang, Y., Wang, J., and Zhang, D. (2005). Application of CPML to Truncate the Open Boundaries of Cylindrical Waveguides in 2.5-dimensional Problems. *Sci. China Ser. F* 48 (5), 656–669. doi:10.1360/04yf0186

Winton, S. C., and Rappaport, C. M. (2000). Specifying PML Conductivities by Considering Numerical Reflection Dependencies. *IEEE Trans. Antennas Propagat.* 48 (7), 1055–1063. doi:10.1109/8.876324

Xie, Z., Komatitsch, D., Martin, R., and Matzen, R. (2014). Improved Forward Wave Propagation and Adjoint-Based Sensitivity Kernel Calculations Using a Numerically Stable Finite-Element PML. *Geophys. J. Int.* 198 (3), 1714–1747. doi:10.1093/gji/ggu219

Yuan, X., Borup, D., Wiskin, J. W., Berggren, M., Eidens, R., and Johnson, S. A. (1997). Formulation and Validation of Berenger's PML Absorbing Boundary for the FDTD Simulation of Acoustic Scattering. *IEEE Trans. Ultrason. Ferroelect., Freq. Contr.* 44 (4), 816–822. doi:10.1109/58.655197

Yuan, X., Borup, D., Wiskin, J., Berggren, M., and Johnson, S. A. (1999). Simulation of Acoustic Wave Propagation in Dispersive media with Relaxation Losses by Using FDTD Method with PML Absorbing Boundary Condition. *IEEE Trans. Ultrason. Ferroelect., Freq. Contr.* 46 (1), 14–23. doi:10.1109/58.741419

Zeng, Y. Q., and Liu, Q. H. (2004). A Multidomain PSTD Method for 3D Elastic Wave Equations. *Bull. Seismol. Soc. Am.* 94 (3), 1002–1015. doi:10.1785/0120030103

Zhang, W., and Shen, Y. (2010). Unsplit Complex Frequency-Shifted PML Implementation Using Auxiliary Differential Equations for Seismic Wave Modeling. *Geophysics* 75 (4), T141–T154. doi:10.1190/1.3463431

Conflict of Interest: The authors declare that the research was conducted in the absence of any commercial or financial relationships that could be construed as a potential conflict of interest.

frontiers | Frontiers in Earth Science

ORIGINAL RESEARCH
published: 07 July 2022
doi: 10.3389/feart.2022.948040

Seismic Tomography of the Trans-North China Orogen and Its Dynamic Implications

Xiaoming Xu[1,2]*, Zhifeng Ding[1,2], Huili Guo[1,2] and Xinfu Li[3]

[1]Institute of Geophysics, China Earthquake Administration, Beijing, China, [2]Key Laboratory of Earthquake Source Physics, China Earthquake Administration, Beijing, China, [3]School of Geophysics and Information Technology, China University of Geosciences, Beijing, China

We present a high-resolution S wave velocity model of the Trans-North China Orogen (TNCO) and its adjacent areas derived from S wave traveltime residuals of teleseismic waveforms recorded by the dense ChinArray seismic network. Our model reveals S wave velocity anomalies beneath the study area, suggesting the strong lateral heterogeneities of the upper mantle structures. The upper mantle of the Datong volcano is dominated by the significant low velocity anomalies. In addition to the low-velocity zone rooted in the mantle transition zone beneath the Datong volcano region, two low velocity layers extend northwestward to the Hetao graben and southwestward to the southern TNCO within depths of 100–300 km, respectively. Based on these low-velocity anomalies, we provide new insights into the origin of the Datong volcano, which may be related to the asthenospheric upwelling originated from the water-rich mantle transition zone and horizontal mantle flows driven by the extrusion northeastward of the Tibetan plateau. A clear velocity contrast in the upper mantle above 300 km depth beneath the Ordos block and the TNCO implies that the Ordos block still preserves thick cratonic root while the lithosphere of the TNCO is modified. We propose that the asthenospheric upwelling and northeastward push of the Tibetan plateau account for the lithospheric deformation of the TNCO and its adjacent areas.

Keywords: trans-north China orogen, datong volcano, seismic tomography, S wave velocity, upper mantle structure

Edited by:
Weijia Sun,
Institute of Geology and Geophysics (CAS), China

Reviewed by:
Dongliang Liu,
Chinese Academy of Geological Sciences (CAGS), China
Zhi Guo,
China Earthquake Administration, China

***Correspondence:**
Xiaoming Xu
xuxiaoming@cea-igp.ac.cn

Specialty section:
This article was submitted to Solid Earth Geophysics, a section of the journal Frontiers in Earth Science

Received: *19 May 2022*
Accepted: *16 June 2022*
Published: *07 July 2022*

Citation:
Xu X, Ding Z, Guo H and Li X (2022) Seismic Tomography of the Trans-North China Orogen and Its Dynamic Implications.
Front. Earth Sci. 10:948040.
doi: 10.3389/feart.2022.948040

INTRODUCTION

The Trans-North China Orogen (TNCO) is an important part of the North China Craton (NCC), formed by the collision between the eastern NCC and western NCC in the Late Paleoproterozoic (Zhao et al., 2001). The TNCO mainly consists of the Taihang mountain, Lüliang mountain and a series of extensional grabens in-between, such as the Weihe graben and Fenhe graben (**Figure 1**). In contrast to the stable Ordos block with the thick and refractory Archean continental nucleus (Zhao et al., 2001), the TNCO has experienced intense tectonic deformation and magmatic activities since the Mesozoic, accompanied by the strong earthquakes (Liu and Wang, 2012). As the largest Quaternary intraplate volcanic group in the NCC (Xu et al., 2005; Fan et al., 2015), the Datong volcano is located in the northern TNCO (**Figure 1**). According to the surface topography, lithospheric thickness (Zhang et al., 2019) and gravity anomalies (Deng et al., 2014), the TNCO is considered as a transition zone between the eastern NCC undergone the dramatic rejuvenation and the western NCC remaining stable

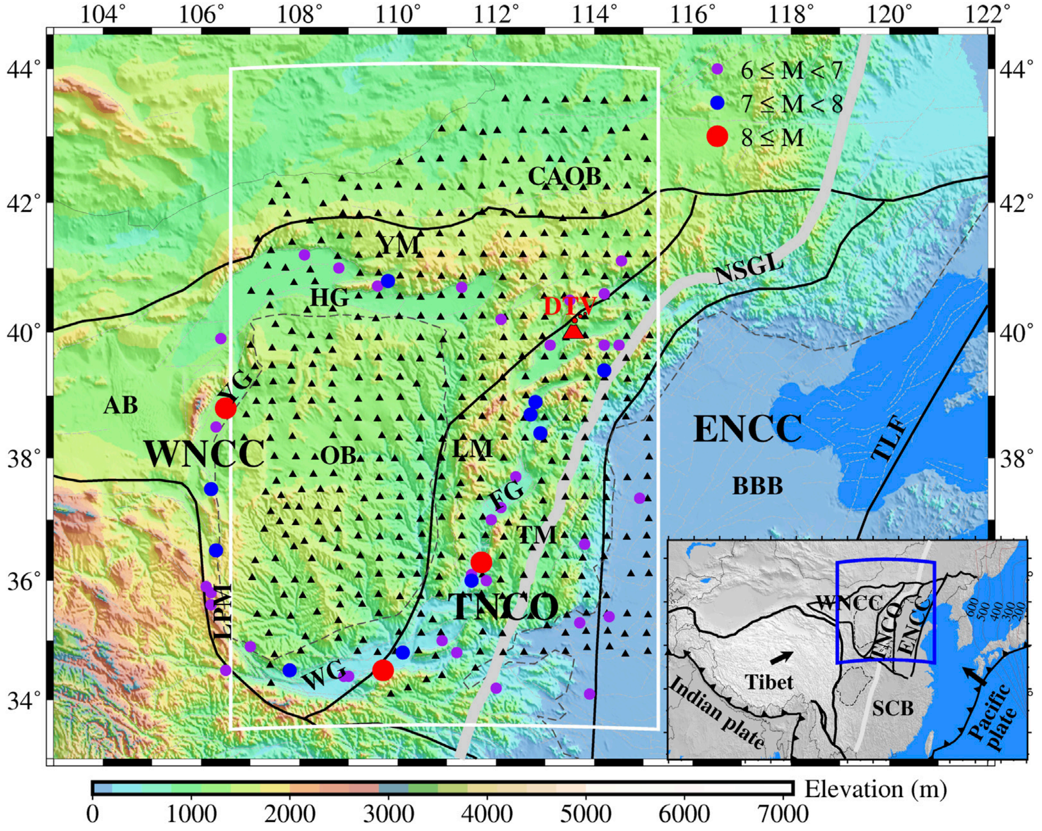

FIGURE 1 | Distribution of seismic stations used in this study. The black triangles represent the seismic stations deployed by ChinArray project. The red volcanic symbol indicates the location of the Datong volcano (DTV). The color circles denote the large historic earthquakes of M ≥ 6 (Liu and Wang, 2012). The thick black lines outline the main tectonic units: the eastern NCC (ENCC), the western NCC (WNCC) and the Trans-North China Orogen (TNCO). The dashed black lines present the boundaries of the Ordos block (OB) and the Bohai bay basin (BBB). The thick gray line indicates the North-South Gravity Line (NSGL). The white rectangle outlines the study area. AB, the Alax black; CAOB, the Central Asia Orogenic Belt; YG, the Yinchuan graben; HG, the Hetao graben; WG, the Weihe graben; FG, the Fenhe graben; LPM, the Liupan mountain; YM, the Yin mountain; LM, the Lüliang mountain; TM, the Taihang mountain; TLF, the Tanlu fault. Inset shows the tectonic setting of the TNCO and its adjacent areas. SCB, the south China block. The black thick arrowhead indicates the absolute plate motion direction from GSRM v2.1 model (Kreemer et al., 2014).

cratonic lithosphere. Therefore, the TNCO and its adjacent areas are ideal places to study the lithospheric deformation and tectonic evolution.

Geochemical and geological studies have suggested that the lithospheric thinning and transformation occurred in the NCC (Xu et al., 2005; Zhu et al., 2011; Wu et al., 2019). In the western NCC, Xu et al. (2005) and Wu et al. (2019) believed that the mantle lithosphere still preserved the oldest crotonic root with a thickness up to 200 km. By comparison, the eastern NCC is characterized by the extensional basin and thinned lithosphere (<80 km) in response to the crustal and deep mantle deformations (Zhang et al., 2019; Zhu et al., 2021). It has been widely accept that these deformations in the eastern NCC were caused by the slab rollback associated with the subduction of the Pacific plate (Zhu et al., 2011; Wu et al., 2019). However, the debates continue regarding the mechanism of the lithospheric deformation in the TNCO. The previous tomographic images suggested that the dehydration of the Pacific stagnant slab resulted in the lithospheric thinning under the TNCO (Zhao, 2004; Huang and Zhao, 2006). Another hypothesis is the horizontal mantle flow escaping northeastward derived from the mantle materials of the Tibetan plateau (Liu et al., 2004). Recently, many observations revealed the existence of the mantle flow driven by the extrusion northeastward of the Tibetan plateau (e.g., Yu and Chen, 2016; Zhang et al., 2016; Gao et al., 2018; Chang et al., 2021). It is essential to obtain the detailed mantle structure of the TNCO and its adjacent areas to further understand the mechanism and dynamic process of the lithospheric deformation.

Seismic tomography is a powerful tool to image the Earth's interior structure. In the past 2 decades, a number of seismic tomography inversions have been performed to construct the 3-D velocity models, focusing on the crustal and upper mantel structures of the TNCO and its adjacent areas (e.g., Zhao, 2004; Huang and Zhao, 2006; Lei, 2012; Xu et al., 2018b; Tao et al., 2018; Dong et al., 2021). Due to the differences in the used data and methods, there are still some contradictions between these models, such as the constraints on the origin of the Datong volcano and lithospheric thinning beneath the TNCO and its adjacent areas. Based on the resolved depth of the low velocity, the upwelling magma of the Datong volcano was attributed to the asthenospheric flow (Liu et al., 2004), lower mantle plum (Lei, 2012) and the dehydration of the Pacific stagnant slab (Zhao, 2004). In addition, the lithospheric thinning is revealed to be spatially heterogeneous under the TNCO and its adjacent areas (Tian et al., 2009; Xu et al., 2018b). The thinning mechanisms is still debated between the lithospheric delamination and mechanical erosion (Zhu et al., 2011; Wu et al., 2019). Thus, it is important to observe the detached lithosphere or large-scale mantle flow in the asthenosphere. The high-resolution velocity model of the crustal and upper mantle beneath the TNCO and its adjacent areas can help us clarify these aforementioned arguments. As the seismic array (**Figure 1**), the densest seismic network in the study area so far, was deployed by the ChinArray project (ChinArray-Himalaya, 2011), the great opportunity is provided to perform seismic tomography inversion and construct the high-resolution 3-D S wave velocity model.

In this paper, we plan to investigate the lithospheric deformation by obtaining the high-resolution 3-D S wave velocity model of the crustal and upper mantle beneath the TNCO and its adjacent areas. At present, a large amount of the high-quality seismic waveforms has been accumulated from the dense seismic array deployed in the TNCO and its adjacent areas (**Figure 1**), which has the highest spatial resolution compared to that used in the previous studies. By picking up the teleseismic S wave traveltime residuals, we perform the seismic tomography inversion to determine the 3-D S wave velocity model of the TNCO and its adjacent areas. Our tomographic results can provide new insights into the mechanism of the lithospheric deformation and improve the understanding on the tectonic evolution of the TNCO and its adjacent areas.

DATA AND METHODS

To measure S wave traveltime residuals, we collected the teleseismic waveforms recorded by 464 portable seismic stations from ChinArray phase III deployment (**Figure 1**). The ChinArray project has operated since August 2011 (ChinArray-Himalaya, 2011), which plans to roll over the whole of mainland China with a dense seismic array consisting of more than 1,000 broadband seismographs. The phase III deployment of ChinArray project conducted from April 2016 to January 2019 covered well the TNCO and its adjacent areas with a station spacing of ~30–40km (**Figure 1**). Each seismograph was equipped with a Guralp CMG-3ESP or CMG-3ESPC seismometer with a corner period of 120 s and a Reftek 130 data logger with a sampling rate of 100 Hz. This array is currently available with the highest station density in this study area.

All earthquake events were selected by the magnitude greater than Ms 5.0 and epicentral distance range of 30°–85°. Then, we rotated the two horizontal components into the radial (R) and transverse (T) directions after removing the means, trends and instrument responses of all seismograms. The waveform correlation method (Rawlinson and Kennett, 2004) was employed to pick up the relative S wave traveltime residuals on the rotated T component within the frequency band range of 0.02–0.2 Hz. In order to obtain the final accurate traveltime residuals, we first trashed the waveforms with low signal-to-noise ratio that were difficult for us to identify the S phases. At least 20 S wave arrival time picks were required for each selected earthquake event. Finally, our dataset used for the final inversion contained a total of 55,935 high-quality relative S wave traveltime residuals from 280 earthquakes. An example showing part of the picked S wave seismograms was demonstrated in **Supplementary Figure S1**. As shown in **Figure 2**, we also plotted the epicenter locations of all used earthquakes. Although most of the teleseismic events come from inside the western Pacific subduction zone and the Java trench, the overall coverages in backazimuth and epicentral distance are reasonably good to provide a crossed and dense distribution of the ray path.

We used the teleseismic tomographic method proposed by Zhao et al. (1994) to perform the 3-D inversion by using the relative S wave traveltime residuals beneath the TNCO and its adjacent areas. The ray paths and traveltimes were calculated accurately by an efficient ray tracing technique (Zhao et al., 1992). The LSQR algorithm (Paige and Saunders, 1982) was used to solve the large and sparse observation equations with damping and smoothing regularizations. We adopted the 1-D modified slightly IASP91 model (Kennett and Engdahl, 1991) by linearly interpolating to compute the velocity perturbation at each grid node set up as shown in **Supplementary Figure S2**. In addition, referring to the Moho depth variation revealed by receiver functions (Li et al., 2014; Xu et al., 2018a; Xu et al., 2021),.the Moho discontinuity was constructed in the initial model (**Supplementary Figure S2B**).

ROBUSTNESS ANALYSIS

The quality and quantity of relative S wave traveltime residuals determine the reliability of tomographic results. To improve the accuracy of picking up the S wave arrival time, the method of P wave particle motions with teleseismic waveforms at period band of 5–50 s (Niu and Li, 2011) was used to estimate the true orientation for each station before rotated the two horizontal components. Then, the waveform correlation method (Rawlinson and Kennett, 2004) was used to further pick up the relative S wave traveltime residuals (**Supplementary Figure S1**). All measured residuals vary between −2.0 and 2.0 s (**Supplementary Figure S3A**). The corresponding error estimates of the relative traveltime residuals is shown in **Supplementary Figure S3B**. We find that most of the error estimates are less than 0.3 s, which indicates the accuracy of our measured S wave traveltime residuals. We also plotted the average traveltime residual and ray path from four directions of northeast, southeast, southwest and northwest for each station (**Supplementary Figure S4**). The directions of the ray path have little effect on the average traveltime residual except for the southeast direction due to the large number of earthquake distribution (**Figure 2**). Generally, the resolution of tomographic inversion depends on the crossed and dense S wave ray paths. **Supplementary Figure S4 and S5** show the distribution of S wave

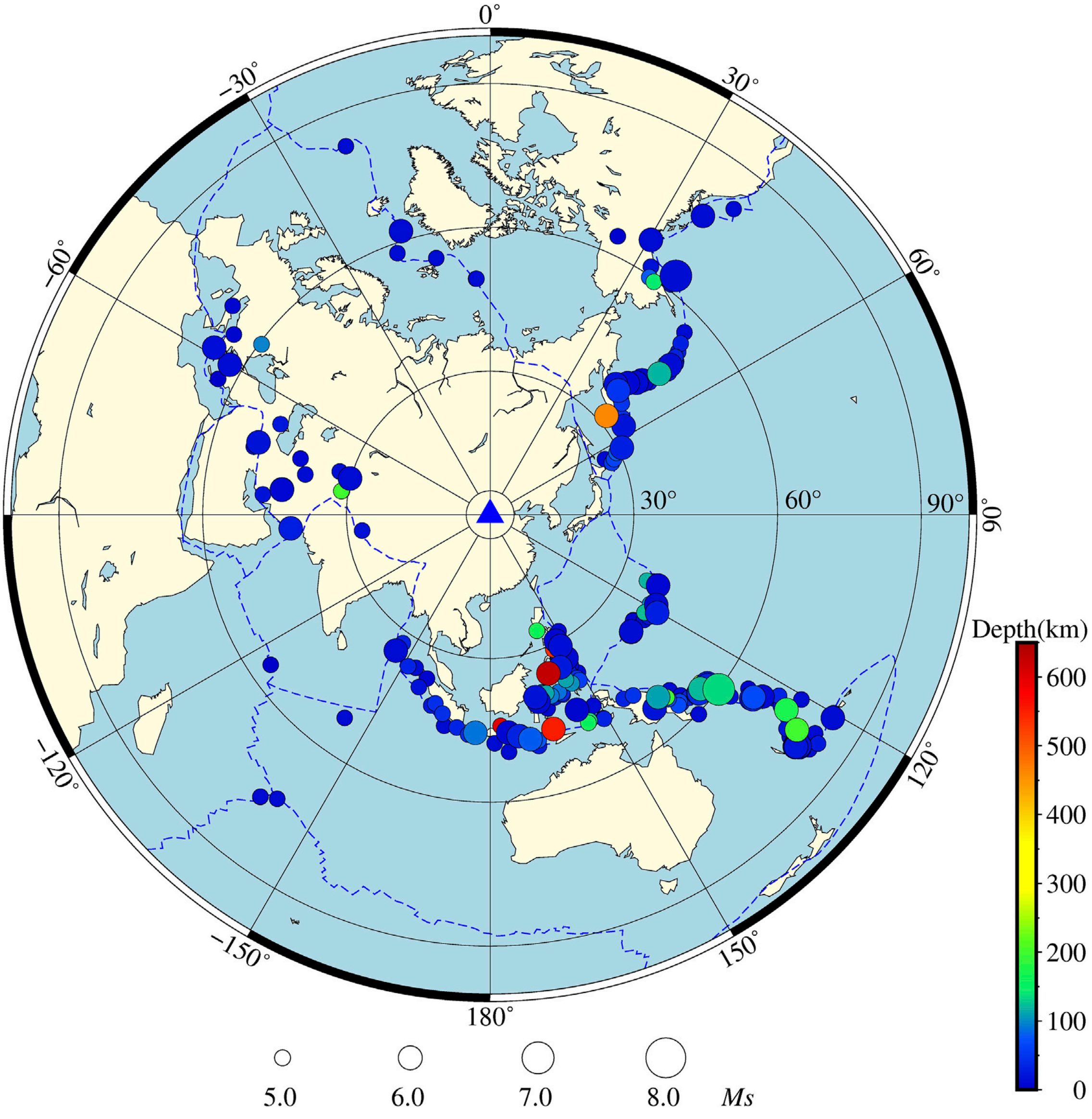

FIGURE 2 | Locations of 280 earthquakes used in this study. The color filed circles show the epicenters. The size of the circles represents the earthquake magnitude and the color indicates event depth. Note that although some events are located inside the 30° circle, all the seismograms we used have an epicentral distance between 30° and 85°.

ray paths used in this study. We find that the study area is covered by the dense and crossed ray paths in both horizontal (**Supplementary Figure S4E**) and vertical (**Supplementary Figure S5**) directions. The ray path density at each grid node is all more than 1,000 at different depths for most of the study area (**Supplementary Figure S6**). Thus, our tomographic results are reliable according to the aforementioned accurate measurements of relative S wave traveltime residuals (**Supplementary Figure S1 and S3**) and dense ray coverage (**Supplementary Figure S4–6**).

For a tomographic inversion, synthetic checkerboard test is usually used to assess the resolution of the inversion results. In this study, we applied the same ray paths as the final tomographic inversion using the real data but different grid size in parameterization of the initial model to perform our checkerboard test with the input velocity perturbation of ±3%. The random noises with a variance of 0.1 s were also added to the synthetic traveltime residuals for simulating the data picking errors. After checking the testing results, we found that the velocity anomalies were well reconstructed at different depths when the horizontal grid spacing was set to 0.5°×0.5° in the synthetic test (**Figure 3**). Therefore, our actual results are robust for the optimal grid spacing of 0.5°×0.5°. In addition, the damping factor is an important parameter to balance the smoothness of the final velocity model and the reduction of the root-mean-square (RMS) traveltime residual. To select a proper damping factor, we

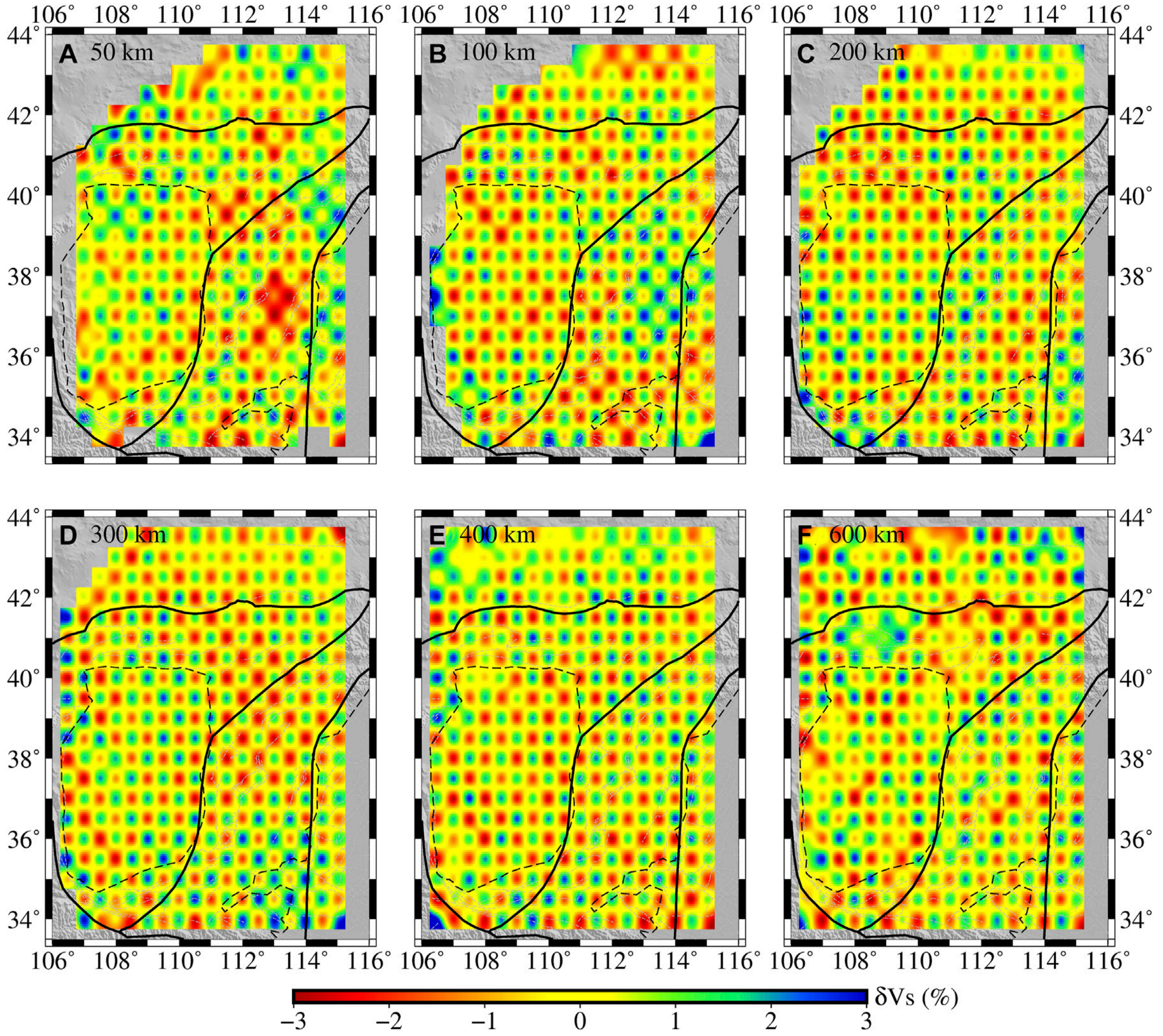

FIGURE 3 | The checkerboard resolution test for the S wave velocity inversion **(A–F)** The recovered results at depths of 50, 100, 200, 300, 400, and 600 km.

conducted many tomographic inversion tests using different values of the damping factor to evaluate the corresponding model smoothness and RMS traveltime residual. **Supplementary Figure S7** displays the trade-off curves between the model smoothness and RMS traveltime residual. The optimal damping factor of 35 was chosen for the final tomographic inversion, which can almost minimize simultaneously the model smoothness and RMS traveltime residual (**Supplementary Figure S7**).

Restoring resolution test is another procedure to further verify the reliability of our tomographic results. According to the distribution of S wave velocity anomalies shown in **Figure 4**, we constructed a synthetic model (**Supplementary Figure S8A**) consisting of the high velocity anomaly beneath the Ordos block and inverted L-shaped low velocity anomaly beneath its surrounding rift grabens on the north and east, respectively. We set the perturbation of −3% and 3% with respect to the low and high velocity anomalies within the depth of 0–200 km. Then, the same ray paths and parameters of the initial model as the real data were adopted to estimate the traveltime residuals of the synthetic model. **Supplementary Figure S8B** shows the results of our restoring resolution test. Although the recovered amplitudes decrease slightly in some regions, the input high and low velocity anomalies are well restored. This means that our tomographic inversion is able to resolve the anomalies beneath the Ordos block and its surrounding regions.

RESULTS

We construct a high-resolution 3-D S wave velocity model of the crustal and upper mantle beneath the TNCO and its adjacent areas from tomographic inversion using the teleseismic relative traveltime residuals. Our obtained velocity model can resolve well the scale of velocity anomaly of about 0.5°. **Figure 4** and **Figure 5** show the six horizontal slices at depths of 50, 100, 200, 300, 400,

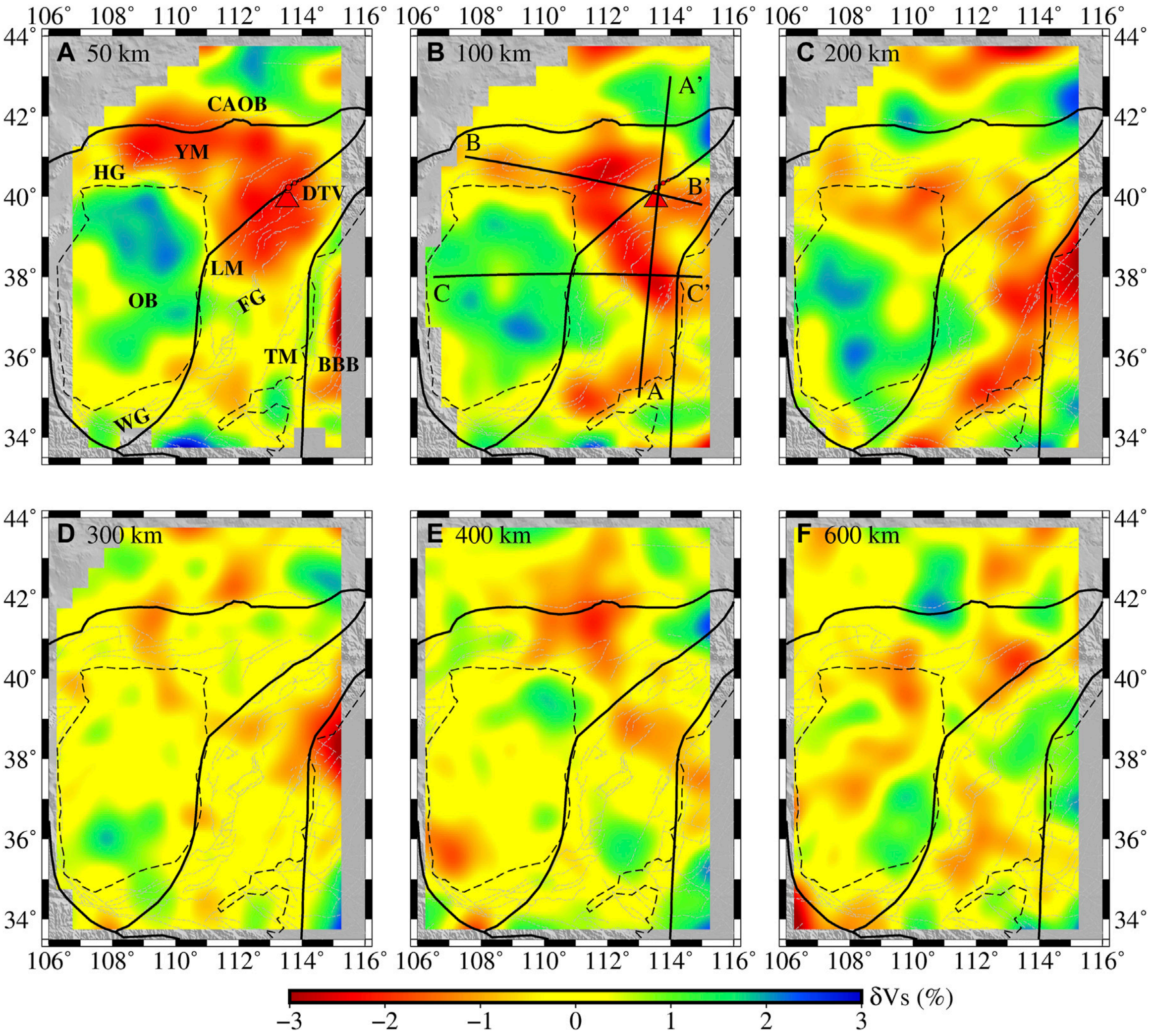

FIGURE 4 | Horizontal slices **(A–F)** of S wave velocity from the seismic tomographic inversion. The depth of each layer is shown in top left corner of each figure. The abbreviations are the same as those defined in the caption of **Figure 1**. The black lines labeled AA′, BB′ and CC′ in figure **(B)** represent the locations of the vertical sections shown in **Figure 5**.

and 600 km and three vertical sections of AA′, BB′ and CC’, respectively. The distribution of S wave velocity presents the significant lateral and vertical variations, indicating the strong structure heterogeneity beneath the study area. In the following sections, we only focus on the upper mantle structures and its implications. The crustal structures are ignored due to the lack of the traveltime data derived from the local and regional earthquakes for the tomographic inversion in this study.

In the horizontal slices of **Figure 4**, the distribution of S wave velocity structure exhibits the quite different patterns between 50–200 km and 300–600 km depths. In particular, the similar characteristics of the velocity structures are shown above 200 km depth although the shapes and amplitudes of the velocity anomalies are slightly different (**Figures 4A–C**). The velocity anomalies are unevenly distributed at depths of 300–600 km (**Figures 4D–F**), which suggests the obvious lateral heterogeneity. We find that the rigid Ordos block is dominated by the prominent high velocity anomalies within 50–200 km depth (**Figures 4A–C**). However, these high velocity anomalies are not completely correlated with the surface tectonic boundary of the Ordos block, accompanied by the low velocity intrusion occurred at the block edge. The significant low velocity anomalies exist under the north and east of the Ordos block above 200 km depth (**Figures 4A–C**), connecting at the Datong volcano region, which suggests the approximate inverted L-shape of the low velocity anomalies. The inverted L-shaped low velocity anomalies are nearly parallel to the strikes of the grabens and orogenic belts, such as the Hetao graben, Fenhe graben, Yin mountain and Taihang mountain. The northern TNCO is characterized by the obvious low velocity anomalies in **Figures 4A–C**, while the elongated low velocity anomalies with a NE-SW trend can be found in the southern TNCO. Especially, the Lüliang mountain is dominated by an alternate distribution of low and high velocity anomalies shown

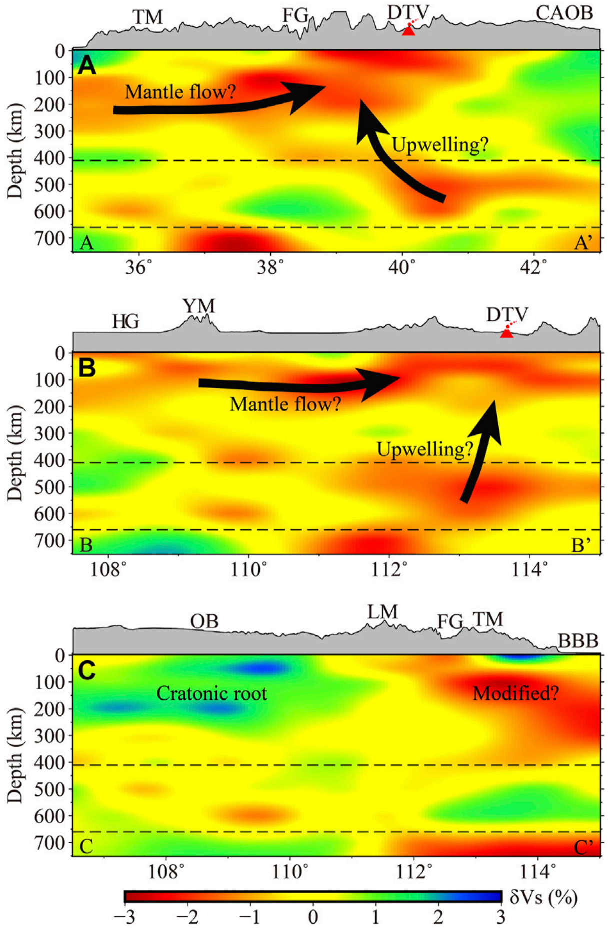

FIGURE 5 | Vertical sections **(A–C)** of S wave velocity along the profiles shown in **Figure 4B**. The surface topography of each section is plotted on the top of each figure. The black thick arrows suggest the possible asthenospheric upwelling and mantle flows. The dashed lines indicate the 410 and 660 km discontinuities. The abbreviations are the same as those defined in the caption of **Figure 1**.

in **Figures 4A–C**. The central Asia orogenic belt is revealed by a complex structure based on our S wave velocity model at depths of 50–600 km.

The vertical sections of AA′ and BB′ are almost perpendicular at the Datong volcano (**Figures 5A,B**), with the strikes of NWW-SEE and NNE-SSW shown in **Figure 4B**, respectively. These two vertical sections are characterized by the prominent low S wave velocity anomaly under the Datong volcano. We find that the prominent low velocity anomaly can be traced down to the mantle transition zone. Besides, two remarkable low velocity layers can be found in the vertical sections of AA′ and BB′ within the depth of about 100–300 km (**Figures 5A,B**), which converge from northwest and southwest below the Datong volcano. The vertical section of CC' crosses the Ordos block and TNCO, and then ends eastward at the western Bohai bay basin (**Figure 4B**). In **Figure 5C**, the obvious high S wave velocity anomaly exists under the Ordos block above the depth of 200 km, while the low velocity anomaly down to about 400 km is located beneath the Taihang mountain and the western Bohai bay basin. This distinct contrast of S wave velocity reflects the difference of the upper mantle structure. In our results, it is absent that the high velocity anomalies were explained by Liu et al. (2017) and Tao et al. (2018) as representing the subducted Pacific plate.

DISCUSSION

Comparisons With Previous Studies

Recently, many velocity models have been constructed by the different tomographic inversions to investigate the structures of the NCC (Huang and Zhao, 2006; Tian et al., 2009; Lei, 2012; Guo et al., 2016; Tao et al., 2018; Xu et al., 2018b; Ai et al., 2019; Yao et al., 2020). However, most of these previous models were estimated based on the permanent stations from the seismic network of China Earthquake Administration with a large station spacing and uneven distribution, which led to their relative low-resolution results. Recently, Cai et al. (2021) and Huang et al. (2021) published the S wave velocity models using the same seismic array as in this study but paid more attention to the shallow structures of the TNCO (<120 km). Compared with these previous studies, our results with high resolution provide new constraints on the deep structures of the TNCO and its adjacent areas.

Our tomographic model illustrates the similar structure patterns revealed by the previous models (Huang and Zhao, 2006; Tian et al., 2009; Lei, 2012; Tao et al., 2018; Xu et al., 2018b), such as the high velocity anomaly beneath the Ordos block and low velocity anomaly under the Datong volcano. However, our results present some different details. For example, the high velocity anomaly in this study, indicating the cratonic root of the Ordos block, is shallower than those in the models of Tian et al. (2009) and Lei (2012), with about 300 and 400 km, respectively. The depth of this high velocity anomaly (~200 km) is roughly consistent with the recent results of the temperature inversion (Guo et al., 2016) and full waveform tomography (Tao et al., 2018), which indicates the Ordos block still preserves the thick and cold cratonic root. However, the outer edge of the high velocity anomaly beneath the Ordos block was invaded by the surrounding low velocity anomalies in a certain extent (**Figure 4**). This phenomenon was also demonstrated by the previous finite-frequency tomography (Xu et al., 2018b) and magnetotelluric inversion (Dong et al., 2014). In addition, the low velocity anomaly suggesting the asthenospheric upwelling shows a complex pattern and is obviously different from the Y-shaped (Lei, 2012) and sloping banded (Tian et al., 2009) anomalies under the Datong volcano region. We find that this low velocity anomaly not only extends down to the mantle transition zone, but also connects with two low velocity layers within about 100–300 km depths from northwest and southwest, respectively. These detailed improvements can be observed mainly due to the high-quality waveforms recorded by the dense seismic array.

Origin of the Datong Volcano

The Datong volcano is one of the most important Quaternary volcanic groups in the NCC, consisting of more than 30 volcanic cones and lava platforms (Fan et al., 2015). Potassium-Argon dating suggested that the last eruption of the Datong volcano ended in the late Pleistocene (0.4 Ma) (Xu et al., 2005). Recently, the high-resolution S wave velocity models delineated that the magma chamber is overlaid by the upper crust with the prominent high velocity anomaly (Cai et al., 2021; Huang et al., 2021), which agrees with the fact that the Datong volcano is inactive at present. The magma of the Datong volcano originated from deep asthenosphere has been revealed by studies on alkali basalt and volcanic debris (Xu et al., 2005; Fan et al., 2015). The large-scale tomographic images demonstrated that the low velocity anomaly under the Datong volcano rooted in the mantle transition zone (Huang and Zhao, 2006; Tian et al., 2009; Tao et al., 2018; Xu et al., 2018b). In fact, the origin and its mechanism of the Datong volcano are still unclear.

Many recent studies have reached a consensus on the hypothesis of the on-going asthenospheric upwelling under the Datong volcano (Ai et al., 2019; Yao et al., 2020; Cai et al., 2021). However, whether the low velocity anomaly indicating this asthenospheric upwelling is related to the dehydration of the Pacific stagnant slab (Zhao, 2004; Huang and Zhao, 2006), lower mantle plum (Lei, 2012) or mantle flows from the Tibetan plateau (Liu et al., 2004) remains controversial. Recent finite-frequency tomography (Xu et al., 2018b) and full waveform tomography (Tao et al., 2018) reported that the western edge of the subducted Pacific slab stagnates at 118–120° E in the mantle transition zone and is far away from the Datong volcano (**Figure 1**). This phenomenon goes against the speculation of the low velocity anomaly caused by the dehydration of the Pacific stagnant slab. Based on most previous tomographic images (Tian et al., 2009; Liu et al., 2017; Xu et al., 2018b; Tao et al., 2018), the low velocity anomaly under the Datong volcano derives from the depth of about 400–600 km and dose not pass down the mantle transition zone, which is obviously contradictory to the hypothesis of the lower mantle plum proposed by Lei (2012). In contrast, the mantle flows within the depth of 100–300 km from the Tibetan plateau was supported to be the main source of the Datong volcanic magma by the conductivity model (Zhang et al., 2016), surface wave (Tang et al., 2013) and P wave (Gao et al., 2018) tomographic images. The results of SKS wave splitting (Yu and Chen, 2016; Chang et al., 2021) also revealed the clockwise turning asthenospheric flow along the Weihe graben driven by the eastward extrusion of the Tibetan upper mantle. Overall, these aforementioned arguments on the origin of the Datong volcano are attributed to the lack of constraints from the regional high-resolution velocity models.

In our high-resolution S wave velocity model (**Figure 4** and **Figure 5**), the complex distribution of the low S wave velocity anomalies is shown under the Datong volcano region. Specifically, the low velocity layers within about 100–300 km depths from northwest (**Figure 5B**) and southwest (**Figure 5A**) connect the vertical low velocity zone rooted in the mantle transition zone beneath the Datong volcano. The NE-SW trending low velocity layer can be observed from the Datong volcano to the southern TNCO, which is roughly consistent with the mantle flow shown in the previous magnetotelluric (Dong et al., 2014), temperature (Guo et al., 2016) and S wave velocity (Tang et al., 2013; Yao et al., 2020) models. Another branch of the low velocity layer spans from the Datong volcano to the Yin mountain and Hetao graben. This mantle flow extended northwestward was also confirmed by the anomalies of the low resistivity (Dong et al., 2014), high temperature (Guo et al., 2016) and low velocity (Yao et al., 2020; Cai et al., 2021). Therefore, these evidences suggest that the origin of the Datong volcano is likely to be related to the two mantle flows from the north and east of the Ordos block, respectively. Next, it is important to understand the formation mechanism of these two mantle flows. Under the effect of the continuous collision between the Indian plate and Eurasia plate since the early Cenozoic (Molnar and Tapponnier, 1975; England and Houseman, 1986), the crustal and upper mantle materials of the Tibetan plateau have escaped to its surrounding areas (Clark and Royden, 2000; Tapponnier et al., 2001; Royden et al., 2008). The lateral extrusion northeastward of the Tibetan plateau has attracted extensive studies (e.g., Meyer et al., 1998; Clark, 2012; Ye et al., 2015; Tian et al., 2021) due to the strong surface deformation in the northeastern margin of the Tibetan plateau. This northeastward movements of the Tibetan plateau have been observed by the GPS measurements and Ps and SKS wave splitting (Xu et al., 2018a; Wang and Shen, 2020; Chang et al., 2021). Especially, the asthenospheric flows from the Tibetan plateau to the Hetao graben and Weihe graben were revealed by the previous seismological observations (Tang et al., 2013; Yu and Chen, 2016; Gao et al., 2018; Chang et al., 2021). Combined with these previous studies, we propose that these two mantle flows shown in **Figure 5** may be the sources for on-going asthenospheric upwelling under the Datong volcano.

In addition, we observe the vertical low velocity zone down into the mantle transition zone under the Datong volcano (**Figures 5A,B**), which can be also found in the previous models (Liu et al., 2017; Xu et al., 2018b; Tao et al., 2018). This vertical low velocity zone coincides with the upwelling of the deep hot mantle materials (Xu et al., 2005; Zhu et al., 2011). However, the cause and mechanism of this asthenospheric upwelling are still unclear. Previous studies indicated that the mantle transition zone could be a major repository for water and have a key role in terrestrial magmatism and plate tectonics (Bercovici and Karato, 2003; Pearson et al., 2014). Besides, the temperature and water content were believed to be the primary causes for the thickness variation of the mantle transition zone (Litasov et al., 2005). Following the equations proposed by Suetsugu et al. (2010), the temperature and water content in the mantle transition zone, approximately −18.4 K and 0.3 wt%, respectively, were calculated using the average S wave velocity of this study and the thickness of the mantle transition zone estimated by Zuo et al. (2020) under the Datong volcano. Considering the deeper 410-km discontinuity of about 422.0 km corresponding to the higher temperature (Zuo et al., 2020), our estimated temperature of −18.4 K may indicate the relative cold lower mantle transition zone, whereas the water content of 0.3 wt% leads to the water-rich mantle transition zone.

This water-rich mantle transition zone beneath the Datong volcano maybe help to materialize the partial melting and the origin of the asthenospheric upwelling. The asthenospheric source also accords with petrological and geochemical analyses on the alkali basalts of the Datong volcano (Xu et al., 2005; Fan et al., 2015). Therefore, the Quaternary Datong volcano is likely to jointly arise from the asthenospheric upwelling rooted in the mantle transition zone and mantle flows driven by the northeastward escape of the upper mantle material from the Tibetan plateau.

Implications for Lithospheric Thinning of the Trans-North China Orogen and Its Adjacent Areas

Since the Mesozoic, the NCC has experienced significant tectonic rejuvenation, accompanied by the widespread magmatism and intense extension (Zhu et al., 2011; Wu et al., 2019). The mantle lithosphere tended to vary from the old cratonic-type to the modified and unstable types from west to east in the NCC (Xu et al., 2018b; Tang et al., 2021), which was confirmed by the gradual thinning of the lithosphere (Chen, 2010; Tang et al., 2013; Zhang et al., 2019). In the eastern NCC, many previous studies have reach the consensus that the lithospheric thinning is mainly relevant to the continental extension caused by the subduction of Pacific plate (e.g., Chen, 2010; Wu et al., 2019; Zhang et al., 2019; Tang et al., 2021). However, the dynamic processes and mechanisms of the lithospheric thinning beneath the TNCO and its adjacent areas are still not fully understood.

In fact, recent tomographic images have illustrated that the mantle lithosphere has been modified partially under the TNCO and its adjacent areas (Xu et al., 2018b; Yao et al., 2020; Dong et al., 2021). The lithospheric delamination and mechanical erosion assumed to account for the mechanisms of the lithospheric modification are still under debate (Wang et al., 2018; Wu et al., 2019). However, these speculation were all based on the asthenosphere-derived upwelling of the hot mantle materials (Dong et al., 2014; Guo et al., 2016; Cai et al., 2021). In this study, we provide a high-resolution S wave velocity model (**Figure 4** and **Figure 5**) to constrain the mantle lithospheric modification beneath the TNCO and its adjacent areas. In contrast to the prominent high S wave velocity anomaly beneath the Ordos block, the inverted L-shaped low velocity anomaly are observed under its surrounding areas in the north and east (**Figures 4A–C** and **Figure 5**). The large-scale low velocity anomaly can be found from the Hetao graben to the Datong volcano region, which agrees well with the thinned lithosphere with the thickness of 80–100 km (Zhang et al., 2019). The low velocity anomalies under the TNCO are locally divided into two parts in the south and north TNCO, respectively. The lithospheric thickness also suggested the coexistence of the thinned lithosphere and remnant cratonic mantle root beneath the TNCO (Zhang et al., 2019). Thus, our observed low velocity anomalies may be in accord with the weak lithosphere where the mantle lithosphere has been modified by the underlying hot asthenospheric materials. Moreover, we find that the low velocity anomalies intrude laterally into the interior of the Ordos block (**Figures 4A–C**). This phenomenon implies the modification of the thick cold lithospheric root occurred beneath the outer edge of the Ordos block. The results of magnetotellric data (Dong et al., 2014) and SKS splitting (Yu and Chen, 2016; Chang et al., 2021) also supported the reginal modification of the cratonic lithosphere under the north and south of the Ordos block. Our model suggests less velocity anomalies below 300 km, which means the mantle structure is close to the reference velocity model. We did not observe the high velocity anomalies beneath the TNCO and its adjacent areas, similar to those interpreted as the delaminated lithosphere by Tian et al. (2009) and Xu et al. (2018b) in deep mantle of the eastern NCC.

According to our obtained high-resolution S wave velocity model, the thinned lithosphere is shown under the TNCO and its adjacent areas (**Figure 4** and **Figure 5**). By analyzing comprehensively our observed S wave velocity anomalies and previous results, we can infer the possible dynamic processes for the lithospheric thinning of the TNCO and its adjacent areas. The two mantle flows driven by the extrusion northeastward of the Tibetan plateau, mentioned in previous section, is likely to erode the thick cratonic lithospheric root beneath the margin of the Ordos block and cause the modifications of the overlying lithosphere. This lithospheric deformation suggests that the effect of the continental collision between the Indian plate and Eurasian plate has far reached northeastward the TNCO region. Besides, the asthenospheric upwelling originated from the water-rich mantle transition zone is also responsible for the lithospheric thinning of the northern TNCO. In general, the asthenospheric upwelling and mantle flows maybe result in the lithospheric thinning under the TNCO and its adjacent areas, and then cause the superficial crustal deformation in response, such as the extensional grabens, strong earthquakes and volcanic activities.

CONCLUSION

A high-resolution 3-D S wave velocity model of the TNCO and its adjacent areas is built by seismic tomography inversion using the teleseismic traveltime residual data recorded by the dense seismic array. Our model shows a prominent lateral heterogeneity of the upper mantle structure across the study area. The Ordos block is featured by significant high velocity anomaly in depths of 0–300 km. We interpret this high velocity anomaly as the preserved thick cratonic root. Two low velocity layers, forming an inverted L-shape, appear in the north and east of the Ordos block. These two low velocity layers are likely to be related to the mantle flows driven by the extrusion northeastward of the Tibetan plateau. We find that the two low velocity anomalies intrude locally into the interior of the Ordos block, which implies the modification of the cratonic root around the outer edge of the Ordos block. An obvious low velocity zone can be found down into the mantle transition zone under the Datong volcano. We infer that this low velocity zone is caused by the hot asthenospheric upwelling originated from the water-rich mantle transition zone. This upward low velocity zone is connected to the two horizontal low velocity layers beneath the Datong volcano. We infer that the asthenospheric upwelling and mantle flows could be responsible for the origin of the Datong volcano and lithospheric thinning beneath the TNCO and its adjacent areas.

DATA AVAILABILITY STATEMENT

The original contributions presented in the study are included in the article/**Supplementary Material**, further inquiries can be directed to the corresponding author.

AUTHOR CONTRIBUTIONS

XX collected the waveform data, plotted the figures used in this study and wrote the manuscript. ZD provided the raw data and guided this work. HG picked up the traveltime residuals and performed the tomography inversion. XL provided useful suggestions. All authors contributed to the article and approved the submitted version.

FUNDING

This work was supported by the National Natural Science Foundation of China (Grant Nos 41974100) and the Special Fund of the Institute of Geophysics, China Earthquake Administration (Grant Nos DQJB16A03, DQJB17A01).

ACKNOWLEDGMENTS

Waveform data for this study are provided by China Seismic Array Data Management Centre at Institute of Geophysics, China Earthquake Administration (doi: 10.12001/ChinArray.Data). All figures are plotted by Generic Mapping Tools (http://gmt.soest.hawaii.edu/home).

SUPPLEMENTARY MATERIAL

The Supplementary Material for this article can be found online at: https://www.frontiersin.org/articles/10.3389/feart.2022.948040/full#supplementary-material

REFERENCES

Ai, S., Zheng, Y., Riaz, M. S., Song, M., Zeng, S., and Xie, Z. (2019). Seismic Evidence on Different Rifting Mechanisms in Southern and Northern Segments of the Fenhe-Weihe Rift Zone. *J. Geophys. Res. Solid Earth* 124 (1), 609–630. doi:10.1029/2018jb016476

Bercovici, D., and Karato, S.-i. (2003). Whole-mantle Convection and the Transition-Zone Water Filter. *Nature* 425, 39–44. doi:10.1038/nature01918

Cai, Y., Wu, J., Rietbrock, A., Wang, W., Fang, L., Yi, S., et al. (2021). S Wave Velocity Structure of the Crust and Upper Mantle Beneath Shanxi Rift, Central North China Craton and its Tectonic Implications. *Tectonics* 40 (4), e2020TC006239. doi:10.1029/2020tc006239

Chang, L., Ding, Z., and Wang, C. (2021). Upper Mantle Anisotropy and Implications beneath the Central and Western North China and the NE Margin of Tibetan Plateau. *Chin. J. Geophys. (in Chinese)* 64 (1), 114–130. doi:10.6038/cjg2021O0315

Chen, L. (2010). Concordant Structural Variations from the Surface to the Base of the Upper Mantle in the North China Craton and its Tectonic Implications. *Lithos* 120 (1-2), 96–115. doi:10.1016/j.lithos.2009.12.007

ChinArray-Himalaya (2011). *China Seismic Array Waveform Data of Himalaya Project*. Beijing: Institute of Geophysics, China Earthquake Administration. doi:10.12001/ChinArray.Data

Clark, M. K., and Royden, L. H. (2000). Topographic Ooze: Building the Eastern Margin of Tibet by Lower Crustal Flow. *Geology* 28 (8), 703–706. doi:10.1130/0091-7613(2000)028<0703:tobtem>2.3.co;2

Clark, M. K. (2012). Continental Collision Slowing Due to Viscous Mantle Lithosphere rather Than Topography. *Nature* 483, 74–77. doi:10.1038/nature10848

Deng, Y., Fan, W., Zhang, Z., and Liang, K. (2014). The Gravity and Isostatic Moho in North China Craton and Their Implications to Seismicity. *Earthq. Sci.* 27 (2), 197–207. doi:10.1007/s11589-013-0019-y

Dong, H., Wei, W., Ye, G., Jin, S., Jones, A. G., Jing, J., et al. (2014). Three-dimensional Electrical Structure of the Crust and Upper Mantle in Ordos Block and Adjacent Area: Evidence of Regional Lithospheric Modification. *Geochem. Geophys. Geosyst.* 15 (6), 2414–2425. doi:10.1002/2014gc005270

Dong, X., Yang, D., Niu, F., Liu, S., and Tong, P. (2021). Adjoint Traveltime Tomography Unravels a Scenario of Horizontal Mantle Flow beneath the North China Craton. *Sci. Rep.* 11 (1), 12523. doi:10.1038/s41598-021-92048-8

England, P., and Houseman, G. (1986). Finite Strain Calculations of Continental Deformation: 2. Comparison with the India-Asia Collision Zone. *J. Geophys. Res.* 91 (B3), 3664–3676. doi:10.1029/JB091iB03p03664

Fan, Q., Zhao, Y., Chen, S., Li, N., and Sui, J. (2015). Quaternary Volcanic Activities in the West of the Daxing'anling-Taihangshan Gravity Lineament. *Bulletin of Mineral. Petrol. Geochem.* 34, 674–681. doi:10.3969/j.issn.1007-2802.2015.04.001

Gao, X., Guo, B., Chen, J., Liu, Q., Li, S., and Li, Y. (2018). Rebuilding of the Lithosphere beneath the Western Margin of Ordos: Evidence from Multiscale Seismic Tomography. *Chinese J. Geophys. (in Chinese)* 61 (7), 2736–2749. doi:10.6038/cjg2018L0319

Guo, Z., Afonso, J. C., Qashqai, M. T., Yang, Y., and Chen, Y. J. (2016). Thermochemical Structure of the North China Craton from Multi-Observable Probabilistic Inversion: Extent and Causes of Cratonic Lithosphere Modification. *Gondwana Res.* 37, 252–265. doi:10.1016/j.gr.2016.07.002

Huang, J., and Zhao, D. (2006). High-resolution Mantle Tomography of China and Surrounding Regions. *J. Geophys. Res.* 111 (B9), B09305. doi:10.1029/2005jb004066

Huang, X., Ding, Z., Ning, J., Niu, F., Li, G., Wang, X., et al. (2021). Sedimentary and Crustal Velocity Structure of Trans-North China Orogen from Joint Inversion of Rayleigh Wave Phase Velocity and Ellipticity and Some Implication for Syn-Rift Volcanism. *Tectonophysics* 819, 229104. doi:10.1016/j.tecto.2021.229104

Kennett, B. L. N., and Engdahl, E. R. (1991). Traveltimes for Global Earthquake Location and Phase Identification. *Geophys. J. Int.* 105, 429–465. doi:10.1111/j.1365-246X.1991.tb06724.x

Kreemer, C., Blewitt, G., and Klein, E. C. (2014). A Geodetic Plate Motion and Global Strain Rate Model. *Geochem. Geophys. Geosyst.* 15, 3849–3889. doi:10.1002/2014GC005407

Lei, J. (2012). Upper-mantle Tomography and Dynamics beneath the North China Craton. *J. Geophys. Res.* 117 (B6), B06313. doi:10.1029/2012jb009212

Li, Y., Gao, M., and Wu, Q. (2014). Crustal Thickness Map of the Chinese Mainland from Teleseismic Receiver Functions. *Tectonophysics* 611, 51–60. doi:10.1016/j.tecto.2013.11.019

Litasov, K. D., Ohtani, E., Sano, A., and Suzuki, A. (2005). Wet Subduction versus Cold Subduction. *Geophys. Res. Lett.* 32, L13312. doi:10.1029/2005gl022921

Liu, M., and Wang, H. (2012). Roaming Earthquakes in China Highlight Midcontinental Hazards. *Eos Trans. AGU* 93 (45), 453–454. doi:10.1029/2012eo450001

Liu, M., Cui, X., and Liu, F. (2004). Cenozoic Rifting and Volcanism in Eastern China: a Mantle Dynamic Link to the Indo-Asian Collision? *Tectonophysics* 393 (1-4), 29–42. doi:10.1016/j.tecto.2004.07.029

Liu, X., Zhao, D., Li, S., and Wei, W. (2017). Age of the Subducting Pacific Slab beneath East Asia and its Geodynamic Implications. *Earth Planet. Sci. Lett.* 464, 166–174. doi:10.1016/j.epsl.2017.02.024

Meyer, B., Tapponnier, P., Bourjot, L., Métivier, F., Gaudemer, Y., Peltzer, G., et al. (1998). Crustal Thickening in Gansu-Qinghai, Lithospheric Mantle Subduction, and Oblique, Strike-Slip Controlled Growth of the Tibet Plateau. *Geophys. J. Int.* 135, 1–47. doi:10.1046/j.1365-246X.1998.00567.x

Molnar, P., and Tapponnier, P. (1975). Cenozoic Tectonics of Asia: Effects of a Continental Collision: Features of Recent Continental Tectonics in Asia Can Be Interpreted as Results of the India-Eurasia Collision. *Science* 189 (4201), 419–426. doi:10.1126/science.189.4201.419

Niu, F., and Li, J. (2011). Component Azimuths of the CEArray Stations Estimated from P-Wave Particle Motion. *Earthq. Sci.* 24 (1), 3–13. doi:10.1007/s11589-011-0764-8

Paige, C. C., and Saunders, M. A. (1982). LSQR: an Algorithm for Sparse Linear Equations and Sparse Least Squares. *ACM Trans. Math. Softw.* 8 (1), 43–71. doi:10.1145/355984.355989

Pearson, D. G., Brenker, F. E., Nestola, F., McNeill, J., Nasdala, L., Hutchison, M. T., et al. (2014). Hydrous Mantle Transition Zone Indicated by Ringwoodite Included within Diamond. *Nature* 507 (7491), 221–224. doi:10.1038/nature13080

Rawlinson, N., and Kennett, B. L. N. (2004). Rapid Estimation of Relative and Absolute Delay Times across a Network by Adaptive Stacking. *Geophys. J. Int.* 157 (1), 332–340. doi:10.1111/j.1365-246X.2004.02188.x

Royden, L. H., Burchfiel, B. C., and van der Hilst, R. D. (2008). The Geological Evolution of the Tibetan Plateau. *Science* 321, 1054–1058. doi:10.1126/science.1155371

Suetsugu, D., Inoue, T., Obayashi, M., Yamada, A., Shiobara, H., Sugioka, H., et al. (2010). Depths of the 410-km and 660-km Discontinuities in and Around the Stagnant Slab beneath the Philippine Sea: Is Water Stored in the Stagnant Slab? *Phys. Earth Planet. Inter.* 183 (1-2), 270–279. doi:10.1016/j.pepi.2010.09.004

Tang, Y., Chen, Y. J., Zhou, S., Ning, J., and Ding, Z. (2013). Lithosphere Structure and Thickness beneath the North China Craton from Joint Inversion of Ambient Noise and Surface Wave Tomography. *J. Geophys. Res. Solid Earth* 118 (5), 2333–2346. doi:10.1002/jgrb.50191

Tang, Y., Ying, J., Zhao, Y., and Xu, X. (2021). Nature and Secular Evolution of the Lithospheric Mantle beneath the North China Craton. *Sci. China Earth Sci.* 64 (9), 1492–1503. doi:10.1007/s11430-020-9737-4

Tao, K., Grand, S. P., and Niu, F. (2018). Seismic Structure of the Upper Mantle Beneath Eastern Asia from Full Waveform Seismic Tomography. *Geochem. Geophys. Geosyst.* 19 (8), 2732–2763. doi:10.1029/2018gc007460

Tapponnier, P., Zhiqin, X., Roger, F., Meyer, B., Arnaud, N., Wittlinger, G., et al. (2001). Oblique Stepwise Rise and Growth of the Tibet Plateau. *Science* 294, 1671–1677. doi:10.1126/science.105978

Tian, Y., Zhao, D., Sun, R., and Teng, J. (2009). Seismic Imaging of the Crust and Upper Mantle beneath the North China Craton. *Phys. Earth Planet. Inter.* 172 (3-4), 169–182. doi:10.1016/j.pepi.2008.09.002

Tian, X., Bai, Z., Klemperer, S. L., Liang, X., Liu, Z., Wang, X., et al. (2021). Crustal-scale Wedge Tectonics at the Narrow Boundary between the Tibetan Plateau and Ordos Block. *Earth Planet. Sci. Lett.* 554, 116700. doi:10.1016/j.epsl.2020.116700

Wang, M., and Shen, Z. K. (2020). Present-Day Crustal Deformation of Continental China Derived from GPS and its Tectonic Implications. *J. Geophys. Res. Solid Earth* 125, e2019JB018774. doi:10.1029/2019jb018774

Wang, K., Zhao, L., Xu, X., and Yang, J. (2018). Heterogeneous Destruction of the North China Craton: Coupled Constraints from Seismology and Geodynamic Numerical Modeling. *Sci. China Earth Sci.* 61 (5), 515–526. doi:10.1007/s11430-017-9142-1

Wu, F.-Y., Yang, J.-H., Xu, Y.-G., Wilde, S. A., and Walker, R. J. (2019). Destruction of the North China Craton in the Mesozoic. *Annu. Rev. Earth Planet. Sci.* 47 (1), 173–195. doi:10.1146/annurev-earth-053018-060342

Xu, Y.-G., Ma, J.-L., Frey, F. A., Feigenson, M. D., and Liu, J.-F. (2005). Role of Lithosphere-Asthenosphere Interaction in the Genesis of Quaternary Alkali and Tholeiitic Basalts from Datong, Western North China Craton. *Chem. Geol.* 224 (4), 247–271. doi:10.1016/j.chemgeo.2005.08.004

Xu, X., Niu, F., Ding, Z., and Chen, Q. (2018a). Complicated Crustal Deformation beneath the NE Margin of the Tibetan Plateau and its Adjacent Areas Revealed by Multi-Station Receiver-Function Gathering. *Earth Planet. Sci. Lett.* 497, 204–216. doi:10.1016/j.epsl.2018.06.010

Xu, X., Zhao, L., Wang, K., and Yang, J. (2018b). Indication from Finite-Frequency Tomography beneath the North China Craton: The Heterogeneity of Craton Destruction. *Sci. China Earth Sci.* 61 (9), 1238–1260. doi:10.1007/s11430-017-9201-y

Xu, X., Ding, Z., Li, L., and Niu, F. (2021). Crustal Anisotropy Beneath the Trans-North China Orogen and its Adjacent Areas from Receiver Functions. *Front. Earth Sci.* 9, 753612. doi:10.3389/feart.2021.753612

Yao, Z., Eric, S., Wang, C., Ding, Z., and Chen, Y. (2020). Asthenospheric Upwelling beneath Northeastern Margin of Ordos Block: Constraints from Rayleigh Surface-Wave Tomography. *Tectonophysics* 790, 228548. doi:10.1016/j.tecto.2020.228548

Ye, Z., Gao, R., Li, Q., Zhang, H., Shen, X., Liu, X., et al. (2015). Seismic Evidence for the North China Plate Underthrusting beneath Northeastern Tibet and its Implications for Plateau Growth. *Earth Planet. Sci. Lett.* 426, 109–117. doi:10.1016/j.epsl.2015.06.024

Yu, Y., and Chen, Y. J. (2016). Seismic Anisotropy beneath the Southern Ordos Block and the Qinling-Dabie Orogen, China: Eastward Tibetan Asthenospheric Flow Around the Southern Ordos. *Earth Planet. Sci. Lett.* 455, 1–6. doi:10.1016/j.epsl.2016.08.026

Zhang, H., Huang, Q., Zhao, G., Guo, Z., and Chen, Y. J. (2016). Three-Dimensional Conductivity Model of Crust and Uppermost Mantle at the Northern Trans North China Orogen: Evidence for a Mantle Source of Datong Volcanoes. *Earth Planet. Sci. Lett.* 453, 182–192. doi:10.1016/j.epsl.2016.08.025

Zhang, Y., Chen, L., Ai, Y., and Jiang, M. (2019). Lithospheric Structure beneath the Central and Western North China Craton and Adjacent Regions from S-Receiver Function Imaging. *Geophys. J. Inter.* 219 (1), 619–632. doi:10.1093/gji/ggz322

Zhao, D., Hasegawa, A., and Horiuchi, S. (1992). Tomographic Imaging ofPandSwave Velocity Structure beneath Northeastern Japan. *J. Geophys. Res.* 97 (B13), 19909–19928. doi:10.1029/92jb00603

Zhao, D., Hasegawa, A., and Kanamori, H. (1994). Deep Structure of Japan Subduction Zone as Derived from Local, Regional, and Teleseismic Events. *J. Geophys. Res.* 99 (B11), 22313–22329. doi:10.1029/94jb01149

Zhao, G., Wilde, S. A., Cawood, P. A., and Su, M. (2001). Archean Blocks and Their Boundaries in the North China Craton: Lithological, Geochemical, Structural and P–T Path Constraints and Tectonic Evolution. *Precambrian Res.* 107 (1-2), 45–73. doi:10.1016/S0301-9268(00)00154-6

Zhao, D. (2004). Global Tomographic Images of Mantle Plumes and Subducting Slabs: Insight into Deep Earth Dynamics. *Phys. Earth Planet. Inter.* 146 (1-2), 3–34. doi:10.1016/j.pepi.2003.07.032

Zhu, R., Chen, L., Wu, F., and Liu, J. (2011). Timing, Scale and Mechanism of the Destruction of the North China Craton. *Sci. China Earth Sci.* 54 (6), 789–797. doi:10.1007/s11430-011-4203-4

Zhu, Y., Liu, S., Zhang, B., Gurnis, M., and Ma, P. (2021). Reconstruction of the Cenozoic Deformation of the Bohai Bay Basin, North China. *Basin Res.* 33 (1), 364–381. doi:10.1111/bre.12470

Zuo, J., Wang, L., and Niu, F. (2020). Multiple Source Downwellings beneath Eastern North China Revealed by 3-D CCP Migration of Receiver Function Data. *J. Asian Earth Sci.* 192, 104266. doi:10.1016/j.jseaes.2020.104266

Conflict of Interest: The reviewer ZG declared a shared affiliation with the authors XX, ZD, HG to the handling editor at the time of review.

frontiers | Frontiers in Earth Science

TYPE Original Research
PUBLISHED 28 September 2022
DOI 10.3389/feart.2022.1008354

OPEN ACCESS

EDITED BY
Weijia Sun,
Institute of Geology and Geophysics (CAS), China

REVIEWED BY
Xiaoming Xu,
China Earthquake Administration, China
Shaolin Liu,
Ministry of Emergency Management, China

*CORRESPONDENCE
Xiaofei Chen,
chenxf@sustech.edu.cn

SPECIALTY SECTION
This article was submitted to Solid Earth Geophysics,
a section of the journal
Frontiers in Earth Science

RECEIVED 31 July 2022
ACCEPTED 16 August 2022
PUBLISHED 28 September 2022

CITATION
Zhang S, Zhang G, Feng X, Li Z, Pan L, Wang J and Chen X (2022), A crustal LVZ in Iceland revealed by ambient noise multimodal surface wave tomography.
Front. Earth Sci. 10:1008354.
doi: 10.3389/feart.2022.1008354

A crustal LVZ in Iceland revealed by ambient noise multimodal surface wave tomography

Sen Zhang[1,2,3], Gongheng Zhang[1,2,3], Xuping Feng[1,2,3], Zhengbo Li[2,3], Lei Pan[2,3], Jiannan Wang[2,3] and Xiaofei Chen[1,2,3]*

[1]Southern Marine Science and Engineering Guangdong Laboratory (Guangzhou), Guangzhou, China, [2]Department of Earth and Space Sciences, Southern University of Science and Technology, Shenzhen, China, [3]Shenzhen Key Laboratory of Deep Offshore Oil and Gas Exploration Technology, Southern University of Science and Technology, Shenzhen, China

The crustal low-velocity zone (LVZ), an important anomaly found in some regional structures of Iceland, is still absent in the Icelandic average velocity structure due to limitations of tomography methods. Using stations from the HOTSPOT experiment and other supplemental stations throughout Iceland, we apply the frequency-Bessel transform method (F-J method) to extract the first two mode dispersion curves from ambient noise data. We obtain an average S-wave velocity (Vs) model of Iceland down to 120 km depth, where two LVZs at depths of 12–22 km and below 55 km are found. The shallow LVZ, whose rationalities are justified using theoretical dispersion curves of certain models to recover themselves, may improve the understanding of the Icelandic average crust. Furthermore, our model shows better representativeness by comparing travel time residuals of the primary wave between observed and synthetic data predicted using different average velocity models. Based on the variations of the Vs gradient, the Icelandic crust with an average thickness of 32 km is divided into the upper crust (0–10 km), middle crust (10–22 km), and lower crust (22–32 km). The asthenosphere starts from the deeper LVZ at 55 km depth, potentially indicating the relatively concentrated melt in this depth range. In this study, crustal LVZs are revealed both in a volcanic active zone and a non-volcanic zone, which may also suggest the LVZ in the average model has more complex origins than the high-temperature zone beneath the central volcanoes. The prevalent thick-cold crustal model of Iceland, considered to rule out the existence of a broad region of partial melt in the crust, also strengthens the possibility of diverse origins. The variations in petrology may also contribute to the crustal LVZ in the average model.

KEYWORDS

Iceland, crust, S-wave low-velocity zone, ambient noise tomography, frequency-Bessel transform method

1 Introduction

The interaction between the spreading Mid-Atlantic rift and Iceland hotspot promotes frequent magmatic events such as eruptions in central volcanoes (blue points in Figure 1) and distinct fissure swarms (blue lines in Figure 1, Johannesson and Saemundsson, 1998) in Iceland. Previous studies based on seismic tomography have revealed a cylindrical low-velocity anomaly in the mantle of Iceland (e.g., Wolfe et al., 1997; Foulger et al., 2001; Allen et al., 2002a; Rickers et al., 2013), which may be a result of the upwelling plume. In addition, some evidence from geochemical anomalies around the ridge also supports the plume hypothesis (e.g., Schilling, 1973; White et al., 1992; Shorttle and Maclennan, 2011).

After the first seismic field observation during the 1960s, a great deal of work has been undertaken to study the crust of Iceland which has obtained similar seismic velocities, but the thickness of the Icelandic crust has been a subject of controversial debate for a long time due to different interpretations of such velocities. There are two dominant but different models of the Icelandic crust. The early thin-hot crust model underlain by an unusual low-velocity uppermost mantle has a thickness of approximately 10–20 km (e.g., Tryggvason, 1962; Pálmason, 1971). The downward extrapolation of near-surface temperature gradients obtained from shallow boreholes in Iceland predicts supra-solidus temperatures and partially molten basaltic material at 10–20 km depths (e.g., Flóvenz and Saemundsson, 1993). In addition, a high-conductivity layer at 10–20 km depths over northeast Iceland, interpreted as the base of the crust, has been detected by magnetotelluric measurements (e.g., Beblo and Bjornsson, 1980).

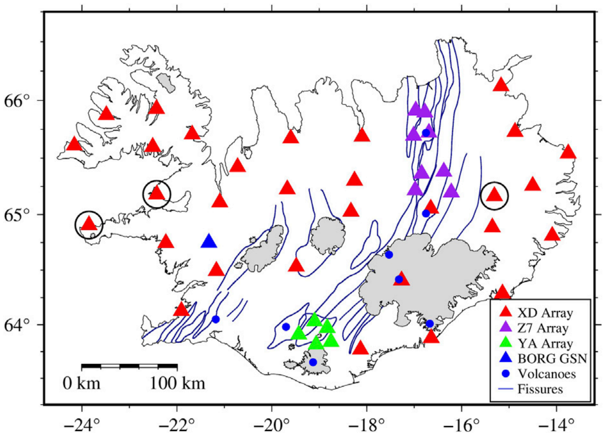

FIGURE 1
Tectonics map of Iceland and seismic stations used in this study. Different seismic networks are identified by triangles with different colors, which include stations from the XD array (red), Z7 array (purple), YA array (green), and BORG (blue). The blue points and lines show major volcanoes and fissure swarms (Johannesson and Saemundsson, 1998), respectively. The glaciers are identified by gray. The stations circled in black are removed finally when we study the average structure in Iceland (see Supplementary Material S1 for further details).

Bjarnason et al. (1993) reported a Moho depth at 20–24 km from wide-angle reflections and a refractor P-wave velocity (Vp) ~7.7 km/s in southwestern Iceland. Additionally, strong P-wave and S-wave reflections have been observed from depths of up to 40 km (Staples et al., 1997; Darbyshire et al., 1998), which leads to an alternative thick-cold crust model with a high-velocity lower crust. Little seismic attenuation with high values of Q in the lower crust also supports this model, which indicates colder crustal temperature below the solidus of gabbro and rules out a broad region of partial melt above Moho (Menke and Levin, 1994; Menke et al., 1995). It can be inferred that the additional layer, referring to the mantle-derived peridotite layer beneath the typical three-layered oceanic crustal structure, will lead to a thin-hot crust model when it is interpreted as an unusual low-velocity upper mantle. However, a thick-cold crust model can be obtained if the additional layer is regarded as a high-velocity lower crust, which has become more prevalent and favored by recent studies (e.g., Darbyshire et al., 2000b; Allen et al., 2002b; Jenkins et al., 2018).

Due to the existence of the plume, the thickness of the Icelandic crust increases in some areas, and the thickest crust is found near the center of the hotspot (Allen et al., 2002b), toward the east (Bjarnason and Schmeling, 2009) or west (Foulger et al., 2003; Li and Detrick, 2003, 2006) of the hotspot. The maximum thickness of the crust is 40 km (Darbyshire et al., 1998; Li and Detrick, 2006), with an average value of 29 km (Allen et al., 2002b). Though many investigations have been conducted on the Icelandic crust structure, including the body wave and surface wave methods (e.g., Allen et al., 2002b; Li and Detrick, 2006), the sensitivity of the low-velocity zone (LVZ) and vertical resolution have some difficulties to be achieved together. Consequently, the average models imaged by different techniques are still pretty vague about the crustal LVZ that has been reported in some regional areas of Iceland (e.g., Darbyshire et al., 2000a; Du et al., 2002; Bjarnason and Schmeling, 2009). Thus, there is still necessitated high-resolution observation of the comprehensive features of the Icelandic crust.

In contrast to traditional seismic methods, ambient noise tomography conquers the defects in the non-homogeneous distribution of seismic events, significantly improving the spatial resolution of seismic images with numerous ray paths. After pioneering works for theoretical foundations (e.g., Aki, 1957; Weaver and Lobkis, 2001; Campillo and Paul, 2003), some specific applications to image velocity structures (e.g., Shapiro and Campillo, 2004; Shapiro et al., 2005; Yang and Ritzwoller, 2008) have greatly promoted the development of ambient noise surface wave tomography, in which extracting dispersion curves from ambient noise data is an essential step. In the past decades, various methods have been developed for extracting the fundamental mode (Capon, 1969; Dziewonski et al., 1969; Levshin and Ritzwoller, 2001; Yao et al., 2006; Park et al., 2007; Luo et al., 2008). However, it is a long-held view that higher modes play an important role in enhancing constraints and suppressing the non-uniqueness of inversion (e.g., Xia et al., 1999; Xia et al., 2003; Pan et al., 2019).

In this study, we apply the recently developed frequency-Bessel transform method (F-J method) (Wang et al., 2019; Xi et al., 2021; Zhou and Chen, 2021) to extract the first two modes of dispersion curves from the ambient noise data of Iceland. We invert the multimodal dispersion curves to obtain a high-resolution average S-wave velocity (V_S) structure of Iceland, which reveals a crustal LVZ. To analyze the possible origins of the low-velocity anomaly, we also circle two subregions, volcanic and non-volcanic zones, and obtain their Vs structures. By recovering different models with their theoretical dispersion curves and comparing the predicted travel time with the observed travel time of the primary wave from earthquake events, we investigate the reliability of this LVZ and the rationality of the average V_S structure.

2 Methods

2.1 The F-J method

Wang et al. (2019) developed the F-J method to extract multimodal dispersion curves from ambient noise cross-correlation functions (NCFs). The method was successfully applied to establish the V_S structures in various areas through the inversion of multimodal dispersion curves (e.g., Wu et al., 2020; Zhan et al., 2020; Li et al., 2022; Ma et al., 2022). We briefly describe the F-J method below.

Wang et al. (2019) defined the F-J spectrum $I(\omega, k)$ as

$$I(\omega, k) = \int_0^{+\infty} \tilde{C}(r,\omega) J_0(kr) r dr, \qquad (1)$$

where ω denotes the angular frequency, k indicates the wave number, J_0 is the zeroth order Bessel function, and $\tilde{C}(r,\omega)$ is the vertical component of the stacked NCF in the frequency domain of two stations separated at r. They further demonstrated that the highlighted parts of the F-J spectrum $I(\omega, k)$ corresponded to dispersion curves. Based on this property of $I(\omega, k)$, they developed the F-J method to extract dispersion curves from the $I(\omega, k)$ image. In this study, to extract dispersion curves from NCFs, we apply the F-J method and a relevant python package CC-FJpy as described by Li et al. (2021).

2.2 Inversion

It has been reported that V_S is more sensitive to the dispersion curve than V_P and density (e.g., Xia et al., 1999; Xia et al., 2003; Pan et al., 2019). To reduce uncertainty, we use empirical relations proposed by Brocher (2005) to calculate V_P according to V_S during inversion. In addition, the ratio of density to V_S is constant through all iterations with an initial density of 2920 kg/m^3 for the initial V_S (Green et al., 2017).

We adopt the inversion algorithm proposed by Pan et al. (2019) to invert the V_S structure parameterized as a 1D multilayered model, which is divided into dozens of homogeneous elemental layers with fixed thickness, and the only unknown parameters to be inverted are the V_S values in each elemental layer. Therefore, the dimension of V_S is the total number of elemental layers. The misfit function of our inversion is formulated as follows:

$$f(\boldsymbol{V_s}) = \frac{1}{m}\sum_i A_i\left[\sum_j \left(c_{ij}^S - c_{ij}^O\right)^2\right] + \alpha\left\|\Delta\left(\boldsymbol{V_s} - \boldsymbol{V_{s\_ref}}\right)\right\|, \qquad (2)$$

where i and j are the indices for modes of dispersion curves and the sampled frequency points, respectively; c_{ij}^S is the synthetic phase velocity; c_{ij}^O is the observed phase velocity; A_i is the weight of the dispersion curve for ith mode; m is the number of modes of the dispersion curve; $\boldsymbol{V_s}$ and $\boldsymbol{V_{s\_ref}}$ are the currently inverted V_S and the initial V_S, respectively; $\alpha\|\Delta(\boldsymbol{V_s} - \boldsymbol{V_{s\_ref}})\|$ is a regularization item to smooth the inversion process avoiding overfitting. In this study, the damping factor α is 0.02 near the maximum curvature of the L-curve (e.g., Hansen, 2001).

The reference model (Supplementary Figure S1) is derived from the average model of Li and Detrick (2006) and the crustal model of Allen et al. (2002b). Due to the decreasing resolution of surface waves with increasing depth, at a depth of 70 km, the thickness of the elemental layer gradually increases from 2 km to adapt to the resolution decrease of deeper penetrating waves. To obtain a robust global optimal solution, 80 dissimilar initial models, randomly selected from a given variation range (± 0.6 km/s) around the reference model, are simultaneously inverted (Supplementary Figure S1). Finally, the best-fitting 50% of the inverted V_S models, the first 50% minimum misfit functions, are weighted average to obtain the final estimated model $\hat{\boldsymbol{m}}$ (red lines in Figures 2C,E):

$$\hat{\boldsymbol{m}} = \frac{1}{\sum_{i=1}^{N} e^{-f(\boldsymbol{m}_i)}} \sum_{i=1}^{N} e^{-f(\boldsymbol{m}_i)} \boldsymbol{m}_i, \qquad (3)$$

where $\boldsymbol{m}_i$ is the converged model whose final misfit function is identified by $f(\boldsymbol{m}_i)$ and N is the number of the best-fitting models.

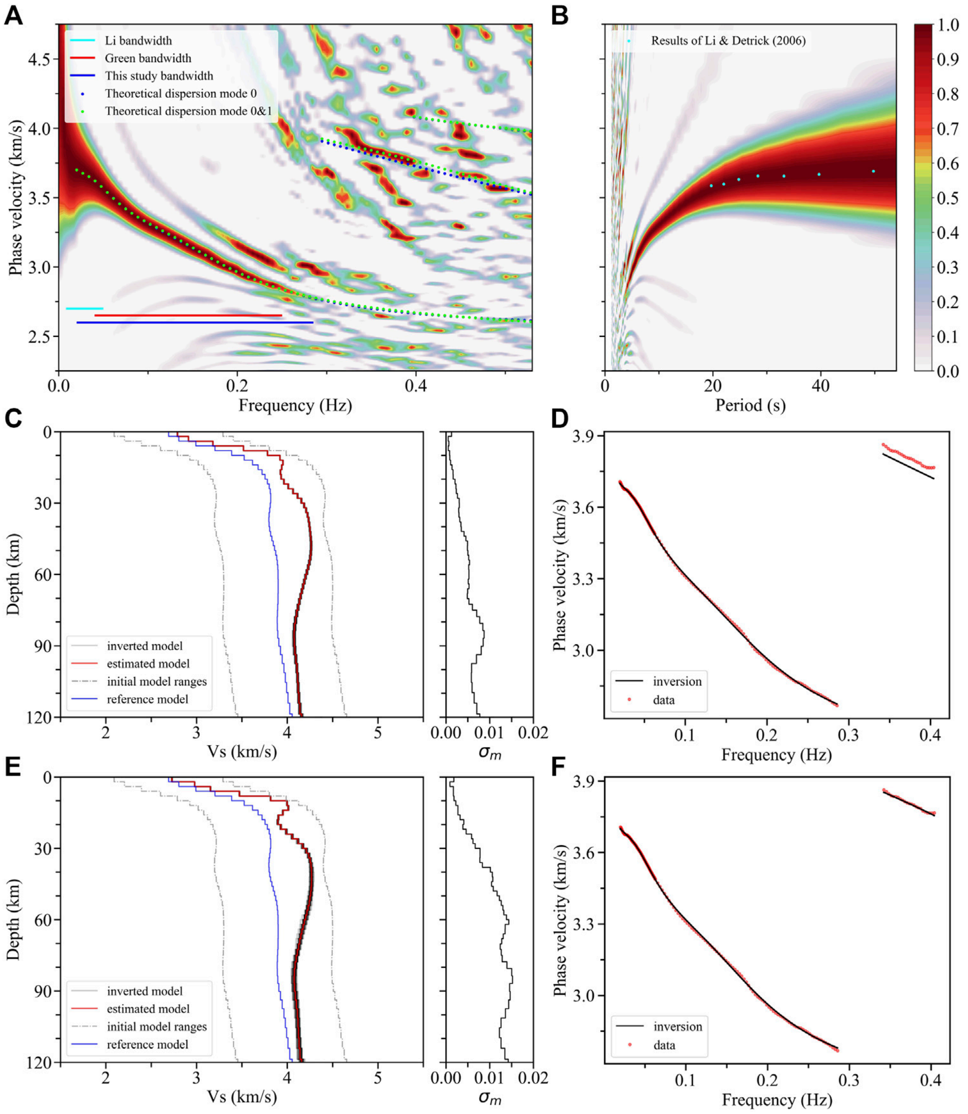

FIGURE 2
F-J spectra and inversion results. **(A)** Icelandic average F-J spectrum obtained by the F-J method in the frequency domain. The cyan solid line denotes the phase velocity bandwidth (0.008–0.050 Hz) obtained by Li and Detrick (2006), the red solid line (0.040–0.250 Hz) is the group velocity bandwidth (Green et al., 2017), and the blue solid line (0.020–0.285 Hz) is this study's result. The blue and green dots denote the theoretical dispersion curves computed from the inverted models. **(B)** Cyan dots extracted from Li and Detrick (2006) are projected to the F-J spectrum in the periodic domain. **(C,E)** The final models (red line) are weighted average from the best-fitting 40 inverted models (gray solid lines with the darker, the greater the weight) using the fundamental mode and first two mode dispersion curves, respectively. The dotted gray lines are the ranges of initial models, while the blue solid line is the reference model, and the black solid line on the right slide represents the standard deviation (σ_m) of every layer. **(D,F)** Fitting between the observed dispersion curves (red dots) and 40 theoretical dispersion curves (black lines) corresponded to the 40 inverted models in Figures 2C,E, respectively.

3 Data processing and results

3.1 Data and the F-J spectra

We apply the vertical component of continuous seismic data recorded by 44 broadband stations across Iceland to analyze the average structure of Iceland. Thirty stations of the XD array (HOTSPOT experiment, red triangles in Figure 1) were operated from July 1996 to July 1998 (e.g., Allen et al., 2002b), along with the global seismic network (GSN) station BORG (blue triangle in Figure 1). Additionally, all data are supplemented by eight stations of the Z7 array (Northern volcanic zone, purple triangles in Figure 1) and five stations of the YA array (Torfajökull 2005, green triangles in Figure 1). To avoid excessive local weights in the average result from two regional NCFs, we select stations from Z7 and YA arrays, mainly concentrated from September 2011 to July 2012 and June to October 2005, respectively. To protect the diffusion hypothesis, we ignore records on days with earthquakes with magnitudes of over M4 in Iceland and offshore.

Cross-correlation processing steps similar to those proposed by Bensen et al. (2007) are applied to seismic noise data. We apply CC-FJpy (Li et al., 2021) to compute NCFs of three different time periods in the frequency domain and obtain symmetrical NCFs in the time domain by inverse Fourier transformation, and the signal-to-noise ratio (SNR) of the latter is also used to conduct quality control (Supplementary Figure S2). The signal window (red lines in Supplementary Figure S2) is built by locating the Rayleigh wave group velocity at 1.7–3.5 km/s, which is translated 45 s outward to obtain the noise window (blue lines in Supplementary Figure S2). The SNR for each NCF is determined using the ratio of the root mean square of the amplitude values in its signal and noise windows, and the SNR is assigned as 4 in this study after a series of tests to both save enough useful information and obtain a clear F-J spectrum. Furthermore, some stations (black circles in Figure 1) that make the average F-J spectrum worse are removed (see Supplementary Material S1).

We apply CC-FJpy (Li et al., 2021) to acquire the F-J spectra (Figures 2A,B) from NCFs, and the fundamental mode dispersion curve could then be extracted from the peak values of the spectra. Figure 2A shows comparisons of the frequency bandwidth of dispersion curve with those of previous studies in this area. Our dispersion range, represented by the blue solid line (0.020–0.285 Hz), has a good balance between high and low frequency ranges. We also extract the dispersion curve of the first higher-mode ranges from 0.343 to 0.403 Hz. Some dispersion points with a period of 20–50 s obtained by Li and Detrick (2006) are projected onto the periodic domain F-J spectrum (Figure 2B), which shows some consistency in the dispersion information obtained from both studies.

3.2 The average S-wave structure

The fundamental dispersion curve is used to invert the average S-wave structure of Iceland (Figures 2C,D), and points with frequencies lower than 0.06 Hz are reserved more densely to provide deeper constraints. We calculate the theoretical dispersion curves of multimodes (blue dots in Figure 2A) of the final model in Figure 2C based on the theory of generalized reflection and transmission coefficients (Chen, 1993), which suggests a good agreement between the fundamental mode dispersion curve and the F-J spectrum energy peak. Since the dispersion curve of the first higher-mode comes close to a portion of the energy peak (Figures 2A,D), we extract the dispersion curve of the first higher-mode and combine it with the fundamental mode dispersion curve to improve the S-wave structure (Figures 2E,F).

To analyze the sensitivity of V_S for dispersion curves of the first two modes at the determined frequency range, we calculate the depth and frequency distribution sensitivity kernel function of the dispersion curves (Aki and Richards, 2002; Pan et al., 2019). The sensitivity of the fundamental mode dispersion curve is widely distributed at all depths and frequencies (Figure 3A), which indicates that the fundamental mode dispersion curve constrains the basic framework of the final model. The sensitivity of the dispersion curve of the first higher-mode, which is mainly concentrated above ~20 km (Figure 3B), provides information on the shallow structure. We also calculate different periods of sensitivity curves for the fundamental mode dispersion curve at periods of 25, 30, 40, and 50 s, whose most sensitivity depths are ~27 km, ~39 km, ~78 km, and ~85 km, respectively (Figure 3C). Although the largest sensitivity value of the dispersion curve at period 50 s is found at a depth of ~85 km, its constraint ability will not be limited to this depth. Finally, we take the model reference depth to 120 km based on the sensitivity distribution.

There are some corrections both on the amplitude of the crustal LVZ and the velocity structure above ~20 km from the constrained model without the first higher-mode (green line in Figure 4A) to the model with the first higher-mode constraint (red line in Figure 4A), which coincide with the sensitivity distribution (Figure 3B). The theoretical dispersion curves computed from the estimated model in Figure 2C correlate well with the fundamental mode energy peak of the F-J spectrum, while there are some differences between the theoretical and observed results for the first higher-mode (blue dots in Figure 2A). This inconsistency may be due to insufficient fundamental mode constraints. Theoretical dispersion curves computed from the estimated model in Figure 2E show a good agreement with the first two modes' energy peaks of the F-J spectrum (green dots in Figure 2A).

Our model has good agreement with the result of Li and Detrick (2006) on the LVZ below ~55 km (Figure 4A), and this LVZ may suggest partial melt in the Icelandic plume head (Allen et al., 2002a) relatively concentrated in this depth range. Additionally, the structure below the crust is significantly lower than that of the ak135 model (Figure 4A) (Kennett et al., 1995), which may result from the existence of a mantle plume beneath Iceland.

3.3 The S-wave structures of two subregions

To provide more evidence on the distribution and origins of the crustal LVZ found in our average model, we capture the velocity structures of two subregions. One located outside the volcanic zone is covered by eight stations from the XD array and

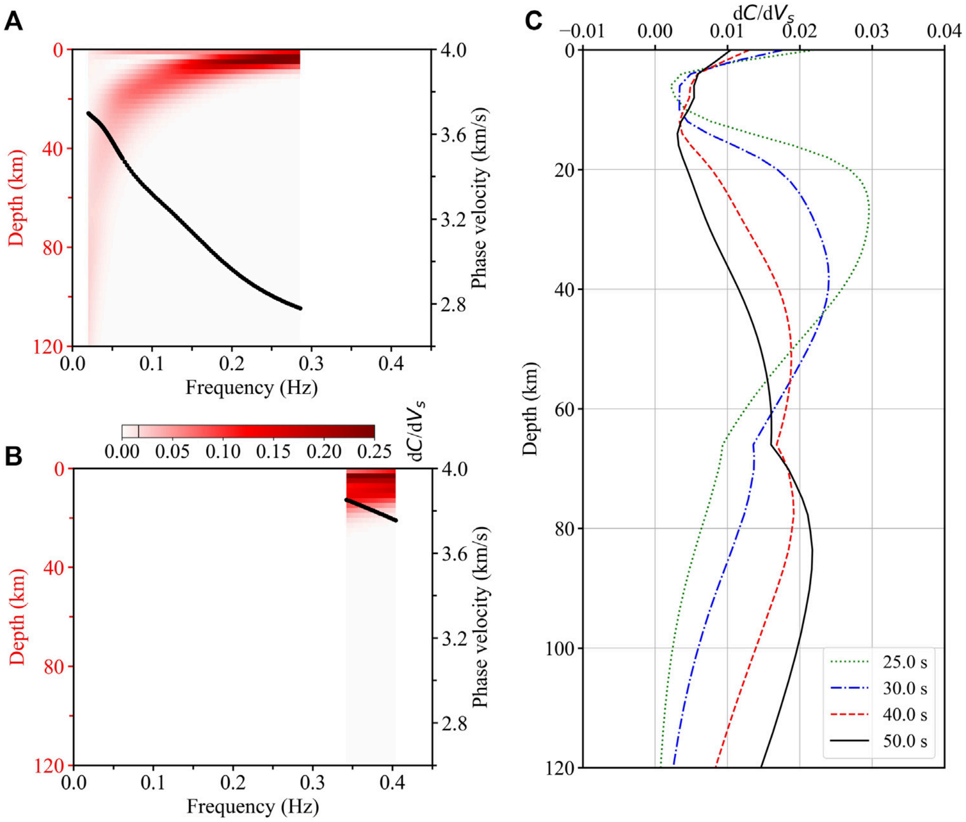

FIGURE 3
Sensitivity analysis: the variations of the partial derivatives of Rayleigh wave first two mode phase velocity relative to Vs with depths and frequencies. The sensitivity of the fundamental mode at the point of 0.02 Hz and 120 km, ~0.015, is identified by a black line in the color bar. Here, *C* is the phase velocity. **(A)** Sensitivity for the fundamental mode dispersion curve (black line). **(B)** Sensitivity for the first higher-mode dispersion curve (black line). **(C)** Sensitivity curves for the fundamental mode dispersion curve at 25, 30, 40, and 50 s.

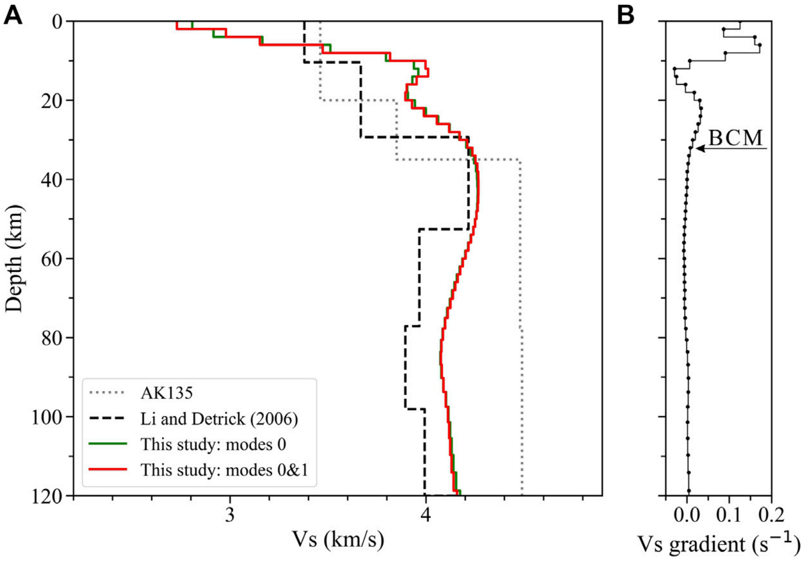

FIGURE 4
(A) Comparisons among average structures constrained by the fundamental mode (green line), first two modes (red line), Icelandic average model (black dashed line) from Li and Detrick (2006), and ak135 model (gray dotted line, Kennett et al., 1995). **(B)** Velocity gradient of each layer in the average model (red line in Figure 4A) is identified by the dotted solid line, where the boundary between the crust and the mantle (BCM) is marked with an arrow.

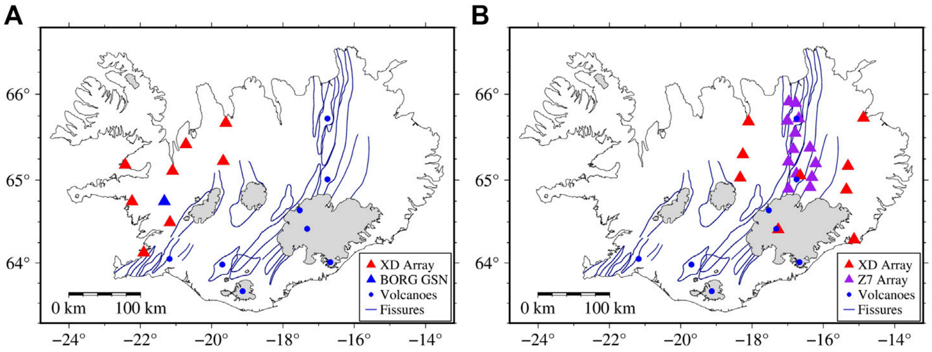

FIGURE 5
Stations coverage of subregions. **(A)** Subregion outside the volcanic zone is covered by the XD array (red angles) and station BORG (blue angle). **(B)** Subregion in the volcanic zone is covered by the XD array (red angles) and Z7 array (purple angles).

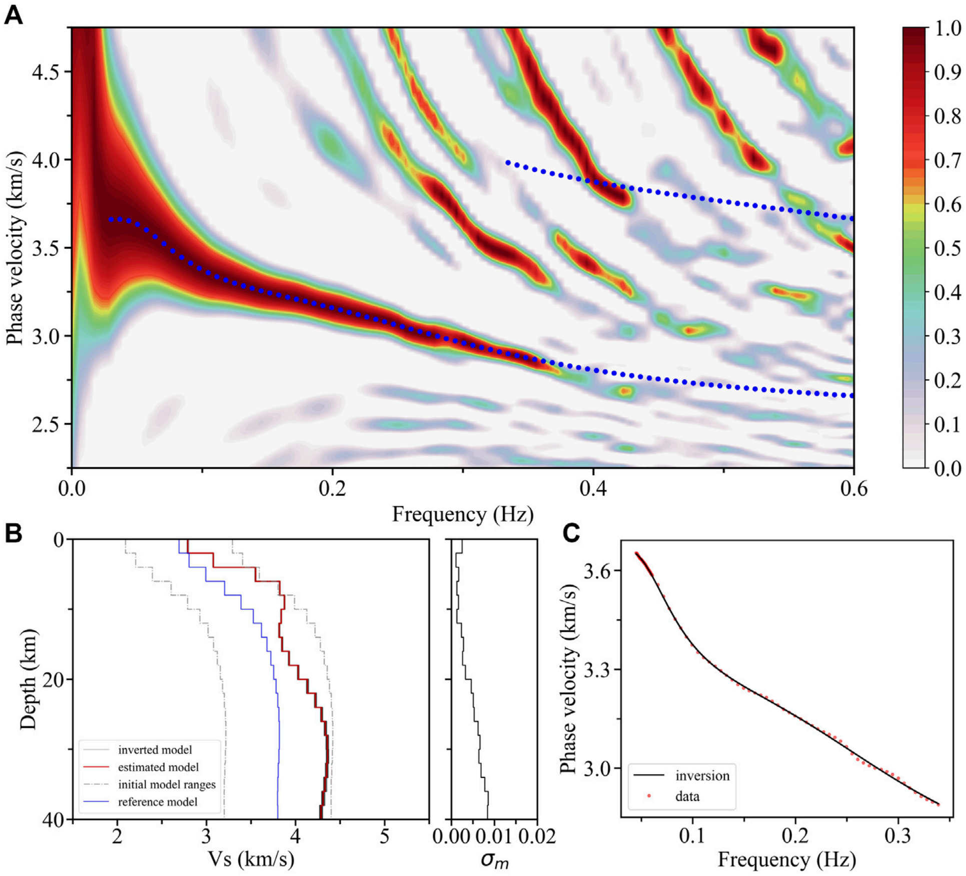

FIGURE 6
F-J spectrum and inversion results from the subregion outside the volcanic zone. **(A)** F-J spectrum and theoretical dispersion curves (blue dotted lines) calculated from the fundamental mode constraint. **(B)** Inversion results and standard deviation (σ_m) of each layer. **(C)** Fitting between the observed dispersion curves (red dots) and theoretical dispersion curves (dark lines).

the station BORG (Figure 5A), while another one located in the volcanic zone has nine stations from the XD array and 13 stations from the Z7 array (Figure 5B). Similar to the analysis of the average structure, we use the F-J method to obtain the dispersion spectra from the ambient noise data here. Multimodal dispersion curves are obtained to invert the structures of subregions, and the theoretical dispersion curves of final models are also projected into the spectra.

We have extracted the fundamental mode dispersion curves both from the F-J spectrum outside the volcanic zone (0.045–0.339 Hz, Figure 6A) and in the volcanic zone (0.041–0.255 Hz, Figure 7A), and the first higher-mode dispersion curve (0.372–0.434 Hz, Figure 7A) from the latter. It should be noted that the suddenly decreased phase velocity of the fundamental mode dispersion peak energy above ~0.27 Hz in the volcanic zone (Figure 7A) may be caused by severe variations in the shallow structure, which cannot be represented by a 1-D model integrating with the deep structure. Taking into account that the sudden change part only occupies a small portion of the total dispersion energy, we eliminate it and integrate the shallow and the deep structures with a 1-D model. The inversion results show that there are crustal LVZs in both subregions. The amplitude of the LVZ with ~4.6% in the volcanic zone (Figure 7B) is greater than that with ~1.5% outside the volcanic zones (Figure 6B) (e.g., Bjarnason and Schmeling, 2009). Therefore, these low-velocity anomalies located in different regions may jointly contribute to the crustal LVZ in the average structure, while the volcanic zones are likely to play more important roles.

3.4 Travel time comparison

To test the rationality of the Icelandic average model, we select four earthquakes on or offshore Iceland in 1997 (yellow stars in Figure 8A, event parameters are shown in Table 1). Primary waves of these four earthquakes have high SNRs, which ensure the determination of primary wave real onset is reliable. Meanwhile, twenty ray paths of primary waves recorded by selected stations of the XD array show a good coverage for the whole of Iceland (Figure 8A).

We use the TauP tool (Crotwell et al., 1999) to calculate the primary wave travel time of all event-station pairs based on the ak135 model (Kennett et al., 1995), the previous Icelandic average model (Li and Detrick, 2006), and the average model in this study, which is compared to the observed actual travel

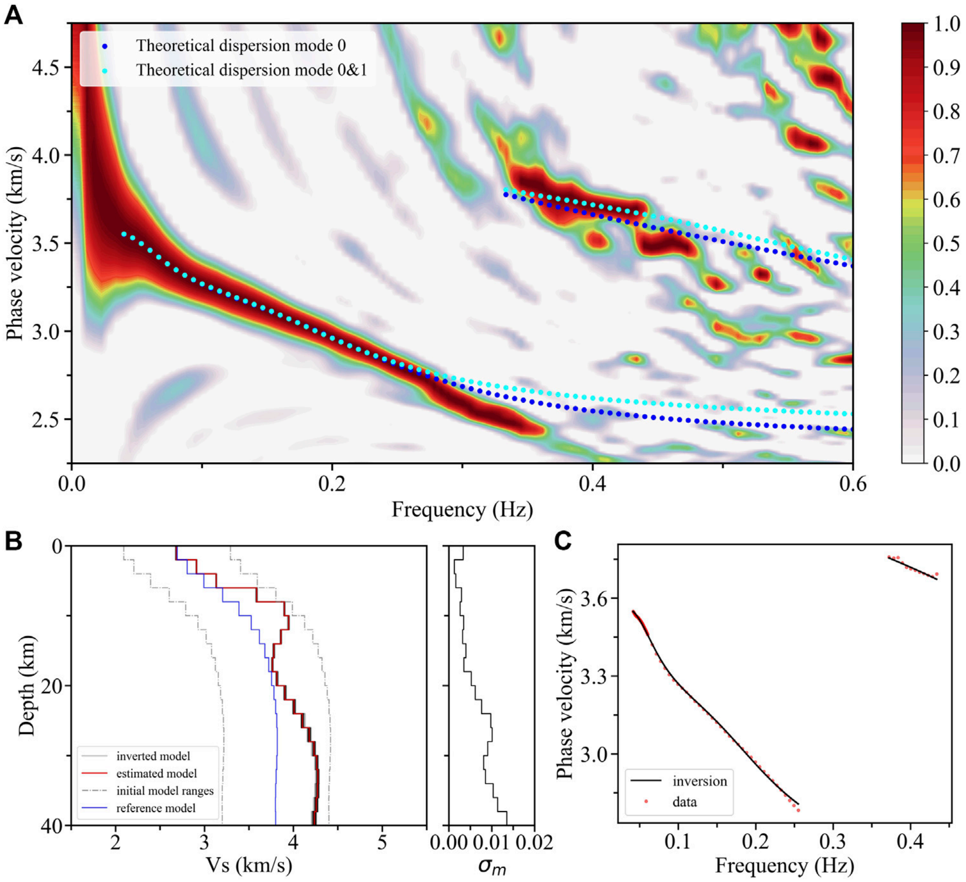

FIGURE 7
F-J spectrum and inversion results from the subregion of the volcanic zone. **(A)** F-J spectrum and theoretical dispersion curves, including the blue and cyan dotted lines calculated from the fundamental and the first two mode constraints, respectively. **(B)** Inversion results and standard deviation (σ_m) of each layer. **(C)** Fitting between the observed dispersion curves (red dots) and theoretical dispersion curves (dark lines).

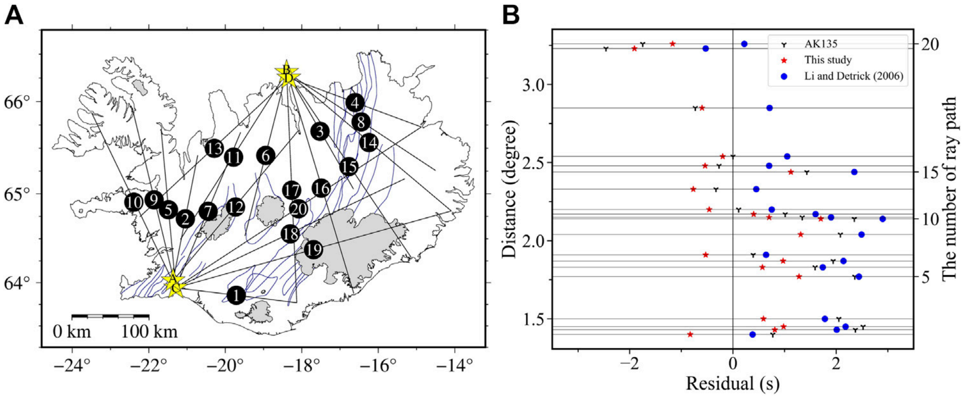

FIGURE 8
Comparison of various travel time calculated from different models and ray paths. **(A)** Distribution of different ray paths and natural earthquakes in Iceland are indicated as black solid lines and yellow stars, respectively. The increasing number represents the gradual increase of path distances, and the letters marked on the stars are event codes. The path combinations of earthquakes and stations can be seen in the Supplementary Table S1. **(B)** Travel time residuals compared to the observed primary wave travel time are calculated from the ak135 model (Kennett et al., 1995), the Icelandic average model (Li and Detrick, 2006) and our average model by the TauP tool (Crotwell et al., 1999), which are marked by different symbols and colors explained as the legend. These paths are sorted by ray distances, and the right vertical axis represents the sorted numbers corresponding to the sequence numbers in Figure 8A.

TABLE 1 Event parameters for the four local earthquakes used in this study.

Code	Date	Time (UTC)	Latitude (°N)	Longitude (°W)	Depth (km)	Magnitude (mb)
A	1997-04-12	23:04:44	64.0231	21.3652	10.0	4.1
B	1997-07-22	16:21:41	66.3101	18.3981	10.0	4.7
C	1997-08-24	03:04:22	63.9422	21.2948	10.0	4.8
D	1997-09-20	15:51:49	66.2503	18.3403	10.0	4.6

time (see Supplementary Table S1 for detailed time data and the combinations of earthquakes and stations). The statistical results of the residuals between the travel time calculated from different models and the observed data are shown in Figure 8B. From a single result such as paths 19 or 20, the travel time residual of Li and Detrick (2006) is smaller than those of the other two models in rift zones, where the crustal velocity is significantly lower than that in other parts of Iceland (e.g., Green et al., 2017). However, in the whole statistics, there are more large positive residuals corresponding to the models from Li and Detrick (2006) and the ak135 model (Kennett et al., 1995) than that of this study, which may indicate that the velocities of these two models are lesser than those of the real structure beneath these paths. The refraction traces of these ray paths calculated by the TauP tool (Crotwell et al., 1999) indicate that most of their deepest refraction positions are less than ~30 km. The comparisons in Figure 4A also reveal the velocities of the two models in the mid-lower crust are lesser than those of our average model at corresponding depths. The positive and negative residuals calculated from our average model are more evenly distributed, and the smaller root mean square value of the residual can be obtained as ~0.95 than that of the previous model (Li and Detrick, 2006) as ~2.78 and the ak135 model (Kennett et al., 1995) as ~2.67. Based on the comprehensive statistical results, the crust model of the average structure obtained in this study has more possibility to better represent the overall velocity characteristics of the Icelandic crust.

4 Discussion

4.1 Tests for the crustal LVZ

The minimal velocity of the crustal LVZ between 12 and 22 km (red line in Figure 4A) is 3.89 km/s, which is approximately 3% lower than the velocity of 4.01 km/s above the LVZ. We also conduct a series of tests to estimate the reliability of the LVZ. For instance, the anomaly is substituted with an incremental structure to create a model (green line in

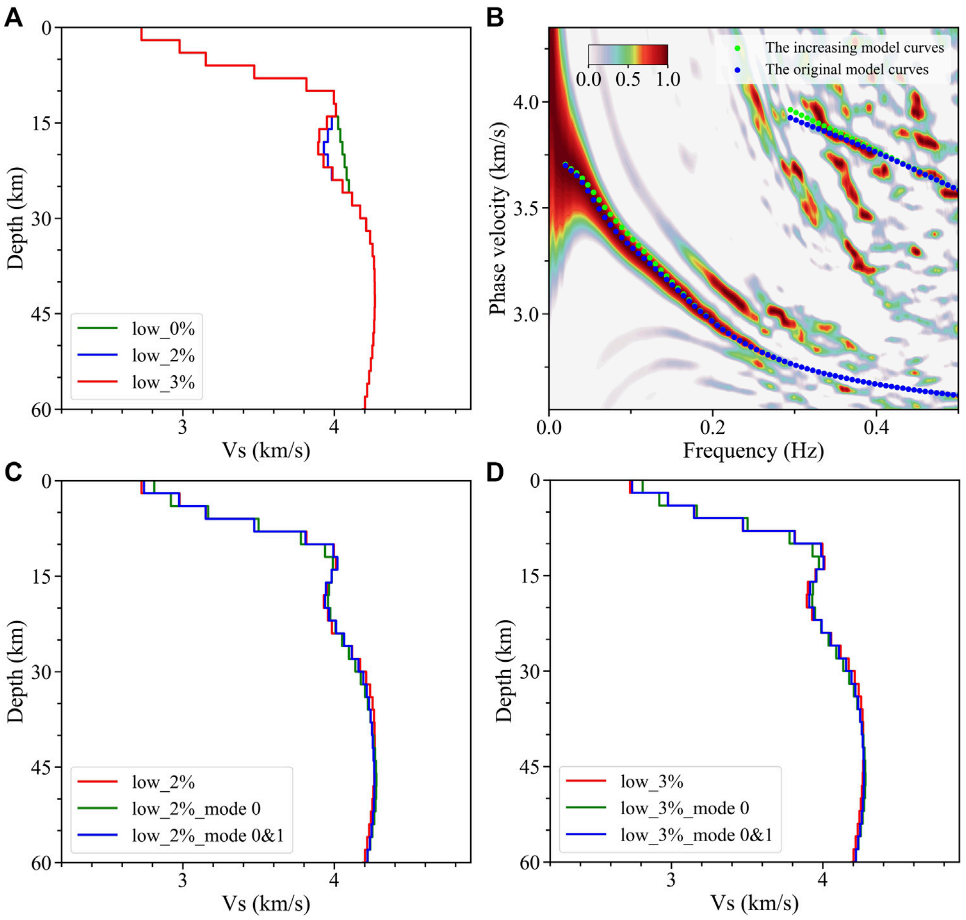

FIGURE 9
Crustal LVZ and model recovery tests of the Icelandic average Vs model. **(A)** Original model with an LVZ at 3% (red line), a new model with an LVZ at 2% (blue line), and an increasing model (green line). **(B)** Theoretical dispersion curves computed from the original (blue dots) and increasing models (green dots) are projected on the average F-J spectrum. **(C)** Comparisons among the new model with an LVZ at 2% (red line) and the models inverted by its theoretical dispersion curves of the fundamental mode (green line) and first two modes (blue line). **(D)** It is the same as Figure 9C; however, the model has an LVZ at 3%.

Figure 9A), whose theoretical dispersion curves are shown in Figure 9B (green dots) and deviate from the energy peak at 0.04–0.14 Hz. However, the theoretical dispersion curves of the original model fit well with the energy peak (blue dots in Figure 9B); thus, the existence of the LVZ in this average V_S model is robust. To detect anomaly resolution, the LVZ is reduced to 2% creating a new model (blue line in Figure 9A), and the inversion results of the first 60 km using theoretical dispersion curves of this model are shown in Figure 9C. The same frequency points of theoretical dispersion curves as those of the dispersion curves in Figure 2 are used to invert, and all other inversion parameters are consistent with those used in Figure 2. Similarly, we compare the original model equipped with LVZ at 3% with the models inverted using the theoretical dispersion curves (Figure 9D). It is observed that the LVZ at 2% (red line in Figure 9C) can be recovered mostly only under the constraint of the fundamental mode dispersion curve (green line in Figure 9C), and the LVZ and shallow structures can be further recovered after the addition of the first higher-mode (blue line in Figure 9C). The same conclusions are obtained for the LVZ at 3%. Therefore, these tests suggest that it can distinguish the LVZ at 3%, especially under the joint constraints of the first two mode dispersion curves.

4.2 Icelandic average crust and low-velocity anomalies

Foulger et al. (2003) reported that although there are some differences among modern seismic studies of the Icelandic crust, a consensus is that the upper crust of Iceland is characterized by a high-velocity gradient, while the velocity gradient in the lower crust decreases by an order of magnitude. These crustal velocity gradients vary in a wide range, such as the western Iceland with steep velocity gradients of up to ~0.45 s^{-1} in Vs at the shallow crust and low-velocity gradients of $\lesssim 0.02$ s^{-1} beneath (Du et al., 2002). There are twofold conditions about the crust in Iceland (Allen et al., 2002b; Bjarnason and Schmeling, 2009): 1) the traditional Moho velocity jump is still in debate due to the absence of strong Pn and Sn phases, and 2) the velocity gradient in the lower crust is an order of magnitude larger than that in the uppermost mantle just as the upper crust and lower crust. Taking into account the features of the Icelandic crust, we try to divide the average crust model of Iceland into three sections with the variations of velocity gradients (as shown in Figure 4B).

The upper crust exhibits high-velocity gradients of up to ~0.17 s^{-1} until the depth of ~10 km. Nevertheless, the comparison between low-velocity gradients of $\lesssim 0.03$ s^{-1} in the mid-lower crust and those of $\lesssim 0.008$ s^{-1} in the top 30 km of the uppermost mantle defines the boundary between the crust and the mantle (BCM) at a depth of ~32 km. In addition, we refer to our average model at 10–22 km depths as the middle crust including an LVZ. The high-velocity gradients of the Icelandic upper crust are generally considered to be due to the reduction of porosity caused by the closure of fractures under lithostatic pressure and the infilling of secondary minerals, as well as the dense parts of unconsolidated lava piles in the upper crust (e.g., Flóvenz and Gunnarsson, 1991). The thickness of the upper crust of 10 km is consistent with the extensive high-velocity gradient layer in Iceland (Jenkins et al., 2018). By sampling a 3-D model, Allen et al. (2002b) obtained an average model with a crustal thickness of ~29 km, which is similar to that in this study. The average crustal thickness is more than four times the normal oceanic crust thickness of ~7 km (White et al., 1992), which may reflect the influence of hotspots on the formation process of the Icelandic crust. If the asthenosphere is defined as the beginning of velocity attenuation below the lithosphere, the average lithospheric thickness of Iceland is ~55 km. The thickness of the lithosphere varying from the thinnest 20 km to the thickest 100 km under different regions in Iceland (Bjarnason and Schmeling, 2009) may support the average result. In addition, Li and Detrick (2006) also confined the mantle lithosphere lid above 60 km based on their velocity profiles in Iceland. The low-velocity anomaly of the asthenosphere below ~55 km may be the result of high temperature and melt accumulation from the deeper hot mantle plumbing that can feed the crustal partial melt.

Abundant receiver function works in Iceland (e.g., Darbyshire et al., 2000a; Du et al., 2002) have revealed significant crustal LVZs, whose thickness and amplitudes also exhibit great variations. By extracting surface wave dispersion information from regional earthquakes, Bjarnason and Schmeling (2009) also observed the presence of LVZs in the depth range of 8–18 km in northern Iceland. Although crustal LVZs in some regional areas of Iceland have been found, this important information is still absent in the pre-existing average structure representing the overall characteristics of Iceland (e.g., Li and Detrick, 2006), which may be ameliorated by our work.

Darbyshire et al. (2000a) reported a prominent LVZ at depths of 10–15 km beneath the central volcano Krafla in northwest Iceland, and Du and Foulger (2001) revealed a substantial LVZ beneath the middle volcanic zone in the lower crust and a similar crustal LVZ is also observed beneath the northern volcanic zone (Figure 7B). These crustal LVZs, observed in volcanic active regions, are generally formed due to anomalously high temperatures and the presence of partial melt at corresponding depths. However, the crustal LVZs outside the volcanic zones observed in this work (Figure 6B) and previous studies (e.g., Bjarnason and Schmeling, 2009), as well as the crustal LVZs existing in the average structure, indicate that the origin of the anomalies may not be so simple, i.e., LVZs are less possible to be mainly confined to below central volcanoes. The thick-cold crust model in Iceland suggests that there is less possibility of a large portion of partial melt above Moho (e.g., Menke and Levin, 1994; Menke et al., 1995), while LVZs may also be caused by compositional changes, anisotropy, or fluids in high pore pressure.

Jenkins et al. (2018) reported the crystallization path of both depleted and enriched mantle melts through a petrological model simplifying the magmatic evolution and crustal accretion. The mineralogical, compositional, and thermodynamic properties also change with depth to affect the crystallization path. The earliest crystallization from bimodal mantle melts is olivine, the first phase on the liquidus curve, forming ultrabasic cumulates at the base of the crust. After further cooling, clinopyroxene and plagioclase mix with olivine to crystallize, and after that, gabbro is the main crystallizing solid rock. The ultrabasic cumulates formed by crystallization have similar seismic velocities to mantle rocks whose velocities are higher than that of gabbroic material (e.g., Maclennan et al., 2001). The Icelandic acidic intrusive bodies mapped by Johannesson and Saemundsson (1989) may further contribute to low-velocity anomalies. Darbyshire et al. (2000a) reported the amplitudes of central and northern crustal LVZs, away from central volcanoes, were similar to the seismic velocity difference between acidic rocks and gabbro. In addition, the anomaly of high-velocity layers containing scoriaceous material in the upper crust (Flóvenz and Gunnarsson, 1991) may promote the velocity contrast with the middle crust. Consequently, the crustal LVZ that we observe in the average structure is likely to be the result of the combined effects of partial melt beneath the central volcanoes and the variations in the petrology of the crust.

5 Conclusion

Based on ambient noise analysis, we use the F-J method to successfully extract Rayleigh phase velocity dispersion curves of the fundamental mode (0.020–0.285 Hz) and first higher-mode (0.343–0.403 Hz) from the continuous broadband ambient noise data recorded at the XD array and some supplement stations in Iceland. Following this, we obtain the average V_S structure down to 120 km depth in Iceland by using multimode dispersion measurements. We observe a crustal LVZ at a depth of 12–22 km, which supplements the characteristics of the Icelandic average crust. We also image the crustal structures in a volcanic zone and a non-volcanic zone, which reveals similar crustal LVZs in both subregions. Considering the gabbro of the middle crust with a lower velocity than that of ultrabasic cumulates at the base, acid intrusion bodies, and high-velocity layer in the upper crust of Iceland, the crustal LVZ may be caused by the lithological composition variations of the crust and the high temperature under the central volcanoes.

Using the changes of the Vs gradient, we also divide the average structure into three parts: upper crust above 10 km depth; middle crust down to 22 km depth, including an LVZ; and the lower crust in the depth range of 22–32 km. The LVZ at 55 km depth below the lithosphere can be regarded as the beginning of the asthenosphere. In addition, we conduct systematic tests to verify the reliability of the crustal LVZ in our average model, which further reveals that the minimum V_S of LVZ is approximately 3% slower than that at the beginning depth of this LVZ. Furthermore, the residual of the predicted primary wave travel time by our model relative to the observed data is smaller than those of other average models, which better supports our average model.

Data availability statement

Datasets for this research are provided by the Incorporated Research Institutions for Seismology (IRIS) from the XD Array (HOTSPOT experiment) (https://doi.org/10.7914/SN/XD_1996, Nolet, 1996), Z7 Array (Northern Volcanic Zone) (https://doi.org/10.7914/SN/Z7_2010, White, 2010), BORG GSN (https://doi.org/10.7914/SN/II, Scripps Institution of Oceanography, 1986), and YA Array (Torfajökull 2005) (http://www.fdsn.org/networks/detail/YA_2005/, Nordic Volcanological Institute, 2005). The earthquake parameters used in this study are supported by IRIS (http://ds.iris.edu/wilber3/find_event). The packages for the F-J method, inversion, and seismic travel time calculation are available in the following references: Li et al. (2021) (https://doi.org/10.1785/0220210042), Pan et al. (2019) (https://doi.org/10.1093/gji/ggy479), and Crotwell et al. (1999) (https://doi.org/10.1785/gssrl.70.2.154).

Author contributions

The specific contributions of each author can be described as follows. Conceptualization: SZ, GZ, XF, and XC; methodology: ZL, LP, JW, and XC; formal analysis: SZ, GZ, XF, and XC; investigation: SZ, GZ, XF, and XC; resources: XC; data curation: SZ and GZ; writing—original draft preparation: SZ; writing—review and editing: XF, ZL, and XC; visualization: SZ, XF, LP, and JW; supervision: XC; project administration: XC; funding acquisition: XC. All authors read and approved the final manuscript.

Funding

This research was supported by National Natural Science Foundation of China (Grant Nos. 41790465 and 92155307), Key Special Project for Introduced Talents Team of Southern Marine Science and Engineering Guangdong Laboratory (Guangzhou) (GML2019ZD0203), Shenzhen Science and Technology Program (Grant No. KQTD20170810111725321), and Shenzhen Key Laboratory of Deep Offshore Oil and Gas Exploration Technology (Grant No. ZDSYS20190902093007855).

Conflict of interest

The authors declare that the research was conducted in the absence of any commercial or financial relationships that could be construed as a potential conflict of interest.

Publisher’s note

Supplementary material

The Supplementary Material for this article can be found online at: https://www.frontiersin.org/articles/10.3389/feart.2022.1008354/full#supplementary-material

References

Aki, K. (1957). Space and time spectra of stationary stochastic waves, with special reference to microtremors. *Bull. Earthq. Res. Inst.* 35, 415–456.

Aki, K., and Richards, P. G. (2002). “Surface waves in a vertically heterogeneous medium,” in *Quantitative seismology*. Editor J. Ellis (Mill Valley, California: University Science Books), 249–330.

Allen, R. M., Nolet, G., Morgan, W. J., Vogfjörd, K., Bergsson, B. H., Erlendsson, P., et al. (2002a). Imaging the mantle beneath Iceland using integrated seismological techniques. *J. Geophys. Res. Solid Earth* 107 (B12), ESE 3-1–ESE 3-16. doi:10.1029/2001JB000595

Allen, R. M., Nolet, G., Morgan, W. J., Vogfjörd, K., Nettles, M., Ekström, G., et al. (2002b). Plume-driven plumbing and crustal formation in Iceland. *J. Geophys. Res. Solid Earth* 107 (B8), ESE 4-1–ESE 4-19. doi:10.1029/2001JB000584

Beblo, M., and Bjornsson, A. (1980). A model of electrical resistivity beneath NE-Iceland, correlation with temperature. *J. Geophys.* 47 (1), 184–190.

Bensen, G. D., Ritzwoller, M. H., Barmin, M. P., Levshin, A. L., Lin, F., Moschetti, M. P., et al. (2007). Processing seismic ambient noise data to obtain reliable broad-band surface wave dispersion measurements. *Geophys. J. Int.* 169 (3), 1239–1260. doi:10.1111/j.1365-246X.2007.03374.x

Bjarnason, I. T., Menke, W., Flóvenz, Ó. G., and Caress, D. (1993). Tomographic image of the mid-Atlantic plate boundary in southwestern Iceland. *J. Geophys. Res. Solid Earth* 98 (B4), 6607–6622. doi:10.1029/92JB02412

Bjarnason, I. T., and Schmeling, H. (2009). The lithosphere and asthenosphere of the Iceland hotspot from surface waves. *Geophys. J. Int.* 178 (1), 394–418. doi:10.1111/j.1365-246X.2009.04155.x

Brocher, T. M. (2005). Empirical relations between elastic wavespeeds and density in the Earth’s crust. *Bull. Seismol. Soc. Am.* 95 (6), 2081–2092. doi:10.1785/0120050077

Campillo, M., and Paul, A. (2003). Long-range correlations in the diffuse seismic coda. *Science* 299 (5606), 547–549. doi:10.1126/science.1078551

Capon, J. (1969). High-resolution frequency-wavenumber spectrum analysis. *Proc. IEEE* 57 (8), 1408–1418. doi:10.1109/PROC.1969.7278

Chen, X. (1993). A systematic and efficient method of computing normal modes for multilayered half-space. *Geophys. J. Int.* 115 (2), 391–409. doi:10.1111/j.1365-246X.1993.tb01194.x

Crotwell, H. P., Owens, T. J., and Ritsema, J. (1999). The TauP Toolkit: Flexible seismic travel-time and ray-path utilities. *Seismol. Res. Lett.* 70, 154–160. doi:10.1785/gssrl.70.2.154

Darbyshire, F. A., Bjarnason, I. T., White, R. S., and Flóvenz, Ó. G. (1998). Crustal structure above the Iceland mantle plume imaged by the ICEMELT refraction profile. *Geophys. J. Int.* 135 (3), 1131–1149. doi:10.1046/j.1365-246X.1998.00701.x

Darbyshire, F. A., Priestley, K. F., White, R. S., Stefánsson, R., Gudmundsson, G. B., and Jakobsdóttir, S. S. (2000a). Crustal structure of central and northern Iceland from analysis of teleseismic receiver functions. *Geophys. J. Int.* 143 (1), 163–184. doi:10.1046/j.1365-246x.2000.00224.x

Darbyshire, F. A., White, R. S., and Priestley, K. F. (2000b). Structure of the crust and uppermost mantle of Iceland from a combined seismic and gravity study. *Earth Planet. Sci. Lett.* 181 (3), 409–428. doi:10.1016/S0012-821X(00)00206-5

Du, Z., Foulger, G. R., Julian, B. R., Allen, R. M., Nolet, G., Morgan, W. J., et al. (2002). Crustal structure beneath western and eastern Iceland from surface waves and receiver functions. *Geophys. J. Int.* 149 (2), 349–363. doi:10.1046/j.1365-246X.2002.01642.x

Du, Z., and Foulger, G. R. (2001). Variation in the crustal structure across central Iceland. *Geophys. J. Int.* 145 (1), 246–264. doi:10.1111/j.1365-246X.2001.00377.x

Dziewonski, A., Bloch, S., and Landisman, M. (1969). A technique for the analysis of transient seismic signals. *Bull. Seismol. Soc. Am.* 59 (1), 427–444. doi:10.1785/bssa0590010427

Flóvenz, Ó. G., and Gunnarsson, K. (1991). Seismic crustal structure in Iceland and surrounding area. *Tectonophysics* 189 (1), 1–17. doi:10.1016/0040-1951(91)90483-9

Flóvenz, Ó. G., and Saemundsson, K. (1993). Heat flow and geothermal processes in Iceland. *Tectonophysics* 225 (1), 123–138. doi:10.1016/0040-1951(93)90253-G

Foulger, G. R., Du, Z., and Julian, B. R. (2003). Icelandic-type crust. *Geophys. J. Int.* 155 (2), 567–590. doi:10.1046/j.1365-246X.2003.02056.x

Foulger, G. R., Pritchard, M. J., Julian, B. R., Evans, J. R., Allen, R. M., Nolet, G., et al. (2001). Seismic tomography shows that upwelling beneath Iceland is confined to the upper mantle. *Geophys. J. Int.* 146 (2), 504–530. doi:10.1046/j.0956-540x.2001.01470.x

Green, R. G., Priestley, K. F., and White, R. S. (2017). Ambient noise tomography reveals upper crustal structure of Icelandic rifts. *Earth Planet. Sci. Lett.* 466, 20–31. doi:10.1016/j.epsl.2017.02.039

Hansen, P. C. (2001). “The L-curve and its use in the numerical treatment of inverse problems,” in *Computational inverse problems in electrocardiology*. Editor P. Johnston (Southampton: WIT Press), 119–142.

Jenkins, J., Maclennan, J., Green, R. G., Cottaar, S., Deuss, A. F., and White, R. S. (2018). Crustal formation on a spreading ridge above a mantle plume: Receiver function imaging of the Icelandic crust. *J. Geophys. Res. Solid Earth* 123 (6), 5190–5208. doi:10.1029/2017JB015121

Johannesson, H., and Saemundsson, K. (1989). *Geological map of Iceland, 1: 500,000, Bedrock geology*. Reykjavik: Icelandic Museum of Natural History and Iceland Geodetic Survey.

Johannesson, H., and Saemundsson, K. (1998). *Geological map of Iceland, 1: 500,000, Tectonics*. Reykjavik: Icelandic Institute of Natural History.

Kennett, B. L. N., Engdahl, E. R., and Buland, R. (1995). Constraints on seismic velocities in the Earth from traveltimes. *Geophys. J. Int.* 122 (1), 108–124. doi:10.1111/j.1365-246X.1995.tb03540.x

Levshin, A. L., and Ritzwoller, M. H. (2001). Automated detection, extraction, and measurement of regional surface waves. *Pure Appl. Geophys.* 158 (8), 1531–1545. doi:10.1007/PL00001233

Li, A., and Detrick, R. S. (2003). Azimuthal anisotropy and phase velocity beneath Iceland: Implication for plume–ridge interaction. *Earth Planet. Sci. Lett.* 214 (1), 153–165. doi:10.1016/S0012-821X(03)00382-0

Li, A., and Detrick, R. S. (2006). Seismic structure of Iceland from Rayleigh wave inversions and geodynamic implications. *Earth Planet. Sci. Lett.* 241 (3), 901–912. doi:10.1016/j.epsl.2005.10.031

Li, Z., Shi, C., Ren, H., and Chen, X. (2022). Multiple leaking mode dispersion observations and applications from ambient noise cross-correlation in Oklahoma. *Geophys. Res. Lett.* 49 (1), e2021GL096032. doi:10.1029/2021GL096032

Li, Z., Zhou, J., Wu, G., Wang, J., Zhang, G., Dong, S., et al. (2021). CC-FJpy: A python package for extracting overtone surface-wave dispersion from seismic ambient-noise cross correlation. *Seismol. Res. Lett.* 92 (5), 3179–3186. doi:10.1785/0220210042

Luo, Y., Xia, J., Miller, R. D., Xu, Y., Liu, J., and Liu, Q. (2008). Rayleigh-wave dispersive energy imaging using a high-resolution linear Radon transform. *Pure Appl. Geophys.* 165 (5), 903–922. doi:10.1007/s00024-008-0338-4

Ma, Q., Pan, L., Wang, J., Yang, Z., and Chen, X. (2022). Crustal S-wave velocity structure beneath the northwestern Bohemian Massif, central Europe, revealed by the inversion of multimodal ambient noise dispersion curves. *Front. Earth Sci.* 10. doi:10.3389/feart.2022.838751

Maclennan, J., Mkenzie, D., Gronvöld, K., and Slater, L. (2001). Crustal accretion under northern Iceland. *Earth Planet. Sci. Lett.* 191 (3), 295–310. doi:10.1016/S0012-821X(01)00420-4

Menke, W., and Levin, V. (1994). Cold crust in a hot spot. *Geophys. Res. Lett.* 21 (18), 1967–1970. doi:10.1029/94GL01896

Menke, W., Levin, V., and Sethi, R. (1995). Seismic attenuation in the crust at the mid-Atlantic plate boundary in south-west Iceland. *Geophys. J. Int.* 122 (1), 175–182. doi:10.1111/j.1365-246X.1995.tb03545.x

Nolet, G. (1996). *Data from: Seismic study of the Iceland hotspot*. International Federation of Digital Seismograph Networks. doi:10.7914/SN/XD_1996

Nordic Volcanological Institute (2005). *Data from:* Torfajokull 2005. International Federation of Digital Seismograph Networks. http://www.fdsn.org/networks/detail/YA_2005/.

Pálmason, G. (1971). *Crustal structure of Iceland from explosion seismology*. Reykjavik: Prentsmiðjan Leiftur.

Pan, L., Chen, X., Wang, J., Yang, Z., and Zhang, D. (2019). Sensitivity analysis of dispersion curves of Rayleigh waves with fundamental and higher modes. *Geophys. J. Int.* 216 (2), 1276–1303. doi:10.1093/gji/ggy479

Park, C. B., Miller, R. D., Xia, J., and Ivanov, J. (2007). Multichannel analysis of surface waves (MASW)—Active and passive methods. *Lead. Edge* 26 (1), 60–64. doi:10.1190/1.2431832

Rickers, F., Fichtner, A., and Trampert, J. (2013). The Iceland–Jan Mayen plume system and its impact on mantle dynamics in the north Atlantic region: Evidence from full-waveform inversion. *Earth Planet. Sci. Lett.* 367, 39–51. doi:10.1016/j.epsl.2013.02.022

Schilling, J. G. (1973). Iceland mantle plume: Geochemical study of Reykjanes ridge. *Nature* 242 (5400), 565–571. doi:10.1038/242565a0

Scripps Institution of Oceanography (1986). *Data from:* Global s*eismograph network* - IRIS/IDA. International Federation of Digital Seismograph Networks. doi:10.7914/SN/II

Shapiro, N. M., and Campillo, M. (2004). Emergence of broadband Rayleigh waves from correlations of the ambient seismic noise. *Geophys. Res. Lett.* 31 (7). doi:10.1029/2004GL019491

Shapiro, N. M., Campillo, M., Stehly, L., and Ritzwoller, M. H. (2005). High-resolution surface-wave tomography from ambient seismic noise. *Science* 307 (5715), 1615–1618. doi:10.1126/science.1108339

Shorttle, O., and Maclennan, J. (2011). Compositional trends of Icelandic basalts: Implications for short–length scale lithological heterogeneity in mantle plumes. *Geochem. Geophys. Geosyst.* 12 (11). doi:10.1029/2011GC003748

Staples, R. K., White, R. S., Brandsdottir, B., Menke, W., Maguire, P. K. H., and McBride, J. H. (1997). Färoe-Iceland ridge experiment: 1. Crustal structure of northeastern Iceland. *J. Geophys. Res. Solid Earth* 102 (B4), 7849–7866. doi:10.1029/96JB03911

Tryggvason, E. (1962). Crustal structure of the Iceland region from dispersion of surface waves. *Bull. Seismol. Soc. Am.* 52 (2), 359–388. doi:10.1785/bssa0520020359

Wang, J., Wu, G., and Chen, X. (2019). Frequency-Bessel transform method for effective imaging of higher-mode Rayleigh dispersion curves from ambient seismic noise data. *J. Geophys. Res. Solid Earth* 124 (4), 3708–3723. doi:10.1029/2018JB016595

Weaver, R. L., and Lobkis, O. I. (2001). Ultrasonics without a source: Thermal fluctuation correlations at MHz frequencies. *Phys. Rev. Lett.* 87 (13), 134301. doi:10.1103/PhysRevLett.87.134301

White, R. (2010). *Data from:* Northern volcanic zone. International Federation of Digital Seismograph Networks. doi:10.7914/SN/Z7_2010

White, R. S., McKenzie, D., and O'Nions, R. K. (1992). Oceanic crustal thickness from seismic measurements and rare Earth element inversions. *J. Geophys. Res. Solid Earth* 97 (B13), 19683–19715. doi:10.1029/92JB01749

Wolfe, C. J., Bjarnason, I. T., VanDecar, J. C., and Solomon, S. C. (1997). Seismic structure of the Iceland mantle plume. *Nature* 385, 245–247. doi:10.1038/385245a0

Wu, G., Pan, L., Wang, J., and Chen, X. (2020). Shear velocity inversion using multimodal dispersion curves from ambient seismic noise data of USArray transportable array. *J. Geophys. Res. Solid Earth* 125 (1), e2019JB018213. doi:10.1029/2019JB018213

Xi, C., Xia, J., Mi, B., Dai, T., Liu, Y., and Ning, L. (2021). Modified frequency–Bessel transform method for dispersion imaging of Rayleigh waves from ambient seismic noise. *Geophys. J. Int.* 225 (2), 1271–1280. doi:10.1093/gji/ggab008

Xia, J., Miller, R. D., and Park, C. B. (1999). Estimation of near-surface shear-wave velocity by inversion of Rayleigh waves. *Geophysics* 64 (3), 691–700. doi:10.1190/1.1444578

Xia, J., Miller, R. D., Park, C. B., and Tian, G. (2003). Inversion of high frequency surface waves with fundamental and higher modes. *J. Appl. Geophy.* 52 (1), 45–57. doi:10.1016/S0926-9851(02)00239-2

Yang, Y., and Ritzwoller, M. H. (2008). Characteristics of ambient seismic noise as a source for surface wave tomography. *Geochem. Geophys. Geosyst.* 9 (2). doi:10.1029/2007GC001814

Yao, H., van Der Hilst, R. D., and de Hoop, M. V. (2006). Surface-wave array tomography in SE tibet from ambient seismic noise and two-station analysis — I. Phase velocity maps. *Geophys. J. Int.* 166 (2), 732–744. doi:10.1111/j.1365-246X.2006.03028.x

Zhan, W., Pan, L., and Chen, X. (2020). A widespread mid-crustal low-velocity layer beneath northeast China revealed by the multimodal inversion of Rayleigh waves from ambient seismic noise. *J. Asian Earth Sci.* 196, 104372. doi:10.1016/j.jseaes.2020.104372

Zhou, J., and Chen, X. (2021). Removal of crossed artifacts from multimodal dispersion curves with modified frequency–Bessel method. *Bull. Seismol. Soc. Am.* 112 (1), 143–152. doi:10.1785/0120210012

frontiers | Frontiers in Earth Science

TYPE Original Research
PUBLISHED 10 January 2023
DOI 10.3389/feart.2022.1080298

Check for updates

OPEN ACCESS

EDITED BY
Lidong Dai,
Institute of geochemistry (CAS), China

REVIEWED BY
Shaolin Liu,
Ministry of Emergency Management, China
Zhi Wei,
Peking University, China

*CORRESPONDENCE
Weijia Sun,
swj@mail.iggcas.ac.cn

SPECIALTY SECTION
This article was submitted to Solid Earth Geophysics,
a section of the journal
Frontiers in Earth Science

RECEIVED 26 October 2022
ACCEPTED 29 November 2022
PUBLISHED 10 January 2023

CITATION
Tang Q, Sun W, Hu J and Fu L-Y (2023), Seismological reference earth model in South China (SREM-SC): Upper mantle. *Front. Earth Sci.* 10:1080298.
doi: 10.3389/feart.2022.1080298

Seismological reference earth model in South China (SREM-SC): Upper mantle

Qingya Tang[1], Weijia Sun[1]*, Jiamin Hu[1,2] and Li-Yun Fu[3,4]

[1]Key Laboratory of Earth and Planetary Physics, Institute of Geology and Geophysics, Chinese Academy of Sciences, Beijing, China, [2]College of Earth and Planetary Sciences, University of Chinese Academy of Sciences, Beijing, China, [3]Shandong Provincial Key Laboratory of Deep Oil and Gas, China University of Petroleum (East China), Qingdao, China, [4]Laboratory for Marine Mineral Resources, Qingdao National Laboratory for Marine Science and Technology, Qingdao, China

This work is the mantle component of constructing the Seismological Reference Earth Model in South China (SREM-SC). Although there has been a wide range of research for imaging the upper mantle structures beneath South China, most of them focus on the large-scale features of the upper mantle, and the depth resolution is insufficient for existing surface wave tomography models to distinguish anomalies below 200 km. This study aims to develop a 3-D upper mantle Seismological Reference Earth Model in South China based on the prior tomography models. The shear wave velocity model comes from the analysis of several seismic surface wave tomography, supplemented by body wave tomography and the P-wave velocity model is constructed by the conversion from S-wave velocity. The radial anisotropy model is calculated from the SV-wave and SH-wave velocity. The Density model of the upper mantle is derived using the empirical relationship linking the density to the shear-wave velocity. The model is grid with 0.5° × 0.5° in latitude and longitude and 5 km interval in depth from 60 to 300 km. The mantle component of Seismological Reference Earth Model in South China is expected to provide a good representation of the upper mantle structures for further detailed studies. The mantle component of Seismological Reference Earth Model in South China provides new insights into upper mantle structures that should be meaningful to reveal the dynamic mechanism and tectonic evolution of South China.

KEYWORDS

South China block, upper mantle, surface waves, body waves, tomography

1 Introduction

The South China Block (SCB), located in the southeast of China, is composed of the Yangtze Craton in the northwest and the Cathaysia Block in the southeast, as illustrated in Figure 1. In the north, the SCB is bounded by the Qinling-Dabie orogenic belt and collided with the North China Craton in the Triassic (Enkin et al., 1992; Cao et al., 2018). In the west, the SCB is eastward compressed by the Tibetan Plateau and separated from the Songpan-Gantze Block by the Longmenshan fault in the northwest. In the southwest, the SCB is surrounded by the Indochina Block through the Ailaoshan-Songma suture zone. In the Southeast, the SCB was subducted by the Pacific plate and the Philippine Sea Plate, resulting in the formation of a trench arc back arc system. The Yangtze Craton and Cathaysia Block collided and amalgamated in the Neoproterozoic (1.1–1.0 Ga) along the Jiangnan orogen (Zhang et al., 2013; Mao et al., 2014; Faure et al., 2017). The current geomorphic characteristics of SCB were finally created under the multi-stage compound structural action of multiple tectonic systems. In Phanerozoic, the SCB experienced long-term plate tectonics and multi-stage superimposition (Zhang et al., 2013). During the Paleozoic, the north, west and south sides of SCB were affected by the closure of the ancient Tethys Ocean; In Late Paleozoic, it collided with the Indochina Block and the North China Block on the north and south, respectively. Since the Mesozoic, large-scale heterogeneous regional metamorphism and diffuse planar magmatic activity were formed (Zhang et al., 2013) under the impact of the collision between SCB and the Indochina Block; And a 1,300 km intracontinental orogenic belt and intensely distributed granite magma were formed (Li and Li, 2007), which were affected by the westward subduction of the Pacific plate. The convergence, compression and relative plate motions of the major tectonic domains (the westward subduction of the Pacific plate, the formation of the Tibet Plateau and northward differential movement of the India Australia plate) in the Mesozoic and Cenozoic led to a complex tectonic environment of the SCB, thus it's necessary to establish a reliable and robust velocity model in order to learn more about the tectonic evolution of SCB.

The evolution process and mechanism of the SCB have been the focus of geoscience research. Several geophysical studies have been conducted to explore the velocity structure, the interface and deformation features of South China in the past decades through the exploitation of dense portable and permanent stations. Many crust and mantle models have been proposed using different data sets and methods, including surface wave tomography (e.g., Li et al., 2013; Bao et al., 2015), body wave tomography (e.g., Zhao et al., 2012; Huang et al., 2015; Sun and Kennett, 2016a, b; Sun and Toksöz, 2006), analysis of receiver function (e.g., He et al., 2014; Guo et al., 2018) and shear wave splitting (e.g., Huang et al., 2011). The large-scale features of the upper mantle of these models are consistent and well delineated, showing a cold lithosphere with fast wave velocity and low Vp/Vs ratio in the Yangtze Craton (e.g., Lebedev and Nolet, 2003; Huang and Zhao, 2006), while the Cathaysia Block shows a low-velocity anomaly and high Vp/Vs ratio. However, these models also show the inconsistency of small-scale structures and the limitation in resolution, which might be attributed to the difference of the data and methods applied in these studies. The receiver function studies concur that the crust and lithosphere are gradually reduction from west to east. The Yangtze Craton is underlain by a thick crust, about 38–46 km (Deng et al., 2014), and a thick mantle lithosphere (extending to over 180 km depth). In the Cathaysia Block, the crustal thickness (Guo et al., 2019) and lithosphere is generally thinner. These regions are part of the circum Pacific tectonic domain and are primarily impacted by the Pacific plate's subduction zone (An et al., 2006). As for the internal deformation of the SCB, it is believed that the anisotropy in eastern China mainly comes from the upper mantle, and the crust and sedimentary layers have little influence on it. The anisotropy of the upper mantle may be related to the collision of the Indian plate with the Eurasian plate and the subduction of the Pacific plate and the Philippine Sea

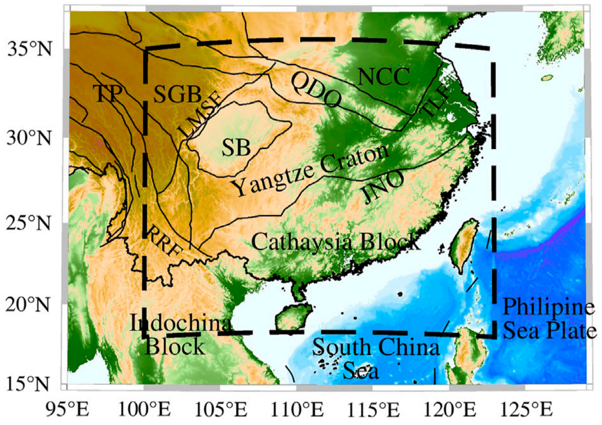

FIGURE 1
Tectonic background of South China Block. TLF, Tanlu fault; RRF, Red River fault; LMSF, Longmenshan fault; NCC, North China Craton; QDO, Qinling-Dabie Orogen; JNO, Jiangnan Orogen; SB, Sichuan Basin; JB, Jiangnan Basin; SGB, Songpan-Gantze Block; TP: Tibetan Plateau.

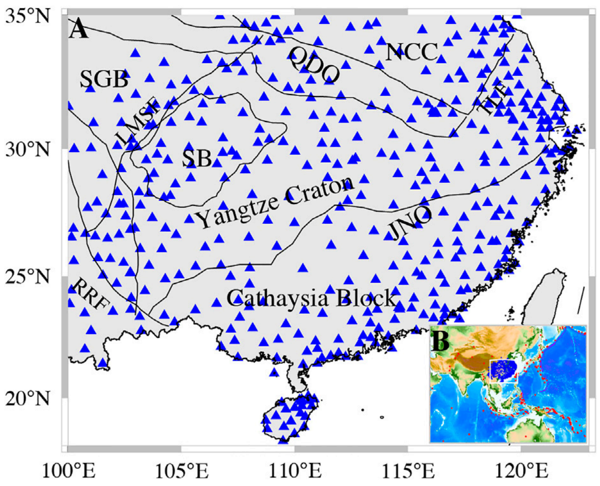

FIGURE 2
(A) Distribution of permanent and portable seismic stations (blue triangles) in the South China Block (B) Insert map: Configuration of seismic stations and seismic events with Ms > 5.5 for the year 2016, to illustrate the potential ray path coverage.

TABLE 1 Previous tomographic models used in this study.

Author	Model	Depth	Depth Interval	Method
Zhou et al. (2012)	V_{sv}	0–199.8 km	0.2 km	Ambient noise and earthquake surface wave tomtigraphy
Bao et a1. (2015)	V_{sv}	1–155 km	2, 5, 10 km	Ambient noise and earthquake surface wave tomtigraphy
Shen et a1. (2016)	V_{sv}	0–199 km	0.5 km	Ambient noise and earthquake surface wave tomography
Tang et al. (2022)	V_{sv}, V_{SH}	50–300 km	5 km	Multimode earthquake surface wave tomography
Han et a1. (2021)	V_{sv}, V_p	0–150 km	5, 10, 20, 30 km	Joint inversion of body wave and surface wave tomography
Gao et al. (2022)	v_{sv}	0–120 km	2, 5 km	Joint inversion of body wave and surface wave tomography

plate under the Eurasian plate (e.g., Wang et al., 2014). To better study the lithospheric structure, we conduct a joint inversion of body- and surface-wave data to determine a high-resolution Vs model of South China.

This study aims to build a reliable 3-D mantle component of Seismological Reference Earth Model in South China (SREM-SC) down to a depth of 300 km based on these different styles of prior tomographic models, which will capture the major features of the upper mantle in South China and serve as an initial model for further study of more detailed velocity structures or prediction of seismic wave fields, and provides new insights into the dynamic process of the lithospheric evolution of the South China.

2 Data resources

The China National Seismic Network Center and domestic research teams (e.g., Zheng et al., 2010) have set up a large number of broadband permanent and portable stations in South China and its surroundings (Figure 2A), providing excellent data resources as the foundation for studying the lithospheric structure. With the numerous earthquakes that occur along the circum-Pacific belt and on the Tibetan Plateau (Figure 2B), these rather dense stations in South China offer a good ray coverage, allowing for the achievement of a decent resolution.

A wide range of techniques have been used to build the 3-D models of the crust and upper mantle utilizing different aspects of seismic records. We accumulated the earth models in the upper mantle of SCB, obtained by the analysis of surface wave dispersion data as well as body waves arrival times (Table 1). We concentrate on the collection of models related to surface waves that combing the ambient noise data and earthquake data. Since the ambient noise correlation offers new data coverage (Shapiro et al., 2005) and shorter period dispersion, this enhances the constraint on the shallow crust. The upper mantle structures from surface waves can be affected by the crustal structure since it has a substantial impact on the propagation of surface waves (Bozdağ and Trampert, 2008; Panning et al., 2010). Therefore, the joint inversion of ambient noise and earthquake surface wave tomography can be helpful to improve the structures in the upper mantle.

The common approach of surface wave tomography is to extract the dispersion information directly from the observed seismogram or secondary observables based on cross correlograms (Cara and Lévêque, 1987). The 3-D shear wave velocities are then obtained by combing and inverting the path-specific dispersion curves either directly without any intermediate steps (Fang et al., 2015) or indirectly through the 2-D phase or group velocity maps. Due to the overlap and coupling of several higher-mode surface waves (Matsuzawa and Yoshizawa, 2019; Pan et al., 2019), the fundamental mode dispersion is typically measured using this approach, and the period range of the dispersion is in the middle to short period. Another approach proposed by Yoshizawa and Kennett (2002) can measure the multimode dispersion from one-single seismogram, including the intermediate step of creating phase velocity maps for multiple modes and frequencies, allowing the incorporation of finite-frequency effects and ray-tracing (Yoshizawa and Kennett 2004; Yoshizawa and Ekström, 2010).

Here, we provide a brief summary of the chosen upper mantle models in SCB. The main contribution to the mantle component of SREM-SC comes from the SV-wave velocity models obtained by surface wave tomography. Zhou et al., (2012) merged the Rayleigh wave group and phase velocity maps at 6–40 s period from ambient seismic noise data with phase velocity maps at 25–70 s derived from earthquakes in the same time frame to construct a 3-D Vsv model of the crust and upper mantle down to a depth of 150 km across SCB. Bao et al. (2015) presented a high-resolution shear-velocity model of the lithosphere (down to about 160 km) beneath China using Rayleigh wave group and phase velocity maps at periods of 10–140 s through the combination of ambient noise and earthquake data. Shen et al. (2016) produced isotropic Rayleigh wave group and phase velocity maps with uncertainty estimates from 8 to 50 s period across the China from ambient noise tomography, and extend them to 70 s period across parts of South China from earthquake tomography. Then, a Bayesian Monte Carlo methodology is used to build a shear-

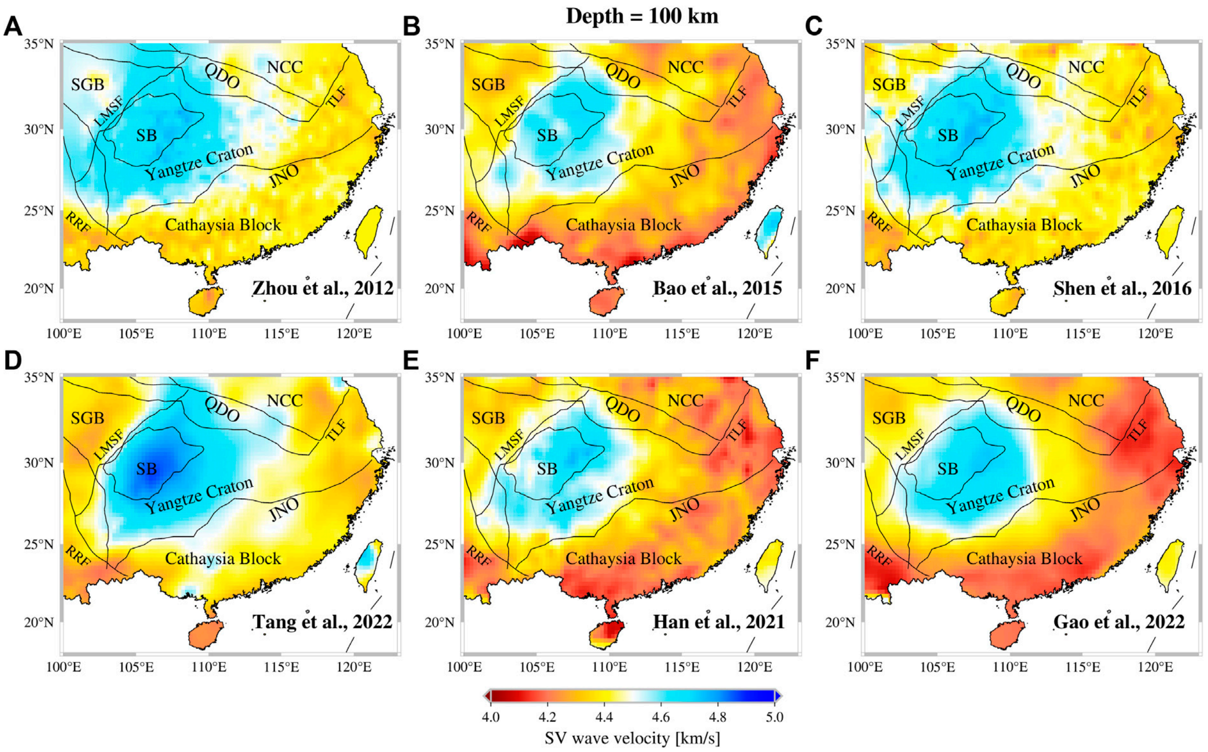

FIGURE 3
Shear wave velocity for the six SV wave models at 100 km depth from **(A)** Zhou et al. (2012) **(B)** Bao et al. (2015) **(C)** Shen et al. (2016) **(D)** Tang et al. (2022) **(E)** Han et al. (2021) **(F)** Gao et al. (2022).

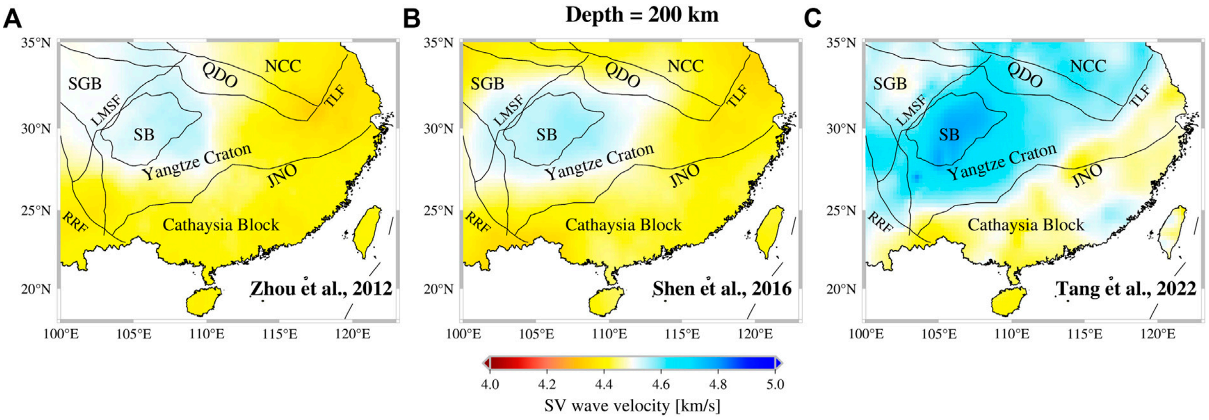

FIGURE 4
Shear wave velocity for the three SV wave models at 200 km depth from **(A)** Zhou et al. (2012) **(B)** Shen et al. (2016), and **(C)** Tang et al. (2022).

wave velocity model that covers the mainland China down to a depth of 150 km. Tang et al. (2022) refilled the inversion depth of the radially anisotropic 3-D shear-wave model of the whole South China Block down to a depth of at least 300 km using the multimode surface wave tomography (Yoshizawa and Ekström, 2010).

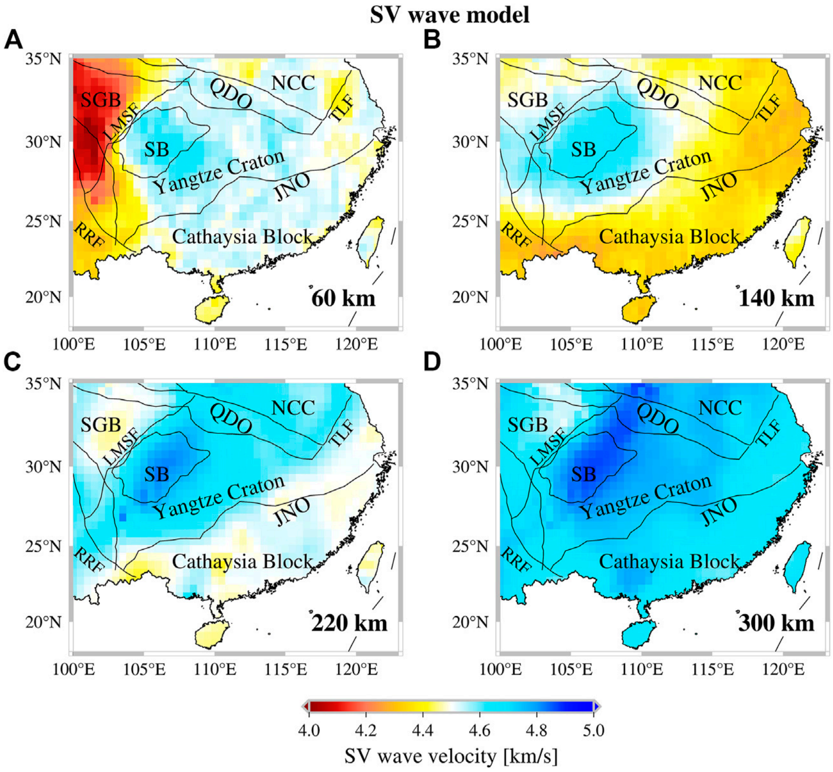

FIGURE 5
SV wave velocity of the mantle component of SREM-SC at depths of **(A)** 60 km **(B)** 140 km **(C)** 220 km, and **(D)** 300 km.

Apart from the surface wave data, we can make use of tomographic studies carried out using body wave arrivals for both P and S waves. Han et al. (2021) presented an updated high-resolution Vs and Vp models of the crust and uppermost mantle of continental China (USTClitho2.0) down to 150 km depth by joint inversion of numerous high-quality arrivals from 11,953 earthquakes and surface wave dispersion data based on the work of Xin et al. (2019) (USTClitho1.0). Gao et al. (2022) conducted research on the joint inversion of earthquake body wave and surface wave data from both earthquake and ambient noise to produce a high-resolution 3D Vs model of the lithosphere in South China. The jointly inverted models are further improved as a result of the complementary strengths of the two data kinds (Gao et al., 2022).

Figure 3 and Figure 4 illustrate the selected models with absolute velocities at depths of 70 km and 140 km. Only one-half of the models show a velocity structure below 150 km. The velocity anomalies of these models in the Yangtze Craton and Cathaysia Block are basically consistent. At 100 km, the western Yangtze Craton shows fast velocity while the Cathaysia Block, eastern Yangtze Craton, and North China Craton exhibit slow velocity. At 200 km, the western Yangtze Craton exhibits high-velocity anomaly and the Cathaysia Block primarily shows low-velocity anomaly despite the diversity of anomalous characteristic. The general consistency between the various models from surface waves and body waves means that the key features of the structure are comparable and well defined, which provides a basis for constructing the mantle component of SREM-SC. Nevertheless, we have to recognize that there are some discrepancies between the basic models due to the different techniques and data sets.

3 Upper mantle models

We establish the representative mantle component of Seismological Reference Earth Model in South China (SREM-SC) on the basis of information available in the earlier studies, by imitating the construction process of the Australian Seismological Reference Model (AuSREM, Salmon et al., 2013; Kennett et al., 2013), rather than conduct a new inversion.

The major control on the mantle component of SREM-SC comes from the shear wave velocity distribution derived from tomographic results. The radial anisotropy, P-wave velocity and density are then conducted from shear wave velocity. The mantle component of SREM-SC is specified in terms of absolute velocities and the primary model nodes are spaced at 0.5° apart in latitude and longitude and 5 km apart in depth from 60 km to 300 km.

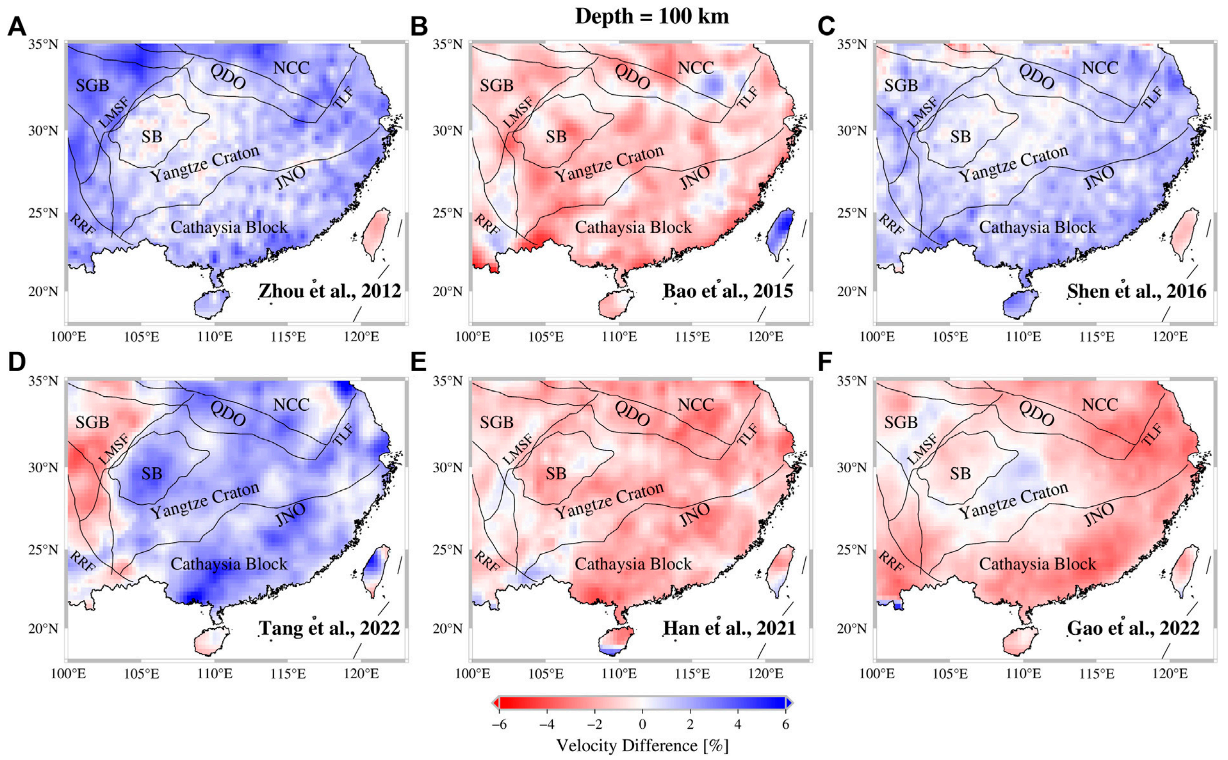

FIGURE 6
Horizontal slices at 100 km depth through SV wave velocity showing the relative velocity difference between regional models of **(A)** Zhou et al. (2012) **(B)** Bao et al. (2015) **(C)** Shen et al. (2016) **(D)** Tang et al. (2022) **(E)** Han et al. (2021) **(F)** Gao et al. (2022) and the mantle component of SREM-SC, respectively.

3.1 Shear wave model

The main contribution to the SV distribution is constructed from the available tomography models mentioned in the last section. Considering the vary grid sizes and depth intervals of these chosen models, we re-interpolate these models to ensure that they share the same range and interval of longitude, latitude and Depths.

In constructing the mantle component of SREM-SC, we seek to provide a representation where the major features are robust and reliable. Therefore, we adopt the linear combinations of these shear-wave velocity models with equal weight to emphasize such features, that is, average these models to obtain the final averaged SV wave model. The tendency is for smaller scale features to be obscured. We give the model same weight because the used seismic stations were similar, which also means that the ray path coverage was comparable.

The horizontal slices of SV wave velocity of the mantle component of SREM-SC are shown in Figure 5. At the uppermost mantle, about 60 km depth (Figure 5A), high-velocity features are observed beneath the Yangtze Craton and Cathaysia Block. While the eastern Tibetan Plateau displays a low-velocity anomaly, which indicates that the uppermost mantle of Tibetan Plateau has undergone significant deformation and high temperature (Bao et al., 2015). The cratonic root beneath Sichuan basin shows fast velocity, extending downward to 300 km, which is consistent with the results of previous studies. For instance, Shan et al. (2016) suggest that the high-velocity root reaches down to at least 250 km beneath the Sichuan Basin. The Cathaysia Block is dominated by a low velocity in the upper mantle as the depth descends (Figures 5B–D), which may reflect the strong mantle upwelling occurred in the late Mesozoic and Cenozoic. As we use absolute velocity, so the wave velocity has a natural tendency to increase with depth (Kennett et al., 2013).

In addition, we discuss the similarities and differences between our average SV wave model and previous regional models. Since the average SV wave model are originated from these regional models, therefore the major features of all these models are concordant through comparison of multiple depths (take Figures 3–5 as examples), and which provides support for the stability of this representative model. As for the differences, it is mainly evaluated through quantitative calculation of relative velocity difference. The model differences at 100 km are displayed in Figure 6 as a percentage relative to the average model. Results show that the velocity difference in most areas was

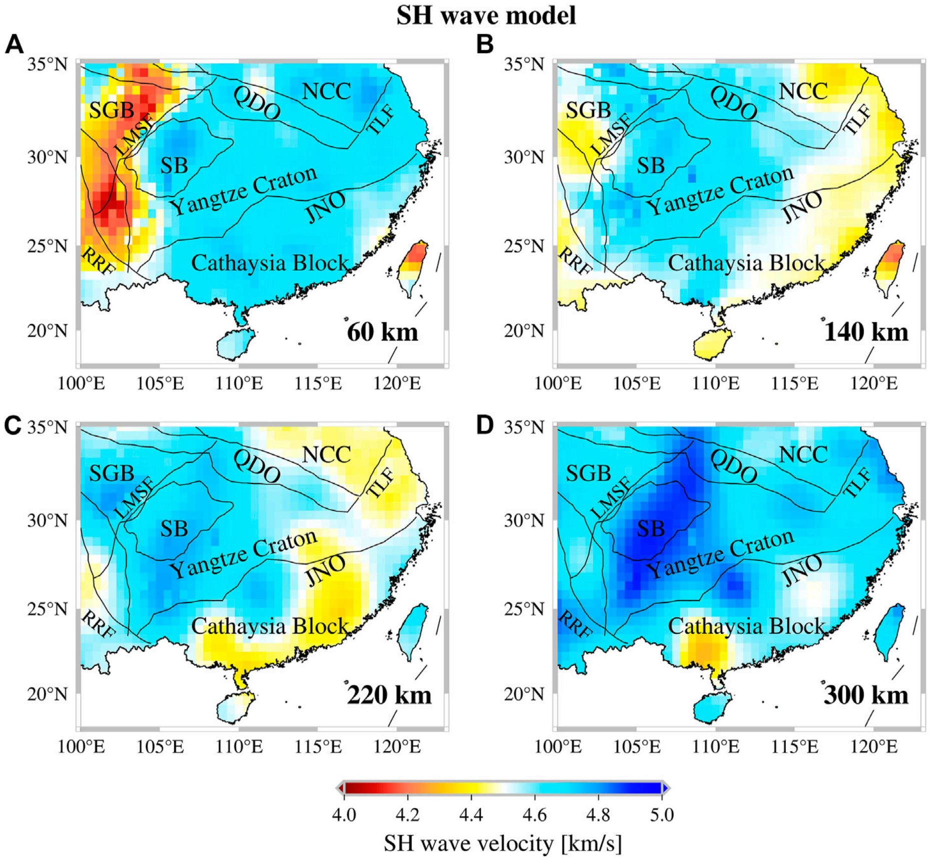

FIGURE 7
SH wave velocity of the mantle component of SREM-SC at **(A)** 60 km **(B)** 140 km **(C)** 220 km, and **(D)** 300 km depths using the result of Tang et al. (2022).

less than 6%. The velocities of our average SV wave model are smaller than the S-wave velocity results obtained by surface wave tomography (Figures 6A,C,D) in the Yangtze Craton and Cathaysia Block, except for the results of Bao et al. (2015). Beneath Sichuan Basin, the average model is closer to the S-wave results obtained by Zhou et al. (2012) and Shen et al. (2016). The results obtained from the joint inversion of body wave and surface wave (Figures 6E,F) are lower than the average model. In the vicinity of the eastern Tibetan Plateau, except for Zhou et al. (2012) and Shen et al. (2016) (Figures 6A,C), other models show slow velocity than the average model.

To date, previous surface wave studies have primarily employed Rayleigh wave phase or group dispersions to obtain the SV-wave structures, thus we have less information about the SH wave distribution. In this case, we tend to use the SH wave model proposed by Tang et al. (2022) as the SH wave representation of the mantle component of SREM-SC. Tang et al. (2022) extracted the fundamental mode to fourth higher-mode Love wave dispersion to construct a 3-D SH-wave velocity model in the entire South China Block using the multimode surface wave tomography.

The SH wave velocity of the mantle component of SREM-SC is displayed in Figure 7. The anomalous features of SH-wave velocity model are consistent with the SV-wave velocity distribution on a large scale, which is characterized by a fast velocity in the western Yangtze craton and a low velocity in the eastern Yangtze craton, the Tibetan Plateau, and the Cathaysia Block. Locally, there are obvious distinctions between SV wave and SH wave velocity anomalies, as shown, the velocity anomaly in the Leizhou Peninsula and southeastern coastal area of Cathaysia Block. Similar low-velocity anomaly has been reported by regional and global tomographic researches, from the surface extends to upper mantle, mantle transition zone, even down to lower mantle. The lowest SH-wave velocity is located beneath southernmost South China at approximately 108°E and 23°N (Figures 7C,D), which is in good agreement with the location of strongest attenuation revealed by teleseismic body wave attenuation tomography (Deng et al., 2021), might be attributed to the deep source mantle plume in this area.

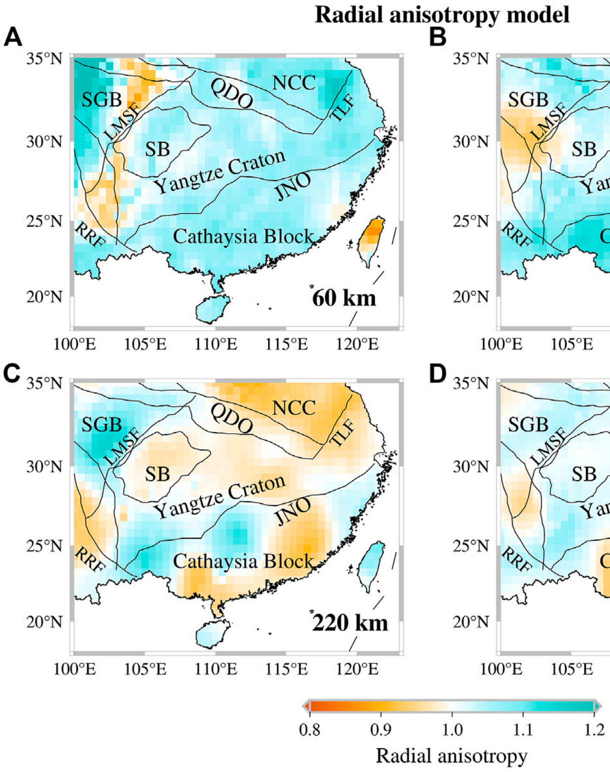

FIGURE 8
Radial anisotropy distribution of the mantle component of SREM-SC at **(A)** 60 km **(B)** 140 km **(C)** 220 km, and **(D)** 300 km depths, determined from the SV wave velocity of SREM-SC and SH wave velocity of Tang et al. (2022).

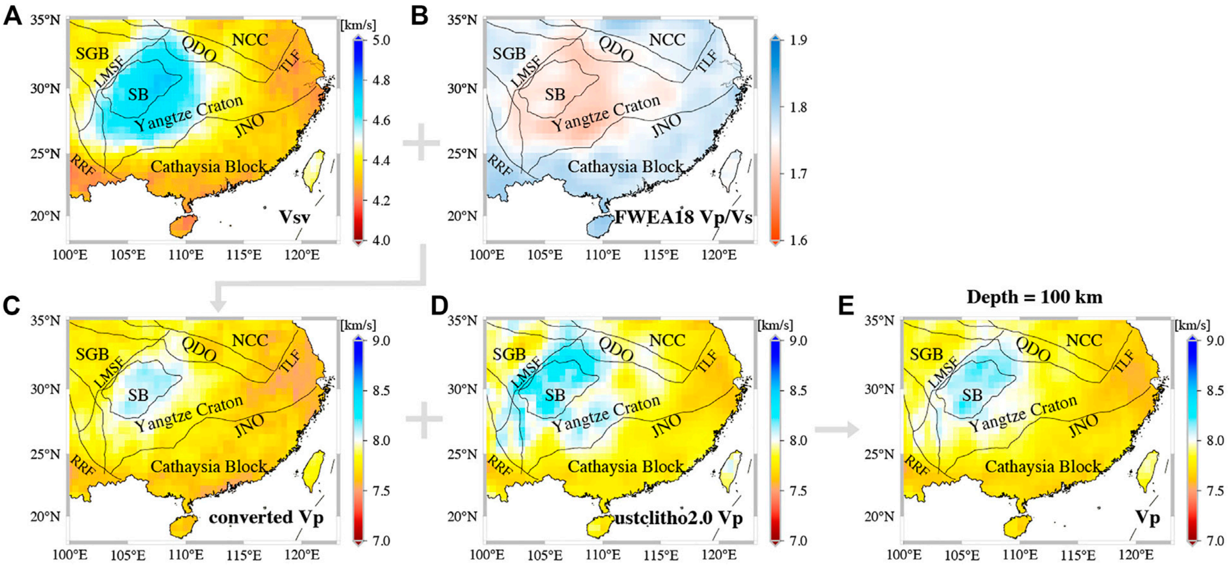

FIGURE 9
The construction process of P wave velocity of the mantle component of SREM-SC keyed at a map view of 100 km depth **(C)** The converted P wave model is obtained by combing **(A)** the averaged SV wave model with **(B)** the Vp/Vs ratio from the FWEA18 model (Tao et al., 2018), and then averaged with **(D)** the P wave velocity from USTClitho2.0 model (Han et al., 2021) to build **(E)** the final P wave velocity of the mantle component of SREM-SC.

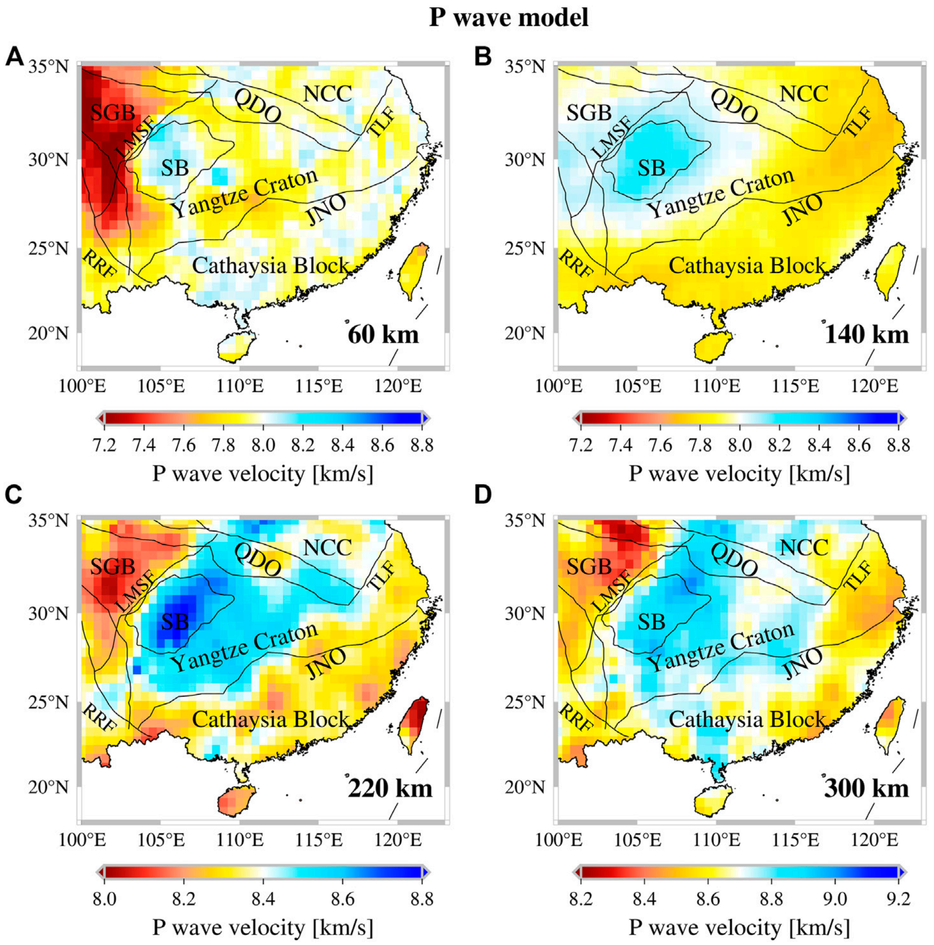

FIGURE 10
P wave velocity of the mantle component of SREM-SC at depths of **(A)** 60 km **(B)** 140 km **(C)** 220 km, and **(D)** 300 km.

3.2 Radial anisotropy

Seismic anisotropy is a crucial tool for identifying crust-mantle material flow and deep material deformation. The intensity and spatial distribution of anisotropy reflect the deformation properties of the earth's interior components; thus, the analysis of radial anisotropy can provide constraints on the formation and evolution of crust-mantle structures (Savage, 1999; Mainprice, 2007). The deformation of the SCB has been explored in earlier researches through a variety of methods (e.g., Yao et al., 2010; Huang et al., 2011; Xie et al., 2013; Liu et al., 2019), however the majority of them focus on the shallow crust and lack depth constraints on the upper mantle.

In this study, we construct a representative radial anisotropy model in the upper mantle of SCB by combining the previously stated SV wave and SH wave models. The definition of radial anisotropy is $\xi = V_{SH}^2/V_{SV}^2$. In general, positive radial anisotropy with $\xi > 1.0$ ($V_{SH} > V_{SV}$) indicates the effects of horizontal shear flow or a horizontally layered structure, whereas negative radial anisotropy with $\xi < 1.0$ ($V_{SH} < V_{SV}$) is interpreted as the influence of vertically oriented structures or mineral alignment.

The radial anisotropy distribution of the mantle component of SREM-SC is illustrated in Figure 8, which is compatible with the work of Tang et al. (2022), who had discussed the similarities and differences between the upper mantle of South China and previous regional and global radial anisotropy models (e.g., Tao et al., 2018; Witek et al., 2021). The study region largely displays positive radial anisotropy at a shallower depth of 60 km (Figure 8A). The Sichuan Basin and its western parts exhibit negative radial anisotropy at 140 km depth (Figure 8B), whereas the Cathaysia Block and Yangtze Craton are dominated by positive radial anisotropy. The Cathaysia Block, Yangtze Craton, NCC, and the eastern Tibetan Plateau gradually exhibit negative radial anisotropy

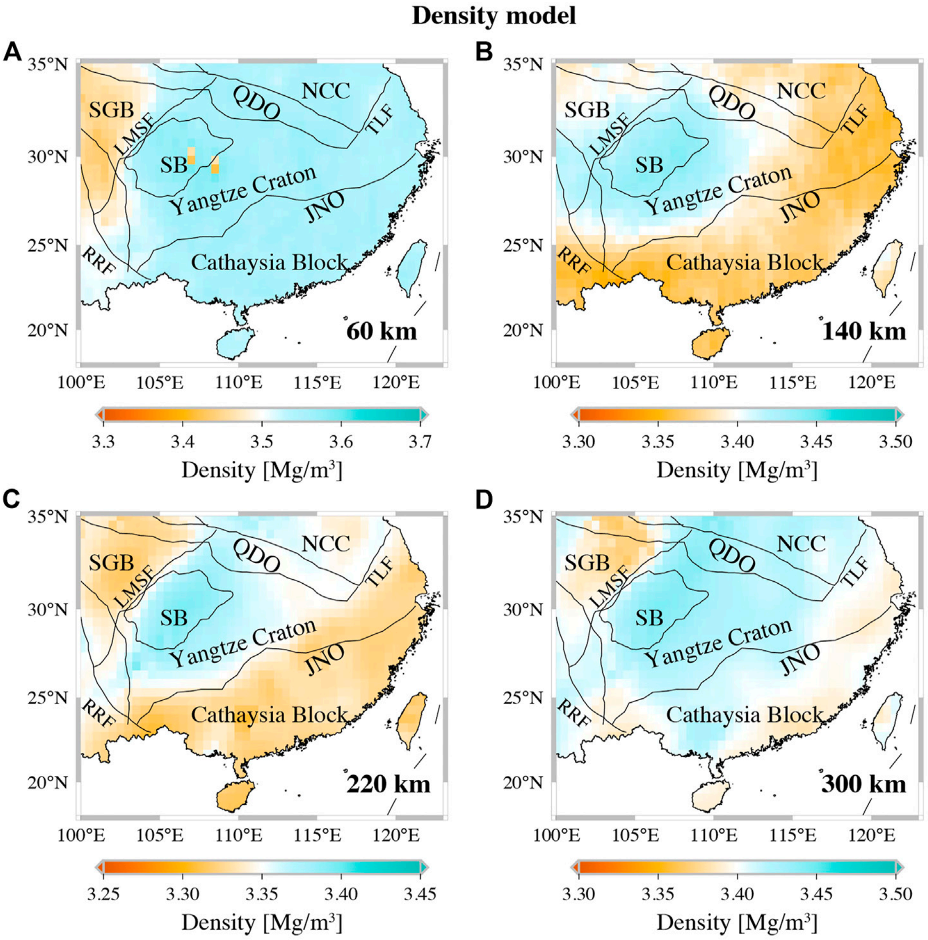

FIGURE 11
The density distribution of the mantle component of SREM-SC at depths of **(A)** 60 km **(B)** 140 km **(C)** 220 km, and **(D)** 300 km, calculated from the empirical relationship proposed by Kennett et al. (2013) between the density and shear wave velocity. The solid black lines in **(A)** denote the location of cross-sections in Figure 12, Figure 13.

with increasing depth; these features are visible on the map at 220 and 300 km depths (Figures 8C,D). At a depth of 300 km, the anisotropy in the Sichuan Basin decreases while the negative anisotropy of the Cathaysia Block increases, especially beneath the Leizhou Peninsula and its environs and the southeastern coastal region. The negative radial anisotropy beneath the Sichuan Basin and its western portion may reflect the influence of the compression of the Tibetan Plateau and the thermal erosion of mantle flow (Tang et al., 2022). The obvious negative radial anisotropy in the asthenosphere of the coastal region of Cathaysia Block reveals that the vertical movement of mantle material is dominant, which may be related to the small-scale mantle convection above the back arc subduction plate due to the subduction of the Philippine Sea plate (Peng et al., 2007). We attribute the signal of negative radial anisotropy and low-velocity anomaly in Leizhou Peninsula and surroundings to the vertical movement of upper mantle, possibly related to the Cenozoic Hainan mantle plume. This point was supported by the direct seismic observations of receiver function analysis. The results of Wei and Shen (2016) beneath the Lei-Qing region reveal that the crustal thickness has been thickened and the mantle transition zone (MTZ) has been thinning, which suggests the upwelling of mantle materials penetrating the MTZ to thicken the local crust.

3.3 P wave model

There are few publicly available data on the P-wave velocity of the upper mantle in the SCB, and the majority of P-wave model come from body wave tomography from wider regions (e.g., Zhao et al., 2012). The vertical resolution of body wave

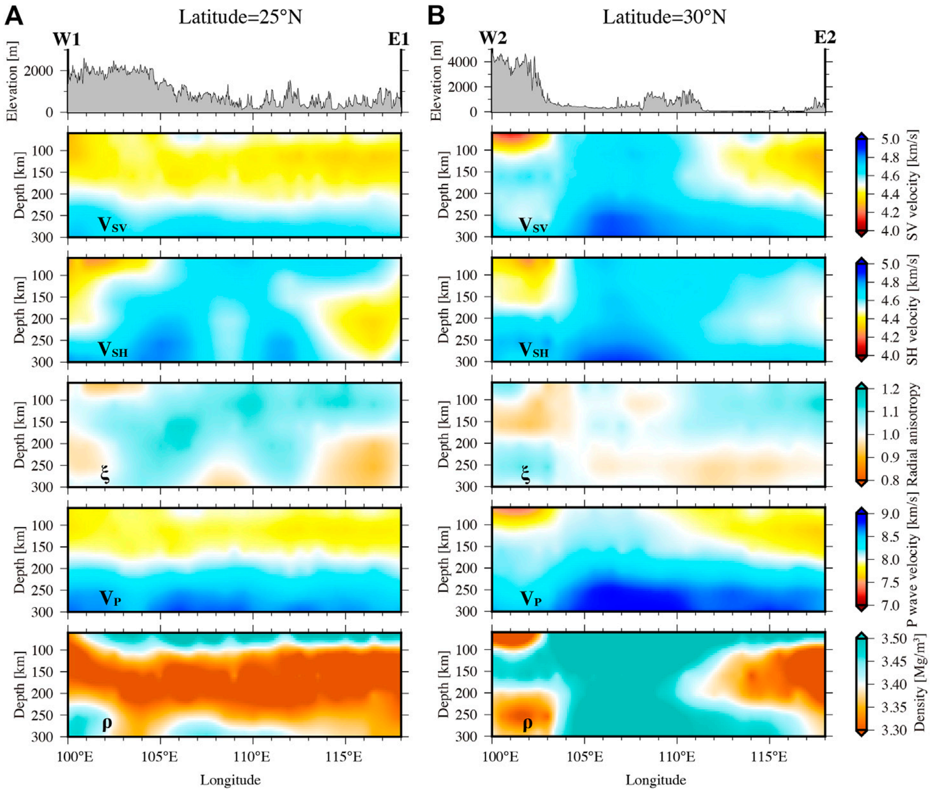

FIGURE 12
Vertical Cross-sections of the mantle component of SREM-SC along profiles **(A)** W1-E1 at 25°N and **(B)** W2-E2 at 30°N indicated in Figure 11A. Topography is plotted above each cross-section, and the red lines are the approximate border of the main tectonic units. YC, Yangtze Craton; CB, Cathaysia Block; TP, Tibetan Plateau; NCC, North China Craton; QDO, Qinling-Dabie Orogen.

tomography is poor compared to the study of surface wave tomography because of steep ray paths. The main information we gather on the P-wave velocity distribution of SCB comes from the full waveform seismic tomography on the upper mantle beneath eastern Asia (Tao et al., 2018) and the joint inversion of body-wave and surface wave tomography down to a depth of 150 km (Han et al., 2021).

The construction process of P wave velocity of the mantle component of SREM-SC is shown in Figure 9. In this study, we first use the Vp/Vs ratio derived from FWEA18 model (Tao et al., 2018) and the SV wave velocity of the mantle component of SREM-SC to obtain a converted P wave velocity, instead of using the empirical relationship between P wave velocity and shear wave velocity (named Brocher's regression fit), which is invalid for shear-wave velocities larger than 4.5 km/s (Brocher, 2005). With equal weights, the converted P wave velocity and the P wave velocity of USTClitho2.0 model (Han et al., 2021) are used to create the averaged P wave model.

The resulting distribution of P wave velocity is shown in Figure 10. We utilize variable color bar to better visualize the results, since the absolute velocity of P wave increases greatly with depth. The anomalous features of P wave model are generally similar with those of the shear wave model except for the 60 km. At a depth of 60 km (Figure 10A), the P wave velocities of SCB clearly demonstrate lateral heterogeneity which is primarily caused by the heterogeneous distribution of P wave velocity in the USTClitho2.0 model (Han et al., 2021). The eastern Tibetan Plateau is characterized by a slow velocity. At depths of 140 km and 220 km, the western Yangtze Carton shows a fast velocity while the Cathaysia Block and eastern Yangtze Craton display a slow velocity. At 300 km, the Cathaysia Block exhibits a low-velocity anomaly compared to the high-velocity anomaly in the Sichuan Basin. Zhao et al. (2012) interpreted the low-velocity anomalies of P and S waves in the upper mantle of the Cathaysia block as a result of the upwelling of hot materials, caused by the dehydration of the Paleo Pacific subduction plate detained in the mantle transition zone in the Mesozoic. The high P wave velocity beneath Yangtze Craton is usually associated with low Vp/Vs ratio, thick lithospheric root and lower temperature.

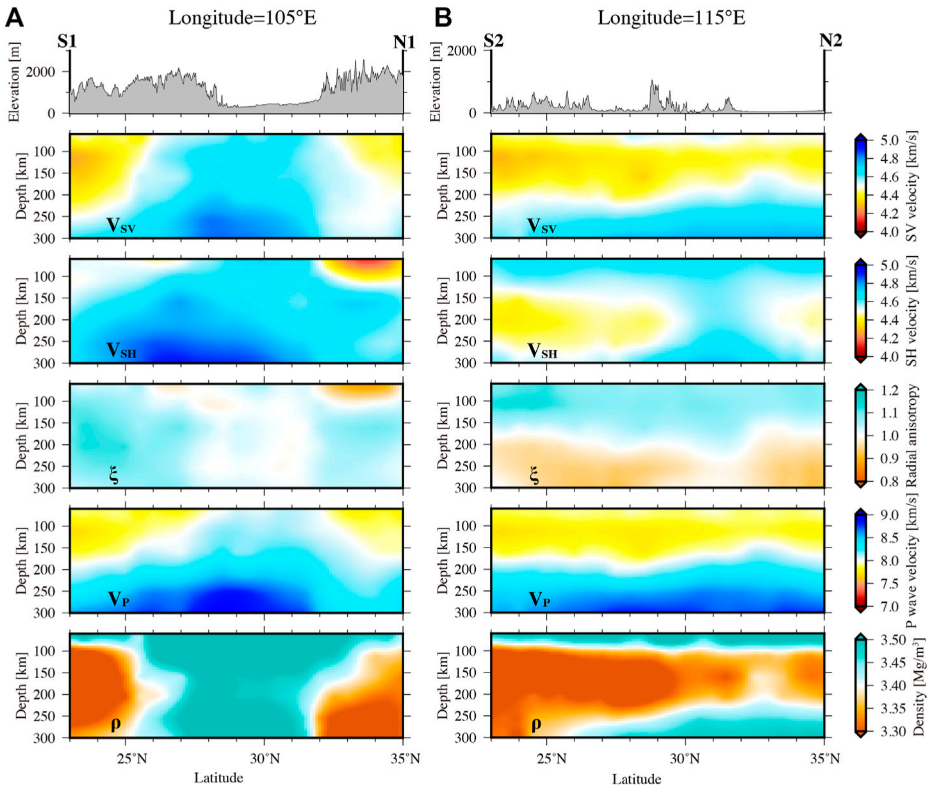

FIGURE 13
Same as Figure 12, but along profiles **(A)** S1-N1 at 105°E and **(B)** S2-N2 at 115°E, indicated in Figure 11A.

3.4 Density model

The density attribute is related to its material composition and temperature structure, as an important basic for understanding the plate tectonic evolution and dynamic processes (Ji et al., 2019). The study on the density of SCB mainly focuses on the crust and uppermost mantle, such as Deng et al. (2014) investigated the 3-D density structure of SCB down to 70 km based on P-wave velocities determined from seismic profiles and Bouguer gravity anomalies, but there is less direct information on the density of the upper mantle.

We have followed an empirical relationship linking the density to the shear-wave velocity proposed by Kennett et al. (2013). They set a threshold $\varepsilon = 2.0 + 0.2 \times (Z - 50)$ for the inclusion of a compositional effect at depth Z in order to compensate for the high cratonic wave velocity in the lithosphere. According to the relative deviations $\delta ln\beta = (Vs - Vref)/Vref$ in shear wave velocity from the *ak*135 model (Kennett et al., 1995) at a particular depth Z greater than or less than ε%, a density scales to a velocity perturbation or absolute velocity are given as follows:

$$\rho = \rho_0 \times (1 + 0.3 \times \delta \ln \beta);\ \ \delta \ln \beta \times 100 \leq \varepsilon\%$$

$$= (13.931 - \mathrm{Vs})/2.7724;\ \ \delta \ln \beta \times 100 \geq \varepsilon\%$$

Where ρ_0 is the reference density taken from the *ak*135 model. The distribution of density in the upper mantle are plotted in Figure 11 as a deviation from the reference density in *ak*135 model. The density distribution of the upper mantle of the SCB has obvious heterogeneity in both horizontal and vertical directions. At a shallow depth of 60 km, the Yangtze Craton and Cathaysia Block demonstrate high density, which is similar with the findings of Deng et al. (2014). The eastern Tibetan Plateau is characterized by low density. As depth increases, the density characteristics of the eastern and western SCB are obviously different, that is the Cathaysia Block shows low density while the Yangtze Craton exhibits high density. At 300 km, the density anomaly of Yangtze Craton is slightly larger than that of the Cathaysia Block. The density distribution pattern has a good correlation with the tectonic unit, the Craton correspond to high density, and the Cathaysia Block correspond to low density, which maybe related to the subduction of Pacific Plate. The density is constructed by quantitative estimation of SV wave velocity, which can be used as the initial of the joint inversion of P wave velocity and gravity in the future to concentrate the advantages of the two methods.

4 Discussion and conclusion

We propose a 3-D representative upper mantle component of Seismological Reference Earth Model in South China (SREM-SC). For the mantle component of SREM-SC, we employ the SV wave velocity as the primary control, and we derive the radial anisotropy, P wave velocity and density based on the relationship between variables with SV velocity.

The mantle component of SREM-SC is illustrated in Figure 12 and Figure 13 which show four representative cross-sections through the SV wave velocity, SH wave velocity, radial anisotropy, P wave velocity and density in both latitude and longitude. Cross-section W1-E1 and W2-E2 crosses the southeastern Tibetan Plateau (TP), Yangtze Craton (YC), and Cathaysia Block (CB). As can be seen in Figure 12A, the Cathaysia Block shows low SV-wave and P-wave velocity. The SH-wave velocity of western Cathaysia Block is higher than the eastern coastal areas. In Figure 12B, significant fast SV-wave, SH-wave and P-wave velocities and high density are shown beneath the Yangtze Craton, especially the western Yangtze Craton. The eastern Yangtze Craton exhibits slow SV-wave, slow P-wave velocity above 200 km and low density. A low-velocity zone exists beneath the Tibetan Plateau in the uppermost mantle. Cross-section N1-S1 and N2-S2 identify these conspicuous features from the longitude perspective. There is an obvious high-velocity zone and high density in the lithosphere and asthenosphere of the western Yangtze Craton, extending from 50 to 350 km (Figure 13A). The slow velocity beneath the eastern Yangtze Craton is indistinguishable from the Cathaysia Block (Figure 13B), and Huang et al. (2009) believed that the low velocity anomaly was due to the thermochemical effect of the subduction of the Sulu Ocean crust.

The SV model is well constrained and we have confidence in the major features. The most noticeable feature of shear wave model and P wave model in the upper mantle is the fast velocity in the Yangtze Craton compared to the low-velocity anomaly in the Cathaysia Block. This is a consistent feature revealed by earlier regional models, for example, the shear wave velocity models described in Section 2, as well as global models. The distribution of radial anisotropy correlates well with the results of Tang et al. (2022), since we adopt their SH wave velocity as the SH wave representation. The research on SH wave determined from Love wave in South China need to be enhanced. By applying the empirical relation constructed by Kennett et al. (2013) to compensate for the effect of high velocity, the density differences are modest and do not show much dependence on the high velocity zones. However, as the seismic S-wave result is the only factor that constrain the density structure, it is preferable to combine the gravity and seismology inversions in order to reduce the non-uniqueness of inversion and improve the horizontal and vertical resolution. At the same time, we realize that the reference model will be further improved based on new information in the future to better construct the lithosphere and asthenosphere boundaries, and attenuation, etc.

The mantle component of SREM-SC provides a good representation of 3-D structure beneath South China Block at a standard 0.5° × 0.5° grid in latitude and longitude and 5 km interval in depth that can be used for a variety of purposes. For instance, gravity modelling and investigations of dynamic topography (Kennett et al., 2013) should benefit from the SREM-SC. The mantle component of SREM-SC provides new insights into upper mantle structures, which should be meaningful to reveal the dynamic mechanism and tectonic evolution of South China. The data set of the mantle component of SREM-SC is added in the Supplementary Material.

Data availability statement

The raw data supporting the conclusion of this article will be made available by the authors, without undue reservation.

Author contributions

The specific contributions of each author can be described as follows. QT: Conceptualization, Methodology, Investigation, Data Curation, Writing-Original Draft, Visualization; WS: Conceptualization, Investigation, Resources, Supervision, Writing-Review and Editing, Funding acquisition; JH: Methodology, Data Curation, Form analysis, Validation, Writing-Review and Editing; L-YF: Resources, Writing-Review and Editing, Project administration, Funding acquisition. All authors contributed to the article and approved the submitted version.

Funding

This research was supported by National Natural Science Foundation of China (Grants No. 41720104006) and the Youth Innovation Promotion Association CAS.

Acknowledgments

We thank the shear wave velocity model beneath the mainland China provided by Xuewei Bao. We thank the excellent models provided by Lei Gao (doi.org/10.5281/zenodo.5650189) and Shoucheng Han (https://github.com/ShouchengHan/USTClitho2.0) and the earth models provided by the China regional seismological reference model achievement center (http://chinageorefmodel.org) and the IRIS DMC Data Products effort (Trabant et al., 2012). All figures were drawn using Generic Mapping Tools (Wessel and Smith, 1991).

Conflict of interest

Publisher's note

Supplementary material

The Supplementary Material for this article can be found online at: https://www.frontiersin.org/articles/10.3389/feart.2022.1080298/full#supplementary-material

References

An, M., and Shi, Y. (2006). Lithospheric thickness of the Chinese continent. *Phys. Earth Planet. Interiors* 159, 257–266. doi:10.1016/j.pepi.2006.08.002

Bao, X., Song, X., and Li, J. (2015). High-resolution lithospheric structure beneath Mainland China from ambient noise and earthquake surface-wave tomography. *Earth Planet. Sci. Lett.* 417, 132–141. doi:10.1016/j.epsl.2015.02.024

Bozdağ, E., and Trampert, J. (2008). On crustal corrections in surface wave tomography. *Geophys. J. Int.* 172 (3), 1066–1082. doi:10.1111/j.1365-246X.2007.03690.x

Brocher, T. M. (2005). Empirical relations between elastic wavespeeds and density in the Earth's crust. *Bull. Seismol. Soc. Am.* 95 (6), 2081–2092. doi:10.1785/0120050077

Cao, X., Flament, N., Müller, D., and Li, S. (2018). The dynamic topography of eastern China since the latest jurassic period. *Tectonics* 37, 1274–1291. doi:10.1029/2017tc004830

Cara, M., and Lévêque, J. J. (1987). Waveform inversion using secondary observables. *Geophys. Res. Lett.* 14, 1046–1049. doi:10.1029/gl014i010p01046

Deng, Y., Byrnes, J. S., and Bezada, M. (2021). New insights into the heterogeneity of the lithosphere-asthenosphere system beneath SouthSouth China from teleseismic body-wave attenuation. *Geophys. Res. Lett.* 48. doi:10.1029/2020gl091654

Deng, Y., Zhang, Z., Badal, J., and Fan, W. (2014). 3-D density structure under South China constrained by seismic velocity and gravity data. *Tectonophysics* 627, 159–170. doi:10.1016/j.tecto.2013.07.032

Enkin, R. J., Yang, Z., Chen, Y., and Courtillot, V. (1992). Paleomagnetic constraints on the geodynamic history of the major blocks of China from the Permian to the present. *J. Geophys. Res.* 97 (B10), 13953. doi:10.1029/92jb00648

Fang, H., Yao, H., Zhang, H., Huang, Y. C., and van der Hilst, R. D. (2015). Direct inversion of surface wave dispersion for three-dimensional shallow crustal structure based on ray tracing: Methodology and application. *Geophys. J. Int.* 201, 1251–1263. doi:10.1093/gji/ggv080

Faure, M., Chen, Y., Feng, Z., Shu, L., and Xu, Z. (2017). Tectonics and geodynamics of South China: An introductory note. *J. Asian Earth Sci.* 141, 1–6. doi:10.1016/j.jseaes.2016.11.031

Gao, L., Zhang, H., Gao, L., He, C., Xin, H., and Shen, W. (2022). High-resolution vs tomography of South China by joint inversion of body wave and surface wave data. *Tectonophysics* 824, 229228. doi:10.1016/j.tecto.2022.229228

Guo, L., Gao, R., Shi, L., Huang, Z., and Ma, Y. (2019). Crustal thickness and Poisson's ratios of South China revealed from joint inversion of receiver function and gravity data. *Earth Planet. Sci. Lett.* 510, 142–152. doi:10.1016/j.epsl.2018.12.039

Han, S., Zhang, H., Xin, H., Shen, W., and Yao, H. (2021). USTClitho2.0: Updated unified seismic tomography models for continental China lithosphere from joint inversion of body-wave arrival times and surface-wave dispersion data. *Seismol. Res. Lett.* 93 (1), 201–215. doi:10.1785/0220210122

He, R., Shang, X., Yu, C., Zhang, H., and Van der Hilst, R. D. (2014). A unified map of Moho depth and Vp/Vs ratio of continental China by receiver function analysis. *Geophys. J. Int.* 199 (3), 1910–1918. doi:10.1093/gji/ggu365

Huang, J., and Zhao, D. (2006). High-resolution mantle tomography of China and surrounding regions. *J. Geophys. Res.* 111, B09305. doi:10.1029/2005JB004066

Huang, Z., Wang, L., Zhao, D., Mi, N., and Xu, M. (2011). Seismic anisotropy and mantle dynamics beneath China. *Earth Planet. Sci. Lett.* 306, 105–117. doi:10.1016/j.epsl.2011.03.038

Huang, Z., Zhao, D., and Wang, L. (2015). P wave tomography and anisotropy beneath Southeast Asia: Insight into mantle dynamics. *J. Geophys. Res. Solid Earth* 120, 5154–5174. doi:10.1002/2015jb012098

Ji, F., Li, F., Zhang, Q., Chen, H., and Xiao, L. (2019). Crustal density structure of the Antarctic continent from constrained 3D gravity inversion. *Chin. J. Geophys. (in Chinese)* 62 (3), 849–863doi. doi:10.6038/cjg2019M0507

Kennett, B. L. N., Engdahl, E. R., and Buland, R. (1995). Constraints on seismic velocities in the Earth from traveltimes. *Geophysical Journal International* 122 (1), 108–124. doi:10.1111/j.1365-246x.1995.tb03540.x

Kennett, B. L. N., Fichtner, A., Fishwick, S., and Yoshizawa, K. (2013). Australian seismological reference model (AuSREM): Mantle component. *Geophys. J. Int.* 192 (2), 871–887. doi:10.1093/gji/ggs065

Lebedev, S., and Nolet, G. (2003). Upper mantle beneath southeast Asia fromSvelocity tomography. *J. Geophys. Res.* 108 (B1). doi:10.1029/2000jb000073

Li, Y., Wu, Q., Pan, J., Zhang, F., and Yu, D. (2013). An upper-mantle S-wave velocity model for East Asia from Rayleigh wave tomography. *Earth and Planetary Science Letters* 377-378, 367–377. doi:10.1016/j.epsl.2013.06.033

Li, Z. X., and Li, X. H. (2007). formation of the 1300-km-wide intracontinental orogen and postorogenic magmatic province in mesozoic South China: A flat-slab subduction model. *Geol.* 35, 179–182. doi:10.1130/g23193a.1

Liu, C., Yao, H., Yang, H. Y., Shen, W., Fang, H., Hu, S., et al. (2019). Direct inversion for three-dimensional shear wave speed azimuthal anisotropy based on surface wave ray tracing: Methodology and application to yunnan, southwest China. *J. Geophys. Res. Solid Earth* 124, 11394–11413. doi:10.1029/2018jb016920

Mainprice, D. (2007). Seismic anisotropy of the deep earth from a mineral and rock physics perspective. *Treatise on Geophysics* 1, 437–491. doi:10.1016/b978-044452748-6.00045-6

Mao, J., Li, Z., and Ye, H. (2014). Mesozoic tectono-magmatic activities in South China: Retrospect and prospect. *Sci. China Earth Sci.* 57 (12), 2853–2877. doi:10.1007/s11430-014-5006-1

Matsuzawa, H., and Yoshizawa, K. (2019). Array-based analysis of multimode surface waves: Application to phase speed measurements and modal waveform decomposition. *Geophys. J. Int.* 218 (1), 295–312. doi:10.1093/gji/ggz153

Pan, L., Chen, X., Wang, J., Yang, Z., and Zhang, D. (2019). Sensitivity analysis of dispersion curves of Rayleigh waves with fundamental and higher modes. *Geophys. J. Int.* 216, 1276–1303. doi:10.1093/gji/ggy479

Panning, M. P., Lekić, V., and Romanowicz, B. A. (2010). Importance of crustal corrections in the development of a new global model of radial anisotropy. *J. Geophys. Res.* 115, B12325. doi:10.1029/2010JB007520

Peng, Y.-J., Huang, Z., Su, W., and Zheng, Y. J. (2007). Anisotropy in crust and upper mantle beneath China continent and its adjacent seas. *Chinese J. Geophys.* 50 (3), 666–674. (In Chinese). doi:10.1002/cjg2.1080

Salmon, M., Kennett, B. L. N., and Saygin, E. (2013). Australian seismological reference model (AuSREM): Crustal component. *Geophys. J. Int.* 192 (1), 190–206. doi:10.1093/gji/ggs004

Savage, M. K. (1999). Seismic anisotropy and mantle deformation: What have we learned from shear wave splitting? *Rev. Geophys.* 37, 65–106. doi:10.1029/98rg02075

Shan, B., Xiong, X., Zhao, K. F., Xie, Z. J., Zheng, Y., and Zhou, L. (2016). Crustal and upper mantle structure of South China from Rayleigh wave tomography. *Geophys. J. Int.* 254, ggw477. doi:10.1093/gji/ggw477

Shapiro, N. M., Campillo, M., Stehly, L., and Ritzwoller, M. H. (2005). High-resolution surface-wave tomography from ambient seismic noise. *Science* 307, 1615–1618. doi:10.1126/science.1108339

Shen, W., Ritzwoller, M. H., Kang, D., Kim, Y., Lin, F.-C., Ning, J., et al. (2016). A seismic reference model for the crust and uppermost mantle beneath China from surface wave dispersion. *Geophys. J. Int.* 206 (2), 954–979. doi:10.1093/gji/ggw175

Sun, W., and Kennett, B. L. N. (2016a). Uppermost mantle P wavespeed structure beneath eastern China and its surroundings. *Tectonophysics* 683, 12–26. doi:10.1016/j.tecto.2016.06.011

Sun, W., and Kennett, B. L. N. (2016b). Uppermost mantle structure beneath eastern China and its surroundings from Pn and Sn tomography. *Geophys. Res. Lett.* 43 (7), 3143–3149. doi:10.1002/2016gl068618

Sun, Y., and Toksöz, M. N. (2006). Crustal structure of China and surrounding regions from P wave traveltime tomography. *J. Geophys. Res.* 111. doi:10.1029/2005jb003962

Tang, Q., Sun, W., Yoshizawa, K., and Fu, L. (2022). Anomalous radial anisotropy and its implications for upper mantle dynamics beneath South China from multimode surface wave tomography. *JGR. Solid Earth* 127–e2021JB023485. doi:10.1029/2021JB023485

Tao, K., Grand, S. P., and Niu, F. N. (2018). Seismic structure of the upper mantle beneath Eastern Asia from full waveform seismic tomography. *Geochem. Geophys. Geosyst.* 19, 2732–2763. doi:10.1029/2018GC007460

Trabant, C., Hutko, A. R., Bahavar, M., Karstens, R., Ahern, T., and Aster, R. (2012). Data products at the IRIS DMC: Stepping stones for research and other applications. *Seismological Research Letters* 83 (5), 846–854. doi:10.1785/0220120032

Wang, C., Chang, L., Ding, Z., Liu, Q., Liao, W., and Flesch, L. M. (2014). Upper mantle anisotropy and crust-mantle deformation pattern beneath the Chinese mainland. *Sci. China Earth Sci.* 57, 132–143. doi:10.1007/s11430-013-4675-5

Wei, S. S., and Chen, Y. J. (2016). Seismic evidence of the Hainan mantle plume by receiver function analysis in southern China. *Geophys. Res. Lett.* 43, 8978–8985. doi:10.1002/2016GL069513

Wessel, P., and Smith, W. H. F. (1991). Free software helps map and display data. *Eos Trans. AGU.* 72 (41), 441. doi:10.1029/90eo00319

Witek, M., Chang, S.-J., Lim, D. Y., Ning, S., and Ning, J. (2021). Radial anisotropy in East Asia from multimode surface wave tomography. *JGR. Solid Earth* 126–e2020JB021201. doi:10.1029/2020JB021201

Xie, J., Ritzwoller, M. H., Shen, W., Yang, Y., Zheng, Y., and Zhou, L. (2013). Crustal radial anisotropy across eastern Tibet and the western Yangtze craton. *J. Geophys. Res. Solid Earth* 118 (8), 4226–4252. doi:10.1002/jgrb.50296

Xin, H., Zhang, H., Kang, M., He, R., Gao, L., and Gao, J. (2019). High-resolution lithospheric velocity structure of continental China by double difference seismic traveltime tomography. *Seismological Research Letters* 90 (1), 229–241. doi:10.1785/0220180209

Yao, H., van der Hilst, R. D., and Montagner, J.-P. (2010). Heterogeneity and anisotropy of the lithosphere of SE Tibet from surface wave array tomography. *J. Geophys. Res.* 115 (B12), B12307. doi:10.1029/2009jb007142

Yoshizawa, K., and Ekström, G. (2010). Automated multimode phase speed measurements for high-resolution regional-scale tomography: Application to north America. *Geophys. J. Int.* 183, 1538–1558. doi:10.1111/j.1365-246X.2010.04814.x

Yoshizawa, K., and Kennett, B. L. N. (2004). Multimode surface wave tomography for the Australian region using a three-stage approach incorporating finite frequency effects. *J. Geophys. Res.* 109. doi:10.1029/2002jb002254

Yoshizawa, K., and Kennett, B. L. N. (2002). Non-linear waveform inversion for surface waves with a neighbourhood algorithm—Application to multimode dispersion measurements. *Geophys. J. Int.* 149, 118–133. doi:10.1046/j.1365-246X.2002.01634.x

Zhang, G., Guo, A., Wang, Y., Li, S., Dong, Y., Liu, S., et al. (2013). Tectonics of South China continent and its implications. *Sci. China Earth Sci.* 56 (11), 1804–1828. doi:10.1007/s11430-013-4679-1

Zhao, L., Allen, R. M., Zheng, T., and Zhu, R. (2012). High-resolution body wave tomography models of the upper mantle beneath eastern China and the adjacent areas. *Geochem. Geophys. Geosyst.* 13 (6). doi:10.1029/2012gc004119

Zheng, X., Jiao, W., Zhang, C., and Wang, L. (2010). Short-Period Rayleigh-wave group velocity tomography through ambient noise cross-correlation in xinjiang, northwest China. *Bulletin of the Seismological Society of America* 100 (3), 1350–1355. doi:10.1785/0120090225

Zhou, L., Xie, J., Shen, W., Zheng, Y., Yang, Y., Shi, H., et al. (2012). The structure of the crust and uppermost mantle beneath South China from ambient noise and earthquake tomography. *Geophys. J. Int.* 189 (3), 1565–1583. doi:10.1111/j.1365-246X.2012.05423.x

Frontiers in Earth Science

TYPE Original Research
PUBLISHED 13 January 2023
DOI 10.3389/feart.2022.1055480

OPEN ACCESS

EDITED BY
Weijia Sun,
Institute of Geology and Geophysics (CAS), China

REVIEWED BY
Caroline Eakin,
Australian National University, Australia
Zhi Wei,
Peking University, China

*CORRESPONDENCE
Andrew Birkey,
abirkey@udel.edu

SPECIALTY SECTION
This article was submitted to Solid Earth Geophysics, a section of the journal Frontiers in Earth Science

RECEIVED 27 September 2022
ACCEPTED 14 December 2022
PUBLISHED 13 January 2023

CITATION
Birkey A and Ford HA (2023), Anisotropic structure of the Australian continent. *Front. Earth Sci.* 10:1055480.
doi: 10.3389/feart.2022.1055480

Anisotropic structure of the Australian continent

Andrew Birkey[1,2]* and Heather A. Ford[1]

[1]Department of Earth and Planetary Sciences, University of California, Riverside, Riverside, CA, United States,
[2]Department of Earth Sciences, University of Delaware, Newark, DE, United States

The Australian continent preserves some of the oldest lithosphere on Earth in the Yilgarn, Pilbara, and Gawler Cratons. In this study we present shear wave splitting and Ps receiver function results at long running stations across the continent. We use these results to constrain the seismic anisotropic structure of Australia's cratons and younger Phanerozoic Orogens. For shear wave splitting analysis, we utilize SKS and SKKS phases at 35 broadband stations. For Ps receiver function analysis, which we use to image horizontal boundaries in anisotropy, we utilize 14 stations. Shear wave splitting results at most stations show strong variations in both orientation of the fast direction and delay time as a function of backazimuth, an indication that multiple layers of anisotropy are present. In general, observed fast directions do not appear to be the result of plate motion alone, nor do they typically follow the strike of major tectonic/geologic features at the surface, although we do point out several possible exceptions. Our Ps receiver function results show significant variations in the amplitude and polarity of receiver functions with backazimuth at most stations across Australia. In general, our results do not show evidence for distinctive boundaries in seismic anisotropy, but instead suggest heterogenous anisotropic structure potentially related to previously imaged mid-lithospheric discontinuities. Comparison of Ps receiver function and shear wave splitting results indicates the presence of laterally variable and vertically layered anisotropy within both the thicker cratonic lithosphere to the west, as well as the Phanerozoic east. Such complex seismic anisotropy and seismic layering within the lithosphere suggests that anisotropic fabrics may be preserved for billions of years and record ancient events linked to the formation, stabilization, and evolution of cratonic lithosphere in deep time.

KEYWORDS

lithospheric diversity: new perspective on structure, composition, and evolution, shear wave splitting, receiver function, anisotropy

1 Introduction

Earth's interior is commonly divided into layers by one of two criteria: composition or rheology. The outermost rheological layer is the lithosphere, a rigid shell that translates coherently above the flowing asthenosphere and is composed of portions of two compositional layers, the crust and the mantle. In some instances, the lithosphere is considered to be that portion of the Earth engaged in plate tectonics and is referred to as the tectosphere (Jordan, 1975). Increasing evidence suggests the lithosphere is heterogeneous in many geophysical properties: magnetotellurics (e.g., Selway, 2018; Bedrosian and Finn, 2021), tomography (e.g., Yoshizawa, 2014), attenuation (e.g., Kennett and Abdullah, 2011), reflectivity (e.g., Kennett et al., 2017), reflection (e.g., Worthington et al., 2015), refraction (Musacchio et al., 2004), shear wave splitting (e.g., Chen et al., 2018), and receiver functions (e.g., Hopper and Fischer, 2015). One of the key findings from some of these studies is that heterogeneity within the Earth's upper mantle is often expressed as anisotropy of material properties such as seismic wavespeeds (Debayle et al., 2016), strength (Vauchez et al., 1998), and electrical conductivity (Du Frane et al., 2005). In this study, we present results at long-running stations across the entire Australian continent from two complementary techniques, shear wave splitting and receiver functions, to provide a detailed accounting of anisotropy within the Australian lithosphere—which in some instances has evolved over billions of years of geologic history. We examine cratonic Australia (regions tectonically inactive for at least one billion years) and the younger, Phanerozoic eastern margin for evidence of preserved and inherited seismic lithospheric structure. Importantly, we observe complex seismic structure not only in the cratons, but also in Phanerozoic Australia.

1.1 Shear wave splitting background

Seismic structures are often assumed to be isotropic—meaning wave speed is not directionally dependent. Yet many of the Earth's constituent minerals have strongly anisotropic crystal forms leading to variations in speed of light or seismic wavespeeds according to the direction energy propagates. The observation of seismic anisotropy in Earth's lithosphere and asthenosphere thus requires the bulk alignment of crystal forms within the crust and/or mantle. At crustal depths, minerals such as quartz, mica, and amphibole are seismically anisotropic (Brownlee et al., 2017). At upper mantle depths, the dominant mineral is olivine, which is strongly anisotropic, exhibiting up to 22.3% single-crystal anisotropy for S-waves (Kumazawa and Anderson, 1969). In the crust, anisotropy may be expressed as either shape-preferred orientation (alignment of fractures or magmatic bodies) or lattice-preferred orientation (alignment of mineral crystals due to strain; LPO). In the mantle, the force of plate motion or convection may create LPO, although shape-preferred orientation may also be present as melt-aligned structures, though this occurs predominantly in rift settings (e.g., Vauchez et al., 2000; Walker et al., 2004). While the mechanics behind LPO formation are complicated, in the upper mantle they can usually be simplified to a case of dislocation glide where shear in crystals mirrors shear due to plate motion, and fast directions are parallel to flow (Karato et al., 2008).

One of the most used methods to image seismic anisotropy is known as shear wave splitting. A shear wave encountering an anisotropic medium will be split into two orthogonal quasi-shear waves (one fast, one slow). As the waves propagate through the medium, they travel at different wave speeds, accruing a delay time between the two waves. Upon reaching a receiver, the delay time between the waves (the combined result of the strength of anisotropy and thickness of the layer) and the fast direction of the medium (or the alignment of mineral crystals) can be measured; see Section 2.1 for more information on this methodology. This method has been used in many different tectonic settings to measure the seismic anisotropy of crust and mantle lithosphere, including subduction zones (Long and Silver, 2008), mid-ocean ridges (Conder, 2007), and tectonically quiescent regions such as cratons (Eakin et al., 2021).

1.2 Ps receiver function background

Earth's interior is composed of rocks with different material properties, such as velocity and density. Strong contrasts in these properties across horizontal to gently dipping layers can result in the conversion from a P-wave to an S-wave, or *vice versa*. These converted phases can be used with the unconverted phase to deconvolve a structural component from the signal. This is known as a receiver function, and has been used to image a number of lithologic and mineralogic boundaries within the Earth such as sediment-basement contacts (Liu et al., 2018), deep crustal mineralogical/seismic structure (Hopper et al., 2017), the crust-mantle boundary (the Moho; Reading and Kennett, 2003), the lithosphere-asthenosphere boundary (Ford et al., 2010), seismic wave speed discontinuities internal to thick lithosphere (known as mid-lithospheric discontinuities; Wirth and Long, 2014), and the mantle transition zone (Ba et al., 2020).

In this study, we present results from Ps receiver functions across Australia. This method provides excellent vertical resolution of seismic boundaries. Because the direct and converted arrivals are time separated, Ps receiver functions image the Moho well. Additionally, backazimuthal variations in the amplitude and polarity of transverse-component receiver functions can be used to detect changes in seismic anisotropy across boundaries (Levin and Park, 1997; Schulte-Pelkum and Mahan, 2014; Park and Levin, 2016). This method has been used to estimate seismic anisotropy in several settings, such as subduction zones (Wirth and Long, 2012), tectonically quiescent interiors (Wirth and Long, 2014; Ford et al., 2016; Chen et al., 2021b), and orogens (Long et al., 2017). However, Moho multiples can obscure arrivals from the uppermost mantle, making them less suitable for imaging the lithosphere-asthenosphere boundary in some instances (Bostock, 1997; Bostock, 1998). Previous continent-wide receiver function studies of Australia provide independent constraints on both the seismic structure of the lithospheric mantle and the depth of lithosphere-asthenosphere boundary, but these studies have assumed a largely isotropic mantle (Ford et al., 2010; Birkey et al., 2021). Calculation of anisotropic Ps receiver functions will improve understanding of the seismic structure and layering of the Australian continent and provide a complementary dataset to shear wave splitting.

1.3 Tectonic background

The Australian continent has a long geologic history spanning the Archean to present. It can be divided into four broad regions (Figure 1). In the western two-thirds of the continent, there are three composite cratons: the West Australian Craton, composed of the Archean Pilbara and Yilgarn Cratons as well as Proterozoic Orogens and basins; the South Australian Craton, with the Archean Gawler Craton in the center, the Proterozoic Curnamona Craton along the eastern margin, and Proterozoic basins between; and the North Australian Craton, composed of the Proterozoic Kimberly Craton in the northwest, and Proterozoic basins and orogens throughout. The North Australian Craton and West Australian Craton were joined together around 1.8 Ga, evidence of which is preserved in the Rudall Complex and Arunta Inlier (Collins and Shaw, 1995; Smithies and Bagas, 1997; Li, 2000). Between 1.3 and 1.1 Ga, the South Australian Craton completed its final docking with the West Australian Craton and North Australian Craton during the Musgrave and Albany-Fraser Orogenies (Clarke et al., 1995; Myers et al., 1996). To the east are a series of Phanerozoic orogens that were accreted to the cratonic core: the Cambrian Delamerian (Marshak and Flöttmann, 1996), the Cambrian to Late Permian Lachlan and Thomson (Murray

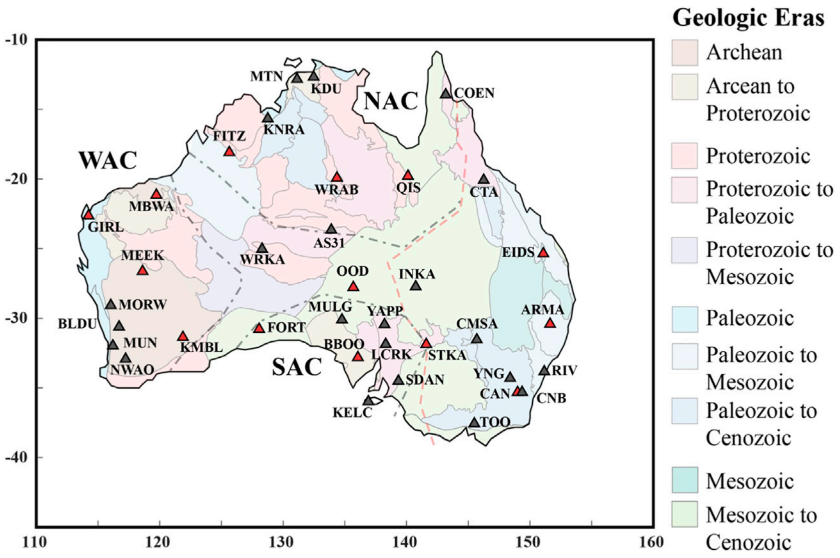

FIGURE 1
Map of stations used in this study. Red triangles indicate stations used in both shear wave splitting and receiver function analysis. Gray triangles indicates stations used only for shear wave splitting. Background shows significant geologic divisions of Australia, simplified from Fraser et al. (2007). Dashed red line shows location of the Tasman Line. Dashed gray lines mark inferred boundaries of cratonic blocks. NAC–North Australian Craton; SAC–South Australian Craton; WAC–West Australian Craton.

and Kirkegaard, 1978; Foster and Gray, 2000), and the Carboniferous to Early Mesozoic New England Orogen (Coney et al., 1990). Separating the cratons and Phanerozoic orogens to the east is the Tasman Line, a boundary inferred predominantly from surface geology (Direen and Crawford, 2003).

1.4 Previous geophysical studies relevant to this study

Previous shear wave splitting studies have indicated complex anisotropic structure of the Australian lithosphere. Continental studies have indicated frequency dependent splitting, implying depth variation in anisotropy (Clitheroe and Van der Hilst, 1998; Özalbey and Chen, 1999). A large percentage of nulls, results indicating no splitting or coming from backazimuths aligned with the fast or slow direction, have been calculated in both continental and local shear wave splitting studies (Özalbey and Chen, 1999; Heintz and Kennett, 2006; Chen et al., 2021a; Eakin et al., 2021). Several studies have indicated potential correlation between fast directions and features observed at the surface or in the crust: at station WRAB (NAC), fast direction is consistent with Proterozoic faulting (Clitheroe and Van der Hilst, 1998); splitting at KMBL in the Yilgarn Craton (WAC) roughly mirrors the trend of the Eastern Goldfields Terrane (Chen et al., 2021b); results from the BILBY network near the North Australian Craton's Tenant Creek Inlier match its geometry (Eakin et al., 2021); and stations in eastern Australia have been shown to have fast directions that are subparallel to the structural trends of Phanerozoic fold belts or the Tasman Line—shown in Figure 1 as a dashed red line (Clitheroe and Van der Hilst, 1998; Heintz and Kennett, 2005; Bello et al., 2019). In general, fast directions across the continent due not mirror apparent plate motion, suggesting a contribution from fossilized lithospheric anisotropy (Clitheroe and Van der Hilst, 1998; Heintz and Kennett, 2005).

Tomographic studies have also examined anisotropy within the Australian lithosphere and asthenosphere. In general, azimuthal anisotropy is weaker above 150 km with complex patterns; below that, fast directions rotate to more N-S, mirroring plate motion (Debayle and Kennett, 2000; Simons et al., 2002; Debayle et al., 2005; Fishwick and Reading, 2008). While these models suggest broad trends such as shallower anisotropy roughly oriented E-W and deeper anisotropy oriented N-S, there are some variations. For instance, Fishwick and Reading (2008) find weak anisotropy within the center of Australia at 75 km, with stronger anisotropy around the edges; while most fast directions are oriented N-S by 250 km, their model suggests complex anisotropy within the WAC and SAC. Simons et al. (2002) constrain complex patterns that do not correlate to surface features down to at least 200 km, with a rotation to more N-S-oriented patterns by 300 km depth. Studies of radial anisotropy have also suggested multilayered anisotropy, with complex changes through the lithosphere and into the asthenosphere (Debayle and Kennett, 2000; Yoshizawa and Kennett, 2015). As with azimuthal anisotropy, radial anisotropy is laterally heterogeneous throughout the continent. The strongest radial anisotropy is observed in Proterozoic suture zones of central Australia, with somewhat weaker radial anisotropy in the NAC and WAC (Yoshizawa and Kennett, 2015).

Anisotropic receiver function analysis of Australia has thus far been relatively limited. Chen et al. (2021b) calculated Ps receiver functions in the Yilgarn Craton and found evidence for multiple layers of anisotropy. Ford et al. (2010) and Birkey et al. (2021) utilized Sp receiver functions to characterize discontinuity structure of the lithospheric mantle—while these analyses did not constrain anisotropy, they found evidence for mid-lithospheric discontinuities within cratonic Australia, which some have argued may be due to anisotropic layering (Rychert and Shearer, 2009; Wirth and Long, 2014).

2 Materials and methods

We used 35 stations for shear wave splitting, including those from the Australian National Seismograph Network (AU, 32 stations; DOI https://dx.doi.org/10.26186/144675), the Global Seismograph Network (IU and II; DOI https://doi.org/10.7914/SN/IU and https://doi.org/10.7914/SN/II), and the French Global Network of Seismological Broadband Stations (G, one station; DOI http://doi.org/10.18715/GEOSCOPE.G). Ps receiver functions used 14 total stations from the same networks: 11 from the AU network, and one each from the IU, II, and G networks. Data used in this study were accessed using the IRIS Data Management Center. They are free and publicly available.

2.1 Shear wave splitting

We used core-refracted phases (i.e., SKS and SKKS) to calculate our shear wave splitting results. These have the benefit of a "reset" due to conversion from P-to-S at the core-mantle boundary; thus, the anisotropy observed at the surface is only due to receiver-side effects (assumed to be dominantly in the upper mantle, though this may not be the case). Phases were limited to 85°–130° epicentral distance to avoid phase contamination, to events M_w 5.5 and greater to maximize the signal-to-noise ratio, and no event depth limits were applied. Signals were filtered at multiple frequency bands between 0.01 and 1.0 Hz to maximize the signal-to-noise ratio. Additionally, changes in splitting parameters with frequency bands have been linked to changes in anisotropy with depth (i.e., higher frequencies are linked to shallower depths and lower frequencies to greater depths; Eakin and Long, 2013), though we do not observe any obvious frequency dependence.

Splits were calculated in an updated version of Splitlab (Wüstefeld et al., 2008; Deng et al., 2017), a free, publicly available MATLAB plugin. All splitting results in this paper are from the rotation correlation method (Bowman and Ando, 1987): this method takes the signal on both components, rotates them in 1° increments, and time shifts them in 0.1 s increments. For each rotation and each time shift, correlation between the signals is calculated. The pair with the maximum correlation represents the fast direction and delay time of the split. One limitation of this method is a systematic misorientation of 45° at near-null directions; this can be accounted for with modeling of the splitting parameters, detailed in Section 3.3 (Wüstefeld and Bokelmann, 2007; Eakin et al., 2019). To check for the quality of splits, we also calculate splitting parameters using the minimum energy and eigenvalue methods (Silver and Chan, 1991). Fast directions between methods within 25° of one another and delay times within 0.4 s are required for fair and null splits, but not poor splits; we show an example split and null in Supplementary Figures S1, 2. Finally, splitting intensity is calculated to check whether the split is a null—a splitting intensity value close to 0 indicates a null value, and in cratons the absolute value tends to be smaller than in other regions. The signal-to-noise ratio was required to be above 5.0. Finally, the shape of the particle motion before and after correction for the preferred fast direction and delay time was examined: before correction particle motion should be elliptical, then rectilinear after correction. We check station orientation using the Latest Assessment of Seismic Station Observations (LASSO).

2.2 Ps receiver functions

Events for Ps receiver function analysis were epicentrally limited to 30°–95° with no depth limit. Stations with more than 5 years of data had a higher magnitude cutoff of 5.8 to maximize the signal-to-noise ratio, while stations with less than 5 years of data had a lower magnitude cutoff of 5.6 to maximize the number of waveforms available. Preprocessing of receiver functions included: cutting traces to identical length; detrending and demeaning waveforms; bandpass filtering from 0.02 to 2.0 Hz; visually sorting waveforms with clear P-wave arrivals; and manually picking P-wave arrivals in the Seismic Analysis Code (SAC). Waveforms were rotated into vertical, radial, and transverse components (with most Ps energy occurring on the radial component). Receiver functions were calculated with a 65 s data window. All backazimuths were calculated in 10° bins with a minimum of two events required per bin. Deconvolution of the daughter phase (Ps wave) was performed in the frequency domain using the multiple-taper spectral correlation method (Park and Levin, 2016). Once deconvolution was performed, receiver functions were migrated from time to depth using the local tomography model AuSREM (Kennett and Salmon, 2012; Kennett et al., 2013; Salmon et al., 2013). We report receiver functions at 0.75 Hz—this frequency provides more clearly separated pulses than 0.5 Hz without introducing higher frequency noise (such as seen at 1.0 or 2.0 Hz).

3 Results

Below we present results first for shear wave splitting, then receiver functions. We describe shear wave splitting results in terms of station-averaged splitting parameters (Section 3.1), then according to backazimuthal variations in said parameters (Section 3.2), and finally in terms of single-layer modeling (Section 3.3). We then describe receiver functions in terms of crustal and Moho structure, followed by mantle structure (Section 3.4).

3.1 Station averaged splitting parameters

A total of 522 non-null splits were calculated. Null results (i.e., non-splitting) are evidence of no anisotropy, weak anisotropy, or alignment of the backazimuth of the incoming wave with a fast or slow direction (Savage, 1999). There was a total of 409 nulls detected. Events for both splits and nulls are clustered around four backazimuths: 30° (199 results), 150° (206 results), 190° (189 results), and 300° (91 results). These correspond to the subduction zone along the northern Pacific plate, the subduction zone along the west coast of South America, the spreading center between the Antarctic and South American plates, and the Himalayan collision zone, respectively (Figure 2).

Shear wave splitting results are often presented as station averages. In Figure 3 we display an arithmetic mean for the average fast direction and delay time at each station, plotted on top of tectonic terranes. Average fast directions at all stations trend either N-S or NE-SW, and there are few correlations between tectonic terranes inferred

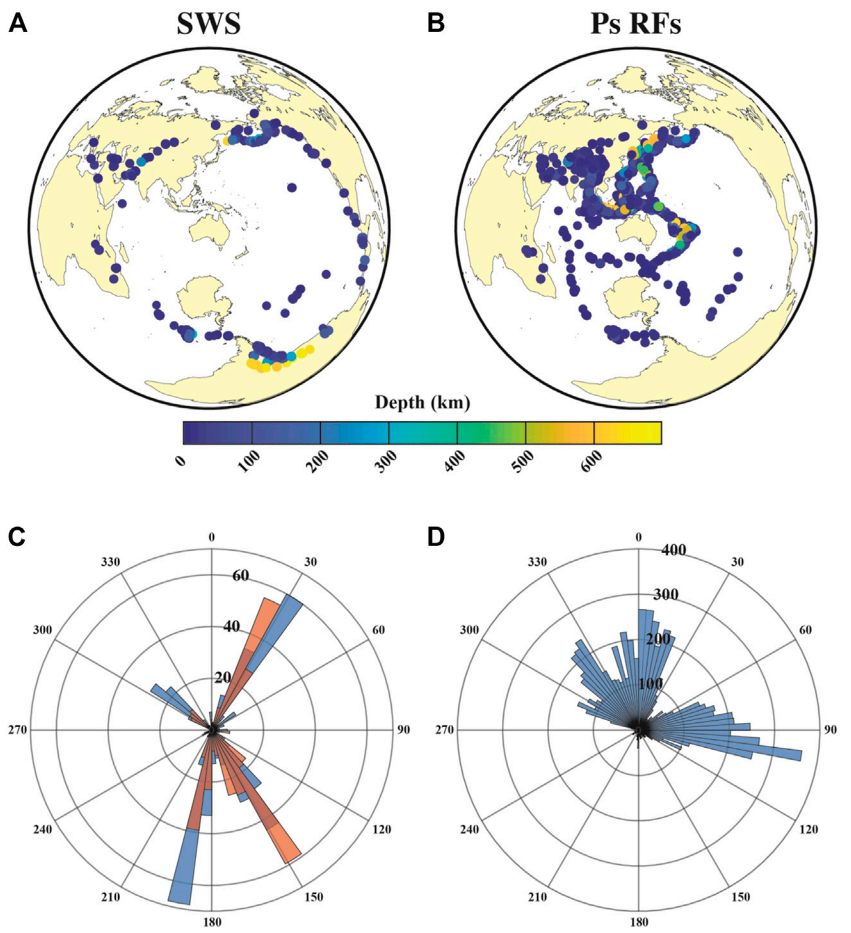

FIGURE 2
Event information for both methods used in this study. **(A)** Map of events used for shear wave splitting, color coded according to event depth. **(B)** Map of events used for receiver functions, color coded according to event depth. **(C)** Polar histogram of event distribution by backazimuth for shear wave splitting. Blue bins are splitting results, while orange bins are null results. **(D)** Polar histogram of event distribution by backazimuth for receiver functions.

at the surface and average fast directions; however, there are slight variations between regions (Supplementary Figures S3). Delay times among all regions tend to be around 0.6 s (Supplementary Figures S4), smaller than the average at stations globally but consistent with previous results in Australia (e.g., Heintz and Kennett, 2005).

In the same figure, we also plot average fast directions against plate motion from a hotspot frame of reference using HS3-NUVEL 1A (Gripp and Gordon, 2002). At 25 of the stations analyzed, fast direction and plate motion disagree by more than 10°. One station (MBWA) has only nulls and is therefore not included in this discussion. The remaining nine stations with a fast direction within 10° of absolute plate motion are ARMA, BBOO CAN, CNB, INKA, MULG, RIV, WRKA, and YNG. Agreement between fast direction and plate motion is often assumed to be the case in tectonically quiescent regions, based on both splitting observations (e.g., Vinnik et al., 1992) and laboratory studies of olivine crystals (Karato et al., 2008). Stations ARMA, CAN, CNB, RIV, and YNG are along the eastern margin of the continent where the lithosphere is younger and thinner, and thus splitting directions may be more heavily influenced by plate motion. While station INKA is on somewhat thicker lithosphere than those ot its east, it is to the east of the Tasman Line—generally recognized as the transition between cratonic and Phanerozoic Australia. Fast directions at station WRKA are clustered near -60° (7 splits) and 60° (8 splits), so the averaging of these two bins results in a near-zero fast direction. Stations BBOO and MULG have clusters of fast directions ~140° apart (near -70° and 70°), again resulting in a fast direction closer to zero. While nine stations have average fast directions in good agreement with plate motion, the averaging of splitting parameters smooths out significant backazimuthal variations seen in the results (see Section 3.2). Therefore, the anisotropic fabric inferred from splitting is not likely to be controlled solely by plate motion even at those stations where there is good agreement between average splitting direction and absolute plate motion. We also note that Additionally, the rotation correlation method can produce systematic 45° misorientations from the true fast direction (Wüstefeld and Bokelmann, 2007; Eakin et al., 2019), which will lead to inaccurate station averages: to address this possibility, we model results by station in Section 3.3.

3.2 Backazimuthal variation in splitting

Layered anisotropy should produce backazimuthal variations in fast direction and delay time. As seen in Figure 4, we observed this in

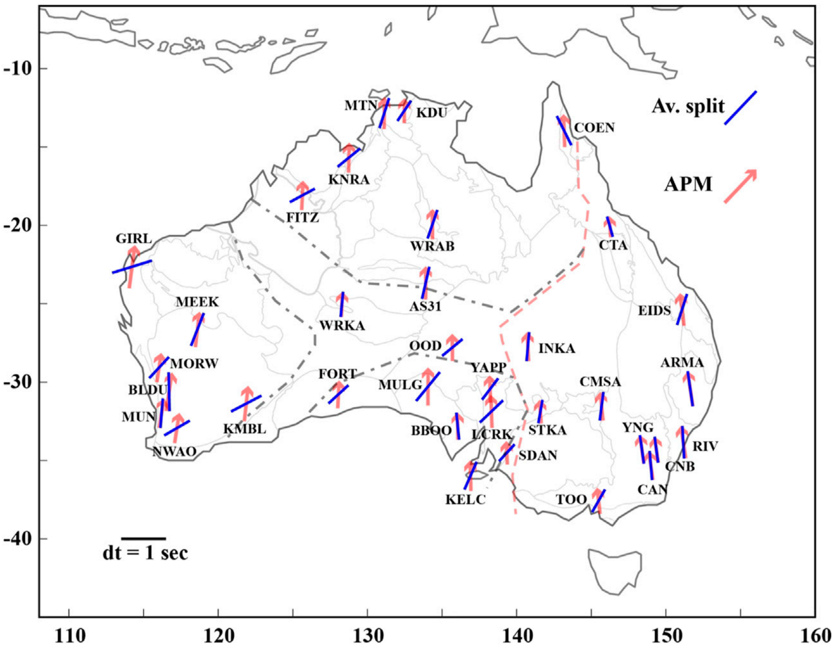

FIGURE 3
Average shear wave splitting parameters plotted against apparent plate motion from the HS3-NUVEL 1A model (Gripp and Gordon, 2002). An example split with a fast direction of 90° and a delay time of 1 s is shown in the lower left.

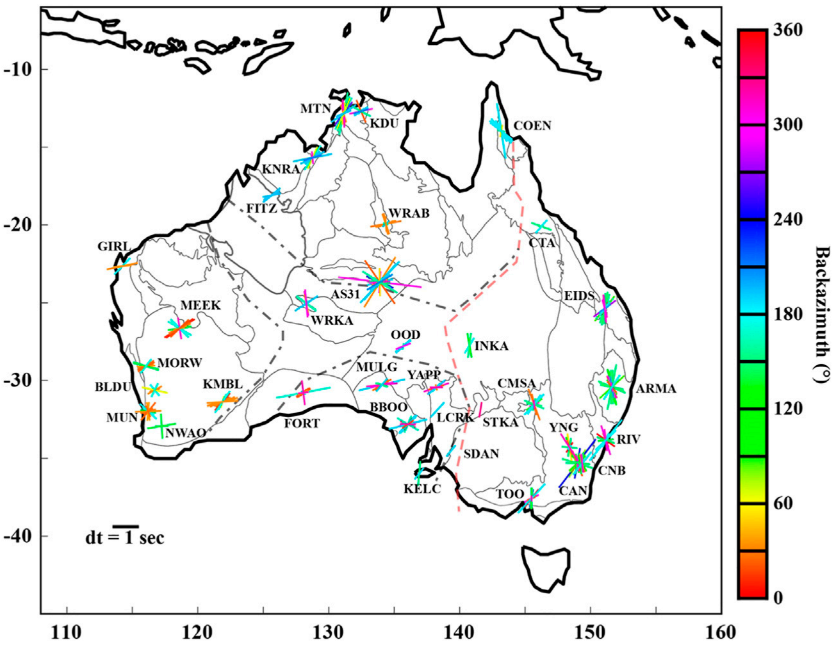

FIGURE 4
Splitting parameters color-coded by backazimuth of the event. An example split with a fast direction of 90° and a delay time of 1 s is shown in the lower left. Note that 0° and 360° are the same backazimuths.

Australia. In general, stations with longer deployment times have more data and more backazimuthal variation in splitting parameters (e.g., stations AS31 and CAN). However, clear variations in backazimuth can be seen at most stations in our study. Below, we examine the results of each region in the context of backazimuthal variations. While results are grouped by region, the varied tectonic histories of each region implies they need not be consistent. We display regional information on splitting in Table 1.

3.2.1 Splitting in phanerozoic Australia

This region contains the most stations (12) and the most non-null splits (190). Absolute plate motion varies somewhat from north to south and from east to west, but in general the Australian plate is moving to the north. Results are shown in Supplementary Figures S5. For each region we calculate the average absolute plate motion among stations; in Phanerozoic Australia, the average absolute plate motion is oriented at -6.40°. While splitting parameters vary significantly by backazimuth, at a given backazimuth there is some consistency in results across stations. We identified the five backazimuths in this region with the most splits: 30°, 90°, 150°, 180°, and 300°. For each of these, we found splits within ±10°, then averaged the fast direction and delay time for each subset of results. At 30° we find 18 splits, with an average fast direction of -6.88° and an average delay time of 0.59 s; this is very close to the direction of absolute plate motion. There are 14 splits in the bin centered around 90°, with an average fast direction of 41.95° and an average delay time of 0.72 s; for these splits, the average fast direction and average absolute plate motion vary by 48.35°. The 150° bin has the most splits (84), and an average fast direction of -23.25° (16.85° different from the average absolute plate motion) with an average delay time of 0.6 s. With 31 splits, the 180° bin has an average fast direction of 16.30° and average delay time of 0.79 s; the average fast direction in this bin vary from average absolute plate motion by 22.7°. Finally, the bin centered at 300° has 27 splits, an average fast direction of 8.97°, and an average delay time of 0.52 s. This last bin has a 15.37° difference between fast direction and plate motion.

In Supplementary Figures S6, we display splits for all stations according to backazimuth and inclination angle. We display splits by backazimuth against fast direction and delay time in Supplementary Figures S7, 8. While average fast directions for Phanerozoic Australia generally mirror absolute plate motion, there is still some change with backazimuth. Notably, at most stations there is a clear NE-SW fast direction orientation at both 0° and 180° backazimuth. Station ARMA has the most splits in this region, with consistency in fast direction at most backazimuths: most splits are oriented close to N-S, except for a handful near ~160° which are oriented closer to E-W. Station EIDS has more complexity in splitting, with most splits oriented NE-SW, but some oriented N-S; there is no consistency in orientation by backazimuth. Finally, station COEN has a deviation from the general trend of stations in this region, with fast directions at 180° backazimuth oriented NW-SE.

3.2.2 Splitting in the North Australian Craton

In the North Australian Craton, the average absolute plate motion is oriented at 1.17°, a slight eastward shift from the average of Phanerozoic Australia. As with splits in Phanerozoic Australia, there is significant backazimuthal complexity in the North Australian Craton, with stations AS31 and MTN having the most splits and the most variability in fast directions and delay times (Supplementary Figures S9). Within this region there are eight stations and 180 splits. Four backazimuths were identified with the most splits (30°, 150°, 195°, and 300°): as with Phanerozoic Australia, we found splits within ±10° of these and averaged fast directions and delay times. For the first bin (30° ± 10°) there are 38 splits, an average fast direction of 35.56°, and an average delay time of 0.63 s; the average fast direction and average absolute plate motion has a large disagreement here of 34.39°. At 150° we found 31 splits, with an average fast direction of -47.43 and an average delay time of 0.58 s; this bin too has a significant disagreement between average fast direction and average absolute plate motion (48.60°). The bin centered at 195° has the most splits (62); the average fast direction is 58.54° (57.37° off from average absolute plate motion) with an average delay time of 0.61 s. Our final bin (300°) has the least splits (21), an average fast direction of 10.69 and an average delay time of 0.72 s; this bin has the smallest difference between absolute plate motion and average fast direction at 9.52°. In general, splits in the North Australian Craton do not agree with plate motion and vary significantly as a function of back azimuth.

Other than a general disagreement between absolute plate motion and station-averaged fast directions, there are no noticeable key trends across the North Australian Craton. We show variations in splitting according to backazimuth and inclination angle at each station in Supplementary Figure S10, and according to backazimuth and fast direction/delay time in Supplementary Figures S11, 12. Rather, most stations in this region exhibit considerable complexity in splitting parameters as a function of backazimuth. For instance, station AS31 has significant variability with backazimuth: splits coming from just west of 180° backazimuth are oriented NE-SW, while those coming from just east of 180° backazimuth are oriented NW-SE; for splits coming from backazimuths less than 90° or greater than 270°, the fast direction is oriented close to E-W. Station WRKA has similar behavior as31 for backazimuths close to 180°. At station WRAB, results are particularly complex and backazimuthally limited. Most splits come from close to 30°, with two dominant orientations: E-W and N-S. However, splits with a steeper incidence angle have the more N-S orientation. Station MTN is the least complex station in this region, with most splits oriented either N-S or NE-SW.

3.2.3 Splitting in the South Australian Craton

In the South Australian Craton, there are eight stations and compared to other areas in our study this region contained the fewest number of splits (72). Average absolute plate motion in the South Australian Craton is oriented at -0.82°. Four backazimuthal bins were identified: 30°, 150°, 180°, and 300°. Again, splits within ±10° of these backazimuths were identified, and an average fast direction and delay time was calculated. Regional backazimuthal splits can be seen in Supplementary Figures S13. At 30°, there are 10 splits, an average fast direction of 54.76° and 0.48 s; the fast direction and absolute plate motion are 55.58° apart. The 150° bin has 15 splits, with an average fast direction of -44.51° (43.69° different from the average absolute plate motion) and an average delay time of 0.44 s. For the 180° bin, there are 21 splits; these have an average fast direction of 51.93° and an averaged delay time of 0.68 s. In this bin, the average fast direction and the average absolute plate motion are 52.75° different. Finally, at the 300° bin, there are 19 splits, an average fast direction of 25.34°, and a delay time of 0.65 s; this last bin has a difference of 26.16° between the average fast direction and absolute plate motion. While fast direction is variable at all backazimuths, those less than 180° have delay times roughly 0.2 s smaller than those greater than 180°.

As seen in Supplementary Figures S14 and Supplementary Figures S15, 16, the most obvious trend in this region is a fast direction that is oriented NE-SW for splits coming from backazimuths just west of 180°. Station BBOO has the most complexity of fast directions in the South Australian Craton, ranging from E-W at ~315°, to NE-SW just west of 180°, and multiple fast directions just east of 180°. Station LCRK has the most consistency, with low delay times and fast directions oriented either NE-SW or E-W.

TABLE 1 Bins with the most splits for each of the four regions. The number of splits, average fast direction ?), and average delay time (dt) per bin are shown.

Phanerozoic Australia				North Australian craton				South Australian craton				Wcst Australian craton			
Bin	Splits	Av. ϕ	Av. dt	Bin	Splits	Av.ϕ	Av. dt	Bin	Splits	Av. ϕ	Av. dt	Bin	Splits	Av. ϕ	Av. dt
30°	18	-6.88°	0.59 s	30°	38	35.56°	0.63 s	30°	10	54.76°	0.48 s	30′	46	57.59°	0.66 s
906°	14	41.95°	032 s	150°	31	-47.43°	0.58 s	150°	15	-44.61°	0.44 s	135°	9	5.57°	0.57 s
150°	84	-23.25°	0.60s	195°	62	58.54°	0.61 s	180°	21	51.93°	0.68 s	180°	11	-8.76°	0.49 5
180°	31	16.30°	0.79s	300°	21	10.69°	0.72 5	3,006	19	25.34°	0.65 5				
300°	27	8.97°	0.52 s												

3.2.4 Splitting in the West Australian Craton

In the West Australian Craton, there are eight stations and 78 splits. Events are more backazimuthally limited here than elsewhere, and we identified only three backazimuths with more than 10 splits (30°, 135°, and 180°). As with all other regions, splits within ±10° of each backazimuth were found and splitting parameters were averaged. See Supplementary Figures S17 for results. The average absolute plate motion is 8.05°, the most eastward orientation for any of the regions. The bin centered at 30° has 46 splits; the average fast direction is 57.59° (49.54° off from the average absolute plate motion) and the average delay time is 0.66 s. At 135°, there are nine splits, with an average fast direction of 5.57° and an average delay time of 0.57 s; this bin has a small misfit from the average absolute plate motion at 2.48°. Our last bin has 11 splits, an average fast direction of -8.76° and an average delay time of 0.49 s. The difference between average fast direction and average absolute plate motion is 16.18° in this bin.

Several broad trends are observed across multiple stations in the West Australian Craton, displayed in Supplementary Figure S18 and Supplementary Figures S19, 20. For instance, at ~30° backazimuth, fast directions at most stations are oriented ENE-WSW (with an exception at MUN, where several splits are oriented more N-S); at 180° backazimuth there is much less consistency in fast direction between stations. At station KMBL, there is a rotation in fast direction from NE-SW close to 0° backazimuth to more E-W moving toward 90° backazimuth, then back to NE-SW at 180°. Station MEEK has a similar orientation for backazimuths just east of 0° but has a rotation to NW-SE orientations just east of 180° backazimuths. Station MUN has significant complexity, with fast direction and delay time varying even for close backazimuths.

3.3 Shear wave splitting modelling

Interpreting shear wave splitting results from the rotation correlation method is complicated by a known 45° misorientation from the true fast direction at near-null backazimuths that produces a sawtooth pattern, and a sinusoidal trend for delay times (e.g., Wüstefeld and Bokelmann, 2007). Eakin et al. (2019) empirically derived the following equations to estimate the true fast direction and delay time:

$$\Phi_{app} = \Phi_{true} - \frac{90}{\pi}\tan^{-1}\cot\left(\frac{\pi}{90}\left(\psi - \Phi_{true}\right)\right) \qquad (1)$$

$$\delta_{app} = \delta_{true}{}^{*}\left|\sin\left(\frac{\pi}{90}\left(\psi - \Phi_{true}\right)\right)\right| \qquad (2)$$

Where Φ is fast direction, ψ is backazimuth, and δt is delay time. Using these equations, we perform a grid search over fast directions ranging from 0° to 180° in 1° increments and delay times ranging from 0.1 s to 4.0 s in 0.1 s increments. We then sum the misfits—the smallest summed misfit is the preferred true fast direction or delay time.

At some stations, this correction accounts for variability in splitting with backazimuth, but at others there is backazimuthal variability that cannot be explained through simple modeling alone. This approach is also better at finding the true fast direction or delay time than a simple averaging scheme, as fast directions that are close to 180° may counteract one another. In Table 2 we show the modeled fast direction and delay time for all stations with more than two non-null splits, as well as the summed misfit values for those models. Supplementary Figures S21 shows the modelling results for all stations included in this analysis.

To quantify which stations have results that are modeled by a single layer of anisotropy with misorientation from the rotation correlation method, we rely on three main criteria. First, there should be more than 10 splits at the station; while we modeled all stations with more than two splits, stations with fewer than 10 generally lack sufficient backazimuthal coverage to determine whether a model fits the data well. Second, the summed misfit between the model and results should be less than 1,000. Third, the difference between the average calculated from the sawtooth function at the same backazimuths as splits and the average of the splits themselves should be less than 25. In addition, we examine the backazimuthal coverage for all stations: some stations with sufficient data and small misfits are backazimuthally limited and thus have insufficient coverage to constrain a single correct model (such as WRAB). In total, we modeled sawtooth functions for 29 stations: 13 (45%) of these were well fit, while 16 (55%) were not. Both well-modeled and unmodeled stations are geographically distributed. Stations with a larger number of splits tend to not be well modeled, though this is not always the case (as at AS31, which has the most splits and is well modeled). We plot all modeled splitting parameters with APM in Figure 5, and the modeled and average splitting parameters in Figure 6. Unlike average fast directions, modeled fast directions do not agree with APM.

3.4 Ps receiver functions

For Ps receiver functions, 8,607 waveforms were used, averaging 615 waveforms per station. Station CAN used the most waveforms (1,135) while station OOD used the fewest (308). The small number of

TABLE 2 Shear wave splitting modeling information.

Modeled Phi										
Station	Phi	Dt	Splits	Misfit	Phi average	Modeled Phi	Phi Misfit	Lon	Lat	Modeled?
ARMA	136	1	44	2000.6	126.16	97.74	28.42	151.63	-30.42	No
AS31	79	0.8	63	557.8	78.75	82.02	3.27	133.9	-23.67	Yes
BBOO	66	0.9	29	208	66.21	80.91	14.70	136.05	-32.809	Yes
BLDU	74	0.6	10	177.6	76.70	88.56	11.86	116.71	-30.614	Yes
CAN	52	0.9	28	1,231.6	41.46	84.85	43.39	148.99	-35.32	No
CMSA	56	0.8	16	491.6	42.63	75.23	32.60	145.69	-31.54	No
CNB	131	0.7	12	468.5	127.42	97.06	30.36	149.36	-34.312	No
COEN	96	0.3	15	441.4	102.73	104.44	1.71	143.18	-13.96	No
CTA	78	0.5	4	8.1	72.50	73.28	0.77	146.25	-20.09	No
EIDS	42	0.8	26	875.3	42.15	67.08	24.93	151.081	-25.37	Yes
FITZ	74	0.7	11	58.2	59.55	63.13	3.58	125.64	-18.09	No
FORT	78	0.5	11	162.2	72.73	81.58	8.85	128.059	-30.779	Yes
GIRL	59	1	4	11.4	70.75	73.60	2.85	114.23	-22.643	No
INKA	55	0.7	5	203.5	43.60	77.38	33.78	140.75	-27.74	No
KDU	71	0.5	11	127	73.91	84.33	10.42	132.47	-12.69	Yes
KMBL	37	0.9	16	75	65.25	63.51	1.74	121.88	-31.37	Yes
KNRA	38	0.9	16	262	49.25	74.80	25.55	128.76	-15.68	Yes
LCRK	47	0.5	9	158.4	62.00	78.49	16.49	138.22	-30.44	No
MEEK	87	0.8	21	201.6	81.14	94.98	13.84	118.61	-26.64	Yes
MORW	50	0.8	11	45.2	58.18	76.95	18.76	116.04	-29.07	Yes
MTN	41	0.9	40	1,452.5	48.63	81.54	32.92	131.13	-12.84	No
MULG	92	1	10	63.9	77.20	76.73	0.47	134.06	-30.28	Yes
MUN	90	0.6	10	323.9	78.90	94.63	15.73	116.21	-31.98	Yes
OOD	27	1	9	22.5	42.78	51.86	9.08	135.69	-27.79	No
RIV	87	0.6	15	500.2	77.60	104.69	27.09	151.16	-33.83	No
TOO	46	0.8	15	215.2	38.60	54.87	16.27	145.49	-37.57	Yes
WRAB	122	0.5	10	312.5	142.60	122.59	20.01	134.36	-19.93	No
WRKA	70	0.4	21	452.8	62.76	100.22	37.46	128.29	-25.04	No
YNG	57	0.5	9	319.2	51.11	91.56	40.44	148.39	-34.29	No

events at station OOD is unsurprising: using the IRIS **M**odular **U**tility for **STA**tisical k**N**owledge **G**athering system (MUSTANG), probability density functions for seismic noise at the station indicate a large amount of noise above the Peterson New High Noise Model (Peterson, 1993). While station CAN is similarly noisy, it has been deployed since 1987 ensuring that there is a much longer period in which to find suitable events of high quality. Events for Ps come primarily from backazimuths between 300° and 120°. In this range there are several plate boundaries, including those of the Australian plate, those along the western Pacific plate, and the complex boundary between the Indian, Eurasian, and Australian plates (Figure 2).

We present Ps receiver function results for nine stations across the Australian continent (Figures 7–10). For the remaining stations the receiver functions are of poor quality or have issues with data availability. For instance, at stations FORT and GIRL we observe large amplitude, ringy phases with frequent polarity flips, consistent with basinal reverberations (Zelt and Ellis, 1989); Ford et al. (2010) also observed shallow crustal reverberations that prevented them from interpreting upper mantle structure at station FORT. Receiver functions were binned by backazimuth, and both the radial (corresponding to SV energy) and the transverse (corresponding to SH energy) component receiver functions were calculated. Energy on the transverse component has been shown to be primarily due to the presence

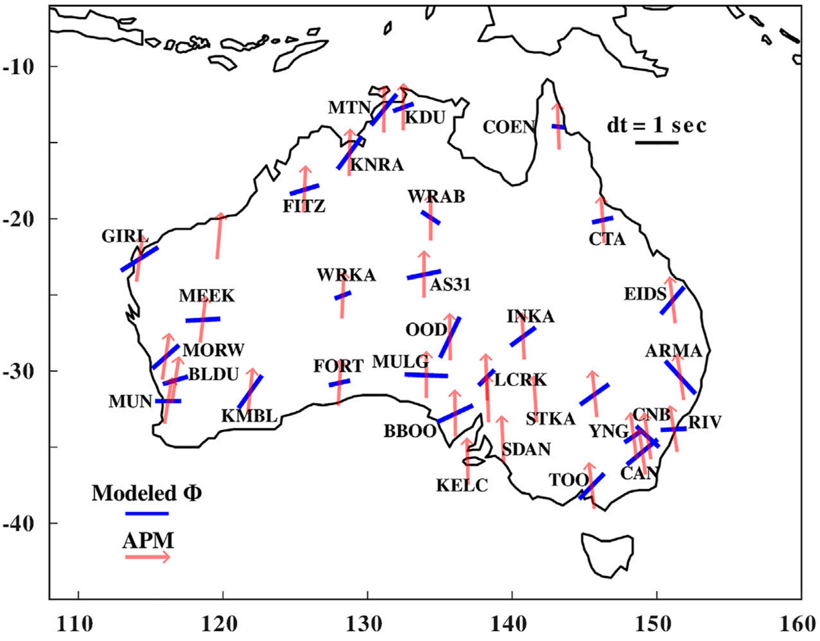

FIGURE 5
Modeled shear wave splitting parameters against apparent plate motion from the HS3-NUVEL 1A model (Gripp and Gordon, 2002). An example split with a fast direction of 90° and a delay time of 1 s is shown in the upper right.

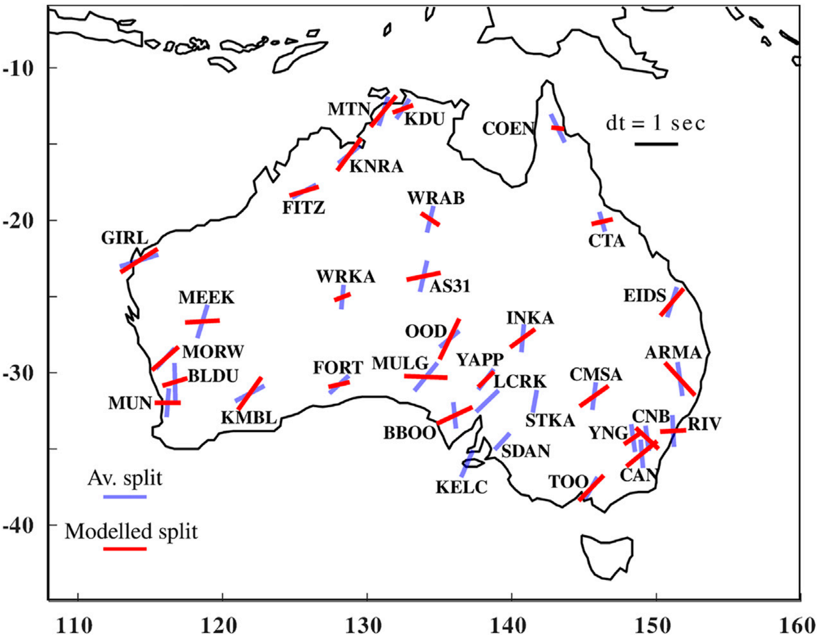

FIGURE 6
Average shear wave splitting parameters against modeled splitting parameters. An example split with a fast direction of 90° and a delay time of 1 s is shown in the upper right.

of isotropic dipping structures or anisotropic boundaries (Levin and Park, 1997; Park and Levin, 2016). In the remaining results sections, we begin by first describing results associated with the crust and Moho, and then describe observed structure of the mantle. We include boundaries that are inferred to be either isotropic, anisotropic or both.

3.4.1 Crust and Moho structure

The depth of the Moho is commonly mapped using Ps receiver functions, which we report below. We compare these results to those reported in the AuSREM (Kennett et al., 2017) and those calculated by Birkey et al. (2021), who used an automated receiver function method

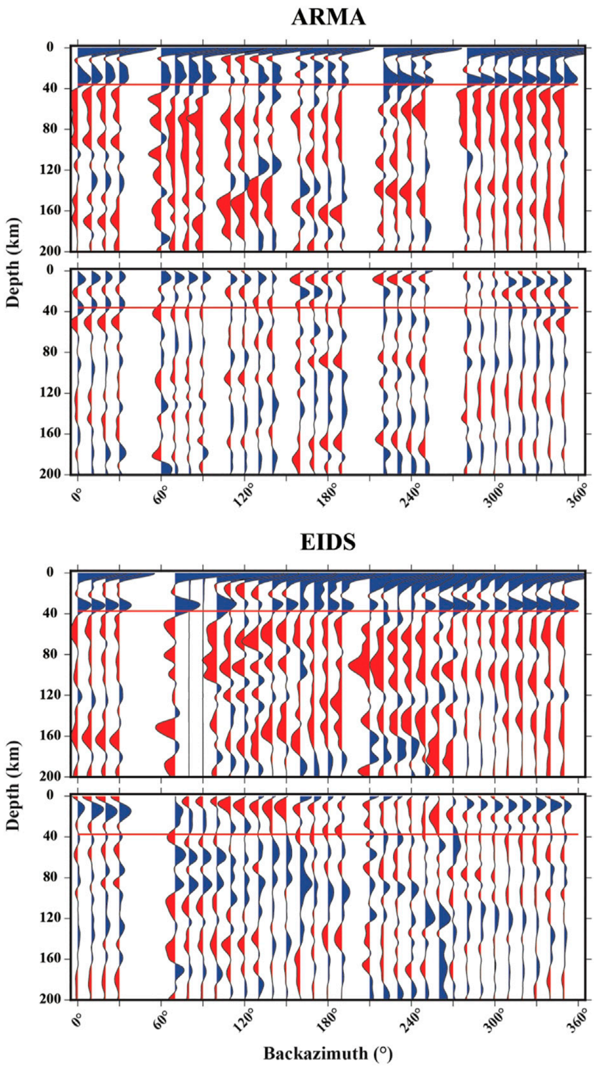

FIGURE 7
Backazimuthally-binned Ps receiver functions from Phanerozoic Australia. Top panel for each is the radial component, bottom panel is the transverse component. Blue pulses indicate a velocity increase with depth; red pulses indicate a velocity decrease with depth. The red line shows the predicted Moho depth for the station-averaged receiver functions. Backazimuth is shown on the *x*-axis, while depth from surface is shown on the *y*-axis.

for both Sp and Ps receiver functions. With Ps receiver functions, the Moho can be identified by its positive polarity (indicating a velocity increase with depth, which is expected moving from the crust to the mantle) on radial component receiver functions. We identify Moho depths using single-station stacked radial-component receiver functions, assuming the Moho is represented by the maximum amplitude positive pulse below the direct arrival located at or near zero at each station. At stations ARMA, BBOO, EIDS, KMBL, MEEK, and WRAB, all three studies estimate similar Moho depths (within 10 km). At two stations (FITZ and OOD), our single-station stacks do not have a clear positive pulse we can associate with the Moho. At station QIS, our estimated Moho depth is within 5 km of the AuSREM estimate, but Birkey et al. (2021) did not include station QIS in their analysis. Previous global observations have indicated that older continents tend to have thicker than average crust (Laske et al., 2013): this is generally confirmed by our receiver functions. There are some exceptions: we estimate the depth of the Moho to be 32 km at station MEEK and 35 km at station KMBL, despite both being within the West Australian Craton—though previous results do potentially indicate a thicker Moho (e.g., Kennett et al., 2012; Birkey et al., 2021). Phanerozoic Australia has a crustal thickness of less than 40 km (30 km at station ARMA and 31 km at station EIDS); the North Australian Craton has the thickest crust of any region in our results, with all stations having a thickness greater than 40 km; all stations within the West Australian Craton have a crustal thickness less than 40 km.

In Phanerozoic Australia, we report results for two stations: ARMA and EIDS (seen in Figure 7). At station ARMA, the positive pulse associated with the velocity increase across the Moho on the radial component is not consistent across all backazimuths, but rather is variable in shape and amplitude, and is observed over a range of depths, between 30 and 40 km, which may be due to a laterally complex Moho. There is some positive and negative energy above the Moho, but most of the negative pulses at around 10 km depth (i.e., immediately below the direct arrival) are likely sidelobes given their timing and low amplitudes. Station EIDS has a slightly more consistent Moho pulse across backazimuths, with a clearer peak around 30 km. We observe both positive (e.g., between 160° and 190° backazimuth around 15 km) and negative energy (e.g., between 100° and 150° backazimuth around 20 km) above the Moho, potentially indicating sharp boundaries in velocity between different crustal layers.

In the North Australian Craton, we report results for three stations: FITZ, QIS, and WRAB (Figure 8). We observe the most variability in the shape and amplitude of the Moho pulse at station FITZ, with some backazimuths having no clear positive pulse associated with the transition from crust to mantle. There is a significant amount of energy above the Moho at ~10 km, with large amplitude negative pulses between 60° and 120°, then again close to 270°: this indicates a lower-velocity layer above the Moho. Station QIS has a more consistent Moho pulse (ranging from 40 to 50 km), particularly between 280° and 350°, where the positive pulses fall roughly at the same depth (~50 km) and have similar amplitudes. There are complex switches between positive and negative pulses above the Moho; for instance, between 120° and 190° backazimuth where a negative pulse at ~10 km is followed by a positive pulse around 20 km, then another negative pulse ranging from 30 to 40 km depth. Station WRAB has the most consistency in the shape of its Moho pulse, with two distinct groups: one between 70° and 180° (at a depth of ~45 km), the other between 250° and 30° (where there appear to be two or more positive pulses connected to one another without one being larger than the others). There is a large amount of positive energy above the Moho, but little negative energy except at ~10 km where small negative pulses may represent sidelobes of the direct arrival.

For the South Australian Craton, we report Ps receiver function results for two stations: BBOO and OOD (Figure 9). Station BBOO has a relatively consistent Moho pulse at all backazimuths around 40 km, and a secondary positive pulse above the Moho around 20 km (which in some cases was the same or greater amplitude than the deeper positive pulse). There is little negative energy in the crustal portion of the receiver function. Station OOD has significantly more complex structure, with little consistency in the Moho pulse, and some backazimuths with unclear Moho arrivals. Between 150° and 170°,

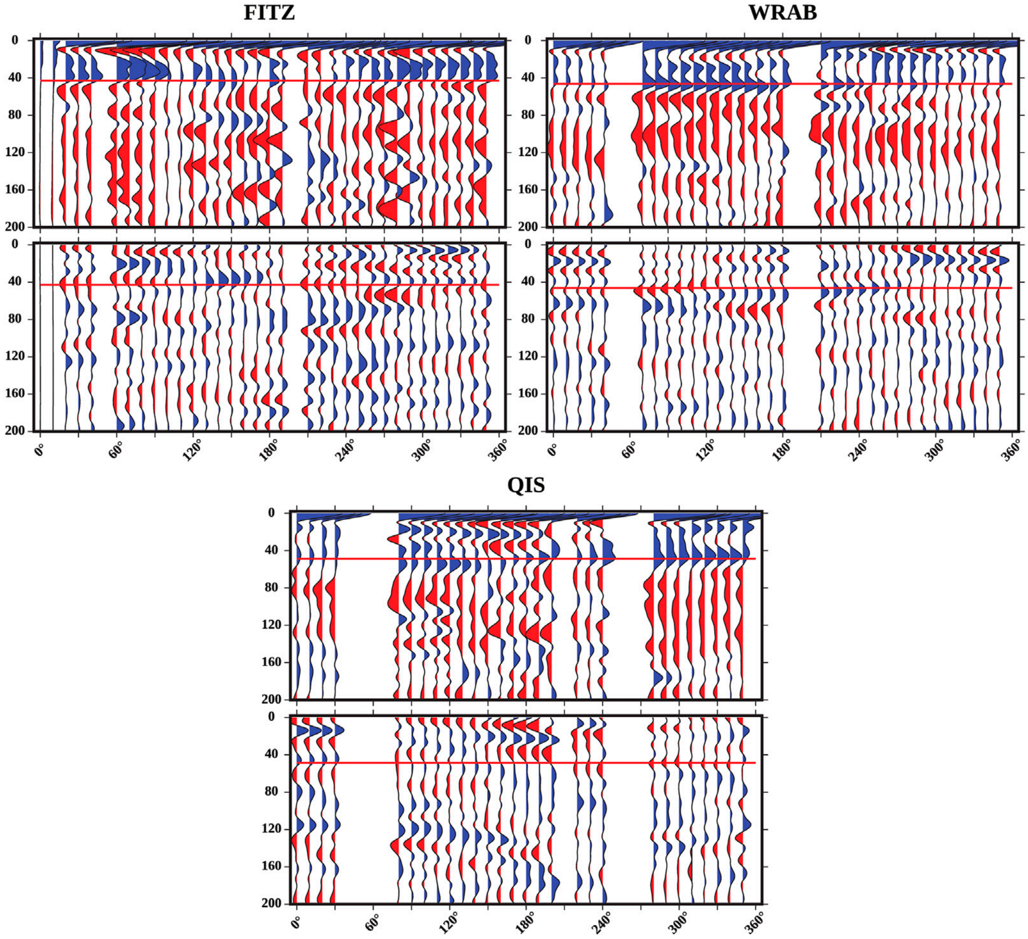

FIGURE 8
Backazimuthally-binned Ps receiver functions from the North Australian Craton (NAC). Cyan lines indicate depth of potential polarity flips, as mentioned in the text. All other features the same as in Figure 7.

there are large amplitude negative pulses above the Moho at ~10 km. There are few other negative arrivals in the sub-Moho portion of the receiver function, but positive arrivals have complex shapes and amplitudes (e.g., between 90° and 160° backazimuth where a secondary positive pulse starts immediately below the direct arrival and increases its depth with increasing backazimuth).

Finally, in the West Australian Craton we report Ps receiver function results for two stations: KMBL and MEEK (shown in Figure 10). Station KMBL has a clear, large, consistent amplitude positive pulse associated with the Moho at all backazimuths, generally around 35 km depth. There is a large amount of positive energy in the crustal portion of the receiver function (usually at ~15 km depth), with minimal negative arrivals. The positive Moho pulse at station MEEK is also generally consistent across backazimuths (between 30 and 35 km), with some variations in pulse shape and amplitude. Like station KMBL, there is significant positive energy at most backazimuths near 15 km depth but few negative arrivals.

Overall, our results show clear Moho arrivals, possible crustal structure such as sediment-basement contacts or low-velocity zones, and some polarity flips above the Moho. As polarity flips are indicative of either dipping layers or anisotropy, this suggests the presence of one or both within the crust. However, we do not observe the two-lobe or four-lobe patterns on the transverse component receiver functions as predicted by modelling (Levin and Park, 1997; Ford et al., 2016; Park and Levin, 2016).

3.4.2 Mantle structure

As stated above, the presence of energy and polarity flips on the transverse component of receiver functions is often interpreted as being due to seismic anisotropy: our receiver functions do have significant energy below the Moho, but it is often difficult to interpret and does not follow predicted patterns of simple two-lobe or four-lobe polarity flips (e.g., Ford et al., 2016).

At station MEEK, we observe several possible polarity flips on the transverse component: first at roughly 80 km depth, then at 120 km depth, and finally at 180 km depth. Birkey et al. (2021) found two significant negative phases at station MEEK using Sp receiver functions: one at 80 km (interpreted to be a mid-lithospheric discontinuity) and one at 129 km (interpreted to be the lithosphere-asthenosphere boundary). All the Ps polarity flips appear to occur over 10s of kilometers. At station KMBL there are several gaps in backazimuthal coverage: between 200° and 240° and between 250° and 300°. These gaps make observations of polarity flips more difficult, but there do appear to be flips at 80 km, 100 km, and

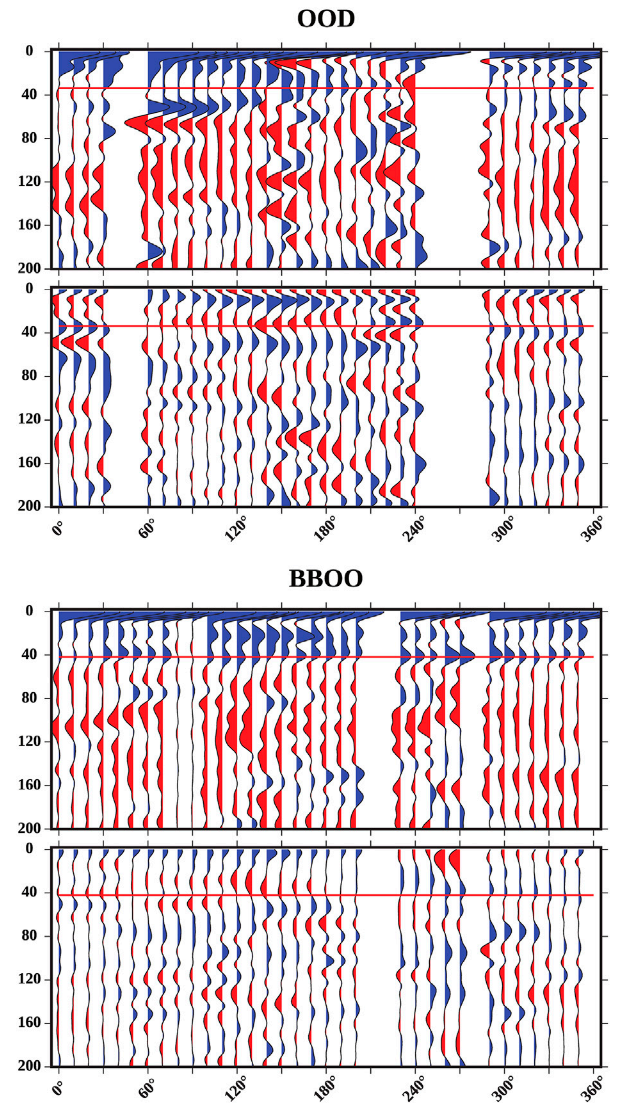

FIGURE 9
Backazimuthally-binned Ps receiver functions from the South Australian Craton (SAC). Features the same as in Figure 7.

160 km. As with station MEEK, these are very gradual, with pulses that extend over 10s of kilometers in depth. Previous studies reported negative phases at 79 km and 113 km, both interpreted to be mid-lithospheric discontinuities (Birkey et al., 2021). Station WRAB has polarity flips at 60 km, 100 km, 140 km, and 180 km. Mid-lithospheric discontinuities were reported at 71, 91, 135, and 198 km (Birkey et al., 2021). We display receiver functions as rose diagrams for all nine stations in Figure 11, ranging from 0 to 200 km depth. Significant complexity is present at most stations.

Our receiver functions indicate complex structure within the Australian lithosphere, as we see significant energy on transverse components with some polarity flips. However, our observed polarity flips are generally not consistent with predicted two-lobe or four-lobe patterns that a sharp boundary in seismic anisotropy would create (e.g., Levin and Park, 1997; Ford et al., 2016; Park and Levin, 2016). Due to the complexity of our results, we cannot easily generate comparative forward models, which would be necessary to infer orientations of seismic anisotropic layering in the mantle. Importantly, we note that we observe polarity flips at several stations (MEEK, KMBL, and WRAB) roughly corresponding to the same depths where Birkey et al. (2021) observed statistically significant negative phases on Sp receiver functions. Correspondence between both sets of receiver functions may indicate that MLDs at least partially arise from the presence of anisotropy at depth. Therefore, the summarizing result of our Ps receiver function analysis is that while anisotropic layering is present, it cannot provide us with unique insight into the orientation of such structures within the Australian lithosphere.

4 Discussion

For clarity, we begin our discussion with a summary of results. Station-averaged shear wave splitting fast direction mostly trend N-S,

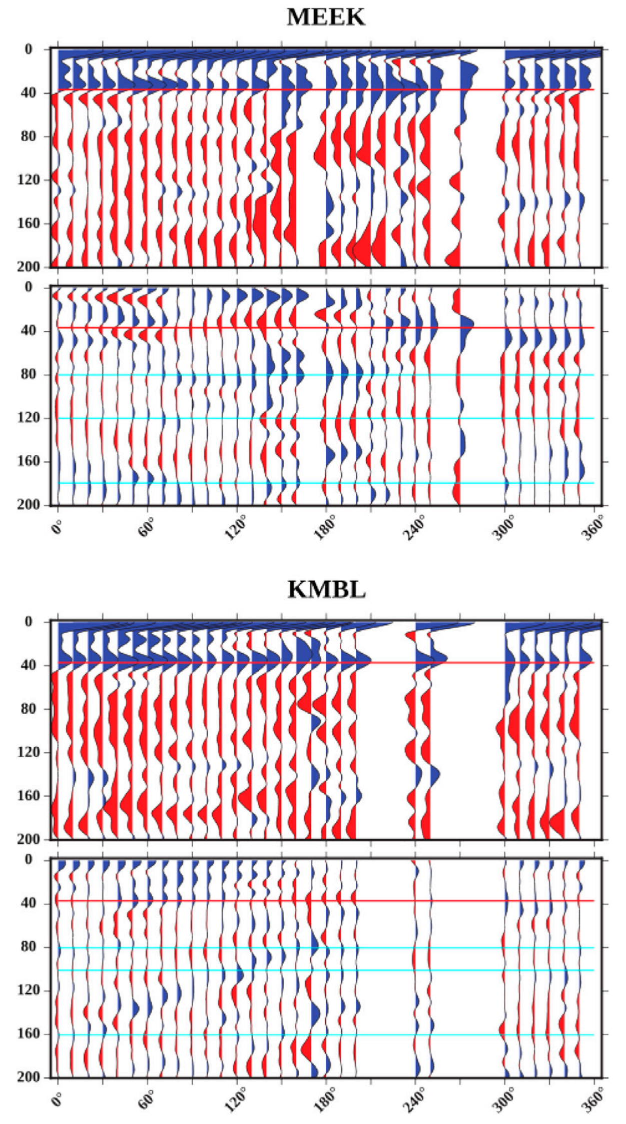

FIGURE 10
Backazimuthally-binned Ps receiver functions from the West Australian Craton (WAC). Cyan lines indicate depths of potential polarity flips, as mentioned in the text. All other features the same as in Figure 7.

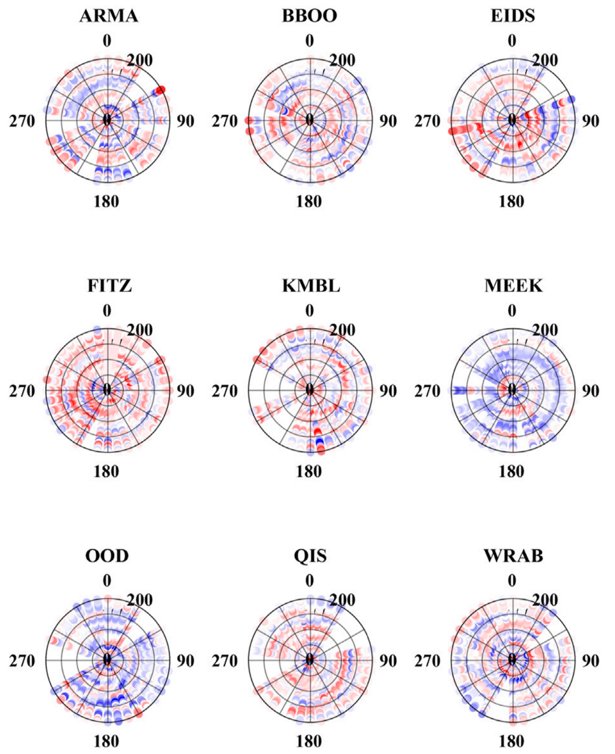

FIGURE 11
Rose diagrams of transverse-component Ps receiver functions, showing backazimuth along the circumference of circles and the depth of the phase increasing from zero at the center to 200 km at the edge. Each dot is color-coded according to the amplitude of the receiver function (blue indicates a positive phase, while red indicates a negative phase).

which is not generally correlated with surface features but does agree well with plate motion (though this is likely due to averaging of disparate results, not anisotropy dominated by shear at the base of the plate). Average delay times for stations across the continent are close to 0.6 s. Individual splits show a clear variation in fast direction and delay time with backazimuth in all regions, which is often seen as diagnostic of complex anisotropy. We also test whether these variations with backazimuth are due to systematic misorientation from the rotation correlation method: this seems to be the case for 13 out of 29 modelled stations. Ps receiver functions show evidence for possible crustal layering and anisotropy (as indicated by polarity flips on the transverse component); they additionally have significant energy at mantle depths with potential polarity flips, though these do not perfectly follow predicted two- or four-lobed patterns. Finally, some of these polarity flips occur at the same depths as mid-lithospheric discontinuities reported in Birkey et al. (2021).

4.1 Comparison of our results to previous shear wave splitting studies

There have been numerous previous studies that have examined the structure of the Australian continent in terms of seismic properties, including anisotropy, and other geophysical constraints (e.g., Debayle and Kennett, 2000; Heintz and Kennett, 2005; Fishwick and Reading, 2008; Ford et al., 2010; Saygin and Kennett, 2012; Wang et al., 2014; Yoshizawa and Kennett, 2015; Tesauro et al., 2020). Seismic anisotropic studies have included continental and regional shear wave splitting analysis (Clitheroe and Van der Hilst, 1998; Özalbey and Chen, 1999; Heintz and Kennett, 2005; Heintz and Kennett, 2006; Bello et al., 2019; Chen et al., 2021a; Eakin et al., 2021), and continental tomographic studies (Debayle, 1999; Debayle and Kennett, 2000; Simons et al., 2002; Debayle et al., 2005; Fishwick and Reading, 2008; Yoshizawa and Kennett, 2015). In this section we primarily focus on comparing our results to other shear wave splitting studies. In Section 4.2. we focus on comparing our shear wave splitting results to constraints from tomography and in Section 4.3. we focus on comparing our receiver function results to relevant studies. Individual and averaged splits are compared to previously published splits in Supplementary Figures S22, 23.

Eakin et al. (2021) examined shear wave splitting through central Australia, including three permanent stations that were also used in this study (stations AS31, MULG, and WRAB). That study found a significant number of null events (consistent with other studies of the Australian continent), average fast directions that paralleled topography, gravity, and magnetic trends with a transition from the Proterozoic orogens in central Australia into the North Australian Craton. They argue that their results indicate fossilized seismic anisotropy within the lithosphere, rather than from the asthenosphere (i.e., plate motion shear). While our average splits from vary significantly from those reported in Eakin et al. (2021), fast directions that were modeled to account for misorientation due to the rotation correlation method are in better agreement. However, their results are reported from the minimum energy method and included PKS phases as well, which may help to explain the discrepancies. They report an average fast direction of 72° at AS31, while our modeled fast direction was 79°. At station MULG; Eakin et al. (2021) found an average fast direction of 75°—our modeled fast direction was 92°, with five splits within 10° of their average. For station WRAB, we report a modeled fast direction of -58°, and seven splits within 10° of the -17° reported by Eakin et al. (2021). While ray paths for PKS and SK(K)S phases are nearly identical in the upper mantle, different epicentral distance ranges are used for each phase to prevent phase contamination: this may result in differences in splitting parameters, especially if there are lower mantle contributions (see Section 4.2). Additionally, very few of the events analyzed were the same between Eakin et al. (2021) and this study. However, we did identify some events in common: six at station AS31, two at station MULG, and two at station WRAB (compared in Table 3). We compare their reported minimum energy splits to our rotation correlation splits and the values we obtained from the minimum energy method. Of the 10 splits in common, seven have comparable values (four at AS31, one at station MULG, and two at station WRAB).

A recent study of seismic anisotropy in the Yilgarn Craton (Chen et al., 2021a) used four of the same stations as used in this study (KMBL, MEEK, MORW, and MUN). We had two additional stations within the Yilgarn: BLDU and NWAO, both roughly in line with stations MORW and MUN along the western margin of the craton. Other than KBML, our modeled fast directions are within 20° of average fast directions reported by Chen et al. (2021a), though our averages do not match theirs as well. Disagreement between the two studies could be a result of variations in methodology or events chosen, or the phases used for splitting—Chen et al. (2021a) includes PKS, SKS, SKKS, and SKiKS phases, while this study has

TABLE 3 Comparison of splits calculated by both this study and Eakin et al. (2021). We display the fast direction ϕ) and delay time (dt) for both the minimum energy method (SC) and the rotation correlation method (RC).

AS31						
Ev. Lat	Ev. Ion	Backazirnuth	Phi (SC)	Phi (RC)	dt (SC)	dt (RC)
-55.52°	-28.26°	190.18°	66.13°		0.55 s	
-55.50°	-2,830°	190.20°	88.20°	51.20°	1.10 s	0.40 s
-56.20°	-26 89°	190.72°	6,072°		0.75 s	
-56.20°	-26.90°	190.70°	58.70°	59.70″	0.70 s	0.70 s
-22 68°	25 16°	241 75°	-76.75°		1 30 s	
-22.70°	25.20°	24,130°	87.70°	80.70′	0.70 s	0.80 S
-36.12°	-101 .0222°	137.53°	71.53°		0.70 s	
-36.10°	-101.10°	137.50°	-86.50°	82.50°	0.60 s	0.60 s
-55.92°	-27 86°	190 23°	66.28°		055 s	
-55.90°	-27.90°	190.30°	68.30°	59.30°	0.70 s	0.60 s
-60.21°	-26.53°	189.66°	81.66°		1.35 s	
-6,020°	-26.60°	189.60°	85.60°	55.60°	1.70 s	0.70 s
MULG						
Ev. Lat	Ev. Ion	Backazimoth	Phi (SC)	Phi (RC)	dt (SC)	dt (RC)
-56.20°	-26.89°	190.52°	80.52°		1.50 s	
-56.20°	-26.90°	190.50°	82.50°	78.50°	2.00 s	1.80 s
-55.69°	-26.30°	190.99°	88.99°		2.35 s	
-55.70°	-26.20°	191.00°	-89.00°	46.00°	3.60 S	0.60 s
WRAB						
Ev. Lat	Ex. Ion	Backazimoth	Phi (SC)	Phi (RC)	dt (SC)	A (s)t (RC)
s)59.03°	-155.12°	29.44°	-24.56°		0.70	
59.00°	-155.10°	29.50°	-26.50°	-18.50°	0.70	0.70
54.58°	-161.77°	31.53°	-24.47°		0.05	
54.50°	-161.70°	31.60°	5.60°	-22.40	1.10	0.70

mostly SKS and SKKS phases. Modeled delay times are in closer agreement: our delay times range from 0.6 s at station BLDU and MUN to 0.9 s at stations KMBL; Chen et al. (2021a) has a similar range, with 0.5 s at station MUN (south of station BLDU) and 0.7 s at station KMBL. Both studies also suggest general disagreement between plate motion and average fast directions. Despite slight differences, the overall conclusion reached by Chen et al. (2021a) is supported by this study: seismic anisotropy is relatively weak but complex in the Yilgarn Craton, in stark contrast to the exceptionally fast plate motion with strong alignment of asthenospheric seismic anisotropy (Debayle et al., 2005).

Our results are not in good agreement with a previous study examining the structure of southeast Australia (Bello et al., 2019). Both studies report complex splitting parameters that frequently do not mirror plate motion. For all four stations used in both studies (CAN, CNB, TOO, and YNG), our average delay times were significantly lower (1.0 s or less at all stations), whereas Bello et al. (2019) estimate average delay times of greater than 1.0 s. Additionally, fast directions are significantly different at all stations. Bello et al. (2019) used a method similar to the eigenvalue method laid out in Silver and Chan (1991) and also deployed a weighted averaging scheme: this contrasts with our use of the rotation correlation method and no weighting in our averages, which may explain some of the differences.

The differences between our results and those of the other studies indicates the need for a careful analysis of the methodological and data differences in shear wave splitting analysis, particularly in regions such as Australia where seismic anisotropy is vertically stratified and laterally complex. Such complexities are supported by our analysis, specifically at those stations where modelling does not match well with observed fast directions and delay times, and echo the findings of previous studies (e.g., Clitheroe and Van der Hilst, 1998; Heintz and Kennett, 2005). In the remaining sections, we compare our splitting results to constraints from receiver functions and tomography.

4.2 Constraining depth-dependent seismic anisotropy

Shear wave splitting is a path-integrated effect from the core-mantle boundary to the surface, thus it cannot provide firm depth constraints without modeling. However, surface waves are sensitive to changes in seismic anisotropy with depth, thus surface wave tomography can help to provide a lens through which we may be able to better understand our splitting results. A recent global tomography model (Debayle et al., 2016) includes an anisotropic component, which indicates clear changes in anisotropy at short lateral scales, and changes with depth similar to previous tomographic models that indicated a transition from complex anisotropy above 150 km depth to plate motion parallel anisotropy below that (e.g., Debayle et al., 2005; Fishwick and Reading, 2008). Of the 13 stations well modeled by a single layer of anisotropy, seven are within 20° of an E-W orientation, roughly in line with what tomography has indicated. The remaining five and the 16 that cannot be modeled require another explanation such as contributions from multiple layers of anisotropy. We examine other potential causes in Section 4.5.

While we did calculate effective splitting parameters in MSAT (Walker and Wookey, 2012) for a four-layer model using values from the model of Debayle et al. (2016), we determined that, because 45% of stations were well fit by a single layer of anisotropy and the remaining stations were backazimuthally limited, additional complexity was not required and did not warrant comparison to Debayle et al. (2016). This agrees with Eakin et al. (2021), who produced several two-layer models and argued that these models did not fit their results and were not strictly preferred over a one-layer model (wherein seismic anisotropy is present solely in the lithosphere).

One potential explanation for the observed discrepancies in the modeled *versus* calculated splitting results may come from seismic anisotropy in the lowermost mantle. Contributions to shear wave splitting are assumed to be predominantly within the upper mantle. However, previous studies have indicated the possibility of lowermost mantle seismic anisotropy as a contribution to Australian shear wave splitting results. Özalbey and Chen, 1999 found anomalous waveforms on transverse component seismograms that did not match the predicted shape for upper mantle shear wave splitting (the time-derivative of the radial component), arguing that these anomalous waveforms were likely due to the presence of heterogeneities within the lowermost mantle. More recent studies have also documented lowermost mantle contributions to shear wave splitting across the globe including Africa (Lynner and Long, 2014; Ford et al., 2015), Australia (Creasy et al., 2017), Eurasia (Long and Lynner, 2015); Iceland (Wolf et al., 2019), North America (Lutz et al., 2020). While these studies show a clear presence of seismic anisotropy within the lowermost mantle, results are often heterogeneous and indicate complex seismic anisotropy. Furthermore, constraints on both dominant slip systems and the mechanism of deformation responsible for development of fabric are poorly constrained. In Supplementary Figures S24, we plot our splits at a depth of 2,700 km against the GyPSuM tomography model (Simmons et al., 2010) for the same depth. Splitting parameters exhibit significant heterogeneity across the region, sampling the lowermost mantle over a region of roughly 60° of latitude and 50° of longitude. As such, it is possible that the lowermost mantle has some contribution to our observations of shear wave splitting. Furthermore, while different phases (i.e., SKS, SKKS, and PKS) have very similar paths in the upper mantle, paths diverge significantly in the lowermost mantle: thus, variations in studies may arise as a result of different phases used, especially if seismic anisotropy in the lowermost mantle has a significant contribution. Phases sampling the lowermost mantle coupled with complex upper mantle seismic anisotropy implies that our results are difficult to model or directly interpret without first concretely identifying contributions from each region, which is beyond the scope of the present study.

4.3 Comparison of receiver functions to previous studies

Our Ps receiver functions indicate complex, heterogeneous structure below the Moho. Additionally, we see gradual changes in polarity (i.e., a shift from a positive to a negative pulse) on backazimuthally-binned transverse component receiver functions. In an isotropic, horizontally stratified system, no energy should be present on the transverse component: thus, the presence of such energy (and more specifically polarity changes of said energy) is diagnostic of either anisotropy or dipping layers. Figures 7–10 show these gradual polarity changes; Chen et al. (2021b) examined four stations (KMBL, MEEK, MORW, and MUN) in the Yilgarn craton and performed a harmonic decomposition to constrain anisotropic structure; this method performs a linear regression to constrain polarity flips and divides the receiver function into a combination of sine and cosine terms (Shiomi and Park, 2008). They report clear evidence for two layers of seismic anisotropy at three of these stations (KMBL, MORW, and MUN). At KMBL, Chen et al. (2021b) report three prominent phases potentially associated with dipping structure or seismic anisotropy: at 58, 87, 101 km. At MEEK, they report prominent phases at 74 and 94 km. While Chen et al. (2021b) utilized harmonic decomposition to analyze their receiver functions, rose diagrams can be used to provide a visual representation of similar trends such as seismic anisotropy or dipping layers (Ford et al., 2016; Park and Levin, 2016). In Figure 12, we plot rose diagrams for both stations at corresponding depths: 60, 90, and 100 km ±5 km for KMBL; 75 and 95 km ±5 km for MEEK. While there are polarity flips at station KMBL, these do not match simple two or four-lobed patterns. For station MEEK, polarity flips are much clearer, particularly at 75 km—this matches well with a two-lobed pattern; Chen et al. (2021b) report a dominant contribution to modelled energy from a two-lobed pattern.

Because receiver functions are sensitive to sharp boundaries, we utilize variations in fast directions with depth from Debayle et al. (2016) to isolate potential depths at which polarity flips on the transverse component of receiver functions might be expected. At station ARMA, there is a single large change in modelled fast direction between 150 km (-89.94°) and 175 km (60.42°). We observe some evidence of a change in polarity at these depths, but these changes are subtle; additionally, this is beneath the predicted depth of the lithosphere-asthenosphere boundary along the eastern margin of the continent. Station BBOO also only has one large change in fast direction, between 70 km (-88.50°) and 90 km (-52.27°) according to Debayle et al. (2016). There are some slight changes in polarity between these two depths in our receiver function results, most consistent with a two-lobed pattern. At station EIDS, there are no large changes in tomographically inferred fast direction within lithospheric depth bounds; while our receiver function results for the station does have some polarity flips, these are not consistent and do not match predicted two-lobed or four-lobed behavior. Tomographically modeled fast directions for station FITZ show a continuous decrease from close to 90° near the surface to a more N-S orientation closer to plate motion at depth; polarity flips are isolated at station FITZ and do

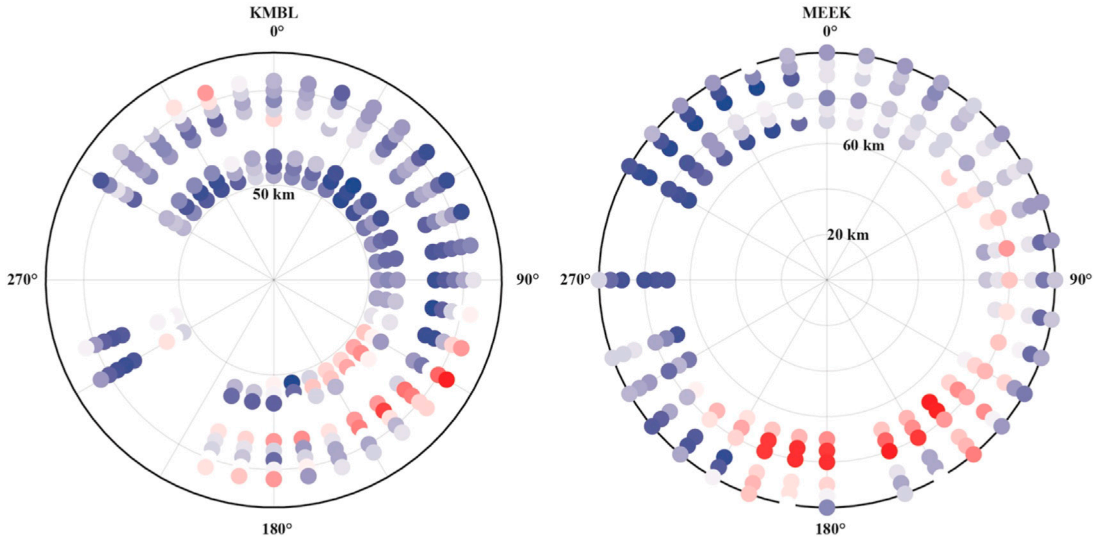

FIGURE 12
Rose diagrams of transverse-component Ps receiver functions for stations used in Chen et al. (2021b) at the depths where their harmonic decomposition indicated polarity changes. Depth increases from zero at the center to 200 km at the edge.

not indicate seismic anisotropy. At station KMBL, the model of Debayle et al. (2016) shows only one large jump in fast direction from -23.30° at 70 km to 35.70° at 90 km—our receiver functions for station KMBL do not show corresponding polarity flips. Station MEEK shows modelled fast directions that are roughly consistent at all depths, yet our receiver functions show a two-lobed polarity flip around 80 km. Between 100 km and 125 km, there is a shift in modelled fast direction (56.60°–18.37°) at station OOD. The transverse component receiver function for station OOD does have complex changes in polarity between these two depths, but the pattern is not an obvious two or four-lobed one. Finally, at station WRAB there is also a change in fast direction between 100 km (-57.80°) and 125 km (13.51°); however, while there are polarity flips on the receiver function, they are complex and do not match predicted patterns associated with seismic anisotropy. It is important to note that these comparisons are not direct ones: while receiver functions and surface wave tomography both provide good depth resolution, receiver functions are sensitive to sharp boundaries whereas tomography characterizes changes in volumetric properties. Thus, a lack of explicit agreement between the two methods does not indicate a lack of seismic anisotropy but rather a combination of gradually changing seismic anisotropy constrained by tomography, with fine scale layering of seismic anisotropy imaged by receiver functions.

4.4 Implications for the nature of the Australian lithosphere

Previous geophysical studies have made clear that the Australian continent has a complex lithospheric structure, with variations in the thickness of the lithosphere and its internal properties. Regional tomography models indicate some broad trends within the continent, such as thicker lithosphere with faster wavespeeds in cratonic Australia and thinner lithosphere with slower wavespeeds along the eastern margin (Kennett et al., 2012). Additionally, the lithosphere appears to increase in thickness in a stepwise fashion westward from the Phanerozoic eastern margin. While the lithosphere is generally thicker in the western two-thirds of the continent, there are still significant variations in the depth of the lithosphere-asthenosphere boundary determined from tomography (Kennett et al., 2012). Topography of the lithosphere-asthenosphere boundary may result in complex mantle flow patterns and edge convection, which would produce its own anisotropic signature (e.g., Chen et al., 2021a; Eakin et al., 2021). Global models show the same broad features in Australia (e.g., Debayle et al., 2016).

While the lithosphere-asthenosphere boundary is generally thought of as step-like change in physical properties, some studies have referred to it instead as the lithosphere-asthenosphere transition because (especially in cratons) it is often not a discrete boundary (Mancinelli et al., 2017). One recent study (Yoshizawa and Kennett, 2015) utilized tomography to examine both the lithosphere-asthenosphere transition and radial seismic anisotropy within the Australian upper mantle. This transition occurs at different depths and has variable thickness across the continent: it is thickest and deepest in central Australia in the Proterozoic sutures between cratons; along the eastern margin of the continent the lithosphere-asthenosphere transition is shallower. Trends in radial seismic anisotropy are similar, with the strongest radial seismic anisotropy in the sutures between cratons, decreases in radial seismic anisotropy from the base of the crust to mid-lithospheric depths in the cratons, and strong radial seismic anisotropy in the asthenosphere along the eastern margin. Global models of azimuthal seismic anisotropy (e.g., Debayle et al., 2016) do show variations in seismic anisotropy with depth and across the continent, though these do not mirror major surficial boundaries. Additional constraints on anisotropy come from Quasi-Love wave scattering (Eakin et al., 2021), which indicates anisotropy in Australia is complex and spatially heterogeneous. This scattering is largely in agreement with previous studies indicating anisotropy within Australia is likely fossilized in the lithosphere and linked to the continent's long tectonic history.

As noted in Section 3.3.2, several of our Ps receiver functions have polarity flips at roughly the same depths as mid-lithospheric discontinuities reported previously (Ford et al., 2010; Birkey et al., 2021). Mid-lithospheric discontinuities seem to be a near-ubiquitous feature of cratonic lithosphere, but their origin is still somewhat unclear. The most common explanations include the presence of current or solidified partial melt, hydrous minerals such as phlogopite, or seismic anisotropy (Selway et al., 2015; Aulbach et al., 2017). Birkey et al. (2021) argue that the most likely explanation for mid-lithospheric discontinuities in Australia is the presence of ancient hydrous minerals; however, they do not rule out the possibility that seismic anisotropy could contribute to the decrease in velocity associated with negative phases observed at mid-lithospheric depths. The polarity flips that we observe occur over 10s of km, which suggests either a thicker layer of seismic anisotropy or a more gradual transition from one fast direction orientation to another. Thus, seismic anisotropy seems likely to not be the sole cause of observed mid-lithospheric discontinuities, although it may provide a contribution, similar to an argument put forward by Ford et al. (2016) for the Wyoming and Superior Cratons. However, it is clear from both this study and previous ones that the Australian lithosphere is anisotropic; such seismic anisotropy must be fossilized within the lithosphere, as there are no obvious explanations for ongoing fabric formation in the lithosphere today. This argument is bolstered by the disagreement between absolute plate motion and the average fast direction of most cratonic stations (except for AS31, MORW, MUN, and WRKA; though an examination of individuals splits makes clear that these stations have significant backazimuthal variability that cannot be explained by plate motion).

In addition to the macroscopic alignment of intrinsically seismically anisotropic minerals, the layering of media with different material properties can also produce seismic anisotropy. Earthquakes originating from Australia have complex high-frequency body-wave codas; Kennett et al. (2017) argue that this is due to multi-scale heterogeneity (i.e., layering occurs at multiple scales). Such heterogeneity could contribute to the complex splitting patterns that are observed in Australia and could be linked to the formation and evolution of the lithosphere.

4.5 Relating observed seismic anisotropy to geologic structure

Simple interpretations of the seismic anisotropy present within the Australian lithosphere are difficult, and readers should be cautious of shear wave splitting results for two primary reasons. First, as noted in this study, there are discrepancies between various published shear wave splitting studies for Australia. As noted above, there are some differences in phases used and methodology: we report our results from the rotation correlation method, which has been shown to have a systematic 45° misorientation in fast direction for near-null backazimuths (Wüstefeld and Bokelmann, 2007; Eakin et al., 2019). Modeling of this sawtooth pattern does resolve some differences, but others remain, underscoring the complexity of seismic anisotropy in the region. Second, contributions to shear wave splitting from the lowermost mantle cannot be ruled out, implying that observed fast directions may be the result of splitting throughout the mantle. This second point is an emerging issue in the calculation of shear wave splitting globally.

Caveats aside, this last section focuses on comparing shear wave splitting and receiver function results from a selected number of stations to the observed geology and inferred tectonic history of the Australian continent. Importantly, while seismic anisotropy can be correlated to specific processes in regions of active tectonism, this is less intuitive for cratons as there may be multiple layers of anisotropy that result in a complex signal not easily linked to specific events. As noted elsewhere, previous studies have indicated the presence of multiple layers of seismic anisotropy within the Australian lithosphere (e.g., Simons et al., 2002). Multiple layers of anisotropy may be a good candidate explanation for many of our results, though there is no apparent reason for the lithosphere of the entire continent to have a roughly consistent fast direction. Additionally, many tectonic events in the Precambrian are poorly constrained, making it difficult to definitively argue for any one cause of the anisotropy we observe (e.g., Chen et al., 2021a).

4.5.1 North Australian Craton

For station COEN (in the Coen Inlier), we report an average fast direction of -28.7°, which deviates from the more N-S direction of plate motion. However, there is evidence for NNW-SSE directed shortening at ~1.65 Ga (Cihan et al., 2006), which could explain our results. Most individual splits are roughly parallel to the predicted direction of shortening, except for a few results that are almost perpendicular (these come from a limited backazimuthal range, however).

At station FITZ, our average fast direction is 62.7°, with individual splits roughly oriented the same direction. These measurements are subparallel to stress orientations in that part of the NAC (the Canning Basin; Bailey et al., 2021)—some studies have indicated a link between presently measured stress and anisotropy; however, we note that stress here is determined from borehole measurements, which only sample the shallow crust. While this region has relatively thick sedimentary cover (several kilometers in some spots), it is not likely that crustal anisotropy alone would be enough to produce the strength of splitting we observe here. We do note, however, that transverse component receiver functions exhibit some polarity flips above the Moho (at ~20 km for instance), which may indicate a crustal contribution to anisotropy.

Stations KDU and MTN are both in the Pine Creek Inlier and have similar average fast directions (32.5° and 18.5°, respectively). Near MTN, there are several faults with strikes subparallel to its average fast direction (Needham et al., 1988). There is some evidence from ocean basins that faults can induce seismic anisotropy parallel to their strike (Faccenda et al., 2008), but this may not be directly applicable to continental settings given the thicker crust and mantle lithosphere. Additionally, individual splitting measurements at MTN vary quite a bit, so while the average fast direction mirrors the strike of local faults, this may not be the cause of the anisotropy. KDU is farther from these faults and is well modeled by a single layer of anisotropy oriented at 71°, implying that anisotropy there cannot be explained by faulting.

KNRA may be the strongest candidate for a station with anisotropy that is well explained by tectonic history. Its modeled fast direction (38°) is similar to the strike of the Halls Creek Orogen (though the station is north of known exposures), and there is evidence for west-dipping subduction in the Proterozoic (Sheppard et al., 1999); fast directions are expected to be trench parallel in such settings, which may explain the average fast direction we report. Individual fast directions do have more variability but are in general similar to the strike of the Halls Creek Orogen.

The average fast direction at WRAB deviates slightly from the trend of the Tenant Creek Inlier. However, one grouping of individual fast directions does mirror the trend, similar to what Eakin et al. (2021) reported; there is another that is roughly perpendicular to that first group. Transverse component receiver functions show some possible polarity flips at lithospheric mantle depths for WRAB, though as noted elsewhere these are not easily modelled. This may indicate complex seismic anisotropy at depth that contributes to the variations in fast direction.

4.5.2 South Australian Craton

We do not find compelling evidence that our results are well explained by surface geologic features, which is not surprising given the Archean age of parts of the craton. Averaged splits at seven stations trend NE-SW, which does not mirror the boundaries of the SAC or any of its components—the one exception being at station FORT where the average fast direction does trend similar to the boundary between the SAC and the Albany-Fraser Orogen to its west and may be explained by compression during Orogenesis.

4.5.3 West Australian Craton

One important feature of the WAC is that some tomographic studies have imaged slightly thinner lithosphere along the western margins of the craton than other portions of cratonic Australia (e.g. Yoshizawa and Kennett, 2015). This is corroborated by Birkey et al. (2021), who saw evidence for the lithosphere-asthenosphere boundary along the western margin of the continent. If the western margin is indeed thinner than central Australia, this could produce edge-driven convection. In turn, this would result in the development of new seismically anisotropic fabrics that may contribute to the shear wave splitting we observe. As many of the stations in the WAC exhibit complex splitting behavior, multiple contributions to the signal are not unexpected. One station that may have a tectonic explanation for its anisotropic signal is MEEK, with a modeled fast direction of 87°. This is roughly parallel to the Capricorn Orogen to its north.

4.5.4 Phanerozoic Australia

Many of the stations in Phanerozoic Australia have average fast directions close to plate motion (roughly N-S), which may be expected for thinner lithosphere with an anisotropic signal dominated by shear at the base of the plate. Two clear exceptions to this are EIDS and TOO, though this seems likely to be a result of more splits coming from backazimuths with fast directions that differ from APM as there are splits at each station that do match APM.

Stations CAN, CNB, and YNG are all in the Lachlan Orogen, with average fast directions that are roughly parallel to geologic features of the orogen in that region as well APM. However, individual splitting measurements vary significantly by backazimuth, with few mirroring plate motion. A previous receiver function study (Girardin and Farra, 1998) did find two layers of anisotropy beneath CAN: an upper layer oriented E-W (possibly linked to E-W extension), and a lower layer oriented N-S (most likely linked to plate motion). This layered anisotropy could explain the results that we observe at all three stations.

5 Conclusion

We present shear wave splitting and Ps receiver function results from permanent stations across the Australian continent. Importantly, both methods indicate that anisotropy within the Australian lithosphere is complex. While average fast directions are similar to absolute plate motion, there is variability in fast direction with backazimuth (diagnostic of said complexity). Even at stations within Phanerozoic Australia, we observe evidence for complex anisotropy from shear wave splitting, suggesting that in many cases multiple layers of seismic anisotropy may be required. However, shear wave splitting cannot directly provide depth constraints—for this we instead rely on Ps receiver functions. These display some changes in polarity on transverse components over 10s of kilometers, suggesting that any changes in seismic anisotropy do not occur as sharp interfaces. Ps receiver functions presented here are also in agreement with previously published Sp receiver functions across Australia, particularly at mid-lithospheric depths. Though results from both methods warrant caution in interpretation, the ancient lithosphere of the Australian continent likely preserves anisotropic fabric related to its formation and evolution, with minimal contributions from present-day plate motion.

Data availability statement

The original contributions presented in the study are included in the article/Supplementary Material, further inquiries can be directed to the corresponding author.

Author contributions

AB performed analysis, wrote original draft, produced figures, and edited drafts. HAF conceptualized the study, secured funding, and edited drafts.

Acknowledgments

We would like to thank Maureen Long and Megan Anderson for their contribution to the formulation of this project. We also thank three reviewers for their helpful suggestions. All data from the following networks were freely and publicly accessed using the IRIS DMC: AU (DOI https://dx.doi.org/10.26186/144675); G (DOI http://doi.org/10.18715/GEOSCOPE.G); II (DOI https://doi.org/10.7914/SN/II); IU (DOI https://doi.org/10.7914/SN/IU).

Conflict of interest

The authors declare that the research was conducted in the absence of any commercial or financial relationships that could be construed as a potential conflict of interest.

Publisher's note

Supplementary material

The Supplementary Material for this article can be found online at: https://www.frontiersin.org/articles/10.3389/feart.2022.1055480/full#supplementary-material

References

Aulbach, S., Massuyeau, M., and Gaillard, F. (2017). Origins of cratonic mantle discontinuities: A view from petrology, geochemistry and thermodynamic models. *Lithos* 268, 364–382. doi:10.1016/j.lithos.2016.11.004

Ba, K., Gao, S. S., Liu, K. H., Kong, F., and Song, J. (2020). Receiver function imaging of the 410 and 660 km discontinuities beneath the Australian continent. *Geophys. J. Int.* 220 (3), 1481–1490. doi:10.1093/gji/ggz525

Bailey, A. H. E., Jarrett, A. J. M., Tenthorey, E., and Henson, P. A. (2021). Understanding present-day stress in the onshore Canning Basin of western Australia. *Aust. J. Earth Sci.* 68 (6), 818–838. doi:10.1080/08120099.2021.1879265

Bedrosian, P. A., and Finn, C. A. (2021). When Wyoming became superior: Oblique convergence along the southern trans-hudson orogen. *Geophys. Res. Lett.* 48 (13), e2021GL092970. doi:10.1029/2021gl092970

Bello, M., Cornwell, D. G., Rawlinson, N., and Reading, A. M. (2019). Insights into the structure and dynamics of the upper mantle beneath Bass Strait, southeast Australia, using shear wave splitting. *Phys. Earth Planet. Interiors* 289, 45–62. doi:10.1016/j.pepi.2019.02.002

Birkey, A., Ford, H. A., Dabney, P., and Goldhagen, G. (2021). The lithospheric architecture of Australia from seismic receiver functions. *J. Geophys. Res. Solid Earth* 126 (4), e2020JB020999. doi:10.1029/2020jb020999

Bostock, M. G. (1997). Anisotropic upper-mantle stratigraphy and architecture of the Slave craton. *Nature* 390 (6658), 392–395. doi:10.1038/37102

Bostock, M. G. (1998). Mantle stratigraphy and evolution of the Slave province. *J. Geophys. Res. Solid Earth* 103 (B9), 21183–21200. doi:10.1029/98jb01069

Bowman, J. R., and Ando, M. (1987). Shear-wave splitting in the upper-mantle wedge above the Tonga subduction zone. *Geophys. J. Int.* 88 (1), 25–41. doi:10.1111/j.1365-246x.1987.tb01367.x

Brownlee, S. J., Schulte Pelkum, V., Raju, A., Mahan, K., Condit, C., and Orlandini, O. F. (2017). Characteristics of deep crustal seismic anisotropy from a compilation of rock elasticity tensors and their expression in receiver functions. *Tectonics* 36 (9), 1835–1857. doi:10.1002/2017tc004625

Chen, X., Levin, V., Yuan, H., Klaser, M., and Li, Y. (2021b). Seismic anisotropic layering in the Yilgarn and Superior cratonic lithosphere. *J. Geophys. Res. Solid Earth* 126 (8), e2020JB021575. doi:10.1029/2020jb021575

Chen, X., Levin, V., and Yuan, H. (2021a). Small shear wave splitting delays suggest weak anisotropy in cratonic mantle lithosphere. *Geophys. Res. Lett.* 48 (16), e2021GL093861. doi:10.1029/2021gl093861

Chen, X., Li, Y., and Levin, V. (2018). Shear wave splitting beneath eastern north American continent: Evidence for a multilayered and laterally variable anisotropic structure. *Geochem. Geophys. Geosystems* 19 (8), 2857–2871. doi:10.1029/2018gc007646

Cihan, M., Evins, P., Lisowiec, N., and Blake, K. (2006). Time constraints on deformation and metamorphism from EPMA dating of monazite in the Proterozoic Robertson River Metamorphics, NE Australia. *Precambrian Res.* 145 (1-2), 1–23. doi:10.1016/j.precamres.2005.11.009

Clarke, G. L., Sun, S. S., and White, R. W. (1995). Grenville-age belts and associated older terranes in Australia and Antarctica. *AGSO J. Aust. Geol. Geophys.* 16 (1), 25–40.

Clitheroe, G., and Van Der Hilst, R. D. (1998). Complex anisotropy in the Australian lithosphere from shear-wave splitting in broad-band SKS records. *Geodyn. Ser.* 26, 73.

Collins, W. J., and Shaw, R. D. (1995). Geochronological constraints on orogenic events in the Arunta inlier: A review. *Precambrian Res.* 71 (1-4), 315–346. doi:10.1016/0301-9268(94)00067-2

Conder, J. A. (2007). Dynamically driven mantle flow and shear wave splitting asymmetry across the EPR, MELT area. *Geophys. Res. Lett.* 34 (16). doi:10.1029/2007gl030832

Coney, P. J., Edwards, A., Hine, R., Morrison, F., and Windrim, D. (1990). The regional tectonics of the Tasman orogenic system, eastern Australia. *J. Struct. Geol.* 12 (5-6), 519–543. doi:10.1016/0191-8141(90)90071-6

Creasy, N., Long, M. D., and Ford, H. A. (2017). Deformation in the lowermost mantle beneath Australia from observations and models of seismic anisotropy. *J. Geophys. Res. Solid Earth* 122 (7), 5243–5267. doi:10.1002/2016jb013901

Debayle, E., Dubuffet, F., and Durand, S. (2016). An automatically updated S-wave model of the upper mantle and the depth extent of azimuthal anisotropy. *Geophys. Res. Lett.* 43 (2), 674–682. doi:10.1002/2015gl067329

Debayle, E., and Kennett, B. L. N. (2000). The Australian continental upper mantle: Structure and deformation inferred from surface waves. *J. Geophys. Res. Solid Earth* 105 (B11), 25423–25450. doi:10.1029/2000jb900212

Debayle, E., Kennett, B., and Priestley, K. (2005). Global azimuthal seismic anisotropy and the unique plate-motion deformation of Australia. *Nature* 433 (7025), 509–512. doi:10.1038/nature03247

Debayle, E. (1999). SV-Wave azimuthal anisotropy in the Australian upper mantle: Preliminary results from automated Rayleigh waveform inversion. *Geophys. J. Int.* 137 (3), 747–754. doi:10.1046/j.1365-246x.1999.00832.x

Deng, J., Long, M. D., Creasy, N., Wagner, L., Beck, S., Zandt, G., et al. (2017). Lowermost mantle anisotropy near the eastern edge of the pacific LLSVP: Constraints from SKS–SKKS splitting intensity measurements. *Geophys. J. Int.* 210 (2), 774–786. doi:10.1093/gji/ggx190

Direen, N. G., and Crawford, A. J. (2003). The tasman line: Where is it, what is it, and is it Australia's rodinian breakup boundary? *Aust. J. Earth Sci.* 50 (4), 491–502. doi:10.1046/j.1440-0952.2003.01005.x

Du Frane, W. L., Roberts, J. J., Toffelmier, D. A., and Tyburczy, J. A. (2005). Anisotropy of electrical conductivity in dry olivine. *Geophys. Res. Lett.* 32 (24), L24315. doi:10.1029/2005gl023879

Eakin, C. M., Flashman, C., and Agrawal, S. (2021). Seismic anisotropy beneath central Australia: A record of ancient lithospheric deformation. *Tectonophysics* 820, 229123. doi:10.1016/j.tecto.2021.229123

Eakin, C. M., and Long, M. D. (2013). Complex anisotropy beneath the Peruvian flat slab from frequency-dependent, multiple-phase shear wave splitting analysis. *J. Geophys. Res. Solid Earth* 118 (9), 4794–4813. doi:10.1002/jgrb.50349

Eakin, C. M., Wirth, E. A., Wallace, A., Ulberg, C. W., Creager, K. C., and Abers, G. A. (2019). SKS splitting beneath Mount St. Helens: Constraints on subslab mantle entrainment. *Geochem. Geophys. Geosystems* 20 (8), 4202–4217. doi:10.1029/2019gc008433

Faccenda, M., Burlini, L., Gerya, T. V., and Mainprice, D. (2008). Fault-induced seismic anisotropy by hydration in subducting oceanic plates. *Nature* 455 (7216), 1097–1100. doi:10.1038/nature07376

Fishwick, S., and Reading, A. M. (2008). Anomalous lithosphere beneath the proterozoic of Western and central Australia: A record of continental collision and intraplate deformation? *Precambrian Res.* 166 (1-4), 111–121. doi:10.1016/j.precamres.2007.04.026

Ford, H. A., Fischer, K. M., Abt, D. L., Rychert, C. A., and Elkins-Tanton, L. T. (2010). The lithosphere–asthenosphere boundary and cratonic lithospheric layering beneath Australia from Sp wave imaging. *Earth Planet. Sci. Lett.* 300 (3-4), 299–310. doi:10.1016/j.epsl.2010.10.007

Ford, H. A., Long, M. D., He, X., and Lynner, C. (2015). Lowermost mantle flow at the eastern edge of the african large low shear velocity province. *Earth Planet. Sci. Lett.* 420, 12–22. doi:10.1016/j.epsl.2015.03.029

Ford, H. A., Long, M. D., and Wirth, E. A. (2016). Midlithospheric discontinuities and complex anisotropic layering in the mantle lithosphere beneath the Wyoming and Superior Provinces. *J. Geophys. Res. Solid Earth* 121 (9), 6675–6697. doi:10.1002/2016jb012978

Foster, D. A., and Gray, D. R. (2000). Evolution and structure of the lachlan fold belt (orogen) of eastern Australia. *Annu. Rev. Earth Planet. Sci.* 28 (1), 47–80. doi:10.1146/annurev.earth.28.1.47

Girardin, N., and Farra, V. (1998). Azimuthal anisotropy in the upper mantle from observations ofP-to-S converted phases: Application to southeast Australia. *Geophys. J. Int.* 133, 615–629. doi:10.1046/j.1365-246x.1998.00525.x

Gripp, A. E., and Gordon, R. G. (2002). Young tracks of hotspots and current plate velocities. *Geophys. J. Int.* 150 (2), 321–361. doi:10.1046/j.1365-246x.2002.01627.x

Heintz, M., and Kennett, B. L. (2005). Continental scale shear wave splitting analysis: Investigation of seismic anisotropy underneath the Australian continent. *Earth Planet. Sci. Lett.* 236 (1-2), 106–119. doi:10.1016/j.epsl.2005.05.003

Heintz, M., and Kennett, B. L. (2006). The apparently isotropic Australian upper mantle. *Geophys. Res. Lett.* 33 (15), L15319. doi:10.1029/2006gl026401

Hopper, E., and Fischer, K. M. (2015). The meaning of midlithospheric discontinuities: A case study in the northern us craton. *Geochem. Geophys. Geosystems* 16 (12), 4057–4083. doi:10.1002/2015gc006030

Hopper, E., Fischer, K. M., Wagner, L. S., and Hawman, R. B. (2017). Reconstructing the end of the Appalachian orogeny. *Geology* 45 (1), 15–18. doi:10.1130/g38453.1

Jordan, T. H. (1975). The continental tectosphere. *Rev. Geophys.* 13 (3), 1–12. doi:10.1029/rg013i003p00001

Karato, S. I., Jung, H., Katayama, I., and Skemer, P. (2008). Geodynamic significance of seismic anisotropy of the upper mantle: New insights from laboratory studies. *Annu. Rev. Earth Planet. Sci.* 36 (1), 59–95. doi:10.1146/annurev.earth.36.031207.124120

Kennett, B. L., Fichtner, A., Fishwick, S., and Yoshizawa, K. (2013). Australian seismological reference model (AuSREM): Mantle component. *Geophys. J. Int.* 192 (2), 871–887. doi:10.1093/gji/ggs065

Kennett, B. L. N., and Abdullah, A. (2011). Seismic wave attenuation beneath the Australasian region. *Aust. J. Earth Sci.* 58 (3), 285–295. doi:10.1080/08120099.2011.550318

Kennett, B. L. N., and Salmon, M. (2012). AuSREM: Australian seismological reference model. *Aust. J. Earth Sci.* 59 (8), 1091–1103. doi:10.1080/08120099.2012.736406

Kennett, B. L. N., Salmon, M., Saygin, E., and Group, A. W. (2012). AusMoho: The variation of Moho depth in Australia. *Geophys. J. Int.* 187 (2), 946–958. doi:10.1111/j.1365-246x.2011.05194.x

Kennett, B. L. N., Yoshizawa, K., and Furumura, T. (2017). Interactions of multi-scale heterogeneity in the lithosphere: Australia. *Tectonophysics* 717, 193–213. doi:10.1016/j.tecto.2017.07.009

Kumazawa, M., and Anderson, O. L. (1969). Elastic moduli, pressure derivatives, and temperature derivatives of single-crystal olivine and single-crystal forsterite. *J. Geophys. Res.* 74 (25), 5961–5972. doi:10.1029/jb074i025p05961

Laske, G., Masters, G., Ma, Z., and Pasyanos, M. (2013). Update on CRUST1. 0—a 1-degree global model of Earth's crust. *Geophys. Res. Abstr.* 15, 2658.

Levin, V., and Park, J. (1997). P-SH conversions in a flat-layered medium with anisotropy of arbitrary orientation. *Geophys. J. Int.* 131 (2), 253–266. doi:10.1111/j.1365-246x.1997.tb01220.x

Li, Z. X. (2000). Palaeomagnetic evidence for unification of the North and West Australian cratons by ca. 1.7 Ga: New results from the kimberley basin of northwestern Australia. *Geophys. J. Int.* 142 (1), 173–180. doi:10.1046/j.1365-246x.2000.00143.x

Liu, G., Persaud, P., and Clayton, R. W. (2018). Structure of the northern Los Angeles basins revealed in teleseismic receiver functions from short-term nodal seismic arrays. *Seismol. Res. Lett.* 89 (5), 1680–1689. doi:10.1785/0220180071

Long, M. D., Ford, H. A., Abrahams, L., and Wirth, E. A. (2017). The seismic signature of lithospheric deformation beneath eastern North America due to Grenville and Appalachian orogenesis. *Lithosphere* 9 (6), 987–1001. doi:10.1130/l660.1

Long, M. D., and Lynner, C. (2015). Seismic anisotropy in the lowermost mantle near the Perm Anomaly. *Geophys. Res. Lett.* 42 (17), 7073–7080. doi:10.1002/2015gl065506

Long, M. D., and Silver, P. G. (2008). The subduction zone flow field from seismic anisotropy: A global view. *science* 319 (5861), 315–318. doi:10.1126/science.1150809

Lutz, K. A., Long, M. D., Creasy, N., and Deng, J. (2020). Seismic anisotropy in the lowermost mantle beneath North America from SKS-SKKS splitting intensity discrepancies. *Phys. Earth Planet. Interiors* 305, 106504. doi:10.1016/j.pepi.2020.106504

Lynner, C., and Long, M. D. (2014). Lowermost mantle anisotropy and deformation along the boundary of the African LLSVP. *Geophys. Res. Lett.* 41 (10), 3447–3454. doi:10.1002/2014gl059875

Mancinelli, N. J., Fischer, K. M., and Dalton, C. A. (2017). How sharp is the cratonic lithosphere-asthenosphere transition? *Geophys. Res. Lett.* 44 (20), 10,189–10,197. doi:10.1002/2017gl074518

Marshak, S., and Flöttmann, T. (1996). Structure and origin of the fleurieu and nackara arcs in the adelaide fold-thrust belt, south Australia: Salient and recess development in the delamerian orogen. *J. Struct. Geol.* 18 (7), 891–908. doi:10.1016/0191-8141(96)00016-8

Murray, C. G., and Kirkegaard, A. G. (1978). The Thomson orogen of the tasman orogenic zone. *Tectonophysics* 48 (3-4), 299–325. doi:10.1016/0040-1951(78)90122-1

Musacchio, G., White, D. J., Asudeh, I., and Thomson, C. J. (2004). Lithospheric structure and composition of the Archean Western Superior Province from seismic refraction/wide-angle reflection and gravity modeling. *J. Geophys. Res. Solid Earth* 109 (B3), B03304. doi:10.1029/2003jb002427

Myers, J. S., Shaw, R. D., and Tyler, I. M. (1996). Tectonic evolution of proterozoic Australia. *Tectonics* 15 (6), 1431–1446. doi:10.1029/96tc02356

Needham, R. S., Stuart-Smith, P. G., and Page, R. W. (1988). Tectonic evolution of the pine Creek inlier, northern territory. *Precambrian Res.* 40, 543–564. doi:10.1016/0301-9268(88)90084-8

Özalaybey, S., and Chen, W. P. (1999). Frequency-dependent analysis of SKS/SKKS waveforms observed in Australia: Evidence for null birefringence. *Phys. earth Planet. interiors* 114 (3-4), 197–210. doi:10.1016/s0031-9201(99)00058-8

Park, J., and Levin, V. (2016). Anisotropic shear zones revealed by backazimuthal harmonics of teleseismic receiver functions. *Geophys. Suppl. Mon. notices R. Astronomical Soc.* 207 (2), 1216–1243. doi:10.1093/gji/ggw323

Peterson, J. R. (1993). Observations and modeling of seismic background noise *(No. 93-322).* Albuquerque, NM: US Geological Survey.

Reading, A. M., and Kennett, B. L. N. (2003). Lithospheric structure of the Pilbara craton, Capricorn orogen and northern Yilgarn craton, western Australia, from teleseismic receiver functions. *Aust. J. Earth Sci.* 50 (3), 439–445. doi:10.1046/j.1440-0952.2003.01003.x

Rychert, C. A., and Shearer, P. M. (2009). A global view of the lithosphere-asthenosphere boundary. *Science* 324 (5926), 495–498. doi:10.1126/science.1169754

Salmon, M., Kennett, B. L. N., and Saygin, E. (2013). Australian seismological reference model (AuSREM): Crustal component. *Geophys. J. Int.* 192 (1), 190–206. doi:10.1093/gji/ggs004

Savage, M. K. (1999). Seismic anisotropy and mantle deformation: What have we learned from shear wave splitting? *Rev. Geophys.* 37 (1), 65–106. doi:10.1029/98rg02075

Saygin, E., and Kennett, B. L. N. (2012). Crustal structure of Australia from ambient seismic noise tomography. *J. Geophys. Res. Solid Earth* 117 (B1). doi:10.1029/2011jb008403

Schulte-Pelkum, V., and Mahan, K. H. (2014). A method for mapping crustal deformation and anisotropy with receiver functions and first results from USArray. *Earth Planet. Sci. Lett.* 402, 221–233. doi:10.1016/j.epsl.2014.01.050

Selway, K. (2018). Electrical discontinuities in the continental lithosphere imaged with magnetotellurics. *Lithospheric discontinuities*, 89–109. doi:10.1002/9781119249740.ch5

Selway, K., Ford, H., and Kelemen, P. (2015). The seismic mid-lithosphere discontinuity. *Earth Planet. Sci. Lett.* 414, 45–57. doi:10.1016/j.epsl.2014.12.029

Sheppard, S., Tyler, I. M., Griffin, T. J., and Taylor, W. R. (1999). Palaeoproterozoic subduction-related and passive margin basalts in the Halls Creek Orogen, northwest Australia. *Aust. J. Earth Sci.* 46 (5), 679–690. doi:10.1046/j.1440-0952.1999.00737.x

Shiomi, K., and Park, J. (2008). Structural features of the subducting slab beneath the Kii Peninsula, central Japan: Seismic evidence of slab segmentation, dehydration, and anisotropy. *J. Geophys. Res. Solid Earth* 113 (B10), B10318. doi:10.1029/2007jb005535

Silver, P. G., and Chan, W. W. (1991). Shear wave splitting and subcontinental mantle deformation. *J. Geophys. Res. Solid Earth* 96 (B10), 16429–16454. doi:10.1029/91jb00899

Simmons, N. A., Forte, A. M., Boschi, L., and Grand, S. P. (2010). GyPSuM: A joint tomographic model of mantle density and seismic wave speeds. *J. Geophys. Res. Solid Earth* 115 (B12), B12310. doi:10.1029/2010jb007631

Simons, F. J., Van Der Hilst, R. D., Montagner, J. P., and Zielhuis, A. (2002). Multimode Rayleigh wave inversion for heterogeneity and azimuthal anisotropy of the Australian upper mantle. *Geophys. J. Int.* 151 (3), 738–754. doi:10.1046/j.1365-246x.2002.01787.x

Smithies, R. H., and Bagas, L. (1997). High pressure amphibolite-granulite facies metamorphism in the Paleoproterozoic Rudall Complex, central Western Australia. *Precambrian Res.* 83 (4), 243–265. doi:10.1016/s0301-9268(96)00051-4

Tesauro, M., Kaban, M. K., and Aitken, A. R. (2020). Thermal and compositional anomalies of the Australian upper mantle from seismic and gravity data. *Geochem. Geophys. Geosystems* 21 (11), e2020GC009305. doi:10.1029/2020gc009305

Vauchez, A., Tommasi, A., Barruol, G., and Maumus, J. (2000). Upper mantle deformation and seismic anisotropy in continental rifts. *Phys. Chem. Earth, Part A Solid Earth Geodesy* 25 (2), 111–117. doi:10.1016/s1464-1895(00)00019-3

Vauchez, A., Tommasi, A., and Barruol, G. (1998). Rheological heterogeneity, mechanical anisotropy and deformation of the continental lithosphere. *Tectonophysics* 296 (1-2), 61–86. doi:10.1016/s0040-1951(98)00137-1

Vinnik, L. P., Makeyeva, L. I., Milev, A., and Usenko, A. Y. (1992). Global patterns of azimuthal anisotropy and deformations in the continental mantle. *Geophys. J. Int.* 111 (3), 433–447. doi:10.1111/j.1365-246x.1992.tb02102.x

Walker, A. M., and Wookey, J. (2012). MSAT—a new toolkit for the analysis of elastic and seismic anisotropy. *Comput. Geosciences* 49, 81–90. doi:10.1016/j.cageo.2012.05.031

Walker, K. T., Nyblade, A. A., Klemperer, S. L., Bokelmann, G. H., and Owens, T. J. (2004). On the relationship between extension and anisotropy: Constraints from shear wave splitting across the East African Plateau. *J. Geophys. Res. Solid Earth* 109 (B8). doi:10.1029/2003jb002866

Wang, L., Hitchman, A. P., Ogawa, Y., Siripunvaraporn, W., Ichiki, M., and Fuji-Ta, K. (2014). A 3-D conductivity model of the Australian continent using observatory and magnetometer array data. *Geophys. J. Int.* 198 (2), 1143–1158. doi:10.1093/gji/ggu188

Wirth, E. A., and Long, M. D. (2014). A contrast in anisotropy across mid-lithospheric discontinuities beneath the central United States—a relic of craton formation. *Geology* 42 (10), 851–854. doi:10.1130/g35804.1

Wirth, E. A., and Long, M. D. (2012). Multiple layers of seismic anisotropy and a low-velocity region in the mantle wedge beneath Japan: Evidence from teleseismic receiver functions. *Geochem. Geophys. Geosystems* 13 (8). doi:10.1029/2012gc004180

Wolf, J., Creasy, N., Pisconti, A., Long, M. D., and Thomas, C. (2019). An investigation of seismic anisotropy in the lowermost mantle beneath Iceland. *Geophys. J. Int.* 219 (1), S152–S166. doi:10.1093/gji/ggz312

Worthington, L. L., Miller, K. C., Erslev, E. A., Anderson, M. L., Chamberlain, K. R., Sheehan, A. F., et al. (2015). Crustal structure of the Bighorn Mountains region: Precambrian influence on Laramide shortening and uplift in north-central Wyoming. *Tectonics* 35 (1), 208–236. doi:10.1002/2015tc003840

Wustefeld, A., and Bokelmann, G. (2007). Null detection in shear-wave splitting measurements. *Bull. Seismol. Soc. Am.* 97 (4), 1204–1211. doi:10.1785/0120060190

Wüstefeld, A., Bokelmann, G., Zaroli, C., and Barruol, G. (2008). SplitLab: A shear-wave splitting environment in matlab. *Comput. Geosciences* 34 (5), 515–528. doi:10.1016/j.cageo.2007.08.002

Yoshizawa, K., and Kennett, B. L. N. (2015). The lithosphere-asthenosphere transition and radial anisotropy beneath the Australian continent. *Geophys. Res. Lett.* 42 (10), 3839–3846. doi:10.1002/2015gl063845

Yoshizawa, K. (2014). Radially anisotropic 3-D shear wave structure of the Australian lithosphere and asthenosphere from multi-mode surface waves. *Phys. Earth Planet. Interiors* 235, 33–48. doi:10.1016/j.pepi.2014.07.008

Zelt, C. A., and Ellis, R. M. (1989). Comparison of near-coincident crustal refraction and extended vibroseis reflection data: Peace River Region, Canada. *Geophys. Res. Lett.* 16 (8), 843–846. doi:10.1029/gl016i008p00843

frontiers | Frontiers in Earth Science

TYPE Original Research
PUBLISHED 16 January 2023
DOI 10.3389/feart.2022.1066265

EDITED BY
Masayuki Obayashi,
Japan Agency for Marine-Earth Science and Technology (JAMSTEC), Japan

REVIEWED BY
Takeshi Akuhara,
The University of Tokyo, Japan
Mei Feng,
Chinese Academy of Geological Science, China

*CORRESPONDENCE
Weilai Wang,
wangwl@cea-igp.ac.cn

SPECIALTY SECTION
This article was submitted to Solid Earth Geophysics,
a section of the journal
Frontiers in Earth Science

RECEIVED 11 October 2022
ACCEPTED 14 November 2022
PUBLISHED 16 January 2023

CITATION
Wang W, Cai G, Wu J and Fang L (2023), The lithospheric S-wave velocity structure beneath the NE Tibetan Plateau and its surrounding craton basins.
Front. Earth Sci. 10:1066265.
doi: 10.3389/feart.2022.1066265

The lithospheric S-wave velocity structure beneath the NE Tibetan Plateau and its surrounding craton basins

Weilai Wang*, Guangyao Cai, Jianping Wu and Lihua Fang

Institute of Geophysics, China Earthquake Administration, Beijing, China

It is essential to investigate the spatial distribution of the lithosphere and asthenosphere in detail, to further obtain the understanding of the effect of plate collision and the process of orogenic movement. From the joint inversion of receiver functions and surface waves, the three-dimensional S-wave velocity structure results down to 200 km depth in the study area were obtained at 1,843 seismic stations. Analysis was performed on the sedimentary thickness, crustal thickness, lower crustal wave velocity, and lithospheric thickness. According to the crustal thickness, we evaluated the distribution of low-velocity zones in the lower crust. The results show that there are low-velocity bodies in the lower crust in the Qinling tectonic belt, but they are not connected, indicating that they may not be able to be used as a channel for material extrusion from the NE Tibetan Plateau at the crustal scale. According to the section results and the depth distribution of the lithosphere-astenosphere boundary, a relatively thick lithosphere exists below the Sichuan Basin and Ordos Basin, and the lithosphere in the east of the study area is relatively thin with a thickness of about 60–80 km, indicating that the lithosphere in the east of the study area has been severely destructed and restructured. The delamination has been observed in the lithosphere under the Songpan-Ganzi Block, showing characteristics of vertical movement of asthenosphere materials. There is a relatively thick low-velocity zone at the top of the mantle lithosphere of the NE plateau; however, it does not exist under the relatively stable Sichuan Basin and the Ordos Block. Compared with the Sichuan Basin and the Ordos Basin at both sides, the Qinling tectonic belt has a low-velocity zone at the depth of 100–160 km, which may be asthenosphere material. In combination with the polarization direction characteristics of the SKS wave, it is clearly observed that asthenospheric material movement exists in an approximate east-west direction beneath the Qinling tectonic belt. Therefore, the asthenosphere beneath the Qinling tectonic belt may serve as an important channel for material extrusion in the NE Tibetan Plateau.

KEYWORDS

receiver function, surface wave, joint inversion, S-wave velocity structure, NE Tibetan Plateau

1 Introduction

Since the Indian-Eurasian plate collision, as the Tibetan Plateau continued to develop toward the northeast (England and Houseman 1986; Tapponnier et al., 2001), the surface uplift and orogeny has occurred in the northeastern margin about 1,000 km away from the convergent front since the middle and late Cenozoic era (Molnar and Tapponnier, 1975). The northward subduction from India to Asia has played an important role in the rise and growth of the plateau. At the northernmost tip of the Tibetan Plateau, the Qilian tectonic belt developed on the southern margin of the North China Craton, and has been shortening along NE-SW at a rate of 13 mm/year (Yin and Harrison, 2000). However, it is unknown whether there is a weak lower crustal flow model on the NE Tibetan Plateau. Therefore, it is of great significance to study the characteristics of the crustal structure in detail, evaluate the lower crustal flow model, and understand the main mechanism of deformation in the northeastern margin of the plateau.

The NE Tibetan Plateau is the intersection area of the Tibetan Plateau Block and the North China Craton/the Yangtze Craton (see Figure 1 for the study area). The Qingling-Dabie orogenic belt is the main component of the gigantic central orogenic belt that crosses China from east to west and divides China into northern and southern parts. It is the structural junction zone of North China and the Yangtze continents and a typical collision orogenic belt (Zhang et al., 1995). With the northward subduction of the Indian lithosphere, the Tibetan asthenosphere has been largely compressed (Huang and Zhao, 2006; Li et al., 2008), and the material in the asthenosphere is compressed similar to the lithosphere (Tapponnier et al., 2001; Vinnik et al., 1992; Silver and Holt, 2002). It is speculated that below the Qinling-Dabie tectonic belt there is an escape channel of the asthenosphere material (Yu and Chen, 2016; Chang et al., 2017). In the tectonic activities, what is the relationship between the lithosphere of the plateau and the lithosphere of the adjacent craton, and the degree of erosion and destruction of the craton lithosphere. The geodynamic process of continental evolution not only occurs on the entire lithosphere scale, but also reaches hundreds of kilometers deep inside the upper mantle. The geophysical background zone with high rigidity of mantle in the lithosphere may hinder the migration of mantle-derived materials derived from the deep region, and the discontinuity between different lithospheres may be a good channel for mantle-derived materials. Therefore, it is essential to investigate the spatial distribution of the lithosphere and asthenosphere in detail, to further the understanding of the effect of plate collision and the process of orogenic movement.

The transformation or destruction of the lithosphere and the distribution of the asthenosphere are related to the hot material activity. According to the transmission characteristics of the body waves, the S-wave velocity structure is closely related to the shear modulus of the earth's internal medium. Compared with the P-wave, the S-wave is more sensitive to the asthenosphere and hot materials. However, most of the studies on the three-dimensional velocity structure above the depth of 150 km in the NE Tibetan Plateau and surrounding craton basins are P-wave travel time tomography (Li et al., 2008; Tian et al., 2009; Tian and Zhao, 2011; Guo et al., 2017). At present, the information regarding S-wave velocity structure of the lithosphere-asthenosphere on the NE Tibetan Plateau mostly comes from large-scale surface wave inversion (Huang et al., 2003; Huang et al., 2009; Bao et al., 2013; Bao et al., 2015; Yang et al., 2013; Wei et al., 2015; Shen et al., 2016; Wei et al., 2017), revealing that the high-velocity body beneath the Ordos and Sichuan basins can extend up to 200 km in depth, while the velocity in the lithosphere on the NE Tibetan Plateau is relatively low. However, since surface waves mainly reflect the average effect of S-wave velocity in a certain range of depth and it is difficult to delineate the fine fluctuation characteristics of important interfaces (such as Moho and lithosphere-astenosphere boundary, LAB), only qualitative discussion of the asthenosphere can be obtained. The receiver function has a unique advantage in determining the depth of the interfaces showing discontinuity of the velocity. The joint inversion can utilize their advantages and effectively reduce the non-uniqueness of the single type data inversion results. The joint inversion of receiver functions and surface wave has been applied to multiple studies on the deep structure of the NE Tibetan Plateau (Zheng et al., 2016; Guo et al., 2017; Li et al., 2017; Wang et al., 2017; Ye et al., 2017; Ye et al., 2018), which have revealed high-resolution structural images of the region and certain observation sections, but the results obtained were basically limited within the depth of 100 km, without revealing relatively complete structural characteristics of lithosphere-asthenosphere. Huang et al. (2009) presented the S-wave velocity structure of the crust and upper mantle (0–300 km) through surface wave tomography and inversion of North China. Wang et al. (2017) used the receiver function and surface wave inversion to obtain the three-dimensional velocity structure down to 100 km depth in the northeastern margin of the Tibetan Plateau, and analyzed the thickness of the sedimentary layer and crust as well as Poisson's ratio in the study area. However, the distribution characteristics of the deep structure of the complete lithosphere and asthenosphere were not given. Detailed images of the deep structure play an important role in understanding the mantle dynamics in NE Tibetan Plateau. Guo and Chen (2017) applied the joint inversion of background noise and the receiver function to obtain a three-dimensional velocity structure within the depth of 100 km in the NE Tibetan Plateau. It is believed that there exists an asthenosphere channel flow from west to east beneath the Qinling-Dabie tectonic belt south of Ordos. Wu et al.

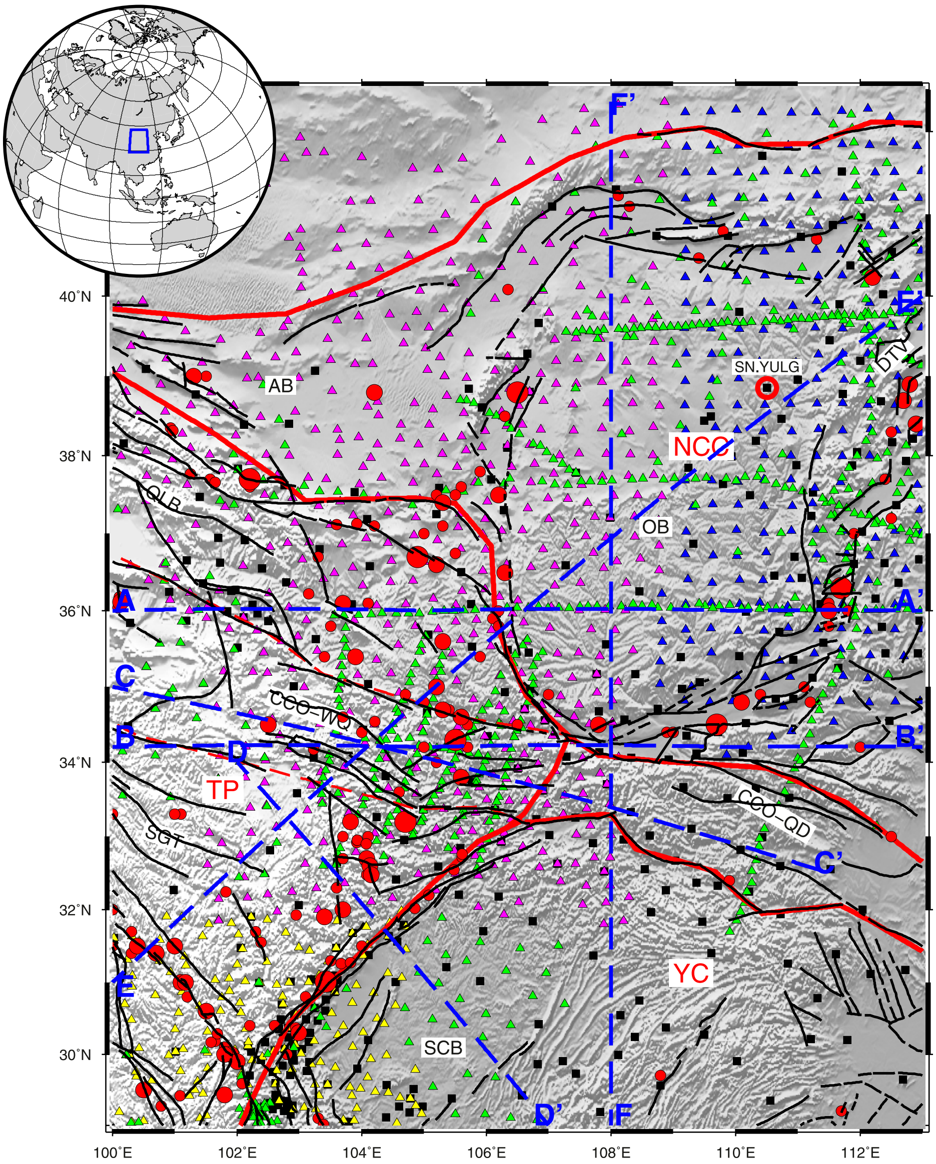

FIGURE 1
Distribution of seismic stations and regional tectonic units (revised from Zhao et al., 2005). Black squares: permanent stations, Yellow triangles: western Sichuan array, Red triangles: ChinArray-Himalaya Phase II, Blue triangles: ChinArray-Himalaya Phase III, Green triangles: Other temporary stations. Red circles mark M ≥6 earthquakes, Blue dashed lines represent sections. and Black lines and red dashed lines represent faults and tectonic boundaries, respectively. TP: Tibetan plateau; YC: Yangtze Craton; CAOB: Central Asia Orogenic Belt; NCC: North China Craton; SGT: Songpan-Garze Terrane; QLB: Qilian tectonic belt; OB: Ordos Block; AB: Alxa Block; CCO: Central China Orogen (or Qinling tectonic belt); WQ: Western Qinling; QD: Qinling Dabie.

(2022) obtained the 3D velocity structure of Ordos and its surrounding areas at a depth down to 200 km from a joint inversion method of receiver function and surface wave. Their results shown the Ordos lithosphere is characterized by thick in the middle and thin in the periphery. However, the 3D structure between the NE Tibetan Plateau and its surrounding cratonic basin is not fully presented.

In this study, we select receiver functions at each station with different filtering parameters and better azimuthal coverage within 2–4 slowness ranges, and stack them to obtain the average receiver functions for different slowness ranges, which can reduce the influence of local lateral inhomogeneity of media near the station and increase the reliability of deep velocity anomalies. By surface wave tomography, the Rayleigh wave phase velocity at periods as long as 150s beneath each station can be obtained. Combing the receiver functions at different slowness ranges with surface dispersion at long periods, the S-wave velocity structure down to 200 km depth can be constrained by the joint inversion. From the observation data of 1,857 broadband seismic stations in the NE Tibetan Plateau and its surrounding areas, the 3D S-wave velocity structure model of the study area within a depth of 200 km is obtained, and the distribution characteristics of the sedimentary layer, crust-mantle boundary, and lithosphere are analyzed. This study explores the characteristics of the NE Tibetan Plateau and its nearby cratonic lithosphere, which has been through transformation and destruction. It will facilitate the in-depth understanding of the deep material migration in this region and geodynamic processes.

2 Data and method

2.1 Data

To obtain the fine structure of the crust and upper mantle and the tectonic characteristics of seismic activity in the NE Tibetan Plateau and the surrounding craton basin, a series of observations from field portable seismic station arrays have been carried out in this region (for example, the western Sichuan array, from October 2006 to July 2009; ChinArray-Himalaya Phase II, from December 2013 to May 2016; ChinArray-Himalaya Phase Ⅲ, from March 2016 to December 2020). Together with the permanent stations in the surrounding area, a densely distributed seismic observation array (1,957 stations) has been formed to cover the whole region (see Figure 1), with an average inter-station distance of approximately 35 km. The receiver function used in the joint inversion in this study is based on the receiver function extraction technique of the maximum entropy deconvolution that obtains high signal-to-noise ratio receiver functions with an epicenter distance between 30°–90° and a magnitude greater than 5.5, recorded at each station in the study area (Wang et al., 2017a).

2.2 Surface wave tomography

Jin and Gaherty (2015) proposed to use dense seismic array to retrieve the phase velocity map of surface wave, and improved it on the basis of Eikonal equation and Helmholtz equation, and developed the automatic surface wave measurement system (ASWMS) to carry out surface wave tomography. In this study, we use the software ASWMS to obtain the phase velocity maps based on Eikonal equation.

The main two steps of the method are as follows (Lin et al., 2009; Jin and Gaherty, 2015; Zhong et al., 2017; Cai et al., 2021):

1) Phase delay measurement between the source and stations. The five parameter Gaussian wavelet function (Gee and Jordan, 1992) can fit the cross-correlation function after the Gaussian narrowband filtering well, in which the Gauss wavelet function is equal to the product of Gaussian envelope function and cosine function, which is usually expressed as:

$$F_i * W_c C(t) \approx AGa\left[\sigma\left(t - t_g\right)\right] \cos\left[\omega\left(t - t_p\right)\right]. \tag{1}$$

F_i is the Gaussian narrow band filter corresponding to the *i*th center frequency; W_c is the window function acting on the cross-correlation function C(t); A is the amplitude factor; Ga is a Gaussian function; σ is half bandwidth; ω is the center frequency of narrowband waveform; t_g and t_p is the group delay time and the phase delay time, respectively. The values of t_g and t_p at different periods can be obtained by Gaussian wavelet function fitting.

2) Phase velocity estimation *via* Eikonal equation. The relationship between phase delay time and slowness vector between two adjacent stations can be expressed by vector field integral

$$\delta_{\tau_p} = \int_{r_i} \vec{S}(\vec{r}) d\vec{r} \tag{2}$$

$\vec{S}(\vec{r})$ is the slowness vector; $\vec{r}_i$ is the *i*th spherical path between the adjacent stations. Formula 2 can be written in discrete form

$$\delta_{\tau_p} = \sum_i \left(S_{R_i} dr_{R_i} + S_{T_i} dr_{T_i}\right) \tag{3}$$

S_{R_i} and S_{T_i} represents the radial and tangential component of the slowness vector at the i-th segment respectively; dr_{R_i} and dr_{T_i} represents the radial and tangential component at the i-th segment of the spherical path discretization between adjacent stations respectively. The objective function for slowness vector inversion is expressed as:

$$\varepsilon_c^2 = \sum \left| \int_{r_i} \vec{S}(\vec{r}) \cdot d\vec{r} - \delta\tau_{p_i} \right|^2 + \lambda\left(\sum \left|\nabla^2 S_R\right|^2 + \sum \left|\nabla^2 S_T\right|^2 \right) \tag{4}$$

The first term of the right-hand side is the mismatch between the observed and the predicted phase delay; the second term is the constraint of slowness smoothness, λ represents the smoothing factor, which is related with frequency.

The study area is divided into the grids of 0.25° × 0.25°, and the surface wave tomography research based on Eikonal equation is carried out. In order to reduce the measurement error of surface wave dispersion, the phase velocity results on each grid point are used to fit the direction and amplitude of the fast wave with π as period to remove the influence of anisotropy. Figure 2 shows the earthquake distribution, station distribution, and surface wave waveform recorded by array. Figure 3 shows the Rayleigh wave phase velocity, the corresponding uncertainty and ray density distribution maps.

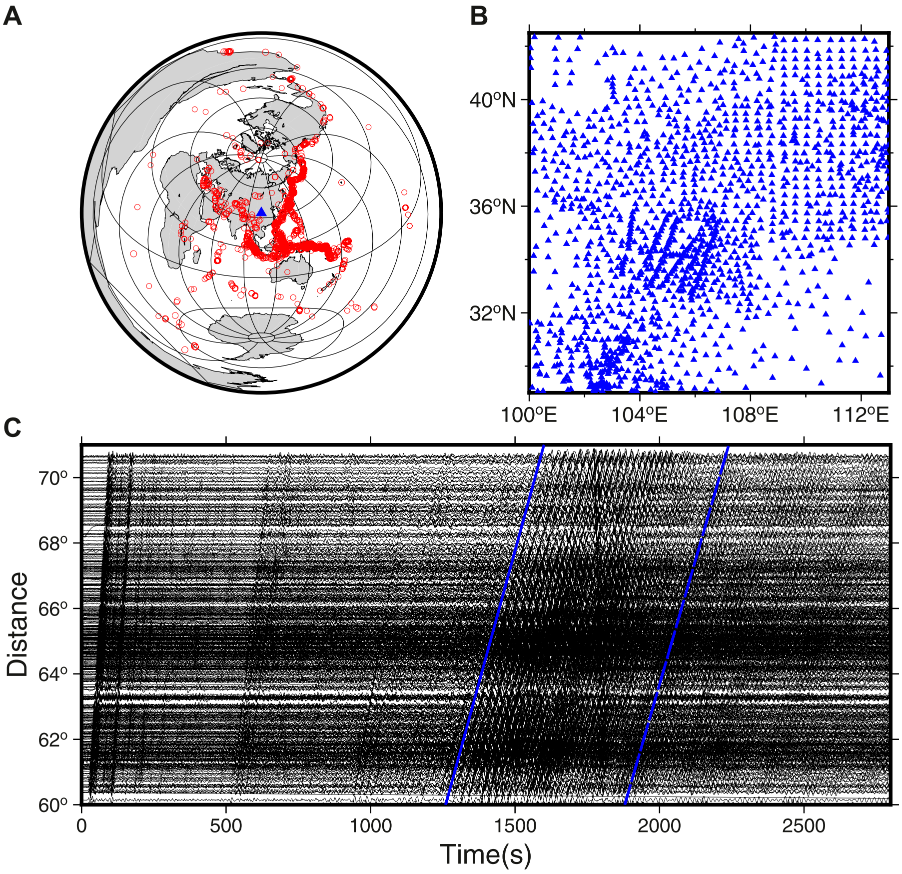

FIGURE 2
(A) Distribution of earthquakes used for surface wave tomography, **(B)** Distribution of stations used for surface tomography. **(C)** The waveforms of the earthquake (Info: 20 April, 2014; at 7.165°S, 155.335°E, 20 km and Mw 6.2) recorded by the ChinArray-Himalaya Phase II. The two blue lines highlight the time windows of Rayleigh wave signal with high signal-to-noise ratio.

2.3 Joint inversion of receiver functions and surface waves

The process of joint inversion of receiver functions and surface waves has been described in detail in Wang W. et al. (2014). Julia et al. (2000) showed that the difference in weight coefficients of receiver functions and surface wave dispersions significantly impacted the inversion results. The inversion problem can be expressed

$$\begin{bmatrix} D \\ \lambda\Delta \end{bmatrix} m \approx \begin{bmatrix} r \\ 0 \end{bmatrix} + \begin{bmatrix} Dm_0 \\ 0 \end{bmatrix} \tag{5}$$

where $\boldsymbol{m}$ is an M-dimensional vector that describes the model, which is a combination of Vs and the depth of each layer; $\boldsymbol{m_0}$ is the known initial model close to the "real" model; $\boldsymbol{D}$ is the partial differential matrix, $\boldsymbol{r}$ is the residual vector; $\boldsymbol{\lambda}$ is the tradeoff parameter between waveform fitting and model smoothness; and the matrix Δ represents a vector of the first differences between shear velocity perturbations in adjacent layers:

$$\Delta = \begin{bmatrix} 1 & -1 & 0 & 0 & \dots \\ 0 & 1 & -1 & 0 & \dots \\ 0 & 0 & 1 & -1 & \dots \\ 0 & 0 & 0 & 1 & \dots \\ \dots & \dots & \dots & \dots & \dots \end{bmatrix} \tag{6}$$

Because the dispersion curve and the receiver function have their own physical units and numbers of data points, Julia et al. (2000) defined a joint prediction error as follows:

$$E_{y|z} = \frac{p}{N_y} \sum_{i=1}^{N_y} \left(\frac{y_i - \sum_{j=1}^{M} Y_{ij} m_j}{\sigma_y} \right)^2 + \frac{1-p}{N_z} \sum_{i=1}^{N_z} \left(\frac{z_i - \sum_{j=1}^{M} Z_{ij} m_j}{\sigma_z} \right)^2 \tag{7}$$

where $\boldsymbol{p}$ is the influence factor for each dataset, which ranges from 0 to 1; **y** and **Y** are the residual receiver function and its partial derivative matrix, respectively; **z** and **Z** are the residual

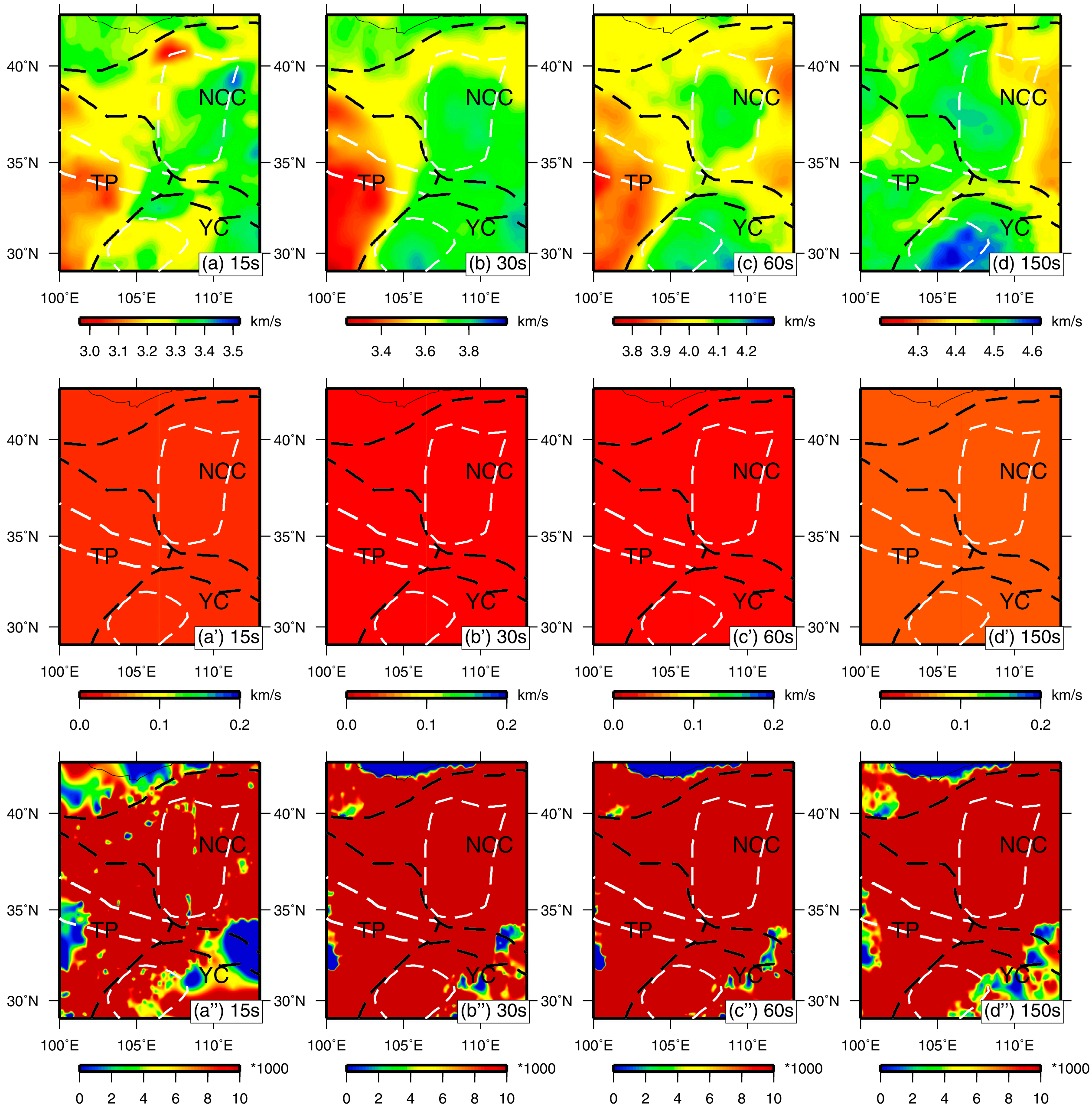

FIGURE 3
The Rayleigh wave phase velocity images **(A–D)**, the corresponding uncertainty images **(A′–D′)** and the density images of surface waves **(A″–D″)** in NE Tibetan Plateau at different periods based on the surface wave Eikonal tomography method. The dotted lines indicate tectonic unit boundaries, as shown in Figure 1.

dispersion curve and its partial derivative matrix, respectively; $\mathbf{N_y}$ and $\mathbf{N_z}$ are the numbers of data points for each dataset; and σ_y^2 and σ_z^2 are the corresponding variances:

$$\sigma_y^2 = \frac{1}{N_y}\sum_{i=1}^{N_y}\left(y_i - \bar{y}\right)^2,\ \sigma_z^2 = \frac{1}{N_z}\sum_{i=1}^{N_z}\left(z_i - \bar{z}\right)^2 \qquad (8)$$

where $\bar{y}$ and $\bar{z}$ are the average values of each dataset.

Considering that there are more receiver function curves than the dispersion curve, the weight coefficient $\boldsymbol{p}$ of fit error for the receiver function varies in the range of 0.1–0.5 (Refer to the Supplementary Materials for the scope selection of $\boldsymbol{p}$), and the weight coefficient of the dispersion curve is 1-$\boldsymbol{p}$. First, we take a random value from 0.1 to 0.5 and assign it to $\boldsymbol{p}$. If the model fails to converge, we regenerate the random model and the value of $\boldsymbol{p}$;

If the cumulative 5 random models cannot converge under the same serial number, we use $\boldsymbol{p} = 0.1$, so that the inversion results tend to converge more easily.

A total of 72 layers are set for the model, including 40 layers of 2 km and 32 layers of 5 km. In this study, the initial S-wave velocities (Vs) of the upper crust, the lower crust, the Moho, and the top of the upper mantle are given as 3.0, 3.5, 4.0, and 4.5 km/s, respectively, and random disturbances of ±1.0, ±0.5, ±1.0 km/s, and ±0.5 km/s are added correspondingly to obtain 20 initial models (as shown in Figure 4D). The smoothing coefficient $\boldsymbol{\lambda}$ that we used is 0.1. Fifty inversion iterations are performed on the obtained initial models. The value of the wave velocity ratio κ (Vp/Vs) in the crust is based on the result of the receiver function h-κ stacking (Wang et al., 2017a; Wang et al., 2017b). According to the global average velocity model AK135 and PREM, the value of the wave velocity ratio κ (Vp/Vs) in the mantle is set at 1.80. The empirical equation $\rho = 0.32Vp + 0.77$ (Birch, 1961) has been applied in this study to determine the density of the medium. The receiver functions obtained by each seismic station are derived from the waveform calculation of two different band-pass filters (0.02–1 Hz and 0.03–0.3 Hz), and the receiver functions in the four slowness ranges (0.04–0.05, 0.05–0.06, 0.06–0.07, and 0.07–0.08) are superimposed separately to determine the average receiver functions in these slowness ranges, which can effectively reduce the influence of the local lateral inequality of the medium near the stations. Figure 4 illustrates the results of the joint inversion under station SN. YULG. According to Figure 4A–C, the receiver function and the surface wave dispersion curve are well fitted. Figure 4E shows the S-wave velocity structure, in which the models with fitting residual less than 1.2 times the minimum fitting error are selected to calculate their average value and standard deviation.

3 Results

3.1 3D Vs model

There are 1,857 stations distributed in the study area. Joint inversions were performed on 1,843 stations, each of which has at least 10 receiver functions and the h-κ stacking quality marked by “very good” or “good” in the papers of Wang et al. (2017a); Wang et al. (2017b), achieving relatively good overall fitting performance. Among them, the inversion fitting residuals of 1,619 stations are less than 5%, 194 stations are between 5–10%, and 30 stations are more than 10%. The inversion results of stations with fitting residuals less than 10% were used to calculate the average of the model within 0.5° grid points. The S-wave velocity distribution was obtained within 200 km of the NE Tibetan Plateau and surrounding basins, of which the results at 9 depths are shown in Figure 5.

Based on the results of the shallow part (Figures 5A,B), the Sichuan Basin, the central Alxa Block, the Ordos Block, and its

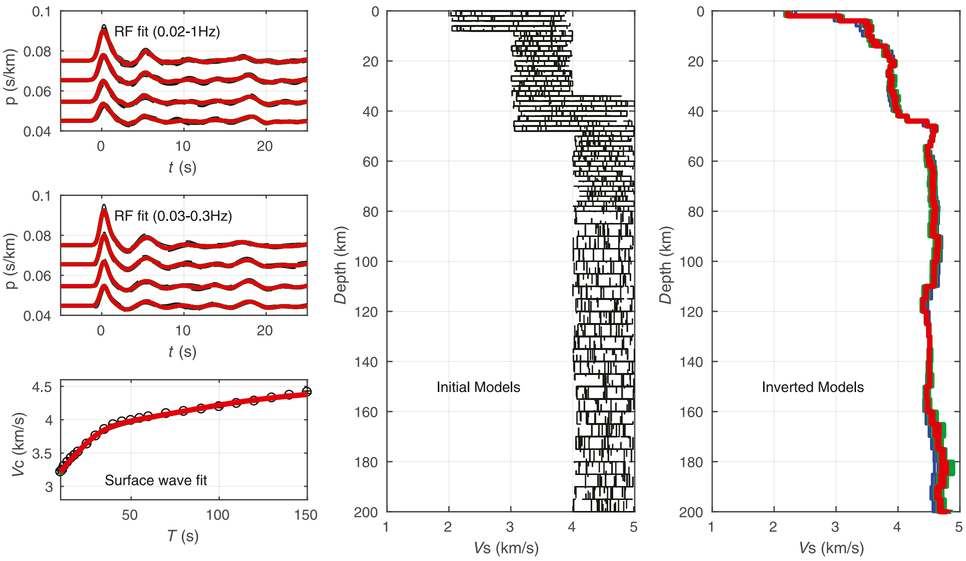

FIGURE 4
The joint inversion results at station SN. YULG located in Ordos block (shown in Figure 1). The 20 random models (black dashed lines) used as initial S-wave velocity models during joint inversion. The S-wave velocity model derived from inversion, where the green lines are models with a small fitted residual (less than 1.2 times the minimum residual), the blue lines are models with a large fitted residual, and the solid red line represents the average value and its standard deviation of the green lines). The stacked receiver functions (black lines) and the fitted curves (red, green and blue lines) for 0.03–0.3 and 0.02–1 Hz, where t refers to time and p refers to horizontal slowness. The Rayleigh wave phase dispersion curve beneath the station (black circles) and the fitted curve (red, green and blue lines), where T refers to period and Vc implies Rayleigh wave phase velocity.

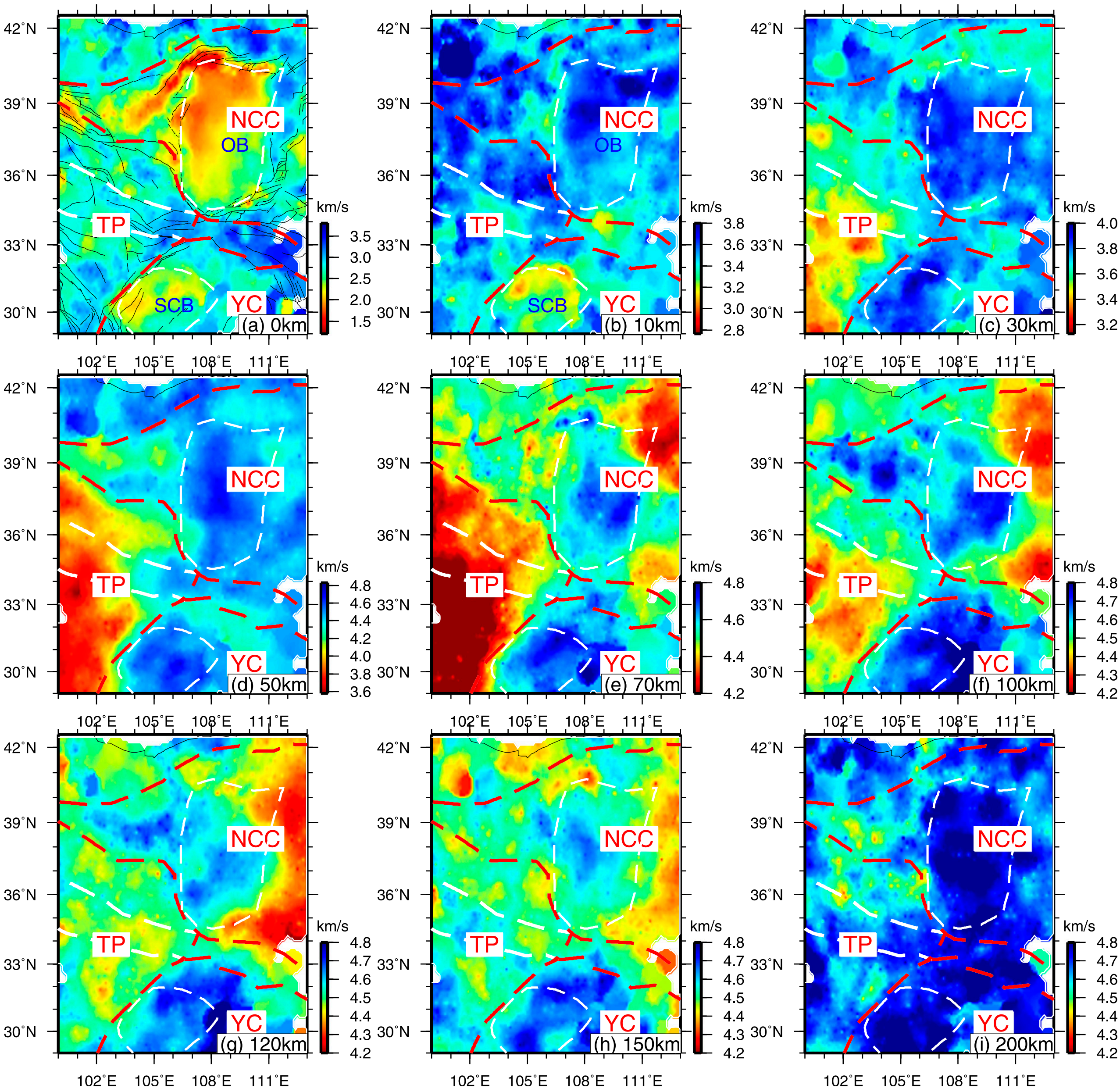

FIGURE 5
S-wave velocity distribution **(A–I)** at different depths from joint inversion of surface waves and receiver functions. The dashed lines indicate tectonic unit boundaries, as shown in Figure 1. Panels **(A–I)** correspond to depths of 0, 10, 30, 50, 70, 100, 120, 150, and 200 km, respectively.

surrounding extensional basin in the study area all exhibit low wave velocity, revealing a typical feature of sedimentary layers, which agrees with the results by Wang et al. (2017a); Wang et al. (2017b) that there are thick Quaternary loose sediments in this area. Searching the maximum value of velocity gradients among 2.5–3.2 km/s in the shallow part of the crust to extract the thickness of the sediment layer (Figure 6A), it shows that there is a huge sedimentary layer in the Sichuan Basin, with the greatest depth more than 6 km in its southwestern part. The Alxa Block, the NW Ordos Block, the Hetao Basin, and Yinchuan Basin also have sedimentary layers with a thickness of 4–8 km. The average S-wave velocity of the shallow sedimentary layer (Figure 6B) is lower in the Alxa Block, and Ordos and its peripheral extensional basins than the Sichuan Basin. This corresponds well to the delay time of the first peak of the P-wave receiver function (Wang et al., 2017a), which may be related to the loose Quaternary sediments. There are almost no low-velocity sedimentary

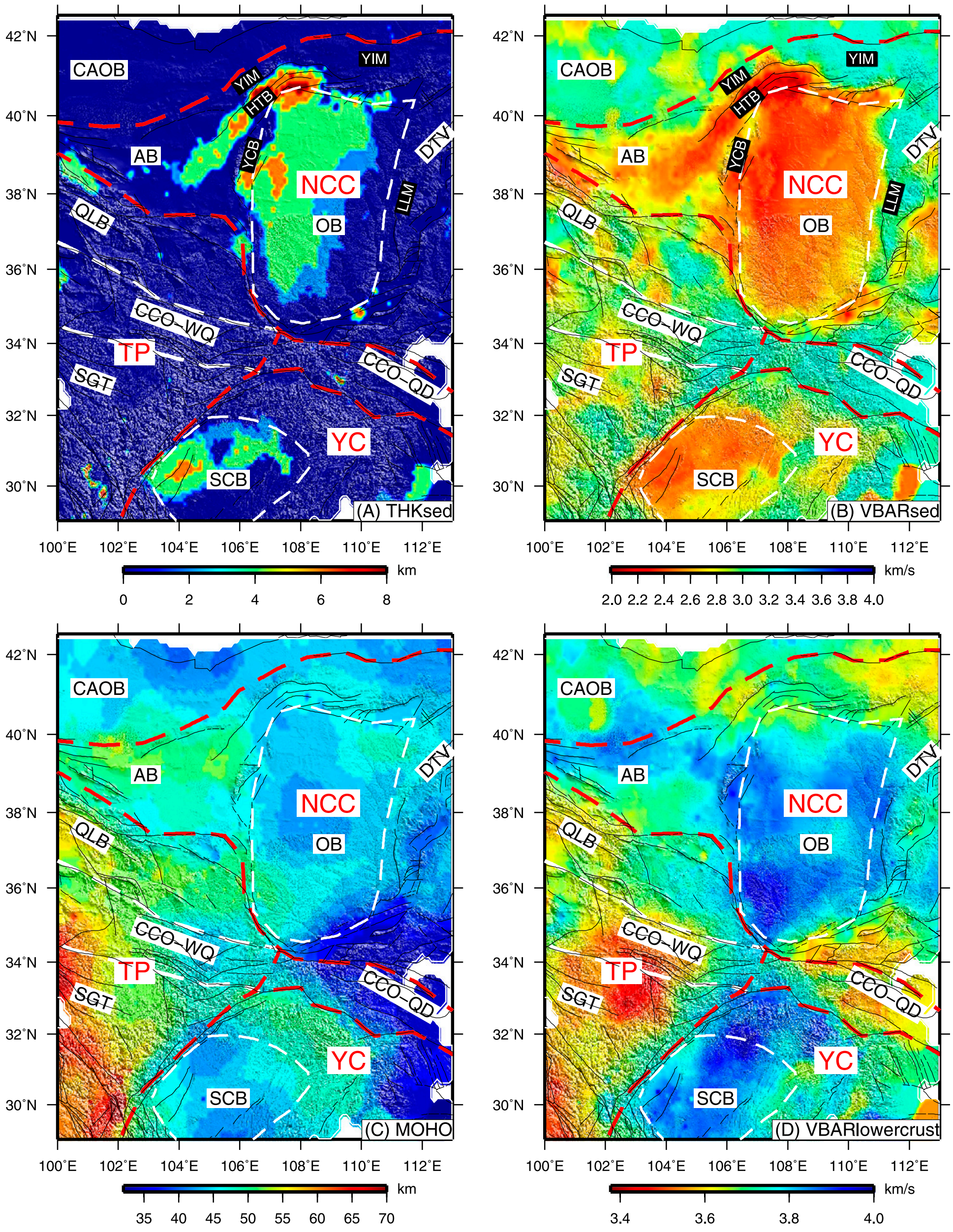

FIGURE 6
Joint inversion results of receiver functions and surface waves: **(A)** Sedimentary thickness; **(B)** Average S-wave velocity in the sediment; **(C)** Crustal thickness; **(D)** Average S-wave velocity in the lower crust. TP, Tibetan plateau; YC, Yangtze Craton; CAOB, Central Asia Orogenic Belt; NCC, North China Craton; SGT, Songpan-Garze Terrane; QLB, Qilian tectonic belt; OB, Ordos Block; AB, Alxa Block; CCO, Central China Orogen (or Qinling tectonic belt); WQ, Western Qinling; QD, Qinling Dabie; DTV, Datong Volcano; YIM, Yin mountain; LLM, Lvliang mountain; SCB, Sichuan basin; YCB, Yinchuan basin; HTB, Hetao basion.

layers in the plateau block, the Qinling tectonic belt, the Central Asia tectonic belt and the Yangtze Craton excluding the Sichuan Basin.

Figure 5C shows the distribution of the middle and lower crust in the study area, illustrating that the Sichuan Basin and the Ordos Block have relatively high wave velocities, and the plateau block and the peripheral area of Ordos are low-velocity zones. Figure 5D roughly reflects the variation of the crustal thickness. We obtain the crustal thickness variations by searching the maximum value of velocity gradients among 4.0–4.3 km/s (Figure 6C). The crustal thickness decreases from about 65 km at the plateau block eastward to about 40 km at the Sichuan Basin and the Ordos Block, and continues to reduce to 30 km at the SE Ordos block, where the thickness of the crust distributed along the Qinling tectonic belt is thinner than that of the Qilian orogenic belt and Songpan-Ganzi Block at both sides of Qinling tectonic belt. According to the crustal thickness, the average S-wave velocity in the depth range of 0.5–0.9 crustal thickness (lower crust) was extracted (Figure 6D). It shows that there are obvious low-velocity characteristics in the lower crust in the NE Tibetan Plateau. The characteristically low Poisson's ratio of the region (Wang et al., 2017a; Wang et al., 2017b) indicates the absence of any partial melting in the lower crust. The wave velocity of the lower crust in the Sichuan Basin and Ordos is relatively high, with a high Poisson's ratio in the north part of Ordos (Wang et al., 2017a), indicating that there may be more mafic components in the crust.

In the 70–200 km slices of the upper mantle (Figures 5E–I), the Sichuan Basin and the Ordos Block show basically high-velocity characteristics from 100 km to 200 km, suggesting that both have a relatively hard and thick lithosphere structure. In some areas, the thickness exceeds 200 km, which agrees with the thickness of the lithosphere obtained by the regional surface wave imaging study (An and Shi, 2006; Huang et al., 2009). The Songpan-Ganzi Block has a low-velocity at 70 km–100 km and a relatively high velocity at 120–200 km, suggesting a partial melting near the top of the mantle in this area. With the continuing increase in the depth, high velocity is again observed, which may be due to the delamination of the lithosphere of the plateau block. The Alxa Block and the eastern section of the Qilian Block change from a medium to high velocity feature at 100–120 km to a low-velocity feature at 150–200 km. This area has a lithosphere of medium thickness. In the north and south of the eastern part of the study area, a low-velocity body appears in the upper mantle from 70 km, and there is a high-velocity body in the middle part. A low-velocity body appears from 120 km and continues to 180 km, indicating that the lithosphere in the east of the study area is the thinnest.

To visually display the lateral structural characteristics across the various tectonic units, the S-wave velocity structure below eight sections are presented (see Figure 7, and the location of the sections is shown in Figure 1). The E-W AA′ section (Figure 7A) traverse the Qilian Block and the southern Ordos Block. The figure display that the middle and lower crust of the Qilian blocks exhibits low-velocity characteristics, while the middle and lower crust of the Ordos Block has a relatively high velocity up to 4 km/s. In the mantle, the Qilian block has a velocity gradient zone immediately below the Moho, which is 30 km thick in the west and decreases to 10 km in the east. The velocity slowly increases in this gradient zone and becomes higher than 4.5 km/s in the depth of 60–80 km. It then gradually declines and exhibits low-velocity features (<4.5 km/s) at the depth of about 150 km. However, the gradient zone in southern Ordos is very thin, and the velocity values of both zones rapidly increase to 4.8 km/s at a depth of 70 km, and maintain at above 4.5 km/s in the depth range of 200 km. This lithospheric feature is also revealed in Li et al. (2018), which used noise and seismic surface wave inversion to obtain the lithospheric structure. However, Huang et al. (2009); Huang (2011) applied surface wave inversion to obtain a much lower wave velocity of Ordos lithospheric, which is quite different from the results of this study and Li et al. (2018).

The BB′ section (Figure 7B) and CC′ section (Figure 7C) spans along the western Qinling tectonic belt and the southeast to Ordos Block, as well as the western Qinling tectonic belt and the Qinling-Dabie tectonic belt. The western Qinling tectonic belt is bounded by 106°E line, where a significant low-velocity layer exists in the lower crust on the west side but not on the east side, consistent with the surface wave tomography results of Huang et al. (2013) and the body wave tomography of Guo et al., 2017. The electrical structure in the deep of the structure obtained by Zhan et al. (2014) shows that a low-resistance layer appears on the west side, and a high-resistance layer appears on the east side of the 106° E boundary. In the mantle, there is a thick velocity gradient zone at the top of the upper mantle beneath the West Qinling Mountains, right below the Moho. A high-velocity body with a velocity above 4.5 km/s only emerges once the depth reaches about 120 km. The Qinling-Dabie tectonic belt is different in that the layer is quite thin from the Moho to the 4.5 km/s contour, and has a high-velocity zone in the lithosphere to 130 km depth. There is a low-velocity zone appears from 130 km depth beneath the BB' section, which is presumed to be an asthenosphere.

The DD′ section (Figure 7D) spans the Songpan-Ganzi Block and the Sichuan Basin. There are low-velocity bodies in the middle and lower crust beneath the west side of the Songpan-Ganzi Block and a relatively thick velocity gradient zone below the Moho with a thickness of about 60 km. High-velocity features appear in the range of 110–180 km in the mantle, and sub-low-velocity layer features show up near 180 km. However, there is no low-velocity layer in the middle and lower crust on the side of the Sichuan Basin, and the S-wave velocity right next to the Moho rapidly increases to 4.8 km/s, and then decreases at a very slow rate at some depths. However, it does not drop to 4.5 km/s within the depth range of 200 km, which also indicates that the basin has a stable lithosphere structure. (Pan et al., 2017) obtained the phase velocity distribution charts of the surface wave showing that Songpan-Ganzi Block has a significant low-velocity layer in the middle and lower crust. Huang et al. (2013) applied surface wave tomography to determine the S-wave velocity structure beneath the Songpan-Ganzi Block, exhibiting that there are low-velocity layers in the crust in the depth range of about 25–45 km. Li et al. (2019) utilized multi-scale tomography to discover that the Songpan-Ganzi Block and the Yangtze Block in the NE Tibetan Plateau display a clear boundary zone in the upper mantle, with a low-velocity anomaly on the west side and a high-velocity anomaly on the east side. This feature is also shown in Figure 7D.

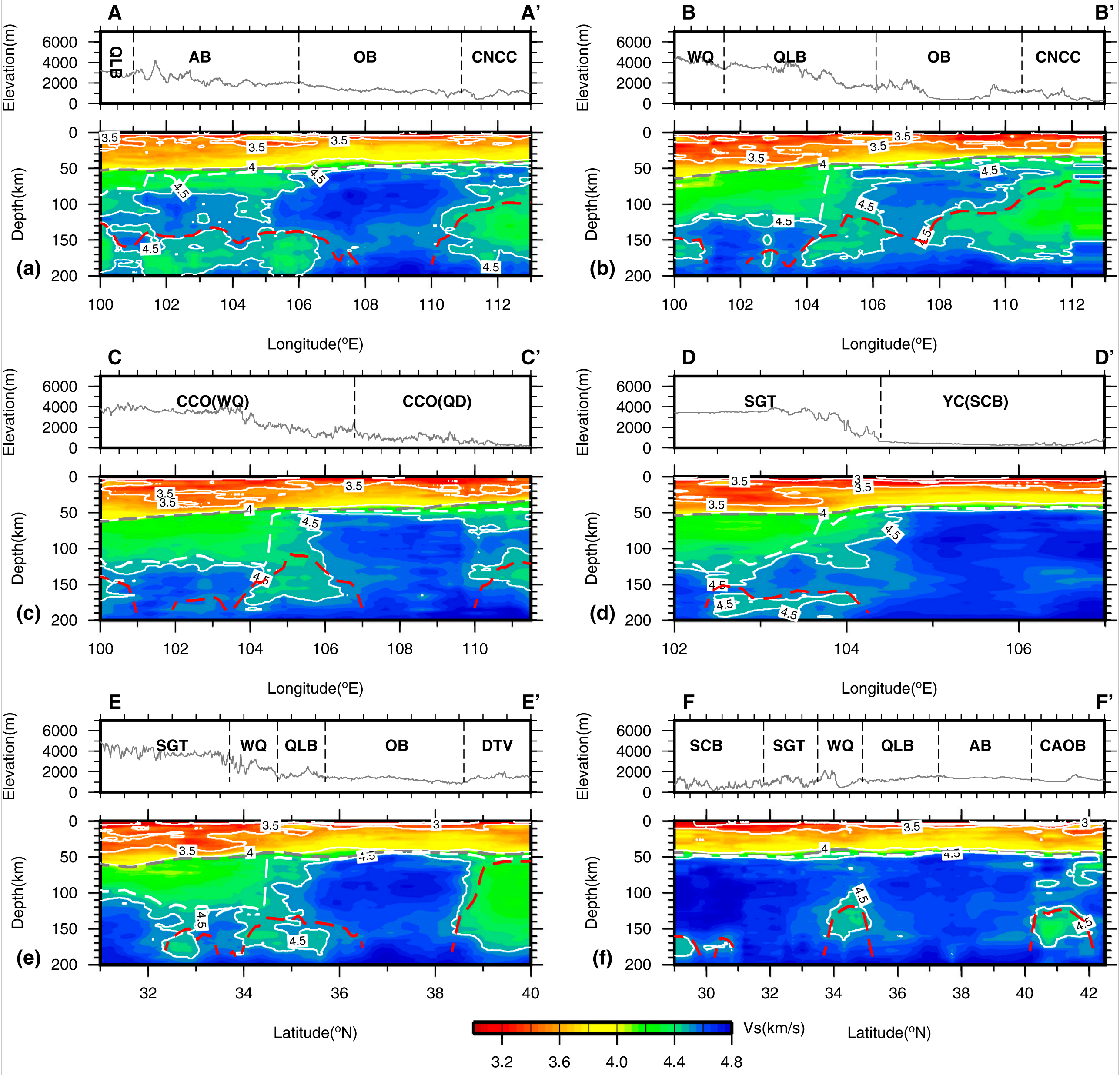

FIGURE 7
S-wave velocity structure beneath 6 sections in the study region. **(A)** AA′ section; **(B)** BB′ section; **(C)** CC′ section; **(D)** DD′ section; **(E)** EE′ section; **(F)** FF′ section. The locations of the six sections are shown in Figure 1. The gray, red and white dashed lines represent the depth of Moho, LAB and the lower boundary of VGZ.

The EE′ section (Figure 7E) spans the Songpan-Ganzi Block, the western Qinling techtonic belt, the Qilian tectonic belt, and the Ordos Block. With the Xianshui River as the boundary (32°N), the high-velocity body below the Moho in the southern Songpan-Ganzi Block mainly appears in the range of 100–200 km; while in the northern Songpan-Ganzi Block (32–34°N), along the section, the gradient zone immediately underneath the Moho gradually becomes thicker and the high-velocity body gradually becomes thinner. While, the lithosphere of the Qilian tectonic belt and the Ordos Block on the north side presents high velocity feature. A weak high-velocity body distributes under the Qinling and Qilian tectonic belts, and the wave velocity under the Datong volcanic area in northeastern Ordos is even lower. In the depth range of 130–180 km, the high-velocity body in the mantle of the

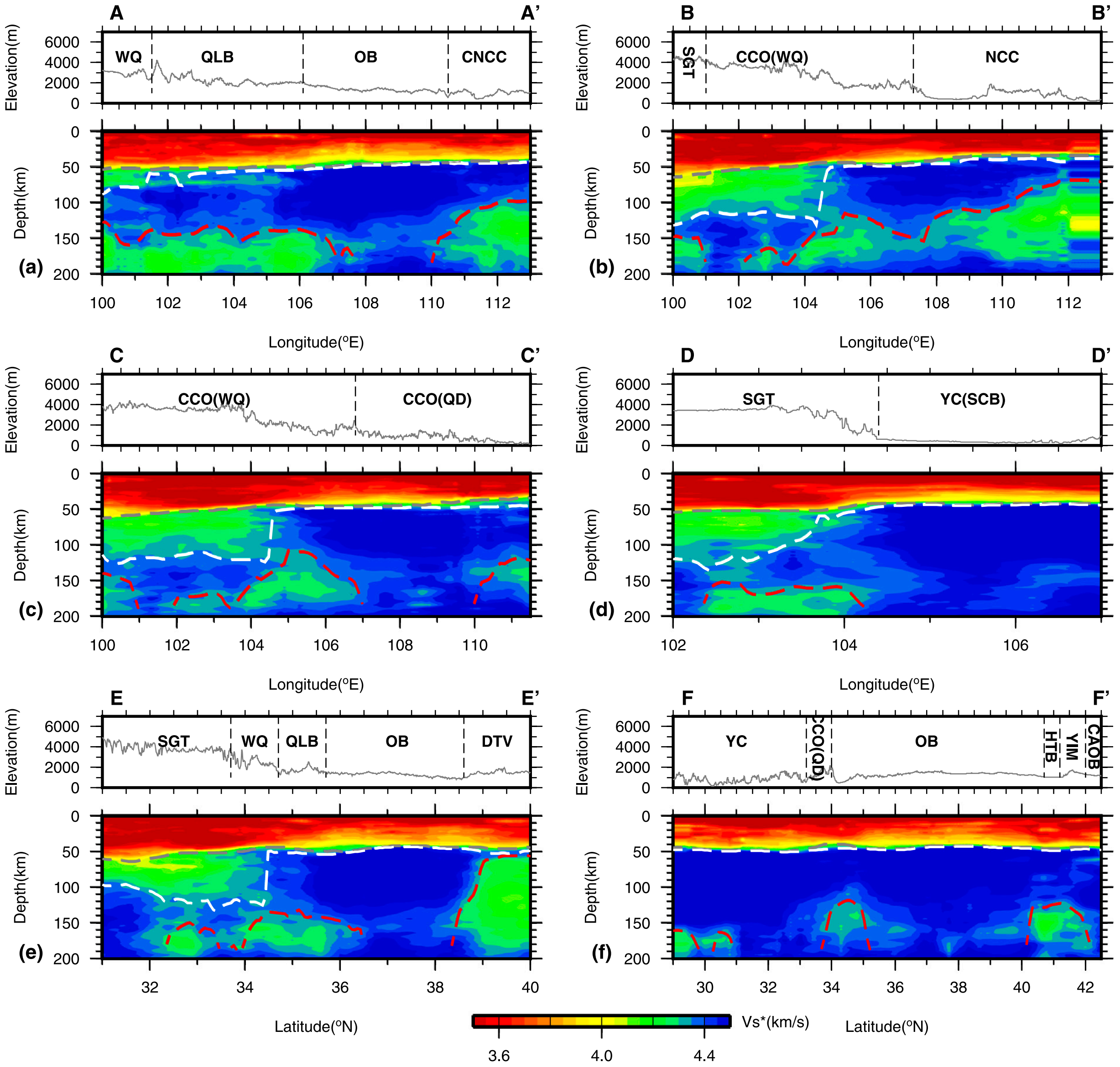

FIGURE 8
Pressure-corrected S-wave2 velocity structure beneath 6 sections in the study region. **(A)** AA′ section; **(B)** BB′ section; **(C)** CC′ section; **(D)** DD′ section; **(E)** EE′ section; **(F)** FF′ section. The locations of the six sections are shown in Figure 1. The gray, red and white dashed lines represent the depth of Moho, LAB, and the lower boundary of VGZ.

Songpan-Ganzi Block and the high-velocity body in the lower part of Ordos are separated by the weak high-velocity body in the Qinling and the Qilian tectonic belts. The S wave receiver function study by Zhang et al. (2013) showed that the lithosphere below the western Qinling tectonic belt was relatively thin, at a thickness of about 125–135 km.

The FF′ section (Figure 7F) spans the eastern margin of the Sichuan Basin, the Qinling tectonic zone, and the Ordos Block and its north side. The sections show that there is no velocity <4.5 km/s in the lower part of the lithosphere in Sichuan Basin and Ordos Basin, and there is a negative gradient interface of 4.5 km/s in the depth of 100 km below the central tectonic belt, while there are several negative gradient interfaces in the depth range of 60–120 km below the northern Hetao Basin of Ordos. Zheng et al. (2018) used the joint inversion of surface wave dispersion and receiver function to determine that the Hetao Basin showed a low-velocity anomaly below 80 km. Chen et al. (2009) also concluded that the thickness of the lithosphere under the Hetao Basin was about 80 km using the S-wave receiver function.

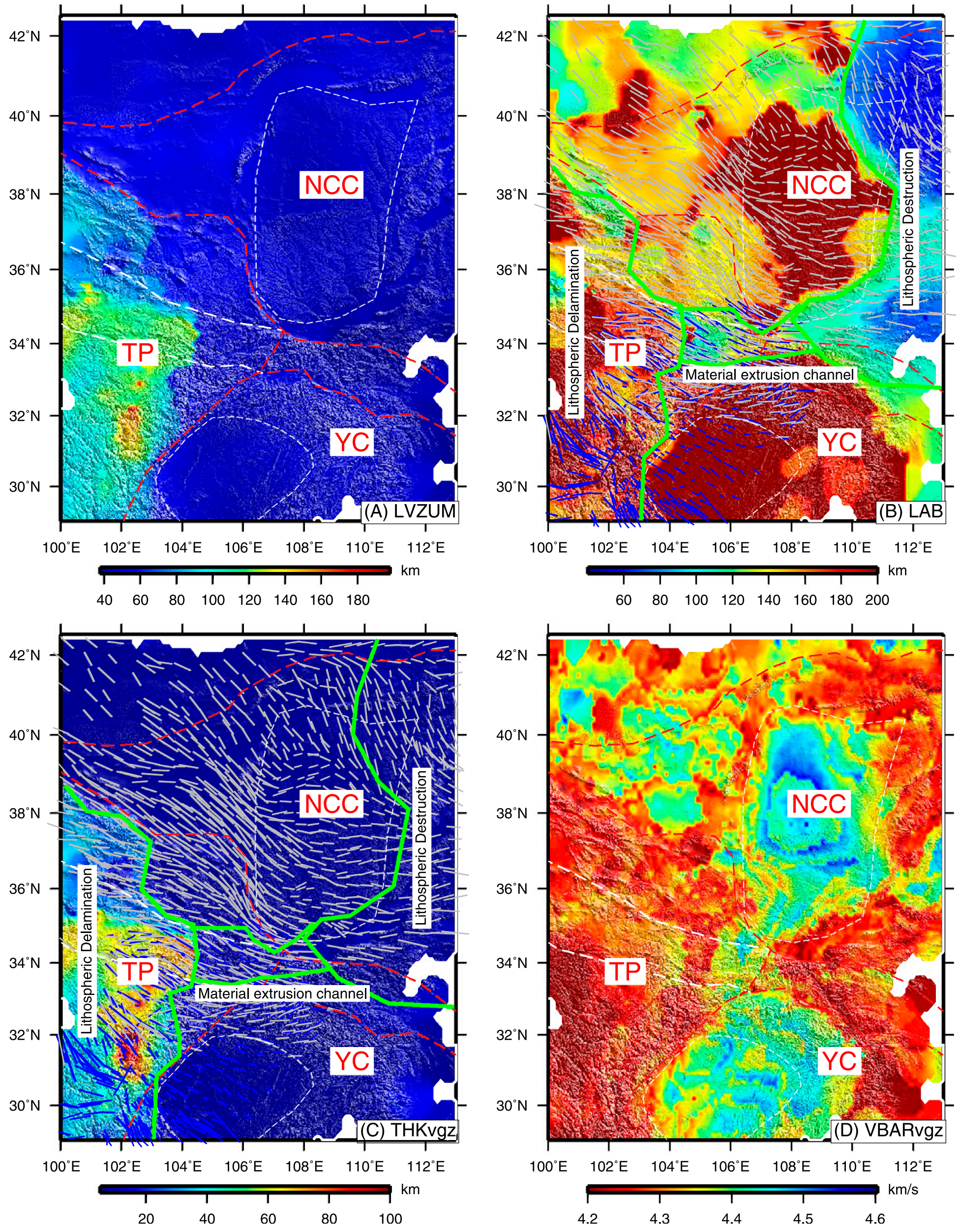

FIGURE 9

(A) The bottom of LVZ in the uppermost mantle: Search for Vs*=4.35 km/s from Moho; **(B)** Lithosphere-asthenosphere boundary: Search for Vs*=4.35 km/s from the Moho downwards and extrema in negative velocity gradient zones, and note that the dark red (200 km) in the figure indicates that the corresponding boundary is not found; **(C)** Thickness of the velocity gradient zone (VGZ) at the uppermost of the mantle lithosphere; **(D)** the average velocity of the VGZ. Blue lines and gray lines represent the SKS wave splitting results from Liu et al. (2020), Liu et al. (2021); Chang et al., 2017; Chang et al., 2021). The green lines indicate the regional scopes of lithospheric delamination, hot material extrusion channel and lithospheric destruction.

Priestley and McKenzie (2006) gave out an empirical relationship between upper mantle S-wave velocity, pressure and temperature: $V_S^* = \frac{V_S}{1+b_v(z-50)}$, where Vs is the S-wave velocity, Vs* is the pressure-corrected velocity of Vs in the upper mantle, b_v is a constant of $3.84*10^{-4}$, z is the depth. Considering that the asthenosphere is characterized by low seismic wave velocity, high temperature, and low vertical gradient, we use a Vs* of about 4.35 km/s after pressure correction as reference marks to determine the base of the lithosphere (Figure 8). Firstly, we searched for the contour of

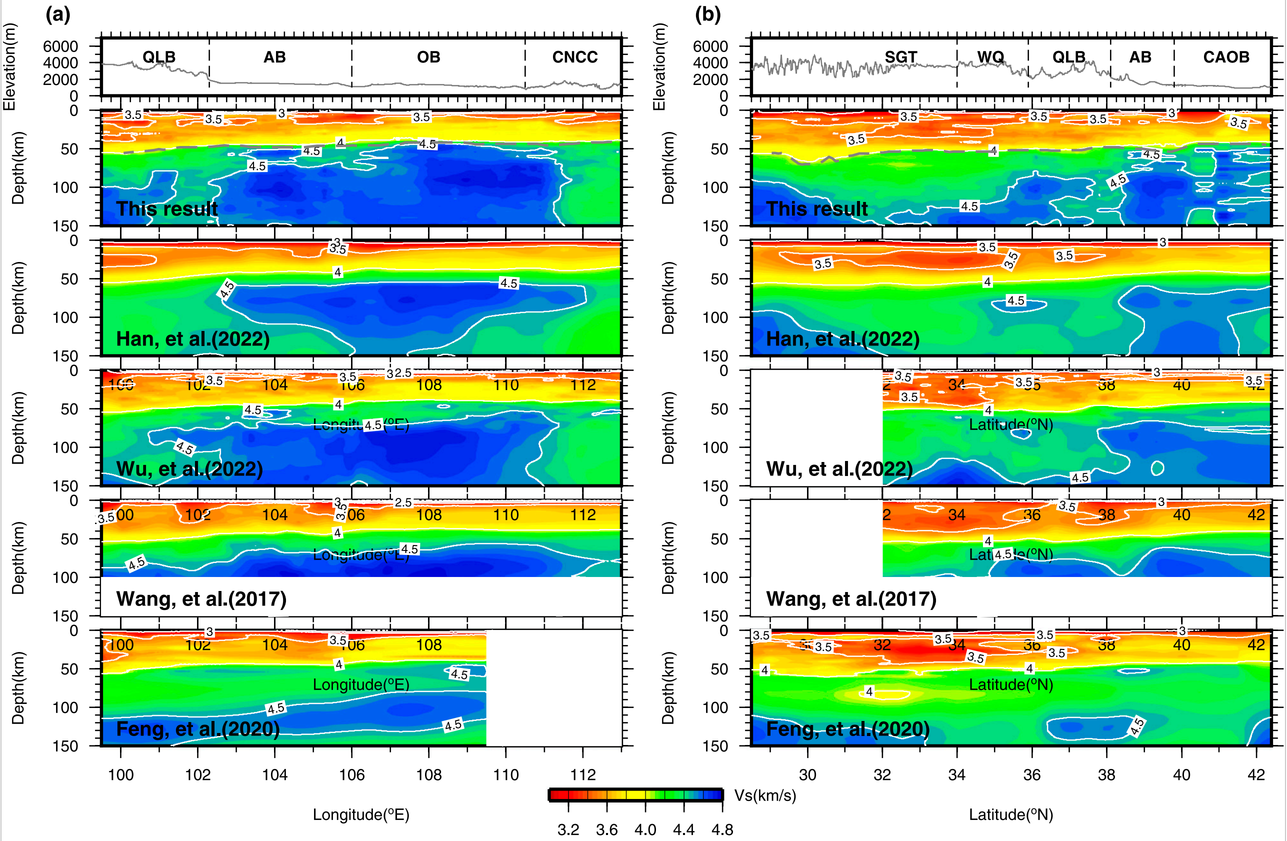

FIGURE 10
The S-wave velocity structure beneath sections along **(A)** latitude line of 38°N **(A)** and **(B)** longitude line of 102°E from this study and previous studies (Wang, et al., 2017; Feng, et al., 2020; Han, et al., 2022; Wu, et al., 2022).

Vs*=4.35 km/s and a positive velocity gradient from the Moho interface, and obtained the distribution of the low velocity zone at the top of the upper mantle (Figure 9A). Then, we searched for the Vs*=4.35 km/s contour with a negative velocity gradient from the Moho and obtained the distribution of the LAB depth (Figure 9B). The dark red area (200 km) indicates that no corresponding interface has been found. Figure 9A shows that the lithosphere under the Sichuan Basin and the Ordos Block is relatively thick, while the lithosphere in the Datong volcanic area in the eastern study area and NE Yangtze Craton is fairly thin with the thickness about 60–80 km. The lithosphere of the Qilian tectonic belt and the Alxa Block is about 150 km thick.

Considering the thickness of the low velocity zone at the top of the upper mantle and the depth of Moho, the thickness of the velocity gradient zone (VGZ) of the upper lithospheric mantle (Figure 9C) and its average wave velocity (Figure 9D) were further obtained. The "velocity gradient zone" is a low velocity layer (<4.5 km/s) beneath Moho, which means that the velocity gradient is very small after entering the mantle (Vs>4.2 km/s), and Vs does not rise to 4.5 km/s quickly, rather than the traditional low-velocity zone between the upper and lower normal velocity layers. For the Songpan-Ganzi Block, the VGZ is about 40 km thick in most parts, and reaches 100 km in some locations. Except for the Tibetan Plateau, the thickness of the velocity gradient zone beneath the surrounding cratonic basins and the Qinling orogenic belt is very thin. According to the results of gravity anomalies on the lithosphere scale (Bi et al., 2016), the authors found that the blocks around the northeastern Tibetan Plateau, such as the Sichuan Basin, Ordos Basin, Alxa block and Qilian tectonic belt, all show prominent positive anomalies, which are still the characteristics of the rigid block. However, the eastern edge of the Songpan-Ganzi Block shows obvious negative anomalies, presumably because the rock is crushed by compressive stress or there is molten crustal and lithospheric material.

3.2 Comparison with previous results

By using double-difference tomography, Han, et al. (2022) obtained high-resolution longitudinal and shear wave velocity models in China. For similar researches in NE Tibetan Plateau and the surrounding areas, some studies used part of the data set and the same method as the current study (e.g., Wang et al., 2017; Wu et al., 2022), and some studies used completely different data set and different methods (e.g., Feng et al., 2017, 2020). We compare our results with four previous studies (Wang et al., 2017; Feng et al., 2020; Han et al., 2022; Wu et al., 2022) beneath two profiles along the latitude line of 38°N and longitude line of 102°E, as shown in Figure 10.

According to Figure 10, there are similar crustal features between this study and the four previous studies: in the lower crust, low velocity zones are found beneath the Songpan-Ganzi block, West Qinling, Qilian tectonic belt and Alxa block, whereas high velocity zone is found beneath the Ordos block. The features are also found in other previous studies (e.g., Zheng et al., 2016; Yang and Zhang, 2018; Zheng et al., 2018; Fu and Xiao, 2020). However, in the upper mantle, large differences are found among different results (Figure 10), and our results are relatively consistent with Wu et al. (2022) and Han et al. (2022). At 38°N (Figure 10A), all studies show that high velocity zones exist beneath the Alxa block and the Ordos block. However, the thickness of velocity gradient zone from Moho to the lithospheric high velocity zone (>4.5 km/s) is different. Beneath Ordos block, in our results, the velocity increases rapidly from Moho downward, which is consistent with the lithospheric P-wave high velocity structure beneath the Wendeng-Alxa Left Banner deep seismic sounding profile (Wang et al., 2014), whereas all the four previous studies mentioned above show relatively thick velocity gradient zones. The reason why our results are different from Wang et al. (2017); Wu et al. (2022) may be that, on the one hand, we used longer period surface wave dispersion data and receiver functions from more stations, and on the other hand, there are some differences in joint inversion processing. Wang et al. (2017) only used a single receiver function for joint inversion; Wu et al. (2022) only used receiver functions with different slowness for joint inversion. In this study, receiver functions with different filters and different slowness are used. In addition, Wu et al. (2022) also inversed the seismic wave velocity ratio of each layer from the joint inversion, however, they did not analyze its reliability which may influence the values of Vs.

4 Discussions

Two models have been finally proposed to explain the formation and deformation of the Tibetan Plateau: 1) rigid plate model (Peltzer and Tapponnier, 1988; Tapponnier et al., 2001) and 2) viscous plate model or lower crustal flow model (England and Houseman, 1988; Royden et al., 1997; Clark and Royden, 2000). The difference between the two models mainly focuses on the composition or state of the crust and mantle material, i.e. the spatial distribution of the partially molten material. The average wave velocity of the lower crust in this paper (Figure 8D) show that there are significant low-velocity layers in the lower crust of the NE plateau block (including the NE Songpan-Ganzi, the western Qinling tectonic belt, and the Qilian tectonic belt). However, these regions have low Poisson's ratio (<0.26) (Wang et al., 2017a), indicating that there is no partial melting in the NE Tibetan Plateau, and there is no ground for lower crustal flow. Li et al. (2014) suggested that the crustal thickening and the local LVZ beneath the northwestern Qilian Orogen reflect an intracrustal response associated with the shortening between the North China Craton and the Tibetan Plateau. This study also shows the craton basins, Qilian tectonic belt and the central part of the central tectonic belt are basically characterized by high velocity, and the low velocity bodies of the lower crust under the central tectonic belt is not connected, which indicates that there is no widespread local melting to support the model of lower crust flow. Previous studies (Agius and Lebedev, 2014; Yang et al., 2019) show that the NE Tibetan Plateau displays negative or weak radial anisotropy, which cannot be adequately explained by the lower crustal flow model. Therefore, the structural deformation of the NE Tibetan Plateau on the crustal scale may be explained more properly by the rigid plate model for the surface lift and orogeny, and the Qinling tectonic belt may not be the channel for material extrusion in the NE Tibetan Plateau on the crustal scale.

At the upper mantle, the material is grouped into a relatively hard solid material (undamaged or not severely damaged lithosphere), and a relatively soft elastoplastic material (asthenosphere and lithosphere material went through severe damage and delamination). The asthenosphere material is in a molten or plastic state, and small stress can cause the flow or convection of the material, which in turn drives the hard lithosphere to move as an integrated body (Qiu et al., 2006). There are two major types of migration for asthenosphere material: 1) horizontal flow migration of asthenosphere material. When the middle and lower parts of the lithosphere of the Indian plate and the Eurasian plate collided in the Tibetan Plateau, the asthenosphere of the Tibetan Plateau went through rheological migration with the main body migrating to the east and southeast of Asia. This process caused the thinning of the asthenosphere in the Tibetan Plateau and the thickening of the asthenosphere in the adjacent region. 2) Vertical flow migration of the asthenosphere material. During the collision process, part of the asthenosphere material migrated vertically upward (Zhong et al., 2017) and mixed with material in the lithosphere. After the collision, these asthenosphere residual materials were mingled and enclosed to the lithosphere.

According to this study, the structure of the lithosphere beneath the Songpan-Ganzi Block is complex. It can be split into an upper lithosphere with low velocity feature and a deeper lithosphere layer that went through delamination. There may be partially molten material under the upper lithosphere, exhibiting an overall lithosphere with weak strength and extensive hot material activities. Ye et al. (2017) observed a low-velocity zone in the upper mantle beneath Songpan-Ganzi using the joint inversion of receiver function and surface wave, and concluded that the hot asthenospheric flows and its effect of thermal erosion caused the delamination of the lithosphere. The low-velocity zone existing at the top of the upper mantle of the Songpan-Ganzi Block adjacent to the Qinling tectonic zone balanced the surface uplift in the boundary zone (Ye et al., 2018). The Sichuan Basin and central Ordos have the thickest lithosphere (>200 km) in the study area. The lithosphere in the Alxa Block, the Qinling tectonic belt and the surrounding areas of Ordos is relatively thick (~150 km). The lithospheric material in these areas exhibits high-velocity characteristics, with an overall high-strength lithospheric structure, suggesting the inability of upward movement of the asthenospheric material. Compared with the stable blocks with high mechanical strength in Ordos and the Sichuan Basin, the Alxa Block is characterized by the coexistence of weak high-velocity anomalies and local weak low-velocity anomalies in the depth range of lithosphere (Guo et al., 2017; Zheng et al., 2018), indicating that the lithosphere in this area may be undergoing deformation and destruction under the compression of material from the NE Tibetan Plateau.

According to the characteristics of surface movement observed by current GPS (Liang et al., 2013), relative to the stable Eurasian plate, the surface material in the northeastern Tibetan Plateau is still thrusting toward the northeast at a rapid rate. The SKS wave splitting study (Figure 9; Chang et al., 2017; Liu et al., 2020; Chang et al., 2021; Liu et al., 2021) reveals that most areas in the west of the study region and the Datong volcano display strong fast-wave polarization in the NW-SE direction, and the Qinling tectonic belt shows a strong fast wave polarization in the E-W direction, while the anisotropy intensity of the Ordos block and Sichuan basin in the middle of the study area are obviously weakened. From Figure 9B, the NE Ordos block and Datong volcanic area have roughly the same lithospheric thickness and SKS fast wave direction, indicating that the lithospheric thinning in the NE Ordos block is related to the volcanic activity. Compared with the central part of Ordos, the SW Ordos block has significantly greater anisotropic strength and a thinner lithosphere, which suggests that the lithosphere in the southwest of Ordos has been reformed and thinned. Compared with the Sichuan Basin and the Ordos Basin at both sides, the Qinling tectonic belt has a low-velocity zone at the depth of 100–160 km, which may be asthenosphere material. The trend of the asthenosphere low velocity zone is roughly the same as the regional SKS wave polarization direction, indicating that there is an obvious nearly east-west asthenosphere material flow under the Qinling tectonic belt, so the Qinling tectonic belt may be an important channel for material extrusion on the NE Tibetan Plateau (Chang et al., 2011; Yu and Chen, 2016; Guo and Chen, 2017).

5 Conclusion

In this study, the S-wave velocity structure results down to 200 km depth in the study area were obtained using the joint inversion of the receiver function and surface wave dispersion. The distribution characteristics of the crust and lithosphere structures in the study area were analyzed in detail, and the deformation mechanism and the characteristics of deep material migration of the NE Tibetan Plateau were further discussed. The results illustrate that a relatively thick sedimentary layer is distributed in the basins of the study area, which is fairly consistent with the geological tectonic background. The crustal thickness shows a drastic lateral change, gradually thinning from west to east. The crustal thickness of the eastern plateau is up to 65 km, followed by the thickness of the Sichuan Basin and Ordos Basin at about 40 km, and the thinnest part occurs in the southeastern region at about 30 km. According to the LAB burial depth distribution obtained in this study, there is a relatively thick lithosphere (>200 km) below the Sichuan and the Ordos Basins, and the thinnest part of the lithosphere in the east is about 60–80 km, suggesting extensive destruction and reformation processes.

The crustal thickness of the Tibetan Plateau shows an overall tendency to gradually decrease outwards, which corresponds to the outward expansion of the plateau. The NE Songpan-Ganzi, the western Qinling, and the Qilian tectonic belts have low-velocity layers in the middle and lower crust. Based on related research, we believe that there is no local melting in this area. Combined with the low Poisson's ratio and radial anisotropy in the region, we conclude that there is no extensive partial melting in the region to support the lower crustal flow model. There are low velocity zones in the lower crust in the Qinling tectonic belt, but they are not connected, indicating that they may not be able to be used as a channel for material extrusion from the NE Tibetan Plateau at the crustal scale.

In the range of mantle, the Songpan-Ganzi Block has a relatively thick low-velocity zone below the Moho, which may be related to the surface uplift and orogeny of the plateau. The lithosphere structure under the Songpan-Ganzi Block is quite complex, displaying signs of delamination and characteristics of vertical migration in the asthenosphere underneath. The Sichuan Basin and the Ordos Block show significant high-velocity anomalies, and have a quite thick lithosphere (>200 km), while the Qinling tectonic belt has a thin lithosphere (100–130 km). Combining with the characteristics of the regional SKS wave polarization direction, there is an explicit asthenosphere material flow on an approximately east-west direction below the Qinling tectonic belt. Therefore, the outward expansion of the material in the NE Tibetan Plateau encountered strong obstruction of the rigid Ordos block and the rigid Sichuan Basin, and formed an important channel for the extrusion of material from west to east beneath the Qinling tectonic belt at the upper mantle scale.

Data availability statement

Publicly available datasets were analyzed in this study. This data can be found here: The Earthquake Science Data Center, Institute of Geophysics, China Earthquake Administration (http://www.esdc.ac.cn/, networks: X3, X2, T1, T0, S0, R4, SC, GS, SN, SX, NM, NX) and the Incorporated Research Institutions for Seismology (IRIS).

Author contributions

WW collected the waveform data, plotted the figures used in this study and wrote the manuscript. GC provided literature research and wrote part of the manuscript. JW guided this work. LF provided useful suggestions. All authors contributed to the article and approved the submitted version.

Funding

This research was supported by National Natural Science Foundation of China (Grant No. 41974058), and the Special Fund of the Institute of Geophysics, China Earthquake Administration (Grant No. DQJB19A35).

Conflict of interest

The authors declare that the research was conducted in the absence of any commercial or financial relationships that could be construed as a potential conflict of interest.

Publisher's note

Supplementary material

The Supplementary Material for this article can be found online at: https://www.frontiersin.org/articles/10.3389/feart.2022.1066265/full#supplementary-material

References

Agius, M. R., and Lebedev, S. (2014). Shear-velocity structure, radial anisotropy and dynamics of the Tibetan crust. *Geophys. J. Int.* 199 (3), 1395–1415. doi:10.1093/gji/ggu326

An, M., and Shi, Y. (2006). Lithospheric thickness of the Chinese continent. *Phys. Earth Planet. Interiors* 159 (3), 257–266. doi:10.1016/j.pepi.2006.08.002

Bao, X., Song, X., and Li, J. (2015). High-resolution lithospheric structure beneath Mainland China from ambient noise and earthquake surface-wave tomography. *Earth Planet. Sci. Lett.* 417, 132–141. doi:10.1016/j.epsl.2015.02.024

Bao, X., Song, X., Xu, M., Wang, L., Sun, X., Mi, N., et al. (2013). Crust and upper mantle structure of the north China craton and the NE Tibetan plateau and its tectonic implications. *Earth Planet. Sci. Lett.* 369, 129–137. doi:10.1016/j.epsl.2013.03.015

Bi, B., Hu, X., Li, L., Zhang, H., Liu, S., and Cai, J. (2016). Multi-scale analysis to the gravity field of the northeastern Tibetan plateau and its geodynamic implications. *Chin. J. Geophys. (in Chinese)* 59 (2), 543–555. doi:10.6038/cjg20160213

Birch, F. (1961). The velocity of compressional waves in rocks to 10 kilobars: 2. *J. Geophys. Res.* 66 (7), 2199–2224. doi:10.1029/JZ066i007p02199

Cai, G., Wang, W., Wu, J., and Fang, L. (2021). Surface wave tomography based on Eikonal tomography in Ordos and adjacent areas. *Chinese Journal of Geophysics* 64 (4), 1215–1226. doi:10.6038/cjg2021O0070

Chang, L., Ding, Z., Wang, C., and Flesch, L. M. (2017). Vertical coherence of deformation in lithosphere in the NE margin of the Tibetan plateau using GPS and shear-wave splitting data. *Tectonophysics* 699, 93–101. doi:10.1016/j.tecto.2017.01.025

Chang, L., Ding, Z., and Wang, C. (2021). Upper mantle anisotropy and implications beneath the central and Western North China and the NE margin of Tibetan Plateau. *Chinese Journal of Geophysics (in Chinese)* 64 (1), 114–130. doi:10.6038/cjg2021O0315

Chang, L., Wang, C., and Ding, Z. (2011). Upper mantle anisotropy in the Ordos Block and its margins. *Sci. China Earth Sci.* 54, 888–900. doi:10.1007/s11430-010-4137-2

Chen, L., Cheng, C., and Wei, Z. (2009). Seismic evidence for significant lateral variations in lithospheric thickness beneath the central and Western North China Craton. *Earth Planet. Sci. Lett.* 286 (1-2), 171–183. doi:10.1016/j.epsl.2009.06.022

Chen, L., Jiang, M. M., Yang, J. H., Wei, Z. G., Liu, C. Z., and Ling, Y. (2014). Presence of an intralithospheric discontinuity in the central and Western North China craton: Implications for destruction of the craton. *Geology* 42, 223–226. doi:10.1130/G35010.1

Clark, M. K., and Royden, L. H. (2000). Topographic ooze: Building the eastern margin of tibet by lower crustal flow. *Geology* 28, 703–706. doi:10.1130/0091-7613(2000)028<0703:tobtem>2.3.co;2

England, P., and Houseman, G. (1986). Finite strain calculations of continental deformation, 2: Comparison with the India–Asia collision zone. *J. Geophys. Res.* 91 (B3), 3664–3676. doi:10.1029/jb091ib03p03664

England, P., and Houseman, G. (1988). The mechanics of the Tibetan Plateau. *Philos. Trans. R. Soc. Lond. Ser.* A326, 301–320.

Feng, M., An, M., and Dong, S. (2017). Tectonic history of the ordos block and qinling orogen inferred from crustal thickness. *Geophysical Journal International* 210 (1), 303–320. doi:10.1093/gji/ggx163

Feng, M., An, M., Mechie, J., Zhao, W., Xue, G., and Su, H. (2020). Lithospheric structures of and tectonic implications for the central–east Tibetan plateau inferred from joint tomography of receiver functions and surface waves. *Geophysical Journal International* 223 (3), 1688–1707. doi:10.1093/gji/ggaa403

Fu, Y., and Xiao, Z. (2020). Ambient noise tomography of Rayleigh and Love wave in Northeast Tibetan plateau and adjacent regions. *Chinese Journal of Geophysics (in Chinese)* 63 (3), 860–870. doi:10.6038/cjg2020N0239

Gee, L., and Jordan, T. (1992). Generalized seismological data functionals. *Geophys. J. Int.* 111 (2), 363–390. doi:10.1111/j.1365-246X.1992.tb00584.x

Guo, H., Ding, Z., and Xu, X. (2017). Upper mantle structure beneath the northern South-Nouth Seismic Zone from teleseismic traveltime data. *Chinese Journal of Geophysics (in Chinese)* 60 (1), 86–97. doi:10.6038/cjg20170108

Guo, X., Gao, R., Li, S., Xu, X., Huang, X., Wang, H., et al. (2016). Lithospheric architecture and deformation of NE Tibet: New insights on the interplay of regional tectonic processes. *Earth and Planetary Science Letters* 449, 89–95. doi:10.1016/j.epsl.2016.05.045

Guo, Z., and Chen, Y. J. (2017). Mountain building at northeastern boundary of Tibetan plateau and craton reworking at ordos block from joint inversion of ambient noise tomography and receiver functions. *Earth and Planetary Science Letters* 463 (34), 232–242. doi:10.1016/j.epsl.2017.01.026

Han, S., Zhang, H., Xin, H., Shen, W., and Yao, H. (2022). USTClitho2.0: Updated unified seismic tomography models for continental China lithosphere from joint inversion of body-wave arrival times and surface-wave dispersion data. *Seismological Research Letters* 93 (1), 201–215. doi:10.1785/0220210122

Huang, J., and Zhao, D. (2006). High-resolution mantle tomography of China and surrounding regions. *J. Geophys. Res.* 111 (B9), B09305. doi:10.1029/2005jb004066

Huang, Z., Li, H., and Xu, Y. (2013). Lithospheric S-wave velocity structure of the North-South Seismic Belt of China from surface wave tomography[J]. *Chinese Journal of Geophysics (in Chinese)*, 56(4): 1121–1131. doi:10.6038/cjg20130408

Huang, Z., Li, H., Zheng, Y., and Peng, Y. (2009). The lithosphere of North China Craton from surface wave tomography. *Earth and Planetary Science Letters* 288 (1-2), 164–173. doi:10.1016/j.epsl.2009.09.019

Huang, Z., Su, W., Peng, Y., Zheng, Y., and Li, H. (2003). Rayleigh wave tomography of China and adjacent regions. *J. Geophys. Res.* 108 (B2). doi:10.1029/2001jb001696

Huang, Z., Tilmann, F., Xu, M., Wang, L., Ding, Z., Mi, N., et al. (2017). Insight into NE Tibetan Plateau expansion from crustal and upper mantle anisotropy revealed by shear-wave splitting. *Earth and Planetary Science Letters* 478, 66–75. doi:10.1016/j.epsl.2017.08.030

Huang, Z. (2011). Velocity anisotropy in the crust and upper mantle of North China. *Chinese J. Geophys.* 54 (3), 169–180. doi:10.1002/cjg2.1598

Jin, G., and Gaherty, J. B. (2015). Surface wave phase-velocity tomography based on multichannel cross-correlation. *Geophysical Journal International* 201 (3), 1383–1398. doi:10.1093/gji/ggv079

Julia, J., Ammon, C. J., Herrmann, R. B., and Correig, A. M. (2000). Joint inversion of receiver function and surface wave dispersion observations. *Geophysical Journal International* 143 (1), 99–112. doi:10.1046/j.1365-246x.2000.00217.x

Li, C., van der Hilst, R. D., Meltzer, A. S., and Engdahl, E. R. (2008). Subduction of the Indian lithosphere beneath the Tibetan Plateau and Burma. *Earth Planet. Sci. Lett.* 274, 157–168. doi:10.1016/j.epsl.2008.07.016

Li, H., Shen, Y., Huang, Z., Li, X., Gong, M., Shi, D., et al. (2014). The distribution of the mid-to-lower crustal low-velocity zone beneath the northeastern Tibetan plateau revealed from ambient noise tomography. *J. Geophys. Res. Solid Earth* 119 (3), 1954–1970. doi:10.1002/2013jb010374

Li, S., Guo, Z., Chen, Y. J., Yang, Y., and Huang, Q. (2018). Lithospheric structure of the Northern Ordos from ambient noise and teleseismic surface wave tomography. *J. Geophys. Res. Solid Earth* 123 (8), 6940–6957. doi:10.1029/2017jb015256

Li, Y., Wang, X., Zhang, R., Wu, Q., and Ding, Z. (2017). Crustal structure across the NE Tibetan Plateau and Ordos Block from the joint inversion of receiver functions and Rayleigh-wave dispersions. *Tectonophysics* 705, 33–41. doi:10.1016/j.tecto.2017.03.020

Li, Z., Guo, B., Liu, Q., Chen, J., Li, S., and Qi, S. (2019). P-wave structure of upper mantle beneath the Northeastern Tibetan Plateau from multi-scale seismic tomography. *Chinese Journal of Geophysics (in Chinese)* 62 (4), 1244–1255. doi:10.6038/cjg2019J0392

Liang, S., Gan, W., Shen, C., Zhou, D., Liu, J., Chen, W., et al. (2013). Three-dimensional velocity field of present-day crustal motion of the Tibetan Plateau derived from GPS measurements. *J. Geophys. Res. Solid Earth* 118 (10), 5722–5732. doi:10.1002/2013jb010503

Lin, F. C., Ritzwoller, M. H., and Snieder, R. (2009). Eikonal tomography: Surface wave tomography by phase front tracking across a regional broad-band seismic array. *Geophysical Journal International* 177 (3), 1091–1110. doi:10.1111/j.1365-246x.2009.04105.x

Liu, J., Wu, J., Wang, W., Cai, Y., and Fang, L. (2021). Seismic anisotropy and implications for lithospheric deformation beneath the Ordos Block and surrounding regions. *Geophysical Journal International* 226 (3), 1885–1896. doi:10.1093/gji/ggab154

Liu, J., Wu, J., Wang, W., Fang, L., and Chang, K. (2020). Seismic anisotropy beneath the eastern margin of the Tibetan Plateau from SKS splitting observations. *Tectonophysics* 785, 228430. doi:10.1016/j.tecto.2020.228430

Molnar, P., and Tapponnier, P. (1975). Cenozoic Tectonics of Asia: Effects of a Continental Collision: Features of recent continental tectonics in Asia can be interpreted as results of the India-Eurasia collision. *Science* 189 (4201), 419–426. doi:10.1126/science.189.4201.419

Pan, J., Li, Y., Wu, Q., Ding, Z., and Yu, D. (2017). Phase velocity maps of Rayleigh wave based on a dense coverage and portable seismic array in NE Tibetan plateau and its adjacent regions. *Chin. J. Geophys.* 60 (6), 2291–2303. doi:10.6038/cjg20170621

Peltzer, G., and Tapponnier, P. (1998). Formation and evolution of strike-slip faults, rifts, and basins during the India-Asia collision: An experimental approach. *J. Geophys. Res. Solid Earth* 93 (B12), 15085–15117.

Priestley, K., and McKenzie, K. (2006). The thermal structure of the lithosphere from shear wave velocities. *Earth Planet. Sci. Lett.* 244 (1-2), 285–301.

Qiu, R., Li, T., Zhou, S., Deng, J., Xiao, Q., and Geng, S. (2006). *The composition and evolution of the lithosphere in China continent (in Chinese)*. Beijing: Geological Publishing House.

Royden, L. H., Burchfiel, B. C., King, R. W., Chen, Z., Shen, F., Liu, Y., et al. (1997). Surface de-formation and lower crustal flow in eastern Tibet. *Science* 276, 788–790. doi:10.1126/science.276.5313.788

Shen, W., Ritzwoller, M. H., Kang, D., Kim, Y., Lin, F. C., Ning, J., et al. (2016). A seismic reference model for the crust and uppermost mantle beneath China from surface wave dispersion. *Geophys. J. Int.* 206 (2), 954–979. doi:10.1093/gji/ggw175

Silver, P., and Holt, W. (2002). The mantle flow field beneath western North America. *Science* 295 (5557), 1054–1057.

Tapponnier, P., Zhiqin, X., Roger, F., Meyer, B., Arnaud, N., Wittlinger, G., et al. (2001). Oblique stepwise rise and growth of the tibet plateau. *Science* 294, 1671–1677. doi:10.1126/science.105978

Tian, Y., and Zhao, D. (2011). Destruction mechanism of the North China craton: insight from P and S wave mantle tomography. *Journal of Asian Earth Sciences* 42 (6), 1132–1145. doi:10.1016/j.jseaes.2011.06.010

Tian, Y., Zhao, D., Sun, R., and Teng, J. (2009). Seismic imaging of the crust and upper mantle beneath the North China Craton. *Physics of the Earth and Planetary Interiors* 172 (3-4), 169–182. doi:10.1016/j.pepi.2008.09.002

Vinnik, L., Makeyeva, L., Milev, A., and Usenko, A. (1992). Global patterns of azimuthal anisotropy and deformations in the continental mantle. *Geophys. J. Int.* 111 (3), 433–447. doi:10.1111/j.1365-246X.1992.tb02102.x

Wang, S., Wang, F., Zhang, J., Jia, S., Zhang, C., Zhao, J., et al. (2014). The P-wave velocity structure of the lithosphere of the North China craton—results from the wendeng-alxa Left banner deep seismic sounding profile. *Sci. China Earth Sci.* 57 (9), 2053–2063. doi:10.1007/s11430-014-4903-7

Wang, W., Wu, J., Fang, L., Lai, G., and Cai, Y. (2017b). Crustal thickness and Poisson's ratio in southwest China based on data from dense seismic arrays. *J. Geophys. Res. Solid Earth* 122, 7219–7235. doi:10.1002/2017JB013978

Wang, W., Wu, J., Fang, L., Lai, G., and Cai, Y. (2017a). Sedimentary and crustal thicknesses and Poisson's ratios for the NE Tibetan Plateau and its adjacent regions based on dense seismic arrays. *Earth and Planetary Science Letters* 462, 76–85. doi:10.1016/j.epsl.2016.12.040

Wang, W., Wu, J., Fang, L., Lai, G., Yang, T., and Cai, Y. (2014a). S wave velocity structure in southwest China from surface wave tomography and receiver functions. *J. Geophys. Res. Solid Earth* 119 (2), 1061–1078. doi:10.1002/2013jb010317

Wang, X., Li, Y., Ding, Z., Zhu, L., Wang, C., Bao, X., et al. (2017). Three-dimensional lithospheric S wave velocity model of the NE Tibetan Plateau and

Western North China Craton. *J. Geophys. Res. Solid Earth* 122 (8), 6703–6720. doi:10.1002/2017jb014203

Wei, X., Jiang, M., Liang, X., Chen, L., and Ai, Y. (2017). Limited southward underthrusting of the Asian lithosphere and material extrusion beneath the northeastern margin of Tibet, inferred from teleseismic Rayleigh wave tomography. *J. Geophys. Res. Solid Earth* 122 (9), 7172–7189. doi:10.1002/2016jb013832

Wei, Z., Chen, L., Jiang, M., and Ling, Y. (2015). Lithospheric structure beneath the central and Western north China craton and the adjacent qilian orogenic belt from Rayleigh wave dispersion analysis. *Tectonophysics* 646, 130–140. doi:10.1016/j.tecto.2015.02.008

Wu, J., Liu, Y., Zhong, S., Wang, W., Cai, Y., Wang, W., et al. (2022). Lithospheric structure beneath Ordos Block and surrounding areas from joint inversion of receiver function and surface wave dispersion. *Sci. China Earth Sci.* 65, 1399–1413. doi:10.1007/s11430-021-9895-0

Yang, Y., Zheng, Y., Chen, J., Zhou, S., Celyan, S., Sandvol, E., et al. (2013). Rayleigh wave phase velocity maps of Tibet and the surrounding regions from ambient seismic noise tomography. *Geochem. Geophys. Geosyst.* 11 (8), 10–1029. doi:10.1029/2010gc003119

Yang, Z., Chen, Y., Zhang, X., and Song, X. (2019). S-wave velocity structure and radial anisotropy in eastern and north-eastern margins of Tibetan plateau. *Chinese Journal of Geophysics (in Chinese)* 62 (12), 4554–4570. doi:10.6038/cjg2019N0149

Yang, Z., and Zhang, X. (2018). Ambient noise Rayleigh wave tomography in the northeastern Tibetan Plateau. *Acta Seismologica Sinica* 40 (1), 1–12.

Ye, Z., Gao, R., Li, Q., Xu, X., Huang, X., Xiong, X., et al. (2018). Eastward extrusion and northward expansion of the Tibetan Plateau&mdash; Discussions for the deep processes of the plateau uplift. *Chin. Sci. Bull.* 63 (31), 3217–3228. doi:10.1360/n972018-00478

Ye, Z., Li, J., Gao, R., Song, X., Li, Q., Li, Y., et al. (2017). Crustal and uppermost mantle structure across the tibet-qinling transition zone in NE tibet: Implications for material extrusion beneath the Tibetan plateau. *Geophys. Res. Lett.* 44 (20), 316–323. doi:10.1002/2017gl075141

Yin, A., and Harrison, T. (2000). Geologic evolution of the Himalayan-Tibetan orogen. *Annu. Rev. Earth Planet. Sci.* 28 (1), 211–280.

Yu, Y., and Chen, Y. J. (2016). Seismic anisotropy beneath the southern Ordos block and the Qinling-Dabie orogen, China: Eastward Tibetan asthenospheric flow around the southern Ordos. *Earth and Planetary Science Letters* 455, 1–6. doi:10.1016/j.epsl.2016.08.026

Zhan, Y., Zhao, G., Wang, L., Wang, J., Chen, X., Zhao, L., et al. (2014). Deep electric structure beneath the intersection area of West Qinling orogenic zone with North-South Seismic tectonic zone in China. *Chinese Journal of Geophysics (in Chinese)* 57 (8), 2594–2607. doi:10.6038/cjg20140819

Zhang, G., Zhang, Z., and Dong, Y. (1995). Nature of main tectono-lithostratigraphic units of the qinling orogen: Implications for the tectonic evolution. *Acta Petrologica Sinica* 11 (2), 101–114.

Zhang, H., Teng, J., Tian, X., Zhang, Z., and Gao, R. (2013). Lithospheric thickness and upper mantle anisotropy beneath the northeastern Tibetan Plateau. *Chinese Journal of Geophysics (in Chinese)* 56 (2), 459–471. doi:10.6038/cjg20130210

Zhang, H., Teng, J., Tian, X., Zhang, Z., Gao, R., and Liu, J. (2012). Lithospheric thickness and upper-mantle deformation beneath the NE Tibetan Plateau inferred from S receiver functions and SKS splitting measurements. *Geophysical Journal International* 191 (3), 1285–1294. doi:10.1111/j.1365-246x.2012.05667.x

Zhao, G., Sun, M., Wilde, S. A., and Sanzhong, L. (2005). Late Archean to Paleoproterozoic evolution of the North China Craton: Key issues revisited. *Precambrian Res.* 136 (3), 177–202.

Zheng, C., Ding, Z., and Song, X. (2018). Joint inversion of surface wave dispersion and receiver functions for crustal and uppermost mantle structure beneath the northern north-south seismic zone. *Chinese Journal of Geophysics (in Chinese)* 61 (4), 1211–1224. doi:10.6038/cjg2018L0443

Zheng, D., Li, H., Shen, Y., Tan, J., Ouyang, L., and Li, X. (2016). Crustal and upper mantle structure beneath the northeastern Tibetan Plateau from joint analysis of receiver functions and Rayleigh wave dispersions. *Geophys. J. Int.* 204 (1), 583–590. doi:10.1093/gji/ggv469

Zhong, S., Wu, J., Fang, L., Wang, W., Fan, L., and Wang, H. (2017). Surface wave Eikonal tomography in and around the northeastern margin of the Tibetan plateau. *Chinese Journal of Geophysics (in Chinese)* 60 (6), 2304–2314. doi:10.6038/cjg20170622

frontiers | Frontiers in Earth Science

TYPE Original Research
PUBLISHED 18 January 2023
DOI 10.3389/feart.2022.1065782

OPEN ACCESS

EDITED BY
Zengxi Ge,
Peking University, China

REVIEWED BY
Yong Yu,
Southern University of Science and Technology, China
Jing Wu,
Institute of Geology and Geophysics (CAS), China

*CORRESPONDENCE
Dinghui Yang,
ydh@tsinghua.edu.cn
Qiusheng Li,
lqs1958@163.com

SPECIALTY SECTION
This article was submitted to Solid Earth Geophysics, a section of the journal Frontiers in Earth Science

RECEIVED 10 October 2022
ACCEPTED 10 November 2022
PUBLISHED 18 January 2023

CITATION
Han R, Yang D, Li Q, Fu W, Zhu G, Zhang H, Chen H and Cheng Y (2023), Structural boundary and deep contact relationship between the Yangtze and Cathaysia Blocks from crustal thickness gradients.
Front. Earth Sci. 10:1065782.
doi: 10.3389/feart.2022.1065782

Structural boundary and deep contact relationship between the Yangtze and Cathaysia Blocks from crustal thickness gradients

Rubing Han[1], Dinghui Yang[1]*, Qiusheng Li[2]*, Wei Fu[3], Gaohua Zhu[4], Hongshuang Zhang[2], Hao Chen[5] and Yongzhi Cheng[2]

[1]Department of Mathematical Sciences, Tsinghua University, Beijing, China, [2]Key Laboratory of Deep-Earth Dynamics of Ministry of Natural Resources, Institute of Geology, Chinese Academy of Geological Sciences, Beijing, China, [3]College of Transportation Engineering, Nanjing Tech University, Nanjing, China, [4]CAS Key Laboratory of Marine Geology and Environment, Center for Ocean Mega-Science, Institute of Oceanology, Chinese Academy of Sciences, Qingdao, China, [5]School of Geophysics and Measurement-Control Technology, East China University of Technology, Nanchang, China

The deep boundary and contact relationship between the Yangtze and Cathaysia Blocks (the major tectonic units of the Southern China Block), as well as the tectonic attributes of the Jiangnan Orogenic Belt, have remained unknown or controversial. Using data recorded by 128 portable broadband stations and 96 permanent stations, we obtained high-resolution images of crustal thickness and Poisson's ratio in the study area. The influences of crustal anisotropy and inclined interface were eliminated by using the newly proposed receiver function H–κ–c stacking method. We then used a gradient analysis method to obtain crustal thickness gradients at the boundary of the Yangtze and Cathaysia Blocks for the first time. Our results reveal that the crustal thickness varies from >38 km in the Qinling–Dabie Orogenic Belt to <30 km east of the Tanlu Fault and Cathaysia Block. Areas with high Poisson's ratios (>0.27) are concentrated on the flanks of the deep fault zone and the continental margin of the study area; those with low Poisson's ratios (<0.23) are concentrated in the Jiangnan Orogenic Belt. Large crustal thickness gradients are found beneath the eastern part of the Jiujiang–Shitai buried fault (>5 km/°). Combined with the velocity structure and discontinuity characteristics at different depths, these findings suggest that the Jiujiang–Shitai fault may constitute a deep tectonic boundary dividing the Yangtze and Cathaysia Blocks on the lithospheric scale. Moreover, our results support that the Cathaysia Block subducted northwestward toward the southeastern margin of the Yangtze Block in the Neoproterozoic, and that the Jiujiang–Shitai buried fault and Jiangshan–Shaoxing fault are the deep and shallow crustal contact boundaries of the two Blocks, respectively; that is, the Yangtze Block overlaps the Cathaysia Block.

KEYWORDS

Yangtze block, Cathaysia block, H-κ-c, gradient analysis, Jiujiang-Shitai buried fault

Introduction

Since the Neoproterozoic, the South China Block has experienced one of the most complex geological evolution processes worldwide, including collision collage, cleavage, destruction, and reconstruction (Shu, 2012; Zhang et al., 2012; Zhang et al., 2013). South China mainly consists of the Yangtze Block (YB), Cathaysia Block (CB), and the northeast-by-east (NEE)-trending Jiangnan Orogenic Belt (JOB) (Li et al., 2003; Charvet, 2013) (Figure 1). As important parts of South China, the YB and CB exhibit obvious differences in crustal composition and tectonic history. The YB is generally regarded as an Archean craton, and its basement, which is outcropped in its western part, is mainly composed of Archean to Proterozoic rocks (Qiu et al., 2000; Jiao et al., 2009). In comparison, the CB in the southeast is relatively young and consists mainly of Neoproterozoic basement and early Paleozoic sedimentary cover (Wang et al., 2007). The JOB (also known as the "Jinning Orogenic Belt" or "Sibao Orogenic Belt") is a linear uplift between the YB and CB. Constituting a set of Neoproterozoic trench-arc-basin assemblages, it is the product of collision–collage between the two Blocks (Zhang et al., 2021). The main part of the JOB is a large, NW-trending thrust fault–fold arc structural system; the inner deformation core comprises a Proterozoic structural uplift belt that is asymmetrical and fan-shaped and derives from the Middle and Late Indosinian to Yanshan periods (Li et al., 2016; Shu et al., 2019). Identifying and analyzing the boundary and collage evolution of the YB and CB is important for the study of tectonic division, magmatic mineralization, and basic geological theory in South China (Shu, 2012). However, owing to the strong alteration of tectonic activities since the Mesozoic and limited data resolution, the deep boundary and contact relationship between the two Blocks, as well as the tectonic attributes and deep dynamic processes of the JOB, remain controversial.

The Jiangshan–Shaoxing fault is widely considered to constitute the boundary between the YB and CB, and the southern boundary of the JOB based on petrology, geochronology, geochemistry, geophysics, and isotope data (e.g., Li and Li, 2003; Li et al., 2009; Cawood et al., 2013; Zhang et al., 2015). However, the location of the northern boundary of the JOB has remained unclear owing to poor exposure of Precambrian lithologies. Knowledge of the crustal structure and its various horizontal rates would provide critical evidence for block-boundary identification. Seismological method is one of the important means of obtaining high-resolution crustal structures. Previous active- and passive-source surveys have obtained the major crustal structural characteristics of South China, promoting the understanding

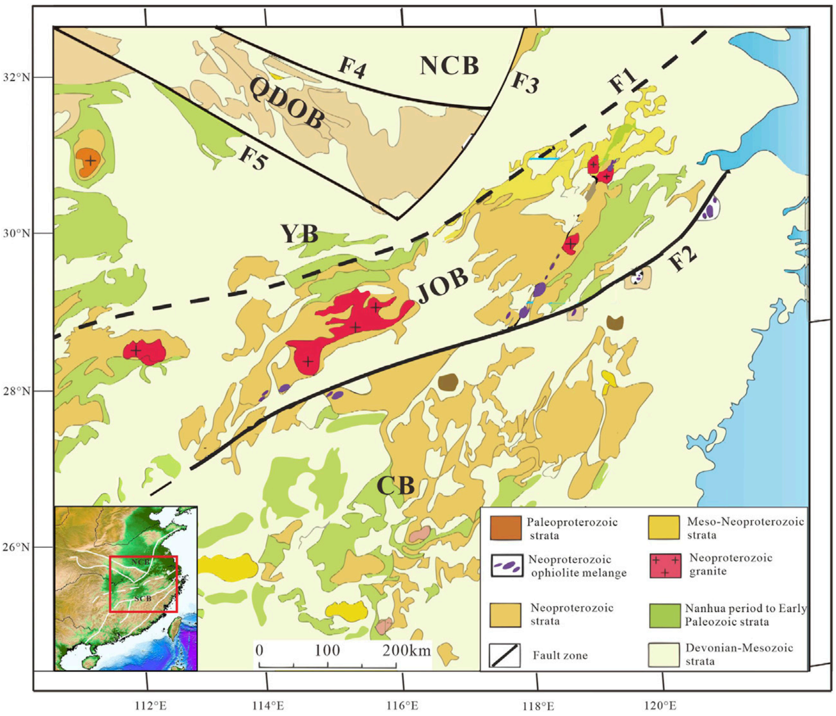

FIGURE 1
Simplified geological map of southeastern China, modified from Shu et al. (2019). NCB, North China Block; SCB, South China Block; YB, Yangtze Block; JOB, Jiangnan Orogenic Belt; QDOB, Qinling–Dabie Orogenic Belt; CB, Cathaysia Block; F1, Jiujiang–Shitai buried fault; F2, Jiangshan–Shaoxing fault; F3, Tanlu fault; F4, Xinyang–Shucheng fault; F5, Xiangfan–Guangji fault. The red rectangle in the illustration at the lower left corner indicates the study area.

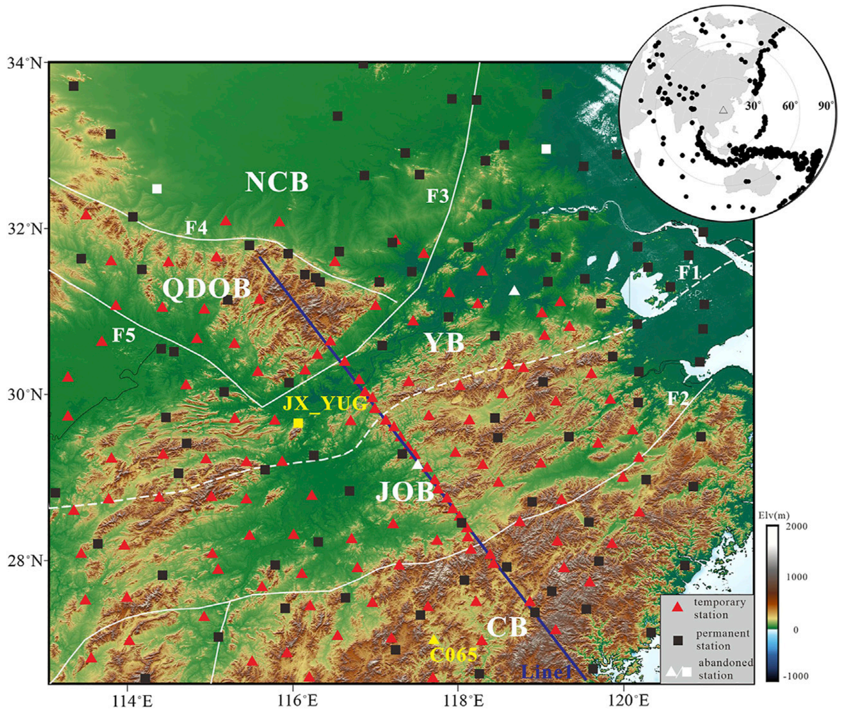

FIGURE 2
Location map of seismic stations and teleseismic events (upper right corner) in Southeastern China. The background color map indicate the topography. The yellow triangles and squares represent the locations of the stations shown in Figure 3 and Figure 4 respectively. Blue solid lines represent CCP stacking section (see Figure 9C, modified from Ye et al., 2019). The triangle and black dots in the upper right corner indicate the center of the study area and teleseismic events, respectively. Main structural lines and fault lines are described in Shu et al. (2019).

of the deep structure and dynamic processes of this continent. Zhang et al. (2005) used wide-angle reflection/refraction data to identify velocity variations of the crustal and uppermost mantle on the two flanks of the Jiangshan–Shaoxing fault zone. The receiver function common conversion point (CCP) stacking results of Huang. (2013) show that the crustal thickness changes significantly on the two flanks of the Jiujiang–Shitai (Jiangnan) buried fault. These high-resolution seismic profile results provide abundant information on the boundary between the YB and CB, but it remains difficult to describe the deep boundaries and understand the relationship between the two blocks because of the limitations of the linear profile. Obvious differences in the lithospheric structure between the YB and CB have been revealed based on a two-dimensional (2-D) network of permanent stations in South China. The lithospheric thickness of the YB is approximately 200 km, the crustal thickness is approximately 45 km, and the crustal composition is mainly mafic. In comparison, a relatively thin lithosphere (approximately 80 km) and crust (approximately 30 km) are present in the CB, and the crustal composition is mainly felsic (Wei et al., 2016; Zhang et al., 2018; Shahzad et al., 2021; Zhang et al., 2021). Previous studies have suggested that the Jiujiang–Shitai fault may constitute the northern boundary of the junction belt between the YB and CB, and have roughly described the spatial distribution of this buried fault zone (He et al., 2013; Guo and Gao, 2018; Zhang et al., 2019; Guo et al., 2019). However, owing to the sparse distribution of permanent stations and low resolution of the horizontal variation characteristics of the crustal structure obtained in previous studies, considerable uncertainty remains with regard to the location of the northern block boundary of the JOB.

Resolving this issue depends on the fine characterization of the 3-D Moho structure with high resolution in the junction belt. Dense seismic arrays can help to obtain high-resolution structural models of the Earth’s interior. The organic combination of this acquisition scheme with permanent network-based observations can yield massive amounts of data, which allow substantial improvements in the spatial resolution of images of the Earth’s interior. Among the multiple data processing methods, the receiver function method can effectively detect velocity discontinuities in the study area through rapid waveform stripping (Chen et al., 2022). In this study, we used data from 128 portable broadband stations and 96 permanent stations with complementary locations to provide enhanced coverage and dense sampling in the study area (Figure 2). The recently proposed receiver function method of “corrected” crustal thickness–average crustal Vp/Vs ratio (H–κ–c) superposition (Li et al., 2019) was utilized to obtain high-resolution images of the crustal thickness and Poisson’s ratio beneath the study area, following harmonic correction. With this framework, we applied a gradient analysis method that is sensitive to crustal thickness (or the Moho depth) to calculate the maximum horizontal gradient of the Moho which may represent the boundary of the YB and CB for the first time. This information provides key evidence for locating the boundary and identifying the directional trends of the main blocks in southeastern China.

Data and method

Data

A total of 128 temporary stations and 96 permanent stations were located in the study area (27°N–34°N, 113°E–123°E), which consists of five main tectonic units from north to south: the southern margin of the North China Block (NCB), the Qinling–Dabie Orogenic Belt (QDOB), the Lower Yangtze Block (YB), the Jiangnan Orogenic Belt (JOB), and the northeast region of the Cathaysia Block (CB). The temporary seismic stations used REFTEK-130 or Q330S+ data collectors, and CMG-3ESP (Band range, 60s-50 Hz) or CMG-3T (Band range, 120s-50 Hz) broadband seismometers with a sampling rate of 100 Hz. The data acquisition project of temporary stations was funded by China Geological Survey (CGS) and the fieldwork was finished cooperatively by Institute of Geology, Chinese Academy of Geological Sciences (IG of CAGS), Peking University (PKU), Nanjing University (NJU), Institute of Earthquake Forecasting of China earthquake Administration (IEF of CEA) and Institute of Geomechanics, Chinese Academy of Geological Sciences (IGM of CAGS) from July 2014 to December 2016, from which a total of 1,710 Gb data was recorded. The data of the permanent seismic stations were obtained from the Data Backup Centre for China Seismograph Network and recorded from January 2013 to December 2017 (Zheng et al., 2009).

According to standard processing flow (Liu et al., 1997; Wu and Zeng, 1998), we first removed the mean value, linear trend, *etc.* Then, we selected an earthquake catalogue corresponding to the study period from the United States Geological Survey (USGS), which contains 1,150 events with magnitudes greater than 5.5, and epicenter distances between 30° and 90°. Next, three-component waveforms (20 s before and 180 s after the first arrival P wave) were bandpass filtered by 0.05–2 Hz and rotated into Z-R-T coordinate to separate energy between the P wave and the conversions (Ps). We selected the data showing obvious first arrival of the P-wave without distortion, and employed time-domain iterative deconvolution to generate radial receiver functions (Ligorría and Ammon, 1999) with a Gaussian coefficient of 3.0. A total of 28,710 receiver functions were chosen for further analysis. Figure 3 shows the receiver function arrangement of No. C065. Ps were identifiable on the delay time diagram at nearly 3–4 s after the first P-wave arrival, and the crustal multiples (PpPs, PpSs+PsPs) were also visible. Good back-azimuthal coverages and epicentral distances were also observed (Figure 3, right). A total of 23,415 receiver function records with obvious first arrivals and high signal-to-noise ratios were chosen for further processing.

H-κ-c method

Crustal thickness (H) can provide key evidence for block boundary identification and is a significant parameter for describing fluctuation of the Moho. The average crustal Vp/Vs ratio (*κ*) reflects the material composition, structure, and physical state of crust.

The receive function H–κ stacking method jointly constrains H and *κ* based on the arrival time relationship between the Moho surface converted wave Ps, crustal multiples PpPs (M1), PsPs+PpSs (M2), and direct P wave information (Zhu and Kanamori, 2000). With different combinations of H and κ, we calculated the theoretical arrival times of Ps, M1, and M2 based on the crustal average velocity of the P wave (Vp). According to the theoretical arrival time, the corresponding amplitude was obtained in the receiver function; then, the amplitude was weighted and summed to acquire the optimal estimation of the combination of H and italic. Compared with the direct P-wave, the calculation expressions for the travel time of Ps, M1 and M2 were as follows:

$$
\begin{aligned}
t_{ps} &= H\left(\sqrt{\frac{\kappa^2}{{V_P}^2}-p^2}-\sqrt{\frac{1}{{V_P}^2}-p^2}\right)\\
t_{M1} &= H\left(\sqrt{\frac{\kappa^2}{{V_P}^2}-p^2}+\sqrt{\frac{1}{{V_P}^2}-p^2}\right)\\
t_{M2} &= 2H\sqrt{\frac{\kappa^2}{{V_P}^2}-p^2}
\end{aligned}
\tag{1}
$$

where t_{ps}, t_{M1}, and t_{M2} represent the arrival time differences of Ps, M1, and M2, respectively, relative to the direct P wave under crustal thicknesses of *H* and κ. *Vp* represents the crustal average P-wave velocity and *p* represents the ray parameter. The weighted sum was calculated as follows:

$$
S(H,\kappa) = w_1 r(t_{Ps}) + w_2 r(t_{M1}) - w_3 r(t_{M2}) \tag{2}
$$

where $r(t)$ is the amplitude of the receiver function; and w_1, w_2, and w_3 represent the proportions of Ps and crustal multiples in the superimposed energy, respectively. The Poisson’s ratio (*δ*) can be obtained from its relationship with Vp/Vs (*κ*): $= 0.5 - \frac{1}{2(\kappa^2-1)}$. Mean square error estimation followed the

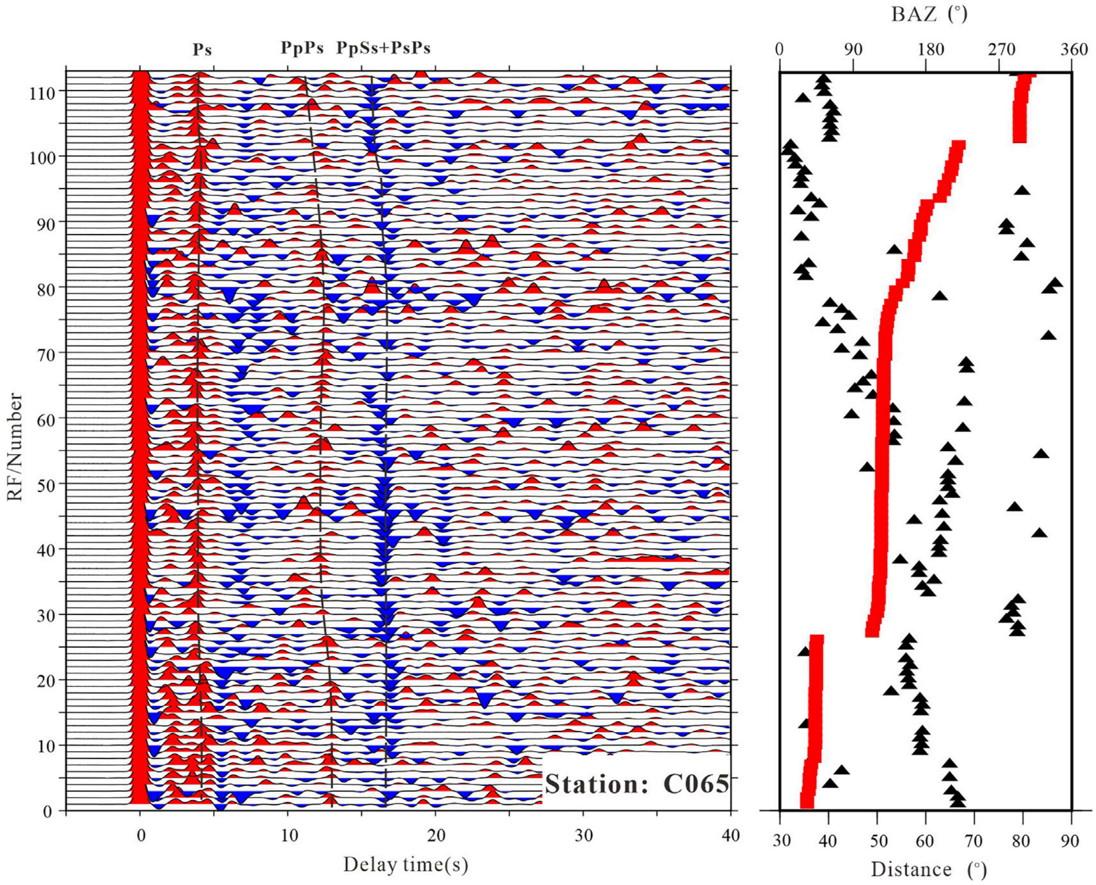

FIGURE 3
Receiver function (RF) records from station C065 (Left). Receiver functions arranged according to the back-azimuth, where the numbers on the horizontal axis denote the latency time of P wave arrival. The seismic phases (Ps, PpPs, PpSs+PsPs) are marked using red and broken lines. Red rectangles represent the back-azimuth, and the black triangles denote epicenter distance distribution.

method of Zhu and Kanamori (2000); that is, when $S(H, \kappa)$ reached the maximum value, it was Taylor expanded and take quadratic differentials for H and κ respectively. In particular:

$$\begin{cases} \sigma_H = 2\sigma_s / \dfrac{\partial^2 s}{\partial H^2} \\ \sigma_k = 2\sigma_s / \dfrac{\partial^2 s}{\partial \kappa^2} \end{cases} \tag{3}$$

mean-square deviations of H and κ, respectively. When the underground structure is relatively simple, the H−κ method can effectively constrain the crustal thickness and Vp/Vs ratio at the station because the arrival times of Ps and crustal multiples vary little with different azimuth angles. Nevertheless, when the crust has an obvious inclined interface (Lombardi et al., 2008) or anisotropic structures (Fang and Wu, 2009), the arrival times of the three phases vary considerably with the back-azimuth, causing the estimation results obtained using the H−κ method to deviate markedly from the real results, and even deviate from the normal range (Hammond, 2014). The inclined Moho surface and inner crustal interface lead to variations of the arrival time of the Ps, M1, and M2 seismic phases with the back-azimuth, taking 360° as the period. S-wave azimuthal anisotropy leads to variation in the arrival time of the seismic phase with the back-azimuth, taking 180° as the period. Moreover, an inclined interface and S-wave azimuthal anisotropy change the polarity of the multi-wave seismic phase, thereby reducing the estimation of the useful seismic phase energy stacking upon H−κ calculation and causing the search results to deviate.

The H−κ−c method represents an improved, "corrected" H−κ technology proposed by Li et al. (2019) considering both the Moho surface inclination and azimuthal anisotropy structure. Basically, harmonic fitting is performed on the three phases to minimize the biases due to the dipping Moho and crustal anisotropy. At present, the H−κ−c method has been widely applied to receiver function imaging of crustal structures in China, elucidating many detailed characteristics of crustal structures (Zhang et al., 2020; Li et al., 2021; Han et al., 2022). In particular, the second-order harmonic equation $F(\theta)$

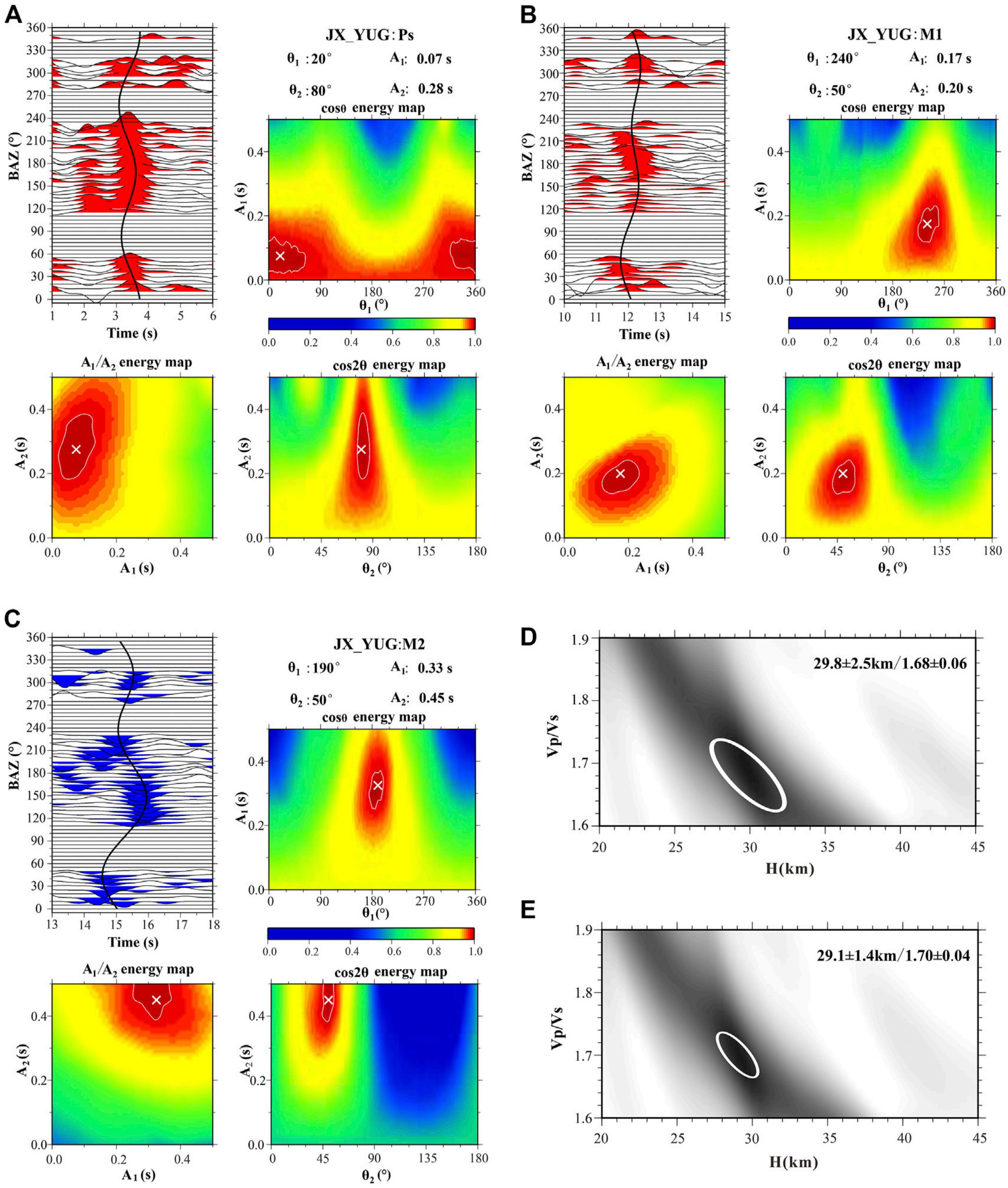

FIGURE 4
Harmonic fitting of Ps **(A)**, M1 **(B)**, and M2 **(C)** for JX_YUG. The black lines represent the arrival times of Ps, M1, and M2 phases. The cross marks indicate the best solutions, and the 99% contours show the empirical uncertainty. H−κ domain energy maps are shown with weighting factors of 0.7/0.2/0.1 **(D)** in H−κ stacking and 0.6/0.3/0.1 **(E)** in H−κ−c stacking. H, κ, and their uncertainties (σH, σκ) are listed in the top right. The error ellipses with one standard deviation (Zhu and Kanamori, 2000) are marked with white circles.

is used to fit the variations of Ps and crustal multiples with the back-azimuth affected by the inclined interface and S-wave azimuthal anisotropy. The harmonic fitting equation is as follows:

$$F(\theta) = A_0 + A_1 \cos(\theta - \theta_1) - A_2 \cos 2(\theta - \theta_2) \tag{4}$$

where $F(\theta)$ represents the arrival time of the Ps and crustal multiples as the back-azimuth (θ) changes, A_0 represents the center arrival time, and A_1, A_2, θ_1, and θ_2 represent the amplitude and phase of the first- and second-order changes, respectively. The harmonic correction is to find the optimal solution in the five-dimensional parameter ($dt=A_0-t_{ref}$, A_1, A_2, θ_1, θ_2) space,

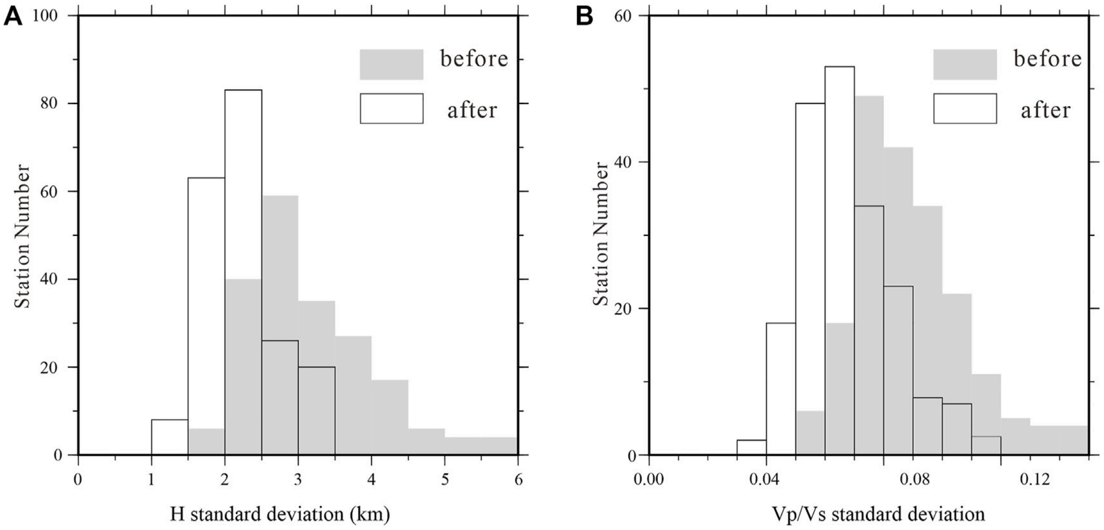

FIGURE 5
Comparison of the H-κ stacking standard deviation both before and after harmonic corrections. **(A)** Histogram of the differences of H (dH). **(B)** Histogram of the difference of Vp/Vs (dκ).

where t_{ref} represents the arrival time of Ps calculated using the traditional H–κ stacking method, and the preliminary search range of each parameter is set as: dt: −1.0 to 1.0 s; A_1, A_2: 0–0.5 s; θ_1: 0–355°; θ_2: 0–175° (Li et al., 2019). A_1 and A_2 can be adjusted if the region is characterized by a larger interface inclination or greater anisotropic strength. In this study, the average crustal Vp (6.3 km/s) value was obtained from the deep seismic profiles (Zheng et al., 2003), and we set the search interval of crustal thickness (H) to be 20–50 km and the Poisson's ratio (κ) to be 1.5–2.0 according to the regional geological characteristics (He et al., 2013; Wei et al., 2016). The weighting factors of the three phases (Ps, M1, and M2) were adjusted from 0.7, 0.2, and 0.1, to 0.6, 0.3, and 0.1, respectively. The weighting of M1 was increased because the harmonic corrections enhanced the coherency of the M1 phase as well as the stacking energy, while the weighting of M2 remained because it was relatively weaker and more complicated.

The detailed steps of the H–κ–c stacking method can be described as follows: 1) use the traditional H–κ method to obtain the reference arrival times t_{ref} of Ps, M1, and M2; 2) apply move-out corrections for all receiver functions to eliminate arrival times caused by different epicenter distances; 3) obtain the harmonic coefficients of the subsequent azimuth changes of Ps, M1, and M2 through harmonic fitting; and 4) use the harmonic parameters obtained in (3) to correct the corresponding Ps and crustal multiples, and apply traditional H–κ stacking again. As shown in Figure 4, the area of the one-sigma error ellipse decreased after harmonic correction. Overall, the standard deviations of H and κ are reduced from an average of ~3.50 km, ~0.08 to an average of ~2.0 km, ~0.06 (Figure 5). This validates the robustness of the H-κ-c method.

Gradient analysis method

In addition, to highlight the spatial distribution of the abrupt lateral Moho variations at the block boundary, we applied a technical strategy and method based on gradient analysis to obtain the first-order derivation of the crustal thickness value along the longitude and latitude directions in the spatial domain, and then conducted vector summation to obtain a "rate of change" distribution map (Xu et al., 2020). Compared with the traditional observation of the absolute value of the thickness, the gradient results provide more abundant information for the study of geological processes and have higher resolution along the block contact boundary. This is helpful in revealing local structural deformation characteristics that may be masked, and in further exploring geological issues such as the deep boundary division of lithospheric block units.

This analysis method requires 2-D imaging results with a large range and high resolution, and our new crustal thickness structure by the H–κ–c stacking method provides an apt basis for this analysis. The maximum horizontal gradient of the Moho is calculated as follows: 1) we applied an equally weighted spatial filter to the crustal thickness values with a filter radius of 30 km; 2) we calculated the first-order difference in the crustal thickness at each node along both the longitudinal and latitudinal directions; 3) we obtained the maximum horizontal gradient

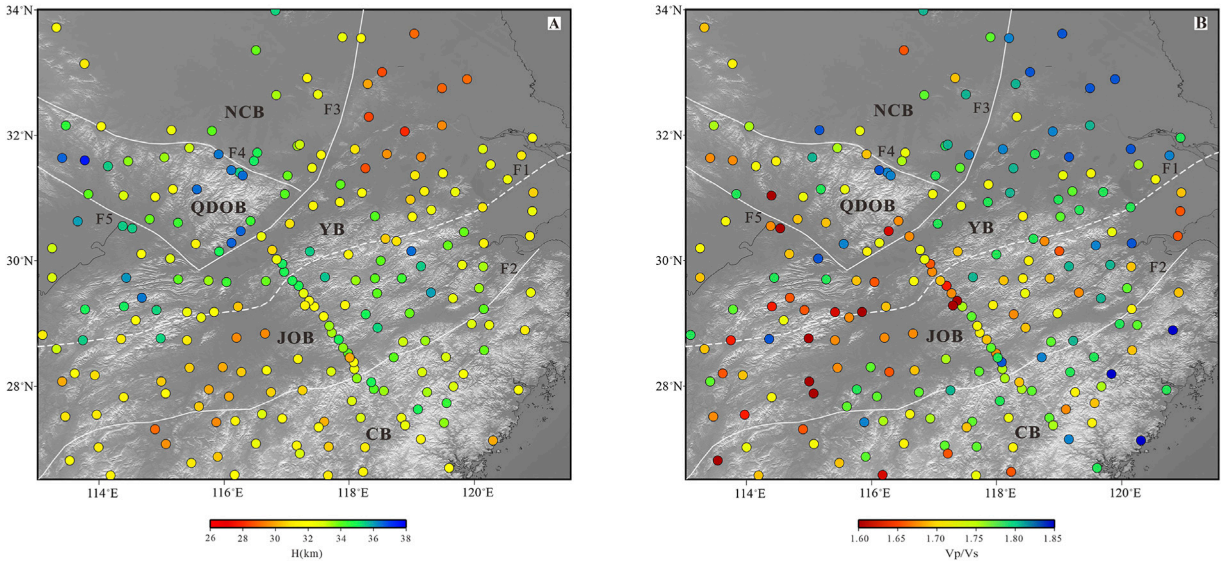

FIGURE 6
Distribution of crustal thickness **(A)** and Vp/Vs ratio **(B)** at the stations. Labels are the same as in Figure 1.

of the Moho from vector summations of the longitudinal and latitudinal gradients.

Results

Crustal thickness and gradients characteristics

We obtained the crustal thickness (H), Vp/Vs ratio, and Poisson's ratio (κ) after harmonic corrections using the H–κ–c stacking technique; the results are shown in Figure 6 and Supplementary Table S1. We abandoned four stations, which are shown in Figure 2, owing to the negative influence of the quality and quantity of station records, site conditions, underground structures, *etc.* In addition, because 19 stations had back-azimuth gaps of >90°, the harmonic correction was void; therefore, H and κ were still calculated using the traditional H–κ method. The statistical results show that the crustal thickness in the study area varies from 28.0 to 37.6 km, with an average value of 32.6 km; the error range was 1.0–3.3 km, and the average error value was 2.2 km. The Vp/Vs ratio varied from 1.63 to 1.82, (average 1.73); the error range was 0.03–0.11, and the average error value was 0.06. The low-error estimates for each station also indicate that the calculation result is reliable; results with relatively large errors were concentrated in the northeast of Jiangsu Province, where the sedimentary layer is relatively thick.

Figure 7 shows the 2-D variation characteristics of the crustal thickness and Poisson's ratio in the study area. Overall, our results reveal that H and κ exhibited obvious zoning and blocking characteristics. The variation from >38 km in the QDOB (the largest crustal thickness) to <30 km east of the Tanlu fault (the smallest crustal thickness) is consistent with the variation in the deep seismic sounding results (Deng et al., 2011; Xu et al., 2014). The resolution of the crustal thickness and Poisson's ratio was markedly improved with the substantial increase in seismic stations. The results further reveal that in the JOB and CB in the southern part of the study area, the crustal thickness generally does not exceed 32 km, whereas in high elevation areas, such as the Huangshan and Wuyishan, the crust is relatively thick (up to approximately 35 km).

Figure 7A illustrates the obvious difference in crustal thickness on the two flanks of the eastern part of the Jiujiang–Shitai buried fault (F1). Except for the relatively high elevation area in the eastern part of the JOB, the crust is relatively thick on the northwest side of F1, approximately 34 km, and relatively thin on the southeast side of F1, approximately 30 km. Figure 8 shows the distribution of the maximum horizontal gradient of the crustal thickness in the study region. A gradient zone with large lateral gradients is visible along the eastern part of the Jiujiang–Shitai buried fault (F1), with the gradient value >5 km/° (indicated by the red arrow), whereas no obvious change is observable along the Jiangshan–Shaoxing fault zone (F2), which is traditionally considered as the boundary between the YB and CB. In addition, the gradient results show that the eastern part of the QDOB is divided into several small blocks. As the deep boundary between the east and west of the Dabie Orogenic Belt, the Shangcheng–Macheng fault (F6) has obvious differences in rock assemblages, tectonic styles, and metallogenic backgrounds on the two flanks (Liu and Zhang,

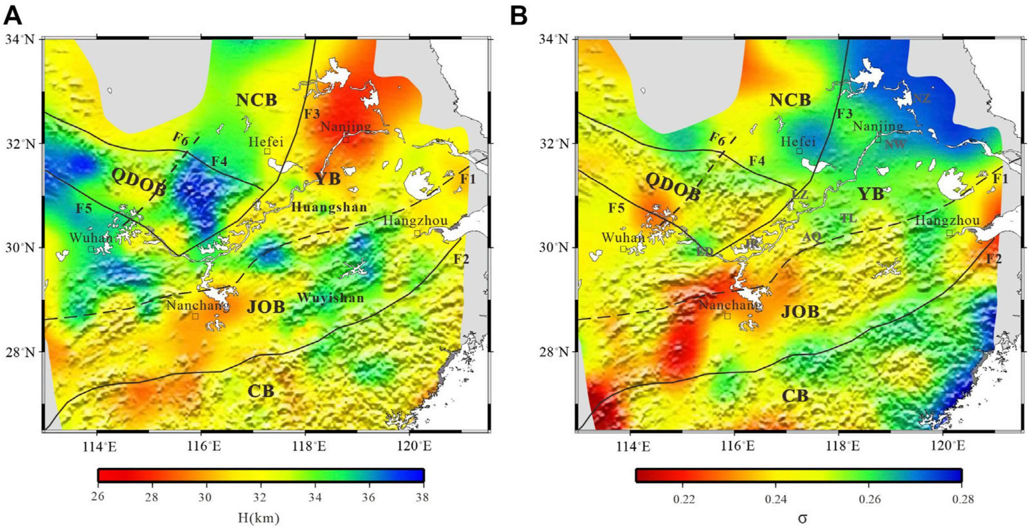

FIGURE 7
Two-dimensional distribution map of crustal thickness **(A)** and Poisson's ratio **(B)** in the study area. NZ, Ningzhen deposits; NW, Ningwu deposits; LZ, Luzong deposits; AQ, Anqing deposits; TL, Tongling deposits; JR, Jiurui deposits; ED, Southeastern Hubei deposits. F6, Shangcheng-Machang fault. Labels are the same as in Figure 1.

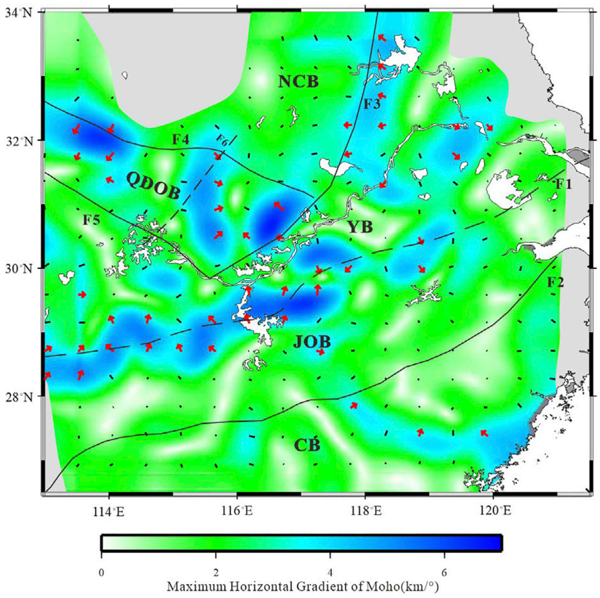

FIGURE 8
Maximum horizontal gradients of the crustal thickness. Short bars denote the directions of maximum gradients for every grid; red arrows show the grids with corresponding gradients >4 km/°. The direction indicated by the arrow indicates that the crustal thickness increases. Labels are the same as in Figure 1.

2013). The gradient results also show that the fault constitutes a deep boundary, and that the variation characteristics of crustal thickness are very clear, which is consistent with previous Pn tomography results (Gu et al., 2016; Yin et al., 2019). As shown in Figure 7A, east of the Tanlu fault (F3), at the site of the NCB and YB impact and bonding, the Moho depth is approximately 28 km, which is 3–5 km thinner than that of the surrounding structural units. The crustal thinning zone is distributed along the NE–SW direction and extends southward to the Jiujiang–Shitai buried fault (F1). The northern end cannot be clearly described as limited by the study area. The gradient results (Figure 8) more clearly describe the boundary of the crustal thinning zone (Shi et al., 2013; Xu et al., 2014).

Poisson's ratio variation

In general, the Poisson's ratio distribution in the study area shows obvious 2-D characteristics and a staggered alternating distribution (Figure 7B). Areas with high Poisson's ratios are concentrated on the two flanks of the Tanlu (F3) and Jiangshan–Shaoxing (F2) faults, as well as the southeast coastal area, with an average value of >0.27. In the bonding zone of the YB and CB, the Poisson's ratio shows obvious low-value distribution characteristics, with an average value of <0.23.

A negative correlation was observed between crustal thickness and Poisson's ratio in the crustal thinning zone on the east side of the Tanlu fault zone (F3), as shown in Figure 7B. In particular, five of the seven ore deposits in the Middle–Lower Yangtze Metallogenic Belt are located in the crustal thinning area (Figure 7B); moreover, over 200 other small ore deposits are also present (Lin et al., 2021), reflecting the close correlation between mineralization and the thinning of crustal thickness.

Discussion

Crustal structure and attribute characteristics

The crustal structure and Poisson's ratio characteristics represent seismological traces in the Earth following the long geological evolution process, which can be used to infer the dynamic mechanism and deformation process of evolution (Chen et al., 2022). Poisson's ratio reflects the rock properties of the crust and is sensitive to the material composition of the crust and subsequent tectonic deformation. Increase in mafic and decreases in quartz lead to an increase in the Poisson's ratio of the rock. Partial melting and an increase in the fluid composition of a two-phase medium also increase Poisson's ratio (Ji et al., 2009).

Existing seismic studies (Shi et al., 2013; Lü et al., 2014, 2015; Xu et al., 2014; Zhang et al., 2015; Zhang et al., 2021) have attributed crustal thinning and Poisson's ratio increases on the east side of F3 to the melting–assimilation–storage–homogenization (MASH) mineralization process (Hildreth and moorbath, 1988; Richards, 2003); in addition, many intermediate-acid intrusive rocks have similar geochemical characteristics to those of adakite rocks, which also directly indicates the existence of strong crust–mantle interaction in this area (Wang and Mo, 1995; Xu et al., 2002). The distribution of high Poisson's ratios (>0.27) is clearly related to large regional fault zones (such as the Tanlu fault). Wan and Zhao. (2012) attributed this relationship to the existence of structural fault-sphere detachment and an oceanic-continental transitional lithosphere. Deep faults provide a channel for magma under plating or ejection and determine the shape of magma differentiation, rise, and emplacement in the crust, which allows more basic magmatic materials to intrude into the crust and become enriched near the fault zone, and provides a good environment for the emplacement of metallogenic materials at shallow depths. This thermal convection and the injection of mantle thermal materials into the continental crust provide a direct driving force for shallow iron–copper polymetallic mineralization (Deng and Wu, 2001). The extension of F3 to the mantle has become a consensus in the geoscience community and is been supported by deep seismic soundings (Zhang et al., 2015; Liu et al., 2015). We speculate that the formation of the magma chamber was accompanied by the thinning of the crust thickness and the increase of Poisson's ratio. The magma rose to the shallow crust along the deep suture zone (such as F3), and large-scale magmatic activity broke out and a variety of deposits were formed on the shallow crust (Lü et al., 2014, 2015; Zhang et al., 2015).

In a tectonic compression environment, felsic rocks are more likely to form pushover structures or folds than mafic rocks under the same temperature and pressure, resulting in a decrease in the crustal velocity ratio with an increase in crustal thickness. In addition, delamination reduces the thickness of some basic rocks in the lower crust, resulting in a decrease in the crustal Poisson's ratio. The Poisson's ratio of the middle part of the JOB is generally low, with an average value of <0.23, forming an obviously low Poisson's ratio belt between the northern and southern borders (i.e., Jiujiang–Shitai buried fault in the north and Jiangshan–Shaoxing fault in the south) (He et al., 2013; Guo et al., 2019). One explanation is that intra continental orogenic movement shortened and thickened the crust in the Mesozoic, with thickening mainly occurring in the upper crust. This multi-stage tectonic action caused the JOB to have a thick upper crust and a low crustal Poisson's ratio (Zhang et al., 2021). Another explanation is related to the crustal thickening under the Mesozoic compression background and the crustal thinning in the later extension background (Chen et al., 2022). The velocity structure obtained using previous wide-angle reflection/refraction seismic sounding data shows that the P-wave velocity of the lower crust varies from 6.2 to 6.6 km/s in the JOB, which is far less than the average velocity of the lower crust for the whole South China Block (Lin et al., 2021). According to geochemical and chronological studies, the South China continent should be dominated by thick crust (>45 km) before the Mesozoic (Zhu and Kanamori, 2000; Zhang et al., 2015). The latest results in this study show that the current average crustal thickness of JOB is about 30 km. All these provide further support for the thinning of the lower crust and reduction of the mafic composition.

Deep boundary between the YB and CB

It is difficult to clearly describe the characteristics of this sharp change in crustal thickness based on absolute thickness results. Blocks that have undergone different evolutionary histories or suffered different degrees of deformation leave records of thickness differences at the boundary during the assembling process; however, traces of structural deformation characteristics along the contact boundaries are often unclear owing to the long geological age and the influence of later reformation. It difficult to capture the precise position of the sharpest change in block thickness based only on the absolute value of Moho depth. Rather, such interpretation hinders the discrimination, identification, and further discussion of the deep contact relationship of the main block boundaries. The maximum horizontal gradients of crustal thickness obtained in this study, which clearly reveal the track of this buried fault (Figure 8). Our results show that the crustal thickness around the Jiangshan–Shaoxing fault (F2), which is traditionally considered as the boundary between the YB and CB (Zhang et al., 2005; Zhang et al., 2013; Zhang et al., 2018), does not vary significantly. However, a significant difference was observed in the crustal thickness variance on the two sides of the Jiujiang–Shitai buried fault (F1). We suggest that F1 may constitute the deep boundary

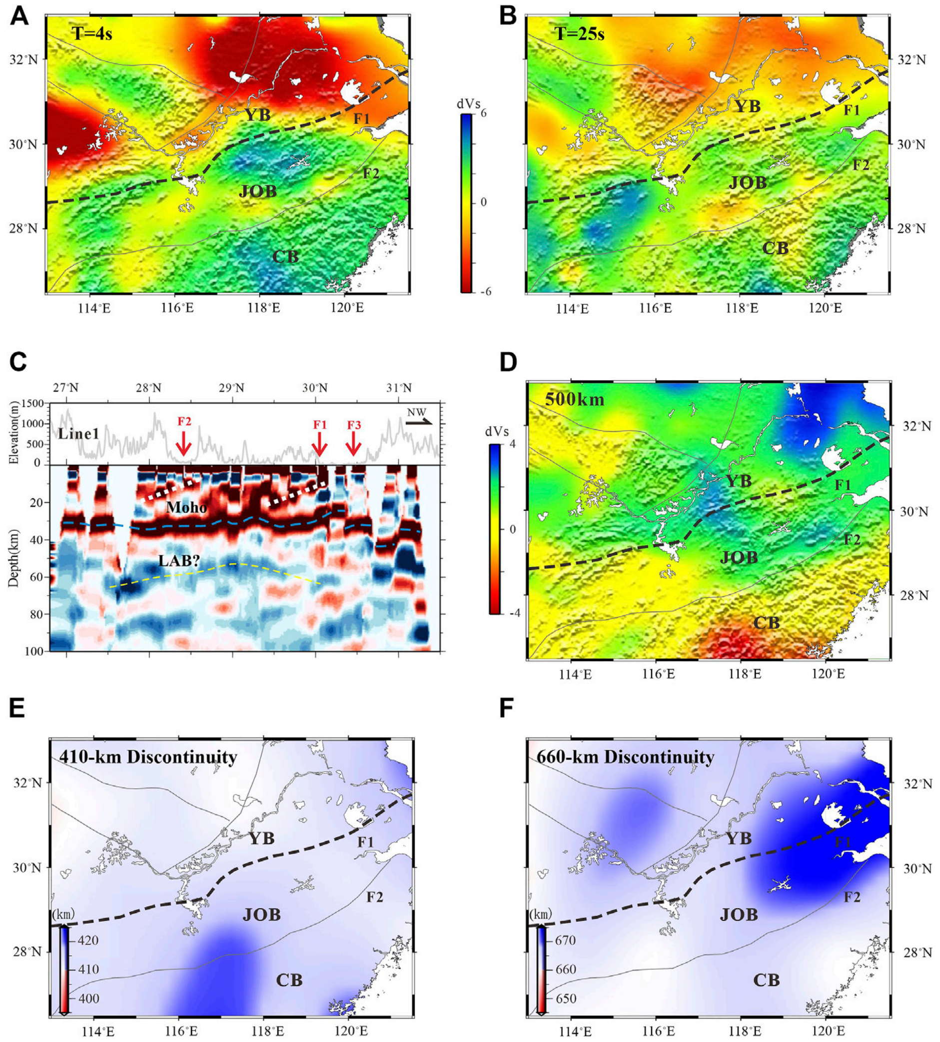

FIGURE 9
Rayleigh wave phase velocity perturbation at periods of 4 s **(A)** and 25 s **(B)** (Ma et al., 2022). Receiver function CCP stacking result **(C)** (Ye et al., 2019). S-wave velocity (Vs) tomography at the depth of 500 km **(D)** (Huang et al., 2021). Topography of the 410-km **(E)** and 660-km discontinuity **(F)** (Han et al., 2020). Labels are the same as in Figure 1.

between the YB and CB. The nature and scale of F2 have been widely recognized as first-order boundary faults between the YB and CB. The explanations for the insignificant abrupt change in the Moho depth on the two sides of F2 are as follows. First, the fault may extend to the base of the crust at a certain angle, resulting in the position of Moho break off not being imaged directly beneath the surface track of the fault (Zhang et al., 2013). Second, as a Neoproterozoic period bonding zone, the deep structure of F2 has been transformed by the subsequent extrusion and extension processes of the South China continent, resulting in relatively weak initial traces of the fault (Zhang et al., 2021). Specifically, the present Moho topography in South China should be the result of the reconstruction of the later tectonic events. Moho surface at the plate splicing part is generally staggered and overlapped due to compression, which leads to unclear Moho imaging (Zhang et al., 2019; Shu et al., 2021). On the one hand, the seismic wave velocity and Poisson's ratio of the crust in the east of South China are relatively low, which is considered to be the result of the lower crustal delamination, which naturally makes the previously thickened crust tend to be average (Lin et al., 2021; Zhang et al., 2021); On the other hand, the subduction and retreat of the Mesozoic ancient Pacific plate resulted in the partial melting of the mantle wedge and the upwelling of the asthenosphere, which led to the overall extension of the crust and partial melting of the bottom (Huang and Zhao, 2006; Li and Li, 2007).

Based on our results, we infer that the central-eastern segment of F1 represents the deep boundary between the YB and CB, whereas F2 is marked as the shallow boundary; that is, the southern margin of the YB overlaps the northern margin of the CB. The subduction direction of CB is believed to be NW based on the polarity of compressional tectonics of the JOB (Guo et al., 1989; Wang and Mo, 1995; Shu, 2012; Yao et al., 2019; Suo et al., 2020). This conclusion is supported by the results of recent ambient noise tomography experiments (Ma et al., 2022). Ma et al. (2022) clearly show that no obvious variation in S-wave velocity is apparent between the two sides of F2, whereas the central-eastern segment of F1 represents the transform boundary between low- and high-velocity during different periods of seismic waves (Figures 9A,B). Guo and Gao. (2018), Guo et al. (2019) also speculated that the JOB has a double-layer basement based on the differences in gravity, magnetic properties, and material composition in the crust. In the central–eastern segment of the JOB, F1 is the front edge of the lower basement of the CB and F2 is the upper basement Frontier of the YB. Moreover, the common conversion point (CCP) stacking result of receiver function also clearly shows that Moho is obviously staggered on both sides of the F1, and the inferred LAB seismic phase (Shan et al., 2021; Yang et al., 2021) also shows discontinuous characteristics (Figure 9C; Ye et al., 2019). The velocity imaging results revealed that the YB and CB show different velocity characteristics in the lithospheric mantle (Wang et al., 2018; Chen et al., 2022). S-wave receiver function showed that the lithosphere thickness in the lower YB and its adjacent regions is about 80–100 km, confirming the characteristics of lithosphere thinning (Zhang et al., 2019). Zhou et al. (2012) used the ambient noise and earthquake tomography to reveal that the west YB has a thicker lithospheric structure (~150 km or more), while the east YB is relatively thin (about 80 km), and the CB is the thinnest, only 60–70 km. However, previous studies have shown that the significant differences between tectonic units in South China are mainly characterized by the response of the crustal deformation (most of them limited within the crust) and magmatic activity, while the mantle lithosphere is entirety stretched during Mesozoic, and even at the block boundary, it will change smoothly. So it is difficult to use the differences of lithospheric structure for determining the minor or local-scale block boundary.

Tomography results reveal the presence of extensive low-velocity anomalies in the upper mantle of southeastern China to the north of F1, along with near-horizontal high-velocity bodies in the mantle transition zone (MTZ), which are similar to those in the North China and Northeast China Blocks. High-velocity anomalies are speculated to be caused by the Pacific subduction plate remaining in the MTZ (Huang and Zhao, 2006; Li and Van Der Hilst, 2010; Huang et al., 2014; Jiang et al., 2021). However, the MTZ in the CB, south of F1, showed no obvious high-velocity anomalies (Figure 9D; Li and Van Der Hilst, 2010; Huang et al., 2021). Moreover, according to a recent 3-D fine structure of the MTZ derived from the receiver function, there is a mantle boundary at 29°N, and the structural characteristics on the two sides are different (Han et al., 2020). Overall, the depth of the 660-km discontinuity declines in the northern study area, and the 410-km discontinuity in the south is partially depressed, accompanied by obvious differences in temperature and water content. The surface projection of the deep boundary (29°N) has good spatial correspondence with the location and strike of F1 (Figures 9E,F). Obvious structural differences of MTZ on the two sides of F1 indicate that the YB and CB above may have different deep mantle dynamic environments.

Amalgamation of the YB and CB

The South China plate has undergone a long and multi-stage process of crustal evolution and continental transformation and exhibits complex and diverse crustal material composition and structural characteristics. The magmatism and metamorphism of the South China plate have resulted in the formation of a complex tectonic pattern of multi-block integration and basin-mountain coupling. One possibility is that the JOB formed between the YB and CB during the Mesoproterozoic Sibao orogeny (1,100–1,000 Ma; Li et al., 2019). Alternatively, shortening and subduction between the YB and CB may have occurred in the Neoproterozoic (~800 Ma) along the Jiujiang–Shitai buried fault on the southeastern margin of the JOB (Shu, 2012; Yao et al., 2014). Furthermore, a third slab-arc model (Zhao et al., 2011) proposed that the CB subducted NW-ward beneath the YB and that the final assembly of these two blocks occurred at approximately 830 Ma according to the compressional tectonic direction of the JOB, which is supported by other study data (Zhang et al., 2015; Xu et al., 2015; Yao et al., 2019; Ma et al., 2022). Based on the slab-arc model and the maximum horizontal gradients of the crustal thickness revealed in this study, combined with the previous research results, the proposed process of amalgamation between the YB and CB since the Neoproterozoic is illustrated in Figure 10.

During the Neoproterozoic, the CB subducted toward the southeastern margin of the YB along the NW- direction and collided with the YB to form a relatively stable South China lithosphere structure, resulting in low greenschist facies metamorphic rocks, ductile shear deformation, and magmatic activity in the southeastern margin of the YB (Shu et al., 2021). The Jiujiang Ms 5.7 main earthquake in 2005 may be the NW trending Yangjishan-Wushan-Tongjiangling fault concealed in the Ruichang basin, and the focal mechanism solution shows a sinistral strike slip fault of reverse nature (Tang et al., 2018). However, due to the focus too shallow, Lü et al. (2008) pointed out that this earthquake mainly corresponds to some small-scale secondary faults, which cannot represent the structure and stress state of the whole main fault. In addition, F1 and F2 are affected by multiple geological tectonic movements in the later period, and only thrust structures remained to present. Therefore, it is difficult to accurately describe their properties with the focal mechanism of current earthquakes. Besides, the deep reflection

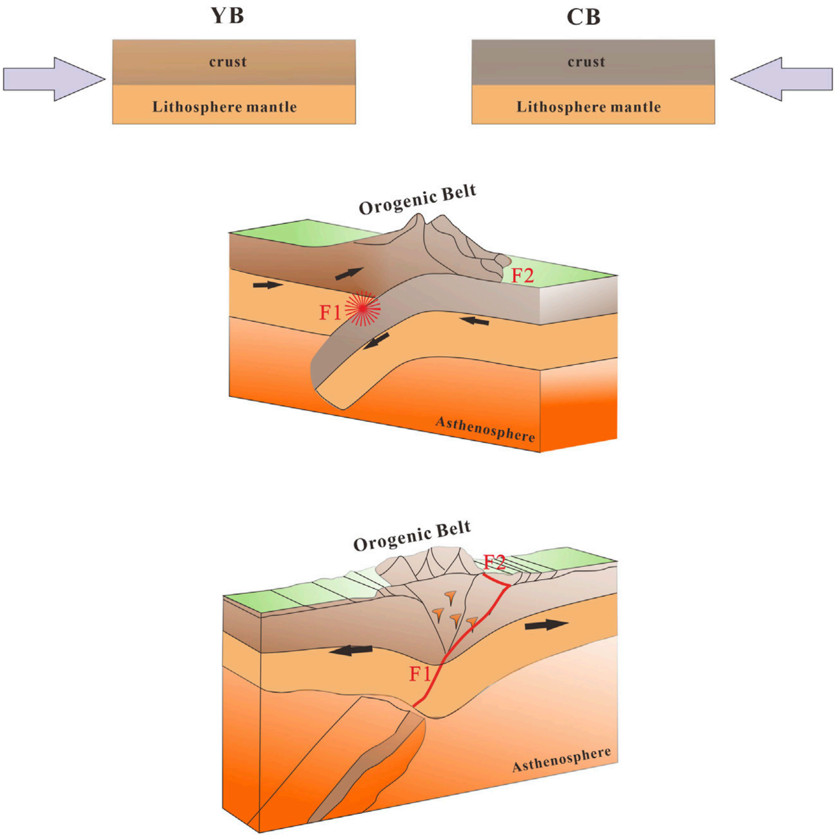

FIGURE 10
Subduction and amalgamation processes of suture zone between the YB and CB. This model describes the process of amalgamation between the YB and CB since the Neoproterozoic. The CB subducted northwest-ward toward the southeastern margin of the YB, and then underwent various geological processes, forming the current tectonic framework. Labels are the same as in Figure 1.

profile clearly shows the low-angle NE-SW thrust characteristics of several buried faults in the crust of eastern South China (Liang, 2014). The thrust feature in the middle and upper YB below the Jiangnan ancient suture can also be presented (Dong et al., 2015), indicating that this thrust fault in southeastern China is widespread. In addition, as shown in Figure 9C, the CCP result of the receiver function also records the thrust characteristics of F1 and F2 in the crust. The NE-trending Jiangnan Neoproterozoic arc Orogenic Belt was formed between the YB and CB, as supported by abundant geological and geophysical evidences related to collisional orogeny, such as strong compressive deformation of the strata, region-scale angular unconformity, ductile shear zone, arc migmatite associated with subduction, high-pressure gneiss, syn-collisional granites, and ophiolite mélange, representing ancient oceanic crust (Shu, 2012; Zhao et al., 2013; Chu et al., 2020). The eastern section of the Jiujiang–Shitai buried fault may represent the deep boundary (mantle-scale) between the CB and YB, whereas the Jiangshan–Shaoxing fault is the surface track, with the CB subducted beneath the YB.

Following collision, the South China Block underwent multiple extensional-compressional processes and metamorphic deformation events, including: Neoproterozoic (approximately 800–750 Ma) rifting events on a lithosphere scale (Shu, 2012; Zhang et al., 2012); early Paleozoic (approximately 460–400 Ma) large-scale metamorphic deformation and magmatic events affecting the middle and lower crust (Wang et al., 2012); early Mesozoic (approximately 260–200 Ma) tectonic-magmatic events characterized by thin-crust tectonics, thrust nappe, and large-scale peraluminous magmatism (Zhao et al., 2013; Li et al., 2017); and late Mesozoic back-arc extension and multi-stage and multi-type magmatic events controlled by the subduction of the Paleo–Pacific Plate (Huang and Zhao, 2006; Li and Li, 2007). The high potassium calc-alkaline granite formed in the late Yanshan period (142–67 Ma) has a higher Poisson's ratio (Zhou et al., 2006; Li et al., 2014). The increasing trend of the crustal Poisson's ratio from inland to coastal areas (Figure 7B) is related to the crustal evolution process since the Mesozoic in South China (i.e., from inland to coastal, the age distribution trend of magmatic rocks is from old to new). The high Poisson's ratio implies the underplating of the deep mafic magma (Ye et al., 2013; Chen et al., 2022). All these tectonic events may have influenced the formation of the present tectonic pattern.

Conclusion

In this study, we investigated teleseismic P-wave receiver functions based on the dense broadband seismic array in plan view, and obtained high-resolution images of crustal thickness and Poisson's ratio in southeastern China that eliminated the influence of crustal S-wave azimuth anisotropy and inclined interface. Consequently, the deep boundary and contact relationship between the YB and CB could be evaluated for the first time based on the variation of the maximum horizontal gradients of the crustal thickness. In particular:

(1) Crustal thickness varies from >38 km in the QDOB to <30 km in the CB and east of the Tanlu fault. Regions with relatively high Poisson's ratios are concentrated on the two flanks of the deep fault zone and the continental margin of the study area (>0.27), whereas those with lower Poisson's ratios are concentrated in the JOB (<0.23).
(2) The depth of the Moho east of the Tanlu fault is approximately 28 km, which is 3–5 km thinner than the geological units on the east and west sides; the fault extends to the vicinity of the Jiujiang–Shitai fault in the south with a strike of SW to NE. Combined with other geological and geophysical data, we infer that the deep structural characteristics of the Tanlu fault are closely related to extensive mineralization.
(3) The eastern section of the Jiujiang–Shitai buried fault constitutes a sharp Moho gradient zone with a maximum horizontal gradient of crustal thickness of >5 km/°. Combined with the velocity structure and discontinuity surface characteristics at different depths, we consider that the Jiujiang–Shitai buried fault may represent the deep structural boundary dividing the YB and CB at the mantle scale.
(4) The subduction and amalgamation model is supported by our results, in which the CB subducted northwest beneath the southern margin of the YB during the Neoproterozoic. The Jiujiang–Shitai fault is considered as the northern boundary of the JOB, whereas the Jiangshan-Shaoxing fault is the southern boundary.

Data availability statement

The original contributions presented in the study are included in the article/Supplementary Material, further inquiries can be directed to the corresponding authors.

Author contributions

RH: writing—original draft. DY: funding, project administration, and review. QL: supervision, provided raw data, and review. WF: conceptualization, formal analysis. GZ: suggesting, investigation. HZ: data processing, methodology. HC: editing. YC: data curation, software.

Funding

This work was supported by the National Natural Science Foundation of China (Grant Nos. 42204097, 91962110, 41774113, and 42104099).

Acknowledgments

We thank Jiangtao Li (Wuhan University), Zhou Zhang (Guangzhou Institute of Geochemistry, Chinese Academy of Science), Mijian Xu (Nanjing University), Nian Wang (Tsinghua University), for providing valuable advice about the discussion. The project was funded by CGS (Grant Nos. 12120114067701, DD20179354) and the fieldwork was finished co-operatively by IG of CAGS, PKU, NJU, IEF of CEA, and IGM of CAGS. The permanent data were supplied by the Data Management Center of the China National Seismic Network. All support is gratefully acknowledged. Most of the figures were made using Generic Mapping Tools (Wessel and Smith, 1998).

Conflict of interest

The authors declare that the research was conducted in the absence of any commercial or financial relationships that could be construed as a potential conflict of interest.

Publisher's note

Supplementary material

The Supplementary Material for this article can be found online at: https://www.frontiersin.org/articles/10.3389/feart.2022.1065782/full#supplementary-material

References

Cawood, P. A., Wang, Y., Xu, Y., and Zhao, G. (2013). Locating South China in rodinia and gondwana: A fragment of greater India lithosphere? *Geology* 41 (8), 903–906. doi:10.1130/G34395.1

Charvet, J. (2013). The neoproterozoic–early paleozoic tectonic evolution of the South China block: An overview. *J. Asian Earth Sci.* 74, 198–209. doi:10.1016/j.jseaes.2013.02.015

Chen, C., Lü, Q., Chen, L., Shi, D., Yan, J., and Ai, Y. (2022a). Crustal thickness and composition in the South China Block: Constraints from earthquake receiver function. *Sci. China Earth Sci.* 65 (4), 698–713. doi:10.1007/s11430-021-9858-x

Chen, L., Wang, X., Wang, X., Wei, Z., and Zhang, J. (2022b). Advances and perspectives for receiver function imaging of the Earth's internal discontinuities and velocity structures. *Rev. Geophys. Planet. Phys.* 53 (0), 1–22. doi:10.19975/j.dqyxx.2022-029

Chu, Y., Lin, W., Faure, M., Allen, M., and Feng, Z. (2020). Cretaceous exhumation of the triassic intracontinental xuefengshan belt: Delayed unroofing of an orogenic plateau across the South China block? *Tectonophysics* 793, 228592. doi:10.1016/j.tecto.2020.228592

Deng, J., and Wu, Z. (2001). Lithospheric thinning event in the lower Yangtze craton and Cu-Fe metallogenic belt in the middle and lower Yangtze River reaches. *Geol. Anhui* 11 (2), 86–91.

Deng, Y., Li, S., Fan, W., and Liu, J. (2011). Crustal structure beneath South China revealed by deep seismic soundings and its dynamics implications. *Chin. J. Geophys.* 54 (10), 2560–2574. doi:10.3969/j.issn.0001-5733.2011.10.013

Dong, S., Zhang, Y., Gao, R., Su, J., Liu, M., and Li, J. (2015). A possible buried paleoproterozoic collisional orogen beneath central South China:Evidence from seismic-reflection profiling. *Precambrian Res.* 264, 1–10. doi:10.1016/j.precamres.2015.04.003

Fang, L., and Wu, J. (2009). Effects of dipping boundaries and anisotropic media on receiver functions. *Prog. Geophys* 24 (1), 42–50.

Gu, Q., Ding, Z., Kang, Q., and Zhao, Q. (2016). Pn wave velocity and anisotropy in the middle-southern segment of the Tan-Lu fault zone and adjacent region. *Chin. J. Geophys.* 59 (2), 504–515. doi:10.6038/cjg20160210

Guo, L., and Gao, R. (2018). Potential-field evidence for the tectonic boundaries of the central and Western Jiangnan belt in South China. *Precambrian Res.* 309, 45–55. doi:10.1016/j.precamres.2017.01.028

Guo, L., Gao, R., Shi, L., Huang, Z., and Ma, Y. (2019). Crustal thickness and Poisson's ratios of South China revealed from joint inversion of receiver function and gravity data. *Earth Planet. Sci. Lett.* 510, 142–152. doi:10.1016/j.epsl.2018.12.039

Guo, L., Shi, Y., Lu, H., Ma, R., Dong, H., and Yang, S. (1989). The pre-Devonian tectonic patterns and evolution of South China. *J. Southeast Asian Earth Sci.* 3 (1-4), 87–93. doi:10.1016/0743-9547(89)90012-3

Hammond, J. (2014). Constraining melt geometries beneath the Afar Depression, Ethiopia from teleseismic receiver functions: The anisotropic H-κ stacking technique. *Geochem. Geophys. Geosyst.* 15 (4), 1316–1332. doi:10.1002/2013GC005186

Han, R., Li, Q., Huang, R., and Zhang, H. (2020). Detailed structure of mantle transition zone beneath southeastern China and its implications for thinning of the continental lithosphere. *Tectonophysics* 789, 228480. doi:10.1016/j.tecto.2020.228480

Han, R., Yang, D., Li, Q., Chen, H., Zhang, H., Ye, Z., et al. (2022). Crustal structure and anisotropy in the Lower Yangtze region and its metallogenic implications. *Front. Earth Sci.* 10, 849088. doi:10.3389/feart.2022.849088

He, C., Dong, S., Santosh, M., and Chen, X. (2013). Seismic evidence for a geosuture between the Yangtze and Cathaysia blocks, south China. *Sci. Rep.* 3 (1), 2200–2207. doi:10.1038/srep02200

Hildreth, W., and Moorbath, S. (1988). Crustal contributions to arc magmatism in the Andes of central Chile. *Contr. Mineral. Pet.* 98 (4), 455–489. doi:10.1007/BF00372365

Huang, H. (2013). The crustal and upper mantle structure and anisotropy beneath the lower Yangtze Craton and its adjacent regions. [dissertation/doctor's thesis]. Nanjing: Nanjing University.

Huang, J., and Zhao, D. (2006). High-resolution mantle tomography of China and surrounding regions. *J. Geophys. Res.* 111 (B9), B09305. doi:10.1029/2005JB004066

Huang, R., Xu, Y., Luo, Y., and Jiang, X. (2014). Mantle transition zone structure beneath Southeastern China and its implications for stagnant slab and water transportation in the mantle. *Pure Appl. Geophys.* 171 (9), 2129–2136. doi:10.1007/s00024-014-0837-4

Huang, Z., Gou, T., and Wang, L. (2021). P and S wave tomography of east-central China: Insight into past and present mantle dynamics. *Tectonophysics* 809, 228859. doi:10.1016/j.tecto.2021.228859

Ji, S., Wang, Q., and Salisbury, M. (2009). Composition and tectonic evolution of the Chinese continental crust constrained by Poisson's ratio. *Tectonophysics* 463, 15–30. doi:10.1016/j.tecto.2008.09.007

Jiang, G., Zhang, G., Zhao, D., Lü, Q., Shi, D., Li, H., et al. (2021). Mantle flow and dynamics beneath central-east China: New insights from P-wave anisotropic tomography. *JGR. Solid Earth* 126 (5), e2020JB020070. doi:10.1029/2020JB020070

Jiao, W., Wu, Y., Yang, S., Peng, M., and Wang, J. (2009). The oldest basement rock in the Yangtze Craton revealed by zircon U-Pb age and Hf isotope composition. *Sci. China Ser. D-Earth. Sci.* 52 (9), 1393–1399. doi:10.1007/s11430-009-0135-7

Li, C., and Van Der Hilst, R. D. (2010). Structure of the upper mantle and transition zone beneath Southeast Asia from traveltime tomography. *J. Geophys. Res.* 115 (B7), B07308. doi:10.1029/2009JB006882

Li, J., Song, X., Wang, P., and Zhu, L. (2019). A generalized H-κ method with harmonic corrections on Ps and its crustal multiples in receiver functions. *J. Geophys. Res. Solid Earth* 124 (4), 3782–3801. doi:10.1029/2018JB016356

Li, J., Wang, X., Zhang, F., Zhou, X., and Shu, X. (2016). A rhythmic source change of the Neoproterozoic basement meta-sedimentary sequences in the Jiangnan Orogen: Implications for tectonic evolution on the southeastern margin of the Yangtze Block. *Precambrian Res.* 280, 46–60. doi:10.1016/j.precamres.2016.04.012

Li, J., Zhang, Y., Zhao, G., Johnston, S., Dong, S., Koppers, A., et al. (2017). New insights into phanerozoic tectonics of South China: Early paleozoic sinistral and triassic dextral transpression in the east wuyishan and chencai domains, NE Cathaysia. *Tectonics* 36 (5), 819–853. doi:10.1002/2016TC004461

Li, W., Chen, Y., and Xu, Y. (2021). Crustal SiO_2 content of the Emeishan Large Igneous Province and its implications for magma volume and plumbing system. *Geochem., Geophys., Geosyst.* 22 (8), e2021GC009783. doi:10.1029/2021GC009783

Li, W., and Li, X. (2003). Adakitic granites within the NE jiangxi ophiolites, South China: Geochemical and Nd isotopic evidence. *Precambrian Res.* 122 (1-4), 29–44. doi:10.1016/s0301-9268(02)00206-1

Li, X., Kind, R., and Yuan, X. (2003). Seismic study of upper mantle and transition zone beneath hotspots. *Phys. Earth Planet. Interiors* 136 (1-2), 79–92. doi:10.1016/S0031-9201(03)00021-9

Li, X., Li, W., Li, Z., Lo, C., Wang, J., Ye, M., et al. (2009). Amalgamation between the Yangtze and Cathaysia blocks in SouthSouth China: Constraints from SHRIMP U–Pb zircon ages, geochemistry and Nd–Hf isotopes of the shuangxiwu volcanic rocks. *Precambrian Res.* 174 (1-2), 117–128. doi:10.1016/j.precamres.2009.07.004

Li, Y., Gao, M., and Wu, Q. (2014). Crustal thickness map of the Chinese mainland from teleseismic receiver functions. *Tectonophysics* 611, 51–60. doi:10.1016/j.tecto.2013.11.019

Li, Z., and Li, X. (2007). formation of the 1300-km-wide intracontinental orogen and postorogenic magmatic province in mesozoic South China: A flat-slab subduction model. *Geol.* 35 (2), 179–182. doi:10.1130/G23193A.1

Liang, F. (2014). Deep structure of the middle part in the middle and lower reaches of Yangtze river: Insights from reflection seismic data. [dissertation/doctor's thesis]. China: Chinese Academy of Geological Sciences.

Ligorría, J., and Ammon, C. (1999). Iterative deconvolution and receiver-function estimation. *Bull. Seismol. Soc. Am.* 89 (5), 1395–1400. doi:10.1785/BSSA0890051395

Lin, J., Xu, T., Cai, H., Lü, Q., Bai, Z., Deng, Y., et al. (2021). Crustal velocity structure of Cathaysia Block from an active-source seismic profile between Wanzai and Hui'an in SE China. *Tectonophysics* 811, 228874. doi:10.1016/j.tecto.2021.228874

Liu, B., Feng, S., Ji, J., Shi, J., Tan, Y., and Li, Y. (2015). Fine lithosphere structure beneath the middle-southern segment of the Tan-Lu fault zone. *Chin. J. Geophys.* 58 (5), 1610–1621. doi:10.6038/cjg20150513

Liu, Q., Rainer, K., and Li, S. (1997). The receiver functions at the stations of the Chinese Digital Seismic Network (CDSN) and their nonlinear inversion. *Chin. J. Geophys.* 3, 356–368.

Liu, S., and Zhang, G. (2013). Mesozoic basin development and its indication of collisional orogeny in the Dabie orogen. *Chin. Sci. Bull.* 58, 827–852. doi:10.1007/s11434-012-5503-6

Lombardi, D., Braunmiller, J., Kissling, E., and Giardini, D. (2008). Moho depth and Poisson's ratio in the Western-Central Alps from receiver functions. *Geophys. J. Int.* 173 (1), 249–264. doi:10.1111/j.1365-246X.2007.03706.x

Lü, J., Zheng, Y., Ni, S., and Gao, J. (2008). Focal mechanisms and seismogenic structures of the Ms5.7 and ms 4.8 jiujiang-ruichang earthquakes of nov. 26, 2005. *Chin. J. Geophys.* 2008 (01), 158–164.

Lü, Q., Dong, S., Shi, D., Tang, J., Jiang, G., Zhang, Y., et al. (2014). Lithosphere architecture and geodynamic model of middle and lower reaches of Yangtze metallogenic belt: A review from SinoProbe. *Acta Pet. Sin.* 30 (4), 889–906.

Lü, Q., Dong, S., Tang, J., Shi, D., and Chang, Y.SinProbe-03-CJ Group (2015). Multi-scale and integrated geophysical data revealing mineral systems and exploring for mineral deposits at depth: A synthesis from SinoProbe-03. *Chin. J. Geophys* 58 (12), 4319–4343. doi:10.6038/cjg20151201

Ma, J., Huang, J., and Fu, Y. (2022). Phase velocity tomography of Rayleigh and Love waves in the suture zone between the Yangtze and Cathaysia Blocks. *Chin. J. Geophys.* 65 (4), 1255–1270. doi:10.6038/cjg2022P0217

Qiu, Y., Gao, S., McNaughton, N., Groves, D., and Ling, W. (2000). First evidence of >3.2 Ga continental crust in the Yangtze craton of south China and its implications for Archean crustal evolution and Phanerozoic tectonics. *Geology* 28 (1), 11–14. doi:10.1130/0091-7613(2000)028<0011:feogcc>2.3.co;2

Richards, J. (2003). Tectono- magmatic precursors for porphyry Cu-(Mo-Au) deposit formation. *Econ. Geol.* 98, 1515–1533. doi:10.2113/gsecongeo.98.8.1515

Shahzad, S., Liu, J., Sun, Y., and Li, C. (2021). Crustal structure and deformation in southeastern China revealed by receiver functions. *J. Asian Earth Sci.* 221, 104937. doi:10.1016/j.jseaes.2021.104937

Shan, B., Zhou, W., and Xiao, Y. (2021). Lithospheric thermal and compositional structure of South China jointly inverted from multiple geophysical observations. *Sci. China Earth Sci.* 64 (1), 148–160. doi:10.1007/s11430-019-9661-4

Shi, D. N., Lü, Q. T., Xu, W. Y., Yan, J. Y., Zhao, J. H., Dong, S. W., et al. (2013). Crustal structure beneath the middle–lower Yangtze metallogenic belt in east China: Constraints from passive source seismic experiment on the mesozoic intra-continental mineralization. *Tectonophysics* 606, 48–59. doi:10.1016/j.tecto.2013.01.012

Shu, L. (2012). An analysis of principal features of tectonic evolution in South China Block. *Geol. Bull. China* 31 (7), 1035–1053. doi:10.3969/j.issn.1671-2552.2012.07.003

Shu, L., Wang, J., and Yao, J. (2019). Tectonic evolution of the eastern Jiangnan region, South China: New findings and implications on the assembly of the Rodinia supercontinent. *Precambrian Res.* 322, 42–65. doi:10.1016/j.precamres.2018.12.007

Shu, L., Yao, J., Wang, B., Faure, M., Charvet, J., and Chen, Y. (2021). Neoproterozoic plate tectonic process and Phanerozoic geodynamic evolution of the South China Block. *Earth. Sci. Rev.* 216, 103596. doi:10.1016/j.earscirev.2021.103596

Suo, Y., Li, S., Cao, X., Wang, X., Somerville, I., Wang, G., et al. (2020). Mesozoic-cenozoic basin inversion and geodynamics in east China: A review. *Earth. Sci. Rev.* 210, 103357. doi:10.1016/j.earscirev.2020.103357

Tang, J., Lü, J., Zeng, X., Yang, Y., Zeng, W., and Duan, L. (2018). Characteristics of focal mechanisms and stress field in the border region of Jiujiang and Ruichang. *J. Geodesy Geodyn.* 38 (08), 791–795+827. doi:10.14075/j.jgg.2018.08.005

Wan, T., and Zhao, Q. (2012). The Genesis of tectono-magmatism in eastern China. *Sci. China Earth Sci.* 55 (3), 347–354. doi:10.1007/s11430-011-4361-4

Wang, H., and Mo, X. (1995). An outline of the tectonic evolution of China. *Episodes* 18 (1), 6–16. doi:10.18814/epiiugs/1995/v18i1.2/003

Wang, X., Li, Q., Zhang, H., and Guo, Chen. (2018). Study of P-wave velocity structure in upper mantle in eastern South China. *Glob. Geol.* 37 (02), 620–626. doi:10.3969/j.issn.1004-5589

Wang, X., Li, X., Li, Z., Li, Q., Tang, G., Gao, Y., et al. (2012). Episodic precambrian crust growth: Evidence from U–Pb ages and Hf–O isotopes of zircon in the nanhua basin, central south China. *Precambrian Res.* 222, 386–403. doi:10.1016/j.precamres.2011.06.001

Wang, Y., Fan, W., Sun, M., Liang, X., Zhang, Y., and Peng, T. (2007). Geochronological, geochemical and geothermal constraints on petrogenesis of the indosinian peraluminous granites in the South China block: A case study in the hunan province. *Lithos* 96 (3-4), 475–502. doi:10.1016/j.lithos.2006.11.010

Wei, Z., Chen, L., Li, Z., Ling, Y., and Li, J. (2016). Regional variation in Moho depth and Poisson's ratio beneath eastern China and its tectonic implications. *J. Asian Earth Sci.* 115, 308–320. doi:10.1016/j.jseaes.2015.10.010

Wessel, P., and Smith, W. (1998). New, improved version of generic mapping tools released. *Eos Trans. AGU.* 79 (47), 579. doi:10.1029/98EO00426

Wu, Q., and Zeng, R. (1998). The crustal structure of Qinghai-Xizang plateau inferred from broadband teleseismic waveform. *Chin. J. Geophys.* 14, (05), 669–679.

Xu, J., Shinjo, R., Defant, M., Wang, Q., and Rapp, R. (2002). Origin of mesozoic adakitic intrusive rocks in the ningzhen area of east China: Partial melting of delaminated lower continental crust? *Geol.* 30 (12), 1111–1114. doi:10.1130/0091-7613(2002)030<1111:oomair>2.0.co;2

Xu, M., Huang, Z., Wang, L., Xu, M., Zhang, Y., Mi, N., et al. (2020). Sharp lateral Moho variations across the SE Tibetan margin and their implications for plateau growth. *J. Geophys. Res. Solid Earth* 125 (5), e2019JB018117. doi:10.1029/2019JB018117

Xu, T., Zhang, Z., Tian, X., Liu, B., Bai, Z., Lü, Q., et al. (2014). Crustal structure beneath the Middle-Lower Yangtze metallogenic belt and its surrounding areas: Constraints from active source seismic experiment along the Lixin to Yixing profile in East China. *Acta Pet. Sin.* 30 (4), 918–930.

Xu, X., Li, Y., Tang, S., Xue, D., and Zhang, Z. (2015). Neoproterozoic to Early Paleozoic polyorogenic deformation in the southeastern margin of the Yangtze Block: Constraints from structural analysis and 40Ar/39Ar geochronology. *J. Asian Earth Sci.* 98, 141–151. doi:10.1016/j.jseaes.2014.11.015

Yang, X., Li, Y., Afonso, J., Yang, Y., and Zhang, A. (2021). Thermochemical state of the upper mantle beneath South China from multi-observable probabilistic inversion. *JGR. Solid Earth* 126 (5), e2020JB021114. doi:10.1029/2020JB021114

Yao, J., Cawood, P., Shu, L., and Zhao, G. (2019). Jiangnan orogen, South China: a~ 970–820 Ma rodinia margin accretionary belt. *Earth. Sci. Rev.* 196, 102872. doi:10.1016/j.earscirev.2019.05.016

Yao, J., Shu, L., Santosh, M., and Zhao, G. (2014). Neoproterozoic arc-Related mafic–ultramafic rocks and syn-collision granite from the Western segment of the jiangnan orogen, South China: Constraints on the neoproterozoic assembly of the Yangtze and Cathaysia blocks. *Precambrian Res.* 243, 39–62. doi:10.1016/j.precamres.2013.12.027

Ye, Z., Li, Q., Gao, R., Guan, Y., He, R., Wang, H., et al. (2013). Seismic receiver functions revealing crust and upper mantle structure beneath the continental margin of southeastern China. *Chin. J. Geophys.* 56 (9), 2947–2958. doi:10.6038/cjg20130909

Ye, Z., Li, Q. S., Zhang, H. S., Li, J. T., Wang, X. R., Han, R. B., et al. (2019). Crustal and uppermost mantle structure across the Lower Yangtze region and its implications for the late Mesozoic magmatism and metallogenesis, eastern South China. *Phys. Earth Planet. Interiors* 297, 106324. doi:10.1016/j.pepi.2019.106324

Yin, W., Lei, J., Du, M., Yang, Y., Mi, Q., Lu, M., et al. (2019). Uppermost-mantle Pn velocity and anisotropic tomography of the Tanlu fault zone and adjacent areas. *Chin. J. Geophys.* 62 (11), 4227–4238. doi:10.6038/cjg2019M0672

Zhang, B., Bao, X., and Xu, Y. (2020). Distinct orogenic processes in the south- and north-central tien Shan from receiver functions. *Geophys. Res. Lett.* 47 (6), e2019GL086941. doi:10.1029/2019GL086941

Zhang, G., Guo, A., Wang, Y., Li, S., Dong, Y., Liu, S., et al. (2013a). Tectonics of South China continent and its implications. *Sci. China Earth Sci.* 56, 1804–1828. doi:10.1007/s11430-013-4679-1

Zhang, L., Jin, S., Wei, W., Ye, G., Jing, J., Dong, H., et al. (2015a). Lithospheric electrical structure of South China imaged by magnetotelluric data and its tectonic implications. *J. Asian Earth Sci.* 98, 178–187. doi:10.1016/j.jseaes.2014.10.034

Zhang, M., Xu, T., Lü, Q., Bai, Z., Wu, C., Wu, Z., et al. (2015b). 3D Moho depth beneath the middle-lower Yangtze metallogenic belt and its surrounding areas: Insight from the wide angle seismic data. *Chin. J. Geophys.* 58 (12), 4360–4372. doi:10.6038/cjg20151203

Zhang, Y., Cen, L., Ai, Y., Jiang, M., Xu, W., and Shen, Z. (2018). Lithospheric structure of the South China block from S-receiver function. *Chin. J. Geophys.* 61 (1), 138–149. doi:10.6038/cjg2018L0226

Zhang, Y., Dong, S., Li, J., Cui, J., Shi, W., and Su, J. (2012). The new progress in the study of mesozoic tectonics of SouthSouth China. *Acta Geosci. Sin.* 33 (03), 257–279. doi:10.3975/cagsb.2012.03.01

Zhang, Y., Shi, D., Lü, Q., Xu, Y., Xu, Z., Yan, J., et al. (2021). The crustal thickness and composition in the eastern South China Block constrained by receiver functions: Implications for the geological setting and metallogenesis. *Ore Geol. Rev.* 130, 103988. doi:10.1016/j.oregeorev.2021.103988

Zhang, Y., Xu, Y., Yan, J., Xu, Z., and Zhao, J. (2019a). Crustal thickness, and its relations to mineralization in the southeastern part of South China: Constraint from the teleseismic receiver functions. *Geol. China* 46 (4), 723–736. doi:10.12029/gc20190404

Zhang, Y. Y., Fang, H., Qiu, G. G., Ai, Y. S., and Zhao, L. (2019b). The lithospheric structure of the lower Yangtze craton and its adjacent regions by S receiver function imaging. *Geol. China* 46 (4), 786–794. doi:10.12029/gc20190409

Zhang, Z., Badal, J., Li, Y., Chen, Y., Yang, L., and Teng, J. (2005). Crust–upper mantle seismic velocity structure across Southeastern China. *Tectonophysics* 395 (1-2), 137–157. doi:10.1016/j.tecto.2004.08.008

Zhang, Z., Xu, T., Zhao, B., and Badal, J. (2013b). Systematic variations in seismic velocity and reflection in the crust of Cathaysia: New constraints on intraplate orogeny in the South China continent. *Gondwana Res.* 24 (3-4), 902–917. doi:10.1016/j.gr.2012.05.018

Zhao, J., Zhou, M., Yan, D., Zheng, J., and Li, J. (2011). Reappraisal of the ages of neoproterozoic strata in SouthSouth China: No connection with the grenvillian orogeny. *Geology* 39 (4), 299–302. doi:10.1130/G31701.1

Zhao, K., Jiang, S., Chen, W., Chen, P., and Ling, H. (2013). Zircon U–Pb chronology and elemental and Sr–Nd–Hf isotope geochemistry of two triassic A-type granites in SouthSouth China: Implication for petrogenesis and indosinian transtensional tectonism. *Lithos* 160, 292–306. doi:10.1016/j.lithos.2012.11.001

Zheng, Q., Zhu, J., Xuan, R., and Cai, X. (2003). An approach to the crustal velocities in southern China. *Sediment. Geol. Tethyan Geol.* 23 (4), 9–13.

Zheng, X., Ouyang, B., Zhang, D., Yao, Z., Liang, J., and Zheng, J. (2009). Construction of the technical system of data Backup Centre for China Seismograph network and its support to wenchuan earthquake researches. *Chin. J. Geophys. (in Chin.* 52 (5), 657–662. doi:10.1002/cjg2.1387

Zhou, L., Xie, J., Shen, W., Zheng, Y., Yang, Y., Shi, H., et al. (2012). The structure of the crust and uppermost mantle beneath South China from ambient noise and earthquake tomography. *Geophys. J. Int.* 189 (3), 1565–1583. doi:10.1111/j.1365-246X.2012.05423.x

Zhou, X., Sun, T., Shen, W., Shu, L., and Niu, Y. (2006). Petrogenesis of mesozoic granitoids and volcanic rocks in SouthSouth China: A response to tectonic evolution. *Episodes* 29 (1), 26–33. doi:10.18814/epiiugs/2006/v29i1/004

Zhu, L., and Kanamori, H. (2000). Moho depth variation in southern California from teleseismic receiver functions. *J. Geophys. Res.* 105 (B2), 2969–2980. doi:10.1029/1999JB900322

frontiers | Frontiers in Earth Science

TYPE Original Research
PUBLISHED 30 January 2023
DOI 10.3389/feart.2022.1080307

EDITED BY
Claudia Piromallo,
Istituto Nazionale di Geofisica e Vulcanologia (INGV), Italy

REVIEWED BY
Ting Yang,
China Earthquake Administration, China
Liang Qiu,
China University of Geosciences, China
Raffaele Di Stefano,
Istituto Nazionale di Geofisica e Vulcanologia (INGV), Italy

*CORRESPONDENCE
Weijia Sun,
swj@mail.iggcas.ac.cn

SPECIALTY SECTION
This article was submitted to Solid Earth Geophysics, a section of the journal Frontiers in Earth Science

RECEIVED 26 October 2022
ACCEPTED 09 December 2022
PUBLISHED 30 January 2023

CITATION
Hu J, Sun W, Liu C, Tang Q and Fu L-Y (2023), Seismological reference earth model in South China (SREM-SC): Crust and uppermost mantle.
Front. Earth Sci. 10:1080307.
doi: 10.3389/feart.2022.1080307

Seismological reference earth model in South China (SREM-SC): Crust and uppermost mantle

Jiamin Hu[1,2], Weijia Sun[1]*, Congcong Liu[1,2], Qingya Tang[1] and Li-Yun Fu[3,4]

[1]Key Laboratory of Earth and Planetary Physics, Institute of Geology and Geophysics, Chinese Academy of Sciences, Beijing, China, [2]College of Earth and Planetary Sciences, University of Chinese Academy of Sciences, Beijing, China, [3]Shandong Provincial Key Laboratory of Deep Oil and Gas, China University of Petroleum (East China), Qingdao, China, [4]Laboratory for Marine Mineral Resources, Qingdao National Laboratory for Marine Science and Technology, Qingdao, China

The South China Block is located on the eastern margin of the Eurasian Plate and the western margin of the Pacific Plate. The South China Block is currently in a tectonically compressed environment, while the Tibetan Plateau is moving eastward and the Philippine Sea Plate is moving westward from geodetic observations. The South China Block is an ideal place to revisit tectonic history from the Archean to Cenozoic, where its information could be well preserved in the crust. In this study, we aim to build the crustal and uppermost mantle component of the Seismological Reference Earth Model in South China (SREM-SC) to provide a background velocity model for geological interpretations and fine-scale velocity inversion. The S-wave velocity model comes from combining models inverted by ambient noise tomography and surface wave tomography. The P-wave velocity model is obtained from converted S-wave velocity and joint inversion tomography. The density model is inferred from an empirical relationship with P-wave velocity. The Moho depth is obtained by a weighted averaging scheme of previously published receiver function results. The P-wave and S-wave velocity models have a grid interval of 0.5° in both latitude and longitude, and with a vertical sampling interval of 5 km down to the 60 km depth. This work provides the 3-D crust and uppermost mantle structures and a representative reference model beneath South China.

KEYWORDS

South China Block, crust, reference model, surface waves, body waves, receiver functions

1 Introduction

The South China Block (SCB), located on the Eurasian Plate's southeast margin and the Pacific Plate's western margin, is an important tectonic unit in the east of the Chinese mainland. It is adjacent to the North China Craton (NCC), bounded by the Qinling-Dabie orogen (QDO) and Tanlu Fault (TLF) in the north, the Songpan-Gantze Block (SGB) and the Tibetan Plateau (TP) in the west (Figure 1). South China Block is composed of two

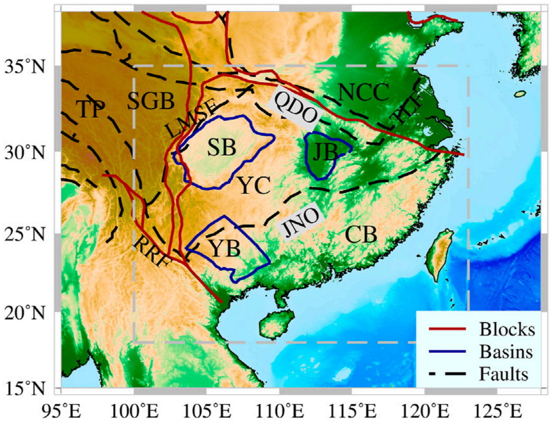

FIGURE 1
Tectonic background of South China Block. Thick red and blue lines indicate the boundaries of the major tectonic units and basins, after Zhang et al. (2003) and Su et al. (2018). Dash black lines indicate the major faults in the Chinese mainland (Deng et al., 2003). TP: Tibetan Plateau; SGB: Songpan-Gantze Block; QDO: Qinling-Dabie Orogen; NCC: North China Craton; TLF: Tanlu Fault; SB: Sichuan Basin; JB: Jianghan Basin; YB: Youjiang Basin; YC: Yangtze Craton; CB: Cathaysia Block; JNO: Jiangnan Orogen; RRF: Red River Fault; LMSF: LongMenShan Fault.

major blocks, the Yangtze Craton and the Cathaysia Block. The Yangtze Craton is mainly composed of the Paleoproterozoic crystalline basement, and the Cathaysia Block is mainly composed of Neoproterozoic basement rocks (Cawood et al., 2013; Zheng et al., 2013). The long period of intense tectonic movements and multistage superposition shaped the present tectonic features of the South China Block. In Neoproterozoic, the Yangtze Craton collided with the Cathaysia Block along the Jiangnan orogenic belt to form the South China block (Zhang et al., 2013; Mao et al., 2014; Yan. et al., 2018a). The North China Craton and the South China block are thought to have collided after the closure of the paleo-Tethys Ocean during the Triassic, resulting in the formation of the Qinling-Dabie orogenic belt (Shu, 2012; He et al., 2013; Wang et al., 2013; Yan et al., 2018b). The South China Block transitioned from Tethysian to Pacific tectonic regimes during the Early-Middle Jurassic, and thus the tectonic environment changed from convergence to extension, which led to large-scale lithosphere thinning, widespread magmatism, and extensive mineralization (Li and Li, 2007; Shu, 2012; Wang et al., 2013; Lü et al., 2014; Qiu et al., 2016; Qiu et al., 2017; Qiu et al., 2022).

Understanding the crustal deformation and dynamic mechanism in South China requires detailed information about crustal structure and composition. In recent years, many geophysical studies have been conducted to image the crustal and uppermost mantle structure using various techniques, such as body wave tomography (He and Santosh, 2016; Sun and Kennett, 2016b; a; Qu et al., 2020), surface wave tomography (Zhou et al., 2012; Bao et al., 2015; Shan et al., 2016), receiver functions (He et al., 2013; He et al., 2014; Song et al., 2017; Zhang et al., 2018), joint inversion tomography (Guo et al., 2018; Guo et al., 2019; Gao et al., 2022), deep seismic reflection profiling (Deng et al., 2011; LÜ et al., 2013), gravity analysis (Deng et al., 2014). Zhou et al. (2012) obtained the 3D S-wave velocity structure in South China through ambient noise and earthquake surface wave tomography and they found that the lithosphere is thick in the western Yangtze Craton but thin in the eastern Cathaysia Block. They hypothesized that the lithosphere of the Yangtze Craton and Cathaysia Block was eroded and thinned due to the flat slab subduction of the Pacific plate. He et al. (2013) obtained the distribution of crustal thickness and Vp/Vs in South China through the receiver function study, and inferred that the Jiujiang-Shitai fault defines a suture zone between the Yangtze Craton and Cathaysia Block. Guo et al. (2018) observed the lateral crustal structure variations beneath South China Block through the joint inversion of the surface wave and receiver functions, which supported the flat slab subduction model proposed by Li and Li (2007). Through joint inversion of body wave and surface wave, Gao et al. (2022) analyzed the thinning mechanism of the lithosphere in South China, and they preferred the flat slab subduction and its rollback model. In addition, a high-velocity belt was found in the middle crust, and they speculated that this high-velocity belt indicated the location of the Neoproterozoic Yangtze Craton and Cathaysia Block. There have been comprehensive geophysical studies in South China, but there are still some unresolved issues due to the complex tectonic events. For example, the location of the suture zone between the Yangtze Craton and the Cathaysia Block is still debated (Wang et al., 2010; He et al., 2013). Several competitive geological models such as the flat-slab subduction model (Li and Li, 2007), the underplating and delamination model (He et al., 2013), and the lateral asthenospheric flow model (Gong and John Chen, 2014) have been proposed for the formation of the Yangtze Craton and Cathaysia Block. Furthermore, different Mesozoic magmatic province formation mechanisms were also controversial (Zhou X. et al., 2006; Li and Li, 2007; Wang et al., 2013).

Kennett et al. (2013) and Salmon et al. (2013) proposed an Australian Seismological Reference Model (AuSREM) using a large amount of seismological information in the Australian region. This 3D seismological reference model not only shows the main structural features of the area but also provides a detailed basic reference model for the future study of the area. The AuSREM plays an important role in Australian research and has been cited more than 100 times so far. Some velocity models in South China have been obtained by different research methods, but there may be significant inconsistencies between various models. We propose a basic reference model for South China like the AuSREM. It is very helpful to solve the above-mentioned controversial issues. The purpose of establishing the crustal and uppermost mantle component of the SREM-SC is to summarize the extensive seismological information and methods in South China over the past decades and to provide 3D

TABLE 1 Nine seismic models were used in this study. (A) Data resources of tomography inversion for the S-wave velocity model used in this study. (B) Data resources of receiver function for crustal thickness model used in this study.

A. Five seismic tomography models				
Author	Grid	Depth grid spacing	Model	Methods
Zhou et al. (2012)	0.5 × 0.5	0.2 km (from 0 to 150 km)	Vs	Ambient noise and earthquake surface wave tomography
Bao et al. (2015)	0.1 × 0.1	2 km (from 1 to 9 km); 5 km (from 12.5 to 77.5 km); 10 km (from 85 to 155 km)	Vs	Ambient noise and earthquake surface wave tomography
Shen et al. (2016)	0.5 × 0.5	0.5 km (from 0 to 199 km)	Vs	Ambient noise and earthquake surface wave tomography
Han et al. (2021)	0.5 × 0.5	0, 5, 10, 15, 20, 30, 40, 60, 80, 100, 120, 150, 180 km	Vs & Vp	Joint inversion of the body wave and surface wave
Gao et al. (2022)	0.5 × 0.5	2 km (from 0 to 30 km); 5 km (from 30 to 120 km)	Vs	Joint inversion of the body wave and surface wave

B. Four crustal thickness models		
Author	Model	Methods
Li et al. (2014)	Moho depth	H—κ stacking of receiver functions (collecting and integrating)
He et al. (2014)	Moho depth & Vp/Vs	H—κ stacking of receiver functions
Wei et al. (2016)	Moho depth & Poisson's ratio	H—κ stacking of receiver functions
Guo et al. (2019)	Moho depth & Vp/Vs	Joint inversion of receiver function and gravity

seismological reference models in South China and its surrounding areas.

The crustal and uppermost mantle component of the SREM-SC is grid-based, with 0.5-degree latitude and longitude sampling. The model grid ranges from 100°E to 121°E in longitude and from 18°N to 35°N in latitude. The properties of each grid point are defined by the sedimentary thickness of the basin, the Moho depth, P-wave velocity (Vp), S-wave velocity (Vs), and density. Using various types of seismic data, we created a database of well-constrained results. The Vs mainly comes from surface wave tomography. The Vp comes from converted Vs and body wave tomography. The density is obtained from the empirical relationship between the Vp and density.

The crustal structure has an important influence on the tomography of the lithospheric mantle and asthenosphere, so the establishment of this model is of great value to improve knowledge of the crustal structure and the seismic tomography work (Salmon et al., 2013). The crustal and uppermost mantle component of SREM-SC provides a reference model for other studies in this area, such as improving earthquake locations, seismic wave propagation modeling, and calculation of crustal corrections.

2 Data resources

We gathered various types of data and then combined them to construct the 3D seismological reference model for crustal and uppermost mantle structures in South China. The data resources for constructing the velocity model mainly come from various joint tomographic inversion results, while the data resources for constructing the Moho depth map are mainly from the receiver function studies.

We have collected five previously published S-wave velocity models for the lithosphere of the South China Block (Table 1). Previous studies have obtained 3D S-wave velocity models of the crust and upper mantle across the South China block by ambient noise and earthquake surface wave tomography (Zhou et al., 2012; Bao et al., 2015; Shen et al., 2016). The empirical Green's functions (EGFs) estimated from the long-time cross-correlation of ambient noise provided shorter periods of dispersions (Shapiro et al., 2005). Therefore, combining both ambient noise and traditional surface wave tomography can get a more detailed lithospheric structure from the shallow crust to the upper mantle (Yao et al., 2006; Yao et al., 2010). Based on the algorithm of Zhang et al. (2014), some studies in South China combined body-wave arrival times and surface wave data to determine a high-resolution 3D S-wave velocity model of the lithosphere (Han et al., 2021; Gao et al., 2022).

We collected some estimations of crustal thickness, Poisson's ratio, and Vp/Vs ratio in the South China Block from previously four published receiver function results (Table 1). The receiver function technique (Zhu and Kanamori, 2000) has become a general seismological method to investigate crustal thickness. It can extract P-to-S converted phases generated at seismic

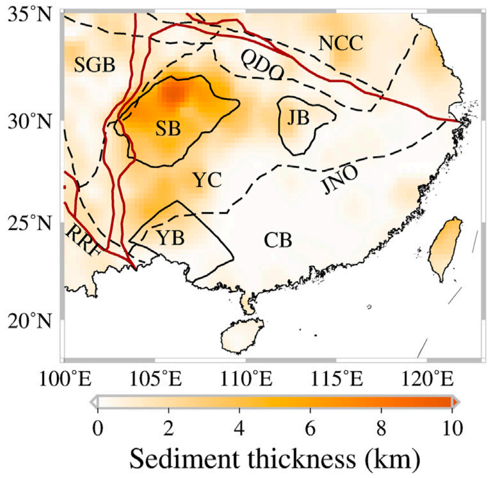

FIGURE 2
The thickness of sediments in the South China Block is based on the study of Laske et al. (2013) and Xiao et al. (2021).

discontinuities effectively in the crust and upper mantle beneath seismic stations. Compared to the absolute velocities, receiver function methods provide better limits on the discontinuities. Li et al. (2014) summarized the crustal thickness of the Chinese mainland based on previous studies. He et al. (2014) integrated the three phases (converted Ps and multiple PpPs and PpSs + PsPs phases) of the Moho to estimate the crustal thickness and average Vp/Vs ratio of continental China using the H-k stacking method of receiver functions (Zhu and Kanamori, 2000). Wei et al. (2016) used the same method but more data to calculate the Moho depth and Poisson's ratios beneath eastern China. Guo et al. (2019) enhanced the method for the joint inversion of gravity and receiver function and apply it to improve the estimates of crustal thickness and Vp/Vs ratio in South China.

3 Sediments thickness

Sediment thickness, seismic properties, and geometrical features of basins can be used to better understand the basin's geological evolution (Zhou J. et al., 2006; Li et al., 2012). CRUST1.0 is the latest and widely used global model of the crust. Based on the existing seismic detection results of active and passive sources, combined with gravity inversion research, the model gives information on sediment thickness, crustal thickness, and velocity structure with 1.0-degree latitude and longitude sampling (Laske et al., 2013). Xiao et al. (2021) provided the thickness of sediments model beneath continental China by using the Rayleigh wave ellipticity, P polarization, and receiver function method.

Based on the model of CRUST1.0 and the study of Xiao et al. (2021), we establish a sedimentary thickness model in South China. We provide a comparison of the different weighting values for the sediment thickness model in the supplementary material (Supplementary Figure S6), evidencing that the weighting values have little effect on the final model. CRUST1.0 is a global model with less data coverage over South China than Xiao et al. (2021), so we think the weighting value 6:4 is an appropriate choice. The final weighting model for the sediment thickness H_{Ref} at any grid point is

$$H_{Ref}(i) = 0.6H_X(i) + 0.4H_C(i) \qquad (1)$$

where H_X comes from the study of Xiao et al. (2021), H_C is the CRUST1.0 model (Laske et al., 2013).

Figure 2 displays the thicknesses of sediment in the South China Block. The thickest deposits are concentrated in the Sichuan Basin and the thickness of sedimentary cover reaches 5–10 km. The deposits are mainly composed of the Palaeozoic and middle Mesozoic strata (Wang et al., 2016; Liu et al., 2021). It has the thickest shales (up to 300 m) and has become China's primary region for shale gas exploration (Zou et al., 2019). The Jianghan and Youjiang basins have no obvious deposits, but they have rich mineral resources and play an important role in the tectonic evolution of the South China block. The Jianghan basin is a typical continental petroliferous basin with salt layers. It is a rifted basin of Cretaceous-Paleogene formed on the Yangtze platform, covering $28,000km^2$ smaller than the Sichuan basin (Lu et al., 2008). These sediments not only contain the uplift information of the surrounding orogenic belt but also preserve the geological information of the evolution of the Yangtze River (Zhang et al., 2008; Lin and Liu, 2019). In the southwestern part of the South China Block, a fabulous amount of gold deposits gathered in the Youjiang basin. The formation of the gold deposits is related to two tectonic evolution events, the collision between the Indosinian Block and the South China Block and the westward subduction of the paleo-Pacific Plate (Su et al., 2018; Jin et al., 2021; Yang et al., 2021). There are few studies on the sediments' seismic velocity distributions presently and so we hope that the sediments thickness of the crustal and uppermost mantle component of the SREM-SC can stimulate the development of more detailed representations of the sediments.

4 Moho depth

The Moho provides an immediate connection between the crustal and mantle component of SREM-SC. We have collected many studies on the crustal thickness in South China using the receiver function method or joint inversion method (Table 1). The left column of Figure 3 shows that the distribution of stations

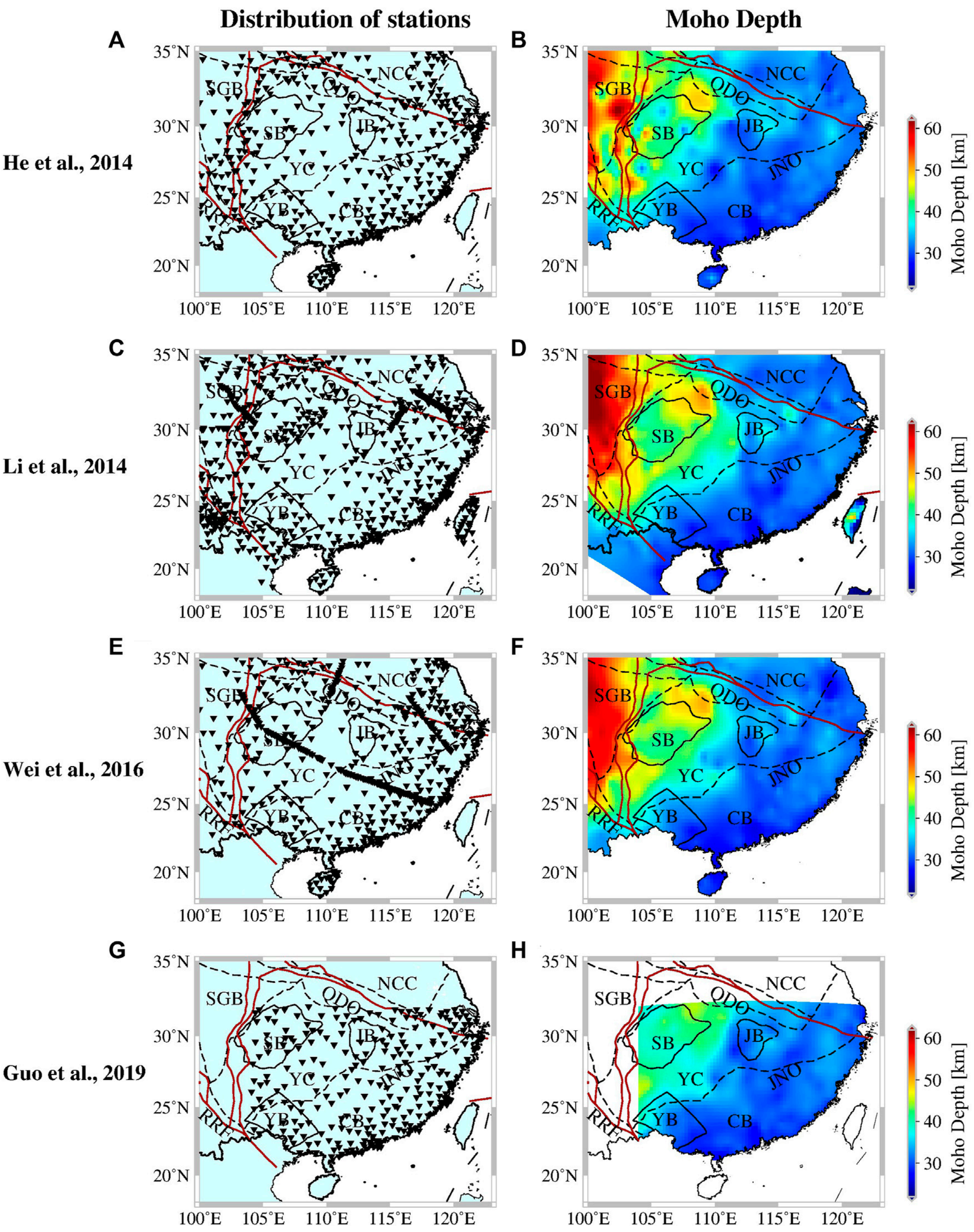

FIGURE 3
Distribution of stations and the Moho depth maps from different studies. **(A,B)** The He et al. (2014) model, **(C,D)** the Li et al. (2014) model, **(E,F)** the Wei et al. (2016) model, **(G,H)** the Guo et al. (2019) model.

in South China is relatively uniform, and some temporary arrays are added in the study of Li et al. (2014) and Wei et al. (2016). The Moho depth of these studies showed great consistency, except in some areas, which may be caused by the different data sets or the details of the method (filters, selection of events, and the parameters).

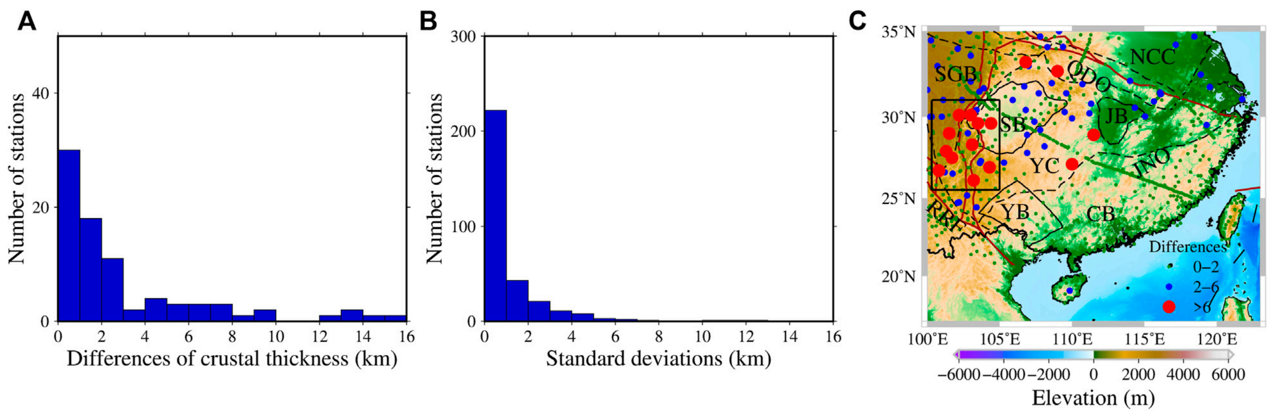

FIGURE 4
Uncertainties of crustal thicknesses determined from receiver function analysis. **(A)** Differences in crustal thickness for stations with two different estimates. **(B)** Standard deviations of crustal thickness for stations with three or more different estimates. **(C)** Distribution of estimates for those stations with large differences.

TABLE 2 Information about stations with standard deviation/difference estimates greater than 6 km.

Lon (°)	Lat (°)	Li et al. (2014) (km)	He et al. (2014) (km)	Wei et al. (2016) (km)	Guo et al. (2019) (km)
100.8	26.7	55	33.11		
109.0	32.7	52	61.2, 32.32	49.1	
101.51	28.99	61.2	39.35	57.88	
111.5	28.9	44			28
103	30.1	43.3	58.73		
101.7	27.5	58.7	38.17	54.5	
102.2	30.1	58.8	44.7		
101.3	27.9	52	38.35		
104.3	26.91		30.61		44
106.8	33.23		35.57	48.25	
103.1	28.3	45.5, 49	34		
103.2	26.1	46.4	56.17		
103.5	29.6	49.6	40.53		
110	27.1	37.8	26.1	39.58	30.5
104.4	29.6	46	53.49	43.96	38.5

For the same station, there may be some differences in longitude and latitude given by different studies. To ensure that the information of the same station can be compared in the statistical process, we regard the station spacing less than 7 km as the same station (If this criterion is smaller, it will lead to the actual same station but be counted many times; If this criterion becomes larger, then closely spaced linear arrays will be miscounted). Based on the above criteria, in our database 397 stations had more than one estimate (2 stations were estimated 6 times, 21 stations were estimated 5 times, 169 stations were estimated 4 times, 121 stations were estimated 3 times, and 84 stations were estimated 2 times) and 499 stations with only one estimation. The dataset used in our study has some redundancy because many stations had multiple estimates of crust thickness. We calculate the difference or standard deviation of stations for stations with multiple estimates to evaluate its uncertainty. Figure 4A shows the differences in crustal thickness for 84 stations with two different measurements. We also calculated the standard deviations for 313 stations with at least three different estimates of the crustal thickness (Figure 4B). The standard deviation/difference of most measurements is within 3 km, but a few of them reach 16 km. We list the specific estimates in Table 2 for each model with a standard deviation/difference greater than 6 km. There is no significant difference in crustal thickness in most study areas, but some areas with complex topography have huge differences, such as the southeastern Tibetan Plateau (Figure 4C). We do not consider the estimates of the crustal thickness with a standard deviation/difference greater than 6 km in the final model.

We have collected more than 800 estimates of crustal thickness from receiver function studies (Figure 5A) in South China after removing poor thickness estimations and redundant data. With denser station distribution, we propose a crustal thickness map in South China. The large-scale features of the result (Figures 5B,C) are similar to those of

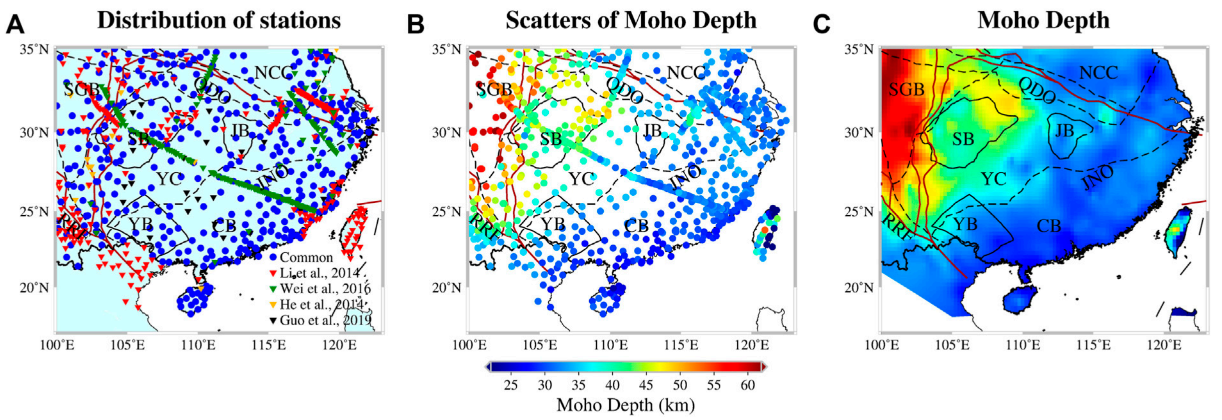

FIGURE 5
(A) Distribution of receiver function data used in this study. Blue circles: Multiple measurements of crustal thickness; red triangles: one measurement from Li et al. (2014); green triangles: one measurement from Wei et al. (2016); yellow triangles: one measurement from He et al. (2014); black triangles: one measurement from Guo et al. (2019). **(B)** Scatters of crustal thicknesses; **(C)** Interpolated results to crustal thicknesses.

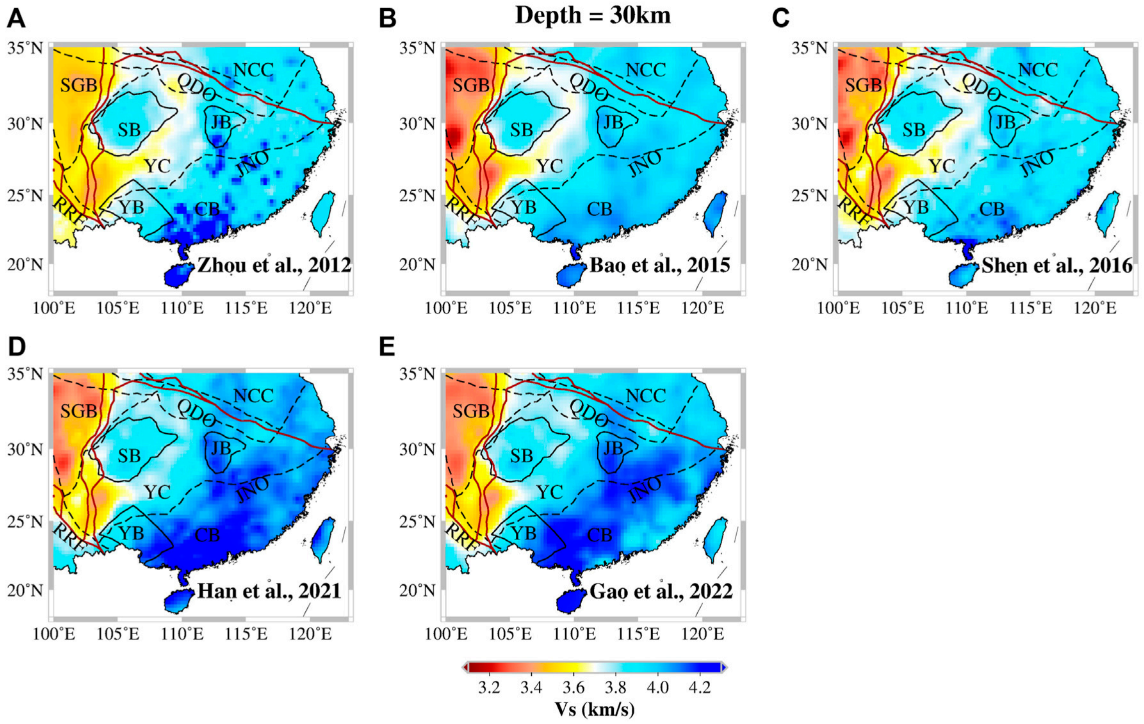

FIGURE 6
Five published S-wave velocity models at a depth of 30 km with the same color bar from **(A)** Zhou et al. (2012), **(B)** Bao et al. (2015), **(C)** Shen et al. (2016), **(D)** Han et al. (2021), **(E)** Gao et al. (2022). The velocity structure on Taiwan island is not reliable due to lacking data in **(A)**.

previous results (Li et al., 2014; Wei et al., 2016). However, in some detail, we integrate the results of all models so that it can represent the general features of the region. The crustal thickness shows a large variation from east to west. The crustal thickness along the coastal region of the Cathaysia Block is about 25–35 km. The western Yangtze Craton is thicker, about 37–48 km. The Songpan-Gantze block has a crustal thickness of up to 60 km.

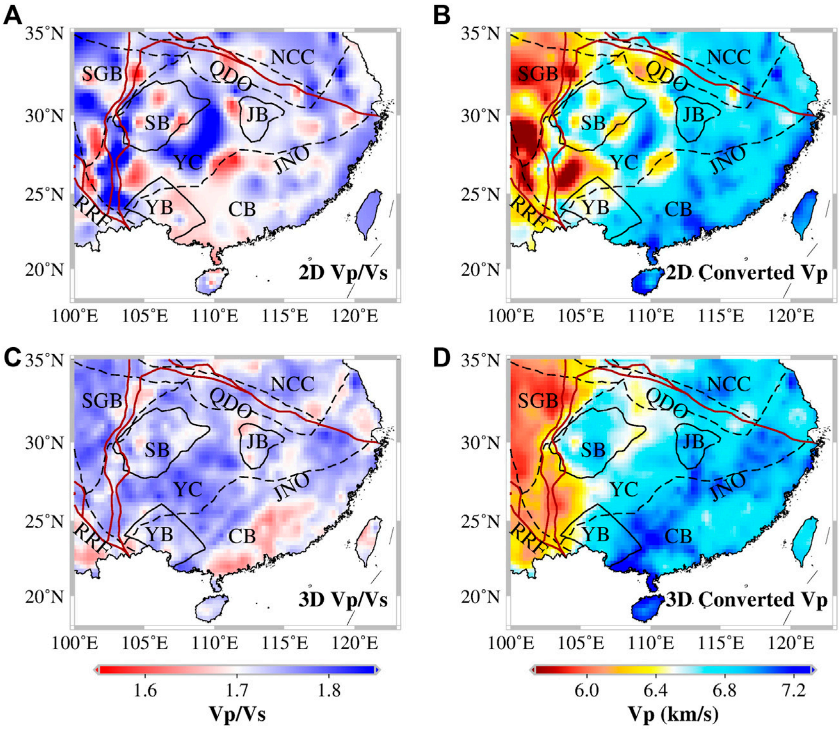

FIGURE 7
Comparison of the estimated values obtained from the conversion of Vs using the two different approaches. **(A)** 2D Vp/Vs ratio obtained by receiver function study (He et al., 2014) and **(B)** the resulting 2D converted Vp. **(C)** 3D Vp/Vs ratio obtained by tomographic study (Han et al., 2021) and **(D)** the resulting 3D converted Vp.

5 Velocity model

5.1 Velocity model construction

With the development of China's earthquake observation system, South China has good data coverage and these studies used the three-component seismogram records from permanent and temporary stations of the China National Seismic Network deployed in South China. The crustal and uppermost mantle component of the SREM-SC is controlled by the S-wave velocity (Vs). S-wave velocity is then used to construct the P-wave velocity (Vp) and density (ρ) fields, as discussed below.

5.1.1 Averaged model of Vs

Since the horizontal grids and vertical sampling intervals of the published velocity models are different, we re-interpolated each model in uniform grids at the same horizontal coordinates (0.5° step) and depth (5 km step), using an inverse distance weighted method (exponent in the inverse distance weighting function is 2). Figure 6 illustrates the selected models with absolute velocities at depth of 30 km. We also show the velocity structure comparison at different depths in the supplementary material (5 km, Supplementary Figure S1; 10 km, Supplementary Figure S2; 20 km, Supplementary Figure S3; 40 km, Supplementary Figure S4; 60 km, Supplementary Figure S5). The velocity anomalies of these models in most areas are consistent. The Sichuan Basin shows low-velocity anomalies in the shallow crust due to the thick sediments. In the middle-lower crust, the low-velocity anomalies are mainly distributed in the Songpan-Gantze Block and the southeastern Tibetan Plateau. And the coast of the Cathaysia Block shows high velocities. The general consistency between the various models from different methods means that the key features of the structure are comparable, which provides a basis for constructing the crustal and uppermost mantle component of SREM-SC. Nevertheless, we must recognize that there are some discrepancies between the models due to the different techniques and data sets, such as the distribution of the low-velocity anomalies in the Sichuan Basin at 5 and 10 km, the value of the velocity anomalies in the Songpan-Gantze Block and the Cathaysia Block at 20–60 km depth.

In order to obtain the average reference model of the study region, we test the models with different weights according to data coverage, resolution, inversion method, and other factors (shown in Supplementary Figure S7 and Supplementary Table S1). By comparing the results of different weights, we find that

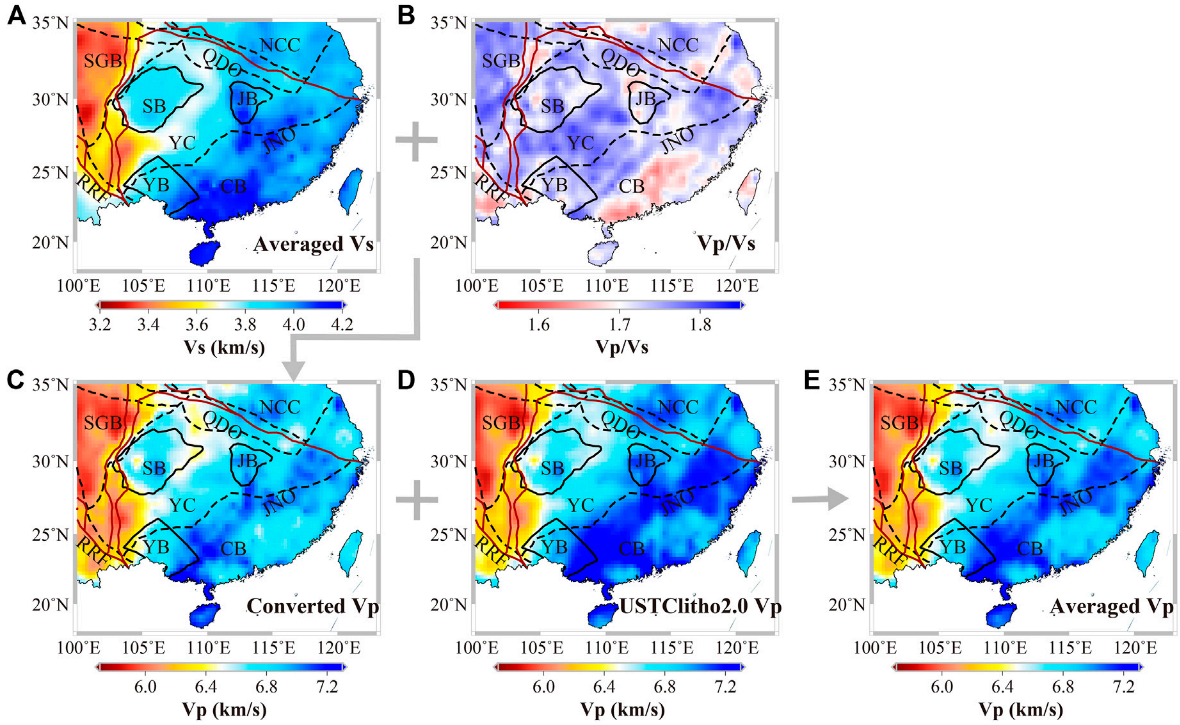

FIGURE 8
The construction process of P-wave velocity for the crustal and uppermost mantle component of SREM-SC keyed at a map view of 30 km depth. **(C)** The converted P-wave velocity model is obtained by combing **(A)** the averaged S-wave velocity model with **(B)** the Vp/Vs ratio obtained from the USTClitho2.0, and then averaged with **(D)** The P-wave velocity from USTClitho2.0 (Han et al., 2021) to build **(E)** the final averaged P-wave velocity for the crustal and uppermost mantle component of SREM-SC.

there is little difference in velocity structure characteristics. It indicates that the velocity structure characteristics of the five models used in our study are very similar at various depths, and it is feasible for us to average the five models. We calculate the original five models (Table 1) with equal weight and obtain an average model that can represent the common characteristics of the study region. To evaluate the results of our average model, we also calculated the difference between each model and the average model at each grid point, as follows:

$$Difference = \frac{Model - AverageModel}{AverageModel} \times 100\% \tag{2}$$

5.1.2 Conversion from Vs to Vp

At present, there are few publicly available 3D P-wave velocity models for the crust and uppermost mantle in South China Block, and the majority of P-wave velocity models come from body wave tomography or the full waveform seismic tomography in the mantle (Zhao et al., 2012; Tao et al., 2018). Therefore, we would like to obtain some other information to help construct the 3D P-wave velocity models. We can estimate the Vp by conversion of Vs using the Vp/Vs ratio. There are two different approaches to getting the Vp/Vs ratio. In the first method, the receiver function studies provide not only an estimate of Moho depth but also the average Vp/Vs ratio of the crust. The ratio obtained by this method is a 2D model, which is the same value at every depth (Figure 7A). In the second method, the USTClitho2.0 provided both the Vp and Vs, we can get the Vp/Vs ratio by dividing these two. The ratio obtained by this method is a 3D model, which is different at every depth (Figure 7C). By comparing the models estimated by the conversion of Vs using the two different approaches, we found that the Vp got from 3D Vp/Vs ratio (Figure 7D) was more consistent with the velocity characteristics than the 2D Vp/Vs ratio (Figure 7B).

Figure 8 shows the construction process of the P-wave velocity of the crustal and uppermost mantle component of SREM-SC. The average Vs model (Figure 8A) combined with the 3D Vp/Vs ratio (Figure 8B) yields a converted Vp field (Figure 8C), and then its combination with the Vp estimates from the joint tomography inversion (Han et al., 2021) (Figure 8D) to produce a final Vp distribution (Figure 8E). Combining these two sets of results, we construct a smooth estimate of the Vp model, which provides a good representation of the velocity structure of the study region.

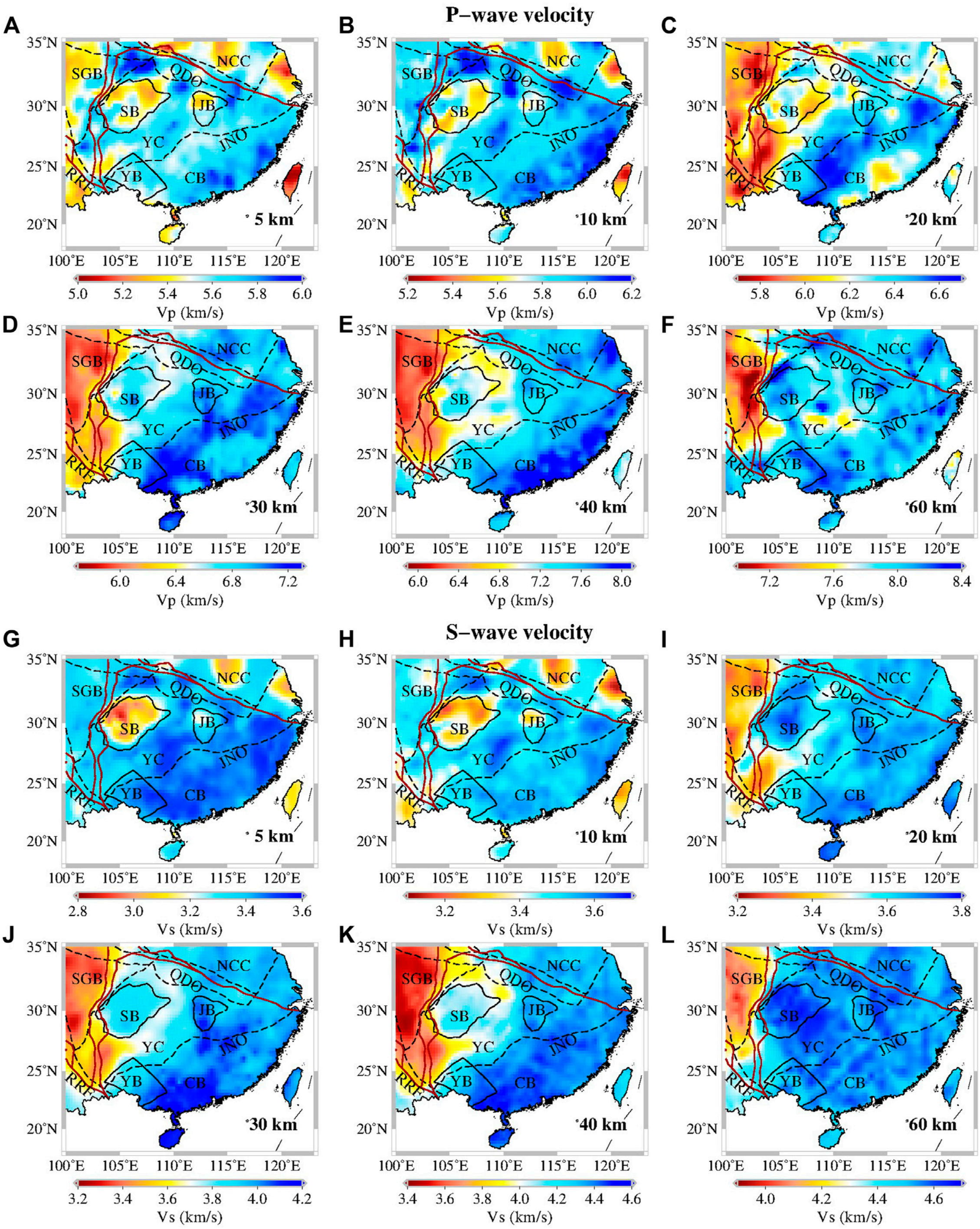

FIGURE 9
P-wave velocity distribution for the crustal and uppermost mantle component of SREM-SC at depths of **(A)** 5 km, **(B)** 10 km, **(C)** 20 km, **(D)** 30 km, **(E)** 40 km, and **(F)** 60 km. S-wave velocity distribution for the crustal and uppermost mantle component of SREM-SC at depths of **(G)** 5 km, **(H)** 10 km, **(I)** 20 km, **(J)** 30 km, **(K)** 40 km, and **(L)** 60 km.

5.1.3 Relation of Vp and density

Velocity and density are two kinds of parameters with good correlation to rock's physical properties. Feng et al. (1986) proposed a linear relationship between velocity and density suitable for local conditions by referring to the Nafe-Drake empirical relationship and combining it with plenty of seismic

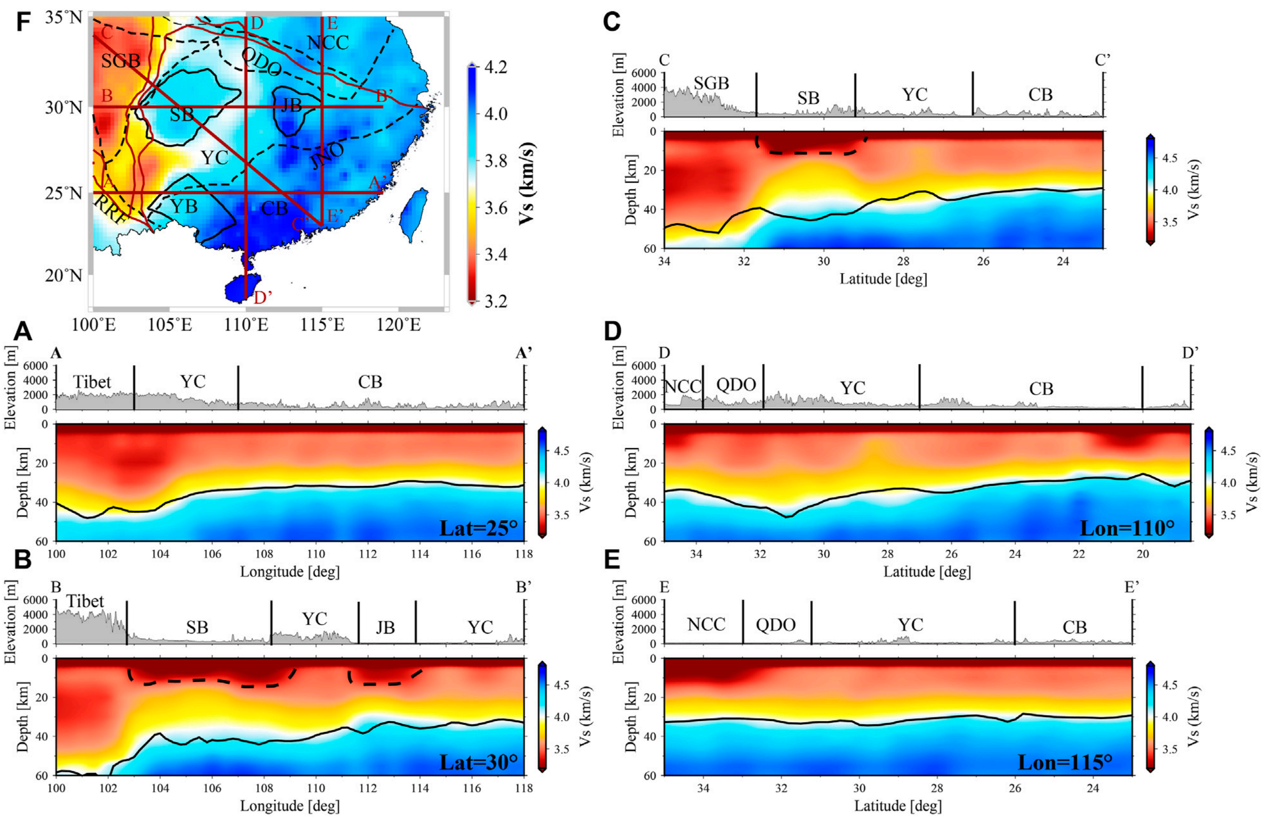

FIGURE 10
Vertical S-wave velocity sections of the crustal and uppermost mantle component of SREM-SC along profiles **(A)** latitude at 25°N, **(B)** latitude at 30°N, **(C)** a diagonal profile CC′, **(D)** longitude at 110°E; **(E)** longitude at 115°E. The profile locations are shown in the map view **(F)** at 30 km. Moho depth of this study (solid black line) is also shown in the map.

data in North China when inversing the 3D potential field of gravity and magnetic. We use the empirical relationship proposed by Feng et al. (1986):

$$\rho = 2.78 + 0.56^{*}\left(v_p - 6.0\right);\ v_p \le 6.0 \tag{3}$$

$$\rho = 3.07 + 0.29^{*}\left(v_p - 7.0\right);\ 6.0 < v_p \le 7.5 \tag{4}$$

$$\rho = 3.22 + 0.20^{*}\left(v_p - 7.5\right);\ v_p > 7.5 \tag{5}$$

5.2 Velocity structure

5.2.1 Horizontal slices

Ambient noise tomography, which is highly sensitive to the existence of sediments, is primarily responsible for determining the upper crust structure (Salmon et al., 2013). Figures 9A,B,G,H display the P-wave velocity and S-wave velocity in the crustal and uppermost mantle component of the SREM-SC at 5 and 10 km depth. At the depth of 5 km, both P-wave and S-wave velocities show low-velocity anomalies in sedimentary basins such as Sichuan Basin and Jianghan Basin, the southeastern North China Craton, and the eastern Tanlu Fault. The low-velocity anomalies of the S-wave correspond well to the Sichuan Basin, while the low-velocity anomalies of the P-wave are scattered, which can also be observed in the Songpan-Gantze Block and Red River Fault. The P-wave and S-wave velocities at 10 km are homogeneous in most regions, except for the Sichuan Basin, where there is still a bit of low velocity due to the thicker sediments. In comparison, the Qinling-Dabie Orogen and the coastal of the Cathaysia Block show high velocities, which could be caused by crystallized basement rocks (Li and Li, 2007).

Figures 9C,D,I,J display the P-wave velocity and S-wave velocity in the crustal and uppermost mantle components of the SREM-SC at 20 and 30 km depth. At depth of 20 km, the velocity distribution characteristics of the P-wave and S-wave are roughly the same. The P-wave velocity in the Jiangnan Orogenic shows high-velocity anomalies. Up to 30 km depth, the velocity structure shows a significant change from west to east and does not correspond to the geological structure like the upper crust structure. The low-velocity anomalies are concentrated in the Songpan-Gantze Block and the southeastern margin of the Tibetan Plateau. These low-velocity anomalies possibly relate

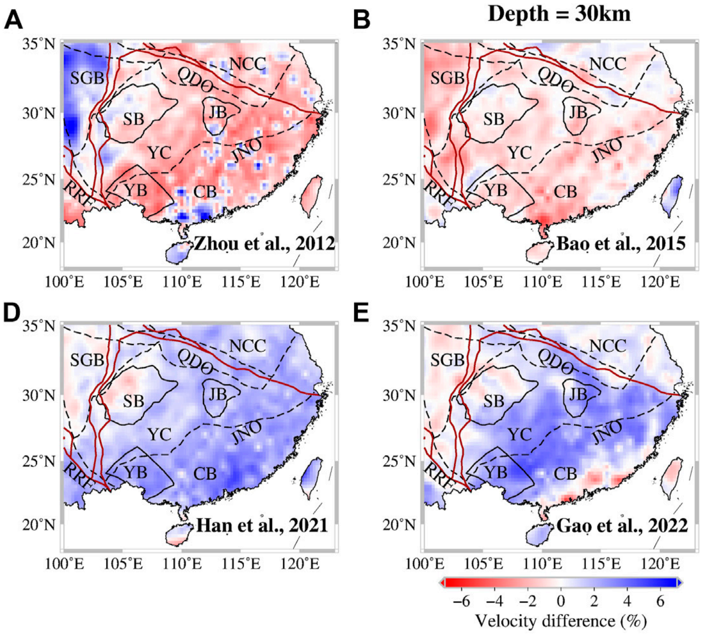

FIGURE 11
Velocity difference of the averaged S-wave velocity model at 30 km depth relative to the models of **(A)** Zhou et al. (2012), **(B)** Bao et al. (2015), **(C)** Shen et al. (2016), **(D)** Han et al. (2021), **(E)** Gao et al. (2022).

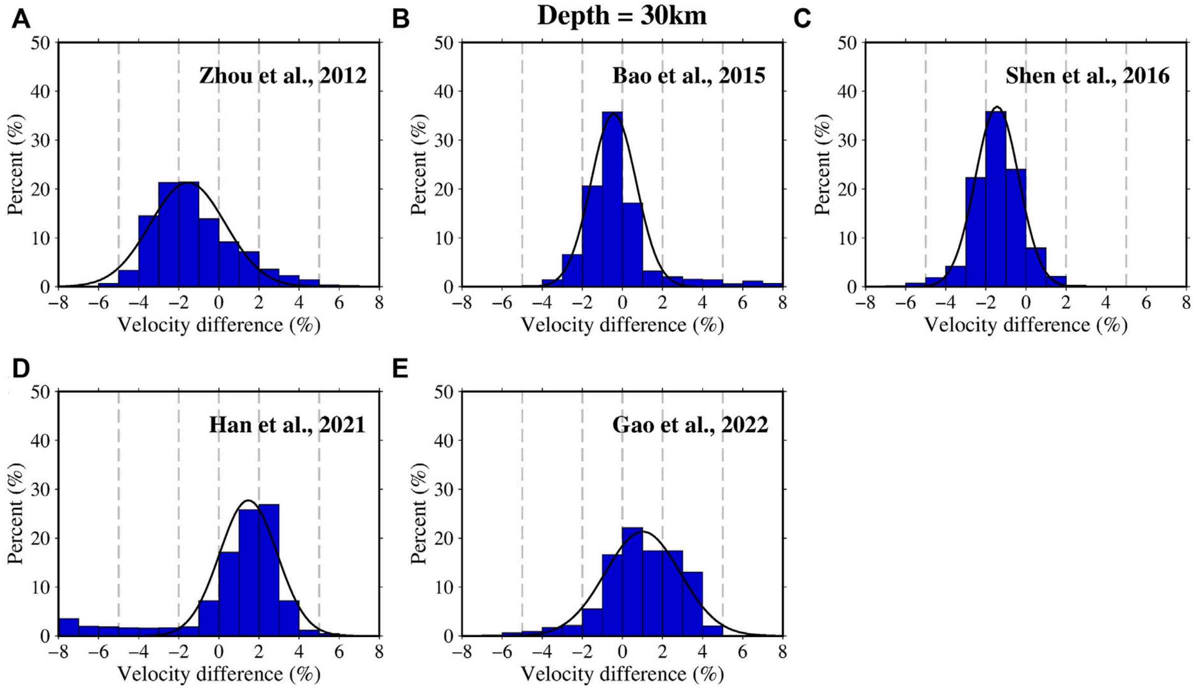

FIGURE 12
Percentage histograms of velocity difference distribution from the average model, calculated at each node, at 30 km depth for **(A)** Zhou et al. (2012), **(B)** Bao et al. (2015), **(C)** Shen et al. (2016), **(D)** Han et al. (2021), **(E)** Gao et al. (2022). The dashed gray lines indicate the velocity difference of 0%, ± 2%, and ± 5%.

to the channel flow in the middle-lower crust beneath Tibet (Clark and Royden, 2000; Royden et al., 2008). We also can see a generally good correlation between the distribution patterns of S-wave velocity, P-wave velocity, and Moho depth discussed in section 4 (Figure 5C), for instance, regions with a thicker crust usually have lower velocity values than regions with a thinner crust.

The P-wave velocity and S-wave velocity in the crustal and uppermost mantle components of the SREM-SC at 40 and 60 km depth are shown in Figures 9E,F,K,L. At the depth of 40 km, the velocity characteristics remain in the same distribution pattern as at 30 km depth. At the depth of 60 km, the whole study area displayed as high velocities, while the southeastern Tibetan Plateau retains some low-velocity characteristics.

5.2.2 Vertical cross sections

Figure 10 shows five representative vertical cross sections through the crustal and uppermost mantle component of the SREM-SC. The sections at latitude 25°N, latitude 30°N, longitude 110°E, longitude 115°E, and an oblique section extending from the southeast to northwest of the study region are presented in depth slices of S-wave velocity at 30 km depth (Figure 10F).

Section AA’ (Figure 10A) crosses the southeastern Tibetan Plateau (TP), southern Yangtze Craton (YC), and Cathaysia Block (CB). A low-velocity zone exists beneath the Tibetan Plateau in this section. Section BB’ (Figure 10B) crosses the Tibetan Plateau, Sichuan Basin (SB), and Jianghan basin (JB), and reaches the eastern Yangtze Craton. There is a low-velocity zone in the middle and lower crust of the Tibetan Plateau, which has a clear boundary with the Sichuan Basin, possibly due to the obstruction of the rigid Sichuan Basin (Clark and Royden, 2000; Royden et al., 2008). At the same time, we can observe a clear Moho depth variation between longitude 102°E and 104°E. In addition, there are low-velocity anomalies below the Sichuan Basin and Jianghan Basin, which are related to their thick sediments, but for these sedimentary basins, there is no fully defined lower boundary. Section CC’ (Figure 10C) crosses the Songpan-Gantze block (SGB), Sichuan Basin, Yangtze Craton, and Cathaysia Block. There is a low-velocity zone beneath the Songpan-Gantze Block in the middle-lower crust, and the Moho depth of the whole section increases from southeast to northwest. We can still observe the low velocities below the Sichuan Basin in the shallow crust. Section DD′ and EE’ (Figures 10D,E) both cross the North China craton (NCC), Qinling-Dabie Orogen (QDO), Yangtze Craton, and Cathaysia Block along longitude. In these two sections, the crustal thickness fluctuates slightly, about 35 km.

By comparing our new Moho depth (Figure 5C) discussed in section 4 with the vertical sections of the S-wave velocity, we found a good correspondence between the Moho depth and the Vs of 4.0 km/s. We can see from these sections that the Moho depth increases from southeast to northwest and crustal thickness is positively correlated with topography.

5.3 Comparison with previous models

We compare our average model with those by Zhou et al. (2012), Bao et al. (2015), Shen et al. (2016), Han et al. (2021), and Gao et al. (2022) at 30 km depth in Figure 11 and the other depths in the supplementary material (Supplementary Figures S8–S12). We also show the histograms of velocity difference distribution for all five models at 30 km depth in Figure 12, and the other depths are shown in the supplementary material (Supplementary Figures S13–S17).

The result shows that the difference in most areas was less than 6%. At the depth of 30 km, the S-wave velocity results obtained by surface wave tomography (Figures 11A–C) are smaller than the average model in the Yangtze Craton and Cathaysia Block, except for the Sichuan Basin of the model of Shen et al. (2016). In the whole study area, except for the Songpan-Gantze block and the parts of the Sichuan Basin, the results obtained from the joint inversion of body wave and surface wave (Figures 11D,E) are higher than the average model. In the vicinity of the Songpan-Gantze block, except for Zhou et al. (2012) (Figure 11A), other all models show lower velocity than the average model. Figure 12 shows the histogram statistics of the velocity difference distribution at 30 km depth, the models of Figures 12B,C are closest to the average model. The velocity obtained by surface wave inversion is generally lower than the average model, while that obtained by joint inversion is generally higher than the average model.

These published five models are obtained by different data sets and inversion methods, so it is difficult to estimate their systematic biases quantitatively. Zhou et al. (2012) and Shen et al. (2016) think the velocity uncertainties are caused by the trade-off between shear velocity perturbations near a boundary and topography. At shallow depths, uncertainties are highest beneath sedimentary basins. At the depths away from crustal interfaces, the uncertainties are much smaller. At deeper depths, the uncertainties maps are controlled by the Moho depth. The highest uncertainty varies from the eastern of the study region to Tibet. The resolution of the model is about 1–2° in eastern China and has no significant difference in South China (Bao et al., 2015). Han et al. (2021) and Gao et al. (2022) conduct the checkerboard test to evaluate the model and the resolution in South China is relatively uniform. Reasons for these differences may include different types of original data, the method of dispersion measurement, inversion initial models, methods and parameters, etc. We do not determine which model is better or worse, we just attempt to analyze the differences and similarities between the previous models and the newly established average model.

6 Conclusion

We propose the crustal and uppermost mantle component of the Seismological Reference Earth Model in South China (SREM-SC) from many published seismic models, which can serve as a new reference model for the velocity structure of the South China lithosphere. The crustal and uppermost mantle component of SREM-SC is grid-based with a 0.5° sampling in both latitude and longitude, and with vertical sampling points at 5 km intervals to the depth of 60 km. Each grid point is defined by the thickness of the sediments, the Moho depth, the P-wave velocity, the S-wave velocity, and density as a function of depth. The S-wave velocity comes from the ambient noise and earthquake surface wave tomography and the information for the P-wave velocity is a combination of estimates by conversion of Vs using the Vp/Vs ratio and the joint inversion. The density is inferred from empirical relationships between P-wave velocity and density. The Moho depth is obtained by weighted averaging of previously published receiver function results.

The crustal and uppermost mantle component of SREM-SC describes the major lithosphere features in South China. However, we must recognize the limitations of this model. There is no dense P-wave velocity information in the crust of South China, and we limit it by conversing from S-wave velocity. The model can be improved by adding more information constraints. The crustal structure has a significant impact on the tomography of the lithospheric mantle and asthenosphere. The establishment of the crustal and uppermost mantle component of SREM-SC is critical for understanding the crustal structure and improving seismic tomography work. And it can also be used as the initial model for seismic wave propagation simulation, crustal correction for tomography inversion, gravity modeling, etc.

Data availability statement

The raw data supporting the conclusion of this article will be made available by the authors, without undue reservation.

Author contributions

JH: Conceptualization, Investigation, Data Curation, Methodology, Writing—Original Draft, Visualization; WS: Conceptualization, Investigation, Resources, Supervision, Writing—Review and Editing, Funding acquisition; CL: Methodology, Writing—Review and Editing; QT: Data Curation, Methodology, Writing—Review and Editing; L-YF: Resources, Writing—Review and Editing, Project administration, Funding acquisition. All authors contributed to the article and approved the submitted version.

Funding

This research was supported by the National Natural Science Foundation of China (Grants No. 41720104006) and the Youth Innovation Promotion Association CAS.

Acknowledgments

We thank the excellent models provided by Xuewei Bao and Zhi Guo. We thank the models provided by China's regional seismological reference model achievement center (http://chinageorefmodel.org). We also appreciate Junliu Suwen for his kind help during the revision process. All Figures in this study are plotted by the GMT (http://gmt.soest.hawaii.edu/home).

Conflict of interest

The authors declare that the research was conducted in the absence of any commercial or financial relationships that could be construed as a potential conflict of interest.

Publisher's note

Supplementary material

The Supplementary Material for this article can be found online at: https://www.frontiersin.org/articles/10.3389/feart.2022.1080307/full#supplementary-material

References

Bao, X., Song, X., and Li, J. (2015). High-resolution lithospheric structure beneath Mainland China from ambient noise and earthquake surface-wave tomography. *Earth Planet. Sci. Lett.* 417, 132–141. doi:10.1016/j.epsl.2015.02.024

Cawood, P. A., Wang, Y., Xu, Y., and Zhao, G. (2013). Locating South China in rodinia and gondwana: A fragment of greater India lithosphere? *Geology* 41 (8), 903–906. doi:10.1130/g34395.1

Clark, M. K., and Royden, L. H. (2000). Topographic ooze: Building the eastern margin of Tibet by lower crustal flow. *Geology* 28 (8), 703–706. doi:10.1130/0091-7613(2000)28<703:TOBTEM>2.0.CO;2

Deng, Q., Zhang, P., Ran, Y., Yang, X., Min, W., and Chen, L. (2003). Active tectonics and earthquake activities in China. *Earth Sci. Front.* 10 (S1), 66–73. doi:10.3321/j.issn:1005-2321.2003.z1.012

Deng, Y., Zhang, Z., Badal, J., and Fan, W. (2014). 3-D density structure under South China constrained by seismic velocity and gravity data. *Tectonophysics* 627, 159–170. doi:10.1016/j.tecto.2013.07.032

Deng, Y., Li, S., Fan, W., and Liu, J. (2011). Crustal structure beneath South China revealed by deep seismic soundings and its dynamics implications. *Chin. J. Geophys. (in Chinese)* 54 (10), 2560–2574. doi:10.3969/j.issn.0001-5733.2011.10.013

Feng, R., Yan, H., and Zhang, R. (1986). Fast inversion method and corresponding programming for 3D potential field. *Acta Geologica Sinica* 4 (3), 390–402.

Gao, L., Zhang, H., Gao, L., He, C., Xin, H., and Shen, W. (2022). High-resolution vs tomography of South China by joint inversion of body wave and surface wave data. *Tectonophysics* 824, 229228. doi:10.1016/j.tecto.2022.229228

Gong, J., and John Chen, Y. (2014). Evidence of lateral asthenosphere flow beneath the South China craton driven by both Pacific plate subduction and the India-Eurasia continental collision. *Terra Nova* 26 (1), 55–63. doi:10.1111/ter.12069

Guo, L., Gao, R., Shi, L., Huang, Z., and Ma, Y. (2019). Crustal thickness and Poisson's ratios of South China revealed from joint inversion of receiver function and gravity data. *Earth and Planetary Science Letters* 510, 142–152. doi:10.1016/j.epsl.2018.12.039

Guo, Z., Gao, X., Li, T., and Wang, W. (2018). Crustal and uppermost mantle structures of the South China from joint analysis of receiver functions and Rayleigh wave dispersions. *Physics of the Earth and Planetary Interiors* 278, 16–25. doi:10.1016/j.pepi.2018.03.001

Han, S., Zhang, H., Xin, H., Shen, W., and Yao, H. (2021). USTClitho2.0: Updated unified seismic tomography models for continental China lithosphere from joint inversion of body-wave arrival times and surface-wave dispersion data. *Seismological Research Letters* 93 (1), 201–215. doi:10.1785/0220210122

He, C., Dong, S., Santosh, M., and Chen, X. (2013). Seismic evidence for a geosuture between the Yangtze and Cathaysia blocks, South China. *Sci Rep* 3, 2200. doi:10.1038/srep02200

He, C., and Santosh, M. (2016). Crustal evolution and metallogeny in relation to mantle dynamics: A perspective from P-wave tomography of the SouthSouth China block. *Lithos* 263, 3–14. doi:10.1016/j.lithos.2016.06.021

He, R., Shang, X., Yu, C., Zhang, H., and Van der Hilst, R. D. (2014). A unified map of Moho depth and Vp/Vs ratio of continental China by receiver function analysis. *Geophysical Journal International* 199 (3), 1910–1918. doi:10.1093/gji/ggu365

Jin, X.-Y., Zhao, J.-X., Feng, Y.-X., Hofstra, A. H., Deng, X.-D., Zhao, X.-F., et al. (2021). Calcite U-Pb dating unravels the age and hydrothermal history of the giant Shuiyindong Carlin-type gold deposit in the golden triangle, South China. *Economic Geology* 116 (6), 1253–1265. doi:10.5382/econgeo.4870

Kennett, B. L. N., Fichtner, A., Fishwick, S., and Yoshizawa, K. (2013). Australian seismological reference model (AuSREM): Mantle component. *Geophysical Journal International* 192 (2), 871–887. doi:10.1093/gji/ggs065

Laske, G., Masters, G., Ma, Z., and Pasyanos, M. (2013). Update on CRUST1.0 - a 1-degree global model of earth's crust. *Geophys. Res. Abstracts* 15, EGU2013–2658.

Li, S., Zhao, G., Dai, L., Liu, X., Zhou, L., Santosh, M., et al. (2012). Mesozoic basins in eastern China and their bearing on the deconstruction of the North China Craton. *Journal of Asian Earth Sciences* 47, 64–79. doi:10.1016/j.jseaes.2011.06.008

Li, Y., Gao, M., and Wu, Q. (2014). Crustal thickness map of the Chinese mainland from teleseismic receiver functions. *Tectonophysics* 611, 51–60. doi:10.1016/j.tecto.2013.11.019

Li, Z.-X., and Li, X.-H. (2007). formation of the 1300-km-wide intracontinental orogen and postorogenic magmatic province in mesozoic South China: A flat-slab subduction model. *Geology* 35 (2), 179. doi:10.1130/g23193a.1

Lin, X., and Liu, J. (2019). A review of mountain-basin coupling of Jianghan and Dongting basins with their surrounding mountains. *Seismology and Geology* 41 (2), 499–520. doi:10.3969/j.issn.0253-4967.2019.02.015

Liu, S., Yang, Y., Deng, B., Zhong, Y., Wen, L., Sun, W., et al. (2021). Tectonic evolution of the Sichuan Basin, southwest China. *Earth-Science Reviews* 213, 103470. doi:10.1016/j.earscirev.2020.103470

Lu, M., Wu, C., and Jiang, J. (2008). Features and Genesis of gas reservoirs in the Jianghan basin. *Natural Gas Industry* 28 (8), 12–14. 1000-0976(2008)28:8<12:JHPDQZ>2.0.TX;2-M.

Lü, Q. T., Dong, S. W., Shi, D. N., Tang, J. T., Jiang, G. M., Zhang, Y. Q., et al. (2014). Lithosphere architecture and geodynamic model of middle and lower reaches of Yangtze metallogenic belt: A review from SinoProbe. *Acta Petrologica Sinica* 30 (4), 889–906.

LÜ, Q., Yan, J., Shi, D., Dong, S., Tang, J., Wu, M., et al. (2013). Reflection seismic imaging of the Lujiang–Zongyang volcanic basin, Yangtze Metallogenic Belt: An insight into the crustal structure and geodynamics of an ore district. *Tectonophysics* 606, 60–77. doi:10.1016/j.tecto.2013.04.006

Mao, J., Li, Z., and Ye, H. (2014). Mesozoic tectono-magmatic activities in South China: Retrospect and prospect. *Science China Earth Sciences* 57 (12), 2853–2877. doi:10.1007/s11430-014-5006-1

Qiu, L., Kong, R., Yan, D.-P., Mu, H.-X., Sun, W., Sun, S., et al. (2022). Paleo–Pacific plate subduction on the eastern Asian margin: Insights from the Jurassic foreland system of the overriding plate. *GSA Bulletin* 134 (9-10), 2305–2320. doi:10.1130/b36118.1

Qiu, L., Yan, D.-P., Tang, S.-L., Wang, Q., Yang, W.-X., Tang, X., et al. (2016). Mesozoic geology of southwestern China: Indosinian foreland overthrusting and subsequent deformation. *Journal of Asian Earth Sciences* 122, 91–105. doi:10.1016/j.jseaes.2016.03.006

Qiu, L., Yan, D.-P., Yang, W.-X., Wang, J., Tang, X., and Ariser, S. (2017). Early to middle triassic sedimentary records in the Youjiang Basin, South China: Implications for indosinian orogenesis. *Journal of Asian Earth Sciences* 141, 125–139. doi:10.1016/j.jseaes.2016.09.020

Qu, P., Chen, Y., Yu, Y., Ge, Z., Li, Q., and Dong, S. (2020). 3D velocity structure of upper mantle beneath SouthSouth China and its tectonic implications: Evidence from finite frequency seismic tomography. *Chinese Journal of Geophysics (in Chinese)* 63 (8), 2954–2969. doi:10.6038/cjg2020N0183

Royden, L. H., Burchfiel, B. C., and van der Hilst, R. D. (2008). The geological evolution of the Tibetan Plateau. *Science* 321 (5892), 1054–1058. doi:10.1126/science.1155371

Salmon, M., Kennett, B. L. N., and Saygin, E. (2013). Australian seismological reference model (AuSREM): Crustal component. *Geophysical Journal International* 192 (1), 190–206. doi:10.1093/gji/ggs004

Shan, B., Xiong, X., Zhao, K. F., Xie, Z. J., Zheng, Y., and Zhou, L. (2016). Crustal and upper mantle structure of South China from Rayleigh wave tomography. *Geophysical Journal International* 208, 1643–1654. doi:10.1093/gji/ggw477

Shapiro, N. M., Campillo, M., Stehly, L., and Ritzwoller, M. H. (2005). High-resolution surface-wave tomography from ambient seismic noise. *Science* 307 (5715), 1615–1618. doi:10.1126/science.1108339

Shen, W., Ritzwoller, M. H., Kang, D., Kim, Y., Lin, F.-C., Ning, J., et al. (2016). A seismic reference model for the crust and uppermost mantle beneath China from surface wave dispersion. *Geophysical Journal International* 206 (2), 954–979. doi:10.1093/gji/ggw175

Shu, L.-S. (2012). An analysis of principal features of tectonic evolution in South China Block. *Geological Bulletin of China* 31 (7), 1035–1053.

Song, P., Zhang, X., Liu, Y., and Teng, J. (2017). Moho imaging based on receiver function analysis with teleseismic wavefield reconstruction: Application to South China. *Tectonophysics* 718, 118–131. doi:10.1016/j.tecto.2017.05.031

Su, W., Dong, W., Zhang, X., Shen, N., Hu, R., Hofstra, A. H., et al. (2018). "Carlin-Type gold deposits in the dian-qian-gui "golden triangle" of southwest China," in *Diversity in carlin-style gold deposits*. doi:10.5382/rev.20.05

Sun, W., and Kennett, B. L. N. (2016a). Uppermost mantle P wavespeed structure beneath eastern China and its surroundings. *Tectonophysics* 683, 12–26. doi:10.1016/j.tecto.2016.06.011

Sun, W., and Kennett, B. L. N. (2016b). Uppermost mantle structure beneath eastern China and its surroundings from Pn and Sn tomography. *Geophysical Research Letters* 43 (7), 3143–3149. doi:10.1002/2016gl068618

Tao, K., Grand, S. P., and Niu, F. (2018). Seismic structure of the upper mantle beneath eastern a sia from full waveform seismic tomography. *Geochemistry, Geophysics, Geosystems* 19 (8), 2732–2763. doi:10.1029/2018gc007460

Wang, M., Hubbard, J., Plesch, A., Shaw, J. H., and Wang, L. (2016). Three-dimensional seismic velocity structure in the Sichuan basin, China. *Journal of Geophysical Research Solid Earth* 121 (2), 1007–1022. doi:10.1002/2015jb012644

Wang, Y., Fan, W., Guo, F., Peng, T., and Li, C. (2010). Geochemistry of mesozoic mafic rocks adjacent to the chenzhou-linwu fault, South China: Implications for the lithospheric boundary between the Yangtze and Cathaysia blocks. *International Geology Review* 45 (3), 263–286. doi:10.2747/0020-6814.45.3.263

Wang, Y., Fan, W., Zhang, G., and Zhang, Y. (2013). Phanerozoic tectonics of the SouthSouth China block: Key observations and controversies. *Gondwana Research* 23 (4), 1273–1305. doi:10.1016/j.gr.2012.02.019

Wei, Z., Chen, L., Li, Z., Ling, Y., and Li, J. (2016). Regional variation in Moho depth and Poisson's ratio beneath eastern China and its tectonic implications. *Journal of Asian Earth Sciences* 115, 308–320. doi:10.1016/j.jseaes.2015.10.010

Xiao, X., Cheng, S., Wu, J., Wang, W., Sun, L., Wang, X., et al. (2021). Shallow seismic structure beneath the continental China revealed by P-wave polarization, Rayleigh wave ellipticity and receiver function. *Geophysical Journal International* 225 (2), 998–1019. doi:10.1093/gji/ggab022

Yan, D. P., Zhou, Y., Qiu, L., Wells, M. L., Mu, H., and Xu, C.-G. (2018a). The longmenshan tectonic complex and adjacent tectonic units in the eastern margin of the Tibetan plateau: A review. *Journal of Asian Earth Sciences* 164, 33–57. doi:10.1016/j.jseaes.2018.06.017

Yan, D. P., Qiu, L., Wells, M. L., Zhou, M. F., Meng, X., Lu, S., et al. (2018b). Structural and geochronological constraints on the early mesozoic north longmen Shan thrust belt: Foreland fold-thrust propagation of the SW qinling orogenic belt, northeastern Tibetan plateau. *Tectonics* 37 (12), 4595–4624. doi:10.1029/2018tc004986

Yang, W. X., Yan, D. P., Qiu, L., Wells, M. L., Dong, J. M., Gao, T., et al. (2021). Formation and forward propagation of the indosinian foreland fold-thrust belt and nanpanjiang foreland Basin in SW China. *Tectonics* 40 (4). doi:10.1029/2020tc006552

Yao, H., van der Hilst, R. D., and de Hoop, M. V. (2006). Surface-wave array tomography in SE Tibet from ambient seismic noise and two-station analysis - I. Phase velocity maps. *Geophysical Journal International* 166 (2), 732–744. doi:10.1111/j.1365-246X.2006.03028.x

Yao, H., van der Hilst, R. D., and Montagner, J.-P. (2010). Heterogeneity and anisotropy of the lithosphere of SE Tibet from surface wave array tomography. *Journal of Geophysical Research* 115 (B12), B12307. doi:10.1029/2009jb007142

Zhang, G., Guo, A., Wang, Y., Li, S., Dong, Y., Liu, S., et al. (2013). Tectonics of South China continent and its implications. *Science China Earth Sciences* 56 (11), 1804–1828. doi:10.1007/s11430-013-4679-1

Zhang, H., Maceira, M., Roux, P., and Thurber, C. (2014). Joint inversion of body-wave arrival times and surface-wave dispersion for three-dimensional seismic structure around SAFOD. *Pure and Applied Geophysics* 171 (11), 3013–3022. doi:10.1007/s00024-014-0806-y

Zhang, P., Deng, Q., Zhang, G., Ma, J., Gan, W., Min, W., et al. (2003). Active tectonic blocks and strong earthquakes in the continent of China. *Science in China (Series D)* 46, 13–24. doi:10.3321/j.issn:1006-9267.2003.z1.002

Zhang, Y., Chen, L., Ai, Y., Jiang, M., Xu, W., and Shen, Z. (2018). Lithospheric structure of the SouthSouth China block from S-receiver function. *Chinese Journal of Geophysics (in Chinese)* 61 (1), 138–149. doi:10.6038/cjg2018L0226

Zhang, Y., Li, C. a., Wang, Q., Chen, L., Ma, Y., and Kang, C. (2008). Magnetism parameters characteristics of drilling deposits in jianghan plain and indication for forming of the Yangtze River three gorges. *Chinese Science Bulletin* 53 (4), 584–590. doi:10.1007/s11434-008-0111-1

Zhao, L., Allen, R. M., Zheng, T., and Zhu, R. (2012). High-resolution body wave tomography models of the upper mantle beneath eastern China and the adjacent areas. *Geochemistry, Geophysics, Geosystems* 13 (6), n/a. doi:10.1029/2012gc00411

Zheng, Y.-F., Xiao, W.-J., and Zhao, G. (2013). Introduction to tectonics of China. *Gondwana Research* 23 (4), 1189–1206. doi:10.1016/j.gr.2012.10.001

Zhou, J., Xu, F., Wang, T., Cao, A., and Yin, C. (2006). Cenozoic deformation history of the qaidam basin, NW China: Results from cross-section restoration and implications for qinghai–tibet plateau tectonics. *Earth and Planetary Science Letters* 243 (1-2), 195–210. doi:10.1016/j.epsl.2005.11.033

Zhou, L., Xie, J., Shen, W., Zheng, Y., Yang, Y., Shi, H., et al. (2012). The structure of the crust and uppermost mantle beneath South China from ambient noise and earthquake tomography. *Geophysical Journal International* 189 (3), 1565–1583. doi:10.1111/j.1365-246X.2012.05423.x

Zhou, X., Sun, T., Shen, W., Shu, L., and Niu, Y. (2006). Petrogenesis of mesozoic granitoids and volcanic rocks in SouthSouth China: A response to tectonic evolution. *Episodes* 29 (1), 26–33. doi:10.18814/epiiugs/2006/v29i1/004

Zhu, L., and Kanamori, H. (2000). Moho depth variation in southern California from teleseismic receiver functions. *Journal of Geophysical Research Solid Earth* 105 (B2), 2969–2980. doi:10.1029/1999jb900322

Zou, C., Zhu, R., Chen, Z.-Q., Ogg, J. G., Wu, S., Dong, D., et al. (2019). Organic-matter-rich shales of China. *Earth-Science Reviews* 189, 51–78. doi:10.1016/j.earscirev.2018.12.002

frontiers | Frontiers in Earth Science

TYPE Original Research
PUBLISHED 02 February 2023
DOI 10.3389/feart.2023.1064835

OPEN ACCESS

EDITED BY
Chunquan Yu,
Southern University of Science and Technology, China

REVIEWED BY
Yosuke Aoki,
The University of Tokyo, Japan
Mingjie Liu,
Southwest Petroleum University, China
Meng Li,
SINOPEC Petroleum Exploration and Production Research Institute, China

*CORRESPONDENCE
Zhong Li,
✉ lizhong@mail.iggcas.ac.cn

SPECIALTY SECTION
This article was submitted to Structural Geology and Tectonics,
a section of the journal
Frontiers in Earth Science

RECEIVED 08 October 2022
ACCEPTED 18 January 2023
PUBLISHED 02 February 2023

CITATION
Liang S, Li Z, Zhang W and Gao Y (2023),
The characteristics of strike-slip faults and their control on hydrocarbon distribution in deep carbonate reservoirs of the central Sichuan Basin.
Front. Earth Sci. 11:1064835.
doi: 10.3389/feart.2023.1064835

The characteristics of strike-slip faults and their control on hydrocarbon distribution in deep carbonate reservoirs of the central Sichuan Basin

Shangzi Liang[1,2], Zhong Li[1,2]*, Wang Zhang[1] and Yang Gao[3]

[1]State Key Laboratory of Lithospheric Evolution, Institute of Geology and Geophysics, Chinese Academy of Sciences, Beijing, China, [2]College of Earth and Planetary Sciences, University of Chinese Academy of Sciences, Beijing, China, [3]Oil and Gas Resources Strategic Research Center of the Ministry of Natural Resources, Beijing, China

The past decade has witnessed a breakthrough in the gas exploration of deep marine carbonates of the central Sichuan Basin. Deep faults research has also attracted increasing attention, as faulting plays an important role in reservoir control. Previous studies have suggested a developed series of high-angle strike-slip fault systems in the central Sichuan Basin, but correlated exploration activities are limited, as distribution rules and dynamic mechanisms remain unclear. In this study, the spectral decomposition coherence method was used to describe the geometric and kinematic characteristics of these strike-slip faults. Using a comprehensive analysis technique to assess the strike-slip fault tectonic activity history, the formation and evolution processes of strike-slip faults and their control on hydrocarbon distribution were examined. The results showed that the deep strike-slip fault system, mostly distributed in the Dengying Formation, can be divided into four stages, three levels, and three groups of orientation, which controlled the structural framework and shape of the central Sichuan area, as well as the zoning from north to south, and blocking from west to east. The faults showed features of layered deformation and staged evolution in the vertical direction. The segmentation of strike-slip faults strongly controls the quality of fractured vuggy reservoirs. Reservoirs of the hard-linked zone of the strike-slip fault are the most developed, followed by those of soft-linked segments, with translational sections of the strike-slip fault being relatively undeveloped. Strike-slip faults are important hydrocarbon migration paths, and their multistage activities have different controlling effects on hydrocarbon accumulation.

KEYWORDS

deep strike-slip faults, deep carbonate reservoir, hydrocarbon distribution, Central Sichuan Uplift, Sichuan Basin

1 Introduction

Global carbonate formations are rich in hydrocarbon resources, and will likely be the most important area for future oil and gas exploration and development. Dedicated research in China has led to globally recognized discoveries in the marine carbonate formations of the Tarim, Sichuan, and Ordos Basins. Recently, carbonate oil and gas exploration has gradually moved into deep (burial depth >4500 m) and ultra-deep (>6,000 m) carbonates with increasing progress in exploration technology, resulting in new discoveries of various oil and gas resources (Liu et al., 2009; Li et al., 2020; He et al., 2021; Liu et al.,2010). Most marine carbonates in China are formed in the lower part of the superimposed basin, characterized by deep burial and ancient origin, and have undergone complex diagenesis along with multi-phase tectonic movements during its geological history. Faults and concomitant joints accompanying the multi-stage tectonic evolution could both act as passageways for oil, gas, hydrothermal, and volcanic fluids, as well as playing an important role in later reservoir transformations and hydrocarbon accumulation.

Since 2006, with the discovery of the Anyue gas field, the Gao Shi 1 and Moxi 8 wells in the central Sichuan area have been drilled and tested to obtain a high-yielding industrial gas flow from the Sinian-Cambrian dolomite reservoir, confirming the huge exploration potential of deeper layers in central Sichuan. Previous studies in this region have focused on tectonic evolution, sedimentary facies distribution, and hydrocarbon migration and accumulation. Influenced by the traditional concept of the stable central Sichuan block, previous studies on the deep fault system of the central Sichuan Basin remain incomplete. Currently, there is consensus on the development of deep strike-slip faults in the central area of the Sichuan Basin, but there are still controversies regarding the distribution pattern, nature, and formation period of said faults. Yin et al. (2013) suggested that deep fault systems formed during the Caledonian tectonic period, and experienced multiple stages of strike-slip fault activity in the Hercynian, Indosinian, Yanshan, and Himalayan epochs. According to Li (2017), strike-slip faults existed in two phases of development, at the end of the Sinian and the end of the Early Cambrian. However, Ma et al. (2018) suggested that the strike-slip faults in the Central Sichuan Uplift experienced two stages of activity: Early Caledonian and Late Hercynian. Su et al. (2020) proposed that the principal fault activity occurred during Himalayan formation, revealed by shallow high-steep faults cutting through the Jurassic strata in central Sichuan, and the deep strike-slip faults are in the same fault system. In the present study, the geometrical and kinematic characteristics of strike-slip faults are described based on filtering and spectrum decomposition techniques. The relationships between strike-slip faults, reservoir modification, and oil–gas accumulation are also discussed. This study has great scientific significance for finding out the development characteristics of the strike-slip faults and their control on hydrocarbon accumulation in stable parts of cratonic basins, including the Ordovician strike-slip faults in Tazhong and Tabei areas of Tarim Basin, and the Triassic Yanchang Formation strike-slip faults in Ordos Basin.

2 Geological setting

2.1 Regional geology

The Sichuan Basin covers an area of approximately 1.8–3.0 $\times 10^5$ km^2 in western China. It is a superimposed basin that developed on the Neoproterozoic crystalline basement of the Yangtze Craton, limited by the Animaqing-Mianlue suture in the north, the Longmenshan tectonic belt in the west, the Ganzilitang suture in the southwest, and the east Sichuan folded belt in the east (Figure 1A; Wei et al., 2019). According to the oil and gas resource evaluation from the China National Petroleum Corporation, the total geological reserves of natural gas in the Sichuan Basin are 3.818×10^{13} m^3, and the total cumulative conventional gas production is ~5.998×10^{11} m^3, making it the largest natural gas producing area in China. Based on the morphological and geometrical characteristics of the present-day top of the Sinian, the Sichuan Basin is divided into five primary tectonic units: the Central Sichuan Uplift, West Sichuan Depression, North Sichuan Depression, East Sichuan High-Steep Fold Belt, and South Sichuan low-steep fold belt (Figure 1A). The Central Sichuan Uplift is located in the central part of the Sichuan Basin, which is characterized by a giant long-axis anticlinal structure spreading to the northeast (Figure 1C), and the structure was fixed in the Yanshan–Himalayan period.

The study area is located in the Central Sichuan Uplift and covers an area of 24,500 km^2. Structural research shows that it contains the GaoShiti-Moxi paleo-uplift, and the Mianzhu-Changning Cratonic internal rifting to the west. The western boundary of the GaoShiti-Moxi paleo-uplift is the north-south striking synsedimentary normal fault F dipping to the west (Figure 1C). There is no other obvious tectonic boundary to the north, east or south, indicating a transitional relationship. The strike-slip fault system (Yin et al., 2013; Ma et al., 2018; Su et al., 2020; Liang and Li, 2022), a product of multiple tectonic movements on the periphery basin, was developed in the deep part of the study area.

Marine carbonates are mainly developed in the Sinian to Middle Triassic, and the Upper Triassic-Quaternary are terrestrial deposits (Figure 2). Taking into account the lithological differences between Sinian-Permian, the lower Triassic-middle Triassic, and upper Triassic, and the unconformities, the central Sichuan area was divided into a lower structural sequence (Sinian-Permian), a middle structural sequence (Lower Triassic-Middle Triassic), and an upper structural sequence (Upper Triassic and its overlying strata). The strike-slip faults in the study area are mainly distributed in the lower structural sequence. The majority of the exploratory wells in the central Sichuan area did not penetrate the Sinian. Industrial hydrocarbon flows revealed by the drilled wells are related to marine carbonates, including the Sinian, Cambrian, Carboniferous, Qixia-Maokou, Changxing, Feixianguan, Jialingjiang, and Leikoupo formations. The Sinian contains two sets of high-quality reservoirs, namely the second and fourth members of the Dengying Formation. Their lithologies are primarily algal-clotted dolomite, algal-stromatolitic dolomite, algal dolarenites, and oncolite, with a wide horizontal distribution stacked vertically against each other. The reservoir in the fourth member of the Dengying Formation has experienced strong karstification of weathering crust, leading to increased reservoir porosity and forming a fracture-void system due to multiple stages of dissolution and tectonic movement. The stratigraphic contacts between the fourth member of the Dengying Formation and overlying Lower Cambrian Qingzhusi Formation are unconformities. Karstification of the reservoir took place near the unconformity of the Dengying Formation, forming the largest deep marine carbonate gas field in China.

2.2 Tectonic evolution of the region

Basement activity and pre-existing basement fractures in the Sichuan Basin are stress concentration zones (Nemcok et al., 2005;

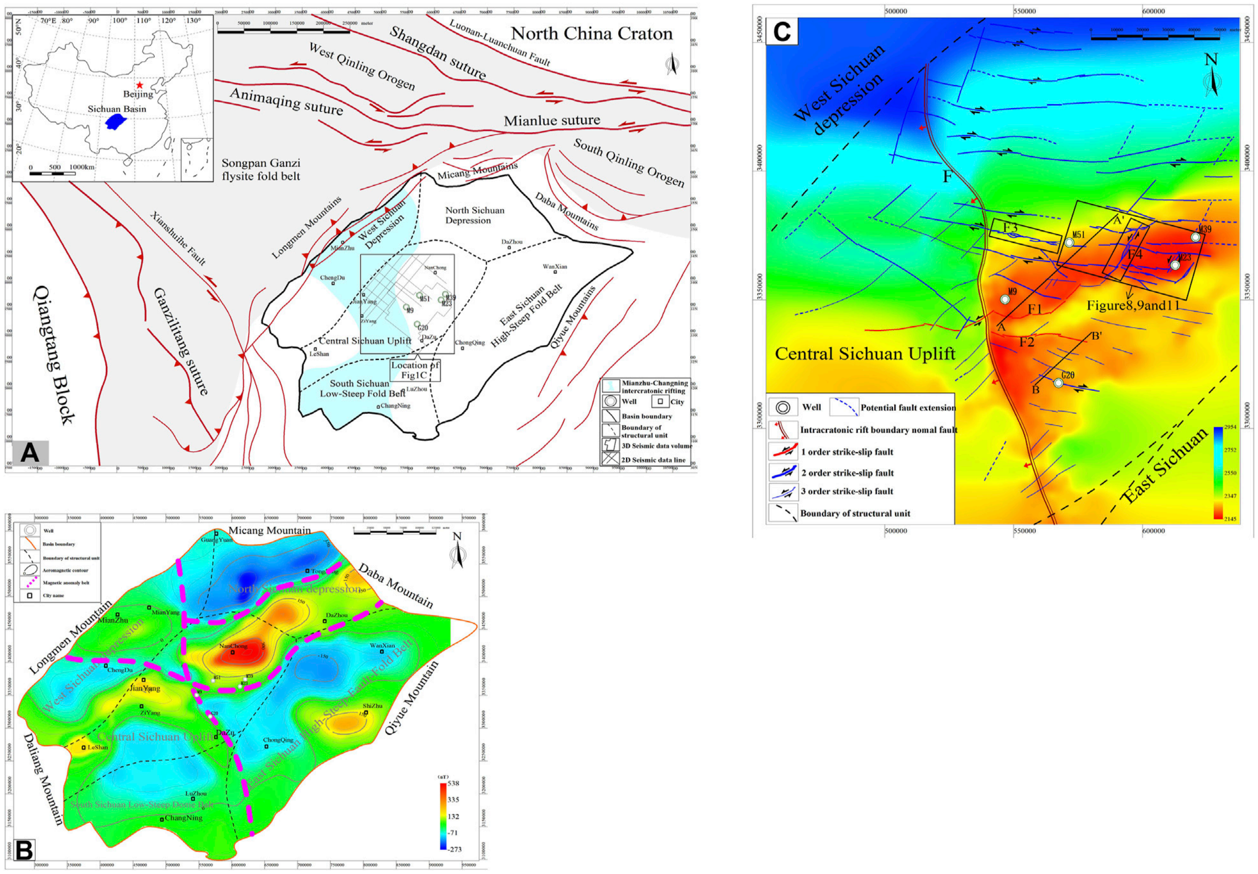

FIGURE 1
(A) Simplified distribution map of the tectonic units of the Sichuan Basin and the surrounding area showing sutures and faults. The map was modified from Wei et al. (2019). **(B)** Isoline of aeromagnetic anomalies in the Sichuan Basin. The map was modified from Gu and Wang. (2014). **(C)** Enlarged view of the central part of Figure 1A showing the distribution of strike-slip faults at the top of Sinian (Z_2dn top) in the Central Sichuan Uplift.

Tong et al., 2010), which not only control the development and evolution of sedimentary cover in the basin, but also are important factors triggering the development of faults within the sedimentary cover. Previous studies have shown that the central area of the Sichuan Basin is to the northeast, near the west–east magnetic anomaly belt (Figure 1B), whereas a negative magnetic anomaly belt developed between the two positive magnetic anomaly belts in the northeast and southwest. A negative magnetic anomaly belt developed between the positive magnetic anomalies in Jianyang and Dazu, and weak positive magnetic anomalies developed to the south of the strong positive magnetic anomalies in Nanchong; therefore, the basement of the central area of the Sichuan Basin is not a unified block, but rather comprises several large tectonic weak zones based on aeromagnetic anomalies (Gu and Wang, 2014). As weak tectonic zones, the basement faults are prone to be active under the regional stress field, which may form the basis of the development of the west-east and north-east strike-slip faults in the central area of the Sichuan Basin.

The fault evolution of the Sichuan Basin is closely related to basin basement activity, and the remote effects are generated by the convergence or divergence of the surrounding plates. From the Late Neoproterozoic to the Cambrian, the paleo-Qinling oceanic crust to the north of the Yangtze Plate was subducted below the Yangtze plate by the influence of the breakup of Rodinia. With an increasing dip in the subduction zone, the dynamic mechanism of the South Qinling Plate changed from a subduction–convergence mechanism to one of retreat–extension (Zhu et al., 2014; 2015; Hu et al., 2015; Xiang et al., 2015; Wang et al., 2017; Zhang et al., 2018), forming an interior rifting of the Yangtze Plate due to the tensional setting (Niu et al., 2003; Stein and Stein, 2013). Simultaneously, the western margin of the Yangtze Plate converged to the northern margin of East Gondwana by subduction (Moghadam et al., 2013; Chen et al., 2018), resulting in a transtensional setting within the Yangtze Plate due to slab pull. Based on the above two factors, the western margin of the Yangtze plate developed the north-south Mianzhu-Changning intracratonic rift (Zhu et al., 2007; Jiang et al., 2011; Liu et al., 2013; Li et al., 2019). The central area of the Sichuan Basin, located at the western margin of the Yangtze plate is influenced by the Mianzhu-Changning intracratonic rift, and includes a series of synsedimentary faults (Figure 3B).

The Yangtze plate drifted slowly northwards in the transtensional setting, reaching a maximum drift rate and rotating anticlockwise during the Ordovician, due to strong tectonic activity (Figure 3A; Feng et al., 2011; Hou et al., 2014). Owing to slab retreat and mantle uplift, the margin and interior of the Yangtze Plate have both extensional and uplift dynamic mechanisms (Figure 3C). Based on the pre-existing tectonic weak zone, the central Sichuan area is subject to oblique transtension near west-east and north-east strike-slip faults.

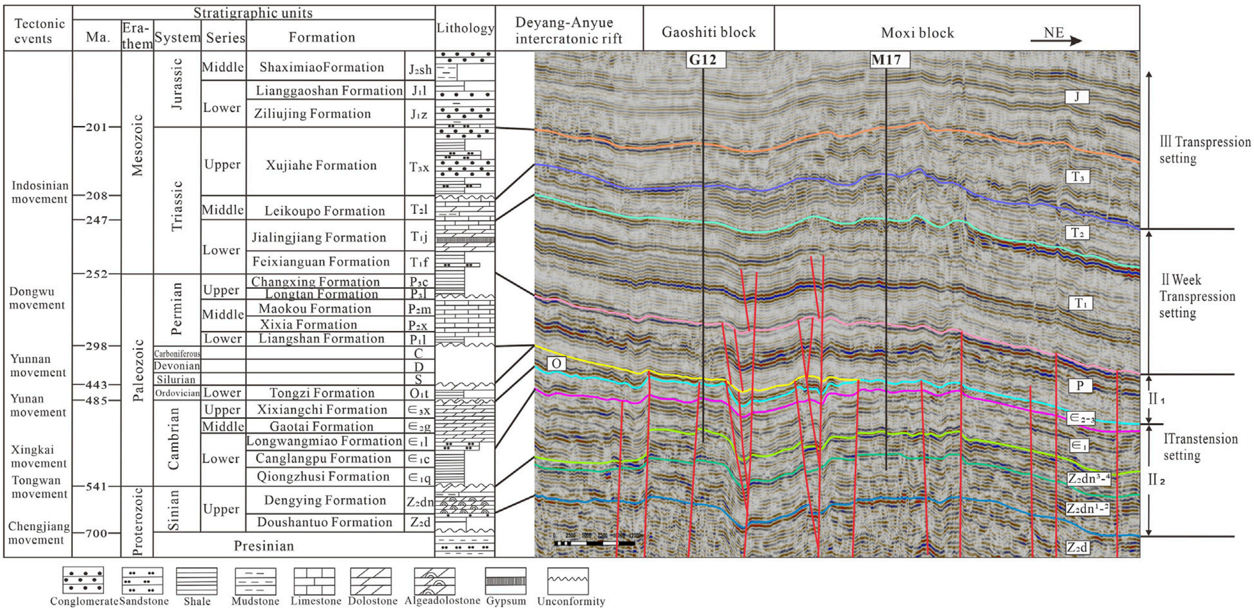

FIGURE 2
Comprehensive tectonostratigraphic column of Central Sichuan Uplift, Sichuan Basin.

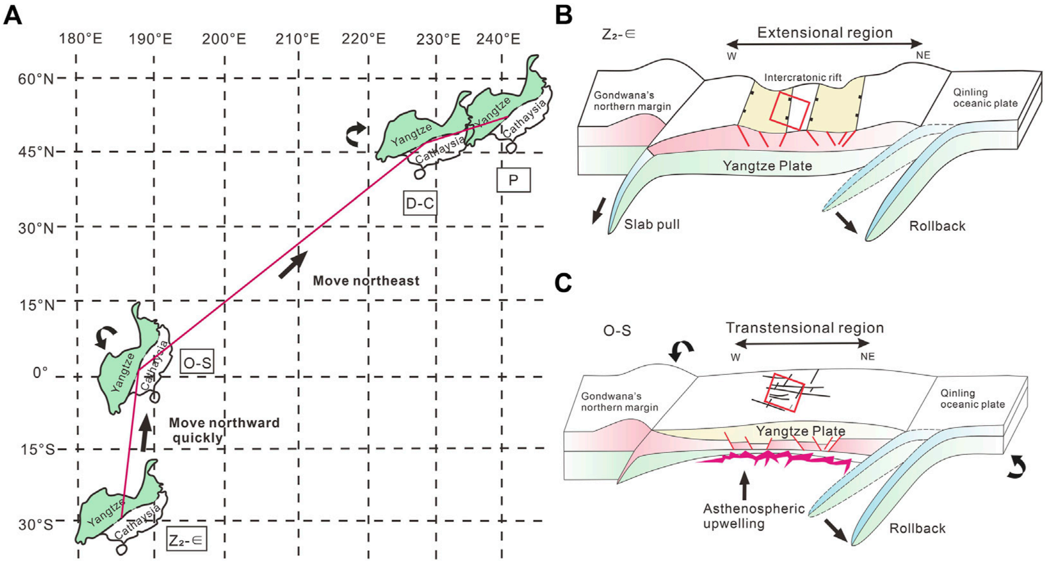

FIGURE 3
(A) The displacement and rotation of the Yangtze Plate from the Sinian to Permian based on palaeomagnetic data by Luo et al. (2004); Feng et al. (2011) and Hou et al. (2014). **(B)** Tectonic evolution of the central area of Sichuan Basin with synsedimentary faults, serving as the east boundary of the Mianzhu-Changning intercratonic rift. **(C)** Tectonic evolution of the central area of Sichuan Basin with strike-slip faults.

Under the influence of the hot doming of mantle uplift, and the opening of the ancient Tethys Ocean, the Sichuan Basin started to rift from the Middle Devonian within the Yangtze Plate, and the Emei basalt eruption reached its maximum in the Late Permian. At the end of the Early Permian, the subduction of the Qiangtang terrain resulted in southwest-northeast transpressional stress, causing north-west rifting of the Yangtze plate, and accelerating the up-arching of the deep "Emei Mantle Column," resulting in rapid eastward movement (Figure 3A; Luo et al., 2004). Here, the coinciding tectonic activity was the strongest. The main faults in the central Sichuan area have undergone inherited development.

Beginning in the Late Triassic, the Upper Yangtze region, including the Sichuan Basin, was mainly influenced by peripheral compressional stress, ending the evolution of the intracratonic rift-style basin, and leading to the development of a series of foreland basins. The strike-slip faults of the central Sichuan area were adjusted and modified in a transpressional regime because of the collocation of the surrounding plates.

3 Data and methods

3.1 Database

Core data, well data, imaging logs, and 2D and 3D seismic data were used in the present study. Core samples were obtained from ten exploratory wells of the fourth member of the Dengying Formation, whereas well data, including conventional electrical log curves and lithological logs, were collected from 80 exploratory wells in the central Sichuan area. The post-stack time migration 3D seismic data covered an area of 8,000 km^2 (Figure 1A), with a cell size of 20 × 20 m, a sampling interval of 2 m, an effective frequency band range of 12–49 Hz, and a deep dominant frequency of 30 Hz (Figure 12). Eleven (11) two-dimensional seismic lines totaled 1,300 km (Figure 1A).

3.2 Methods

As the depth increases, the resolution and dominant frequency of seismic data will decrease. The Strike-slip fault has the characteristics of small displacements and is difficult to identify. To enhance the sensitivity of different scales of faults from seismic data, this study used an improved coherence technique based on spectral decomposition to describe medium-small scale faults. The original full spectral-band post-stack time migration seismic data were decomposed into 15, 25, 35, and 45 Hz frequency-divided data. The results showed that the seismic profiles from the 35 Hz frequency-split data had higher resolution and clearer breakpoints; thus, the 35 Hz frequency band was identified as the dominant frequency for deep fault spectrum decomposition processing in this area. The edge-preserving filtering method (An et al., 2021) can effectively protect discontinuous boundary information, improve the signal-to-noise ratio, and enhance the continuity of seismic events. After spectral decomposition and filtering, the seismic data were used as a carrier to extract coherent attributes, curvature, and ant-tracking data along the target layer to characterize the faults and fractures (Ma et al., 2020).

When a significant acoustic impedance difference exists between the reservoir and non-reservoir rocks, the reservoir can be predicted using conventional post-stack seismic attributes. The porosity of the carbonate rocks of the Sinian Dengying Formation calculated from its logging curve decreased with increasing acoustic impedance, revealing a negative correlation; therefore, the porosity ranges can be used to define the acoustic impedance values of the reservoir and non-reservoir rocks. Compared with the post-stack seismic amplitude method, the principal component analysis (PCA) of the frequency-decomposed amplitude can significantly improve reservoir thickness prediction. The post-stack seismic data were subdivided into low-, mid-, and high-frequency panels, extending the amplitude tuning range, and improving the amplitude-thickness linear relationship (Zeng, 2017). The frequency-decomposed amplitude attributes extracted from the low-, mid-, and high-frequency panels were transformed into principal components, extracting most of the seismic attribute information (Chopra and Marfurt, 2007). The relationship between the frequency-decomposed amplitude principal components and reservoir thickness at the well site was fitted and calculated. In this study, 15 wells were used for the fitting calculation, and the correlation coefficient (R^2) between the predicted and actual values was 0.78. The predicted results for the other five blind-testing wells fell within the predicted trend, indicating that the seismic prediction results were credible.

4 Results

4.1 Strike-slip fault characteristics from seismic data

Based on the refined interpretation of the processed seismic data, three groups of deep strike-slip faults trending north-east, north-west, and west-east were identified in the study area, and the fault structure styles in both section and planar distribution patterns were clarified. At the eastern boundary of the Deyang-Anyue intracratonic rift, the nearly north-south trending synsedimentary fault F separated the western and eastern fields of the study area (Figure 1C). The region in the west primarily shows north-west and north-east trending strike-slip faults, whereas the eastern field is developed with north-east, north-west, and nearly west-east trending strike-slip faults. Fault F1 divided the study area into the northern Moxi structure and the southern Gaoshiti structure. Compared to the Gaoshiti structure, the Moxi structure shows more faults and stronger fault activity. In the Moxi structure and its northern slope, the strike-slip faults exhibit north-west, north-east, and nearly west-east trends that are roughly perpendicular to the central area of the Sichuan Basin. The entire major fault consists of several segmental faults with different dips and throws, and the planar structural characteristics vary along the strike. Together, with the coherent attributes extracted from the seismic data processed by spectrum decomposition and filtering (Figure 4), and fault characterization by the ant-tracking technique, the planar distribution pattern of strike-slip faults exhibits echelons, oblique intersections, and arc shapes. The Gaoshiti structure and its southern slope mainly developed northwest trending faults, and generally, the single north-west trending fault exhibited a short extension distance and vertically ended at the bottom of the Permian. The fine coherence map shows that secondary faults within north-west trending faults are distributed in an en-echelon arrangement, further confirming that the north-west trending faults are dextral strike-slip faults. In general, the number of faults in the southern belt (Gaoshiti structure and its southern slope) is markedly less than in the northern belt (Moxi structure and its northern slope). The structural pattern of the strike-slip fault assemblage is classified into three levels according to the activity periods, extension length, and horizon cut-through by fault (Figure 1C). For example, fault F1 serves as the boundary of the Moxi structure: it penetrates the basement, terminates upward in the Triassic, shows a large fault throw, a long distance of planar

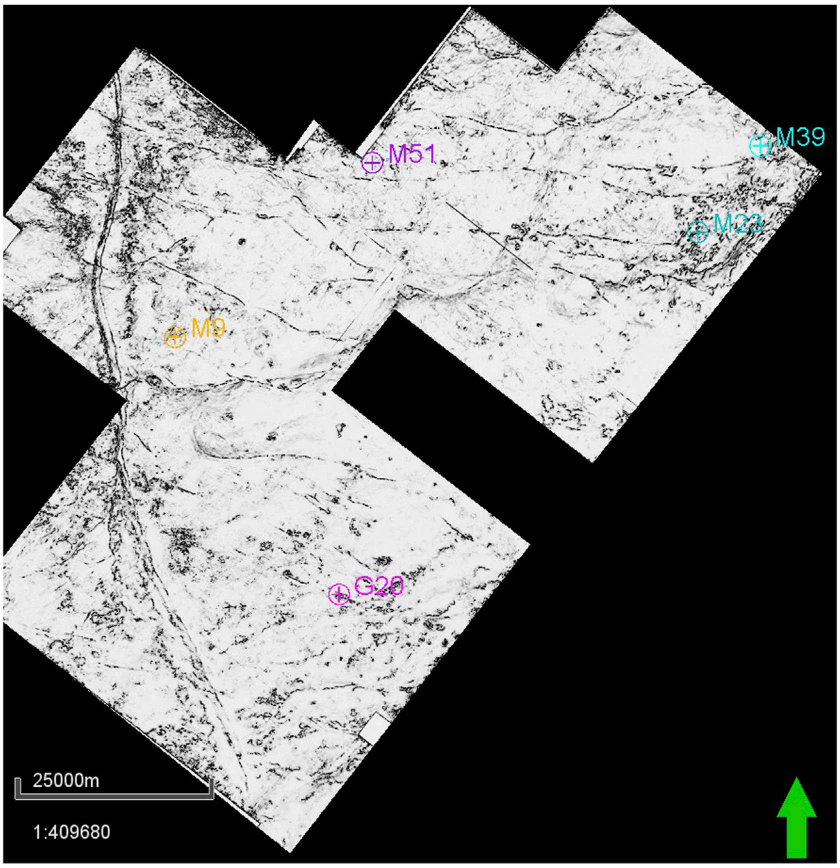

FIGURE 4
Fine coherent map of the top surface of the Dengying Formation in the 3D seismic area. See Figure 1A for location.

extension, a significant horizontal slip displacement, and multi-stage activity. It is therefore considered a first-grade fault. Second-grade faults present a smaller scale than the first-grade, generally extend across the Sinian, and end during the Cambrian, which controls the development of secondary fault blocks.

The seismic sections displayed in Figure 5 represent typical images of deep strike-slip faults mapped to 3D seismic volumes (Figures 1C, 4). These faults are characterized by steeply dipping, half-flower positive flower, and negative flower structures in the study area. Owing to the superposition of multistage structural deformations, multiple flower structures develop in local areas, forming a superposition of these structures on the seismic profile. The steeply dipping fault is characterized by the development of a single main fault without branch faults. Its fracture zone is narrow and steep, with small fault throws, most of which are transtensional. As a special vertical configuration style of the main and branch faults, the flower structure is one of the typical signs for the identification of strike-slip faults. The strike-slip faults in the central Sichuan area show a negative flower structure feature during the Sinian-Ordovician, similarly indicating that the nature of the faults is transtensional. Owing to the lithological differences between the Permian and its underlying strata, the influence of large unconformities formed by the superposition of multiple unconformities between the Permian strata and its underlying strata, as well as the structural deformation of strike-slip faults are characterized by layered deformation in the longitudinal fault systems in the study area. The faults in the Permian are in the form of small grabens or horsts, which partly converge downward in the boundary of the lower flower structure, and partly in the middle main sliding surface, revealing that the fault development position and strength in the Permian are closely related to the lower strike-slip fault and later fault activity. Some of the strike-slip faults terminate upward in the Triassic, and develop a positive flower structure, forming a raised stratigraphic deformation along the faults, or exhibiting the characteristics of small horsts.

4.2 Linkage and segmentation of strike-slip faults

Previous studies have suggested that the growth of large faults does not evolve from an infinite extension of a secondary fault, but rather from a series of secondary splays (segments) that rupture, spread, grow, interact, and link in a similar orientation (Kim and Sanderson, 2005; Aydin and Berryman, 2010). According to the stress and strain in the overlapping and tip zones of the fault, the fault formation process is characterized by segmentation (Choi et al., 2016; Khalil and Mccday, 2016). Segments are isolated from each other at intervals of hundreds of meters, showing disconnection and no interaction, and can be considered as isolated fault segments. Soft-linked segments are generally

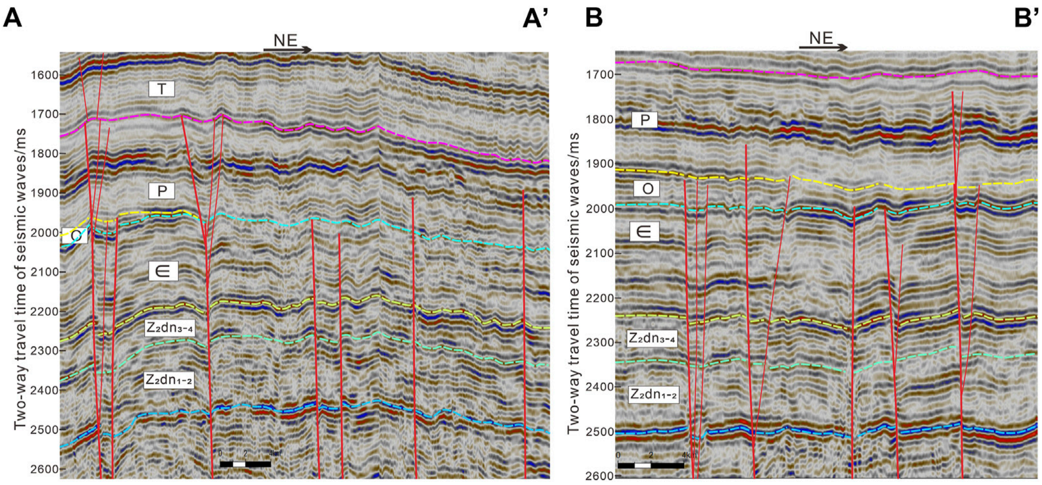

FIGURE 5
Interpreted 3D seismic section **(A)** A′ and **(B)** B′ showing the strike-slip faults. See Figure 1B for locations.

subparallel and overlap in the map view. The overlapping areas of the soft-linked segments lack significant interaction and obvious deformation. The hard-linked zone shows complex fault networks, with a more complicated overlapping area in the seismic profile (Figures 6B, 7B, C), suggesting stronger interaction and deformation in the overlap zones. Based on the coherent attribute map extracted from the seismic data that was processed by spectrum decomposition and filtering, different parts of the strike-slip faults in the study area have different structural and planar configuration styles, showing obvious segmentation. To reveal the segmentation characteristics of the strike-slip faults in the study area, the north-west trending fault F3, and north-east trending fault F4 are described and analyzed in this study.

Strike-slip fault F3 is located in the northern part of the study area (Figure 1C) and extends in a north-west direction. The seismic profile displayed in Figure 6 represents a typical image of F3, which is composed of multiple segments overlapping each other by different fault types to reveal different segmentation along the fault strike. Figure 6B shows the hard-linked zone, and the main fault is characterized by bifurcation and intertwining from the braided structure section in the plane, exhibiting a transtensional fault with a negative flower structure in the profile. The translational section is a linear extension in the plane, and a highly steep erect fault in the profile, showing few secondary splays, with smaller vertical fault displacements and transtensional features (Figure 6C). Figure 6D shows an overlapping zone with right-lateral and right-stepping arrangements in the plane. The interior part of the overlapping zone is in a stretching state, as revealed by the descending block or semi-flower structure in the profile.

The strike-slip fault F4 is a north-east trending fault located in the eastern part of the study area (Figure 1C), and the main fault shows different segmentation characteristics along the fault strike from south to north (Figure 7A). Figure 7B shows the hard-linked zone, segments connecting with each other in the plane, and secondary splays developed in a complicated manner in the overlapping zone, complicating the fault network, while several branch faults converge and merge into a surface in the profile, forming a positive flower structure. Similar to Figures 7B, C, the hard-linked zone segments in which the cut and left laterally displace the north-west trending fault, developed more fractures due to local stress concentration. Figure 7D shows a steep upright fault with linear extension in the plan, while Figure 7E shows the tip of the strike-slip fault, consisting of several branch faults and a main fault, the latter showing a horsetail splay structure in the plane and a semi-flower structure in the profile.

4.3 Analysis of strike-slip fault active periods

Several researchers have conducted extensive studies on the timing of these strike-slip faults (Yin et al., 2013; Li, 2017; Ma et al., 2018; Su et al., 2020); however, their results have been inconclusive. In this study, based on the investigation of the tectonic evolution of the Central Sichuan area, the active periods of strike-slip faults were determined by jointly using the differences in fault structural styles in different strata, and the fault-cut horizon.

The eastern boundary fault of the Mianzhu-Changning rift serves as the most important normal fault that controls the development of the Gaoshiti-Maoxi paleo uplift, and even the Sinian-Early Cambrian tectonic framework of the entire basin. From the Late Sinian to Early Cambrian, during the Tongwan movement and Xingkai taphrogenesis, strike-slip faults were initially formed in the study area. Due to the uplift and erosion of the Leshan Longnüsi Paleo-uplift that developed in the Early Paleozoic, the Ordovician-Carboniferous was missing in the central Sichuan Basin. Drilling revealed that the Ordovician in the study area was overlapped from southeast to northwest, which was retained only in the Gaoshiti structure area, and missing in the Moxi structure area (Figures 2, 5). As first-order faults, the southern boundary fault F1 of the Moxi structure, and the northern boundary fault F2 of the Gaoshiti structure had similar structural characteristics in the seismic profile, showing three periods of activity (Figure 2). The fault cuts through the Sinian

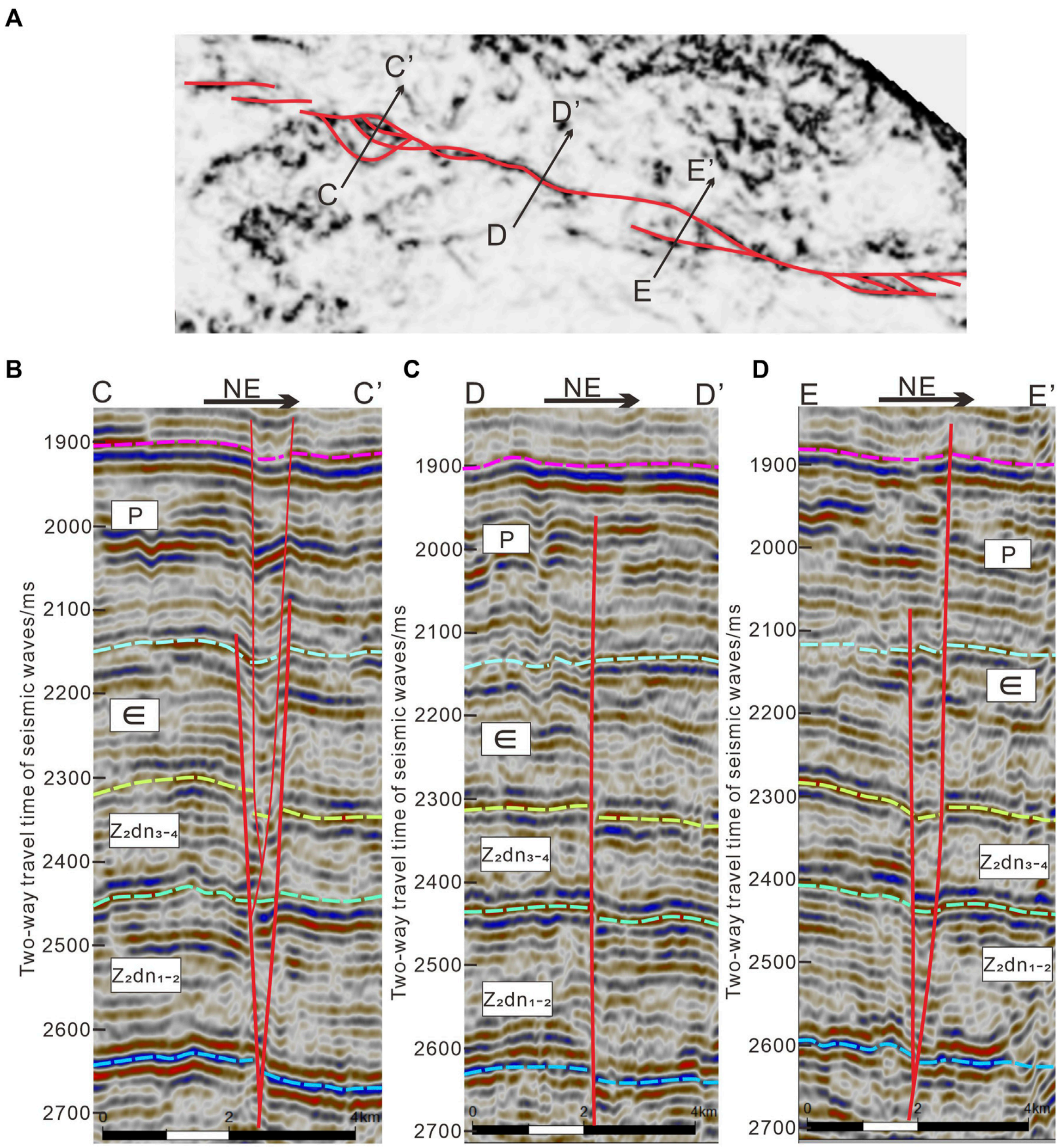

FIGURE 6
(A) The coherence horizon slice of the top of the Sinian, showing segmentation characteristics of the strike-slip fault F3. See Figure 1B for location. **(B–D)** are interpreted seismic sections of the strike-slip fault F3 from west to east. The location of the seismic sections is shown in Figure 6A.

to Lower Triassic strata from bottom to top, while appearing as a highly steep upright strike-slip structure in the Dengying Formation and diverging upward in the Cambrian and Ordovician into a positive flower-like structure. This structure of the Permian was superimposed on the Ordovician, and two flower-like structures were formed. Accordingly, it can be inferred that the strike-slip faults have experienced two fault activities during the deposition of the Ordovician and Permian. The faults formed during the process of fold deformation appear to be perpendicular to the strata (Su et al., 2014a; Su et al., 2014b); therefore, it is speculated that the small horst of the reverse faults perpendicular to the strata in the Triassic may be related to the activities of the Indosinian-Himalayan period subjected to compressional stresses around the basin, which was the third stage of the strike-slip fault.

5 Discussion

5.1 Superimposed, transformed, reservoir beds

Previous studies have considered that, influenced by diagenetic compaction and cementation, the porosity in carbonate rocks gradually decreases with increasing burial depth. It is difficult to form effective reservoirs in ultradeep formations larger than

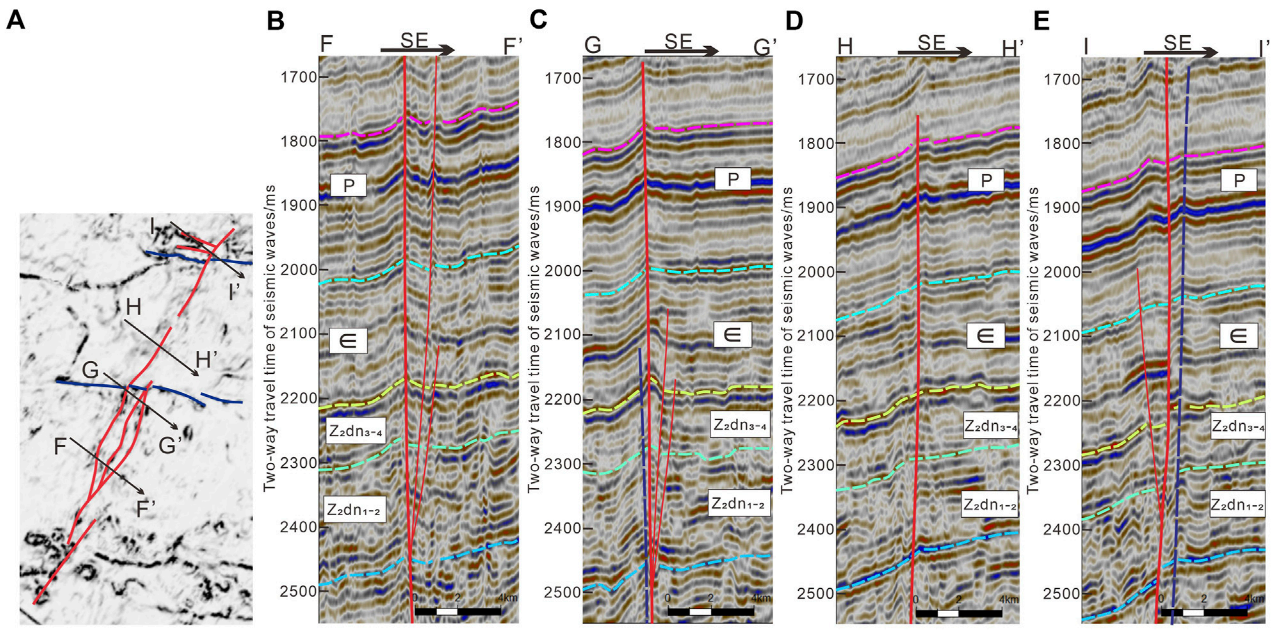

FIGURE 7
(A) The coherence horizon slice of the top of the Sinian, showing segmentation characteristics of the strike-slip fault F4. See Figure 1B for location. **(B–E)** are the interpreted seismic sections of the strike-slip fault F4 from south to north. The location of the seismic sections is shown in Figure 7A.

6,000 m (Schmoker and Hally, 1982; Ehrenberg et al., 2010; Ehrenberg et al., 2009); however, since the 1990s, China has discovered several deep or ultra-deep large-scale carbonate reservoirs in the Tarim and Sichuan Basins, which have often later undergone significant transformations. Therefore, fault activity and the associated fracture development are particularly important for the formation of high-quality ancient carbonate reservoirs. For example, the fracture-void karst reservoir is developed in the Sinian Dengying Formation of the Sichuan Central Region, and multi-phase fault activities have a strong impact on the late modification of the reservoir, promoting the formation of fractures and increasing the storage space of the reservoir.

Prior research has shown that fractures are composed of both fault cores and fault damage zones (Caine et al., 1996; Aydin, 2000; Kim et al., 2004; Childs et al., 2009; Faulkner et al., 2010; Matonti et al., 2012; Choi et al., 2016; Ostermeijer et al., 2022; Kim et al., 2000). Specifically, fault-damage zones develop branching faults and fractures, while their corresponding degree of development and width are influenced by various factors, such as fault size, stratigraphic lithology, and diagenesis (Tondi, 2007; Agosta et al., 2012; Rotevatn and Bastesen, 2012; Michie, 2015; De Graaf et al., 2017). Typically, the greater the distance from the fault core, the less is the fracture development (Mitchell and Faulkner, 2009; Faulkner et al., 2010; Torabi and Berg, 2011; Johri et al., 2014a). For deep carbonate formations, fault-associated damage zones can effectively improve reservoir performance. Indeed, previous researchers have studied fracture frequency and fault damage zone boundaries at three scales of fracture systems—macro-, medium-, and micro-fractures—based on logs, cores, and thin sections (Wu et al., 2019; Shi et al., 2022). Numerical simulation models with reservoir fracture parameters have been used to calculate the influence range of major faults that can reach 600–2000 m, and the fracture within the influenced zone is characterized by high density (Xu et al., 2019). The prediction map of fractures based on 3D seismic attributes in the eastern part of the study area reveals the relationship between the distribution characteristics of the fault damage zone and major faults (Figures 8, 9). There are well-developed fractures closer to the major faults owing to stronger tectonic deformation. Many strike-slip faults are composed of multiple segments overlapping each other by different fault types to show different segmentation along the fault strike. The degree of fracture development in different segment types varies according to differential structural style and stress state. On the plot in Figure 10, fault F4 can be divided into five segments horizontally, with the highest throw values, and highest seismic attribute values, reflecting that fractures occur in the hard-linked zone. This suggests that the higher fault throws absorb far more deformation and strain, promoting development of micro-cracks and fractures which are crucial for reservoir transformation. The southern segment I of fault F4 includes soft-linked segments with various displacements. Because they offset the north-west trending faults, the intersection shows significant displacement and greater fracture development. Segments II and IV are linear extensions of the fault plane with less displacement. Secondary splays and fractures in the translational section of the strike-slip fault are less developed, as the structural deformation is mainly concentrated in the main faults, indicating that the surrounding fault damage zones and fractures are limited in development. Segment III shows a braided structure of intersecting transpressional and transtensional faults, maintaining high fracture density, which are the most developed fault damage zones. The northern segment V has mainly

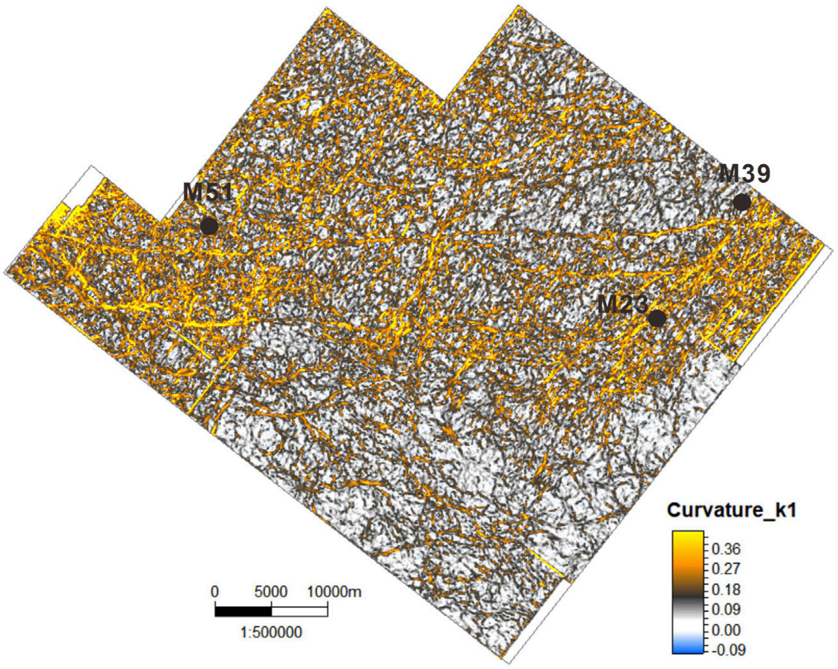

FIGURE 8
Prediction map of fractures of the top of the Sinian based on 3D seismic attributes. See Figure 1B for location.

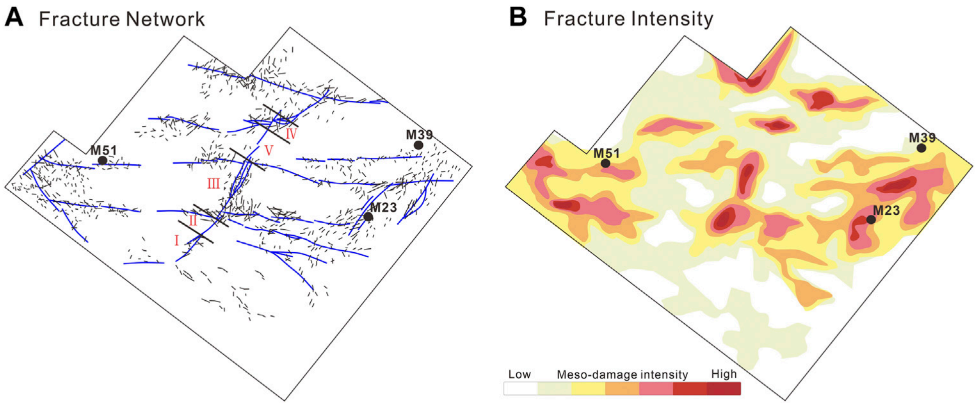

FIGURE 9
Conceptual model showing the damage zone fault and fracture network **(A)** and fracture intensity **(B)**. See Figure 1C for location.

transpressional faults which offset the north-west trending faults, displaying great displacement. The intersection between north-east and north-west faults in the study area shows strong fault activity, producing a wider range of influence, and developing more branch faults and fractures. Faults and their associated fractures serve as high-speed channels for fluid migration, increasing the permeability of reservoirs and enhancing the fluid flow. During the Late Neoproterozoic to Early Cambrian, the faults were active and broke through the surface, providing channels for atmospheric fresh water to flow downward along the fractures. Simultaneously, atmospheric fresh water caused dissolution of the rocks surrounding the fractures and cracks, forming a 3D fracture-void network. The secondary pores in the reservoir are often too scattered to form an effective interconnection; therefore, unfilled or partially filled fractures can create an interconnected network for isolated pores and form a fracture-pore system at a certain scale, thereby increasing reservoir permeability (Figure 11). The reservoir exhibits low frequency, medium amplitude, and medium continuity reflection characteristics on the seismic profile (Figure 12). The 3D seismic attributes were used to describe the planar distribution of the carbonate reservoir of the Fourth Member Dengying Formation in the eastern part of the study area (Figure 13). It was found that the

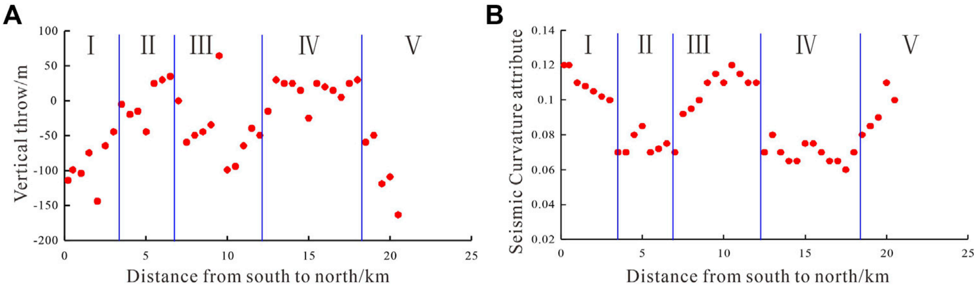

FIGURE 10
(A) The fault segmentation and variations of fault throw along strike-slip fault F4. **(B)** Distance versus Seismic attribute reflecting fractures (see the fault location in Figures 1C, 9A).

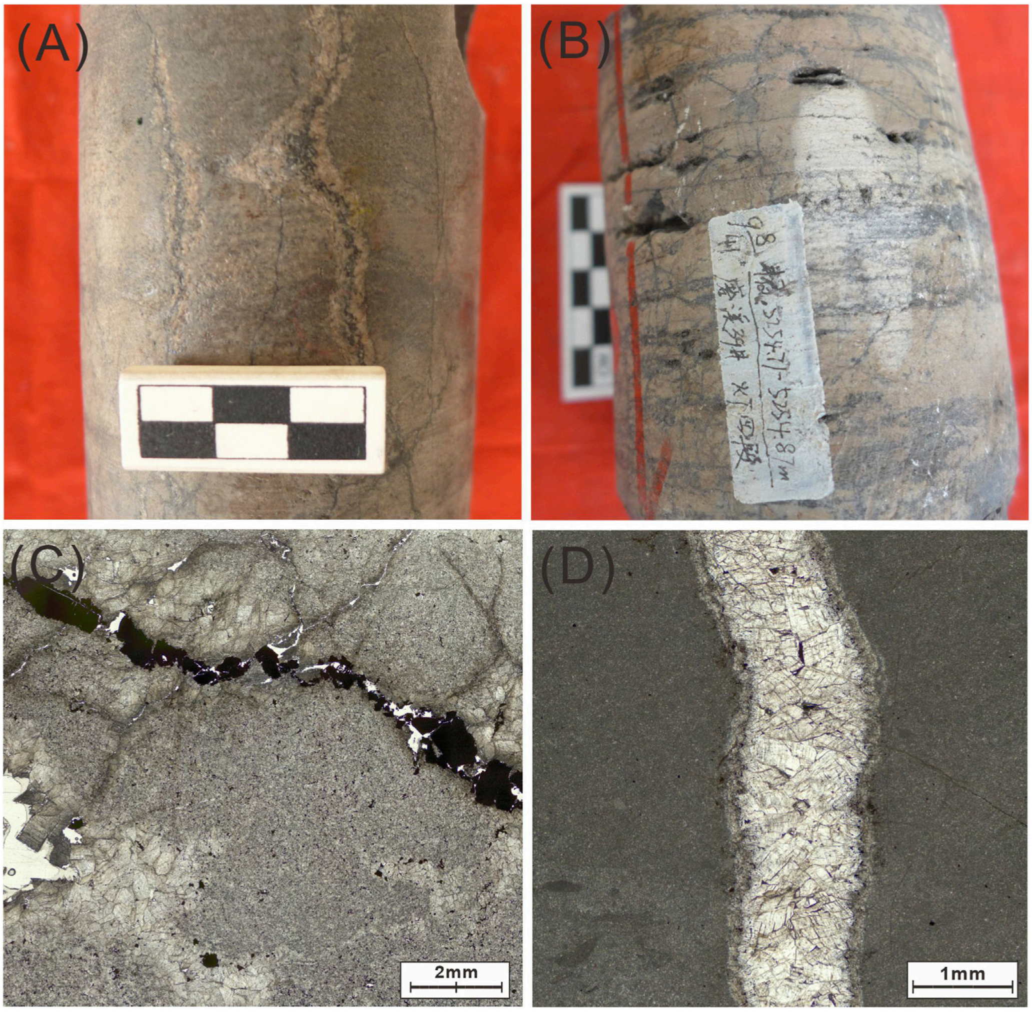

FIGURE 11
Typical photos showing the fractured rocks from the cores **(A, B)** and thin sections **(C, D)** in the Dengying reservoir in Central Sichuan Basin. **(A)** High angle dissolved fracture in clotted dolomite, filled with the saddle dolomite and bitumen, Well M51, 5358.83 m; **(B)** Reticulated structural fractures with dissolution cavities developed. Well M39, 5254.71 m; **(C)** Partially filled structural fractures connecting intergranular pores, Well G20, 5184.4 m, plane polarized light; **(D)** Saddle dolomite vein filling along the fractures, Well M105, 5329.5 m, plane polarized light.

reservoir is mainly distributed along the strike-slip fault. The closer the main fault was, the more fractures developed, providing more channels for fluid migration. Differential segmentation of the strike-slip fault is associated with varying reservoir quality. The hard-linked zone, such as the braided structure section, formed by bifurcation and interweaving of branch faults where fractures are developed, is

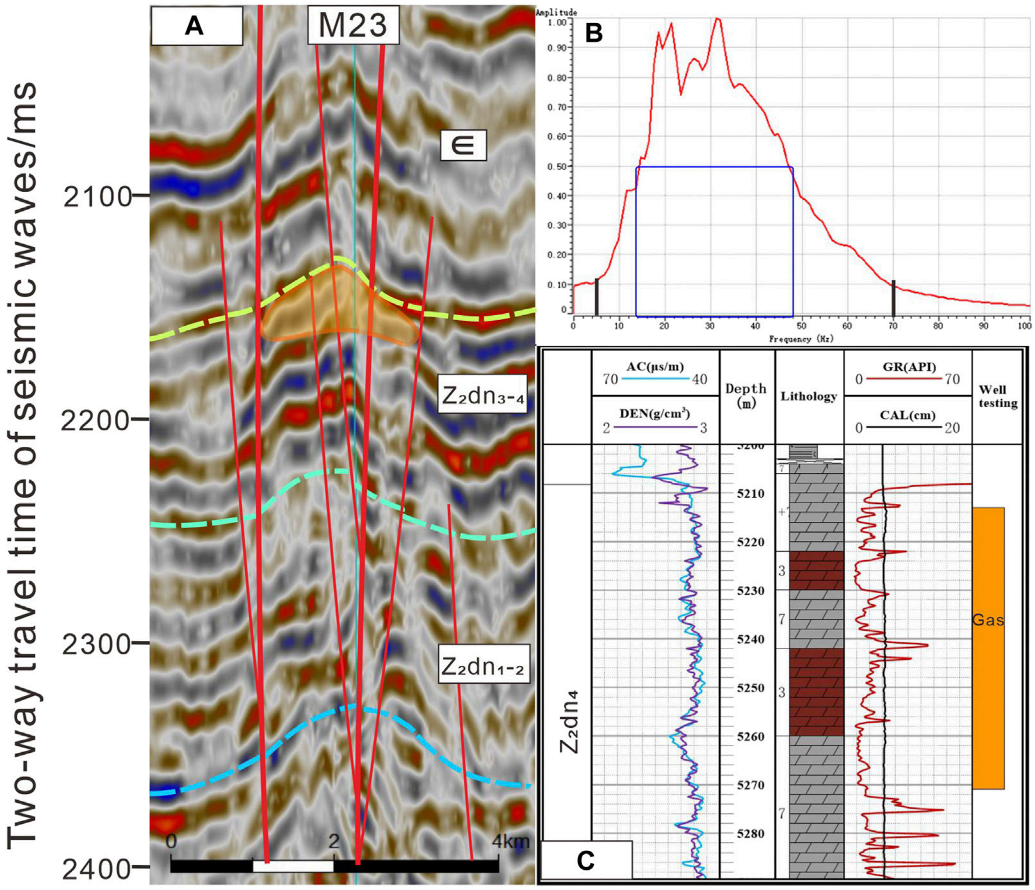

FIGURE 12
(A) Reservoir response characteristics of seismic profile crossing the key well. The range of the orange circle corresponds to **(C)**. **(B)**Seismic bandwidth map. **(C)**The drill columnar section of Well M23 in Dengying Formation.

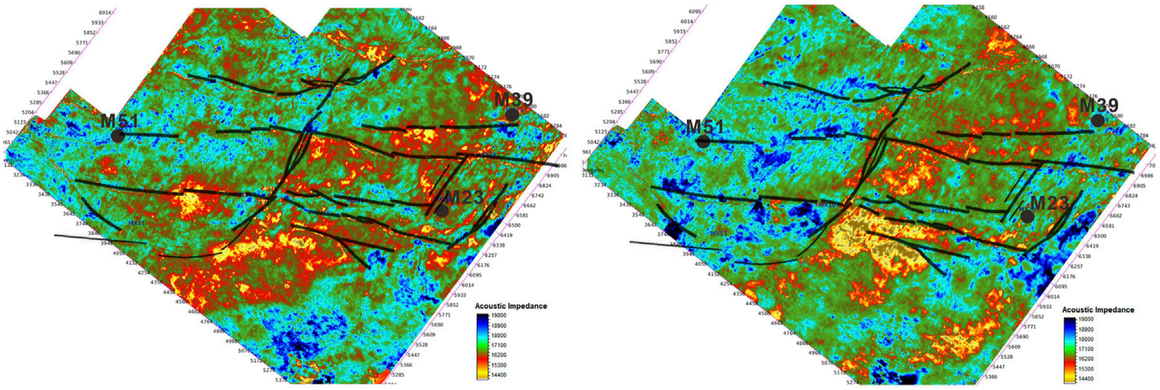

FIGURE 13
The fracture and fracture-void reservoirs are represented by the colors of P-impedance attribute from red to yellow. The P-impedance attribute of 3D seismic data was processed with the Jason Poststack module between the 10 ms below the top of Dengying Formation (left) and 10–30 ms below the top of Dengying Formation (right).

conducive to the development of high-quality reservoirs. Such development is attributed to faults and fractures serving as downwelling channels for shallow groundwater, and upwelling channels for deep hydrothermal fluids, which increases the contact area between the fluids and the original rock, thus creating favorable conditions for the development of karst reservoirs. The soft-linked segments include few secondary splays, forming moderate quality reservoirs. Compared to other sections, few fractures developed in the translational sections of the strike-slip fault, suggesting poor reservoir quality.

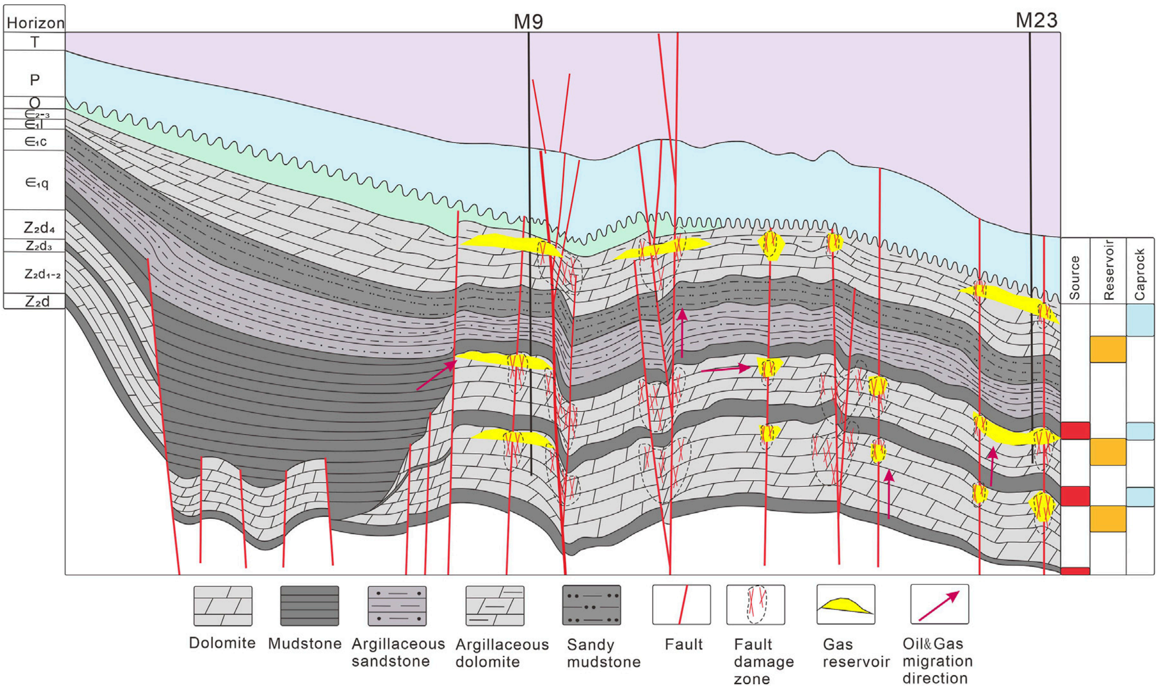

FIGURE 14
The transport and accumulation model of oil and gas in central Sichuan Basin. The oil/gas migrated from the deeper hydrocarbon sources into the multiple reservoirs. Early dense oil accumulation and late condensate gas accumulation developed due to migration along the strike-slip faults.

5.2 Hydrocarbon migration pathway

The Sichuan Basin has deposited huge amounts of sedimentary rock since the Sinian and has developed several hydrocarbon source rocks and source-reservoir-cap rock assemblages. Research has shown that the three main hydrocarbon source rocks are the Cambrian Qiongzhusi Formation mudstone, Silurian Longmaxi Formation mudstone, and coal-bearing mudstone of the Xujiahe Formation, as well as others, such as the mudstone of the Shisantuo Formation, Lower Permian mudstone, Upper Permian mudstone, and Lower Jurassic mudstone. There are many hydrocarbon-bearing formations, covering almost all formations from the Sinian to the Jurassic. The Sinian source-reservoir-cap rock assemblages are the first, and the oldest marine formation source-reservoir-cap rock combinations in the central Sichuan area, with mudstone of the Doushantuo Formation, the Third member Dengying Formation, and the Cambrian Qiongzhusi Formation mudstone comprising the main hydrocarbon source rocks, algal dolomite of the Second member and Fourth member Dengying Formations serving as the reservoirs, and the Lower Cambrian mudstone as the main cap rock, containing three types of combinations: Upper-Source and Lower-Reservoir, Upper-Source and Lateral- Reservoir, and Lower-Source and Upper-Reservoir (Figure 14).

Based on the seismic interpretation results of the whole study area, and oil and gas shows from the exploration, the development of high-quality dolomite reservoirs and fault activity in the central area of the Sichuan Basin determines hydrocarbon migration and accumulation (Figure 14), whereas the development of faults and prolonged active periods are conducive to communicating with the effective source rock, serving as favorable conditions for the production of oil and gas pathways. When source rocks start to produce hydrocarbons, the reservoir of the Sinian Dengying Formation already has storage space, which provides favorable conditions for the formation of paleo-oil reservoirs and crude oil cracking *in situ*. Many studies have been conducted on the oil and gas charging time, as well as the hydrocarbon accumulation period of the Sinian Dengying Formation in the central area of the Sichuan Basin (Liu et al., 2009; Luo et al., 2015; Wang et al., 2016; Shen et al., 2021), and concluded that there were three periods of hydrocarbon accumulation: The first peak period of oil accumulation occurred at the end of the Silurian, but the hydrocarbon supply from source rocks was a continuous process that could have advanced to the early-middle Ordovician at the earliest. This may be the main reason why various scholars considered oil accumulation to have occurred during the Ordovician-Silurian, when a series of strike-slip faults formed with inherited activities in the Late Sinian-Early Cambrian across the central area of the Sichuan Basin. The Wuyi-Yunkai orogeny in the whole Yangtze region occurred due to regional extensional stress, thereby developing secondary splays, and fault damage zones around the main strike-slip faults. Simultaneously, the uplifting stratum suffered significant weathering and denudation, resulting in a wide range of reservoirs being created, with large-scale oil charging. In the late Permian-Early Triassic, the uplift and denudation of formations caused by the rise of the Emeishan mantle plume and the massive eruption of basalts reactivated the faults. The hydrothermal event related to the eruption of the Emeishan basalts caused a large amount of thermal fluid upwelling along these faults and fractures, leading to dissolved carbonate reservoirs, and improved reservoir performance. With the maturation and charging of hydrocarbons, peak oil accumulation occurred during the second stage. During the Yanshan–Xishan epoch, the crude oil in the Sinian Dengying Formation cracked into gas at great depths and high temperatures, creating the peak period of natural gas accumulation.

6 Conclusion

(1) Based on 2D and 3D seismic data in the central area of the Sichuan Basin, systematic interpretation of the deep fracture system suggests that steeply dipping faults and flower-like structures were mainly developed in the study area. The three groups of north-west, north-east, and nearly west-east striking faults in the study area exhibit differences in the structural patterns of the southern and northern regions. The planar combination styles of strike-slip faults consist of an en-echelon arrangement, oblique intersection, and arc shape. The slip faults are classified into three levels according to their activity duration, structural deformation degree, and extension length. Owing to the differences between the upper and lower structural styles of the fault system, location of the fault cut-through layer, and deformation characteristics of the strata, the active stage of strike-slip faults is considered to have occurred in four phases: Late Archean-Early Cambrian, Ordovician, Permian, and Triassic. Generally, a strike-slip fault consists of several segments with different dipping and fault throws, leading to planar structural characteristics that change along the fault strike. The interior of the strike-slip fault is composed of linear translational, overlapping, and braided segments. The translational section is a linear extension of the fault plane with a steep upright fault profile. The overlapping section includes an extensional or contractional segment controlled by its rotational direction relative to the step, whereas the braided section contains interlocking transtensional or transpressional structural segments.

(2) The control of strike-slip faults on fracture development in the study area is significant, including the control of main faults on secondary splays and fracture development. The degree of intensity and period of fault activity impacts the development of the surrounding fracture zones, with a greater distance from the fault resulting in lower density and intensity of fracture. Segmentation of strike-slip faults governs the distribution of karst reservoirs in the Sinian Dengying Formation. The most developed reservoirs are in the overlapping and braided sections, and relatively undeveloped reservoirs are in the linear translational sections.

(3) Deep strike-slip faults have great significance for oil and gas exploration in the central Sichuan Basin. Small fault and fracture systems induced by major fault activities can form interconnections for isolated pores, effectively improving reservoir properties, and increasing oil and gas production. Deep fault activities cause tectonic deformation of the surrounding rock, which can control the formation of traps. These serve as favorable channels for oil and gas migration, effectively communicating with hydrocarbon source rocks and reservoirs, and resulting in the formation of oil and gas reservoirs.

Data availability statement

The original contributions presented in the study are included in the article/supplementary material, further inquiries can be directed to the corresponding author.

Ethics statement

Ethical review and approval was not required for the study on human participants in accordance with the local legislation and institutional requirements. Written informed consent for participation was not required for this study in accordance with the national legislation and the institutional requirements.

Author contributions

SL collected and processed the data, plotted the figures used in this study, and wrote the manuscript. ZL guided this work. WZ provided helpful discussions and suggestions. YG offered constructive comments. All authors contributed to the article and approved the submitted version.

Funding

This research was funded by the Strategic Priority Research Program of the Chinese Academy of Sciences (Grant No. XDA14010201).

Conflict of interest

The authors declare that the research was conducted in the absence of any commercial or financial relationships that could be construed as a potential conflict of interest.

Publisher's note

References

Agosta, F., Ruano, P., Rustichelli, A., Tondi, E., Galindo-Zaldívar, J., and Sanz de Galdeano, C. (2012). Inner structure and deformation mechanisms of normal faults in conglomerates and carbonate grainstones (Granada Basin, Betic Cordillera, Spain): Inferences on fault permeability. *J. Struct. Geol.* 45, 4–20551. doi:10.1016/j.jsg.2012.04.003

An, S., Chen, Y., Luo, M., and Yan, S. (2021). Three dimensional fault enhancement technique based on multidirectional recognition. *Acta Sci. Nat. Univ. Pekin.* 57, 653–659.

Aydin, A. (2000). Fractures, faults and hydrocarbon entrapment, migration and flow. *Mar. Pet. Geol.* 17, 797–814. doi:10.1016/S0264-8172(00)00020-9

Aydin, A., and Berryman, J. G. (2010). Analysis of the growth of strike-slip faults using effective medium theory. *J. Struct. Geol.* 32, 1629–1642. doi:10.1016/j.jsg.2009.11.007

Caine, J. S., Evans, J. P., and Forster, C. B. (1996). Fault zone architecture and permeability structure. *Geol* 24, 1025–1028. doi:10.1130/0091-7613(1996)024<1025:fzaaps>2.3.co;2

Chen, Q., Sun, M., Long, X., Zhao, G., Wang, J., Yu, Y., et al. (2018). Provenance study for the Paleozoic sedimentary rocks from the west Yangtze Block: Constraint on possible link of South China to the Gondwana supercontinent reconstruction. *Precambrian Res.* 309, 271–289. doi:10.1016/j.precamres.2017.01.022

Childs, C., Manzocchi, T., Walsh, J. J., Bonson, C. G., Nicol, A., and Schöpfer, M. P. J. (2009). A geometric model of fault zone and fault rock thickness variations. *J. Struct. Geol.* 31, 117–127. doi:10.1016/j.jsg.2008.08.009

Choi, J. H., Edwards, P., Ko, K., and Kim, Y. S. (2016). Definition and classification of fault damage zones: A review and a new methodological approach. *Earth-Science Rev.* 152, 70–87. doi:10.1016/j.earscirev.2015.11.006

Chopra, S., and Marfurt, K. J. (2007). *Seismic attributes for prospect identification and reservoir characterization[R]*. Tulsa: Society of Exploration Geophysicists.

Ehrenberg, S. N., Nadeau, P. H., and Steen, Ø. (2009). Petroleum reservoir porosity versus depth: Influence of geological age. *Bulletin* 93, 1281–1296. doi:10.1306/06120908163

Ehrenberg, J. H. (2010). *Oil and gas exploration of cambrian-ordovician carbonate in Tarim Basin*. Beijing: Petroleum Industry Press.

Faulkner, D. R., Jackson, C. A. L., Lunn, R. J., Schlische, R. W., Shipton, Z. K., Wibberley, C. A. J., et al. (2010). A review of recent developments concerning the structure, mechanics and fluid flow properties of fault zones. *J. Struct. Geol.* 32, 1557–1575. doi:10.1016/j.jsg.2010.06.009

Feng, Y., Wen, Z., Zheng, Q., Mao, X., Hou, F., Qi, J., et al. (2011). A review of progress in paleocontinent reconstruction research in China. *Mar. Geol. Front*. Available at: http://www.jhyqy.com.cn/en/article/id/f7e86fbd-0297-47a3-96ce-3f72bfd32fb8 27, 41–49.

Gu, Z., and Wang, Z. (2014). The discovery of neoproterozoic extensional structures and its significance for gas exploration in the central sichuan block, Sichuan Basin, south China. *Sci. China Earth Sci.* 57, 2758–2768. doi:10.1007/s11430-014-4961-x

He, Z. L., Ma, Y. S., Zhu, D. Y., Duan, T. Z., Geng, J. H., Zhang, J. T., et al. (2021). Theoretical and technological progress and research direction of deep and ultra-deep carbonate reservoirs. *Oil Gas. Geol.* 42, 533–546. doi:10.11743/ogg20210301

Hou, F., Zhang, X., Feng, Y., Sun, J., Wen, Z., Gao, Z., et al. (2014). Paleogeographic reconstruction and tectonic evolution of major blocks in China since Paleozoic. *Mar. Geol. Quart. Geol.* 34, 9–26. doi:10.3724/SP.J.1140.2014.06009

Hu, F., Liu, S., Santosh, M., Deng, Z., Wang, W., Zhang, W., et al. (2015). Chronology and tectonic implications of neoproterozoic blocks in the South qinling orogenic belt, central China. *Gondwana Res.* 30, 24–47. doi:10.1016/j.gr.2015.01.006

Jiang, G. Q., Shi, X. Y., Zhang, S. H., Wang, Y., and Xiao, S. (2011). Stratigraphy and paleogeography of the ediacaran Doushantuo Formation (ca. 635-551Ma) in south China. *Gondwana Res.* 19, 831–849. doi:10.1016/j.gr.2011.01.006

Johri, M., Dunham, E. M., Zoback, M. D., and Fang, Z. (2014a). Predicting fault damage zones by modeling dynamic rupture propagation and comparison with field observations. *J. Geophys. Res. Solid Earth* 119, 1251–1272. doi:10.1002/2013JB010335

Khalil, S. M., and Mcclay, K. R. (2016). 3D geometry and kinematic evolution of extensional fault-related folds, NW Red Sea, Egypt. *Geol. Soc. Lond. Spec. Publ.* 439, 11. doi:10.1144/sp439.11

Kim, Y. S., Andrews, J. R., and Sanderson, D. J. (2000). Damage zones around strike-slip fault systems and strike-slip fault evolution, Crackington Haven, Southwest England. *Geosci. J.* 4, 53–72. doi:10.1007/bf02910127

Kim, Y. S., Peacock, D. C. P., and Sanderson, D. J. (2004). Fault damage zones. *J. Struct. Geol.* 26, 503–517. doi:10.1016/j.jsg.2003.08.002

Kim, Y. S., and Sanderson, D. J. (2005). The relationship between displacement and length of faults: A review. *Earth-Science Rev.* 68, 317–334. doi:10.1016/j.earscirev.2004.06.003

Li, S. (2017). Study on fault characteristics in moxi-gaoshiti area, Sichuan Basin. [Master's thesis]. East China: CUPB.

Li, Y., Xue, Z., Cheng, Z., and Jiang, H. (2020). Progress and development directions of deep oil and gas exploration and development in China. *China Pet. explor.* 25, 46–57. doi:10.3969/j.issn.1672-7703.2020.01.005

Li, Z., Ran, B., Xiao, B., and Song, J. (2019). Sinian-Early Cambrian uplift-depression pattern in the northern margin of Sichuan Basin and its significance for oil and gas exploration. *Earth Sci. Front.* 26, 59–85.

Liang, S., and Li, Z. (2022). Development characteristics and formation mechanism of deep strike-slip faults in Central Sichuan basin based on seismic data interpretation. *Fresenius Environ. Bull*. Available at: https://www.prt-parlar.de/download_feb_2022/ 31 (06), 6230–6240.

Liu, S., Ma, Y., Cai, X., Xu, G., Wang, G., Yong, Z., et al. (2009). Characteristic and accumulation process of the natural gas from sinian to lower paleozoic in Sichuan Basin, China. *J. Chengdu Univ. Technol. Sci. Technol. Ed.)* 36, 345–354.

Liu, W., Meng, Q., Zhang, G., and Zhang, L. (2010). Geologic characteristics of oil and gas reservoir in old Lower Paleozoic and Sinian carbonate rocks. *Mar. Orig. Pet. Geol.* 15, 15–20.

Liu, S., Sun, W., Luo, Z., and Song, J. (2013). Xingkai geo-fissure movement and oil and gas exploration of lower assemblage in Sichuan Basin. *Chengdu Univ. Technol. Chin. J. Sci. Nat. Sci. Ed.)* 40, 511–520. doi:10.1016/s1876-3804(13)60057-9

Luo, B., Luo, W. J., Wang, W., Wang, Z., and Shan, S. (2015). Formation mechanism of the sinian natural gas reservoir in the leshan-longnvsi paleo-uplift, Sichuan Basin. *Nat. Gas. Geosci.* Available at: http://www.nggs.ac.cn/EN/10.11764/j.issn.1672-1926.2015.03.0444 26, 444–455.

Luo, Z., Liu, S., Liu, S., Yong, Z., Zhao, X., and Sun, W. (2004). The action of "Emei mantle plume" on the separation of the Yangtze plate from the Tarim plate and its significance in exploration. *Acta Geosci. Sin.* 25, 515–522.

Ma, D., Wang, Z., Duan, S., Gao, J., Jiang, Q., Jiang, H., et al. (2018). Strike-slip faults and their significance for hydrocarbon accumulation in Gaoshiti-Moxi area, Sichuan Basin, SW China. *Petroleum Explor. Dev.* 45, 851–861. doi:10.1016/S1876-3804(18)30088-0

Ma, Y., Li, H., Liu, K., Gu, H., and Ren, H. (2020). Application of ant tracking technology based on frequency division coherence in fault characterization of Tahe Oilfield. *Geophys. Prospect. Pet.* 59, 258–266. doi:10.3969/j.issn.1000-1441.2020.02.012

Matonti, C., Lamarche, J., Guglielmi, Y., and Marié, L. (2012). Structural and petrophysical characterization of mixed conduit/seal fault zones in carbonates: Example from the Castellas fault (SE France). *J. Struct. Geol.* 39, 103–121. doi:10.1016/j.jsg.2012.03.003

Michie, E. A. H. (2015). Influence of host lithofacies on fault rock variation in carbonate fault zones: A case study from the island of Malta. *J. Struct. Geol.* 76, 61–79. doi:10.1016/j.jsg.2015.04.005

Mitchell, T. M., and Faulkner, D. R. (2009). The nature and origin of off-fault damage surrounding strike-slip fault zones with a wide range of displacements: A field study from the atacama fault system, northern Chile. *J. Struct. Geol.* 31, 802–816. doi:10.1016/j.jsg.2009.05.002

Moghadam, H. S., Khademi, M., Hu, Z., Stern, R. J., Santos, J. F., and Wu, Y. (2013). Cadomian (Ediacaran-Cambrian) arc magmatism in the ChahJam- Biarjmand metamorphic complex (Iran): Magmatism along the northern active margin of Gondwana. *Gondwana Res.* 27, 439–452. doi:10.1016/j.gr.2013.10.014

Nemcok, M., Schamel, S., and Gayer, R. (2005). *Thrustbelts: Structural architecture, thermal regimes and petroleum systems*. New York: Cambridge University Press.

Niu, Y., O'Hara, M. J., and Pearce, J. A. (2003). Initiation of subduction zones as a consequence of lateral compositional buoyancy contrast within the lithosphere: A petrological perspective. *J. Pet.* 44, 851–866. doi:10.1093/petrology/44.5.851

Ostermeijer, G. A., Aben, F. M., Mitchell, T. M., Rockwell, T. K., Rempe, M., and Farrington, K. (2022). Evolution of co-seismic off-fault damage towards pulverisation. *Earth Planet. Sci. Lett.* 579, 117353. doi:10.1016/j.epsl.2021.117353

Rotevatn, A., and Bastesen, E. (2012). Fault linkage and damage zone architecture in tight carbonate rocks in the suez rift (Egypt): Implications for permeability structure along segmented normal faults. *Sp* 374, 79–95. doi:10.1144/sp374.12

Schmoker, J. W., and Hally, R. B. (1982). Carbonate porosity versus depth: A predictable relation for south Florida. *AAPG Bull.* 66, 2561–2570.

Shen, A., Zhao, W., Hu, A., Wang, H., Feng, L., and Wang, Y. (2021). The dating and temperature measurement technologies for carbonate minerals and their application in hydrocarbon accumulation research in the paleo-uplift in central Sichuan Basin, SW China. *Pet. explor. Dev.* 48, 476–487. doi:10.1016/s1876-3804(21)60045-9

Shi, J., Zhao, X., Pan, R., Zeng, L., and Luo, W. (2022). Natural fractures in the deep Sinian carbonates of the central Sichuan Basin, China: Implications for reservoir quality. *J. Petroleum Sci. Eng.* 216, 110829. doi:10.1016/j.petrol.2022.110829

Stein, S., and Stein, C. A. (2013). Thermo-mechanical evolution of oceanic lithosphere: Implications for the subduction process and deep earthquakes. *Wash. D.C. Am. Geophy. Union Geophys. Monogr. Ser.* 96, 1–17. doi:10.1029/gm096p0001

Su, N., Yang, W., Yuan, B., Dai, X., Wang, X., Wu, S., et al. (2020). Structural features and deformation mechanism of transtensional faults in Himalayan period, Sichuan Basin. *Earth Sci.* 46, 1–7. doi:10.3799/dqkx.2020.202

Su, N., Zou, L. J., Shen, X., Guo, F., Ren, Y., Xie, Y., et al. (2014b). Fracture patterns in successive folding in the western Sichuan Basin, China. *J. Asian Earth Sci.* 81, 65–76. doi:10.1016/j.jseaes.2013.12.003

Su, N., Zou, L. J., Shen, X., Wu, W., Zhang, G., Kong, F., et al. (2014a). Identification of fracture development period and stress field analysis based on fracture fabrics in tectonic superposition areas. *Arab. J. Geosci.* 7, 3983–3994. doi:10.1007/s12517-013-1063-6

Tondi, E. (2007). Nucleation, development and petrophysical properties of faults in carbonate grainstones: Evidence from the San Vito Lo Capo peninsula (Sicily, Italy). *J. Struct. Geol.* 29, 614–628. doi:10.1016/j.jsg.2006.11.006

Tong, H., Cai, D., Wu, Y., Li, X., Li, X., and Meng, L. (2010). Activity criterion of pre-existing fabrics in non-homogeneous deformation domain. *Sci. China Earth Sci.* 53, 1115–1125. doi:10.1007/s11430-010-3080-6

Torabi, A., and Berg, S. S. (2011). Scaling of fault attributes: A review. *Mar. Petroleum Geol.* 28, 1444–1460. doi:10.1016/j.marpetgeo.2011.04.003

Wang, R., Xu, Z., Santosh, M., Xu, X., Deng, Q., and Fu, X. (2017). Middle Neoproterozoic (ca. 705-716 Ma) arc to rift transitional magmatism in the northern margin of the Yangtze Block: Constraints from geochemistry, zircon U-Pb geochronology and Hf isotopes. *J. Geodyn.* 109, 59–74. doi:10.1016/j.jog.2017.07.003

Wang, Z., Wang, T., Wen, L., Jiang, H., and Zhang, B. (2016). Basic geological characteristics and accumulation conditions of Anyue giant gas field, Sichuan Basin. *China Offshore Oil Gas.* 28, 45–52.

Wei, G., Wang, Y., and Xiao, S. (2019). *Structural characteristics and oil and gas in Sichuan Basin [M]*. Beijing, Science Press.

Wu, G., Gao, L., Zhang, Y., Ning, C., and Xie, E. (2019). Fracture attributes in reservoir-scale carbonate fault damage zones and implications for damage zone width and growth in the deep subsurface. *J. Struct. Geol.* 118, 181–193. doi:10.1016/j.jsg.2018.10.008

Xiang, Z., Yan, Q., White, J. D. L., Song, B., and Wang, Z. (2015). Geochemical constraints on the provenance and depositional setting of Neoproterozoic volcaniclastic rocks on the northern margin of the Yangtze Block, China: Implications for the tectonic evolution of the northern margin of the Yangtze Block. *Precambrian Res.* 264, 140–155. doi:10.1016/j.precamres.2015.04.012

Xu, K., Dai, J., Feng, J., and Ren, Q. (2019). Fault system and its controlling effect on fracture distribution in Moxi-Gaoshiti block, Sichuan Basin, China. *J. Southwest Pet. Univ.* 41, 10–22. doi:10.11885/j.issn.1674-5086.2018.01.10.01

Yin, J., Gu, Z., and Li, Q. (2013). Characteristics of deep-rooted faults and their geological significances in Dachuanzhong area, Sichuan Basin. *Oil Gas. Geol.* 34, 376–382. doi:10.11743/ogg20130314

Zeng, H. (2017). RGB blending of frequency panels: A new useful tool for high-resolution 3D stratigraphic imaging. *Interpretation* 5, 1–46. doi:10.1190/segam2017-17494930.1

Zhang, J., Zhang, H., and Li, L. (2018). Neoproterozoic tectonic transition in the South Qinling Belt: New constraints from geochemistry and zircon U-Pb-Hf isotopes of diorites from the Douling Complex. *Precambrian Res.* 306, 112–128. doi:10.1016/j.precamres.2017.12.043

Zhu, M., Zhang, J., and Yang, A. (2007). Integrated ediacaran (sinian) chronostratigraphy of south China. *Palaeogeogr. Palaeoclimatol. Palaeoecol.* 254, 7–61. doi:10.1016/j.palaeo.2007.03.025

Zhu, X., Chen, F., Liu, B., Zhang, H., and Zhai, M. (2015). Geochemistry and zircon ages of mafic dikes in the South Qinling, central China: Evidence for Late Neoproterozoic continental rifting in the northern Yangtze block. *Int. J. Earth Sci. Geol. Rundsch)* 104, 27–44. doi:10.1007/s00531-014-1056-z

Zhu, X., Chen, F., Nie, H., Siebel, W., Yang, Y., Xue, Y., et al. (2014). Neoproterozoic tectonic evolution of South Qinling, China: Evidence from zircon ages and geochemistry of the Yaolinghe volcanic rocks. *Precambrian Res.* 245, 115–130. doi:10.1016/j.precamres.2014.02.005

frontiers | Frontiers in Earth Science

TYPE Original Research
PUBLISHED 20 February 2023
DOI 10.3389/feart.2023.1065911

OPEN ACCESS

EDITED BY
Weijia Sun,
Institute of Geology and Geophysics
(CAS), China

REVIEWED BY
Weijuan Meng,
Tsinghua University, China
Mikhail Rodkin,
Institute of Earthquake Prediction Theory
and Mathematical Geophysics (RAS),
Russia

*CORRESPONDENCE
Jianping Wu,
✉ wjpwu@cea-igp.ac.cn
Lihua Fang,
✉ flh@cea-igp.ac.cn

SPECIALTY SECTION
This article was submitted to
Solid Earth Geophysics,
a section of the journal
Frontiers in Earth Science

RECEIVED 10 October 2022
ACCEPTED 08 February 2023
PUBLISHED 20 February 2023

CITATION
Liu J, Wu J, Fang L, Chang K, Yang T, Wang C, Wang H and Wang S (2023), Characteristics of azimuthal anisotropy in SE Tibetan plateau and its relationship with the background of block structure. *Front. Earth Sci.* 11:1065911.
doi: 10.3389/feart.2023.1065911

Characteristics of azimuthal anisotropy in SE Tibetan plateau and its relationship with the background of block structure

Jing Liu[1], Jianping Wu[1]*, Lihua Fang[1]*, Kai Chang[2], Ting Yang[1], Changzai Wang[1], Huaifu Wang[3] and Shuang Wang[4,5]

[1]Insititute of Geophysics, Beijing, China, [2]National Institute of Natural Hazards, Beijing, China, [3]The 3rd Research Institute of CETC, Beijing, China, [4]New Engineering Industry College, Putian University, Putian, Fujian, China, [5]College of Information Engineering, Sanming University, Sanming, Fujian, China

The southeastern Tibetan Plateau, which includes the Tibetan Plateau, Yangtze Block, and Cathaysia Block, is geotectonically situated in the compound part of the Tethys-Himalayan tectonic domain and the Peninsular Pacific tectonic domain. It is one of the critical regions for studying the scientific problems of plateau material lateral escape, lithosphere deformation, geotectonic properties of blocks, and deep dynamics. In this study, we use ambient noise data recorded by 401 broadband stations to obtain high-resolution short-period (T = 4–32 s) Rayleigh wave azimuthally anisotropic phase velocity maps. These could provide fresh clues for an in-depth understanding of the crust-mantle velocity structure, deformation mechanism, and geotectonic evolution in the southeastern Tibetan Plateau. Within the Simao block, the strikes of the faults and the orientations of the principal compressive stress of the stress field both generally coincide with the fast-wave polarization direction (FPD). The FPD near the Lancangjiang fault zone in the west is in the NE-SW direction, near the Wuliangshan fault zone in the center is near the NS direction, and near the Red River fault zone in the east is the NW-SE direction. We estimate that the compressive stress in the southwest direction of the Tibetan Plateau material has a controlling effect on the crustal deformation of the Simao block, which is likewise blocked by the Lincang granite belt, resulting in strong tectonic deformation. The FPD of the crust in the middle Red River fault zone is NS direction, significantly different from the fault strike. Combining with the seismic activity and GPS results, the depth of 8 km below the surface of the middle Red River fault is completely locked, and we conclude that the anisotropy of the upper crust of the middle part of the Red River fault zone is related to the action of the regional tectonic stress field. Taking into account geochemical and thermochemical results, we speculate that the complex tectonic stress at the junction of the blocks leads to prominent regional characteristics of the FPDs of azimuthal anisotropy in the crust, suggesting that the Shizong-Mile fault zone may be the western boundary between the Yangtze block and the Cathaysia block.

KEYWORDS

azimuthal anisotropy, ambient noise tomography (ANT), Tibetan plateau (TP), simao block, yangtze block, cathaysian block

1 Introduction

The southeastern Tibetan Plateau (TP) is the Frontier zone and the deep material escape zone for the NE collision and extrusion of the Indian plate and the Eurasian continent (Figure 1A). There are the Tengchong block (TCB), Baoshan block (BSB), Simao block (SMB), Chuanxibei block (CXB), Dianzhong block (DZB) and other tectonic units in the area. Since the Cenozoic, it has experienced intense tectonic deformation and frequent seismic activities (Su and Qin, 2001), making it an ideal place to study the interaction among blocks and deep tectonic deformation.

Seismic anisotropy is one of the effective methods to study the deformation of the crust and upper mantle. The upper crustal anisotropy is related to the shape-preferred orientation of microstructures such as lamellae, joints, and fractures in the rock. Furthermore, the anisotropy of the mid-to-lower crust and upper mantle is related to the lattice-preferred orientation of anisotropic minerals such as amphibole, mica, and peridotite. We study seismic anisotropy to understand the relationship between medium and anisotropy, anisotropy and strain, and the relationship between strain and crustal movement. These help us infer the tectonic activities that might have operated in the past and those working at present. Some scholars have studied the SKS-wave splitting measurement in the southeastern TP and believe that, unlike the vertically coherent deformation of the crust and mantle inside the TP, the crust-mantle deformation in the southeastern TP is decoupled (Silver and Chan, 1991; Flesch et al., 2005; Lev et al., 2006; Chang et al., 2015; Huang et al., 2015). However, Wang et al. (2008) believed that the vertical coherent deformation model could also explain SKS-wave splitting measurements outside the TP. The anisotropy obtained by SKS-wave splitting measurement is the cumulative effect of the anisotropy on the path from the core-mantle boundary to the surface, which is difficult to determine the depth of the anisotropic layer. Chen et al. (2013) and Cai et al. (2016) speculated that the crust and upper mantle deformation in the southern study area decoupled. However, Pms anisotropy can only reveal the average anisotropy characteristic of the entire crust. Due to the dispersive properties of surface waves, surface waves of different periods are sensitive to structure information at different depths. Therefore, compared with SKS wave splitting and Pms anisotropy, surface wave azimuthal anisotropy can provide better constraints on the depth variation of anisotropy.

By using the seismic surface wave and ambient noise data, some researchers illustrate the azimuthal anisotropy of the TP and its vicinities (Yao et al., 2010; Lu et al., 2014; Wang et al., 2015; Liu et al., 2019; Liang et al., 2020; Zhu et al., 2021). These studies reveal the anisotropy on a large scale, i.e., mid-to-lower crust and upper mantle depth range, which provides essential evidence for the internal

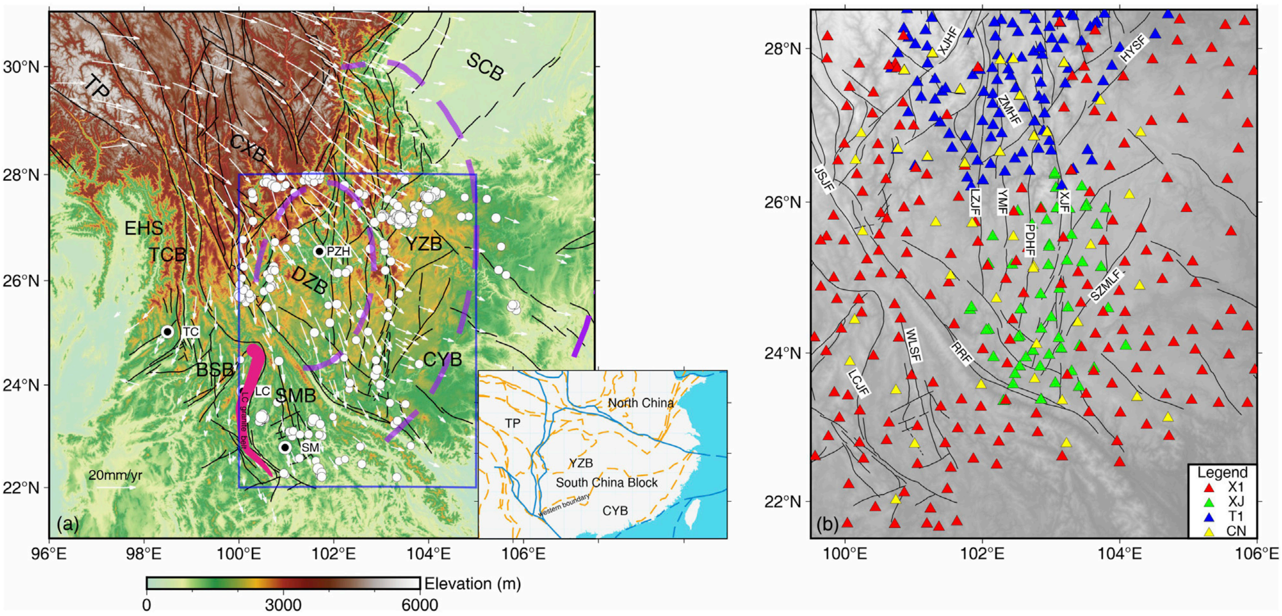

FIGURE 1
(A) Geological setting of the southeastern Tibetan Plateau. The blue rectangle marks the imaging domain in this study. The tectonic units in the southeastern Tibetan Plateau include the Tibetan Plateau (TP), Sichuan Block (SCB), Chuanxibei block (CXB), Dianzhong Block (DZB), Baoshan Block (BSB), Tengchong Block (TCB), eastern Himalayan syntaxis (EHS), Yangtze Block (YZB) and Cathaysian Block (CYB). The two subblocks around the DZB are the Chuanxibei block (CXB) and Simao Block (SMB). The black lines denote major faults. The dotted line inside the DZB demarcates the inner zone of the Emeishan large igneous province (ELIP), while the purple dotted line outside the DZB demarcates the intermediate zone of the ELIP. The white dots indicate the earthquake at the periods from June 2010 to July 2022 (download from https://earthquake.usgs.gov/earthquakes/search/). The white arrows denote the GPS velocity field (Zhao et al., 2015) of the SE Tibetan Plateau relative to the stable Eurasia. The rose-red band indicates the Lincang (LC) granite belt. The bottom-right inset highlights Main block boundary lines. **(B)** Distributions of the stations used in our tomography study. Red, green, blue and yellow triangles show the location of the ChinArray seismic network (ChinArray, 2006), Xiaojiang Array (Wu et al., 2013), Chuanxi Array (Liu et al., 2014) and permanent seismic stations in the southeastern Tibetan Plateau (Zheng et al., 2010), respectively. The abbreviations for which are as follows: ANHF: Anninghe Fault; ZMHF: Zemuhe Fault; XJF Xiaojiang Fault; XJHF: Xiaojinhe Fault; JSJF: Jinshajiang Fault; RRF: Red River Fault; LCJF: Lancangjiang Fault; SZMLF: Shizong-Mile Fault; WLSF: Wuliangshan Fault; LZJF: Lvzhijiang Fault; YMF: Yumen Fault; PDHF: Puduhe fault; HYSF: Huayingshan Fault. LC, PZH, TC and SM represent the cities of Lincang, Panzhihua, Tengchong and Simao, respectively.

structure and deformation dynamic mechanism of the crust and upper mantle in the southeastern TP. However, there is still a debate about the interactions between the sub-blocks and their natural properties. For example, the SMB, located between the Red River Fault zone (RRF) and the Lancangjiang Fault zone (LCJF), is spread from NW to SE (Figure 1). It is adjacent to the Dianzhong block in the north and the Baoshan block in the west. Significant tectonic deformation has occurred since Cenozoic. Geological studies propose a variety of different structural deformation modes. It mainly includes the pushing out effect during lateral rotational extrusion of crustal blocks in the southeastern TP (Tanaka et al., 2008; Kondo et al., 2012; Tong et al., 2013); the extrusion effect of the thrust fault in Lincang (LC) granite foundation from west to east (Gao et al., 2015), and the blocking effect of Lincang granite foundation on the lateral clockwise rotational extrusion movement of SMB (Xu et al., 2017). The eastern boundary between the YZB and the CYB can be made with certainty (Zhang et al., 2005; Zhang et al., 2015; Guo et al., 2019; Ma et al., 2022), but the western border is more controversial (Zhu et al., 2019). The edge of the west is difficult to discern because of the lack of outcrops of the combined geological landmarks (ophiolites, island arc igneous rocks), the thick cover in the later period, and the multi-stage structure and magmatic intrusion. The one point of views is the Shizong-Mile fault (SZMLF, Figure 1B) (Dong et al., 2002; Guo et al., 2009).

In our study, we collect the continuous waveform data recording by dense seismic arrays of the permanent China National-backbone stations and mobile broadband stations (Figure1B). We adopt ambient noise tomography to acquire high-resolution Rayleigh wave phase velocity azimuthal anisotropy in this area. It provides new evidence for the tectonic evolution and dynamic process of the crust and upper mantle in the southeastern TP.

2 Data and methods

2.1 Data acquisition and processing

In this study, we collected the continuous waveform data recorded by three temporal seismic arrays: 195 stations of the ChinArray (X1) between October 2011 and October 2012, 114 stations of the Chuanxi array (CX) between October 2006 and July 2009 (Liu et al., 2014), and 50 stations of the Xiaojiang array (XJ) between January 2009 and December 2010 (Wu et al., 2013). In addition, we also use data recorded by 42 permanent stations of the Sichuan and Yunnan regional seismic networks for 1 year in 2009. There are 401 seismic stations in total in our study region. The average interstation space is about 30 km. The dense station distribution enhances the azimuthal coverage and path density, especially in DZB, compared with previous studies (e.g., Lu et al., 2014; Wang et al., 2015). Figure 1B shows the station distribution. Most stations are equipped with Guralp CMG-3ESPS seismometer (60s–50 Hz) and Reftek 130 digitizer.

The data processing technique for ambient noise tomography is currently in a relatively advanced stage. It mainly includes single station data preprocessing, empirical Green's function extraction, phase velocity dispersion measurement, phase velocity tomography, and surface wave azimuthal anisotropy inversion. Empirical Green's functions (EGFs) are derived from the cross-correlation functions between each station pair using the vertical component of continuous waveform following the method of Bensen et al. (2007) and Fang et al. (2009). Phase velocity dispersions from EGFs are measured using the far-field representation of the surface-wave Green's function and image transformation technique following Yao et al. (2006). Figure 2 shows example of Z-Z cross-correlation functions (CCFs) between stations randomly selected from XJ array. The CCFs are filtered at 5–40 s period band. Figure 3 shows an example of the dispersion measurement of the phase velocity.

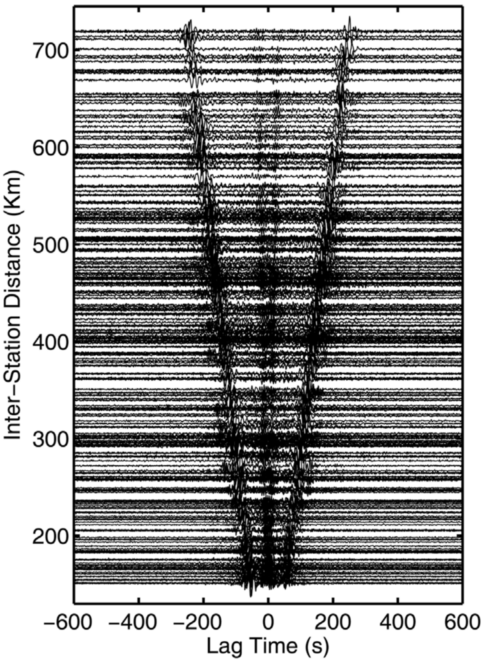

FIGURE 2
Example of Z-Z CCFs between stations randomly selected from XJ array. The CCFs are filtered at 5–40 s period band.

2.2 Surface wave tomography inversion

In the case of weak anisotropic medium and ignoring 4φ terms, Rayleigh wave phase velocity $c(\omega, M, \varphi)$ at an arbitrary point M for each angular frequency ω and azimuth φ can be expressed as (Smith and Dahlen, 1973):

$$c(\omega, M, \varphi) = c_0(\omega)\left[1 + \alpha_0(\omega, M) + \alpha_1(\omega, M)\cos 2\varphi + \alpha_2(\omega, M)\sin 2\varphi\right] \quad (1)$$

Where $c_0(\omega)$ is the reference phase velocity, α_0 and $\alpha_i\,(i = 1, 2)$ are the isotropic phase velocity perturbation and the azimuthal anisotropy coefficients, respectively. During the inversion, these parameters are determined using the continuous regionalization method of Montagner (1986) and the generalized inversion algorithm of Tarantola and Valette (1982) for each period. The

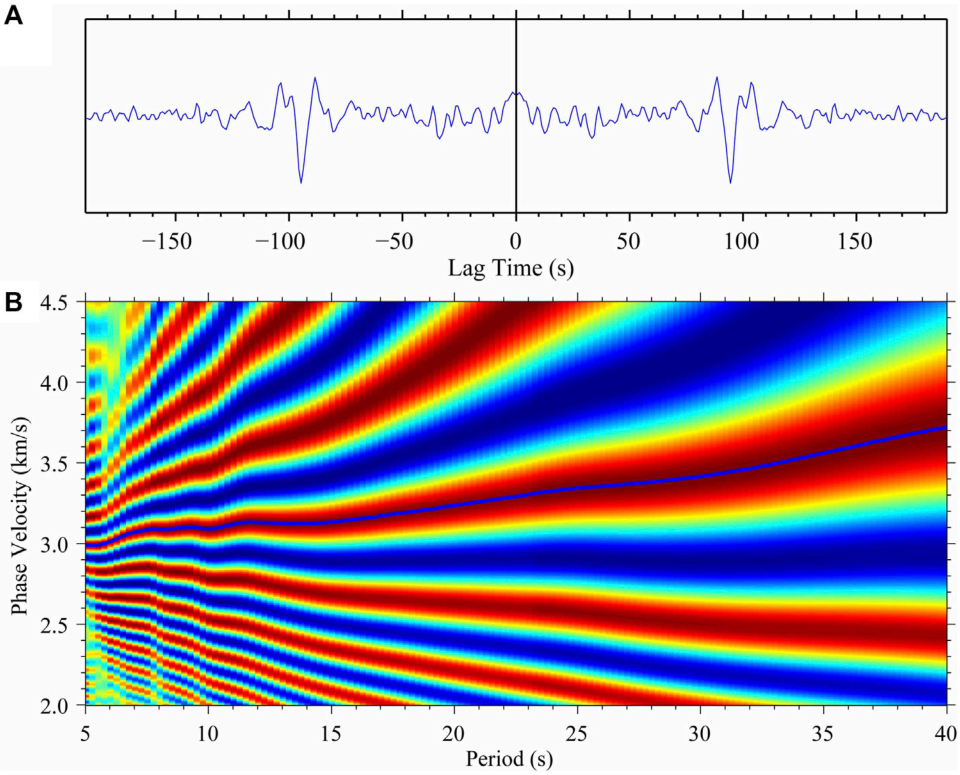

FIGURE 3
Example of dispersion measurement. **(A)** The 4-month cross-correlation obtained between stations XJ03 and XJ42 using vertical recordings. **(B)** FTAN diagram obtained after multiple filter analysis. The abscissa is represented with periods, and the ordinate is represented with phase velocity.

magnitude of the anisotropy, Λ, and the Fast-wave Polarization Direction (FPD), Φ, are determined with Equations 2, 3, respectively.

$$\Lambda = \frac{\left[\alpha_1^2(\omega, M) + \alpha_2^2(\omega, M)\right]^{1/2}}{1 + \alpha_0(\omega, M)} \tag{2}$$

$$\Phi = \frac{1}{2}tan^{-1}\frac{\alpha_2(\omega, M)}{\alpha_1(\omega, M)} \tag{3}$$

The inversion for $\alpha_i\,(i = 0, 1, 2)$ is controlled by three parameters: the standard error of phase velocity measurements, δd, the *a priori* parameter error, δp (which constrains the anomaly amplitude), and the correlation length Lc (which constrains the smoothness of the resulting model). In our inversion, following Yao et al. (2010), we set δd to 2% for all measurements. For a given α_0, δp is set to be twice that of the standard deviation (in percent) of all observed phase velocities at each period with a minimum value of 0.15 km/s. For α_1 and α_2, δp is set to be 1.5% of the average phase velocity at each period. In this study, we focus on short and intermediate period surface wave. It may result in artificial velocity anomaly if the correlation length Lc is too small. So we set the correlation length $Liso=max$ (30 km, C_0*$T/2$) for the isotropic term, where C_0 is the average phase velocity at a certain period, T. The correlation length for the azimuthally anisotropic parameters is set to be 2^*L_{iso} at the corresponding period.

2.3 Resolution tests

The knowledge of the resolution is vital in the interpretation of the tomography results. Artificial values may be introduced in inversion due to insufficient data and poor ray path coverage. Following Simons (2002) and Yao et al. (2010), we performed checkerboard tests to assess the resolution of our model. We calculated the synthetic data from input models with a 1°×1° anisotropic pattern along with the fast azimuthal axis-oriented NE and NW, with 5% isotropic anomalies at each period (Figure 4A). We added the random error with a maximum of 1% to the synthetic data. We performed the inversion with the same parameters as for the actual data.

The checkerboard tests indicate that for the azimuthal anisotropy parameters, the 1°×1° patterns are well recovered throughout our study area (Figures 4B–D). The azimuthal anisotropy is not well recovered in the margin due to relatively poor azimuthal path coverage. Generally, checkerboard tests provide qualitative information about spatial resolution. However, we must remember that the checkerboard test differs from the inversion of actual data due to its inherent limitations, as pointed out by previous studies (e.g., Simons, 2002). For example, the limits of ray approximation, the horizontal smoothing imposed in the inversion, and the trade-off between lateral heterogeneities and anisotropy (Pandey et al., 2015).

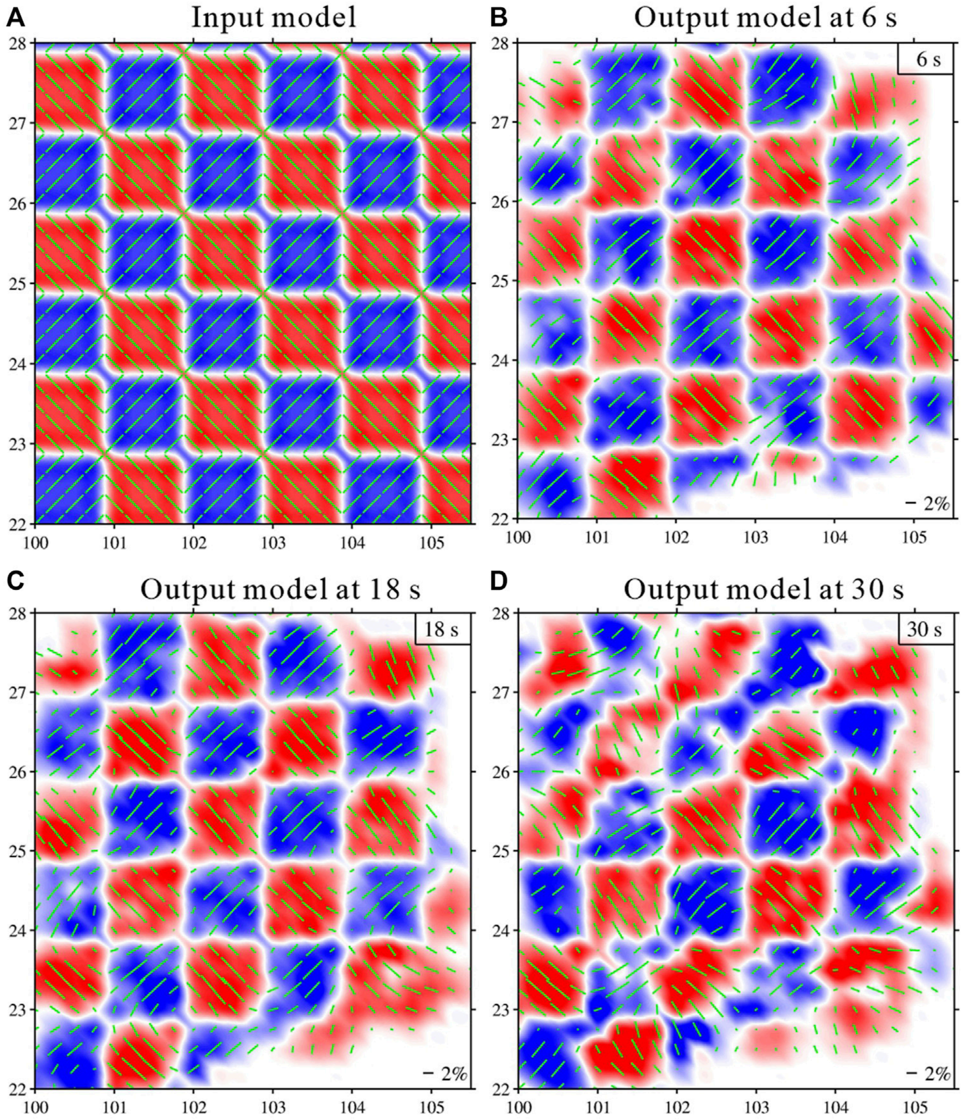

FIGURE 4
Checkerboard tests of azimuthal anisotropy with 1°×1° grid. **(A)** Input model; **(B)**, **(C)**, **(D)** are output model after inversion.

Tarantola and Valette (1982) pointed out that calculating the posterior covariance operator of the model parameters after inversion can estimate the posterior error and resolution of the inversion parameters. If the posterior error is significantly smaller than the prior error, the inversion results are reliable, and the resolution is high. Conversely, when the posterior error is close to the prior error, it indicates that the data cannot resolve the parameter. Figure 5 shows the posterior error distribution of the anisotropic intensity after inversion. Its amplitude is much smaller than the prior error of the anisotropic intensity and the anisotropic intensity in the study area. Taking 10s as an example, in the central, the posterior errors of the anisotropic intensity Ac are all less than 0.3%. Therefore, the inversion results are reliable for regions with anisotropy strength greater than 2%.

3 Results

The Rayleigh surface wave phase velocity and azimuthal anisotropy are obtained by inversion according to the mixed path dispersion curve. The different periods reflect the structural differences in different depth ranges. Compared with the S-wave velocity inverted by a single node, the reliability of the phase velocity at different periods is higher. We select six periods for discussion according to the phase velocity characteristics at each period. Figures 6A–F show isotropic phase velocity and azimuthal anisotropy maps at six periods. Moreover, the background is the absolute value of the isotropic phase velocity. The length and azimuth of the short black bars indicate the magnitude of the azimuthal anisotropy and the FPD, respectively.

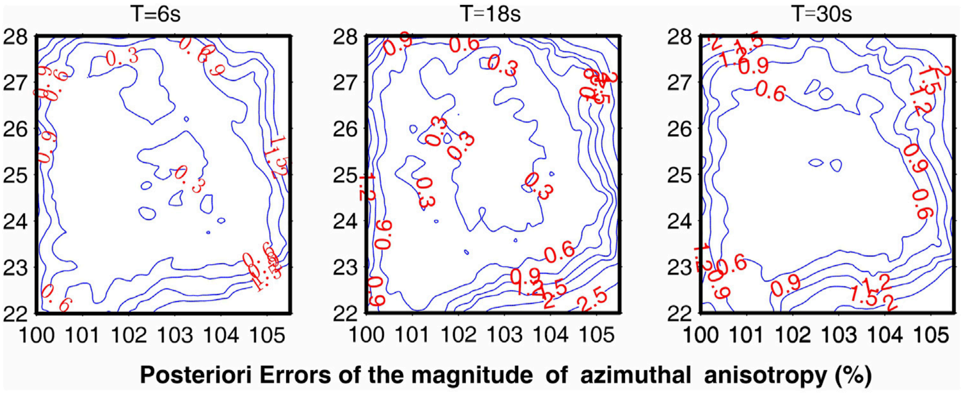

FIGURE 5
posterior errors (in percent) of (right) the magnitude of azimuthal anisotropy at T = 6, 10, and 20 s.

At short periods (4–10 s), the phase velocity mainly reflects the characteristics of the upper crustal structure. The phase velocity distribution is consistent with the surface geological structure. The SMB exhibits low velocity, associated with thick sedimentary layers in this area, consistent with the S-wave velocity results of Liu et al. (2019). There are high-velocity anomalies in the vicinity of Panzhihua (PZH) and the east of the Shizong-Mile fault (SZMLF) zone. An N-S-orientated high-velocity belt along the Lvzhijiang (LZJF) and Yimen faults (YMF) through the Red River Fault (RRF). The FPD of surface wave azimuthal anisotropy is nearly N-S direction in the Dianzhong block and SMB, which is consistent with the strike of the Xiaojiang fault (XJF). In the high-velocity body of PZH, the magnitude of azimuthal anisotropy is weak. The FPD to the east side of the XJF zone is NE. The FPD to the east of the SZMLF is NW-SE direction as a whole, which is significantly different from its adjacent areas.

At intermediate periods (14–20 s), the phase velocity mainly reflects the mid-crustal structure, and its sensitivity range is about 10–25 km. The area near PZH and east of the SZMLF still exhibits high-velocity anomalies. Still, the area of high-velocity anomalies near the PZH area has begun to decrease. After 20 s period, high-velocity anomalies began to appear on the west side of the SMB. The azimuthal anisotropic characteristics at intermediate periods are similar to the short periods. The FPDs to the northeastern SZMLF changed from NW-SE to N-S direction. Furthermore, the FPDs to the south of the eastern RRF zone are nearly E-W direction, and the magnitude of azimuthal anisotropy is relatively strong.

At long periods (>20 s), the phase velocity is sensitive to the structures in the mid-to-lower crust. For example, the SZMLF is the boundary between the YZB and CYB. The high-velocity anomaly on the east side is parallel to the strike of the SZMLF. As the period increases, the area of high-velocity anomalies near the PZH area continues to decrease. After 30 s period, this high-velocity anomaly almost disappeared. The azimuthal anisotropic characteristics seem to be those at 12–20 s periods. The FPDs in the DZB and SMB are still in a close N-S direction. After 24 s, the FPDs in the northern CYB changed from NW-SE and nearly NS to NE-SW. The FPDs to the south of the eastern RRF zone are still near the E-W direction.

4 Discussion

4.1 Crustal deformation mechanism of simao block and its surrounding areas

The SMB has frequent seismic activities, dominantly about magnitude 6.0, showing the characteristics of stronger and less large earthquakes. The present crustal deformation and intense earthquake activities in this area are closely related to the collision of the Indian plate and the Eurasian plate and the lateral extrusion of the TP. Therefore, understanding the velocity structure and anisotropy characteristics will help us further understand the dynamic relationship between the present crustal deformation process and the material extrusion in the southeastern TP.

The velocity anomaly in the SMB is heterogeneous. At 14–32 s periods, it is mainly sensitive to the S-wave velocity structure in the depth range of 20–45 km (Figure 7). The area near the Wuliangshan fault zone (WLSF) continues to exhibit low-velocity anomalies, and the other areas show relatively high-velocity anomalies relative to short periods. Regarding azimuthal anisotropy (Figures 8A, B), the FPDs in the SMB show noticeable regional variance. In the central, the FPDs are generally similar to the fault strikes and the orientation of the principal compressive stress (Sheng et al., 2022). Among them, the FPD near the LCJF in the west is NE-SW direction, the FPD near the WLSF zone in the middle is near the N-S direction, and the FPS near the RRF zone in the east is NW-SE direction. These phenomena are consistent with the phase velocity azimuthal anisotropy of Wang et al. (2015), the group velocity azimuthal anisotropy of Lu et al. (2014), and Pms anisotropy (Chen et al., 2013; Sun et al., 2015; Cai et al., 2016) (Figure 9B).

Previous studies have shown that the RRF experienced a left-lateral strike-slip movement at 32–17 Ma and transformed into a right-lateral strike-slip movement at about 5 Ma (Gilley et al., 2003). In contrast, the XJF zone started to experience an initial left-lateral strike-slip movement from the Middle Miocene to the Early Pliocene (about 17–5 Ma) (Roger et al., 1995). At this time, the Chuandian diamond block (including the CXB and DZB) began to rotate and extrude clockwise along the XJF. During this process, the Chuandian

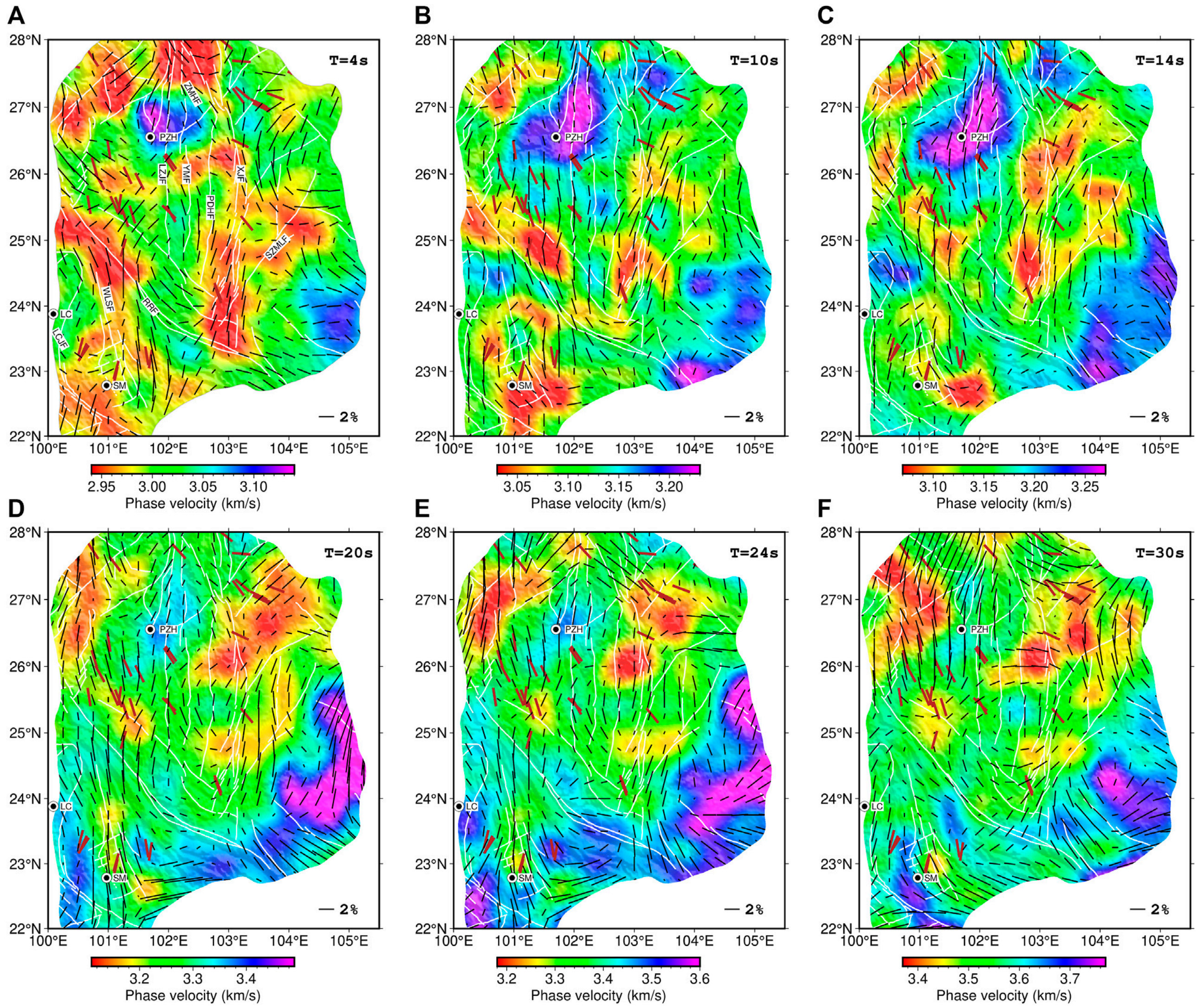

FIGURE 6
Variation of absolute Rayleigh phase velocities (color image) and azimuthal anisotropy (short black bars) in the crust and uppermost mantle beneath southeastern Tibetan Plateau at different periods **(A-F)**. The color bars show the color scale of phase velocities (km/s). The short brown bars are the P-axis directions of the principal stress based on the focal mechanism solution (Ekström et al., 2012). The abbreviations of geological units are defined in the caption of Figure 1.

diamond block was bound to have a robust southward extrusion on the SMB. Since the Oligocene (37–21 Ma), the Lincang granite in the southern SMB has experienced a gradual uplift from south to north (Shi et al., 2006). Furthermore, with the obstruction of the Lincang granite belt, the crustal structure of the central SMB was deformed strongly, forming a northwardly protruding honeycomb-shaped structure.

Therefore, when subjected to compressive stress in the southwest direction of the Chuandian diamond block, the crust of the eastern SMB underwent shear deformation, forming crustal anisotropy parallel to the strike of the RRF. Meanwhile, the crust of the western SMB was blocked by the Lincang granite belt and strongly deformed, forming crustal anisotropy parallel to the strikes of the Lincang granite belt and the LCJF. Likewise, the central is in the transition zone of differential deformation on both sides, forming near N-S trending crustal anisotropy, which is almost consistent with the extensive development of folds and thrust structures in the Mesozoic-Cenozoic strata in the block (Guan et al., 2006).

The SMB has undergone 50°–70° clockwise rotational deformation under the combined action of the Chuandian diamond block since the Pliocene (Sato et al., 2007). The GPS velocity field shows that, relative to the South China block, the NNE pushing caused by the collision of the Indian plate and the Eurasian plate (Wang and Shen, 2020) and the gravitational potential energy generated by the plateau uplift resulted in the eastward extrusion of the TP (Li et al., 2021). After encountering the obstruction from the stable South China block, the TP material moved southeast and southward, causing the Chuandian diamond block to rotate clockwise around the eastern Himalayan tectonic

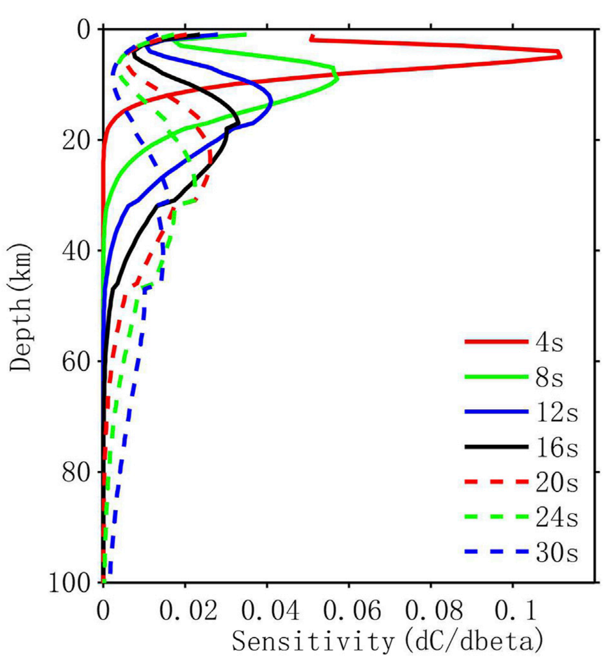

FIGURE 7
Sensitivity kernels of Rayleigh wave phase velocity at different periods.

knot. Therefore, we infer that the compressive stress in the southwest direction of the Chuandian diamond block has a controlling effect on the crustal deformation of the SMB, and the west of the block was blocked by the Lincang granite belt and experienced intense tectonic deformation (Figure 10).

In the middle RRF and its vicinity, the anisotropic FPD at 4–24 s periods (corresponding to the crustal depth range, Figure 7) is near the N-S direction (Figure 5), showing a large angle with the fault strike. The azimuthal anisotropy of the surface wave group velocity, Pms anisotropy, and S-wave azimuthal anisotropy (Figure 9B) also show almost the same characteristics (Lu et al., 2014; Cai et al., 2016; Liu et al., 2019). The RRF zone, as a critical plate boundary cutting the Moho surface (Wang et al., 2014), did not cause the FPD of the anisotropy in the crust to be parallel to the strike of the fault. The tectonic stress field obtained from the focal mechanism (Xu, 2001; Wu et al., 2004; Xu et al., 2016) and the GPS velocity field (Jin et al., 2019) show that the maximum principal stress in the vicinity of the middle RRF zone is in the near N-S direction, which is consistent with the FPD of azimuthal anisotropy (Figure 9A). The anisotropy of the upper crust is generally considered to be related to the shape preferred orientation of microstructures (Rabbel and Mooney, 1996; Crampin and Peacock, 2008). Secondly, fault zones may also affect it, but the influence is limited (Gao et al., 2011). The GPS velocity field (Figure 1A) and seismic activity suggest that the middle RRF zone is completely locked from the surface to 8 km depth (Zhao et al., 2015; Wang et al., 2022). We speculate that the anisotropic material in the upper crust of the middle RRF zone may not have a dominant arrangement along the fault strike but is related to the action of the regional tectonic stress field (Figure 10).

4.2 Constraints on the western boundary between Yangtze Block and Cathaysia Block

At 4–32 s periods, the Rayleigh surface wave phase velocities in the eastern and western sides of the SZMLF have noticeable velocity differences (Figures 8A, B, D), which correspond well with the S-wave and P-wave velocity variations (Wu et al., 2013; Yang et al., 2020). Unlike the velocities on the west side of the fault zone with the periods changing, the east side of the fault zone continues to show relatively high phase velocity anomalies. The apparent velocity differences may reflect the inhomogeneity of the crustal structures and lithologies on both sides. The receiver function showed the crustal thickness on both sides of the SZMLF differs up to 10 km (Wang et al., 2017) (Figure 8D). The geochemical study of the volcanic rocks in the northern SZMLF zone shows that it is mainly alkaline basalt, characterized by low TiO_2 and high Al_2O_3, which is different from the Emeishan continental overflow basalt with high TiO_2 and low Al_2O_3 characteristics (Dong et al., 2002). The Bouguer gravity anomaly and the equilibrium gravity anomaly along both sides of the SZMLF zone are high in the north and low in the south, which shows that the SZMLF is the block boundary separating the YZB and CYB with different crustal structures. In addition, the thermochemical states of the upper mantle in South China based on multi-observation probability inversion (Yang et al., 2021) show that in the lithospheric mantle, the average density in this region also takes the SZMLF zone as the western boundary to separate the YZB and CYB. Coupled with the complex tectonic stress at the junction of the blocks leading to prominent regional characteristics of the FPDs, we infer that the SZMLF zone may be the western boundary between the YZB and CYB in the crust (Figure 10).

The SCB located at the northwest of the YZB. In the northeastern study area, the crustal anisotropy of the southern SCB at 4–20 s periods is dominated by NE-SW and NEE-SWW trends (Figure 8C), which is consistent with the NE-SW trend of the surface eastern Sichuan fold belt (Li et al., 2014; Xiong et al., 2016). The shear wave splitting of local earthquakes (Tai et al., 2015), Pms anisotropy (Sun et al., 2012), and S-wave azimuthal anisotropy (Zhu et al., 2021) also show the same crustal anisotropy characteristics. Since the Cenozoic, the eastward compressive stress of the TP may have been transmitted to the eastern Sichuan fold belt through the hard SCB, leading to an uplift of the east Sichuan fold belt (1–2 mm/a) in this area (Shi et al., 2016; Yuan et al., 2018). We believe that the azimuthal anisotropy of the upper crust is related to the high-angle stratigraphic directional arrangement caused by the eastern Sichuan fold belt deformation, which can be considered as the response evidence for the eastward extrusion of the TP. At 22–34 s periods (Figures 9B, C), the FPD of the azimuthal anisotropy is mainly in the NW-SE direction, and the anisotropy amplitude is greater than 2%, basically consistent with the direction and magnitude of the SKS anisotropy (Liu et al., 2020). We deduce that the lithosphere has undergone significant deformation.

4.3 Crustal structure characteristics and deformation mechanism of the dianzhong block

At the period of 4–30 s, the area near PZH exhibits high phase velocity anomaly (Figure 8C), which is in good agreement with the

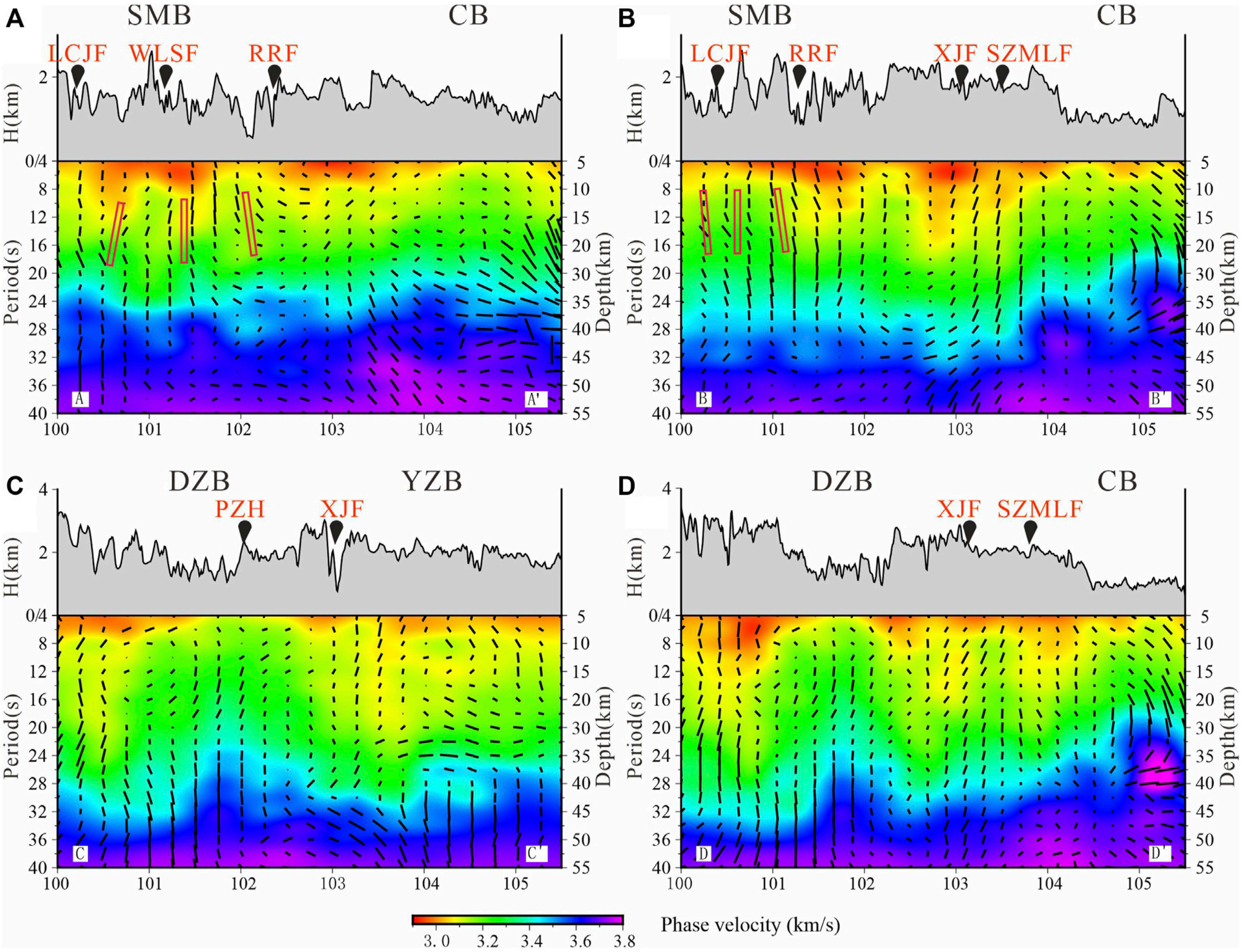

FIGURE 8
Absolute isotropic phase velocities across the four profiles shown in Figure 8D (black lines). The red bars indicate that the fast-wave polarization direction (FPD) of azimuthal anisotropy shows a regional variation. the FPD near the LCJF in the west is NE-SW direction, the FPD near the WLSF zone in the middle is near the N-S direction, and the FPS near the RRF zone in the east is NW-SE direction. The depth corresponding to each period is calculated in terms of the sensitive kernel in Figure 7. Topography is depicted above each profile as the black fonts and the red fonts above it, marking the location of major faults along each profile. The red bars denote the tendency of anisotropic direction. The abbreviations for fault names (red) are the same as in Figure 1. The tectonic units are shown as the black fonts on each topographic area.

characteristics of high Poisson's ratio, high wave velocity, high resistivity, high density, positive magnetic anomaly, and low terrestrial heat flow (Chen et al., 2015; Wang et al., 2017; Wu et al., 2013; Cheng et al., 2017; Shen et al., 2015; Xu et al., 2015; Teng et al., 2019), all distributed in the inner core of the Emeishan large igneous rock province. Moreover, the FPDs in the vicinity of PZH have the characteristics of the NS direction at 4–30 s periods. Another notable feature is a large area of low-velocity anomalies near the Xiaojinhe fault (XJHF) zone in the north, which is consistent with the S-wave velocity obtained by Liu et al. (2014). The phase velocities are sensitive to the S-wave velocities of the mid-to-lower crust at 20–34 s periods (Figure 7). Within this period, the FPD near the northern XJHF zone gradually changed from NS to NE-SW direction, roughly parallel to the fault zone.

Geochemical and regional geological studies (Xu and Zhong, 2001) indicated that during the period of 263-251Ma in the Late Permian, a famous tectonic activity occurred in the western YZB, the magmatic activity of the Emeishan great igneous rock province (Xu and Chung, 2001), whose dynamic mechanism may be related to mantle plume activity. Both sources of intracrustal magmatic intrusions and eruptive basalts come from the deep mantle. According to the dome structure and basalt thickness, the active center of the mantle plume is located near PZH (Shen et al., 2007; Xu and Zhong, 2001). We speculate that the high-velocity anomaly in the crust may be formed by the cooling and crystallization of a large number of high-density basic and ultramafic rock intrusions under the PZH area during the uplifting process of the early mantle plume (Wu et al., 2013; Yang et al., 2014; Zheng et al., 2016).

The XJHF, as the western boundary of the Yangtze block, obliquely cuts the Chuandian diamond block into two sub-blocks in CXB and DZB (Xiang et al., 2002; Xu et al., 2003). The topographic differences between the two sides of the XJHF fault

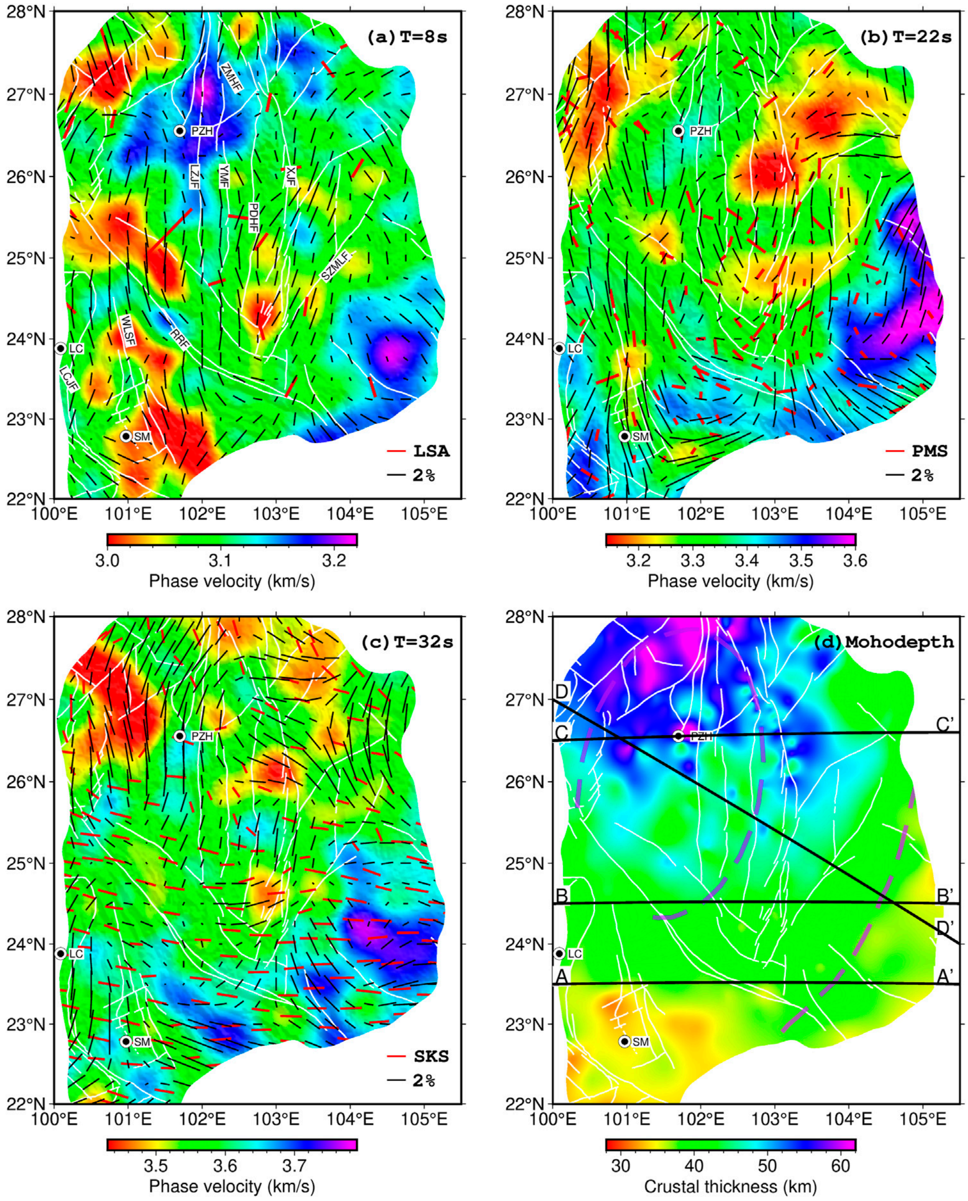

FIGURE 9
Comparison of the previous seismic anisotropy results and our azimuthal anisotropy at different periods. **(A)** Azimuthal anisotropy of Rayleigh wave at period 8 s vs. the Local Seismic Anisotropy (LSA) (Shi et al., 2009, 2012; Gao et al., 2012); **(B)** Azimuthal anisotropy of Rayleigh wave at period 22 s vs. the Pms phase splitting of receiver function (Sun et al., 2012; Chen et al., 2013; Cai et al., 2016); **(C)** Azimuthal anisotropy of Rayleigh wave at period 32 s vs. the SKS/SKKS phases splitting (Chang et al., 2015); **(D)** Distribution of Moho depth (Wang et al., 2017).The abbreviations of geological units are defined in the caption of Figure 1.

zone are significant. To the north of the fault zone, many peaks with altitudes of 4500–6500 m, and the average altitude exceeds 3500 m. While the average altitude to the south of the fault zone rapidly drops to about 2000 m.

Geological investigations have shown that differential movements on both sides of the fault zone are apparent. The horizontal slip rate values of the sub-block in CXB toward SE are 2 mm/a higher than those of the DZB. Since the Late Quaternary, the average differential upward and downward movement rates have reached 1.0–1.3 mm/a (He et al., 1993; Xu et al., 2003). Furthermore, there are also considerable differences in vertical movements observed by level (Liang et al., 2013). What causes the significant differential motion between the two sub-blocks within the Chandian diamond block? Seismic tomography results show (Liu et al., 2014; Wang et al., 2020) that there is a pronounced lower crustal flow in the CXB, and the flow direction is consistent with the extrusion direction of the block to the south. We suggest that the southward extrusion of the TP material is blocked by the hard intracrustal masses with PZH as the core, resulting in a rapid uplift of the northern topography.

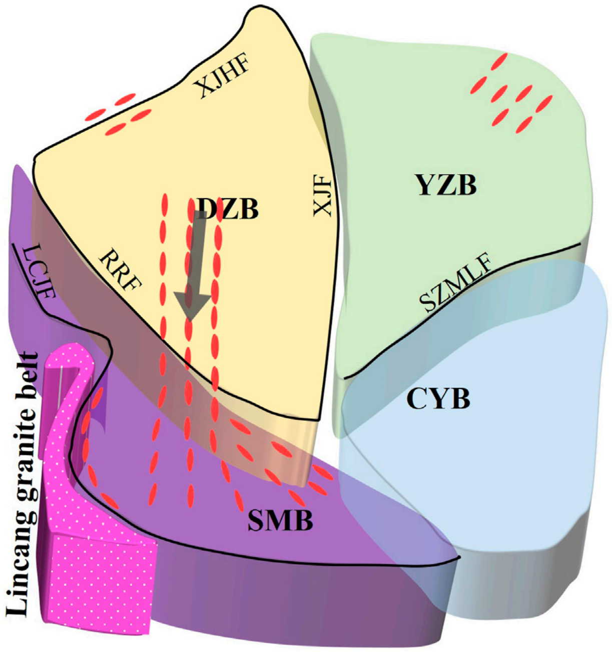

FIGURE 10
A cartoon summarizing the deformation pattern of the crust in the southeastern Tibetan Plateau. We estimate that the compressive stress in the southwest direction of the Tibetan Plateau material has a controlling effect on the crustal deformation of the Simao block, which likewise blocked by the Lincang granite belt, resulting in strong tectonic deformation. The anisotropy of the upper crust of the middle Red River fault zone is related to the regional tectonic stress field. And the Shizong-Mile fault zone may be the western boundary between the Yangtze block and the Cathaysia block. The red ellipses denote the FPD of the Rayleigh-wave phase velocity in the crust. The black arrow denotes the movement direction of the Dianzhong block relative to the South China block (Wang et al., 2020). The black lines denotes the faults.

5 Conclusion

We present an azimuthally anisotropic phase velocity model of the crust and uppermost mantle beneath the southeastern TP from surface wave dispersion. A summary of our major findings and the structural features revealed by the azimuthally anisotropic model is as follows.

1. The azimuthal anisotropy and phase velocity in the SMB show noticeable regional variance. Subject to compressive stress in the southwest direction of the Chuandian diamond block, the crust of the eastern SMB underwent shear deformation, forming crustal anisotropy parallel to the strike of the RRF. Meanwhile, the crust of the western Simao block was blocked by the Lincang granite belt and strongly deformed, forming crustal anisotropy parallel to the strikes of the Lincang granite belt and the LCJF. Likewise, the central is in the transition zone of differential deformation on both sides, forming near N-S trending crustal anisotropy, which is almost consistent with the extensive development of folds and thrust structures in the Mesozoic-Cenozoic strata in the block. We infer that the compressive stress in the southwest direction of the Chuandian diamond block has a controlling effect on the crustal deformation of the SMB, and the west was blocked by the Lincang granite belt and experienced strong tectonic deformation.
2. In the middle RRF and its vicinity, the anisotropic FPD at 4–24 s periods is near N—S direction, showing a large angle with the fault strike. The anisotropic material in the upper crust of the middle RRF zone may not have a dominant arrangement along the fault strike but is related to the action of the regional tectonic stress field.
3. At 4–32 s periods, the Rayleigh surface wave phase velocities in the eastern and western sides of the SZMLF have noticeable velocity differences, which correspond well with the S-wave and P-wave velocity variations. Coupled with the complex tectonic stress at the junction of the blocks leading to prominent regional characteristics of the FPDs, we infer that the SZMLF zone may be the western boundary between the Yangtze and Cathaysia blocks in the crust.
4. Azimuthal anisotropy and Rayleigh surface-wave phase velocity show a pronounced lower crustal flow in the Chuanxibei sub-block, and the flow direction is consistent with the extrusion direction of the block to the south. The southward extrusion of the Tibetan Plateau material is blocked by the hard intracrustal masses with Panzhihua as the core, resulting in a rapid uplift of the northern topography.

Data availability statement

Publicly available datasets were analyzed in this study. This data can be found here: the China Seismic Array Data Management Center at the Institute of Geophysics, China Earthquake Administration.

Author contributions

JL and LF designed the method and programmed the codes; all authors participated in writing, revising, and approving the final manuscript.

Funding

This work was supported by grants 42204070, U2039204 and U2139205 from the National Natural Science Foundation of China, 2021M702988 from the China Postdoctoral Science Foundation, and 2020-S-39 from guiding science and technology projects in Sanming City.

Acknowledgments

Thanks to the China Seismic Array Data Management Center at the Institute of Geophysics, China Earthquake Administration for preparing the waveform data. We are also grateful to the editor and two reviewers for their comments.

Conflict of interest

The authors declare that the research was conducted in the absence of any commercial or financial relationships that could be construed as a potential conflict of interest.

Publisher's note

References

Bensen, G. D., Ritzwoller, M. H., Barmin, M. P., Levshin, A. L., Lin, F., Moschetti, M. P., et al. (2007). Processing seismic ambient noise data to obtain reliable broad-band surface wave dispersion measurements. *Geophys. J. Int.* 169, 1239–1260. doi:10.1111/j.1365-246X.2007.03374.x

Cai, Y., Wu, J., Fang, L., Wang, W., and Yi, S. (2016). Crustal anisotropy and deformation of the southeastern margin of the Tibetan Plateau revealed by Pms splitting. *J. Asian Earth Sci.* 121, 120–126. doi:10.1016/j.jseaes.2016.02.005

Chang, L., Ding, Z., and Wang, C-Y. (2015). Upper mantle anisotropy beneath the southern segment of North-South tectonic belt, China. *Chin. J. Geophys. (in Chinese)* 58 (11), 4052–4067. doi:10.6038/cjg20151114

Chen, Y., Li, W., Yuan, X., Badal, J., and Teng, J. (2015). Tearing of the Indian lithospheric slab beneath southern Tibet revealed by SKS-wave splitting measurements. *Earth Planet. Sci. Lett.* 413, 13–24. doi:10.1016/j.epsl.2014.12.041

Chen, Y., Zhang, Z., Sun, C., and Badal, J. (2013). Crustal anisotropy from Moho converted Ps wave splitting analysis and geodynamic implications beneath the eastern margin of Tibet and surrounding regions. *Gondwana Res* 24, 946–957. doi:10.1016/j.gr.2012.04.003

Cheng, Y. Z., Tang, J., Cai, J. T., Chen, X. B., Dong, Z. Y., and Wang, L. B. (2017). Deep electrical structure beneath the Sichuan-Yunnan area in the eastern margin of the Tibetan plateau. *Chinese Journal of Geophysics* 60 (6), 2425–2441.

ChinArray (2008). China seismic array waveform data, China Earthquake Administration. doi:10.12001/ChinArray.Data

Crampin, S., and Peacock, S. (2008). A review of the current understanding of seismic shear-wave splitting in the Earth's crust and common fallacies in interpretation. *Wave Motion* 45 (6), 675–722. doi:10.1016/j.wavemoti.2008.01.003

Dong, Y. P., Zhu, B. Q., Chang, X. Y., and Zhang, G. W. (2002). Geochemistry of the basalts from north of the shizong-mile belt, eastern yunnan province: Constraints on the tectonic framework of the south China continent. *Acta Petrologica Sinica* 18 (1), 37–46. doi:10.3321/j.issn:1000-0569.2002.01.005

Ekström, G., Nettles, M., and Dziewoński, A. M. (2012). The global CMT project 2004-2010: Centroid-moment tensors for 13,017 earthquakes. *Phys. Earth Planet. Inter.* 200-201, 1–9. doi:10.1016/j.pepi.2012.04.002

Fang, L., Wu, J., and Lu, Z. (2009). Rayleigh wave group velocity tomography from ambient seismic noise in North China. *Chinese Journal of Geophysics* 52 (3), 663–671. *(in Chinese)*.

Flesch, L. M., Holt, W. E., Silver, P. G., Stephenson, M., Wang, C. Y., and Chan, W. W. (2005). Constraining the extent of crust-mantle coupling in central Asia using GPS, geologic, and shear wave splitting data. *Earth Planet. Sci. Lett.* 238, 248–268. doi:10.1016/j.epsl.2005.06.023

Gao, Y., Wu, J., Fukao, Y., Shi, Y., and Zhu, A. (2011). Shear wave splitting in the crust in North China: Stress, faults and tectonic implications. *Geophys. J. Int.* 187, 642–654. doi:10.1111/j.1365-246X.2011.05200.x

Gao, Y., Shi, Y., Wu, J., and Tai, L. (2012). Shear-wave splitting in the crust: Regional compressive stress from polarizations of fast shear-waves. *Earthq. Sci.* 25, 35–45. doi:10.1007/s11589-012-0829-3

Gao, L., Yang, Z., Tong, Y., Wang, H., and An, C. (2015). New paleomagnetic studies of cretaceous and Miocene rocks from jinggu, Western yunnan, China: Evidence for internal deformation of the lanping-simao terrane. *J. Geodyn.* 89, 39–59. doi:10.1016/j.jog.2015.06.004

Gilley, L., Harrison, T., Leloup, P., Ryerson, F., Lovera, O., and Wang, J. (2003). Direct dating of left-lateral deformation along the Red River shear zone, China and Vietnam. *Journal of Geophysical Research Solid Earth* 108 (B2). doi:10.1029/2001jb001726

Guan, Y., Wang, J., Li, P., Cao, D., and Liu, J. (2006). Characteristics of the middle axial tectonic belt in the Lanping-Simao basin, Western Yunnan, and its research significance. *Geology in China* 33 (4), 832–841. doi:10.3969/j.issn.1000-3657.2006.04.013

Guo, L., Liu, Y., Li, C., Xu, W., and Ye, L. (2009). SHRIMP zircon U–Pb geochronology and lithogeochemistry of Caledonian granites from the Laojunshan area, southeastern Yunnan province, China: Implications for the collision between the Yangtze and Cathaysia blocks. *Geochemical Journal* 43, 101–122. doi:10.2343/geochemj.1.0012

Guo, L., Gao, R., Shi, L., Huang, Z., and Ma, Y. (2019). Crustal thickness and Poisson's ratios of South China revealed from joint inversion of receiver function and gravity data. *Earth Planet. Sci. Lett.* 510, 142–152. doi:10.1016/j.epsl.2018.12.039

He, H., Fang, Z., and Li, P. (1993). A preliminary approach to the fault activityof southern segment on xiaojiangwest branch fault. *Journal of Seismological Research* 16 (3), 291–298.

Huang, Z., Wang, L., Xu, M., Ding, Z., Wu, Y., Wang, P., et al. (2015). Teleseismic shear-wave splitting in SE Tibet: Insight into complex crust and upper-mantle deformation. *Earth Planet. Sci. Lett.* 432, 354–362. doi:10.1016/j.epsl.2015.10.027

Jin, H., Gao, Y., Su, X., and Fu, G. (2019). Contemporary crustal tectonic movement in the southern Sichuan-Yunnan block based on dense GPS observation data. *Earth and Planetary Physics* 3 (1), 53–61. doi:10.26464/epp2019006

Kondo, K., Mu, C., Yamamoto, T., Zaman, H., Miura, D., Yokoyama, M., et al. (2012). Oroclinal origin of the Simao arc in the Shan-Thai block inferred from the cretaceous palaeomagnetic data. *Geophys. J. Int.* 190, 201–216. doi:10.1111/j.1365-246X.2012.05467.x

Lev, E., Long, M. D., and van der Hilst, R. D. (2006). Seismic anisotropy in Eastern Tibet from shear wave splitting reveals changes in lithospheric deformation. *Earth Planet. Sci. Lett.* 251, 293–304. doi:10.1016/j.epsl.2006.09.018

Li, C., He, D., Sun, Y., He, J., and Jiang, Z. (2014). Structural characteristic and origin of intra-continental fold belt in the eastern Sichuan basin, South China Block. *J. Asian Earth Sci.* 111, 206–221. doi:10.1016/j.jseaes.2015.07.027

Li, Y., Hao, M., Song, S., Zhu, L., Cui, D., Zhuang, W., et al. (2021). Interseismic fault slip deficit and coupling distributions on the Anninghe-Zemuhe-Daliangshan-Xiaojiang fault zone, southeastern Tibetan Plateau, based on GPS measurements. *J. Asian Earth Sci.* 219, 104899. doi:10.1016/j.jseaes.2021.104899

Liang, S., Gan, W., Shen, C., Xiao, G., Liu, J., Chen, W., et al. (2013). Three-dimensional velocity field of present-day crustal motion of the Tibetan Plateau derived from GPS measurements. *Journal of Geophysical Research Solid Earth* 118 (10), 5722–5732. doi:10.1002/2013jb010503

Liang, C., Liu, Z., Hua, Q., Wang, L., Jiang, N., and Wu, J. (2020). The 3D seismic azimuthal anisotropies and velocities in the eastern Tibetan plateau extracted by an azimuth-dependent dispersion curve inversion method. *Tectonics* 39. doi:10.1029/2019TC005747

Liu, Q. Y., Van Der Hilst, R. D., Li, Y., Yao, H. J., Chen, J. H., Guo, B., et al. (2014). Eastward expansion of the Tibetan Plateau by crustal flow and strain partitioning across faults. *Nat. Geosci.* 7, 361–365. doi:10.1038/ngeo2130

Liu, C., Yao, H., Yang, H. Y., Shen, W., Fang, H., Hu, S., et al. (2019). Direct inversion for three-dimensional shear wave speed azimuthal anisotropy based on surface wave ray tracing: Methodology and application to yunnan, southwest China. *J. Geophys. Res. Solid Earth* 124, 11394–11413. doi:10.1029/2018JB016920

Liu, J., Wu, J., Wang, W., Fang, L., and Chang, K. (2020). Seismic anisotropy beneath the eastern margin of the Tibetan Plateau from SKS splitting observations. *Tectonophysics* 785, 228430. doi:10.1016/j.tecto.2020.228430

Lu, L., He, Z., Ding, Z., and Wang, C. (2014). Azimuth anisotropy and velocity heterogeneity of Yunnan area based on seismic ambient noise. *Chinese Journal of Geophysics (in Chinese)* 57 (3), 822–836. doi:10.6038/cjg20140312

Ma, J., Huang, J., and Fu, Y. (2022). Phase velocity tomography of Rayleigh and Love waves in the suture zone between the Yangtze and Cathaysia Blocks. *Chinese Journal of Geophysics (in Chinese)* 65 (4), 1255–1270. doi:10.6038/cjg2022P0217

Montagner, J. (1986). Regional three-dimensional structures using long-period surface waves. *Ann. Geophys.* 4 (B3), 283–294.

Pandey, P., Ramegowda, V., and Senthil-Kumar, M. (2015). Shared and unique responses of plants to multiple individual stresses and stress combinations: Physiological and molecular mechanisms. *Frontiers in Plant Science* 6, 723. doi:10.3389/fpls.2015.00723

Rabbel, W., and Mooney, W. D. (1996). Seismic anisotropy of the crystalline crust: What does it tell us? *Terra Nova* 8 (1), 16–21. doi:10.1111/j.1365-3121.1996.tb00721.x

Roger, F., Calassou, S., Lancelot, J., Malavieille, J., Mattauer, M., Zhiqin, X., et al. (1995). Miocene emplacement and deformation of the Konga Shan granite (Xianshui He fault zone, west Sichuan, China): Geodynamic implications. *Earth and Planetary Science Letters* 130 (1-4), 201–216. doi:10.1016/0012-821x(94)00252-t

Sato, K., Liu, Y., Wang, Y., Yokoyama, M., Yoshioka, S. Y., Yang, Z., et al. (2007). Paleomagnetic study of cretaceous rocks from Pu'er, Western yunnan, China: Evidence of internal deformation of the indochina block. *Earth and Planetary Science Letters* 258 (1-2), 1–15. doi:10.1016/j.epsl.2007.02.043

Shen, C., Mei, L., Xu, Z., X., Tang, J., and Tian, P. (2007). Fission track thermochronology evidence for Mesozoic-Cenozoic uplifting of Daba Mountain, central China. *Acta Petrologica Sinica* 23 (11), 2901–2910. doi:10.1631/jzus.2007.B0900

Shen, C. Y., Yang, G. L., Tan, H. B., Xuan, S. B., Wu, G. J., and Wang, J. (2015). Gravity anomalies and crustal density structure characteristics of profile Weixi-Guiyang. *Chinese Journal of Geophysics* 58 (11), 3952–3964. (in Chinese). doi:10.6038/cjg20151106

Sheng, S., Wan, Y., Hu, X., Gong, M., and Zhang, S. (2022). The influence of moderate earthquakes on the crustal stress field inferred from 5 moderate earthquakes in Yingjiang area. *Chinese Journal of Geophysics* 65 (6), 2063–2073. (in Chinese). doi:10.6038/cjg2022P0151

Shi, X. B., Qiu, X. L., Liu, H. L., Chu, Z. Y., and Xia, B. (2006). Thermochronological analyses on the cooling history of the Lincang granitoid bathotith, Western Yunnan. *Acta Petrologica Sinica* 22 (2), 465–479. doi:10.1016/j.sedgeo.2005.11.009

Shi, Y. T., Gao, Y., Wu, J., and Su, Y. J. (2009). Crustal seismic anisotropy in yunnan, southwestern China. *J. Seismol.* 13, 287–299. doi:10.1007/s10950-008-9128-9

Shi, Y., Gao, Y., Su, Y., and Wang, Q. (2012). Shear-wave splitting beneath yunnan area of southwest China. *Earthq. Sci.* 25, 25–34. doi:10.1007/s11589-012-0828-4

Shi, H., Shi, X., Glasmacher, U. A., Yang, X., and Stockli, D. F. (2016). The evolution of eastern Sichuan basin, Yangtze block since Cretaceous: Constraints from low temperature thermochronology. *Journal of Asian Earth Sciences* 116, 208–221. doi:10.1016/j.jseaes.2015.11.008

Silver, P. G., and Chan, W. W. (1991). Shear wave splitting and sub continental mantle deformation. *J. Geophys. Res.* 96, 16429–16454. doi:10.1029/91jb00899

Simons, D. (2002). Understanding effective treatments of myofascial trigger points. *Journal of Bodywork and movement therapies* 6 (2), 81–88. doi:10.1054/jbmt.2002.0271

Smith, M., and Dahlen, F. (1973). The azimuthal dependence of Love and Rayleigh wave propagation in a slightly anisotropic medium. *Journal of Geophysical Research* 78 (17), 3321–3333. doi:10.1029/jb078i017p03321

Su, Y., and Qin, J. (2001). Strong earthquake activity and relation to regional neotectonic movement in sichuan-yunnan region. *Geological Review* 17 (1), 24–34. (in Chinese). doi:10.3969/j.issn.1001-4683.2001.01.004

Sun, Y., Niu, F., Liu, H., Chen, Y., and Liu, J. (2012). Crustal structure and deformation of the SE Tibetan plateau revealed by receiver function data. *Earth Planet. Sci. Lett.* 349350, 186–197. doi:10.1016/j.epsl.2012.07.007–

Sun, Y., Liu, J., Zhou, K., Chen, B., and Guo, R. (2015). Crustal structure and deformation under the Longmenshan and its surroundings revealed by receiver function data. *Phys. Earth Planet. Inter.* 244, 11–22. doi:10.1016/j.pepi.2015.04.005

Tai, L. X., Gao, Y., Liu, G., and Xiao, Z. (2015). Crustal seismic anisotropy in the southeastern margin of Tibetan plateau by ChinArray data: Shear-wave splitting from temporary observations of the first phase. *Chinese Journal of Geophysics* 58 (11), 4079–4091. (in Chinese). doi:10.6038/cjg20151116

Tanaka, K., Mu, C., Sato, K., Takemoto, K., Miura, D., Liu, Y., et al. (2008). Tectonic deformation around the eastern Himalayan syntaxis: Constraints from the Cretaceous palaeomagnetic data of the Shan-Thai Block. *Geophys. J. Int.* 175, 713–728. doi:10.1111/j.1365-246X.2008.03885.x

Tarantola, A., and Valette, B. (1982). Generalized nonlinear inverse problems solved using the least squares criterion. *Reviews of Geophysics* 20 (2), 219–232. doi:10.1029/rg020i002p00219

Teng, J., Song, P., Dong, X., Liu, Y., Ma, X., and Yan, Y. (2019). The crust-mantle structure and geophysical boundary field characteristics of Panzhihua ancient mantle plume" relics. *Chinese Journal of Geophysics* 62 (9), 3296–3320. (in Chinese). doi:10.6038/cjg2019L0153

Tong, Y. B., Yang, Z., Zheng, L., Xu, Y. L., Wang, H., Gao, L., et al. (2013). Internal crustal deformation in the northern part of Shan-Thai Block: New evidence from paleomagnetic results of Cretaceous and Paleogene redbeds. *Tectonophysics* 608, 1138–1158. doi:10.1016/j.tecto.2013.06.031

Wang, C. Y., Flesch, L. M., Silver, P. G., Chang, L. J., and Chan, W. W. (2008). Evidence for mechanically coupled lithosphere in central Asia and resulting implications. *Geology* 36, 363–366. doi:10.1130/G24450A.1

Wang, F. Y., Pan, S. Z., Liu, L., Liu, B. F., Zhang, J. S., Deng, X. G., et al. (2014). Wide angle seismic exploration of yuxi-lincang profile—the research of crustal structure of the red river fault zone and southern yunnan. *Chinese Journal of Geophysics* 57 (10), 3247–3258. (in Chinese). doi:10.6038/cjg20141013

Wang, Q., Gao, Y., and Shi, Y. (2015). Rayleigh wave azimuthal anisotropy on the southeastern front of the Tibetan Plateau from seismic ambient noise. *Chinese Journal of Geophysics* 58 (11), 4068–4078. (in Chinese). doi:10.6038/cjg20151115

Wang, W., Wu, J., Fang, L., Lai, G., and Cai, Y. (2017). Crustal thickness and Poisson’s ratio in southwest China based on data from dense seismic arrays. *J. Geophys. Res. Solid Earth* 122, 7219–7235. doi:10.1002/2017JB013978

Wang, H., Wu, J., Zhou, S., Fang, L., Wang, W., and Liu, Y. (2020). Rayleigh wave azimuthal anisotropy in the Southeastern Tibetan Plateau from Eikonal tomography. *Chinese Journal of Geophysics* 63 (3), 1070–1084. (in Chinese). doi:10.6038/cjg2020N0104

Wang, J., Xu, C., Wen, Y., Zang, J., and Xian, Z. (2022). Characteristics of segmentation and interseismic coupling along the Red River fault from GPS observations. *Chinese Journal of Geophysics* (4), 1240–1254. (in Chinese). doi:10.6038/cjg2022P0174

Wang, M., and Shen, Z. (2020). Present-Day crustal deformation of continental China derived from GPS and its tectonic implications. *J. Geophys. Res. Solid Earth* 125. doi:10.1029/2019JB018774

Wu, J., Ming, Y., and Wang, C. (2004). Source mechanism of small-moderate earthquakes and tectonic stress field in Yunnan Province. *Acta Seismologica Sinica* 17 (5), 509–517. doi:10.1007/s11589-004-0032-2

Wu, J., Yang, T., Wang, W., Ming, Y., and Zhang, T. (2013). Three dimensional P wave velocity structure around Xiaojiang fault system and its tectonic implications. *Chinese J. Geophys.* 56, 2257–2267. *(in Chinese)*. doi:10.6038/cjg20130713

Xiang, H. F., Xu, X. W., Guo, S. M., Zhang, W. X., Li, H. W., and Yu, G. H. (2002). Sinistral thrusting along the Lijiang-Xiaojinhe fault since quaternary and its geologic-tectonic significance-Shielding effect of transverse structure of intracontinental active block. *Seismology and Geology* 24 (2), 188–198.

Xiong, X., Gao, R., Wang, H., Zhang, J., and Guo, L. (2016). Frozen subduction in the Yangtze block: Insights from the deep seismic profiling and gravity anomaly in east Sichuan fold belt. *Earthq. Sci.* 29, 61–70. doi:10.1007/s11589-016-0140-9

Xu, X., Wen, X., Zheng, R., Ma, W., Song, F., and Yu, G. (2003). Pattern of latest tectonic motion and its dynamics for active blocks in Sichuan-Yunnan region, China. *Science in China Series D Earth Sciences* 46 (2), 210–226. doi:10.3969/j.issn.1674-7240.2003.z1.017

Xu, T., Zhang, Z., Liu, B., Chen, Y., Zhang, M., Tian, X., et al. (2015). Crustal velocity structure in the Emeishan large igneous province and evidence of the Permian mantle plume activity. *Science China Earth Sciences* 58 (7), 1133–1147. doi:10.1007/s11430-015-5094-6

Xu, Z., Huang, Z., Wang, L., Xu, M., Ding, Z., Wang, P., et al. (2016). Crustal stress field in yunnan: Implication for crust-mantle coupling. *Earthq. Sci.* 29, 105–115. doi:10.1007/s11589-016-0146-3

Xu, Y., Tong, Y., Wang, H., and Yang, Z. (2017). Paleomagnetic constrains on the reversed S shaped structure deformation of the lanping—simao basin in the southeastern xizang (tibet) plateau. *Geological Review (in Chinese)* 63 (3), 19. doi:10.16509/j.georeview.2017.03.002

Xu, Y. G., and Chung, S. L. (2001). The Emeishan large igneous province: Evidence for mantle plume activity and melting conditions. *Geochimica* 30 (1), 1–9.

Xu, Z. H. (2001). A present-day tectonic stress map for eastern Asia region. *Acta Seismologica Sinica* 14 (5), 524–533. doi:10.1007/bf02718059

Yang, T., Wu, J., Fang, L., and Wang, W. (2014). Complex structure beneath the southeastern Tibetan plateau from teleseismic P-wave tomography. *Bull. Seismol. Soc. Am.* 104, 1056–1069. doi:10.1785/0120130029

Yang, Y., Hu, S., Yao, H., Fang, L., and Wu, J. (2020). Crustal shear wave velocity and radial anisotropy in the Xiaojiang fault zone system (SE Tibet) revealed by ambient noise interferometry. *Tectonophysics* 792, 228594. doi:10.1016/j.tecto.2020.228594

Yang, X., Li, Y., Afonso, J. C., Yang, Y., and Zhang, A. (2021). Thermochemical state of the upper mantle beneath south China from multi-observable probabilistic inversion. *J. Geophys. Res. Solid Earth* 126. doi:10.1029/2020JB021114

Yao, H., Van Der Hilst, R. D., and de Hoop, M. V. (2006). Surface-wave array tomography in SE Tibet from ambient seismic noise and two-station analysis - I. Phase velocity maps. *Geophys. J. Int.* 166, 732–744. doi:10.1111/j.1365-246X.2006.03028.x

Yao, H., Van Der Hilst, R. D., and Montagner, J. P. (2010). Heterogeneity and anisotropy of the lithosphere of SE Tibet from surface wave array tomography. *J. Geophys. Res. Solid Earth* 115, B12307. doi:10.1029/2009JB007142

Yuan, P., Jiang, W., Wang, K., and Sneeuw, N. (2018). Effects of spatiotemporal filtering on the periodic signals and noise in the GPS position time series of the crustal movement observation network of China. *Remote Sensing* 10 (9), 1472. doi:10.3390/rs10091472

Zhang, Z., Badal, J., Li, Y., Chen, Y., Yang, L., and Teng, J. (2005). Crust-upper mantle seismic velocity structure across Southeastern China. *Tectonophysics* 395, 137–157. doi:10.1016/j.tecto.2004.08.008

Zhang, L., Jin, S., Wei, W., Ye, G., Jing, J., Dong, H., et al. (2015). Lithospheric electrical structure of South China imaged by magnetotelluric data and its tectonic implications. *J. Asian Earth Sci.* 98, 178–187. doi:10.1016/j.jseaes.2014.10.034

Zhao, B., Huang, Y., Zhang, C., Wang, W., Tan, K., and Du, R. (2015). Crustal deformation on the Chinese mainland during 1998–2014 based on GPS data. *Geod. Geodyn.* 6, 7–15. doi:10.1016/j.geog.2014.12.006

Zheng, C., Ding, Z. F., and Song, X. D. (2016). Joint inversion of surface wave dispersion and receiver functions for crustal and uppermost mantle structure in Southeast Tibetan Plateau. *Chinese Journal of Geophysics* 59 (9), 3223–3236. doi:10.6038/cjg20160908

Zheng, X. F., Yao, Z. X., Liang, J. H., and Zheng, J. (2010). The role played and opportunities provided by igp dmc of china national seismic network in wenchuan earthquake disaster relief and researches. *Bull. Seismol. Soc. Am.* 100, 2866–2872. doi:10.1785/0120090257

Zhu, G., Yu, J. H., Zhou, X., Wang, X., and Wang, Y. (2019). The Western boundary between the Yangtze and Cathaysia blocks, new constraints from the Pingbian Group sediments, southwest South China Block. *Precambrian Res* 331, 105350. doi:10.1016/j.precamres.2019.105350

Zhu, Z., Wang, X., Liu, Z., and Liang, C. (2021). Seismic anisotropy in the southeastern margin of the Tibetan Plateau revealed by ambient noise tomography based on high-density array. *Acta Geophys. Sin.* 64, 823–837. doi:10.6038/cjg2021O0440

frontiers | Frontiers in Earth Science

TYPE Original Research
PUBLISHED 24 February 2023
DOI 10.3389/feart.2023.1078434

OPEN ACCESS

EDITED BY
Chunquan Yu,
Southern University of Science and Technology, China

REVIEWED BY
Hanchao Jian,
Woods Hole Oceanographic Institution, United States
Tianze Liu,
University of California, San Diego, United States

*CORRESPONDENCE
Zhiming Bai,
✉ bbzzmm@mail.iggcas.ac.cn

SPECIALTY SECTION
This article was submitted to Solid Earth Geophysics, a section of the journal Frontiers in Earth Science

RECEIVED 24 October 2022
ACCEPTED 13 February 2023
PUBLISHED 24 February 2023

CITATION
Bai Z, Zhao L, Xiao W, Xu T and Badal J (2023), P-wave velocity structure and implications for magmatism and metallogenesis in the southern Altaids: Constraint from wide-angle seismic data along the Altai-Eastern Tianshan traverse. *Front. Earth Sci.* 11:1078434.
doi: 10.3389/feart.2023.1078434

P-wave velocity structure and implications for magmatism and metallogenesis in the southern Altaids: Constraint from wide-angle seismic data along the Altai-Eastern Tianshan traverse

Zhiming Bai[1]*, Liang Zhao[1], Wenjiao Xiao[2,1], Tao Xu[1] and José Badal[3]

[1]State Key Laboratory of Lithospheric Evolution, Institute of Geology and Geophysics, Chinese Academy of Sciences, Beijing, China, [2]National Key Laboratory of Ecological Security and Resource Utilization in Arid Areas, Xinjiang Institute of Ecology and Geography, Chinese Academy of Sciences, Urumqi, China, [3]Physics of the Earth, Sciences B, University of Zaragoza, Zaragoza, Spain

Altaids in the Central Asian Orogenic Belt (CAOB) is one of the world's largest orogenic belts containing mineral deposits. Together with the Junggar terrain they open an important window to study the Paleozoic tectonic evolution of the CAOB. In this paper, we analyze a 637-km-long wide-angle refraction/reflection seismic profile across the Altai-Eastern Tianshan orogenic belt in the southern Altaids, conducted in September 2018 using 10 large explosive charges fired in drilled holes. We use a traveltime inversion method to reconstruct the lithospheric P-wave velocity structure along the profile. The lithosphere is composed of a 43-55-km-thick crust, a ~10-km-thick crust-mantle transition layer beneath the Altai Mountain, and a ~25-km-thick layer of lithospheric mantle. The results clearly reveal: a prominent Moho uplift beneath the Yemaquan Island Arc, two major crustal-scale low-velocity anomalies (LVAs) beneath the Yemaquan Arc and Bogda Mountain, and three high-velocity anomalies (HVAs) near the surface around the Kalatongke, Yemaquan and Kalatage mining areas. We hypothesize that the subduction of the Paleo-Asian Ocean occurred with strong mantle upwelling. We suggest that continued compression of the Paleo-Asian Ocean causes the delamination of lithosphere, as well as asthenospheric material upwelling and magma underplating into the crust. Consistently, Paleozoic mafic-ultramafic rocks and mantle-derived minerals related to gold, copper and nickel deposits, are widely extended in the area. Our results show that the P-wave velocity-depth curves for deeper depths (>30 km) in the southern Altai and Junggar Basin are close to those of the continental arcs and global continent average. Despite powerful Paleozoic subduction activity, orogeny and volcanism strongly modified the lower crust in the region, part of ancient continental crust was still preserved below the southern Altai and Junggar Basin. In addition, the upper part (depth 5–30 km) of the velocity-depth curve for the Junggar Basin is close to that of the Costa Rica volcanic front and the British Columbia accreted terrain, suggesting that Paleozoic orogenic activity has intensively reconstructed the upper-middle crust beneath the Junggar Basin.

KEYWORDS

wide-angle seismic profiling, P-wave velocity structure, magmatism and metallogenesis, east Altai-Tianshan traverse, central Asian orogenic belt

Highlights

Crustal structure across the Altai-Eastern Tianshan orogenic belt with a 637-km-long wide-angle seismic profile

Prominent HVAs around the Kalatongke, Yemaquan and Kalatage mining areas.

Apparent LVAs related to the subduction of the Paleo-Asian Oceanic plate.

Signifcant Moho uplift and a crust-mantle transition layer beneath the Altai Mountain due to mantle upwelling.

Upper-middle crustal property of Junggar Basin similar to the Costa Rica volcanic front and the British Columbia accreted terrain.

Introduction

Altaids is part of the central Asian orogenic belt, which is found among the large cratons in Eastern Europe (Poland), Siberia, North China, and Tarim. It is the largest continental metallogenic domain in the world (Xiao et al., 2015; Xiao et al., 2018). This region experienced the Precambrian mantle plume explosion, Paleo-Asian Ocean closure, multi-oceanic basin, multiple subduction and complex multidirectional convergent accretion orogenic process during the Paleozoic. All these processes gave rise to a series of tectonic and thermal events, including subduction and magma accretion, and produced world-class gold, copper and other mineral resources. Hence, the investigation of the physical structure, geodynamics and metallogeny of the central Asian orogenic belt has become an attractive Frontier topic in the field of geosciences.

North Xinjiang in western China has undergone strong plate accretion, orogenic processes and magma events in the Paleozoic due to which ophiolite suites, mafic and ultramafic rocks and multi-type metal deposits were produced, including the Kalatongke copper-nickel mine and the Dunbastao gold deposit along the Erqis fault, the Cu-Au metallogenic systems represented by the Qingshuiquan, Shuangquan and Nanmingshui ore deposits (of orogenic, porphyry and epithermal hydrothermal type, respectively) along the Kalamaili fault, and the Kalatage porphyry copper-gold deposit near the southern margin of the Altai-Eastern Tianshan traverse. However, there is still a lack of knowledge and lively controversy regarding the tectonic evolution and metallogeny process in the southern Altaids.

First, despite some geological evidence has shown that the late Paleozoic ultramafic rocks and widely developed Cu-Ni, Ti-Fe and Cr-Fe deposits in the Altai-Eastern Tianshan are closely related to mantle-derived magma (e.g., Mao et al., 2006; Dong et al., 2009; Qian et al., 2011; Wang et al., 2013), the properties of the crustal material and the structural characteristics beneath different blocks need further investigation. For example, whether or not there was a preserved mafic component or special structure related to the Paleozoic subduction or orogenic process in the crust remains an interesting question that limits the discussion of metallogenic mechanism and regional geodynamics.

Based on active seismic source data acquired along the Altai-Altyn geological section, Wang et al. (2003) and Wang et al. (2004) obtained the seismic velocity structure and Poisson's ratio of the crust. Their results show that the crustal thickness is about 50 km for most segments of the profile, although it increases up to 56 km in southern Altai Mountain and decreases up to 46 km in the Junggar Basin; they also revealed some local high-velocity anomalies (HVAs) with Vp greater than 7.0 km/s and high Poisson's ratio of 0.26–0.28 below the Altai Mountain and Junggar Basin. A basic composition was suggested for the upper-middle crust and mafic granulite for the lower crust. Nevertheless, due to several drawbacks, such as a fairly large firing spacing of 63–125 km, a receiver spacing of 2–4 km, and an incomplete observation system, the zones of interest, such as orogenic belts, main sutures and the typical areas of mineral concentration were not sufficiently illuminated, so the fine-scale velocity structure of the region and the Paleozoic tectonics and metallogenic mechanism were not fully determined.

Second, the existence of an ancient basement is still a matter of discussion. For example, it was believed that Altaids had a Precambrian basement in the past (17-8 Ga or later), which was supported by the Sm-Nd age and the Nd isotopic pattern age (Hu et al., 2000; Hu et al., 2000; Fang et al., 2002). However, some studies based on the average zircon age of gneiss have questioned whether there is an ancient basement in the Altai orogen (e.g., Long et al., 2008; Sun et al., 2008). Nd isotope mapping shows that the central part of the deep crust in the Altai orogenic belt is old and the southern margin is new; there is an ancient basement in the lower part of the central block; most of the crustal growth below the Altai Mountains is in a horizontal direction (Wang et al., 2010; Wang et al., 2020). Faced with this scenario, geophysical evidence is still lacking.

The Junggar Basin has experienced multiple periods of north-south compression, basin-forming evolution and tectonic deformation since the Paleozoic (He et al., 2005). Wu. (1986) suggested that the basement of the Junggar Basin was composed of Cambrian-Carboniferous oceanic basins, intra-oceanic island arcs, and micro-continent blocks. Some studies (e.g., Li et al., 2000; Qu et al., 2008) inferred that the eastern Junggar Basin has late Pre-Ordovician continental crustal basement, and Qu et al. (2008) even point out that the basement layer is continental crust characterized by a "double basement." However, based on the results of isotopic and geochemical research, other authors (e.g., Hu et al., 2000; Wang et al., 2019) inferred that the basement layer of Junggar Basin is formed by oceanic crust, and that it may be the trace of a residual oceanic basin with a crust younger than the Altai and Tianshan Mountains. Despite this, mapping results of the Altai–East Junggar–East Tianshan regional isotope corridor show that the East Junggar granites have high $\varepsilon_{Nd}(t)$ (+8–+1) and low T_{DM} (0.7-0.5 Ga) values, which implies that it is young material from the mantle; the deep material mainly has a relatively new (juvenile crust) structural composition (Hf model age is 0.67–0.20 Ga), and the Junggar orogen belt is dominated by vertical growth (Wang et al., 2020).

Against this background, in September 2018, we conducted a 637-km-long wide angle, deep seismic sounding (DSS) experiment

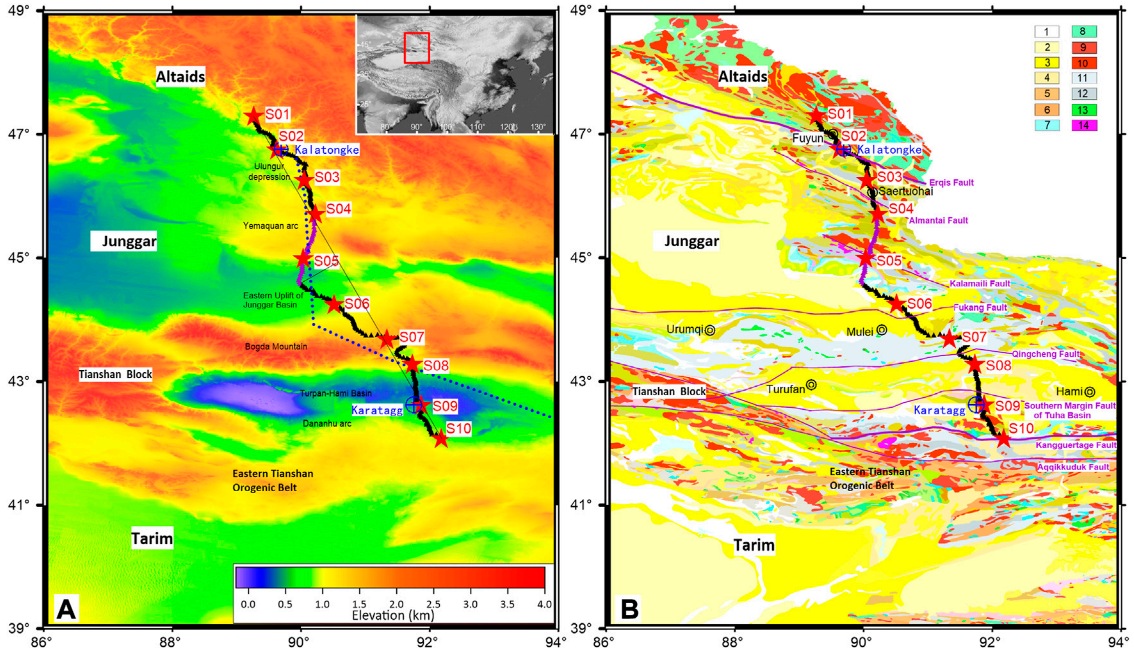

FIGURE 1
The topography **(A)** and geological setting **(B)** of Altai-Tianshan DSS profile. Black triangles: EPS-type digital seismographs; purple triangles: PDS-2 type digital seismographs; red stars: shot point locations (S01-S10). The blue dashed line in Panel **A** denotes the location of old DSS line given by Wang et al. (2003) in this region. The lithology in Panel **B**: 1) Quaternary Holocene alluvial deposits. 2) Upper Pleistocene and Holocene weathered sedimentary. 3) Upper Pleistocene and Holocene water sedimentary. 4) Tertiary sedimentary. 5) Lower Proterozoic. 6) Middle Proterozoic. 7) Mesozoic. 8) Paleozoic. 9) Devonian-Permian granites and granodiorites. (10) Proterozoic granites and granodiorites. (11) Middle Carboniferous sedimentary and volcanic rocks. (12) Early Carboniferous andesites and basalts; (13) Gabbro and diabase. (14) Peridotite and diabase peridotite.

across the Altai-Eastern Tianshan traverse to acquire field wide-angle seismic data. The goal was to reconstruct the crust-upper mantle structure, understand the Palaeozoic accretion and mountain building process in the frame of the ancient Asian Ocean plates, and explore the potential tectonic mechanism for mineral deposits in the area. With the collected seismic data, we adopted the traveltime inversion method Rayinvr (Zelt and Smith, 1992; Zelt and White, 1995) to reconstruct the lithospheric structure of the region more clearly, and finally acquired its seismic properties related to the Paleozoic subduction and block collage activities in the region.

Junggar geological setting

The north-south Altai-Eastern Tianshan profile is located on the eastern margin of the Junggar terrane. It starts at the Altai Mountains and passes through Altaids, Ulungur depression, Yemaquan Arc, eastern uplift of the Junggar Basin, Bogda Mountain, Turpan-Hami Basin and the Dananhu-Tousuquan Arc near the Kanggur suture zone (Figure 1).

The Altai Mountains show many geological records related to Paleozoic ridge subduction, such as adakites, niobium-rich basalts, boehmites, peridotites, A-type granites, bimodal volcanic rocks, ophiolite in back-arc basin, Alaska-type basic-ultrabasic complex, metamorphic belts, acid dyke swarm, *etc.* Xiao et al. (2019) pointed out that the main body of the Altai magmatic arc is formed by the subduction and accretion of the Paleo-Asian Ocean during the Paleozoic.

The Ulungur depression is near the south of Altai Mountains and has a Carboniferous basement layer, and also an upper Triassic, Jurassic and Cretaceous sedimentary layer (Zhu, 2009; Chen et al., 2010), where rich oil-gas resources were explored in the last 10 years. The Erqis ophiolite belt and the Almantai ophiolite belt are located on its north and south sides, respectively (Figure 1). The Yemaquan Arc between the Almantai and Kalamaili ophiolite belts is a part of the eastern Junggar orogenic belt whose folded basement is a volcanic marble basin.

The Junggar Basin has a Cambrian-Carboniferous basement layer consisting of an ocean basin, island arc and microcontinents (Wu, 1986; Bian et al., 2010). From Carboniferous to Cenozoic time, it has experienced multistage tectonic superposition and developed rich oil and gas resources (Zheng et al., 2018).

Bogda Mountain in the southern half of the reference profile has a mid-height mountain and low-hill topography that has been strongly eroded and cut; its main body is composed of a series of Carboniferous marine volcanic-sedimentary rocks coming from small-scale granites, diorites, potash feldspar granites and gabbro-diabase (Gu et al., 2001), although its two sides are Permian conglomerate, sandstone, siltstone and basalts (Su et al., 2005).

TABLE 1 Shot point locations and respective shot charges.

Shot code	Latitude N	Longitude E	Altitude (m)	Charge (kg)
S01	47.37628	89.13358	1,086	3,000
S02	46.73469	89.61982	993	3,000
S03	46.24046	90.04805	996	2,520
S04	45.69111	90.22572	1,192	1,992
S05	44.97589	90.02917	948	2,016
S06	44.23106	90.51181	842	3,000
S07	43.66926	91.33282	1,639	1,992
S08	43.26058	91.72744	797	1,992
S09	42.60164	91.86958	525	2,520
S10	42.05881	92.17778	838	3,000

The Turpan-Hami Basin on the south side of Bogda Mountain (Figure 1) is a continental intermountain basin formed by the Indochina-Yanshanian movement and especially by the northward extrusion of the Indian Plate since the Miocene (Yu and Fu, 1993). Here the basement is composed of Devonian, Carboniferous, and Lower Permian marine intermediate bases, intermediate acid volcanic rocks, volcanic tuffaceous sandstones, mudstones, limestones and Variccian acid magmatic rocks.

The Dananhu-Tousuquan Island Arc at the southernmost end of the profile is part of the eastern Tianshan orogenic belt, and the adjacent Kanggurtag (Figure 1) belt is thought to preserve clear evidence of the subduction of the Paleo-Asian oceanic plate and the arc-continent collision. The Paleozoic strata developed in this belt are composed of basic igneous rocks, acid igneous rocks, volcanic sedimentary rocks, clastic rocks and limestones (Xu et al., 2005). The intrusive rocks are mainly composed by granite, granodiorite, monzogranite, *etc.* The basic-ultrabasic complexes, whose ages range from the Middle Ordovician (Xiao et al., 2004) to the Permian (Li et al., 2006; Wang et al., 2019), are extensively exposed here.

Data

Seismic data acquisition

The seismic experiment was carried out in September-October 2018. The 637-km-long wide-angle reflection/refraction profile, with an azimuth near N30W, was deployed from the Altai Mountain to the eastern Tianshan orogenic belt (Figure 1).

Several holes were drilled and explosive charges were fired under the control of the Geophysical Exploration Centre of the China Earthquake Administration, which was in charge of acquiring seismic data. Field operations were carried out using a dense coverage observation system consisting of 10 shots that were recorded by 595 three-component digital seismographs spaced ~1 km apart. Charges of 2–3 tons of explosive were fired at shot points spaced at 54–89 km. The locations of the shot points from S01 to S10, their respective altitudes and the triggered charges are given in Table 1.

The 5-minute-long seismic signals recorded by digital seismographs were initially sampled at 200 Hz, and then band-pass filtered within the 1–10 Hz frequency band for P-waves. Besides this, to make the seismic reflections more clear to identify, we firstly normalized the records, then enlarged the signal by multiplying the signal-to-noise ratio (SNR) and constant 2.5 so as to make the reflections to be confidently picked, where SNR=Amp/(Amp+Amp0), Amp is the average amplitude within short time-window (0.4 s) around each time-point, and the Amp0 is the minimum average amplitude within 0.4 s before this time-point. All common shot gathers are plotted on a reduced time scale by velocity of 6.0 km/s (Figure 2).

The other gathers for shots S03-S10 has been included in the Supplementary Files. Shot numbers locate at the lower left corner of each graph, and the time axis were reduced at a velocity of 6.0 km/s. Picked traveltime data are drawn as blue lines, while final velocity model traveltimes are drawn as red triangles. Moreover, the slope of the lines at the lower right corner indicates the apparent velocities of the first arrival phase Pg and Pn, which were labeled as red digits in the diagrams.

To apply a 2-D modeling approach for this crooked shot-receiver array, the shot locations are projected perpendicularly onto the line between shots S01 and S10 while maintaining the true source-receiver offsets for subsequent modeling, however this crooked profile indicates the out-of-plane sampling and averaging of structure by the final 2-D model.

Seismic phases on the record sections

Based on the 10 shots fired and the seismic gathers we pick 7,991 travel time data, which can be classified into eight groups: first arrivals of Pg waves, intracrustal reflections P1, P2, P3, Moho reflections Pm1 and Pm2, PL reflections from the bottom of the lithosphere, and first arrivals of the refracted Pn phase along the top of the upper mantle.

The first Pg arrivals can be generally observed at offsets of up to 90–130 km with an apparent P-wave velocity of 5.81–6.38 km/s (Figure 3). The Pg traveltimes at some places are obliviously delayed, which include the south to shots S03, S05, S07, S08 and the north to

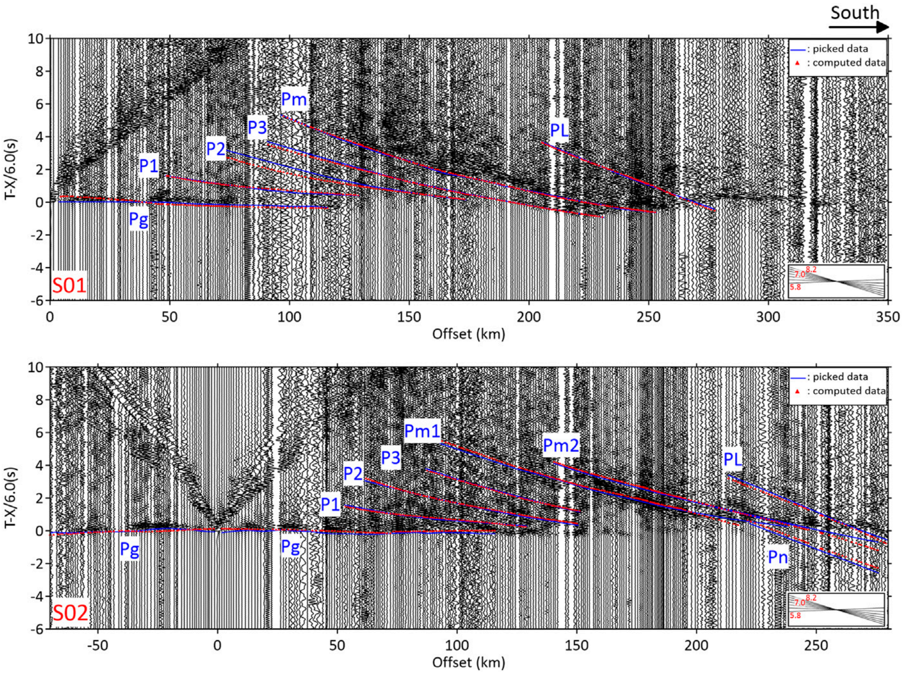

FIGURE 2
Shot gathers for shot S01 and S02. The other gathers for shots S03-S10 has been included in the suppmentary files. Shot numbers locate at the lower left corner of each graph, and the time axis were reduced at a velocity of 6.0 km/s. Picked traveltime data are drawn as blue lines, while final velocity model traveltimes are drawn as red triangles. Moreover, the slope of the lines at the lower right corner indicates the apparent velocities of the first arrival phase Pg and Pn, which were labeled as red digits in the diagrams.

shot S09. These delayed data agree with a surface depression or sedimentary basins, such as the Ulungur depression, Junggar Basin and Turpan-Hami Basin (Tuha basin). Secondly, the Pg traveltime curves of south branch for shots S02 and S04, and north branch for shots S05, S07 and S10 (Figure 2), show an apparently high P-wave velocity of 6.2–6.4 km/s, which means high velocity anomalies (HVAs) in the shallow crust beneath the Yemaquan Arc, Bogda Mountain, Dananhu Arc, and around the Kalatongke and Kalatage mining areas. Moreover, some Pg traveltime curves (south branch for shots S01 and S09) extend as a horizontal line, which indicates that the apparent P-wave velocity is nearly 6.0 km/s.

The intracrustal reflections P1, P2, P3 come from the interfaces C1, C2, and C3, respectively, at average depths of 18.0, 29.7 and 40.17 km, and reveal average velocities of 6.11, 6.35 and 6.49 km/s (Figures 2, 3) computed from the well-known $X^2 - T^2$ relationship for reflections (Bamford, 1978). In general, the P1 reflection has large amplitude for all shots, indicating that the layers above and below of the C1 interface have a large P-wave impedance contrast. The reflected phases P2 and P3 show the characteristics of continuity and strong amplitude in most sections, such as the southern branch for S02, S05, S06 and the northern branch of S07 and S09 for phase P2, and the southern branch of S02, S03, S04, S05 and northern branch for S07 and S10 for phase P3 (Figure 2), despite the fact that some branches present characteristics of weak energy or little continuity.

The Moho reflection Pm1 extends over a offset of 90–280 km with strong apparent amplitude and reveals a P-wave velocity of 6.60 km/s and an approximate crustal thickness of 51.0 km (Figures 2, 3). The Pm1 phases clearly arrive earlier at offsets of around 135 km and 200 km, as can be seen for the southern branch for S03 and the northern branch for S05, respectively, indicating that Moho uplift likely exists beneath the Yemaquan Arc.

The reflection Pm2 from the bottom of crust beneath the Altai Mountain appears clearly identified at an offset range of 100–270 km, such as the south branch for S02 and the north branch for S03 and S04, suggesting an average crustal thickness of 61.4 km and a velocity of 6.77 km/s (Figures 2, 3). The apparent high P-wave velocity of 6.77 km/s suggests that a transition layer between the crust and the mantle probably exists below Altai Mountain.

The southern records for shots S02, S03, S04 and the northern records for shots S06 and S07 show a clear Pn phase whose average apparent P-wave velocity varies from 7.8 km/s to 8.4 km/s (Figures 2, 3). The reflected phase PL is identified on the southern records for shots S01, S02, S04, S05 and on the northern records for shots S06, S07, S08 and S10. This event covers an offset from ~200 km to ~300 km and indicates an average lithospheric thickness of 85.8 km and a velocity of 7.20 km/s.

To display all the above data together, in Figure 3A we show in parentheses depths and seismic velocities deduced from the identified seismic phases on each record section, and in Figure 3B the spatial distribution of velocities and depths together with possible reflection limits based on previously calculated back-projected locations (dotted lines), which were determined using the $X^2 - T^2$ method from the above traveltime data. The regional lithosphere shows some basic features: both the Moho discontinuity and the lithosphere-asthenosphere boundary

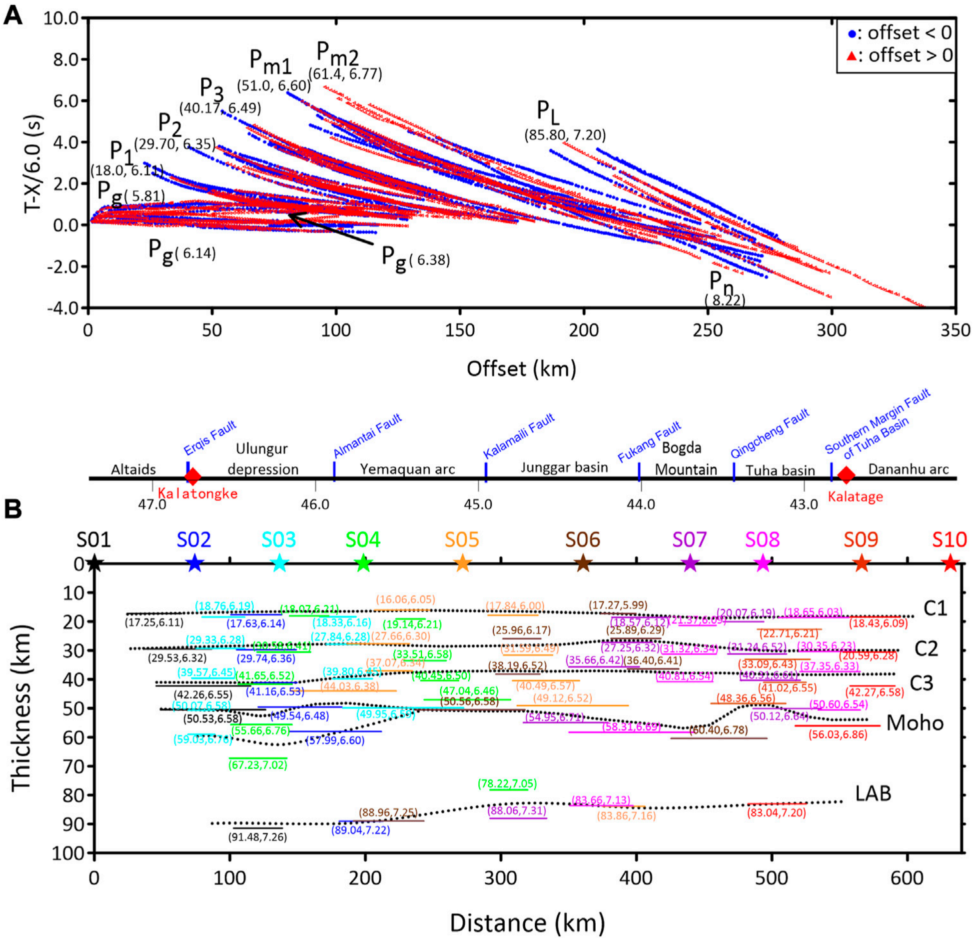

FIGURE 3
(A) Traveltime-offset curves on a reduced time scale by velocity of 6.0 km/s. In parentheses: reflection depths and P-wave velocities deduced from the seismic phases previously identified on each record section. Both the observed data (blue dotted lines) and the calculated data from the final velocity model (red triangles) have also been included for further comparison. **(B)** Spatial distribution of back-projected velocities, depths and possible reflections (dotted lines) based on the X^2-T^2 method. Top: structures and faults traversed by the profile; red diamonds mark the location of the Kalatongke and Kalatage mineral deposits to the north and south of the profile, respectively.

(LAB) below Altai Mountain lie deeper than in other sections; they are also deeper below Bogda Mountain, while the Moho below the Tuha Basin is uplifting significantly.

Methods

Forward and inverse modeling

To model the seismic events described above, we constructed an initial 2-D model using a combination of forward modeling of amplitudes and traveltimes by trial-and-error (Cerveny et al., 1977; Cerveny and Psencik, 1984), and then inverting the structure of the lithosphere using the ray inversion method (Zelt and Smith, 1992; Zelt and White, 1995; Zhang et al., 2013).

The 2-D ray-tracing equations are a pair of first-order ordinary differential equations that can be written in two ways (Cerveny et al., 1977; Cerveny and Psencik, 1984; Xu et al., 2014):

$$\frac{dz}{dx} = \cot\theta, \ \frac{d\theta}{dx} = \frac{(v_z - v_x \cot\theta)}{v} \tag{1}$$

or

$$\frac{dx}{dz} = \tan\theta, \ \frac{d\theta}{dz} = \frac{(v_z \tan\theta - v_x)}{v} \tag{2}$$

with initial conditions

$$x = x_0, \ z = z_0, \quad \theta = \theta_0$$

The variable θ is the angle between the tangent to the ray and the z-axis, v is the wave velocity and v_x and v_z are partial derivatives of velocity with respect to the x and z coordinates, respectively (z is positive downward). The point (x_0; z_0) is the source location and θ_0 is the ray take-off angle. Formula 1 is solved with x as the integration variable when the ray path is near-horizontal, and Formula 2 is solved with z as the integration variable when the ray path is near-vertical (Zelt & Smith, 1992).

Assuming that the traveltime inversion is a linear problem around a starting model, its equation is expressed as:

TABLE 2 Ray tracing details for individual seismic phases.

Seismic phase	Number of picked data	RMS s)	χ2
Pg	1,632	0.183	3.459
P1	965	0.139	0.686
P2	1,137	0.154	0.706
P3	1,185	0.126	0.457
Pm1	1917	0.151	0.893
Pm2	244	0.145	0.577
PL	631	0.146	0.634
Pn	280	0.102	0.502

RMS: root-mean-square error; χ^2 is the chi-squared value which can be described as the formula $\chi^2 = \frac{1}{n}\sum_1^n \frac{(t_i^c - t_i^o)^2}{u_i^2}$, where the t_i^c is the i-th computed travel-time data, t_i^o is the i-th observed travel-time data, and u_i is the i-th uncertainty travel-time data corresponding to the observed data.

$$\mathrm{A}\,\Delta\mathrm{m} = \Delta\mathrm{t} \tag{3}$$

where A is the matrix of partial derivatives of the traveltime with respect to the model parameters, Δm is the perturbation vector of the model parameters (velocity or interface depth), and Δt is the traveltime residual vector. Based on a layered structure model, Zelt and Smith (1992) proposed a ray inversion method to simultaneously invert two-dimensional velocities and interface structures using damped least squares. The final damped least squares solution for traveltime inversion is:

$$\Delta\mathrm{m} = \left(\mathrm{A}^{\mathrm{T}}\mathrm{C}_{\mathrm{t}}^{-1}\mathrm{A} + \mathrm{D}\mathrm{C}_{\mathrm{m}}^{-1}\right)^{-1}\mathrm{A}^{\mathrm{T}}\,\mathrm{C}_{\mathrm{t}}^{-1}\,\Delta\mathrm{t} \tag{4}$$

and the model resolution matrix is given by such formula:

$$\mathrm{R} = \left(\mathrm{A}^{\mathrm{T}}\mathrm{C}_{\mathrm{t}}^{-1}\mathrm{A} + \mathrm{D}\mathrm{C}_{\mathrm{m}}^{-1}\right)^{-1}\mathrm{A}^{\mathrm{T}}\,\mathrm{C}_{\mathrm{t}}^{-1}\,\mathrm{A} \tag{5}$$

Here A is the matrix of partial derivatives of the travel time with respect to the model parameters; D is the global damping factor, whose value determines the resolution of the model and the trade-off between stability and the magnitude of the parameter perturbation; $\mathrm{C_t}$ and $\mathrm{C_m}$ are the estimated diagonal data matrix and diagonal model covariance matrix, respectively. The diagonal elements of the resolution matrix R range between zero and one and indicate the degree of averaging or linear dependence of the true model as represented by the inverted model (Zelt and Smith, 1992).

The Pg and P1 traveltime data were used to invert the shallow structure of the upper crust above the C1 interface (~0–18.0 km depth), Next, we fix this shallow crustal structure and invert the velocity structure of the layer between the C1 and C2 interfaces (~18.0–29.7 km depth) using P2 data. Similarly, we repeat this procedure to invert the velocity structure of the layer between the C2 and C3 interfaces using P3 data, the layer between C3 and the Moho using Pm1 data, the crust-mantle transition layer beneath Altai Mountain from Pm2 data, and finally the top mantle layer from data Pn and PL data. In the practice of the progressive construction layer by layer, we first inverted its average velocity and bottom depth, and then we inverted for its lateral variations in velocities and boundary depth. With this top-down approach, the structure of the lithosphere was finally constructed.

Based on the described method, we repeated forward and inverse modelling until an acceptable fit to observed traveltimes was obtained, thus yielding the final velocity model. The observed and calculated traveltimes for all shot gathers are plotted in Figure 3A, where the observed data are drawn as blue dotted lines and the calculated final velocity model data are dotted as red triangles.

Table 2 contains the number of selected data for each seismic phase identified, used for inversion, and also the results of the travel time fit in terms of root mean square (RMS) error and the corresponding chi-squared value χ^2 (Zelt and Smith, 1992; Zelt and White, 1995). To complement and traveltime modeling, amplitudes were calculated using dynamic ray tracing (Cerveny and Psencik, 1984). We've also computed the ray-path coverage and synthetic seismogram for each shot to check the reliability of our final velocity model and reproduce previous seismic events such as Pg, Pn and other reflections.

Reliability tests

To verify the lateral resolution of the preferred model, we carried out a test similar to the classical checkerboard test, whose procedure was described by Zhang et al. (2011). We first add ±0.3 km/s alternating velocity perturbations to each velocity node and ±1.0 km depth perturbations (Figure 4B) to each depth node of the initial crustal velocity model (Figure 4A); then we computed the synthetic traveltime data for each phase; finally we inverted the velocity and depth perturbations to then obtain the parameter perturbations of the last computed model by subtracting the starting model (Figure 4C).

Besides this, to assess the reliability of the inverted two variables on the final velocity model, we illustrated the diagonal elements of resolution matrix R (Formula 5) in Figure 4D, on which the elements for velocity nodes were drawn in black circles and those for depth nodes were drawn in red triangles; the closer the resolution value is to 1.0, the more reliable the final parameter acquired at a particular location. As can be seen, most of the lithospheric structure investigated by the reference DSS profile shows high resolution values close to 1.0.

Therefore we successfully recovered the checkerboard pattern over the entire illuminated area of the lithosphere, although the

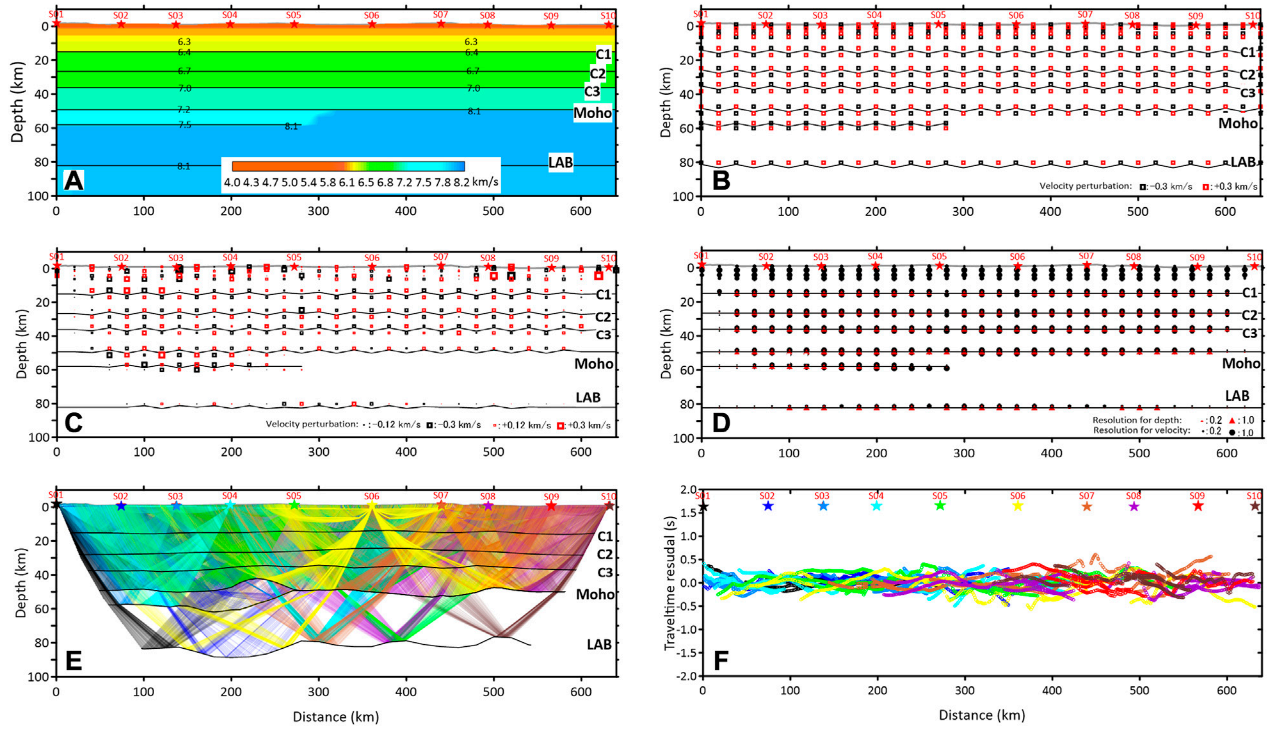

FIGURE 4
Reliability assessment of the final seismic velocity model. **(A)**: the initial homogenious velocity model; **(B)**. the velocity and depth perturbation model, for which the positive and negative velocity perturbation of 0.3 km/s are alternatively added to the velocity nodes on the initial model, and meanwhile the depth perturbation of 1.0 km are alternatively added to the depth nodes on the initial model; **(C)**. the recovered velocity and depth perturbation model; **(D)**. the diagonal elements of resolution matrix for the depth and velocity nodes, where the red triangle indicate the element for depth node, while the black dot indicate the element for velocity node; **(E)**. the ray-path coverage for different shot points; **(F)**. the time-residuals for different shot points.

perturbation amplitudes were somewhat reduced. The structures within the central part of the profile and below Altai Mountain appear to be well recovered and thus more reliable.

The reliability of the final velocity model also depends on the distance between shots, the interval between receivers, and the number of data collected for each phase. The illumination of the lithosphere by ray coverage along the wide-angle seismic profile is shown in Figure 4E; this illustration confirms that most of the profile is covered by a dense seismic ray network and indicates that both the final inverted velocities and the depths at their correspondent positions are successfully illuminated. Finally, the travel-time resudal for each shot gather are plotted in Figure 4F. It has a minor average residual of 0.152 s and shows that generally there exist a good match between the computed and observed data, suggesting that our final model based on the travel-time fit has been satisfactorily resolved.

Results

The reconstructed P-wave velocity lithospheric structure below the reference profile is shown in Figure 5. The information is completed with the age profile of the study region (Figure 5A) according to the Nd isotopic model (TDM) (Wang et al., 2020). The results show a 43-55-km-thick crust, a 25 km-thick upper mantle layer, and ~10-km-thick crust-mantle transition layer beneath southern Altai (Figure 5B). This model reveals: 1). A prominent Moho uplift beneath the Yemaquan Arc; 2). Two crustal-scale major LVAs beneath the Almantai suture and Bogda Mountain; and 3). Three shallow HVAs (P velocity of about 6.3 km/s) distributed around the Kalatongke, Yemaquan and Kalatage mining areas, respectively.

As mentioned above, the Altai-Alkin crustal velocity profile was also constructed based on DSS data (Wang et al., 2003). It shows an average crustal thickness of about 50 km, and also that the southern Altai Mountain has the thickest crust with a thickness of 56 km, followed by Bogda Mountain with a crustal thickness of 54 (Figure 5D). As a whole, our final P-velocity model (Figure 5B) agrees with these characteristics: for example, the average depth of the Moho is 51 km; Southern Altai Mountain and Bogda Mountain have thicker crust with a thickness of 51 and 55 km, respectively; the Junggar Basin and the Yemaquan Arc have thinner crust with a thickness of 49 and 43 km, respectively, and the Moho boundaries have similar geometry. However, compared to the model given by Wang et al. (2003), ours provides a high-resolution P-velocity structure: a crust-mantle transition layer with an high-velocity anomaly (HVA), a ~25 km thick lithosphere below the Moho, a significant Moho uplift below the Yemaquan Arc, and a prominent low-velocity anomaly (LVA) of depth 15–50 km below the upper crust of Bogda Mountain. The Moho uplift revealed by our model around latitude 45.5ºN (Figure 5B), below the Yemaquan Arc, is a clear feature recently verified by Liu et al. (2014) and Yang et al.

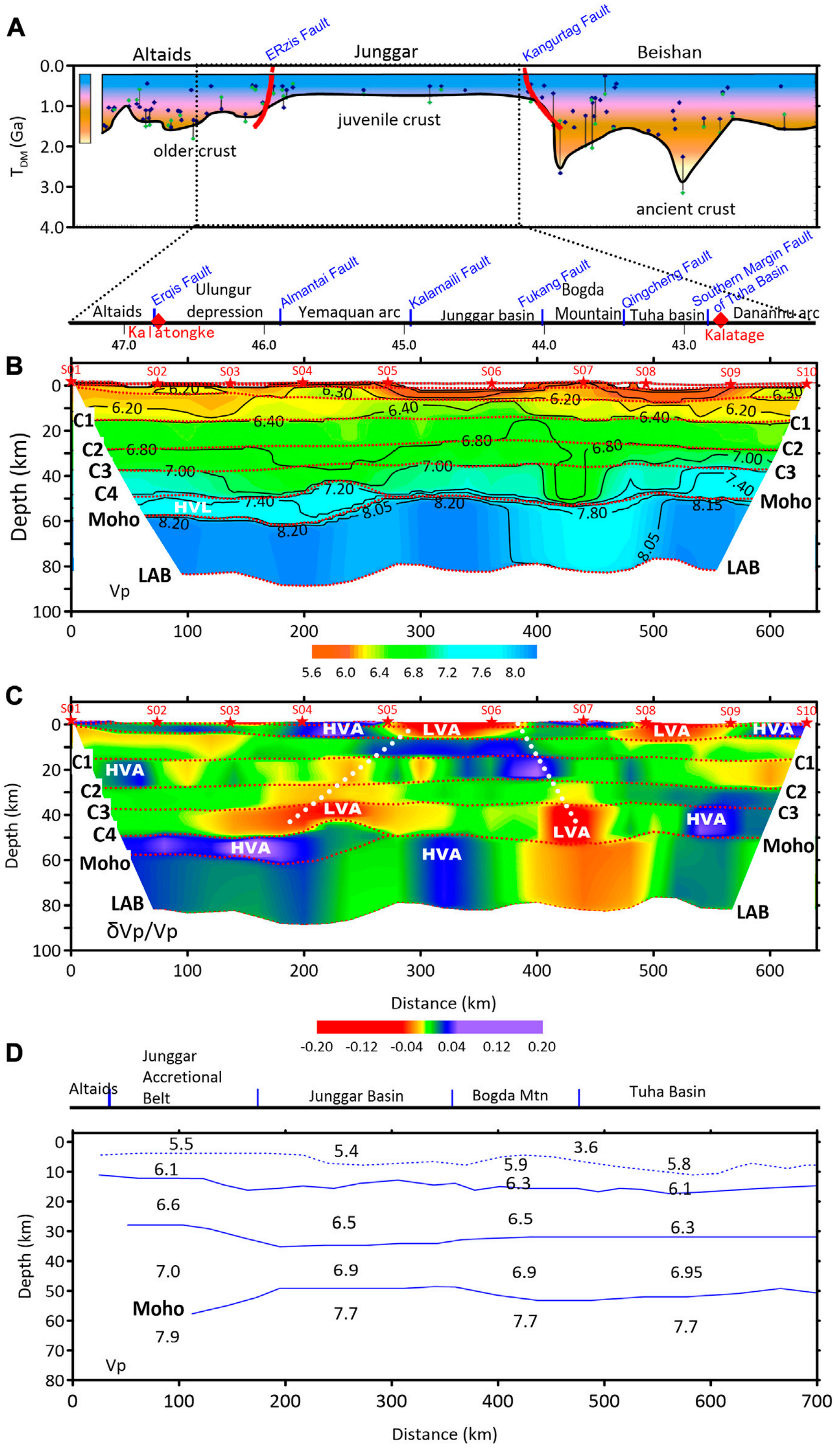

FIGURE 5

Reconstructed P-wave velocity model and comparison with other models. **(A)** Nd isotopic model age (T_{DM}) profile along the study region (revised from Wang et al., 2020). **(B)** Final reconstructed P-wave velocity model (velocity values in km/s). **(C)** Velocity perturbation percentage of the final model once subtracted and then divided by the average Vp velocity of the same velocity layer. The white dashed lines denote possible Paleozoic subduction. **(D)** For comparison purposes, this plot includes the neighboring crustal P-wave velocity structure provided by Wang et al. (2003). Structures and faults traversed by the profile are indicated on top of the plots; red diamonds mark the location of the Kalatongke and Kalatage mineral deposits to the north and south of the profile, respectively.

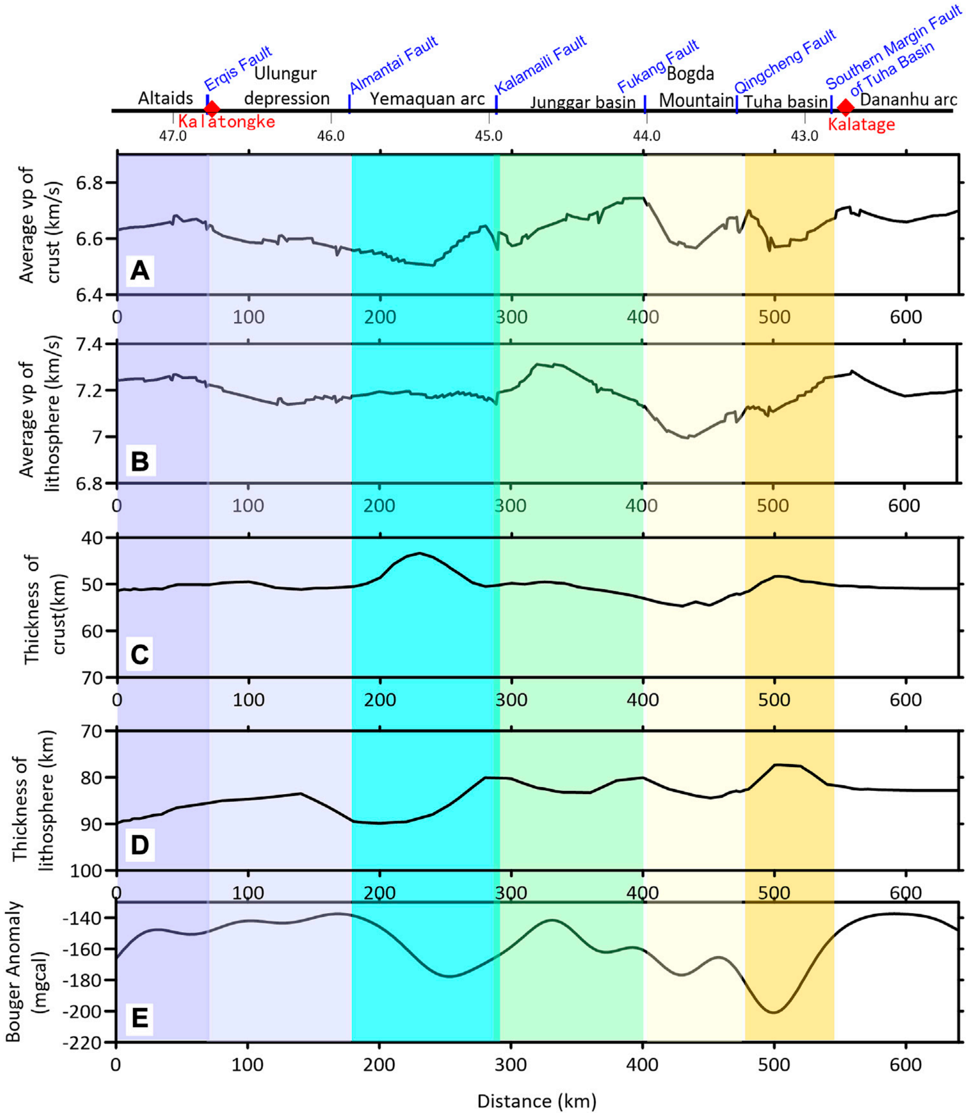

FIGURE 6
Physical parameters for different blocks (highlighted by vertical color bands) based on the final P-wave velocity model. **(A)** Average Vp of the crust. **(B)** Average Vp of the lithosphere. **(C)** Thickness of the crust. **(D)** Thickness of the lithosphere. **(E)** Bouguer gravity anomalies along this profile (extracted from the XGM2019 gravity field model obtained by the Technical University of Munich in 2019). Top: structures and faults traversed by the reference profile; red diamonds mark the location of the Kalatongke and Kalatage mineral deposits to the north and south of the profile, respectively.

(2022) from receiver functions, when describing the geometry of the crustal interface based on dense short-period seismic data.

The LAB depth of ~77–90 km generally agrees with the LAB depth of ~70–100 km in the region obtained by An and Shi. (2006) and depth of ~50–110 km given by Pasyanos et al. (2011) (Litho1.0 model). The significant HVA in the top mantle below the Junggar Basin (Figure 5B) has also been detected by full-wave ambient noise tomography by Lü et al. (2019), showing the Junggar high velocity zone in slices at depths of 42 and 60 km.

Besides this, two prominent LVAs at depth of ~20–40 km were also detected on both sides of the Junggar Basin by ambient seismic noise tomography (Kong et al., 2021): the northern mid-lower crustal LVA shows that it subducts northward beneath the Altaids, while the southern one subducts southward beneath the Bogda Mountain. Our final model (Figure 5B) supports these two different LVAs whose shapes fully agree with our results.

Discussion

Main characteristics of the lithosphere structure by blocks

Southern Altaids

To show at a glance the main features of the lithospheric structure along the Altai-Tianshan profile, in Figure 6 we show both the average Vp and the thickness of crust and lithosphere based on the final P-wave velocity model, while in Figure 7 we include the velocity-depth curves

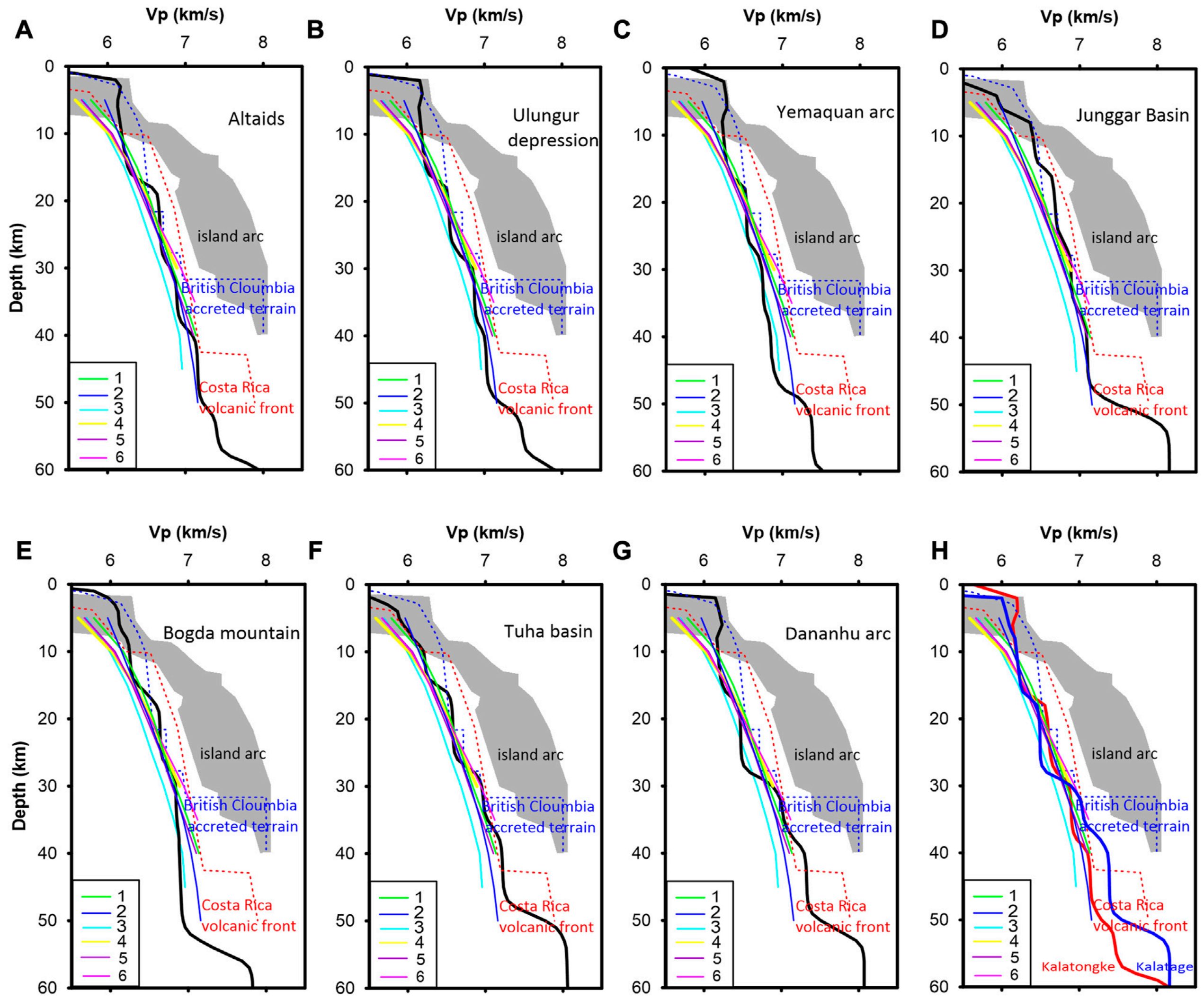

FIGURE 7
(A–G) P-wave velocity curves *versus* depth for each of the distinct blocks crossed by the reference profile (thick black lines) compared to the curves deduced for other regions. **(H)** Same for Kalatongke (thick red line) and Kalatage (thick blue line) mining areas. Velocity-depth curves for other tectonic provinces (Christensen and Mooney, 1995): 1, continental arcs; 2, global average for continent; 3, orogens; 4, extended crust; 5, shields and platforms; 6, rifts. The grey shaded area represents the range of velocities inferred in island arcs from wide-angle seismic surveys (Calvert, 2011).

extracted for each of the blocks crossed by the reference profile for comparison with the curves deduced for other regions.

Our model reveals a deeper LAB below the southern Altaids (Figure 6D), a crust-mantle transition layer (~50–60 km) with high Vp values of 7.2–7.4 km/s, and also two apparent HVAs located within the middle-crust and the top mantle (Figures 5B, C). The velocity-depth curve for this region (Figure 7A) also shows high Vp values for the crust (6.65 km/s) and the rest of the lithosphere (7.25 km/s). All of this evidence is consistent with mantle-derived rocks and minerals, such as the alkaline iron-rich high titanium basalt series related to ilmenite deposits, the tholeiitic basalt–calc-alkaline series related to copper-ickel deposits, and the ophiolite type rocks with rich Mg and poor Fe characteristic related to chromite deposits (Wang et al., 2013).

He et al. (1994) proposed that Altaids contains a continental margin from the late Precambrian to the early Paleozoic, and that subduction of oceanic crust could have occurred in the Paleozoic (Windley et al., 2002; Xiao et al. al., 2004). The mid-lower part (depth >10 km) of the average Vp curve (Figure 7A) is close to that of the continental arcs and global continent average (Christensen and Mooney, 1995). This suggests that, despite the strong Paleozoic subduction and orogenic process, it still retains traces of the ancient components of the pre-Early Paleozoic continental crust, confirming that it is a Japanese-type arc (Xiao et al., 2015; Xiao et al., 2018).

The slab window caused by the subduction of mid-ocean ridges was used to explain the origin of adakite, Nb-rich basalt, high-Mg andesite and Devonian high-grade metamorphic complexes around southern Altai (Zhao et al., 2006; Windley et al., 2007; Sun et al., 2008; Shen et al., 2010; Xiao et al., 2018), and it is believed that there were two oceanic ridge subductions in the late Paleozoic in the southern margin of Altai. Also, there are orogenic gold deposits such as the Kalatongke, Tokuzibayi and Donbastau copper-nickel deposits in the Erqis shear zone in the southern margin of Altai. Chronological studies (e.g., Han et al., 2007; Li et al., 2007) show that the above deposits were formed in the Carboniferous-Permian. The ore magma originated from the upper mantle and is the product of upward intrusion or tectonic-magmatic-fluid activity of mafic magma in a post-collisional extensional environment.

Ulungur depression

The Ulungur Depression is the northeastern part of the Junggar Basin (Figure 1), which is a late Paleozoic-Mesozoic and Cenozoic multi-cycle superimposed basin, with rich oil and gas resources (Zhu, 2009; Chen et al., 2010). Our velocity model (Figures 5B, C) shows that two LVAs exist within the shallow and lower crust. The former corresponds to the thick sedimentary layer of this place. The latter could be interpreted to mean that the top mantle is quite hot and that there is probably a strong thermal interaction across the Moho boundary, which could be related to the high heat flow observed in the Ulungur depression (Jiang et al., 2019) compared to other values of the eastern Junggar area.

Figure 6 shows relatively low average Vp values for the crust (6.59 km/s) and lithosphere (7.16 km/s), respectively. The velocity-depth curve for this region (Figure 7B) also shows that the Vp value of the deepest part of this block (depth>25 km) is clearly less than that of the global continent average (Christensen and Mooney, 1995), and it is also close to the curve of orogens.

Yemaquan Arc

The Yemaquan Arc is located between the Almantai and Kalamaili ophiolite belts and is a part of the eastern Junggar orogenic belt (Figure 1). The folded basement of the Yemaquan continental block is a flysch volcanic basin, and its southern continental margin volcanic arc is covered with Devonian acid volcanic and pyroclastic rocks, neritic terrigenous clastic rocks from the late Early Devonian to the Early Carboniferous, and post-collisional alkaline granite bedrock (Li et al., 1990).

This arc is located in the larger Kalamaili area, where gold deposits represented by the Jinshuiquan, Shuangquan, Nanmingshui and Sujiquandong deposits are developed, forming a set of metallogenic gold systems related to the late Paleozoic collisional orogeny.

Han et al. (2006) showed that the Kalamaili granite belt is a huge NW-trending batholith, which is caused by magmatic events in the post-collision extensional environment of late Paleozoic 330–280 Ma. Zhang et al. (2015) believed that the Late Carboniferous–Permian post-collisional tectonics dominated the major metallogenic systems in this area. These authors proposed that extensional strike-slip structure produced by continental lithospheric delamination and asthenospheric mantle upwelling, crust-mantle magma interaction, and mixed-fluid action is the geodynamic mechanism of metal mineralization in the Karamaili area.

Our model clearly shows that a LVA exists within the middle-lower crust (Figure 5B and especially Figure 5C). This can be attributed to marine sediments or rocks brought to this depth due to Paleozoic subduction. Our model also reveals two apparent HVAs, one shallow near the surface and the another one within the upper mantle (Figure 5C), and a significant Moho uplift (Figure 6C). Based on above geological evidences, we suggest that the LVA, HVAs and Moho uplift of this area could be correlate with Paleozoic post-collision delamination after subduction in this region, and moreover these evidences were probably preserved in the lithosphere due to the lack of strong tectonics during the Mesozoic-Cenozoic period.

Above disclosed clear Moho uplift matches with the imaging results given by Yang et al. (2022), and this block has thinnest crust with a minimum thickness of ~43.0 km (Figure 6C), a thicker lithosphere with a maximum thickness of up to 90.0 km (Figure 6D), while it has the lowest local Bouger anomaly value of −178 mgcal (Figure 6E). This low gravity anomaly agrees with the apparent LVA within the middle-lower crust (Figure 5C), and the low average Vp value of the crust whose minimum is only 6.5 km/s (Figure 6A). The corresponding velocity-depth curve (Figure 7C) shows that the Vp value for the deeper part of this block (depth>25 km) is clearly similar to that of the orogens curve, suggesting a powerful Paleozoic subduction and orogeny around this area.

Junggar basin

This area has a high average Vp value for the lithosphere, whose maximum reaches 7.30 km/s (Figure 6B), and a high local Bouguer anomaly value whose maximum is −142 mgcal (Figure 6E). Our velocity model shows that, except for the LVA corresponding to the surface sedimentary cover, there are two HVAs below the surface LVA and within the upper mantle (Figures 5B, C).

The upper segment of the Junggar Basin velocity curve (depth <30 km) is similar to those of the Costa Rican volcanic front (Gazel et al., 2015) and the British Columbia accreted terrain (Morozov et al., 1998), while the deeper part (depth >30 km) of the velocity curve is close to those of the continental arcs or global continental average (green and blue curves in Figure 7D). This implicates that the shallow structure of the ancient continental crust below the Junggar Basin has been modified enormously due to the strong Paleozoic subduction and orogeny in this area.

Bogda Mountain

Previous studies (Guo et al., 2003; Zhang et al., 2015) have revealed that Bogda Mountain has successively experienced the back-arc basin splitting in the Early Carboniferous, subduction during the Late Carboniferous, with extension in the Early Permian (Xiao et al., 2004), until reaching stability in the Middle-Late Permian and finally reactivating due to the long-range effect of the India-Tibet collision since the Neogene.

Our velocity model shows that although there is a HVA near the surface, a significant LVA is found within the middle-lower crust and uppermost mantle (Figures 5B, C). This LVA is consistent with the velocity pattern provided by Kong et al. (2021), both of which support the idea that the Paleo-Asian Ocean had subducted southward below the Bogda block (Xiao et al., 2004; 2018; Li et al., 2022). Likewise, this block shows a local low average Vp velocity of 6.57 km/s for the crust (Figure 6A) together with the lowest velocity of 7.0 km/s for the mantle Figure 6B). Furthermore, the upper segment (10–30 km) of the velocity-depth curve is similar to that of a continental arc, while the velocity for the deeper segment (depth >30 km) is clearly less than that of the rifts and orogens (Figure 7E). We suppose it indicates that the original deep structure of the lithosphere has been completely modified since the Paleozoic.

Turpan-Hami basin

The Turpan-Hami Basin southeast of Bogda Mountains (Figure 1) is a continental intermountain basin formed by Mesozoic-Cenozoic tectonic movements, especially the northward extrusion of the Indian Plate since the Miocene. It began to be formed from the Late Permian, and experienced complicated stages of tectonic evolution, such as marginal fault depression, fault-depression transition, expansion depression, *etc.*, which caused it to develop thick sedimentary strata (Yu and Fu, 1993).

Our velocity model shows that in addition to a prominent LVA in the shallow crust, corresponding to a thick sedimentary layer whose maximum thickness reaches 8.0 km, there are also two apparent HVAs within the lower crust and the upper mantle (Figure 5C). This block is characterized by having the minimum value of the Bouger anomaly of −202 mgal (Figure 6E), average Vp velocity of 6.56 km/s for the crust (Figure 6A), crustal thickness of 48.4 km (Figure 6C) and lithospheric thickness of 77.5 km (Figure 6D). The upper segment (5–30 km) of the velocity-depth curve is similar to that of the continental arcs, while the velocity at deeper depth (>30 km) is close to that of the Costa Rica volcanic front (Figure 7F). Therefore, we deduce that the powerful orogeny and volcanism caused by the subduction of the Tianshan Paleozoic Ocean slab completely modified the original middle-lower crust in this basin.

Dananhu Arc

The Dananhu Arc is a part of the East Tianshan orogenic belt (Figure 1). It is located tectonically at the intersection of the Siberian plate, the Junggar terrane and the Tarim Basin (Windley et al., 1990; Xiao et al., 2004; Li et al., 2006), so it is an important window to study the convergence of ancient plates and the accretion of crustal collages. A series of igneous rocks, intrusive rocks and basic-ultrabasic complexes are widely developed in this island-arc belt, whose ages start from the Middle Ordovician (Xiao et al., 2004) and last until around the Permian (Li et al., 2006; Wang et al., 2019). Studies have shown that during the evolution of this block, it has experienced multiple stages of plate tectonic activity, such as plate subduction and collision, plate convergence-extension, and crustal ocean-land transition (Qin et al., 2002; Qin et al., 20011; Chen et al., 2016).

Our velocity model (Figure 5C) shows HVAs near the surface (depth <7.0 km) and in the middle-lower crust (depth >29.0 km) that can be correlated with the southern Kangurge structural belt, along of which there is ophiolite of the Cambrian-Silurian (416–494 Ma) widely exposed (Li et al., 2020). We assume that these HVAs suggest the strong orogeny and volcanism due to the northward subduction of the Paleozoic Tianshan Ocean slab.

This block has the maximum value of the Bouger anomaly of −137 mgcal (Figure 6E) and high average Vp velocity values of 6.69 km/s (Figure 6A) and 7.22 km/s (Figure 6B) for the crust and lithosphere, respectively. The middle segment (10–31.5 km) of the velocity-depth curve is close to that of the continental arcs or rifts, while the Vp value at deeper depth (>31.5 km) is much greater than that of the Costa Rica volcanic front (Figure 7G). These results support the idea that mantle-derived magma was powerfully introduced into the shallow crust and lower crust due to the Paleozoic subduction and inter-slab collage around the eastern Tianshan area.

On the tectonic evolution

The formation of Altaids is the product of the long-term subduction of the Paleo-Asian Ocean through a complex process dating back to ~1.0 Ga (Khain et al., 2002) and that continued until ~250 Ma (Windley et al., 2007; Xiao et al., 2018). Figure 5A illustrates the Nd isotopic model age (T_{DM}) profile along the study region (revised from Wang et al., 2020), which shows that although most blocks have developed a juvenile crust whose age is generally less than 500 Ma, the southern Altai has preserved the oldest crust. This is consistent with the respective velocity-depth curves (Figure 7), which shows that the deeper part velocity-depth curve (depth >25 km) is close to that of the global average of continent (in blue). On the other hand, those depart part curves (depth >25 km and in black) of the blocks Yemaquan arc, Bogda Mountain, Tuha basin and Dananhu arc are far from the blue curve, and it suggests the mid-lower crust within these younger blocks has been modified enormously due to the Paleozoic crust-mantle interaction related to subduction and orogeny.

Altaids has a complex paleogeography with multiple islands and seas (Hsü et al., 1991; Xiao et al., 2008; Pan et al., 2009); its western segment is a multi-oceanic basin, multiple subduction zone, complex multidirectional accretionary orogeny (Xiao et al., 2008), and large-scale oroclinal bending during accretionary orogeny (Sengör et al., 1993; van der Voo, 2004; Xiao et al., 2015; 2018).

According to recent results given by Yang et al. (2022), a large number of Paleo-Asian oceanic basins may be trapped during supercontinent formation, and hence make up a large proportion of the juvenile continental crust. They proposed that when the Tarim collage joined the amalgamating Kazakhstan and Tuva-Mongol oroclines in the late Permian-middle Triassic, the Junggar ocean have been protected by both the curvilinear oroclinal belt of the Kazakhstan orocline and the rectilinear lines of the northern Tarim (Xiao et al., 2015; Xiao et al., 2018), thus the remnant ocean basins in eastern and western Junggar were preserved in the complicated multiple convergence process (Yang et al., 2022).

Figure 5C shows that beneath the Yemaquan Arc, ocean slabs subducted northward of the Paleo-Asian Ocean were preserved within the lower crust, which is consistent with the results given by Yang et al. (2022); while another southward subducted ocean slab locates beneath Bogda Mountain, according to the geological results given by Xiao el a. (2004) and Li et al. (2022). Moreover, we have found significant Moho uplift beneath the Yemaquan Arc (Figure 6C), which could be attributed to uplift of mantle material from the depths due to Paleozoic subduction or delamination.

Implications for the metallogenic mechanism

Orogenic deposits exist along the Erqis shear belt on the southern margin of the Altai (Figure 1, north segment of the profile), such as the Kalatongke copper-nickel deposit and the Tokuzibayi and Donbastao gold deposits. The early Permian Kalatongke copper-nickel sulfide deposit (around the shot point S02, Figure 1) is the largest copper-nickel mine in Xinjiang, and its mineralization is related to mafic-ultramafic rocks. Previous petrological and geochemical studies (Wang et al., 2000; Han et al., 2006; Han et al., 2011; Li et al., 2007) revealed that the cited deposits were formed in the Carboniferous-Permian and that the ore-forming magma originated from the upper mantle due to ascending intrusion of mafic magma or magmatic-tectonic fluid activity in a post-collision extensional environment.

Our velocity model shows an HVA in the middle crust between 20 and 30 km depth, a crust-mantle transition layer, and another HVA in the top mantle (Figure 5C). Also, the Vp value from 7.1 to 7.6 km/s corresponding to the deepest section (depth >40 km) of the velocity-depth curve (thick red line in Figure 7H) is greater than the global average for the continent (thin blue line in Figure 7H). These geophysical data support the earlier mantle-derived metallogenic mechanism, and we hypothesize that the strong convergence and continued northward compression of the Paleoasiatic oceanic plate caused delamination of the lithosphere in this region, leading to upwelling of mantle material from of the asthenosphere and subsequent intrusion into the lower crust and thus forming the crust-mantle transition zone. Hence, ore-bearing magma and hydrothermal fluid outcropped along deep faults and fissures to eventually form widespread copper and nickel deposits on the surface.

In the eastern Tianshan area of Xinjiang (Figure 1, south end of the profile), a large number of Permian mafic-ultramafic plutons developed, forming multiple magmatic copper-nickel sulfide deposits and vanadium-titanium magnetite deposits (Mao et al., 2006). Previous studies (Mao et al., 2010; Lü et al., 2019; Zhou et al., 2019) revealed that a series of mafic intrusions (Early Permian) originated in the mantle environment in the Kalatage mining area near the shot point S09 (Figure 1), and also in the Red Sea massive Cu-Zn deposit (Early Devonian) and the Yawan copper-nickel sulphide deposit (Early Permian). It is speculated that deep crustal faults and fractures provided the magma upwelling channel.

The Vp value corresponding to the deepest section (depth >30 km) of the velocity-depth curve for the Kalatage mineral area (thick blue line in Figure 7H) is clearly higher than any other for continental arcs, rifts and Costa Rica volcanic front. Considering the HVAs near the surface and in the lower crust and top mantle (Figure 5C), and the aforementioned ore-forming mechanism for the Kalatage area (Xiao et al., 2004; Li et al., 2006; Mao et al., 2010; Lü et al., 2019; Zhou et al., 2019), we understand that the original deep crust and top mantle undergone a strong modification due to the northward subduction of the Paleozoic Tianshan Ocean slab and the associated orogenic process. In the course of this process, mantle-derived magma and mineral-bearing hydrothermal fluids emerged along deep faults and fractures and then formed mineral deposits around the eastern Tianshan area, such as the Kalatage and Huangshan-Jingerquan copper-nickel mine.

Conclusion

In this study, we analyze a 637-km-long wide-angle refraction/reflection seismic profile deployed at the Altai-Eastern Tianshan orogenic belt, southern Altaids, in 2018. Based on the reconstructed lithospheric P-wave velocity structure, we draw the following conclusions.

1) The main structural features of the regional lithosphere are a 43-55-km-thick normal crust, a ~10 km-thick crust-mantle transition layer beneath the Altai Mountain, and a ~25 km-thick layer of lithospheric mantle.
2) Clearly identified features include: a prominent Moho uplift below the Yemaquan Island Arc, two major crustal-scale low-velocity anomalies below Yemaquan and Bogda Mountain, and three high-velocity surface anomalies around the Kalatongke, Yemaquan and Kalatage mining areas. Combining these features with complementary geological information, we conclude that subduction of Paleo-Asian Ocean plate, strong mantle upwelling and a powerful orogeny occurred within the explored area in the southern Altaids.
3) High-velocity anomalies in the upper crust and the crust-mantle transition layer imply that magma coming from the deep mantle may be a key factor for regional mineralization around the Central Asian Orogenic Belt, such as the Kalatongke copper-nickel sulfide deposit on the Erqis suture, and the Cu-Zn and copper-nickel sulfide deposits of Kalatage area near the Konggurtage suture. Continued compression of the Paleo-Asian Oceanic plate during the post-collision period may be the cause of widespread and intense tectonic activity, such as lithospheric thickening and delamination, most likely leading to asthenospheric material upwelling and mantle magma underplating into the crust. Hence, the presence of mafic-ultramafic rocks and mantle-derived minerals such as gold, copper and nickel, which are widely distributed in the region.
4) Our results show that the velocity-depth curves for the deeper crust (depth >30 km) in the southern Altaids and Junggar Basin are similar to those of the continental arcs and global continent average, while the curves for the other blocks in the region, such as Yemaquan Arc, Bogda Mountain, Tuha Basin and Dananhu Arc, keep great dissimilarity with them. This indicates that despite powerful Paleozoic subduction activity, orogeny and volcanism have strongly modified the lower crust in the region, although part of the ancient continental crust was still preserved beneath southern Altaids and Junggar Basin. Moreover, the upper part (depth 5–30 km) of the velocity-depth curve for the Junggar Basin is close to that of the Costa Rica volcanic front, suggesting that Paleozoic orogenic activity has intensely rebuilt the upper-middle crust below the Junggar Basin.

Data availability statement

The raw data supporting the conclusion of this article will be made available by the authors, without undue reservation.

Author contributions

ZB organized the field project, proposed the viewpoint, acquired seismic data, implemented the algorithm, performed data processing, and analyzed the results. LZ and WX were responsible for proposing the point of view, discussing the results and the conclusions. TX was responsible for data processing, analysis of results and graphic illustrations. JB contributed to the analysis and interpretation of the results, as well as to the writing of much of the manuscript.

Funding

This work was supported by the National Nature Sciences Foundation of China (42130807, 41888101), the National Key Research and Development Project of China (2017YFC0601206), and the K.C. Wong Education Foundation (GJTD-2019-04).

Acknowledgments

We would like to thank the Geophysical Exploration Centre of the China Earthquake Administration, for their efforts in hole-drilling, source triggering, and in the acquisition of field seismic data. We appreciate the guidance, suggestions and discussions with Profs. Laicheng Miao and Xiaobo Tian from the Institute of Geology and Geophysics of the Chinese Academy of Sciences. We are especially grateful to Prof. C.A. Zelt for providing us with the inversion software package used in this study. We would like to thank two reviewers for their insightful criticisms and helpful comments and suggestions that have helped us substantially improve the presentation of this study.

Conflict of interest

The authors declare that the research was conducted in the absence of any commercial or financial relationships that could be construed as a potential conflict of interest.

Publisher's note

Supplementary material

The Supplementary Material for this article can be found online at: https://www.frontiersin.org/articles/10.3389/feart.2023.1078434/full#supplementary-material

SUPPLEMENTARY FIGURE S1
Shot gathers S03-S06, the diagrams also displayed the vertical component of seismic records, which were also reduced with the velocity 6.0 km/s.

SUPPLEMENTARY FIGURE S2
Shot gathers S07-S10, the diagrams also displayed the vertical component of seismic records, which were also reduced with the velocity 6.0 km/s.

SUPPLEMENTARY FIGURE S3
Ray coverage of the DSS profile for all shots.

SUPPLEMENTARY FIGURE S4
Computed synthetic seismograms based on the final velocity model for all shots.

References

An, M. J., and Shi, Y. L. (2006). Lithospheric thickness of the Chinese continent. *Phys. Earth Planet. Interiors* 159, 257–266. doi:10.1016/j.pepi.2006.08.002

Bamford, D. (1978). Interpratation of wide-angle reflection travel-time in tealistic crust-mantle structures. *J. Geophys.* 44, 219–230.

Bian, W. H., Hornung, J., Liu, Z., Wang, P., and Hinderer, M. (2010). Sedimentary and palaeoenvironmental evolution of the Junggar Basin, Xinjiang, Northwest China. *Palaeobiodiversity and Palaeoenvironments* 90 (3), 175–186. doi:10.1007/s12549-010-0038-9

Calvert, A. J. (2011). "The seismic structure of island arc crust," in *arc-continent collision. Frontiers in Earth Sciences*. Editors D. Brown and P. D. Ryan (Berlin: Springer-Verlag), 87–119.

Cerveny, V., Molotkov, I., and Psencik, I. (1977). *Ray method in seismology*. Prague, Czechoslovakia: University of Karlova.

Cerveny, V., and Psencik, I. (1984). SEIS83-Numerical modeling of seismic wave fields in 2-D laterally varying layered structures by the ray method, in E. R. Engdahl *Documentation of Earthquake Algorithms*. 36–40. Boulder, Colorado: World Data Cent. A for Solid Earth Geophys, Rep. SE-35.

Chen, X. J., Zhang, K., and Zhou, J. (2016). Geochronology and geochemistry characteristics of the early Permian monzogranite and dioritic enclaves of east Tianshan and their tectonic implications. *Acta Geol. Sin.* 90 (9), 2334–2354.

Chen, Z. K., Xie, G. J., and Zhang, F. S. (2010). Petroleum geologic characteristics and exploration strategy in Wulungu depression of Junggar Basin. *Xinjiang Geol.* 28 (1), 61–64. doi:10.3724/SP.J.1077.2010.01195

Christensen, N. I., and Mooney, W. D. (1995). Seismic velocity structure and composition of the continental crust: A global view. *J. Geophys. Res.* 100, 9761–9788. doi:10.1029/95jb00259

Dong, L. H., Xu, X. W., Qu, X., and Li, G. M. (2009). Tectonic setting and formation mechanism of the circum-Junggar porphyritic copper deposit belts. *Acta Petrol. Sin.* 25 (4), 713–737.

Fang, T. H., Wang, J. B., Zhang, J. H., and Ding, R. F. (2002). Proterozoic basaltic magma intrusion event in the Altay. *Xinjiang Chin. Geol.* 29 (1), 48–54. doi:10.3969/j.issn.1000-3657.2002.01.009

Gazel, E., Hayes, J. L., Hoernle, K., Kelemen, P., Everson, E., Holbrook, W. S., et al. (2015). Continental crust generated in oceanic arcs. *Nat. Geosci.* 8, 321–327. doi:10.1038/ngeo2392

Gu, L. X., Hu, S. X., Yu, C. S., Wu, C. Z., and Zhengfu, Yan Z. F. (2001). Initiation and evolution of the Bogda subduction-torn-type rift. *Acta Petrol. Sin.* 17 (4), 585–597. doi:10.3321/j.issn:1000-0569.2001.04.009

Guo, L. Z., Zhu, W. B., Ma, R. S., Sun, Y., and Wang, F. (2003). Discussion on the structural coupling. *Geotect. Metallogenia* 27 (3), 197–205. doi:10.1016/S0955-2219(02)00073-0

Han, B. F., He, G. Q., Wang, X. C., and Guo, Z. J. (2011). Late carboniferous collision between the Tarim and Kazakhstan–yili terranes in the Western segment of the south tian Shan orogen, central asia, and implications for the northern Xinjiang, Western China. *Earth-Science Rev.* 109, 74–93. doi:10.1016/j.earscirev.2011.09.001

Han, B. F., Ji, J. Q., Song, B., Chen, L. H., and Zhang, L. (2006a). Late Paleozoic vertical growth of continental crust around the Junggar Basin, Xinjiang, China (Part I): Timing of post-collisional plutonsim. *Acta petrol. Sin.* 22 (5), 1077–1086. doi:10.3321/j.issn:1000-0569.2006.05.003

Han, C. M., Xiao, W. J., Zhao, G. C., Mao, J. W., Li, S. Z., Yan, Z., et al. (2006b). Major types, characteristics and geodynamic mechanism of Upper Paleozoic copper deposits in northern Xinjiang, northwestern China. *Ore Geol. Rev.* 28, 308–328. doi:10.1016/j.oregeorev.2005.04.002

Han, C. M., Xiao, W. J., Zhao, G. C., Qu, W. J., and Du, A. D. (2007). Re-Os dating of the Kalatongke Cu-Ni deposit, Altay Shan, NW China, and resulting geodynamic implications. *Ore Geol. Rev.* 32, 452–468. doi:10.1016/j.oregeorev.2006.11.004

He, D. F., Zhai, G. M., and Kuang, J. (2005). Distribution and tectonic features of paleo-uplifts in the Junggar. *Basin,Chinese J. Geol.* 40 (2), 248–261. doi:10.3321/j.issn:0563-5020.2005.02.009

He, G. Q., Li, M. S., Liu, D. Q., Tang, Y. L., and Zhou, R. H. (1994). *Paleozoic crustal evolution and mineralization in Xinjiang of China*. Urumuqi:Xinjiang: People's Publishing House, 1–437.

Hsü, K. J., Wang, Q. C., Li, J. L., and Hao, J. (1991). Geologic evolution of the neimonides: A working hypothesis. *Eclogae Geol. Helvetiae* 84, 1–35.

Hu, A. Q., Jahn, B., Zhang, G. X., and Zhang, Q. (2000). Crustal evolution and phanerozoic crustal growth in northern Xinjiang: Nd isotopic evidence. Part I. Isotopic characterization of basement rocks. *Tectonophysics* 328 (1/2), 15–51. doi:10.1016/s0040-1951(00)00176-1

Jiang, G. Z., Hu, S. B., Shi, Y. Z., Zhang, C., Wang, Z. T., and Hu, D. (2019). Terrestrial heat flow of continental China: Updated dataset and tectonic implications. *Tectonophysics* 753, 36–48. doi:10.1016/j.tecto.2019.01.006

Khain, E. V., Bibikova, E. V., Kröner, A., Zhuravlev, D. Z., Sklyarov, E. V., Fedotova, A. A., et al. (2002). The most ancient ophiolite of the central asian fold belt: U–Pb and Pb–Pb zircon ages for the dunzhugur complex, eastern sayan, Siberia, and geodynamic implications. *Earth Planet. Sci. Lett.* 19, 311–325. doi:10.1016/s0012-821x(02)00587-3

Kong, X. Y., Wu, J. P., and Liu, J. (2021). S-Wave velocity structure inversed by ambient noise tomography in Xinjiang tien Shan and its surrounding areas. *Earthq. Res. China* 16, 43–58. doi:10.3969/j.issn.1001-4683.2021.01.005

Li, G. M., Shen, Y. C., Liu, T. B., Shen, P., and Zhou, N. W. (2007). Metallogenic evolution of tuokuzibayi gold deposit in southern altay, north Xinjiang: Evidence from characteristics of quartz vein systems, isotopic geochemistry and Ar-Ar chronology. *Mineral. Deposits* 26 (1), 15–32. doi:10.1007/s11434-007-0015-5

Li, H. D., Zhou, J. B., Li, G. Y., Wang, B., Chen, Z., and Wang, H. Y. (2022). Nature and evolution of the south tianshan mountains—beishan mountains-solonker-changchun suture. *Geol. Rev.* 68 (3), 797–816. doi:10.16509/j.georeview.2022.02.061

Li, J. Y., He, G. Q., Xu, X., Li, H. Q., Sun, G. H., Yang, T. N., et al. (2006). Crustal tectonic framework of northern Xinjiang and adjacent regions and its formation. *Acta Geol. Sin.* 80 (1), 148–167.

Li, J. Y., Xiao, X. C., and Chen, W. (2000). Late Ordovician continental basement of the eastern Junggar Basin in Xinjiang, NW China: Evidence from the Laojunmiao metamorphic complex on the northeast basin margin. *Regional Geol. China* 19 (3), 297–302.

Li, J. Y., Xiao, X. C., Tang, Y. C., Zhao, M., and Feng, Y. M. (1990). Main characteristics of late paleozoic plate tectonics in the southern part of east Junggar, Xinjiang. *Geol. Rev.* 36 (4), 305–316. doi:10.16509/j.georeview.1990.04.003

Li, Z. P., Wu, L., and Yan, L. L. (2020). Spatial and temporal distribution of ophiolites and regional tectonic evolution in Northwest China. *Geol. Bull. China* 39 (6), 783–817.

Liu, W. X., Liu, G. Z., Zhou, G., Zhang, H. M., Xu, H. L., and Wang, H. C. (2014). Joint inversion of receiver function and surface wave dispersion for crust and upper mantle S-wave velocity structure beneath the Tianshan and its adjacent region. *Acta Seismol. Sin.* 36 (1), 20–31. doi:10.3969/j.issn.0253-3782.2014.01.002

Long, X. P., Sun, M., Yuan, C., Xiao, W. J., and Cai, K. (2008). Early Paleozoic sedimentary record of the Chinese Altai: Implications for its tectonic evolution. *Early Paleoz. Sediment. Rec. Chin. Altai Implic. its Tect. Evol. Sediment. Geol.* 208, 88–100. doi:10.1016/j.sedgeo.2008.05.002

Lü, X. Q., Mao, Q. G., Sun, L. Y., Chen, L. L., Guo, N. X., and Liang, K. R. (2019a). Discovery of the yueyawan Cu-Ni deposit, eastern tianshan, NW China and its geological implications. Mineral exploration. *Mineral. Explor.* 10 (3), 547–554. doi:10.3969/j.issn.1674-7801.2019.03.018

Lü, Z., Gao, H., Lei, J., Yang, X., Rathnayaka, S., and Li, C. (2019b). Crustal and upper mantle structure of the TienShan orogenic belt from full-wave ambient noise tomography. *J. Geophys. Res. Solid Earth* 124, 3987–4000. doi:10.1029/2019JB017387

Mao, J. W., Franco, P., Zhang, Z. H., Chai, F. M., Yang, J. M., Wu, H., et al. (2006). Late variscan post-collisional Cu- Ni sulfide deposits in East Tianshan and altay in China: Principal characteristics and possible relationship with mantle plume. *Acta Geol. Sin.* 80 (7), 925–942. doi:10.1016/S1001-8042(06)60011-0

Mao, Q. G., Fang, T. H., Wang, J. B., Wang, S. L., and Wang, N. (2010). The geochronology studies of the early Paleozoic Honghai massive sulfide deposits and its geological significance, Kalatage belt in Eastern Tianshan Mountain, Xinjiang, Northwest China. *Acta Petrol. Sin.* 26 (10), 3017–3026.

Morozov, I. B., Smithson, S. B., Hollister, L. S., and Diebold, J. B. (1998). Wide-angle seismic imaging across accreted terranes, southeastern Alaska and Western British Columbia. *Tectonophysics* 299 (4), 281–296. doi:10.1016/s0040-1951(98)00208-x

Pan, G. T., Xiao, Q. H., Lu, S. N., Deng, J. F., Feng, Y. M., Zhang, K. X., et al. (2009). Subdivision of tectonic units in China. *Geol. China* 36 (1), 1–28.

Pasyanos, M. E., Masters, T. G., Laske, G., and Ma, Z. (2014). LITHO1.0: An updated crust and lithospheric model of the Earth. *J. Geophys. Res. Solid Earth* 119, 2153–2173. doi:10.1002/2013JB010626

Qian, H., Jiang, M., Xiao, W. J., Zhao, D. P., Wang, Y., Zhang, L. S., et al. (2011). Seismic tomography of Tianshan-Junggar region and its lithospheric structure,Acta. *Seismol. Sin.* 33 (3), 327–341. doi:10.3969/j.issn.0253-3782.2011.03.006

Qin, K. Z., Fang, T. H., Wang, S. L., Zhu, B. Q., Feng, Y. M., Yu, H. F., et al. (2002). Plate tectonics division, evolution and metallogenic settings in eastern Tianshan Mountains, Northwest China. *Xinjiang Geol.* 20 (4), 302–308. doi:10.3969/j.issn.1000-8845.2002.04.002

Qin, K. Z., Su, B. X., Sakyi, P. A., Tang, D. M., Li, X. H., Sun, H., et al. (2011). SIMS zircon U–Pb geochronology and Sr–Nd isotopes of Ni–Cu-bearing mafic–ultramafic intrusions in eastern tianshan and beishan in correlation with flood basalts in Tarim Basin (NW China): Constraints on a ca. 280 Ma mantle plume. *Am. J. Sci.* 311, 237–260. doi:10.2475/03.2011.03

Qu, G. S., Ma, Z. J., Shao, X. Z., and Zhang, X. K. (2008). Basements and crust structures in Junggar Basin. *Xinjiang Pet. Geol.* 29 (6), 669–674.

Sengör, A. M. C., Natal'in, B. A., and Burtman, V. S. (1993). Evolution of the Altaid tectonic collage and Palaeozoic crustal growth in Eurasia. *Nature* 364, 299–307. doi:10.1038/364299a0

Shen, X. M., Zhang, H. X., and Ma, L. (2010). Ridge subduction and the possible evidences in Chinese Altay, Xinjiang. *Geotect. Metallogenia* 34 (2), 181–195. doi:10.1017/S0004972710001772

Su, L. S., Zhu, W. B., Wang, B., Faure, M., Charvet, J., and Cluzel, D. (2005). The post-collision intracontinental rifting and olistostrome on the southern slope of Boda Mountains, Xing jiang. *Acta Petrol. Sin.* 21 (1), 25–36. doi:10.1196/annals.1298.024

Sun, M., Yuan, C., Xiao, W. J., Long, X. P., Xia, X. P., Zhao, G. C., et al. (2008). Zircon U–Pb and Hf isotopic study of gneissic rocks from the Chinese Altai: Progressive accretionary history in the early to middle Palaeozoic:Progressive accretionary history in the early to middle. *Palaeoz. Chem. Geol.* 247, 352–383. doi:10.1016/j.chemgeo.2007.10.026

van der Voo, R. (2004). Paleomagnetism, oroclines, and growth of the continental crust. *GSA Today* 14, 4–9. doi:10.1130/1052-5173(2004)014<4:poagot>2.0.co;2

Wang, D. H., Chen, Y. C., Xu, Z. G., and Lin, W. W. (2000). Cu-Ni-(PGE) sulfide metallogenic series in north Xinjiang. *Mineral. Deposits* 19 (2), 147–155. doi:10.3969/j.issn.0258-7106.2000.02.006

Wang, G. C., Zhang, M., Feng, J. L., Liao, Q. An. M. J., Zhang, X. H., Kang, L., et al. (2019a). New understanding of the tectonic framework and evolution during the neoproterozoic- paleozoic era in the East Tianshan mountains. *J. Geomechanics* 25 (5), 798–819. doi:10.2090/j.ssn.1006-6616.2019.25.05.066

Wang, T., Huang, H., Song, P., Wu, H. H., Zhang, J. J., Tong, Y., et al. (2020). Studies of crustal growth and deep lithospheric architecture and new issues:exemplified by the central asian orogenic belt (northern Xinjiang). *Earth Sci.* 45 (7), 2326–2344. doi:10.3799/dqkx.2020.172

Wang, T., Tong, Y., Li, S., Zhang, J. J., Shi, X. J., Li, J. Y., et al. (2010). Spatial and temporal variations of granitoids in the altay orogen and their implications for tectonic setting and crustal growth: Perspectives from Chinese altay. *Acta Petrologica Mineralogica* 29 (6), 595–618. doi:10.3969/j.issn.1000-6524.2010.06.002

Wang, W., Meng, Y., Wang, K., Su, X. H., Yu, J. Y., Lü, S., et al. (2019b). Zircon U-Pb ages, geochemical characteristics and petrogenesis of ringed pluton in the Hancaohu area, eastern Tianshan Mountains of Xinjiang. *Geol. Bull. China* 38 (5), 777–789.

Wang, Y. W., Wang, J. B., Li, D. D., Long, L. L., Tang, P. Z., Shi, Y., et al. (2013). Types, temporal-spatial distribution and metallogenic lineage of ore deposits related to mantle-derived magma in northern Xinjiang. *Mineral. Deposits* 32 (2), 223–243. doi:10.3969/j.issn.0258-7106.2013.02.001

Wang, Y. X., Mooney, W. D., Yuan, X., and Coleman, R. G. (2003). The crustal structure from the Altai Mountains to the Altyn Tagh fault, northwest China. *J. Geophys. Res.* 108 (B6), 552. doi:10.1029/2001JB000552

Wang, Y. X., Han, G. H., Jiang, M., Mooney, W. D., and Coleman, R. G. (2004). Crustal structure along the geosciences transect from Altay to Altun Tagh. *Chinese Journal of Geophysics* 47 (2), 240–249. doi:10.3321/j.issn:0001-5733.2004.02.010

Windley, B. F., Alexeiev, D., Xiao, W., Kröner, A., and Badarch, G. (2007). Tectonic models for accretion of the Central Asian orogenic belt. *J. Geol. Soc.* 164, 31–47. doi:10.1144/0016-76492006-022

Windley, B. F., Allen, M. B., Zhang, C., Zhao, Z. Y., and Wang, G. R. (1990). Paleozoic accretion and Cenozoic redeformation of the Chinese Tien Shan range, central Asia. *Geology* 18, 128–131. doi:10.1130/0091-7613(1990)018<0128:paacro>2.3.co;2

Windley, B. F., Kroner, A., Guo, J., Qu, G., Li, Y., and Zhang, C. (2002). Neoproterozoic to paleozoic geology of the Altai orogen, NW China: New zircon age data and tectonic evolution. *J. Geol.* 110, 719–737. doi:10.1086/342866

Wu, Q. F. (1986). Structural evolution and prospects of Junggar Basin. *Xinjiang Geol.* 4 (3), 1–19.

Xiao, W. J., Han, C., Yuan, C., Sun, M., Lin, S., Chen, H., et al. (2008). Middle cambrian to permian subduction-related accretionary orogenesis of northern Xinjiang, NW China: Implications for the tectonic evolution of central asia. *J. Asian Earth Sci.* 32, 102–117. doi:10.1016/j.jseaes.2007.10.008

Xiao, W. J., Song, D., Windley, B. F., Li, J., Han, C., Wan, B., et al. (2019). Accretionary processes and metallogenesis of the central asian orogenic belt: Advances and perspectives. *Sci. China Earth Sci.* 63, 329–361. doi:10.1007/s11430-019-9524-6

Xiao, W. J., Windley, B. F., Sun, S., Li, J., Huang, B., Han, C., et al. (2015). A tale of amalgamation of three Permo-Triassic collage systems in Central Asia: Oroclines, sutures, and terminal accretion. *Ann. Rev. Earth Planet Sci.* 43, 477–507. doi:10.1146/annurev-earth-060614-105254

Xiao, W. J., Windley, B. F., Han, C., Liu, W., Wan, B., Zhang, J., et al. (2018). Late Paleozoic to early Triassic multiple roll-back and oroclinal bending of the Mongolia collage in Central Asia. *Earth-Science Rev.* 186, 94–128. doi:10.1016/j.earscirev.2017.09.020

Xiao, W. J., Zhang, L. C., Qin, K. Z., Sun, S., and Li, J. L. (2004). Paleozoic accretionary and collisional tectonics of the eastern tianshan (China): Implications for the continental growth of central asia. *Am. J. Sci.* 304, 370–395. doi:10.2475/ajs.304.4.370

Xu, X. Y., Ma, Z. P., Xia, Z. C., Xia, L. Q., Li, X. M., and Wang, L. S. (2005). Discussion of the sources and characteristics on Sr, Nd, Pb isotopes of the Carboniferous to

Permian post-collision granites from Tianshan. *Northwest. Geol.* 38 (2), 1–17. doi:10.3969/j.issn.1009-6248.2005.02.001

Xu, T., Li, F., Wu, Z. B., Wu, C. L., Gao, E. G., Zhou, B., et al. (2014). A successive three-point perturbation method for fast ray tracing in complex 2D and 3D geological models. *Tectonophysics* 627, 72–81. doi:10.1016/j.tecto.2014.02.012

Yang, X. S., Tian, X. B., Windley, B. F., Zhao, L., Lu, Y., Yuan, H., et al. (2022). The role of multiple trapped oceanic basins in continental growth: Seismic evidence from the southern Altaids. *Geophys. Res. Lett.* 49, e2022GL098548. doi:10.1029/2022GL098548

Yu, R. L., and Fu, H. (1993). Formation, evolution of Turpan-Hami basin and its petroliferous prospective evaluation. *Xinjiang Pet. Geol.* 14 (3), 217–227.

Zelt, C. A., and Smith, R. B. (1992). Seismic traveltime inversion for 2-D crustal velocity structure. *Geophys. J. Int.* 108, 16–34. doi:10.1111/j.1365-246x.1992.tb00836.x

Zelt, C. A., and White, D. J. (1995). Crustal structure and tectonics of the southeastern Canadian Cordillera. *J. Geophys. Res.* 100, 24255–24273. doi:10.1029/95jb02632

Zhang, D., Lu, Y. M., Ge, L. S., Wang, Z. H., Li, B., Fan, J. J., et al. (2015a). Metallogenic systems of polymetallic gold and copper deposits and related metallogenic geodynamic model in Karamaili of eastern junggar, Xinjiang. *Geol. Rev.* 61 (4), 797–816. doi:10.16509/j.georeview.2015.04.008

Zhang, Y., Li, Z., Nie, F., Tian, X., and Shi, Y. (2015b). Age, provenance and tectonic evolution of Late Paleozoic strata in Bogda Mountain, Xinjiang: Evidence from detrital zircon U-Pb geochronology. *Chin. J. Geol.* 50, 155–181. doi:10.3969/j.issn.0563-5020.2015.01.010

Zhang, Z. J., Klemperer, S., Bai, Z. M., Chen, Y., and Teng, J. W. (2011). Crustal structure of the Paleozoic Kunlun orogeny from an active-source seismic profile between Moba and Guide in East Tibet, China. *Gondwana Research* 19, 994–1007.

Zhang, Z. J., Bai, Z. M., Klemperer, S. L., Tian, X. B., Xu, T., Chen, Y., et al. (2013). Crustal structure across northeastern Tibet from wide-angle seismic profiling: Constraints on the Caledonian Qilian orogeny and its reactivation. *Tectonophysics* 606, 140–159. doi:10.1016/j.tecto.2013.02.040

Zhao, Z. H., Guo, Z. J., and Han, B. F. (2006). Comparative study on of the permian basalt from the beishan area, eastern Xinjiang uygur autonomous region and gansu province, and its tectonic significance. *Acta Petrol. Sin.* 22, 1279–1293. doi:10.3321/j.issn:1000-0569.2006.05.018

Zheng, M. L., Tian, A., Yang, T., He, W., Chen, L., Wu, H., et al. (2018). Structural evolution and hydrocarbon accumulation in the eastern Junggar Basin. *Oil Gas Geol.* 39 (5), 907–917. doi:10.11743/ogg20180506

Zhou, G. C., Wang, Y. W., Shi, Y., Xie, H. J., Li, D. D., and Guo, B. R. (2019). Geochronology and geochemistry of mafic intrusions in the Kalatag area, eastern Tianshan. *Acta Petrol. Sin.* 35 (10), 3189–3212. doi:10.18654/1000-0569/2019.10.14

Zhu, R. F. (2009). Oil-source analysis in south slope of eastern wulungu depression, Junggar Basin. *Nat. Gas. Geosci.* 20 (3), 400–404.

Frontiers in Earth Science

TYPE Original Research
PUBLISHED 13 March 2023
DOI 10.3389/feart.2023.1067239

OPEN ACCESS

EDITED BY
Weijia Sun,
Institute of Geology and Geophysics (CAS), China

REVIEWED BY
Liang Qiu,
China University of Geosciences, China
Eh Tan,
Academia Sinica, Taiwan
Shaohua Yang,
Chinese Academy of Geological Sciences (CAGS), China
Yajin Pang,
China Earthquake Administration, China

*CORRESPONDENCE
Jie Liao,
✉ Liaojie5@mail.sysu.edu.cn

SPECIALTY SECTION
This article was submitted to Solid Earth Geophysics,
a section of the journal
Frontiers in Earth Science

RECEIVED 11 October 2022
ACCEPTED 31 January 2023
PUBLISHED 13 March 2023

CITATION
Lei T, Liao J, Li Z-H, Liu M and Li L (2023), Patched removal of the mantle lithosphere under orogens: A systematic numerical study.
Front. Earth Sci. 11:1067239.
doi: 10.3389/feart.2023.1067239

Patched removal of the mantle lithosphere under orogens: A systematic numerical study

Tian Lei[1], Jie Liao[1,2,3]*, Zhong-Hai Li[4], Mian Liu[5] and Lun Li[1]

[1]School of Earth Sciences and Engineering, Sun Yat-sen University, Guangzhou, China, [2]Southern Marine Science and Engineering Guangdong Laboratory, Zhuhai, China, [3]Guangdong Provincial Key Lab of Geodynamics and Geohazards, Guangzhou, China, [4]Key Laboratory of Computational Geodynamics, College of Earth and Planetary Sciences, University of Chinese Academy of Sciences, Beijing, China, [5]Department of Geological Sciences, University of Missouri, Columbia, MO, United States

Delamination or convective thinning could cause large-scale and complete removal of the mantle lithosphere under orogens. However, geological and geophysical observations suggest that patched removal of the mantle lithosphere has occurred in some orogens, such as the northeastern Tibetan Plateau, the central Tianshan, and the central Andes. Dislocation-creep-induced strain localization cannot promote effective removal of the mantle lithosphere to the Moho on a small-scale. Recent rheological studies propose that dislocation-accommodated grain boundary sliding (DisGBS) may dominate upper mantle deformation. DisGBS could make the lower lithospheric mantle rheologically weaker than dry olivine. With 2-D high-resolution thermo-mechanical modeling, we systematically investigated the conditions for the initiation of small-scale lithospheric thinning under orogens and explored the minimum range of removal of the mantle lithosphere. The numerical results indicate that classic convective drip cannot effectively thin the mantle lithosphere to the Moho on a small-scale. In contrast, small-scale thinning can be induced by lithospheric heterogeneity with DisGBS and plasticity. The rheological heterogeneity can be verified by magmatism and metasomatism under the central Andes and orogens between terranes under the northeastern Tibetan Plateau or in Tianshan.

KEYWORDS

small-scale thinning, rheological heterogeneity, dislocation-accommodated grain boundary sliding, numerical modeling, orogen

1 Introduction

Lithospheric mantle removal under orogens (e.g., the Himalayan–Tibetan Plateau, Central Anatolia, and Colorado) is often explained by delamination or convective thinning (Bird 1978; Bird 1979; Owens & Zandt 1997; Molnar et al., 1998; Gogus et al., 2017). Both delamination and convective thinning are driven by the negative buoyancy in the lithospheric mantle (and sometimes the eclogitized lower crust), even though the growth period of instability and the rheological control of them are different (Levander et al., 2011; Beall et al., 2017; Lei et al., 2019). The long wavelength of downwelling thickened lithosphere leads to mantle lithosphere thinning, and the range of the initial wavelength is commonly larger than the thickness of the mantle lithosphere (Conrad & Molnar 1997; Houseman & Molnar 1997). A laterally homogeneous rheological structure of the lithosphere with dislocation creep or diffusion creep is usually assumed in previous models of delamination or convective thinning, which predict large-scale peeling off of the mantle lithosphere (Bird, 1978; Bird 1979; Schott & Schmeling 1998; Morency & Doin 2004; Göğüş & Pysklywec 2008a; Göğüş & Pysklywec 2008b; Bajolet et al., 2012; Wang & Currie 2015; Beall et al., 2017; Lei et al., 2019). However, patched removal of the mantle lithosphere, with insignificant mafic magmatism, has been observed in the interior of collisional plates and the margin of subducting plates, such as the northeastern Tibetan Plateau, the Tianshan, and the central Andes (Beck & Zandt 2002; Schurr et al., 2006; Ducea 2011; Ducea et al., 2013; Li et al., 2022; Zhang et al., 2022). The width of detachment approaches the layer thickness of the mantle lithosphere under these orogens (~100–200 *km*). Such patched removal of the mantle lithosphere under orogens cannot be readily explained by existing models of delamination or convective thinning because the convective dripping resulting from the short wavelength of perturbation tends to occur near the bottom of the mantle lithosphere and cannot remove the entire mantle lithosphere to the Moho (Conrad & Molnar 1997; Houseman & Molnar 1997; Currie et al., 2008; Lorinczi and Houseman, 2009; Ducea 2011; Beall et al., 2017; Liao et al., 2017).

Rheological weakening is the key factor for small-scale mantle lithosphere removal under orogens, that is, removal from the bottom of the mantle lithosphere to the Moho. However, dislocation creep and diffusion creep overestimate the upper mantle's viscosity (van Hunen et al., 2005; Billen, 2008), which may not effectively promote the patched removal of the mantle lithosphere (Currie et al., 2008; Liao et al., 2017). Recent rheological studies indicate that dislocation-accommodated grain boundary sliding (DisGBS), which differs from dislocation creep or diffusion creep, may dominate the deformation of olivine in the Earth's upper mantle (Tomohiro and Takaaki, 2015). The estimated viscosity of the upper mantle controlled by DisGBS is independent of depth and is lower than that of dislocation creep, indicating that the local mantle lithosphere may experience significant deformation *via* strain localization or hydration activity.

The mantle lithosphere in the northeastern Tibetan Plateau, the Tianshan, and the Central Andes manifests obvious rheological heterogeneities. Geological and geophysical observations indicate that the northeastern Tibetan Plateau consists of multiple terranes with contrasting lithologies, thermal states, and rheological structures. Patches of seismically fast and slow anomalies have been observed beneath the northeastern Tibetan Plateau (Deng et al., 2018). For example, the mantle lithosphere in the Songpan–Ganzi and southern Kunlun–Qaidam terranes has probably been removed, with traces of delaminated pieces. The entire mantle lithosphere in North Qilian has been removed, together with the base of the crust, leading to the sudden decrease of the Moho depth (Deng et al., 2018). This interpretation is consistent with the rapid uplift of the Qilian block at the Miocene-Quaternary from recent magnetostratigraphy and tectonosedimentology (Fang et al., 2013). Young volcanic rocks are exposed (<6 Myr) in the western North Qilian Mountains (Xia et al., 2011). Therefore, lithospheric heterogeneities may play a key role in the shortening of the northeastern Tibetan Plateau (Wang et al., 2008; Yin and Dang, 2008; Zhang and Wang, 2014; Deng et al., 2018). Compared with the Tarim Craton and Kazakh lithosphere (Li et al., 2022), the crust and mantle lithosphere of the sandwiched central Tianshan are assumed to be much rheologically weaker. The intracontinental deformation of the central Tianshan is controlled by rheological heterogeneity (Huangfu et al., 2021; Li et al., 2022). In contrast, the mantle lithosphere under the central Andes does not involve multiple terranes and sutures, thus differing from the northeastern TP and central Tianshan. The tectonic history of subduction has induced the migration of aqueous fluids from the subducting Nazca plate and may also lead to the weakening of the localized mantle lithosphere under the central Andes, which is related to variations in magmatism and metasomatism (Kay & Kay 1993; Beck & Zandt 2002; Jing et al., 2020; Contreras-Reyes and Diaz, 2021). Geochemical constraints show that the peridotite melting of mantle-derived magmatism may have occurred within a volcanic field over short time scales (1–5 Myr) in the Altiplano–Puna Plateau. The pattern of melting is consistent with the convective removal of the small-scale mantle lithosphere under the Altiplano–Puna Plateau (Ducea et al., 2013). Could such rheological heterogeneity in the mantle lithosphere account for the observed small-scale lithosphere thinning? Furthermore, with lithospheric heterogeneities, how does DisGBS regulate the removal of the whole lithospheric mantle? Can Rayleigh–Taylor instability developing in the perturbations of short wavelengths remove the mantle lithosphere with DisGBS to the Moho in the homogenous rheological model? In order to address these questions, we constructed a series of 2-D high-resolution thermo-mechanical models with homogeneous mantle lithosphere, including uniformly distributed perturbations, localized weak mantle lithosphere, and multiple terranes/blocks to systematically investigate the dynamics and rheological constraints of the small-scale removal of the mantle lithosphere under orogens.

2 Numerical model

2.1 Governing equations

We simulated lithospheric thinning in collisional orogens by numerically solving the governing equations of mass, momentum, and energy conservation in two-dimensional (2-D) finite difference models with a marker-in-cell technique (Gerya & Yuen 2003). The governing equations are as follows:

$$\frac{\partial v_i}{\partial x_i} = 0,$$

$$\frac{\partial \sigma_{ij}^{'}}{\partial x_j} - \frac{\partial P}{\partial x_i} + \rho g_i = 0, \tag{1}$$

$$\rho c_p \left(\frac{\partial T}{\partial t} + v_i \frac{\partial T}{\partial x_i} \right) = \frac{\partial}{\partial x_i} \left(k \frac{\partial T}{\partial x_i} \right) + H_r + H_a + H_s,$$

where v is velocity, σ' is the deviatoric stress tensor, P is pressure, ρ is density, g is gravity acceleration, c_p is heat capacity, T is temperature, k is thermal conductivity, H_r is the radioactive heating rate, H_a is the adiabatic heating rate ($H_a = T\alpha(DP/DT)$, α is thermal expansivity, and H_s is the shear heating rate ($H_s = \sigma_{i}^{'}\dot{\varepsilon}_{ij}$, $\dot{\varepsilon}$ strain rate tensor).

For the density of a specific rock type, ρ depends on pressure (P) and temperature (T):

$$\rho_{P,T} = \rho_0 [1 - \alpha(T - T_0)][1 + \beta(P - P_0)], \tag{2}$$

where ρ_0 is the reference density under the conditions of P_0 = 0.1 MPa and T_0 = 298 K (i.e., pressure and temperature at Earth's surface); α and β are the thermal expansion coefficient and the compressibility coefficient.

TABLE 1 Viscous flow laws used in the numerical experiments.

Id symbol	Flow law	E ($kJmol^{-1}$)	V ($JMPa^{-1}mol^{-1}$)	n	$\log_{10}A_D$ ($m^pMPa^{-n-r}s^{-1}$)
RA	Disl (wet quartzite)	154	8	2.3	−3.49
RB	Disl (plagioclase An_{75})	238	8	3.2	−3.48
RC	Disl (dry olivine)	532	8	3.5	4.39
RD	DisGBS (wet olivine)	423	17.6	3.0	−4.89

Table based on Ranalli (1995), which compiled original data from Kirby (1983), Kirby and Kronenberg (1987), and Ranalli and Murphy (1987). Data on dislocation-accommodated grain boundary sliding (DisGBS) are from Tomohiro and Takaaki (2015).

TABLE 2 Material properties used in the numerical experiments.[a]

Section	Material[b]	ρ_0 ($kg\ m^{-3}$)	k[c] ($Wm^{-1}K^{-1}$)	Viscous flow law[d]	Plastic[e] C_0 (MPa)	Plastic[e] $\sin(\phi_{dry})\lambda$
All plates	Asthenosphere (7)	3300	K_3	RD	10–1	0.6–0.3
Strong terrane	Upper crust (1)	2700	K_1	RA	10–1	0.15–0.075
	Lower crust (2)	3000	K_2	RB	10–1	0.15–0.075
	Mantle lithosphere (5)	3300	K_3	RC	10–1	0.6–0.3
Weak terrane	Upper crust (3)	2700	K_1	RA	10–1	0.15–0.075
	Lower crust (4)	3000	K_2	RA	10–1	0.15–0.075
	Mantle lithosphere (6)	3300	K_3	RD	10–1	Varied
References[f]		1,2	3	4,5	6	6

[a] Isobaric heat capacity $C_p = 1000 J\ kg^{-1}K^{-1}$, thermal expansion coefficient $\alpha = 3 \times 10^{-5}K^{-1}$, and compressibility coefficient $\beta = 1 \times 10^{-5}MPa^{-1}$ are used for all rock types.

[b] Numbers of materials correspond to Figure 1.

[c] $K_1 = [0.64 + \frac{807}{T_k+77}] \exp(0.00004P_{MPa})$; $K_2 = [1.18 + \frac{474}{T_k+77}] \exp(0.00004P_{MPa})$; $K_3 = [0.73 + \frac{1293}{T_k+77}] \exp(0.00004P_{MPa})$

[d] Parameters of viscous flow laws are shown in Table 1.

[e] strain weakening effect is applied for plastic rheology, in which both cohesion (C_0) and the effective friction coefficient $\sin(\varphi_{dry})\lambda$ decrease with strain increase. The cut-off values shown in the table correspond to the strain '0–1'.

[f] References 1–6 are Turcotte and Schubert (2002), Bittner and Schmeling (1995), Clauser and Huenges (1995), Ranalli (1995), Tomohiro and Takaaki (2015), and Vogt et al. (2012), respectively.

2.2 Viscoplastic rheology

1 Viscous rheology

$$\eta_{ductile} = \dot{\varepsilon}_{II}^{\ \frac{1-n}{n}} \left(A_D^{-1} G^p f_{H_2O}^{-r}\right)^{\frac{1}{n}} \exp\left(\frac{E+PV}{nRT}\right), \tag{3}$$

where $\dot{\varepsilon}_{II} = (\dot{\varepsilon}_{ij}\dot{\varepsilon}_{ij})^{1/2}$ is the second invariant of the strain rate tensor; A_D, the pre-exponential viscous factor; E, the activation energy; V, the activation volume; G, the grain size; f_{H_2O}, the water fugacity; and n (creep exponent) are experimentally determined flow law parameters (Table 1). The parameter R is the gas constant, p is the grain size exponent, and r is the water fugacity exponent.

Dislocation-accommodated grain boundary sliding is used in our numerical model. Recent studies have proposed that DisGBS may dominate upper mantle deformation (Hansen et al., 2011; Tomohiro and Takaaki, 2015). DisGBS is more effective at a larger strain rate and a smaller grain size, which is consistent with the upper mantle of orogens under convergence. We have applied the same rheological profile for DisGBS to the weak mantle lithosphere and asthenosphere, indicating that the mantle lithosphere of weak terrane is weakened from potential fluid/melt during previous oceanic subduction or terrane accretion. Consequently, the relatively low viscosity based on wet olivine rheology and low plastic strength are applied for the lithospheric mantle of the weak terrane (Tables 1, 2). We used the effective viscosity of "wet quartzite" for both the lower and upper crust of weak terrane (Tables 1, 2). In contrast, the flow law of "wet quartzite" is used for the upper continental crust and "Plagioclase An_{75}" for the lower continental crust in the strong terrane (Tables 1, 2). "Dry olivine" for the lithospheric mantle and the asthenosphere (Tables 1, 2) is generally used for the strong continental lithosphere of the strong terrane, where the fluid/melt weakening effects are neglected; thus, a high plastic effective friction coefficient ($\sin(\varphi_{dry})\lambda = 0.6 \sim 0.3$) is used for the dry and strong lithospheric mantle.

2 Drucker–Prager plasticity

The extended Drucker–Prager yield criterion (e.g., Ranalli, 1995) is adopted in our model to simulate the viscoplastic behavior of the lithosphere:

$$\eta_{plastic} = \frac{\sigma_{yield}}{2\dot{\varepsilon}_{II}}, \qquad \sigma_{yield} = C_0 + P\sin\left(\phi_{dry}\right)\lambda, \tag{4}$$

where $\eta_{plastic}$ is the viscosity of the Drucker–Prager plasticity, σ_{yield} is the yield stress, P is the dynamic pressure, C_0 is the residual rock strength at $p=0$, and φ_{dry} is the internal frictional angle of dry rocks. λ is the pore fluid/melt coefficient that controls the brittle strength of fluid/melt containing porous or fractured media: $\lambda = 1 - \frac{P_{fluid/melt}}{P}$.

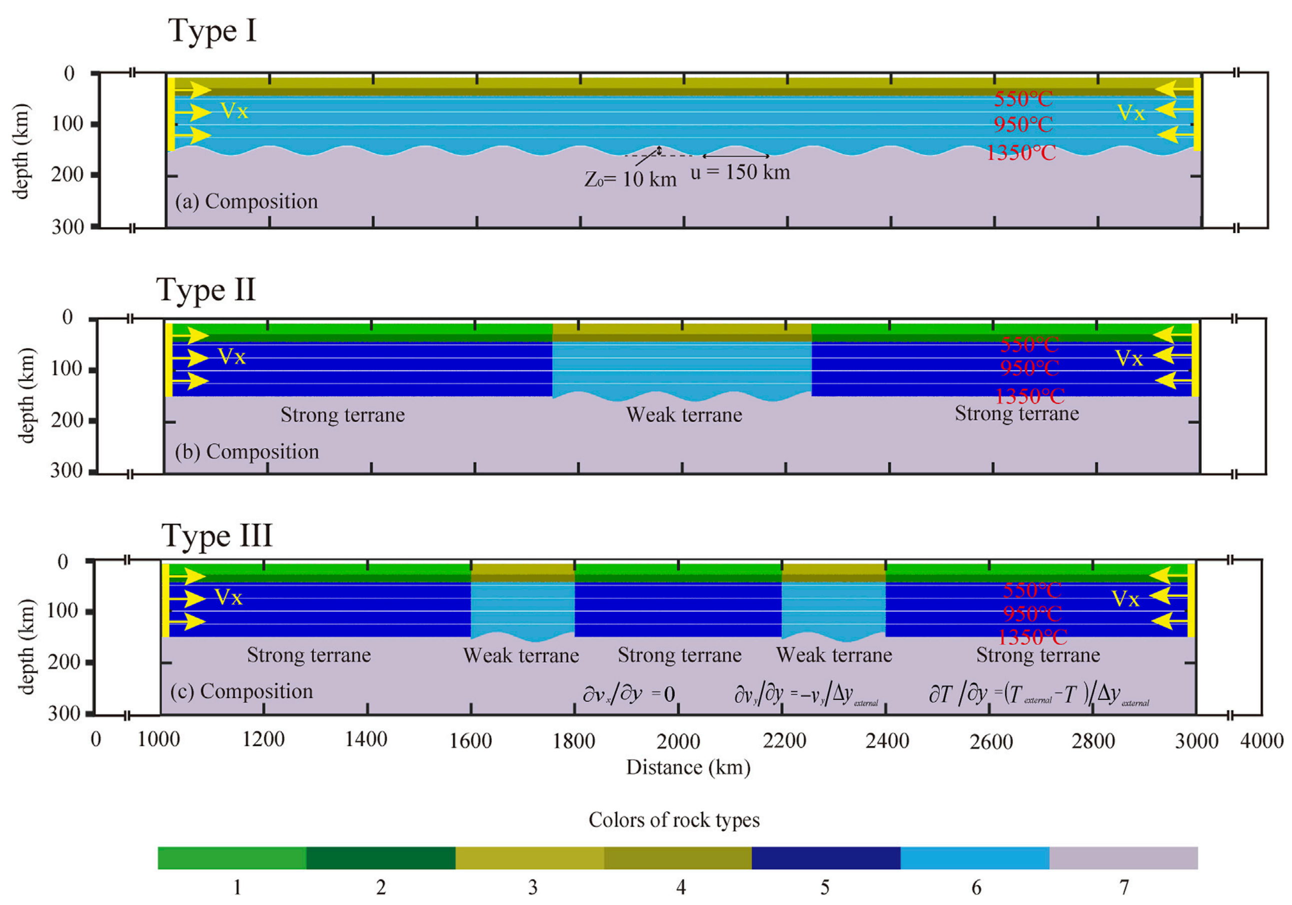

FIGURE 1
Reference model and boundary conditions. **(A)** Composition field of the homogenous model with initial wavelength (u=150 km) and perturbation (Z_0 = 10km). Enlargement (2000×400 km) of the numerical box (4,000×400 km) is shown. White lines are isotherms in ˚C with intervals of 200 ˚C. Initial convergence rates ($V_x = \pm 4.5 + 4.5 cm/yr$) are imposed on the small internal domains in the left and right parts, respectively (yellow arrow). **(B)** Composition field of heterogeneity model with a single weak block. **(C)** Composition field of the heterogeneity model with two weak blocks. Colors indicate the different rock types; 1, 2: continental upper and lower crust of the strong terrane; 3, 4: continental upper and lower crust of the weak terrane; 5: lithospheric mantle of the strong terrane; 6: lithospheric mantle of the weak terrane; 7: asthenosphere.

Because the fluid/melt parameter $P_{\mathrm{fluid/melt}}$ is not directly calculated in the model, we use a range of "$\sin(\varphi_{\mathrm{dry}})\lambda$" values to represent the effective friction coefficient, based on previous systematic investigations (e.g., Gerya & Meilick 2011; Vogt et al., 2012; Li et al., 2016). The strain weakening effect is included in the plastic rheology, in which both the cohesion C_0 and effective friction coefficient $\sin(\varphi_{\mathrm{dry}})\lambda$ decrease with increased strain, as shown in Table 2.

The minimum value of the viscous or plastic viscosity defines the effective viscosity in the model (Ranalli 1995):

$$\eta_{eff} = \min\left(\eta_{ductile}, \eta_{plastic}\right). \tag{5}$$

2.3 Initial model configuration and boundary conditions

Large-scale models ($4000 \times 400\ km$) were built to study the dynamics of the small-scale removal of the mantle lithosphere. Using a non-uniform rectangular numerical grid, the collision zone is represented by $1 \times 1\ km$ high-resolution grids, while $5 \times 1\ km$ grids are used for the rest of the model domain. More than 15 million active Lagrangian markers are used to trace and mark internal lithological boundaries, material properties, and temperature. Although the model length is 4,000 km, the deformation localizes in a relatively narrow (ca. 250 km and 1,000 km) region of interest. The effects of the Earth's curvature are, therefore, neglected in this simplified Cartesian model.

The lithosphere includes a 20-km thick upper crust, a 15-km thick lower crust, and a 105-km thick lithospheric mantle, underlain by the asthenosphere. Some orogens, such as the central Andes, northeastern Tibetan Plateau, and Tianshan, could have experienced a series of subduction and lithospheric detachments (Ducea et al., 2013; Deng et al., 2018; Jing et al., 2020; Huangfu et al., 2021; Li et al., 2022) which could have reduced the viscosity of the mantle (Lei et al., 2019). Moreover, the lithospheric mantle under continental orogens that are adjacent to a subduction zone, such as South America and the Gibraltar Arc, may be modified by subducting plates, leading to the development of secondary downwelling in the continental interior (Levander and Berzada, 2014). Consequently,

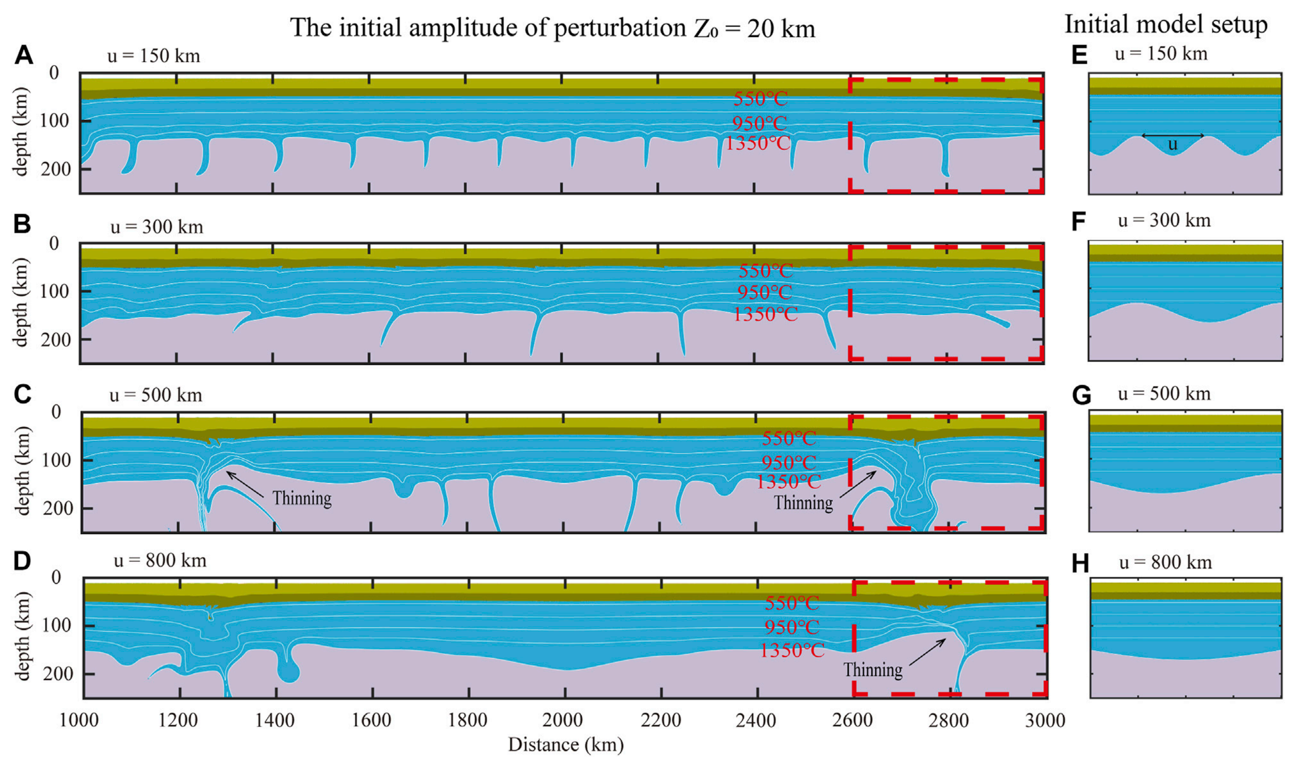

FIGURE 2
Effects of various wavelengths on the homogenous model. The model integrates the dislocation-accommodated grain boundary sliding (n=3, r=1.25, p=1), with a constant initial perturbation of $Z_0 = 20 km$ and a convergence velocity of $v_x = \pm 4.5 + 4.5 cm/yr$. **(A–D)** Constant initial perturbation ($Z_0 = 20 km$) and different wavelengths (u=150 km–1000 km). White lines are isotherms with 200°C intervals. **(E–H)** Initial model at t = 0 Myr corresponding to the red boxes in **(A–D)**.

three groups of models were constructed to simulate the small-scale removing mantle under orogens, and a series of initial perturbations are integrated into the models of Type I~Type III. In the model of Type I, the lithosphere is set to be weak and homogeneous, and a series of initial perturbations with a constant wavelength (u) and perturbation (Z_0) are designed at the bottom of the mantle lithosphere (Figure 1A). In the model with heterogeneous rheology (Type II and Type III), the lithosphere is divided into strong and weak terranes, with the initial perturbation imposed on the bottom of the mantle lithosphere in the weak terrane (Figures 1B, C). The properties of various rock types are summarized in Tables 1 and 2. We assumed the same reference density ρ_0 for the mantle lithosphere and asthenosphere (Table 2). Thus, the gravitational instability of the mantle lithosphere arises from the thickening of the weak lithospheric mantle, which becomes denser than the asthenosphere because of the lower temperature. The initial thermal structure of the lithosphere (the white lines in Figure 1A) is laterally uniform with a linear gradient from 0℃ at the surface to 1350℃ at the bottom of the lithosphere (Turcotte & Schubert 2002). The initial adiabatic thermal gradient in the asthenosphere is 0.5℃•km^{-1}.

The velocity boundary conditions in the model of heterogeneity rheology include free slip for the left, right, and top boundaries and a permeable boundary for the lower boundary (Burg & Gerya 2005; Li et al., 2016). This infinity-like external free-slip condition along the lower boundary implies a free slip condition to be satisfied at about 100 km below the base of the model. The external free slip allows global conservation of mass in the computational domain and is implemented by using the following limitation for velocity components at the lower boundary: $\partial v_x/\partial y = 0$ and $\partial v_y/\partial y = -v_y/\Delta y_{external}$, where $\Delta y_{external}$ is the vertical distance from the lower boundary to the external boundary where free slip ($\partial v_x/\partial y = 0,\ v_y = 0$) is satisfied. The lithosphere is pushed from both sides with a constant convergence velocity (V_x) imposed on the left and the right parts of the models (Figure 1A).

The thermal boundary conditions contain a fixed temperature (0 ℃) at the upper boundary and zero horizontal heat flux across the vertical boundaries. For the lower thermal boundary, a constant temperature condition is imposed at a great depth (1,000 km) below the bottom of the model to allow both temperature and vertical heat flux to vary along the permeable lower boundary of the model domain and to be adjusted dynamically during the model's evolution (Li et al., 2016).

3 Model results

3.1 Type I model with uniformly distributed perturbations

In the case of the homogeneous mantle lithosphere, models of classical delamination predict a large-scale peeling of the

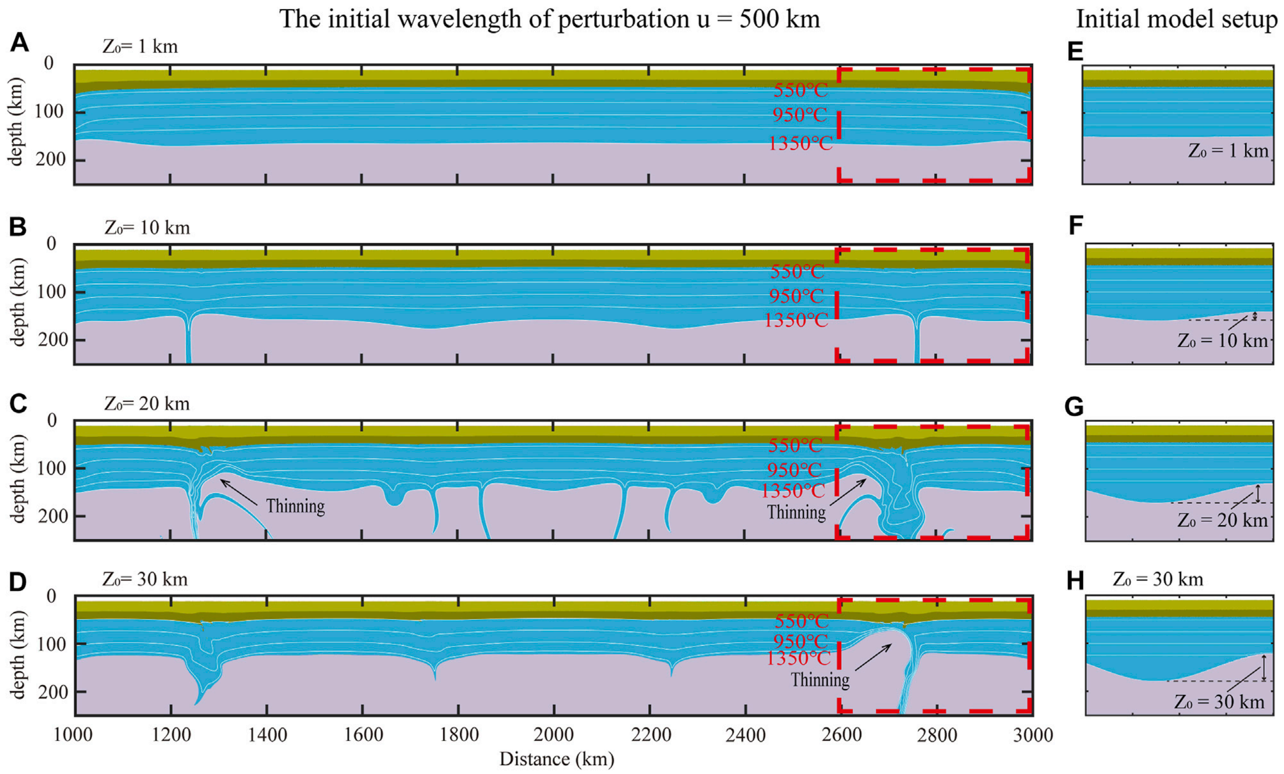

FIGURE 3
Effects of various amplitudes on the homogenous model. The model integrates the dislocation-accommodated grain boundary sliding (n=3, r=1.25, p=1) with a constant initial wavelength of $u = 500km$ and a convergence velocity of $v_x = \pm 4.5 + 4.5cm/yr$. **(A–D)** Constant initial wavelength ($u = 500\ km$) and different perturbation ranges ($Z_0 = 1km - 30km$). White lines are isotherms with 200°C intervals. **(E–H)** Initial model at t = 0 Myr corresponding to the red boxes in **(A–D)**.

mantle lithosphere (Bird 1978, 1979; Lei et al., 2019), which may not adequately explain the small-scale lithospheric mantle removal under some orogens. Rayleigh–Taylor instability could occur in small-scale drips when viscosity is relatively low (Beall et al., 2017; Lei et al., 2019). However, will short wavelength drips remove the mantle lithosphere from its base to the Moho? In order to answer this question, we have performed a series of 2-D numerical experiments to systematically investigate the effects of DisGBS and plasticity on the removal of the mantle lithosphere with uniformly distributed perturbations.

3.1.1 Effect of perturbation wavelength on model evolution

In this case, we used dislocation-accommodated grain boundary sliding (DisGBS) and plasticity (λ = 0.001) to study the effects of perturbation wavelength on convective thinning. Figure 2 shows the model results of different perturbation wavelengths from 150 km to 800 km with constant amplitude ($Z_0 = 20km$) at 3.4 Myr, where convergent velocity $v_x = \pm 4.5 + 4.5cm/yr$. When the initial perturbation wavelength is small ($u = 150km - 300km$), the drips cannot effectively remove the mantle lithosphere (Figures 2A, B). In contrast, with a larger wavelength initial perturbation ($u = 500km - 800km$), the lower mantle lithosphere can be easily removed by the drips (Figures 2C, D).

3.1.2 Effect of perturbation amplitude on model evolution

In addition to various perturbation wavelengths, different perturbation amplitudes can also play an important role in convective thinning. Figure 3 shows the model results of different amplitudes from 1 km to 30 km with a constant of wavelength ($u = 500km$) at 3.4 Myr. With a small perturbation amplitude (Figure 3A, $Z_0 = 1km$), no convective dripping occurs. When the initial perturbation amplitude $Z_0 = 10km$, the drips developed on the bottom of the mantle lithosphere; however, this process cannot effectively remove the lithospheric mantle to the Moho (Figure 3B). With a large amplitude ($Z_0 = 20km$), obvious convective dripping developed on the bottom of the mantle lithosphere, leading to lower mantle lithosphere removal from ~150 km to ~100 km (Figure 3C). Furthermore, in the case of perturbation amplitude $Z_0 = 30km$, the drips effectively induced a removal of the mantle lithosphere from ~150 km to ~50 km (Figure 3D).

3.2 Type II model with a weak block

Natural orogens often consist of numerous terranes with contrasting lithologies, thermal states, and rheological structures, or have experienced localized weakening in the mantle lithosphere through metasomatism induced by subduction or collision (Ducea

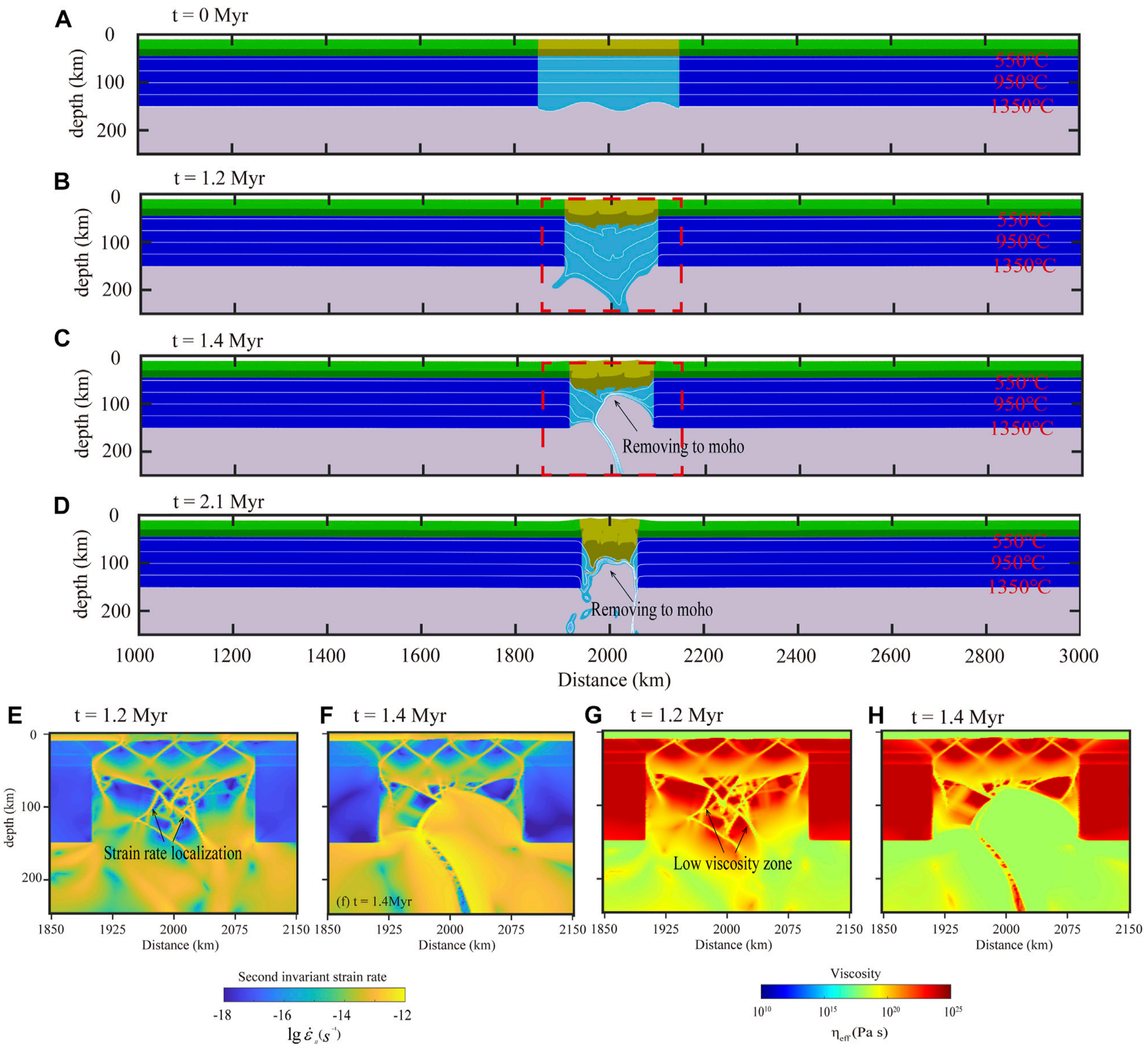

FIGURE 4

Model evolution with heterogeneity. Dislocation-accommodated grain boundary sliding (n=3, r=1.25, and p=1) and plastic yielding (λ = 0.001) are used for the weak mantle. **(A–D)** Results of the composition field (L = 300 km). **(E,F)** Effective viscosity of the model. **(G,H)** Second invariants of the strain rate in the model. Colors of the composition field indicate the different rock types (Figure 1). White lines are isotherms with 200°C intervals. Time (Myr) of evolution is shown in each panel.

et al., 2013; Deng et al., 2018; Jing et al., 2020). Could such rheological heterogeneity explain the observed small-scale lithospheric thinning? In order to solve these problems, we performed a series of experiments with localized weak lithospheric mantle to systematically investigate the effects of DisGBS and plasticity on the removal of the mantle lithosphere with a weak block.

3.2.1 Effect of weak crust and mantle

In the first set of models, we studied the effects of the weak crust and mantle lithosphere on the removal of the mantle lithosphere. Figure 4 shows the model results with DisGBS and significant plastic yielding (λ = 0.001). At the beginning of the experiment, the localized weak mantle lithosphere is thickened by small scale drips (Figure 4B). With further convergence, the obvious fragmentary or small-scale thinning of the mantle lithosphere occurs in the section of weak lithosphere with weak crust (Figures 4C, D). Figures 4E–H show the corresponding effective viscosity and the second invariant of the strain rate. It shows that the strain rate localization goes through the entire mantle lithosphere by conjugate slip and has reduced viscosity in the same way.

The model in Figure 4 assumes a constant width of L = 300 km for the weak terrane. Furthermore, we tested the model with different widths of weak terrane (Figure 5). When the width of the weak block is small (L = 100 km), converging continents lead to pure shear thickening under weak terrane (Figure 5A). In contrast, the obvious removal of

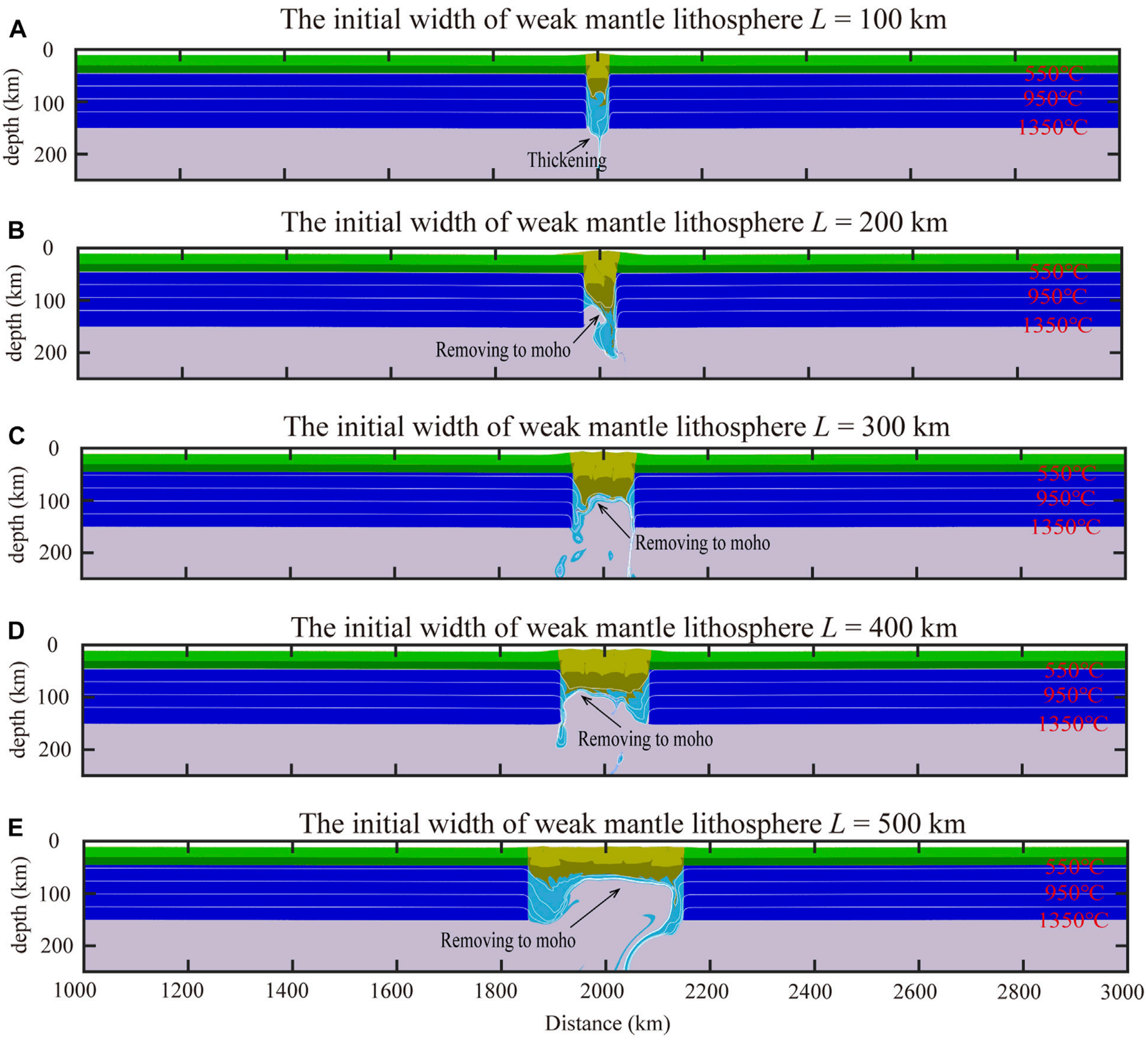

FIGURE 5
Range of effective thinning in the weak terrane. Dislocation-accommodated grain boundary sliding (n=3, r=1.25, and p=1) and plastic yielding (λ = 0.001) are used for the weak mantle. **(A–E)** Composition field with different widths L = 100 km–500 km in the weak mantle lithosphere. Time (Myr) of the models **(A–E)** is, respectively, 0.6 Myr, 1.6 Myr, 2.1 Myr, 2.6 Myr, and 2.3 Myr. Colors of the composition field indicate the different rock types (Figure 1). White lines are isotherms with 200°C intervals.

lithospheric mantle under weak terrane, with thickened crust, occurs at a width of L = 200 km (Figure 5B). The decreasing of plastic equivalent viscosity with high strain rates explains the quick development of instability in the lithospheric mantle on both sides of the weak terrane. This leads to the upwelling of the asthenosphere to the bottom of the crust to trigger delamination under weak terrane. With the increasing width of weak terrane, convective dripping can effectively remove the lithospheric mantle to the Moho without apparently thickened crust (Figures 5C–E).

3.2.2 Effect of localized weak mantle lithosphere

In this set of models, the localized weak mantle lithosphere, with a strong crust, is added into model setup to simulate the effects of the local weak mantle lithosphere on the small-scale thinning. Figure 6 shows the evolution results of the composition field with localized weak mantle, where the plastic yield is 0.001. When the width of the weak mantle lithosphere is small (L = 100–200 km), the drips could not cause effective removing under the weak mantle lithosphere (Figures 6A, B). In comparison with models of weak terrane (Figure 5), the removal of lithospheric mantle occurs in the critical width of the weak region (L = 300 km), which is larger than the weak terrane model (Figure 5). With the increasing width of weak regions, convective dripping can effectively remove the lithospheric mantle to the Moho without apparently thickened crust (Figures 6D, E).

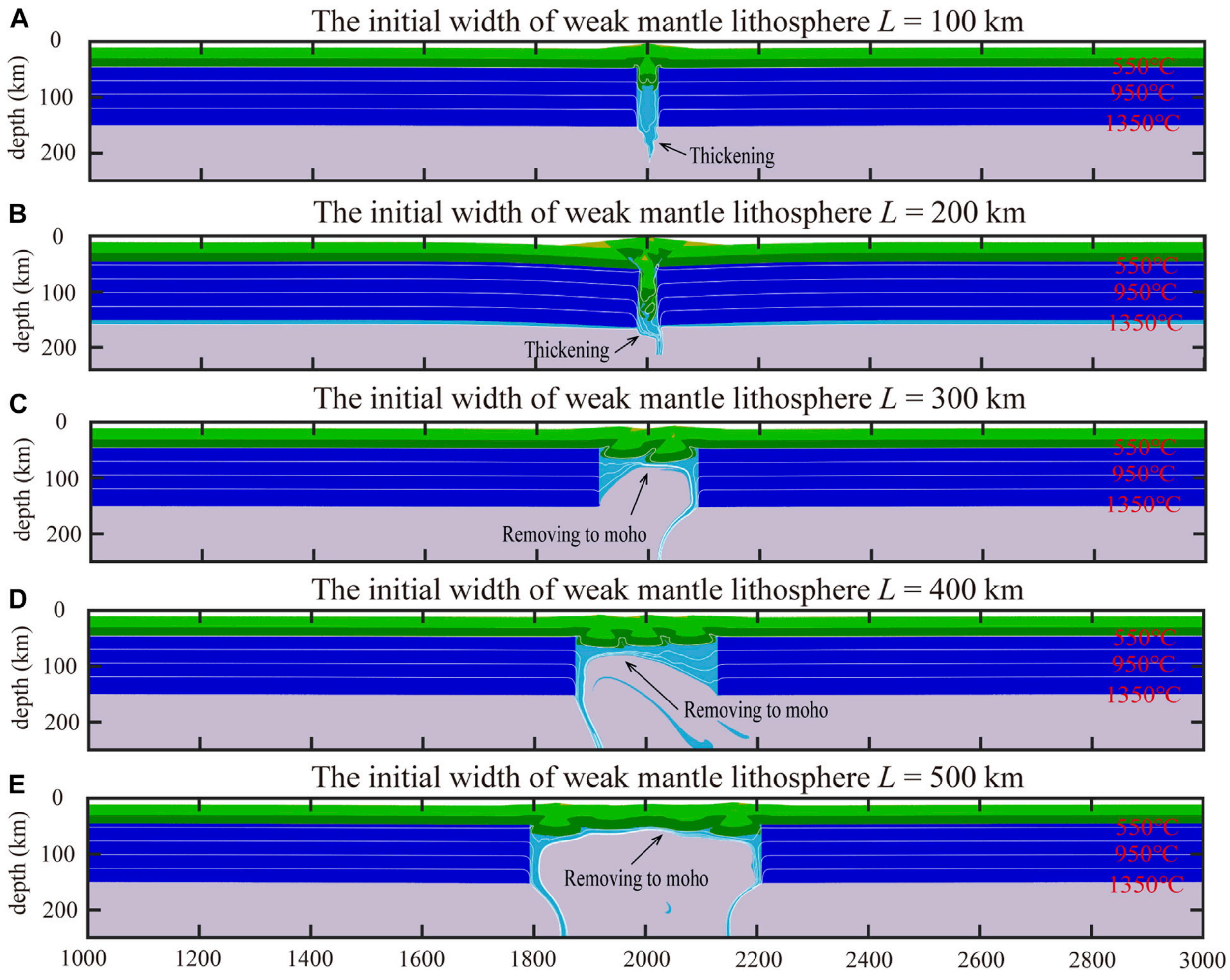

FIGURE 6
Range of effective thinning in the weak mantle lithosphere. Dislocation-accommodated grain boundary sliding (n=3, r=1.25, and p=1) and plastic yielding (λ = 0.001) are used for the weak mantle. **(A–E)** Composition field with different widths L = 100 km–500 km in the weak mantle lithosphere. Time (Myr) of the models **(A–E)** is, respectively, 0.7 Myr, 2.0 Myr, 1.4 Myr, 1.7 Myr, and 2.1 Myr. Colors of the composition field indicate the different rock types (Figure 1). White lines are isotherms with 200°C intervals.

3.3 Type III model with multiple rigid and weak blocks

We have further considered the effects of multiple weak terranes (Deng et al., 2018). Figure 7 shows the corresponding composition, effective viscosity, and the second invariant of the strain rate field. These results illustrate the feedback between strain rates and effective viscosity when DisGBS and plastic yielding are considered. Developed drips occur in the weak terrane and promote the mantle lithosphere peeling off to the crust (Figures 7A–D). As with the model results of a single section of weak terrane (Figure 4), strain weakening reduces both viscous and plastic viscosity, causing localized drips to develop in the bottom of the mantle lithosphere and the further removal of crust (Figures 7E–J). Like the model results of a single weak block (Figure 5), the effective thinning of the mantle lithosphere occurs in the weak terrane, when its width falls into the range of 200 km to 400 km (Figures 8B–D), except when L = 100 km (Figure 8A).

4 Discussion

4.1 Comparisons of the three types of models

Our study indicates that small-scale mantle lithosphere removal can develop under orogens, depending on the rheology of the mantle lithosphere. Here, we compare the effects of the rheological structure on the patched or small-scale removal of mantle lithosphere.

4.1.1 Homogeneous model (type I)

Given that dislocation-accommodated grain boundary sliding and plasticity is integrated into the mantle lithosphere of weak terranes, convective removing could occur with dripping; however, in that case it tends to occur in the model with a large perturbation wavelength and amplitude (Figures 2, 3). To quantify the effect of the initial perturbation wavelength and amplitude on the magnitude of the removal of the mantle lithosphere, we conducted an “available

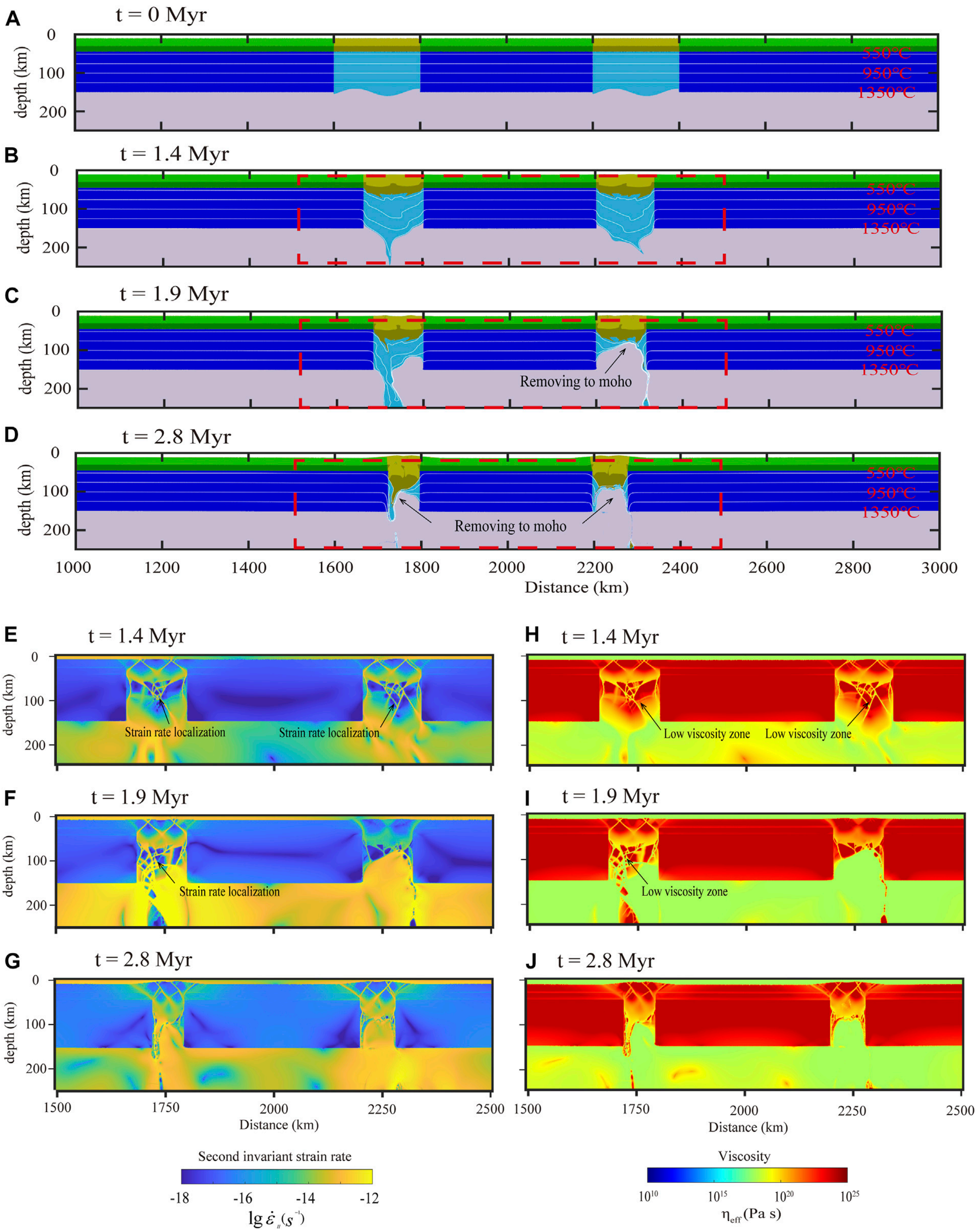

FIGURE 7
Model evolution with the heterogeneity of multiple weak terranes. Dislocation-accommodated grain boundary sliding (n=3, r=1.25, and p=1) and plastic yielding (λ = 0.001) are used for the weak mantle. **(A–D)** Results of the composition field (L = 200 km). **(E–J)** Effective viscosity and the second invariants of the strain rate of the model.

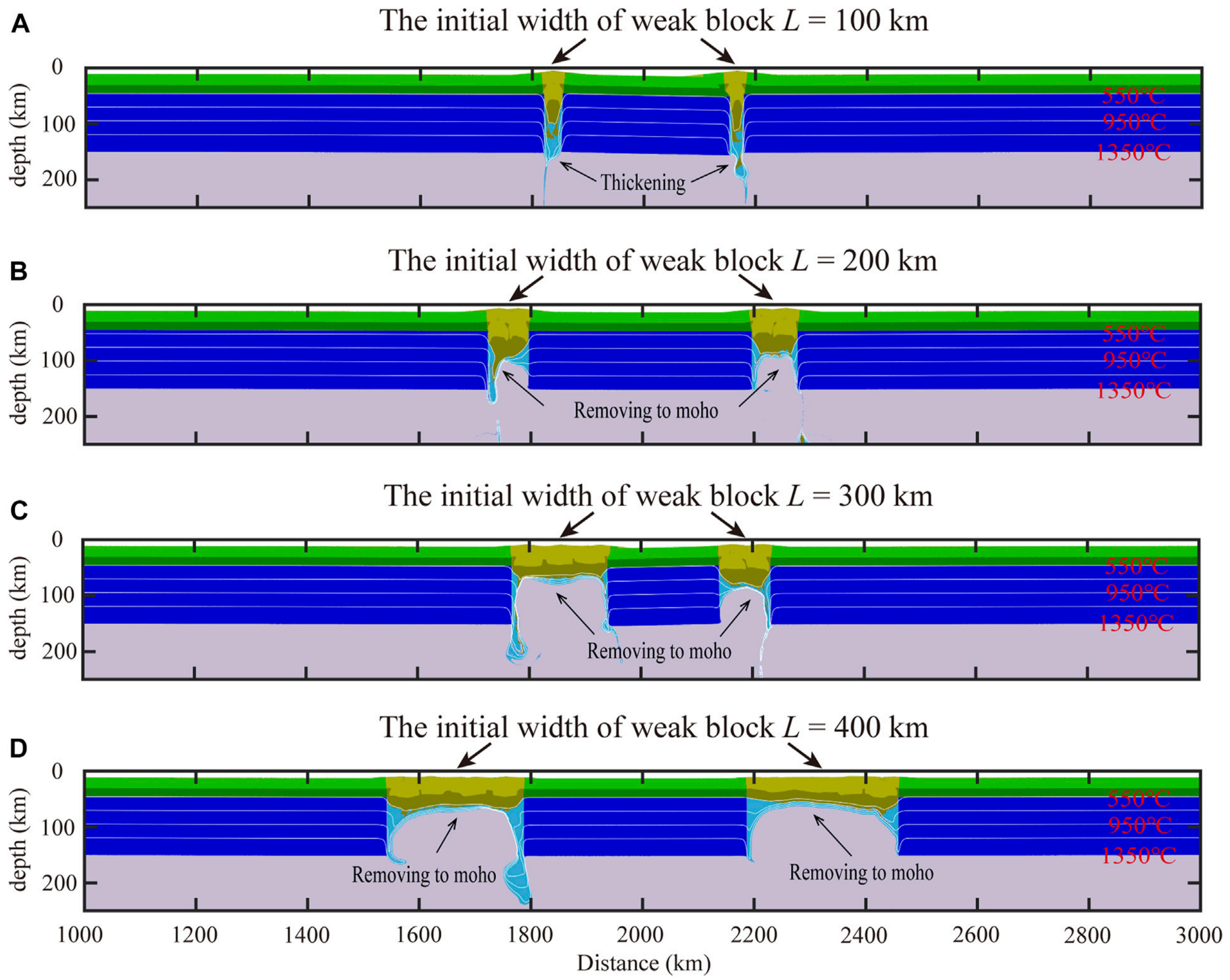

FIGURE 8
Model evolution with the heterogeneity of multiple weak terranes with different widths. Dislocation-accommodated grain boundary sliding (n=3, r=1.25, and p=1) and plastic yielding (λ = 0.001) are used for the weak mantle. **(A–D)** Composition field with different widths L = 100 km−400 km in the weak mantle lithosphere. Time (Myr) of the model **(A–D)** is 1.6 Myr, 2.8 Myr, 2.7 Myr, and 3.2 Myr, respectively. Colors of the composition field indicate the different rock types (Figure 1). White lines are isotherms with 200°C intervals.

buoyancy" scaling analysis. The degree of convective instability depends on the thickness of a potentially unstable layer, which can be caused by the mechanical thickening of the layer. In this study, based on Conrad and Molnar (1999), the gravitational instability of the mantle lithosphere with thickness h can be represented by a Rayleigh number, Ra_n:

$$Ra_n = \left(\frac{\rho_m g \alpha T_0}{n B_m}\right)^n \frac{\lambda^2 h Z_0{}^{n-1}}{\kappa} F_n, \tag{6}$$

where n = 3 is the creep exponent of the accommodated grain boundary sliding (Table 1), T_0 is the temperature difference across the layer, g is the gravitational acceleration, α is the thermal expansion coefficient, κ is the thermal diffusivity, ρ_m is the density of mantle lithosphere, B_m is the rheological strength parameter of the mantle lithosphere, h is the layer thickness of the mantle lithosphere, λ is the initial wavelength, and Z_0 is the initial perturbation amplitude. This number is similar to the standard Rayleigh number with the additional factor F_n, which is the "available buoyancy" of the layer. F_n is calculated by the integral of the negative buoyancy divided by viscosity (Conrad & Molnar 1999). This integrates the variation of density, viscosity, and temperature with depth in an unstable layer; the dimensionless growth rate should depend only on the wavelength of the initial perturbation. Numerical experiments show that the layer will be unstable when Ra_3 is greater than 100 (Conrad & Molnar 1999; Conrad 2000).

In our models, the mantle lithosphere density profile depends on pressure and temperature, while the effective viscosity profile is given by both plasticity and the background strain rate associated with convergence. Figure 9 shows the calculated Ra_3 as a function of layer thickness at different initial perturbation wavelengths and amplitudes, respectively. At the small amplitude (Z_0 = 1 km), the analysis indicates that the whole mantle lithosphere remains stable, with $Ra_3 < 100$ for all thicknesses (Figure 9A). This agrees with the model result that indicates that the mantle lithosphere is stable and thickened during convergence when the small amplitude is applied

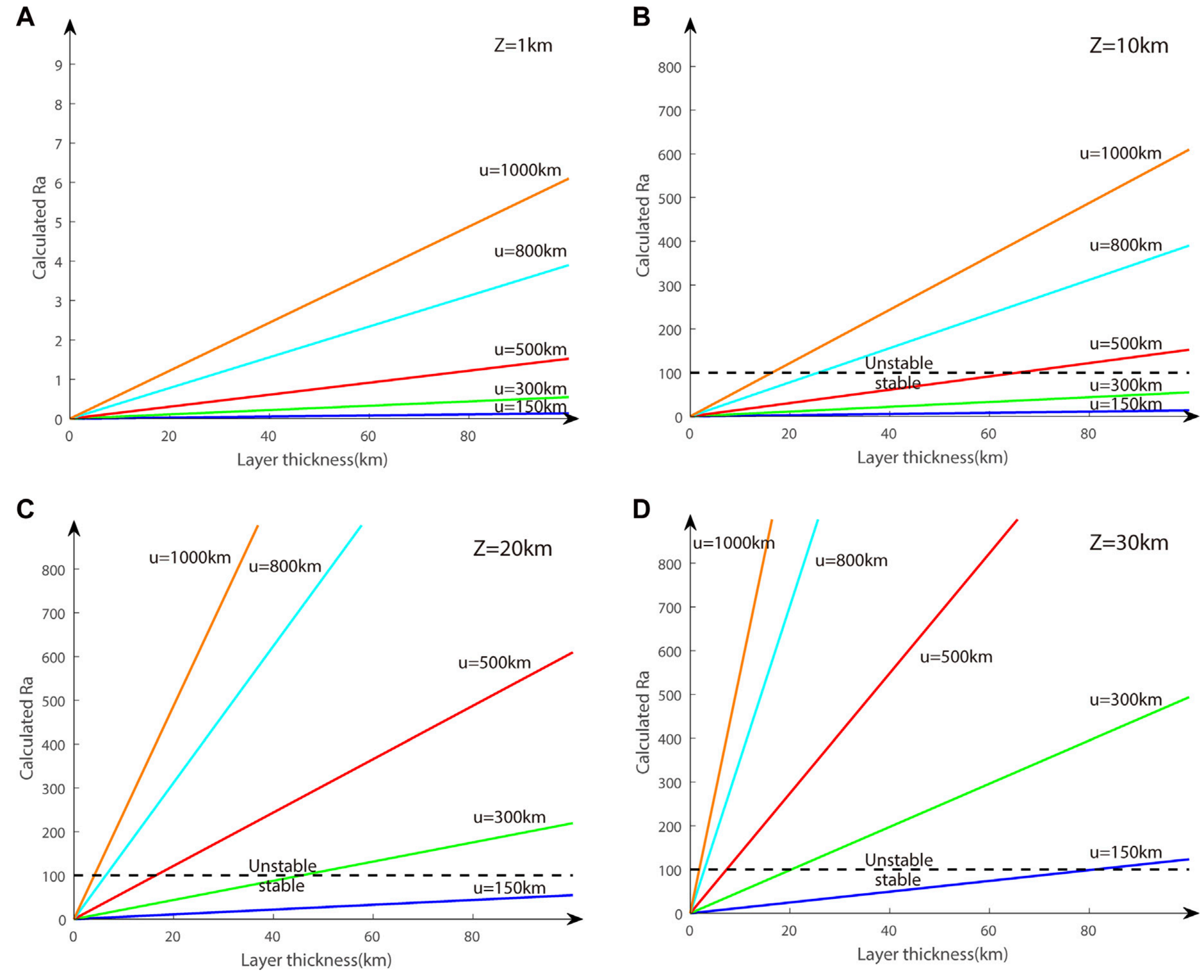

FIGURE 9

(A) Predicted stability (Ra_3) as a function of layer thickness (measured from the base of the lithosphere) for the constant initial perturbation $\Delta L_0 = 1km$ with variations in the initial wavelength. The critical layer thickness (h_{crit}) occurs at $Ra_3 = 100$, indicating the minimum lithospheric mantle thickness that may be removed by Rayleigh–Taylor instability. **(B)** Predicted stability (Ra_3) as a function of layer thickness for the constant initial perturbation $\Delta L_0 = 10km$ with variations in the initial wavelength. **(C)** Predicted stability (Ra_3) as a function of layer thickness for the constant initial perturbation $\Delta L_0 = 20km$ with variations in the initial wavelength. **(D)** Predicted stability (Ra_3) as a function of layer thickness for the constant initial perturbation $\Delta L_0 = 30km$ with variations in the initial wavelength. Dislocation-accommodated grain boundary sliding (Table 1) and plastic yielding ($\lambda = 0.001$) are used for the semi-analytical model (Eq. 6).

(Figure 3A). When the initial perturbation amplitude Z_0 falls in the range of 10 km to 30 km, the calculations show that the large wavelength of the initial perturbation becomes easier to super-exponentially grow and further remove part of the mantle lithosphere (Figures 9B–D). The thickness h_{crit} represents the minimum amount of mantle lithosphere that may be removed by gravitational instability, which indicates that the critical Ra_3 of 100 is obtained for layer thickness. In the models with the larger amplitude ($Z_0 = 20\ km$), the calculated critical Ra_3 of 100 is obtained for the layer thickness of ~45 *km*, ~18 *km*, ~8 *km*, and ~5 *km*, corresponding to perturbation wavelengths of 300 *km*, 500 *km*, 800 *km*, and 1,000 *km* (Figure 9C). Because the initial amplitude ($Z_0 = 20\ km$) is larger than the critical thickness h_{crit}, corresponding to a wavelength range of 500 km–1000 km, the gravitational instability will develop at the base of mantle lithosphere. The results agree with the models, which indicate that the mantle lithosphere is unstable with dripping at a large wavelength of the initial perturbation (Figures 2C, D). For the same reason, in the models with constant wavelength (u=500 *km*), the calculated critical Ra_3 of 100 is obtained for a layer thickness of ∞, ~65 *km*, ~18 *km*, and ~10 *km*, corresponding to the respective perturbation amplitudes of 1 *km*, 10 *km*, 20 *km*, and 30 *km* (Figures 9A–D), where ∞ indicates that the mantle lithosphere is stable during convergence (Figure 3A). When the initial perturbation amplitude is 10 *km*, the minimum amount of removal of the mantle lithosphere h_r (~65 *km*) is larger than the initial amplitude Z_0 (~10 *km*) with a 500 *km* initial wavelength (Figure 9B); this indicates that the evolution of the model with a 10 *km* initial amplitude will have difficulty reaching super-exponential growth and the removal of the mantle lithosphere (Figure 3B). In contrast, with the initial amplitude $Z_0 = 20\ km$, super-exponential growth develops at the base of the mantle lithosphere (Figure 3C) because the initial

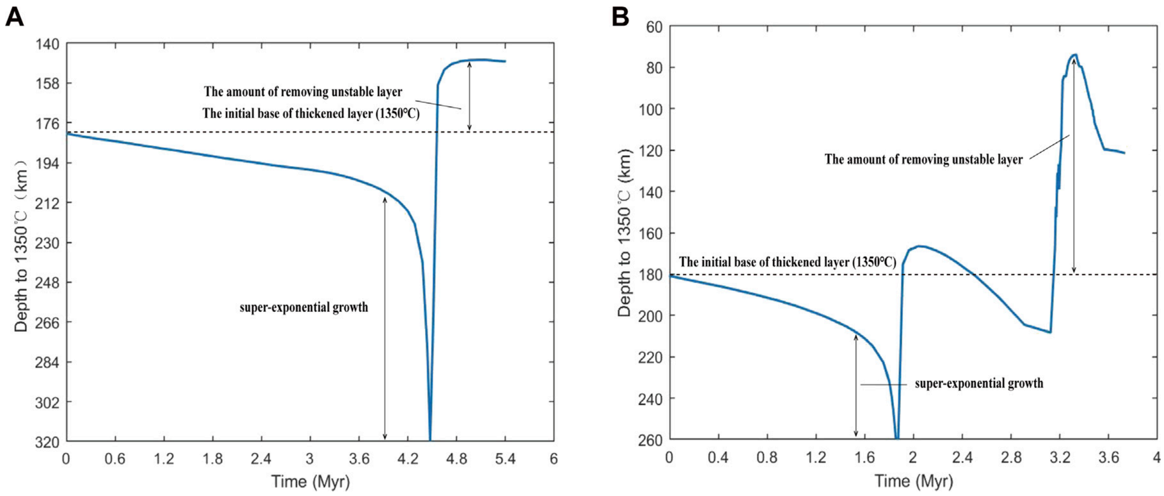

FIGURE 10
Evolution of the average depth of the 1350℃ isotherm for the model of Type I with the constant initial perturbation $Z_0 = 20km$ and initial wavelength $u = 800\ km$. **(A)** Dislocation-accommodated grain boundary sliding (Table 1) is integrated into the model; **(B)** dislocation-accommodated grain boundary sliding (Table 1) and plastic yielding (λ = 0.001) are integrated into the model.

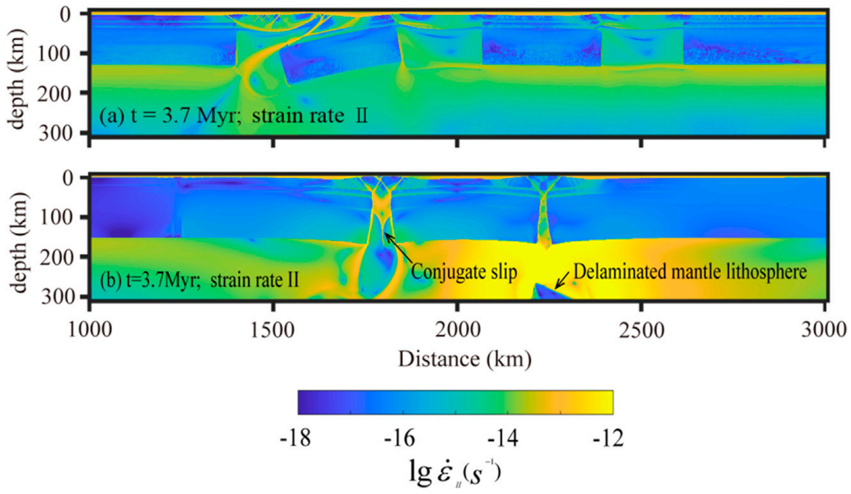

FIGURE 11
(A) Second invariants of the strain rate in the weak mantle lithosphere with dislocation creep (modified from Lei et al., 2020). **(B)** Second invariants of the strain rate in the weak mantle lithosphere with dislocation-accommodated grain boundary sliding (Table 1).

amplitude ($Z_0 = 20\ km$) is larger than the critical thickness h_{crit} (~18 *km*), corresponding to a wavelength of 500 *km* (Figure 9C).

The thickness h_{crit} only estimates the minimum amount of the layer of removal by instability. Larger thicknesses are also potentially unstable (Ra_3 >100 in Figures 9B, C). The rapid growth triggered by larger instability also depends on the convergence and weakening of strain rate localization. Thickening of the mantle lithosphere by horizontal shortening can lead to dripping to remove it in several obvious ways, which include the lithosphere weakening with increasing strain rate—as is expected for the mantle lithosphere with non-Newtonian viscosity (Molnar et al., 1998; Lei et al., 2019). Moreover, the effect of plasticity promotes dripping to remove the larger quantity of the mantle lithosphere than the model without plasticity. Figure 10 shows the amount of removed mantle in the models with an initial wavelength of 800 km and amplitude of 20 km, as well as a convergence velocity of 4.5 *cm/yr*. First, the models show that super-exponential growth occurs with a thickening of ~30 *km*, which is calculated from the depth of the initial base of the thickened layer (1350℃) to the depth at which the initial

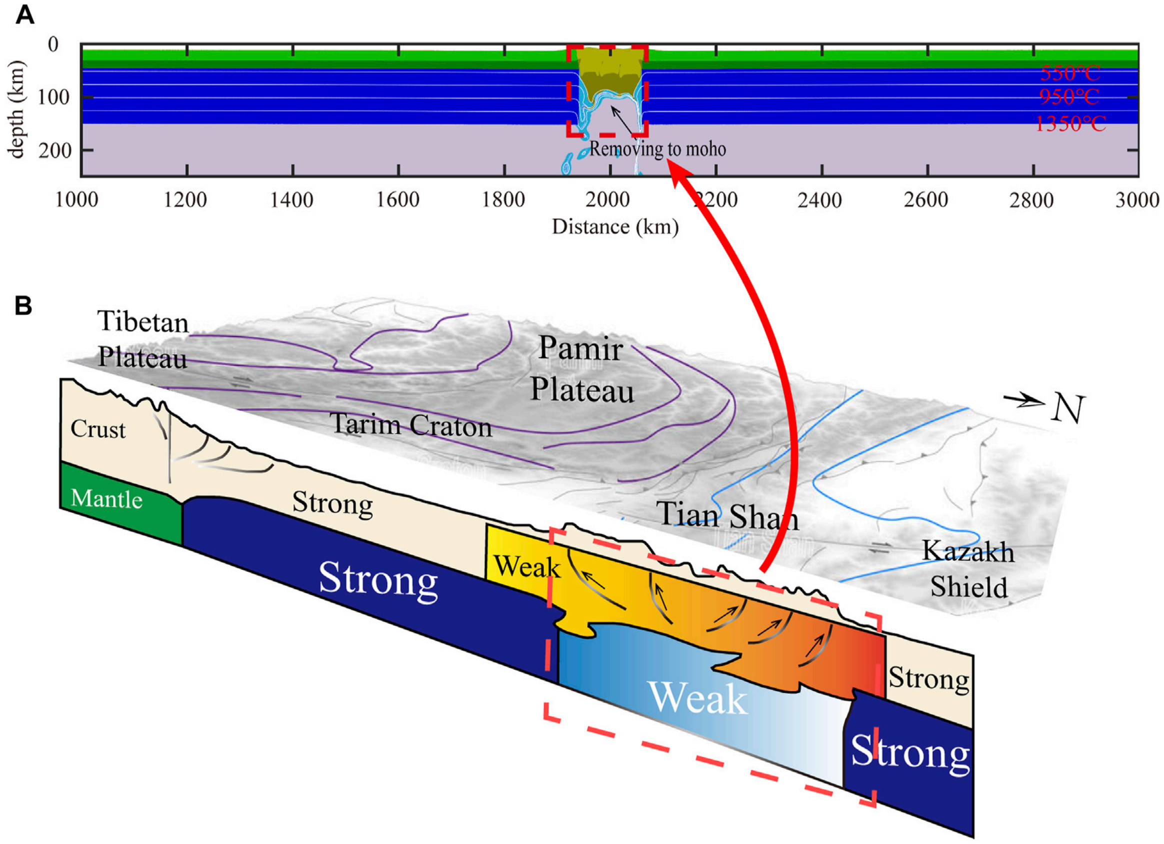

FIGURE 12
Patched/small-scale lithospheric removal and rheological heterogeneity under central Tianshan. **(A)** Model result with a weak block, based on dislocation-accommodated grain boundary sliding and plastic yielding (λ = 0.001). **(B)** Weaker lithosphere under the central Tianshan than the surroundings (Kazakh Shield and Tarim Craton), modified from Li et al., 2022.

thickening develops super-exponential growth (Figures 10A, B). Second, the model with DisGBS (Figure 10A) shows that the thickness of the removed layer ($Ra_3 > 100$) is ~30 km. In comparison, the larger amount of the removed layer (~110 km) of $Ra_3 > 100$ occurs in the model with plasticity (Figure 10B), which indicates that plasticity promotes instability to remove the larger amount of potentially unstable mantle lithosphere ($Ra_3 > 100$).

4.1.2 Heterogeneity model (type II and type III): Strain rate localization

Classical delamination and convective thinning are used to account for the removal of the mantle lithosphere with a homogeneous rheological structure, driven by dripping behaviors (Beall et al., 2017; Lei et al., 2019). Delamination would trigger large-scale peeling-off of the mantle lithosphere, which cannot explain the patched removal of the lithosphere under the Central Andes and the northeastern Tibetan Plateau (Ducea 2011; Lei et al., 2019). The feedback between the strain rate localization and reduced viscosity, based on dislocation creep, is concentrated at the base of the homogeneous lithosphere.

For orogens related to ocean-to-continent subduction, strong hydration processes can lead to local weakening of the mantle lithosphere and cause rheological heterogeneity. The feedback between the strain rate and effective viscosity can reduce the rheological strength of weak mantle lithosphere, causing patched removal of the mantle lithosphere under orogens (Figure 6). On the other hand, the model with multiple weak terranes and weak crust displays obviously patched removal of the mantle lithosphere, indicating a larger parameter range for lithospheric removal than the model of a local weakening mantle lithosphere (Figure 4 and Figure 5). However, the strain rate localization caused by dislocation creep (Ranalli 1995) cannot lead to conjugate slip, which instead promotes the small scale removal of mantle lithosphere (Lei et al., 2020). In contrast, dislocation-accommodated grain boundary sliding can promote strain rate localization in weak terranes, which causes the local weak mantle lithosphere to sink into the asthenosphere by dripping (Figure 11).

Systematic numerical modeling suggests that the rheological range of the small-scale removal of the mantle lithosphere and the associated critical width depends on the heterogeneity in the rheological structure. The mantle lithosphere removal to the Moho in small-scale regions requires low plastic yielding stress (λ = 0.001) (Figure 5). In comparison, the model results with localized weak mantle lithosphere and strong crust indicate that obvious removal

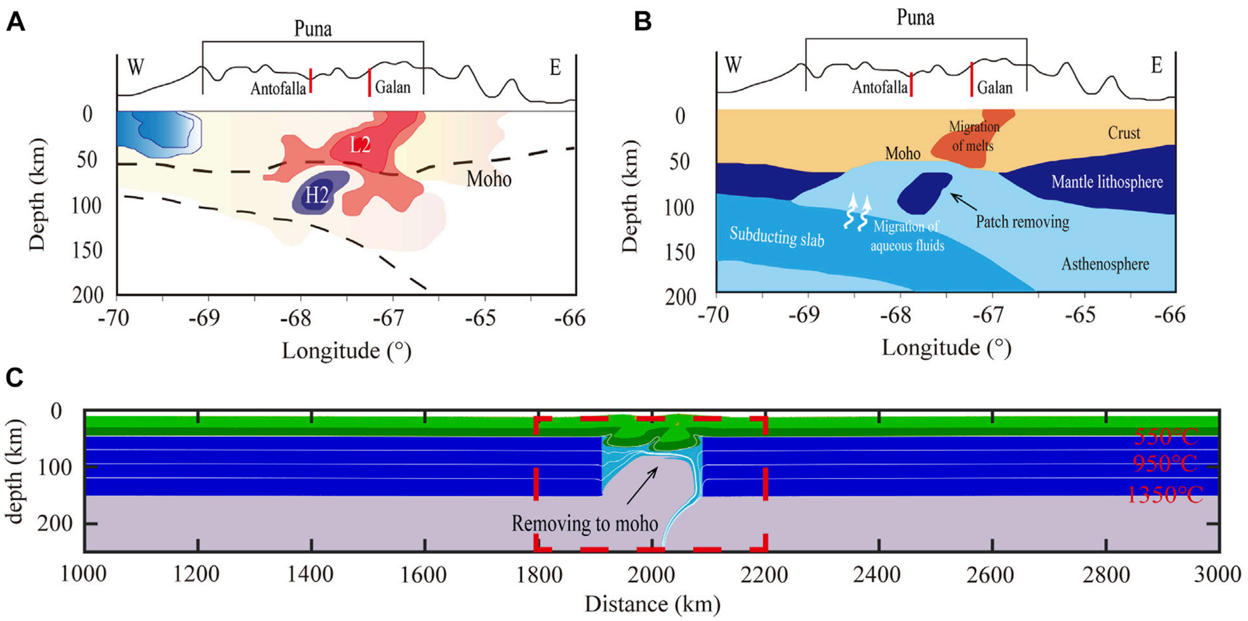

FIGURE 13
Patched/small-scale lithospheric removal under the southern Puna Plateau. **(A)** Vp perturbations under the southern Puna Plateau. The high-velocity body "H2" is interpreted as the small-scale removed lithosphere (modified from Jing et al., 2020), which causes the upwelling of fluids and melts into the crust, triggering the volcanic eruption of Cerro Galan (L2). **(B)** Interpretation cartoon under the southern Puna Plateau (modified from Jing et al., 2020). Water was released from the slab due to the dehydration reaction, which promotes the localized weak mantle lithosphere and further causes small-scale thinning under the southern Puna Plateau. **(C)** Model result with a weak mantle lithosphere, based on dislocation-accommodated grain boundary sliding and plastic yielding (λ = 0.001).

can occur with the condition of low plastic yielding stress (λ = 0.001) and larger critical width (~300 *km*) than is the case with weak block/terranes (Figure 6).

4.2 Geological applications

The history of surface uplift and magmatism is key to discerning delamination or convective thinning under orogens (Göğüş & Pysklywec 2008a; Göğüş & Pysklywec 2008b; Li et al., 2016; Huangfu et al., 2018; Lei et al., 2019). However, it is difficult to identify the patched or fragmental removal of mantle under orogens by means of the two geological indicators because patched removal causes neither symmetric pattern of convective thinning nor migration of delamination.

Adiabatic upwelling of asthenospheric mantle triggered by dripping has been regarded as the most significant expected geological response (Kay & Kay 1993; Ducea & Saleeby 1998). However, it is difficult for small drip with short wavelength to remove the whole mantle lithosphere, which further restricts adiabatic upwelling of the asthenosphere in a few million years (Beall et al., 2017). Thus, it cannot account for the patched removal of lithospheric mantle (to the Moho) and rapid magmatism in the northeastern Tibetan Plateau, Tianshan, and central Andes (Ducea 2011; Ducea et al., 2013; Deng et al., 2018). The results of numerical modeling shed light on the tectonic evolution of orogens with localized weak mantle of metasomatism or the suture between terranes.

4.2.1 Northeastern Tibetan Plateau and Tianshan

The growth of the northeastern TP has been accompanied by continuous lithosphere-scale shortening since the Neogene, during which the inherited lithospheric heterogeneities have played a key role in this shortening (Wang et al., 2008; Yin and Dang, 2008; Zhang and Wang, 2014). The joint inversion of receiver functions reveals patches of seismically fast and slow anomalies in the mantle (Deng et al., 2018). This removal of the mantle lithosphere with patches under the northeastern Tibetan Plateau is reconciled in the models with weak lithospheric blocks (Figures 7A–D).

The central Tianshan together with the adjacent Kazakh Shield to the north and Tarim Craton to the south manifest obvious rheological heterogeneity (Bing et al., 2022; Li et al., 2022; Zhang et al., 2022). Previous studies attributed large-scale intracontinental subduction to the rapid uplift of the central Tianshan since ~11 Myr, including the northward subduction of the Tarim Craton or the southward subduction of the Kazakh Shield (Gilligan et al., 2014; Zhang et al., 2022). However, the major shortening of the lithosphere is distributed throughout the Tianshan orogen (Thompson et al., 2002; Zubovich et al., 2010). Geophysical investigations reveal a weak block in the central Tianshan and a range of low-velocity anomalies in the lithosphere beneath the Tianshan at a depth of ~180 km, indicating a local high temperature and weak rheology there (Lei and Zhao, 2007; Li et al., 2009). The weak mantle lithosphere and crust beneath the Tianshan accommodates strain induced by the distant India–Asia collision, which may have promoted the small-scale removal of the mantle lithosphere in the Tianshan since the Miocene. Our numerical model with localized weak crust and the mantle lithosphere shed light on the mantle lithosphere of the weak block, which is consistent with a high temperature mantle lithosphere presently under the Tianshan and can explain the onset of rapid uplift of the Tianshan since ~11 Myr (Figure 12).

4.2.2 Central Andes

Another case with small-scale removal of the mantle lithosphere is the central Andes. In contrast to the northeastern TP, the mantle lithosphere under the central Andes does not include multiple terranes. The orogeny of the central Andes commenced in the Cenozoic (particularly in the past 30 Myrs). However, the Nazca Plate has been subducting along the western margin of the South American Plate for more than 200 Myrs (Isacks 1988; Allmendinger and Gubbels, 1996; Sobolev and Babeyko, 2005). This long history of subduction has caused a migration of aqueous fluids from the subducting Nazca plate, which may weaken the localized mantle lithosphere under the central Andes (Jing et al., 2020; Contreras-Reyes and Diaz, 2021; Wu et al., 2022). Geochemical constraints and geophysical data indicate a small-scale removal of the mantle lithosphere under the central Andes, with a pattern of melting in accordance with the process of small-scale foundering/dripping (<50 km diameter) of the thickened mantle lithosphere in the Altiplano–Puna Plateau, where mafic volcanic regions on the plateau manifest individual dripping (Drew et al., 2009; Ducea et al., 2013). This may be caused by the localized removal of the weak mantle lithosphere under the Altiplano–Puna Plateau. Geophysical observations also indicate a similar patched removal of lithospheric mantle under the southern Puna Plateau. This process is related to the activity of water released from the Nazca slab. Figure 13 shows the patched/small-scale removal of the mantle lithosphere under the southern Puna Plateau and that the low-velocity body beneath Cerro Galan (L2) reaches the greatest depth as it extends up to ~50 km deep into the crust. This indicates that the localized weak mantle lithosphere may be removed, followed by adiabatic upwelling of the asthenosphere. Meanwhile, a high velocity body (H2) is located beneath the Moho, indicating patched or small-scale removal of the lithosphere (Jing et al., 2020). These processes may be well explained by the results of numerical modeling with a localized weak lithosphere (Figure 13C), in which the local weakness of the mantle lithosphere is dominated by DisGBS and strong plastic yielding ($\lambda = 0.001$).

5 Conclusion

Using high-resolution thermomechanical modeling, we have numerically investigated the small-scale removal of the mantle lithosphere under orogens. Based on both localized weak mantle lithosphere and numerous terranes, we explored the water fugacity and plastic yielding for the model of the small-scale removal of the mantle lithosphere. The main conclusions from this study are as follows:

(1) Classical convective dripping cannot effectively thin the mantle lithosphere on a small scale because it could occur with a large initial wavelength and an amplitude of perturbation that even comprises dislocation-accommodated grain boundary sliding (DisGBS) and plasticity.

(2) Patched removal of the mantle lithosphere is induced by a localized weak block (weak crust and mantle lithosphere) with DisGBS and low plastic yield stress, which can occur in the model with the width of the weak block larger than 200 km, similar to the central Tianshan. The strain rate localization extends through the whole mantle lithosphere by conjugate strike-slip, which causes patched removal of the mantle lithosphere. In comparison, when a low rheological strength is only set to the mantle lithosphere, dripping can effectively remove the mantle lithosphere with the larger width of the weak mantle (~300 km) than the weak block. This result can better account for the patched removal of the mantle lithosphere under the Altiplano–Puna Plateau in the central Andes, which may have been weakened by previous terrane accretion or oceanic subduction.

(3) Lithospheric heterogeneities due to terrane accretion can promote patched thinning beneath weak terranes. Such segmental removal of the mantle lithosphere differs from models with a homogeneous rheological structure. These results can better explain the patched thinning of the mantle lithosphere under the northeastern Tibetan Plateau, where the lithosphere consists of multiple terranes.

Data availability statement

The original contributions presented in the study are included in the article/Supplementary Material; further inquiries can be directed to the corresponding authors.

Author contributions

TL and JL designed the study. TL wrote the manuscript. Z-HL, ML, and LL helped improve the manuscript with some suggestions. All authors contributed to the article and approved the submitted version.

Funding

This research is financially supported by NSFC projects (U1901214, 41974104, and 91855208) and the Guangdong project 2017ZT07Z066. Numerical simulations were run with the clusters of the National Supercomputer Center in Guangzhou (Tianhe-II).

Conflict of interest

The authors declare that the research was conducted in the absence of any commercial or financial relationships that could be construed as a potential conflict of interest.

Publisher's note

References

Allmendinger, R. W., and Gubbels, T. (1996). Pure and simple shear plateau uplift, Altiplano-Puna, Argentina and Bolivia. *Tectonophysics* 259, 1–13. doi:10.1016/0040-1951(96)00024-8

Bajolet, F., Galeano, J., Funiciello, F., Moroni, M., Negredo, A. M., and Faccenna, C. (2012). Continental delamination: Insights from laboratory models. *Geochem. Geophys. Geosystems* 13, 1525–2027. doi:10.1029/2011gc003896

Beall, A. P., Moresi, L., and Stern, T. (2017). Dripping or delamination? A range of mechanisms for removing the lower crust or lithosphere. *Geophys. J. Int.* 210, 671–692. doi:10.1093/gji/ggx202

Beck, S. L., and Zandt, G. (2002). The nature of orogenic crust in the central Andes. *J. Geophys. Res. Solid Earth* 107 (10), ESE7-1–ESE7-16. doi:10.1029/2000jb000124

Billen, M. I. (2008). Modeling the dynamics of subducting slabs. *Annu. Rev. Earth Planet* 36, 325–356. doi:10.1146/annurev.earth.36.031207.124129

Bing, F. Z., Xue, W. B., and Yi, X. X. (2022). Seismic anisotropy in the central Tien Shan unveils rheology-controlled deformation during intracontinental orogenesis. *Geology* 50, 812–816. doi:10.1130/g49633.1

Bird, P. (1979). Continental delamination and the Colorado plateau. *J. Geophys. Res. Solid Earth* 84 (13), 7561–7571. doi:10.1029/jb084ib13p07561

Bird, P. (1978). Initiation of intra continental subduction in the Himalaya. *J. Geophys. Res. Solid Earth* 83 (10), 4975–4987. doi:10.1029/jb083ib10p04975

Bittner, D., and Schmeling, H. (1995). Numerical modelling of melting processes and induced diapirism in the lower crust. *Geophys. J. Int.* 123, 59–70. doi:10.1111/j.1365-246x.1995.tb06661.x

Burg, J. P., and Gerya, T. V. (2005). The role of viscous heating in barrovian metamorphism of collisional orogens: Thermomechanical models and application to the lepontine dome in the central alps. *J. Metamorph. Geol.* 23, 75–95. doi:10.1111/j.1525-1314.2005.00563.x

Clauser, C., and Huenges, E. (1995). "Thermal conductivity of rocks and minerals," in *Rock Physics and phase relations*. Editor T. J. Ahrens (Washington D. C.: AGU), 105–126. Reference Shelf 3.

Conrad, C. P. (2000). Convective instability of thickening mantle lithosphere. *Geophys. J. Int.* 143, 52–70. doi:10.1046/j.1365-246x.2000.00214.x

Conrad, C. P., and Molnar, P. (1999). Convective instability of a boundary layer with temperature and strain-rate-dependent viscosity in terms of 'available buoyancy. *Geophys. J. Int.* 139, 51–68. doi:10.1046/j.1365-246x.1999.00896.x

Conrad, C. P., and Molnar, P. (1997). The growth of Rayleigh–Taylor type instabilities in the lithosphere for various rheological and density structures. *Geophys. J. Int.* 129 (1), 95–112. doi:10.1111/j.1365-246x.1997.tb00939.x

Contreras-Reyes, E., Diaz, D., Bello-Gonzalez, J. P., Slezak, K., Potin, B., Comte, D., et al. (2021). Subduction zone fluids and arc magmas conducted by lithospheric deformed regions beneath the central Andes. *Sci. Rep.* 11, 23078. doi:10.1038/s41598-021-02430-9

Currie, C. A., Huismans, R. S., and Beaumont, C. (2008). Thinning of continental backarc lithosphere by flow-induced gravitational instability. *Earth Planet. Sci. Lett.* 269 (3-4), 436–447. doi:10.1016/j.epsl.2008.02.037

Deng, Y. F., Li, J. T., Song, X. D., and Zhu, L. (2018). Joint inversion for lithospheric structures: Implications for the growth and deformation in northeastern Tibetan plateau. *Geophys. Res. Lett.* 45 (9), 3951–3958. doi:10.1029/2018gl077486

Drew, S. T., Ducea, M. N., and Schoenbohm, L. M. (2009). Mafic volcanism on the Puna Plateau, NW Argentina: Implications for lithospheric composition and evolution with an emphasis on lithospheric foundering. *Lithosphere* 1, 305–318. doi:10.1130/l54.1

Ducea, M. N. (2011). Fingerprinting orogenic delamination. *Geology* 39 (2), 191–192. doi:10.1130/focus022011.1

Ducea, M. N., Seclaman, A. C., Murray, K. E., Jianu, D., and Schoenbohm, L. (2013). Mantle-drip magmatism beneath the Altiplano-Puna plateau, central Andes. *Geology* 41 (8), 915–918. doi:10.1130/g34509.1

Ducea, M., and Saleeby, J. B. (1998). A case for delamination of the deep batholithic crust beneath the Sierra Nevada, California. *Int. Geol. Rev.* 40, 78–93. doi:10.1080/00206819809465199

Fang, X., Liu, D., Song, C., Dai, S., and Meng, Q. (2013). Oligocene slow and Miocene-quaternary rapid deformation and uplift of the Yumu Shan and north Qilian Shan: Evidence from high-resolution magnetostratigraphy and tectonosedimentology. *Geol. Soc. Lond. Spec. Publ.* 373 (1), 149–171. doi:10.1144/SP373.5

Gerya, T. V., and Meilick, F. I. (2011). Geodynamic regimes of subduction under an active margin: Effects of rheological weakening by fluids and melts. *J. Metamorph. Geol.* 29 (1), 7–31. doi:10.1111/j.1525-1314.2010.00904.x

Gerya, T. V., and Yuen, D. A. (2003). Characteristics-based marker-in-cell method with conservative finite-differences schemes for modeling geological flows with strongly variable transport properties. *Phys. Earth Planet. Interiors* 140 (4), 293–318. doi:10.1016/j.pepi.2003.09.006

Gilligan, A., Roecker, S. W., Priestley, K. F., and Nunn, C. (2014). Shear velocity model for the Kyrgyz Tien Shan from joint inversion of receiver function and surface wave data. *Geophys. J. Int.* 199, 480–498. doi:10.1093/gji/ggu225

Gogus, O. H., and Pysklywec, R. N. (2008a). Mantle lithosphere delamination driving plateau uplift and synconvergent extension in eastern Anatolia. *Geology* 36 (9), 723–726. doi:10.1130/g24982a.1

Gogus, O. H., and Pysklywec, R. N. (2008b). Near-surface diagnostics of dripping or delaminating lithosphere. *J. Geophys. Reserch* 113, B11404. doi:10.1029/2007jb005123

Gogus, O. H., Pysklywec, R. N., Şengör, A., and Gün, E. (2017). Drip tectonics and the enigmatic uplift of the central anatolian plateau. *Nat. Commun.* 8, 1538. doi:10.1038/s41467-017-01611-3

Hansen, L. N., Zimmerman, M. E., and Kohlstedt, D. L. (2011). Grain boundary sliding in San Carlos olivine: Flow law parameters and crystallographic-preferred orientation. *J. Geophys. Reserch* 116, B08201. doi:10.1029/2011jb008220

Houseman, G. A., and Molnar, P. (1997). Gravitational (Rayleigh-Taylor) instability of a layer with non-linear viscosity and convective thinning of continental lithosphere. *Geophys. J. R. Astronomical Soc.* 128, 125–150. doi:10.1111/j.1365-246x.1997.tb04075.x

Huangfu, P. P., Li, Z. H., Gerya, T., Fan, W., Zhang, K. J., Zhang, H., et al. (2018). Multi-terrane structure controls the contrasting lithospheric evolution beneath the Western and central–eastern Tibetan plateau. *Nat. Commun.* 9, 3780. doi:10.1038/s41467-018-06233-x

Huangfu, P. P., Li, Z. H., Zhang, K. J., Fan, W., Zhao, J., and Shi, Y. (2021). India-Tarim lithospheric mantle collision beneath Western Tibet controls the Cenozoic building of Tian Shan. *Geophys. Res. Lett.* 48, e2021GL094561. doi:10.1029/2021GL094561

Isacks, B. L. (1988). Uplift of the Central Andean plateau and bending of the Bolivian orocline. *J. Geophys. Res.* 93, 3211–3231. doi:10.1029/jb093ib04p03211

Jing, C., Sofia, K. K., Yuan, X., Heit, B., Wu, H., Yang, D., Schurr, B., et al. (2020). Lithospheric delamination beneath the southern Puna plateau Resolved by local earthquake tomography. *J. Geophys. Res.* 125, e2019JB019040. doi:10.1029/2019JB019040

Kay, R. W., and Kay, S. M. (1993). Delamination and delamination magmatism. *Tectonophysics* 219, 177–189. doi:10.1016/0040-1951(93)90295-u

Kirby, S. H., and Kronenberg, A. K. (1987). Rheology of the lithosphere: Selected topics. *Rev. Geophys* 25, 1219–1244. doi:10.1029/rg025i006p01219

Kirby, S. H. (1983). Rheology of the lithosphere. *Rev. Geophys. Space Phys.* 21, 1458–1487. doi:10.1029/rg021i006p01458

Lei, J., and Zhao, D. (2007). Teleseismic P-wave tomography and the upper mantle structure of the central Tien Shan orogenic belt. *Phys. Earth Planet. Interiors* 162, 165–185. doi:10.1016/j.pepi.2007.04.010

Lei, T., Li, Z. H., and Liu, M. (2020). Dynamics of small-scale removing of mantle lithosphere under orogens. *Chin. J. Geophys.* 63 (10), 3727–3739.

Lei, T., Li, Z. H., and Liu, M. (2019). Removing mantle lithosphere under orogens: Delamination versus convective thinning. *Geophys. J. Int.* 219 (2), 877–896. doi:10.1093/gji/ggz329

Levander, A., Berzada, M. J., Niu, F., Humphreys, E. D., Palomeras, I., Thurner, S. M., et al. (2014). Subduction-driven recycling of continental margin lithosphere. *Nature* 515, 253–256. doi:10.1038/nature13878

Levander, A., Schmandt, B., Miller, M., Liu, K., Karlstrom, K., Crow, R., et al. (2011). Continuing Colorado plateau uplift by delamination-style convective lithospheric downwelling. *Nature* 472 (7344), 461–465. doi:10.1038/nature10001

Li, W., Chen, Y., Yuan, X. H., Xiao, W., and Windley, B. F. (2022). Intracontinental deformation of the Tianshan Orogen in response to India-Asia collision[J]. *Nat. Commun.* 13, 3738. doi:10.1038/s41467-022-30795-6

Li, Z. H., Liu, M., and Gerya, T. V. (2016). Lithosphere delamination in continental collisional orogens: A systematic numerical study. *J. Geophys. Res. Solid Earth* 121, 5186–5211. doi:10.1002/2016jb013106

Li, Z. W., Roecker, S., Zhihai, L., Bin, W., Haitao, W., Schelochkov, G., et al. (2009). Tomographic image of the crust and upper mantle beneath the Western Tien Shan from the MANAS broadband deployment: Possible evidence for lithospheric delamination. *Tectonophysics* 477, 49–57. doi:10.1016/j.tecto.2009.05.007

Liao, J., Wang, Q., Taras, G., and Ballmer, M. D. (2017). Modeling Craton destruction by hydration-induced weakening of the upper mantle. *J. Geophys. Res. Solid Earth* 122, 7449–7466. doi:10.1002/2017jb014157

Lorinczi, P., and Houseman, G. (2009). Lithospheric gravitational instability beneath the southeast Carpathians. *Tectonophysics* 474 (1), 322–336. doi:10.1016/j.tecto.2008.05.024

Molnar, P., Houseman, G. A., and Conrad, C. P. (1998). Rayleigh—taylor instability and convective thinning of mechanically thickened lithosphere: Effects of non-linear viscosity decreasing exponentially with depth and of horizontal shortening of the layer. *Geophys. J. Int.* 133 (3), 568–584. doi:10.1046/j.1365-246x.1998.00510.x

Morency, C., and Doin, M. P. (2004). Numerical simulations of the mantle lithosphere delamination. *J. Geophys. Res. Solid Earth* 109 (3), B03410. doi:10.1029/2003jb002414

Owens, T. J., and Zandt, G. (1997). Implications of crustal property variations for models of Tibetan plateau evolution. *Nature* 387, 37–43. doi:10.1038/387037a0

Ranalli, G., and Murphy, D. C. (1987). Rheological stratification of the lithosphere. *Tectonophysics* 132 (4), 281–295. doi:10.1016/0040-1951(87)90348-9

Ranalli, G. (1995). *Rheology of the Earth, deformation and flow process in Geophysics and* geodynamics. 2nd ed. London: Chapman & Hall, 413.

Schott, B., and Schmeling, H. (1998). Delamination and detachment of a lithospheric root. *Tectonophysics* 296 (3-4), 225–247. doi:10.1016/s0040-1951(98)00154-1

Schurr, B., Rietbrock, A., Asch, G., Kind, R., and Oncken, O. (2006). Evidence for lithospheric detachment in the central Andes from local earthquake tomography. *Tectonophysics* 415 (1-4), 203–223. doi:10.1016/j.tecto.2005.12.007

Sobolev, S. V., and Babeyko, A. Y. (2005). What drives orogeny in the Andes? *Geology* 33, 617–620. doi:10.1130/g21557ar.1

Thompson, S. C., Weldon, R. J., Rubin, C. M., Abdrakhmatov, K., Molnar, P., and Berger, G. W. (2002). Late quaternary slip rates across the central Tien Shan, Kyrgyzstan, central Asia. *J. Geophys. Res. Solid Earth* 107, ETG 7-1–ETG 7-32. doi:10.1029/2001jb000596

Tomohiro, O., Takaaki, K., Higo, Y., Funakoshi, K. I., Suzuki, A., Kikegawa, T., et al. (2015). Dislocation-accommodated grain boundary sliding as the major deformation mechanism of olivine in the Earth's upper mantle. *Sci. Adv.* 1 (9), e1500360. doi:10.1126/sciadv.1500360

Turcotte, D. L., and Schubert, G. (2002). *Geodynamics*. 2nd ed. New York: Cambridge Univ, 456.

van Hunen, J., Zhong, S., Shapiro, N. M., and Ritzwoller, M. H. (2005). New evidence for dislocation creep from 3-D geodynamic modeling of the Pacific upper mantle structure. *Earth Planet, Lett.* 238, 146–155. doi:10.1016/j.epsl.2005.07.006

Vogt, K., Gerya, T., and Castro, A. (2012). Crustal growth at active continental margins: Numerical modeling. *Phys. Earth Planet. Interiors* 192-193, 1–20. doi:10.1016/j.pepi.2011.12.003

Wang, H. L., and Currie, C. A. (2015). Magmatic expressions of continental lithosphere removal. *J. Geophys. Res. Solid Earth* 120, 7239–7260. doi:10.1002/2015jb012112

Wang, Q., Wyman, D. A., Xu, J., Dong, Y., Vasconcelos, P. M., Pearson, N., et al. (2008). Eocene melting of subducting continental crust and early uplifting of central Tibet: Evidence from central-Western Qiangtang high-K calc-alkaline andesites, dacites and rhyolites. *Earth Planet. Sci. Lett.* 272 (1-2), 158–171. doi:10.1016/j.epsl.2008.04.034

Wu, Y., Liao, J., Guo, F., Wang, X. C., and Shen, Y. (2022). Styles of trench-parallel mid-ocean ridge subduction affect Cenozoic geological evolution in circum-Pacific continental margins. *Geophys. Res. Lett.* 49. doi:10.1029/2022GL098428

Xia, L. Q., Li, X. M., Ma, Z. P., Xu, X., and Xia, Z. (2011). Cenozoic volcanism and tectonic evolution of the Tibetan Plateau. *Gondwana Res.* 19 (4), 850–866. doi:10.1016/j.gr.2010.09.005

Yin, A., Dang, Y. Q., Zhang, M., Chen, X. H., and McRivette, M. W. (2008). Cenozoic tectonic evolution of the Qaidam basin and its surrounding regions (Part 3): Structural geology, sedimentation, and regional tectonic reconstruction. *Geol. Soc. Am. Bull.* 120 (7-8), 847–876. doi:10.1130/B26232.1

Zhang, B. F., Bao, X. W., and Xu, Y. X. (2022). Seismic anisotropy in the central Tien Shan unveils rheology-controlled deformation during intracontinental orogenesis. *Geology* 50, 812–816. doi:10.1130/g49633.1

Zhang, Z., Wang, Y., Houseman, G. A., Xu, T., Wu, Z., Yuan, X., et al. (2014). The Moho beneath Western Tibet: Shear zones and eclogitization in the lower crust. *Earth Planet. Sci. Lett.* 408, 370–377. doi:10.1016/j.epsl.2014.10.022

Zubovich, A. V., Wang, X. q., Scherba, Y. G., Schelochkov, G. G., Reilinger, R., Reigber, C., et al. (2010). GPS velocity field for the Tien Shan and surrounding regions. *Tectonics* 29, TC6014. doi:10.1029/2010tc002772

Frontiers in Earth Science

Investigates the processes operating within the major spheres of our planet

Advances our understanding across the earth sciences, providing a theoretical background for better use of our planet's resources and equipping us to face major environmental challenges.

Discover the latest Research Topics

See more →

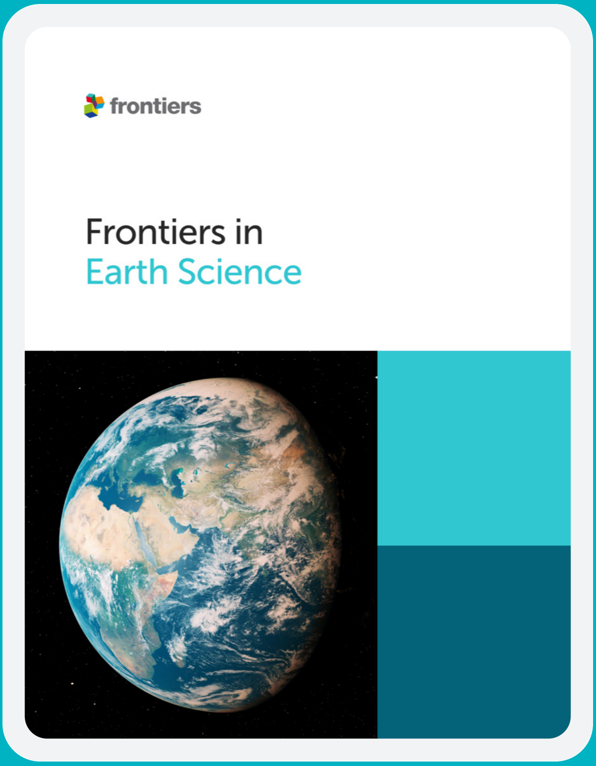
frontiers

Frontiers in
Earth Science

Frontiers

Avenue du Tribunal-Fédéral 34
1005 Lausanne, Switzerland
frontiersin.org

Contact us

+41 (0)21 510 17 00
frontiersin.org/about/contact